

University of Nottingham
UK | CHINA | MALAYSIA



Engineering and Physical Sciences Research Council

Molecular Metal Oxides for Electrochemical Energy Storage

Neelam Sahar Mughal

4275192

School of Chemistry

A thesis submitted to the University of Nottingham for the Degree of Doctor of Philosophy

March 2021

Acknowledgements

My biggest thanks go to my supervisors, Dr Darren Walsh and Dr Graham Newton. Thank you both so much for being incredibly supportive mentors, giving me a tremendous amount of guidance, pep talks and periodic reality checks. I truly appreciate the both of you, you have made me a better scientist and taught me so much. I am grateful for all the advice you have given me for both scientific and non-scientific matters. Similarly, a special thanks to Dr Jamie Cameron for his motivational talks, unwavering support, sharing great stories and being incredibly hilarious.

I would also like to thank my fellow PhD students, in particular Dr Jack Jordan, Sharad Amin and Dr Alexander Kibler. You have all been present in my PhD journey right from the very beginning and it has never once been dull. I will treasure all the laughs, stress, and embarrassing photos we've accumulated over the years. I can confidently say my life is more interesting with you guys in it, and our Japan memories are precious.

I have been lucky enough to meet so many wonderful people during my time in Nottingham. Thank you to the Walsh and Licence groups for helping me when I first started in the CNL, especially Grace Lowe, Matt Bird and Sean Goodwin for teaching me how to do electrochemistry and always having interesting discussions. Thanks to my fellow foodies, Astrid Delorme and Meike Leu for being so supportive and making my time in the CNL and Nottingham so enjoyable. I would like to thank the Mokaya group and Alison Taylor for her friendship, accommodating me in her lab and teaching me about BET and farm animals. Thank you to Lisa Hampson and Laís Dias Ferreira for their kindness and sharing in my PhD woes, you are both wonderful humans. I may have started off as your mentor, Heather Damian and Catherine Peake, but I am so grateful to the two of you for the friendship that followed. Thank you, Cath, for proofreading my work and providing a stream of constant encouragement, I will never forget it. A special thanks to the best masters students, Rory McNulty and

Jack Castle. Rory your passion for science is infectious, thank you for being interested in my work and always being happy to help. Jack C, I appreciate all the troubleshooting you've provided me and keeping me company when I was frequently trapped in the glovebox. Thank you to everyone else in the NAMI Group, I have truly cherished working in such a dynamic and collaborative atmosphere.

Thank you to Emily Smith, David Scurr and Julie Watts for their expertise in XPS and ToF-SIMS. I would also like to thank Perislava Williams and the EPSRC CDT in Sustainable Chemistry for providing me with so many valuable opportunities.

Words cannot express my gratitude for my family, closest friends and my husband Ash, for supporting me during the toughest times and indulging my PhD journey.

Publications

The following article has been published as a result of the work undertaken during the course of this PhD program:

N. S. Mughal, D. A. Walsh and G. N. Newton, Functionalization of Carbon Surfaces Tunes the Redox Stability of Polyoxometalate@Carbon Electrodes, ACS Appl. Energy Mater., 2020, **3**, 12308–12315.

.

Abstract

The work presented in this thesis is a multifaceted approach to the fabrication of low cost and high performance composite electrode materials. The incorporation of polyoxometalates (POMs) within carbonaceous materials represents an important platform for creating bespoke electrode materials. Both materials have high degrees of tuneability with respect to the structure,, electrochemical performance and surface chemistry.

Chapter 1 provides an overview into the evolution of Li-ion battery technology. This section highlights how the concerted efforts of battery chemists since the discovery of Alessandro Volta's 'voltaic pile' have led to the commercialisation of batteries in today's society. The challenges of Li-ion technology moving forward are addressed and POMs are subsequently introduced as a promising candidate for the batteries of the future.

The electrochemical behaviour of a library of plenary and modified POMs is assessed. The obtained redox profiles are examined in detail for aqueous and organic solvents, including a battery electrolyte. The tuneable and versatile nature of the studied POMs is discussed with respect to addenda metal substation, transition metal substitution and hybridisation. Interesting cation – dependent electrochemistry in the presence of metal ions (Li^+/Na^+/Mg^{2+}) is also presented.

The proceeding chapter describes the preparation of a surface modified conductive carbon black, by way of chemical oxidation. The material is characterised and compared to its unmodified analogue. POMs are incorporated on to the two different matrices. The composite materials are analysed and tested using cyclic voltammetry in a range of different solvents, including a battery electrolyte. The effect of surface oxidation of carbon on the retention of POMs during electrochemical cycling is explored.

Subsequently, the penultimate chapter corroborates the electrochemical performance of the POM/carbon composites observed thus far.

The unmodified carbon POM composite and the surface oxidised carbon POM analogue are used as the positive electrode in lithium metal test batteries. The performance is assessed with regards to reversible redox POM chemistry and achieving capacities close to that of the calculated theoretical value. For batteries, one size does not fit all, and as such, different experimental parameters and electrode preparation techniques are probed to inform future experimental design.

The final chapter explores a novel method for the preparation of POM-activated carbon based composite electrodes. This approach seeks to apply the principles of template design to prepare dimensionally controlled porous architectures with POMs encapsulated in the pores. Such a method, if successfully controlled, could assure mechanically robust redox active composite materials for energy storage applications.

Contents

1. Introduction..... 1
   1.1 Battery Fundamentals..... 1
      1.1.1 Rechargeable Batteries..... 4
      1.1.2 Lithium Metal as an Electrode Material..... 5
      1.1.3 First Era of Primary Lithium Batteries..... 6
      1.1.4 Rechargeable Lithium Batteries..... 7
      1.1.5 Intercalation Positive Electrodes..... 7
      1.1.6 Challenges of a Lithium Metal Negative Electrode..... 8
      1.1.7 Naissance of the Li-ion Battery..... 10
      1.1.8 Working Principle of the 'Rocking Chair Battery'..... 11
      1.1.9 Negative Electrode Materials for Li-ion Batteries..... 13
      1.1.10 Positive Electrode Materials for Li-ion Batteries..... 15
   1.2 Polyoxometalates (POMs)..... 22
      1.2.1 Principles of Bonding and Formation..... 22
      1.2.2 Synthesis..... 24
      1.2.3 Structure..... 25
      1.2.4 Electronic Properties of POMs..... 32
      1.2.5 Merits of POMs as Energy Materials..... 34
   1.3 References..... 37
2. Solution Phase Voltammetry of Polyoxometalates in Non-Aqueous & Aqueous Solvents..... 44
   2.1 Introduction..... 44
   2.2 Approach..... 45
   2.3 Aims..... 50
   2.4 Results & Discussion..... 51
      2.4.1 Voltammetry in Organic Solvents – DMF..... 51
      2.4.2 Modified Polyoxometalate..... 63
      2.4.3 Voltammetry in Organic Battery Solvent..... 70
      2.4.4 Voltammetry in Aqueous Solvents – 1M H_2SO_4..... 79
      2.4.5 Cation – dependent Electrochemistry..... 86
   2.5 Conclusion & Future Work..... 119
   2.6 Experimental..... 121
   2.7 References..... 126
3. Preparation & Characterisation of Polyoxometalates Supported on Vulcan Carbon..... 130
   3.1 Introduction..... 130
   3.2 Aims..... 134
   3.3 Results & Discussion..... 134
      3.3.1 Preparation..... 134

3.3.2 Structural Characterisation..... 135
3.3.3 Surface Characterisation.....137
3.3.4 Textural Characterisation..... 141
3.3.5 Electrochemical Characterisation in 1M Sulphuric Acid..... 143
3.3.6 Electrochemical Characterisation in Perchlorate-based Electrolytes.....154
3.3.7 Electrochemical Characterisation in Battery Solvent..... 182
3.3.8 Oxidation Using Acidic Polyoxometalates..... 186
3.4 Conclusion..... 207
3.5 Experimental.....209
3.6 References..... 211
4. Evaluation of POM/Vulcan Electrodes in Lithium Batteries..... 214
4.1 Introduction..... 214
4.2 Approach..... 219
4.3 Aims..... 224
4.4 Results & Discussion..... 224
4.4.1 Preliminary Characterisation.....224
4.4.2 Prediction of Galvanostatic Behaviour of POM/Vulcan Electrodes.....229
4.4.3 Preparation & Cell Assembly.....233
4.4.4 Battery Components..... 234
4.4.5 Performance of $\{K_6W_{18}\}$@[O]V versus $\{K_6W_{18}\}$@V as a Positive Electrode.... 235
4.4.6 Investigating the Effect of Calendaring on Electrode Performance $\{K_6W_{18}\}$@[O]V versus $\{K_6W_{18}\}$@V..... 247
4.4.7 Effect of Increasing the Potential Window..... 259
4.4.8 Effect of Narrowing the Potential Window.....267
4.4.9 Effect of Removing Super P.....271
4.5 Conclusions & Future Work.....276
4.6 Experimental.....279
4.7 References..... 281
5. Dimensionally Controlled Polyoxometalate Impregnated Activated Carbons..... 284
5.1 Introduction..... 285
5.2 Approach..... 288
5.3 Aims.....290
5.4 Results & Discussion..... 291
5.4.1 Preliminary Characterisation.....291
5.4.2 In-situ Carbonisations – Set 1.....303
5.4.3 In-situ Carbonisations – Set 2.....316
5.5 Conclusions & Future Work.....331
5.6 Experimental.....333
5.7 References..... 337
6. Conclusions & Future Prospects.....340

1. Introduction

Our planet is facing formidable energy challenges due to several factors such as the rising levels of anthropogenic CO_2, increasing global population and an unrelenting dependency on fossil fuels.[1] The empirical evidence from recent trends and the rise of organisations such as the Faraday Institution and UK Battery Industrialisation Centre, suggest that renewable energy sources will be an important paving stone in the pathway to a sustainable, decarbonised and secure electrical grid. Favouring the use of decarbonised electricity inevitably leads to dramatic changes in supply and demand, coupled with the variability of renewable sources and seasonal profile of electricity demand for heat. Thus, the intermittent nature of renewables inextricably drives towards harnessing, storing and delivering this abundance of energy in efficient and affordable ways.

Electrochemical energy storage is a strong option poised to meet these challenges. This type of technology refers to the process of converting electrical energy into a storable form and then reconverted back into electrical energy when it is needed.[2] Established forms of electrochemical energy storage include Li-ion batteries[3], supercapacitors[4] and fuel cells[5]. It is difficult to overstate the importance of batteries in our future. Batteries play a crucial role in decreasing greenhouse gas emissions and providing clean, low-carbon energy to our homes, businesses and vehicles. Batteries are also important in powering the digital economy as well an ever-growing number of portable electronics. Therefore, it is of profound interest to scientists to research and develop energy storage technologies to combat the vicissitudes of climate change.

1.1 Battery Fundamentals

The evolution of any given device is of course influenced by its history, and such is the case with batteries. A battery consists of a series of one or more electrochemical cells. An electrochemical cell is a device that is capable of generating electrical energy from the energy liberated during a chemical reaction. It was in the end of the 18th century that the discovery of this type of

cell was made. Alessandro Volta demonstrated the production of electricity through his invention of the 'voltaic pile'. This was composed of an alternating sequence of two different metals; zinc and silver disks that were separated by a cloth soaked in brine solution. He found that the amount of current produced varied when different metals were used, and it was in this way that he defined the electrochemical series. It can be argued that Volta's discovery is romantically related to Luigi Galvani's work at the time on 'animal electricity' but it is without a doubt that it was Volta's invention of the electric pile that paved the way for electrochemistry as a new experimental discipline.[6]

Battery cells store chemical energy in their electroactive electrode materials. This chemical energy can be converted into electrical energy on demand, typically by means of an electrochemical oxidation – reduction reaction. Batteries are categorised into two types: primary and secondary. Both batteries have three main components (Figure 1):

1. The negative electrode – also known as the anode where oxidation takes place and electrons are liberated to the external circuit;

2. The positive electrode – cathode – electrons are accepted from the external circuit and the reduction reaction takes place;

3. The electrolyte – which separates both negative and positive terminals and is the medium for charge transfer such as shuttling ions between the two electrodes in the cell. The electrolyte is typically a liquid solvent with dissolved salts, acids, or alkalis to impart ionic conductivity. It must be a non – conductor of electrons to avoid self-discharge of the cell.

Primary, or non-rechargeable batteries, are supplied fully charged and once they have been discharged (released their energy), they are discarded and cannot be reused. In secondary, or rechargeable batteries, the electrochemical reaction is reversible and thus can be recharged by applying a current from an external source in the opposite direction of discharge. These batteries can discharge into a load and be re-charged many times.

The terms anode and cathode refer to the function of the electrode and not its structure. In primary batteries, the negative and positive terminals are identified as the anode and cathode respectively. Oxidation occurs at the anode whilst reduction takes place at the cathode. The electrodes in a rechargeable battery are appropriately referred to as negative and positive, as the function of the electrodes is dependent on which way the current is flowing.

A conventional current describes the direction in which positive electronic charges move. Electrons have a negative charge, so the flow of electrons is opposite to current flow. During discharge, the anode is oxidised, releasing electrons. These flow in an external circuit towards the cathode which is subsequently reduced. The cathode is the positive terminal since negative electrons flowing in constitutes a positive current going out; therefore, the anode is the negative terminal. For a secondary battery, the opposite holds true during charge (taking electrical energy from a current provided by an external source) where the cathode is negative, and the anode is positive.

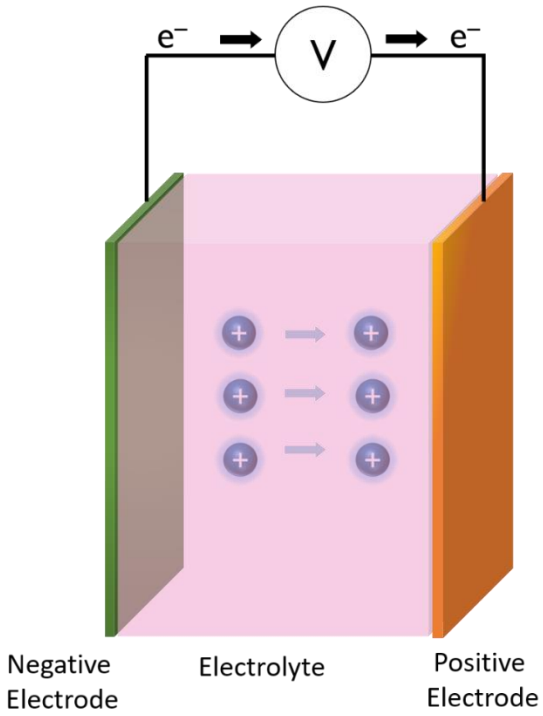


Figure 1 - The three main components of a battery: negative electrode and positive electrode separated by a conductive electrolyte. Electron flow depicts discharge process.

1.1.1 Rechargeable Batteries

Further down the timeline of battery evolution, French scientist Gaston Planté invented the first commercialised rechargeable battery in 1859; the lead-acid battery. The cell comprises of a lead negative electrode and a lead oxide (PbO_2) positive electrode, with a sulphuric acid electrolyte.[7] During discharge, lead (IV) oxide is reduced to lead (II) sulphate ($PbSO_4$) and lead is oxidised to also yield $PbSO_4$. It is one of the most used batteries today in photovoltaics and the automobile industry by virtue of its low cost and good performance.[8]

A direct competitor to the lead-acid battery emerged in 1899. The nickel-cadmium battery invented by Swedish engineer, Waldemar Jungner. Though the initial cost of materials was much more expensive than the lead-acid battery, Ni-Cd batteries offered higher specific energy/energy density (energy stored in watt-hours per unit of mass or volume respectively), long cycle life, tolerance of high charge and discharge rates, high resistance to mechanical abuse and ability to operate at low tempetaures.[9,10] However, Ni-Cd batteries possess a unique feature that makes them unsuitable: a pronounced memory effect. This means highly repetitive shallow charge–discharge cycling where the battery is not fully discharged before being recharged, causes the battery to lose its capacity, thus requiring reconditioning. The primary trade-off however is the use of the heavy metal cadmium which poses a major environmental threat and is highly toxic to human life.

Although modified by innovations in construction design and in materials packaging, lead-acid and nickel-cadmium systems form the foundation of today's popular commercial batteries used in automobile applications such as starting, lighting and ignition, portable tools and back-up power supplies.[11,12]

For the technology at the time, these batteries were sufficient and thus advancement in the field came to a relative standstill for more than a century. It was later in the 1960s that technological innovation surged and called for portable energy. Innovations such as the likes of implantable medical devices required high-energy dense and long-lasting energy sources. The military

required high-energy and high-power sources and the eruption of the consumer electronics market demanded revolutionised batteries. It was abundantly clear that these conventional batteries would be inadequate in the face of rapid innovative progress. Fundamentally these batteries were limited by their respective electrode combinations that offered limited values of specific capacity (maximum amount of charge that can be withdrawn from a battery under specified conditions of discharge, in ampere-hours per gram, Ah g^{-1}). These batteries were also too heavy and too big to function efficiently for the evolving technology.

Cardiac pacemakers are an illustrative example. one of the earliest examples of such a device used a primary zinc-mercury battery. The resultant device was heavy and bulky and ran out of charge after two years, requiring patients to undergo another operation to replace them.[13] Clearly moving forward, the development of new concept batteries boasting higher energy densities and longer operational life are required.

1.1.2 Lithium Metal as an Electrode Material

A breakthrough in the hunt for batteries with higher specific energy and energy density was made when lithium metal was explored as an electrode material. Metals possess properties that make them well suited as electrode materials for batteries. They are readily oxidised from their metallic state to produce ions and electrons as shown in the following half reaction:

$$\mathrm{M} \rightarrow \mathrm{M}^{n+} + ne^{-}$$

The metal can conduct the liberated electrons and therefore becomes the negative electrode for a given cell. Metals that have been commonly used as negative electrodes in commercial batteries are listed in Table 1.[14] The 'redox couple' denotes the ion formed as a product of the oxidation half – reaction. The 'standard reduction potential' is a measure of the tendency of that ion to be reduced back to its metallic state. The 'electrochemical capacity' is a property defined as the amount of electric charge (i.e., capacity) that can be produced per gram of the metal in the specified oxidation half – reaction.

Table 1 - Commonly used metals for metal negative electrodes and their properties.

Metal	Atomic Weight	Density/ g cm $^{-3}$	Redox Couple	Standard Reduction Potential/V	Electrochemical Capacity/mAh g $^{-1}$
Lithium	6.94	0.53	Li/Li^+	–3.04	3.86
Sodium	22.99	0.97	Na/Na^+	–2.71	1.17
Magnesium	24.31	1.74	Mg/Mg^{2+}	–2.70	2.21
Aluminium	26.98	2.70	Al/Al^{3+}	–1.66	2.98
Calcium	40.08	1.54	Ca/Ca^{2+}	–2.87	1.34
Iron	55.85	7.86	Fe/Fe^{2+}	–0.45	0.96
Zinc	65.39	7.14	Zn/Zn^{2+}	–0.76	0.82
Cadmium	112.41	5.64	Cd/Cd^{2+}	–0.40	0.48
Lead	207.2	11.30	Pb/Pb^{2+}	–0.13	0.26

Lithium has the most negative reduction potential. The implication of this is that the Li^+ ion has the lowest tendency to be reduced back to Li, but more importantly this reduction potential signifies that lithium metal shows the highest tendency to be oxidised to Li^+. Additionally, lithium has the highest electrochemical capacity, which is thanks to its exceptionally low atomic weight. This translates to a greater quantity of charge per unit weight through the use of a lithium metal negative electrode.[15]

One of the earliest batteries incorporating lithium was the lithium-iodine (Li-I) battery, developed in a bid to replace the zinc-mercury battery used in pacemakers.[13] The Li-I battery greatly improved the efficiency of pacemakers, reduced their weight and size as well as extending their operational life.[16]

1.1.3 First Era of Primary Lithium Batteries

The development of high-performance battery systems commenced in the 1960s and focussed on primary batteries employing metallic lithium as the

anode. A broad range of positive electrode materials were available on the market such as lithium-sulphur dioxide[17] (Li-SO_2) in 1969, lithium–carbon monofluoride[18] (Li-CF_x) commercialised by Matsushita in 1973 and lithium–manganese oxide[19] (Li-MnO_2) batteries commercialised by Sanyo in 1975. Due to the reactivity of lithium towards water, various non-aqueous solvents were explored as the electrolyte. These ranged from organic solvents such as propylene carbonate and to inorganic ones such as thionyl chloride and lithium perchlorate.[20] These cells were used for LED fishing floats, cameras, digital watches and memory backup applications.

1.1.4 Rechargeable Lithium Batteries

The success of these commercialised primary batteries intensified research efforts to implement lithium chemistry into rechargeable technology. At the time, there were no apparent difficulties at the negative electrode side since it was assumed that the lithium ions liberated during discharge would plate back onto the lithium metal upon charge. Hence initial research sought to identify new positive electrode materials that could partake in reversible lithium uptake and endure long cyclability.

1.1.5 Intercalation Positive Electrodes

The development of “intercalation” or “insertion” electrodes in 1978 was revolutionary.[21] This type of positive electrode is constructed from a host lattice, a crystalline or partially crystalline solid, in which a guest species i.e. lithium can be intercalated (inserted) interstitially during discharge and subsequently de-intercalated (extracted) during recharge with little or no structural alteration to the host. Electric current is generated by the migration of Li-ions from the lithium metal negative electrode to the intercalative positive electrode through the electrolyte during discharge. Reversing this process results in the removal of Li-ions from the positive electrode and returning to the negative electrode to produce the charged state.

Metal chalcogenides such as titanium disulphide (TiS_2) possess a layered structure and can exchange Li-ions across it with minimal lattice expansion. In

1973 and 1974, Whittingham applied TiS_2 as the cathode for batteries and subsequently demonstrated a 2.5 V cell in 1976.[22] The implementation of this type of positive electrode material led to the first commercial rechargeable lithium batteries appearing in the late 1970s to early 1980s. Exxon (now Exxon Mobil) in the USA used TiS_2 and Moli Energy (now E-One Moli Energy) in Canada used molybdenum disulphide (MoS_2) as positive electrode materials, both using liquid organic electrolytes.[23,24]

For a long time, TiS_2 was the most promising intercalation material for positive electrodes in rechargeable lithium batteries. However, when exposed to air, TiS_2 reacts to form malodourous hydrogen sulphide compounds. As such, commercial interest in TiS_2 waned because it had to be synthesised under completely sealed conditions. This was time-consuming and extremely expensive. TiS_2 was eventually superseded by other layered materials but, nonetheless TiS_2 is an important conceptual milestone.

In the hunt for new materials capable of intercalating lithium-ions at higher potentials, Goodenough explored the oxide equivalents of metal chalcogenides (MX_2, where X = O). In 1980, Goodenough and Mizushima demonstrated the electrochemical removal of lithium from $LiCoO_2$ and constructed a 4 V rechargeable lithium cell with a lithium metal anode.[25]

1.1.6 Challenges of a Lithium Metal Negative Electrode

However, the early rechargeable lithium cells were plagued with operational faults and safety problems (Figure 2). The crux of the matter was the high reactivity of lithium metal with the electrolyte, forming a passivation layer on the surface of the anode. This layer is known as the solid electrolyte interface (SEI) and is permeable to Li-ions which allows the ongoing of the discharge process. The SEI consists of polymeric and inorganic materials which prevent ongoing, irreversible reactions between the lithium and electrolyte. A robust SEI layer is essential for the reversible transport of Li-ions. However, a poorly formed SEI with the non-uniform deposition of lithium-ions during charge incites the formation of needle-like lithium crystals, known as dendrites.[26] This

process consumes the electrolyte by continuous reformation of the SEI with each cycle and also lowers the energy density of the cell. Additionally, this process also results in high safety risks. These dendrites are electrochemically inactive however they are chemically reactive, such that the dendritic growth can pierce the separator, resulting in an internal short-circuit or thermal runaway. [27]

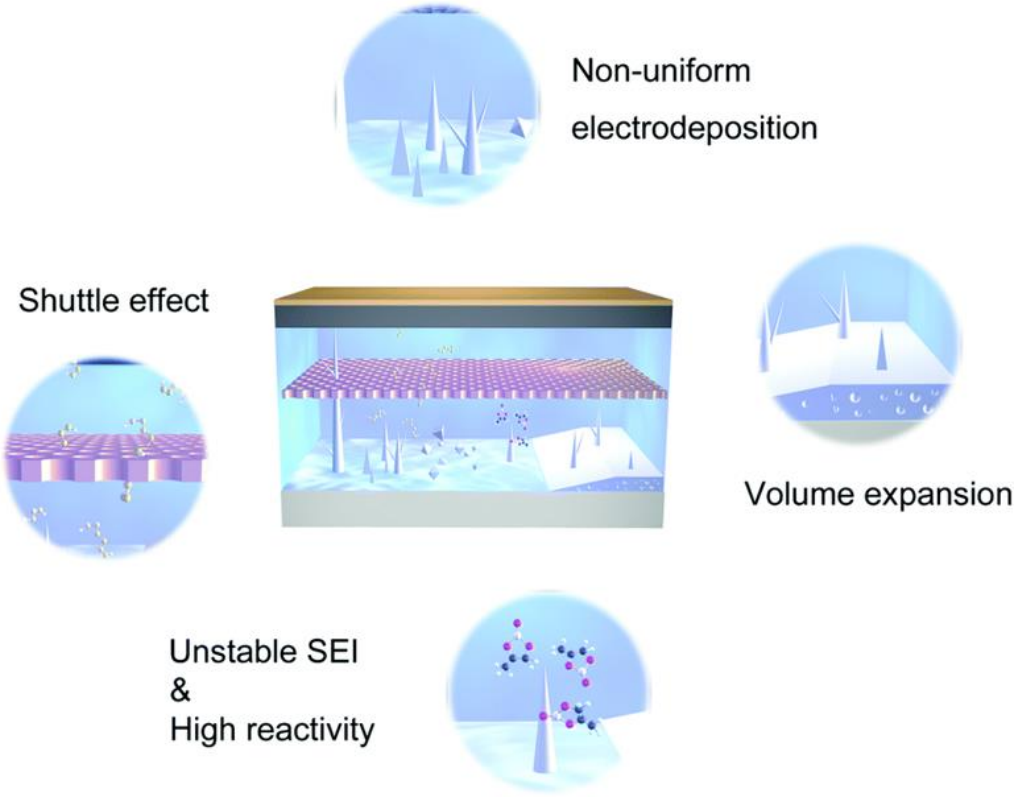


Figure 2 - Challenges in the design of lithium metal batteries include non- uniform electrodeposition, volume expansion, high reactivity of lithium metal/unstable SEI, and shuttling of active cathode materials. Reproduced from[27] with permission from the Royal Society of Chemistry.

The promise of ultrahigh capacity from using lithium metal was the impetus of an overwhelming amount of research on electrolyte formulations in a bid to suppress, even eliminate, the dendritic growth. Perchlorate electrolytes were discontinued for safety reasons due to the very strong oxidising nature of the $LiClO_4$ salt and very reactive fine powder deposits during recharge. Amongst the various electrolyte systems investigated, one approach was to try and promote homogeneous lithium deposition. The feasibility of this approach was

established by Armand in 1978 through the use of a polymer electrolyte; a complex between a lithium salt and a coordinating polymer (e.g. lithium triflate and poly (ethylene oxide) PEO).[28,29] In spite of this and other research in the area, lithium-polymer rechargeable batteries never reached large scale commercialisation because the operational risks associated with a lithium metal electrode were never completely overcome.

Another notable example of a novel electrolyte was reported by an Israeli company. They showed that metallic lithium electrode was highly stable in a solution of $LiAsF_6$ in 1,3 -dioxolane.[30] The lithium was stable up to 120 °C due to excellent surface passivation and over 300 discharge cycles were reported.[31] It was also found that the redox reaction between the $LiAsF_6$ salt and the dioxolane solvent shut down the cell chemistry at temperatures exceeding 125 °C thus preventing thermal runaway.[32] However the problems associated with a lithium anode were not completely eliminated and dendrite formation, particularly at high charge rates still resulted in capacity fade.[33] Metallic lithium was the natural choice as a negative electrode material during the 1970s and 1980s, with researchers seeking to capitalise on its unrivalled high specific energy, despite its dendrite issues. However, fire incidents due to rechargeable lithium batteries in electronic devices, coupled with subsequent manufacturer recalls, dampened the general enthusiasm for metallic lithium anodes and they largely fell out of favour.

1.1.7 Naissance of the Lithium-ion Battery

The term 'Lithium-ion' identifies batteries that do not contain metallic lithium but rather the principal ion that is being shuttled. Lithium-ion batteries are the result of a 'host-guest' concept that embraced the combination of two intercalative electrodes, one capable of accepting Li-ions (lithium sink) and the other capable of releasing Li-ions (lithium source). In this dual-intercalation system, Li-ions are shuttled between the two electrodes during the discharge – charge cycle. This type of system is also known by its moniker "rocking – chair battery". The "rocking-chair" concept was confirmed experimentally by employing lithiated oxides ($Li_6Fe_2O_3$, $LiWO_2$) as negative electrodes and other

oxides (WO_3, TiS_2, V_2O_5) as positive eletrodes.[34,35] Though these offered enhanced safety and cycle life vs lithium metal batteries, they were accompanied by a penalty in energy density, and thus they never reached commercialisation.[36]

On the basis of this seminal concept, the most pertinent question for Li-ion batteries moving forward was how to improve the energy density in order to realise commercialisation. A breakthrough was made when it was discovered that carbonaceous materials such as graphite or amorphous carbon could be applied as intercalation host anodes. This discovery was based on earlier studies of lithium intercalation into graphite chemically[37] and electrochemically.[38] Japanese researchers at Asahi Kasei Corporation also discovered that petroleum coke could reversibly intercalate Li-ions at a low potential of ~0.5 V vs Li/Li^+, without encountering structural destruction.[39] Notably, these carbonaceous materials are of low cost and displayed only minor volume changes upon lithiation. Additionally, intercalation occurs at a potential close to the reduction potential of metallic lithium, making high energy density Li-ion batteries achievable.

Indeed, in 1991 Sony commercialised this lithium-ion technology through the introduction of a high energy dense (80 Wh kg^{-1}; 200 Wh L^{-1}) and high voltage (≈ 3.7 V) cell based on petroleum coke as the negative electrode, $LiCoO_2$ as the positive electrode and a non-aqueous electrolyte.[40,41] This was revolutionary for the portable electronics industry.

1.1.8 Working Principle of the 'Rocking Chair Battery'

As alluded to previously, intercalation involves reversibly incorporating and removing lithium ions within host structures without significant structural disruption to the host. Figure 3 illustrates the intercalation process during discharge. During discharge, the Li^+ ions de-intercalate from the negative electrode, graphite, and migrate towards the positive electrode, $LiCoO_2$, and intercalate into the lattice. The electrons travel in an external circuit simultaneously, in the same direction as the Li^+ ions, whereas current moves in

the opposite direction to the Li^+ ions. During charge, a higher voltage than that produced by the battery is applied, forcing the current to pass in the reverse direction. Thus, the Li^+ ions are de-intercalated from the ordered lattice of $LiCoO_2$ and move to become intercalated between the graphene sheets.

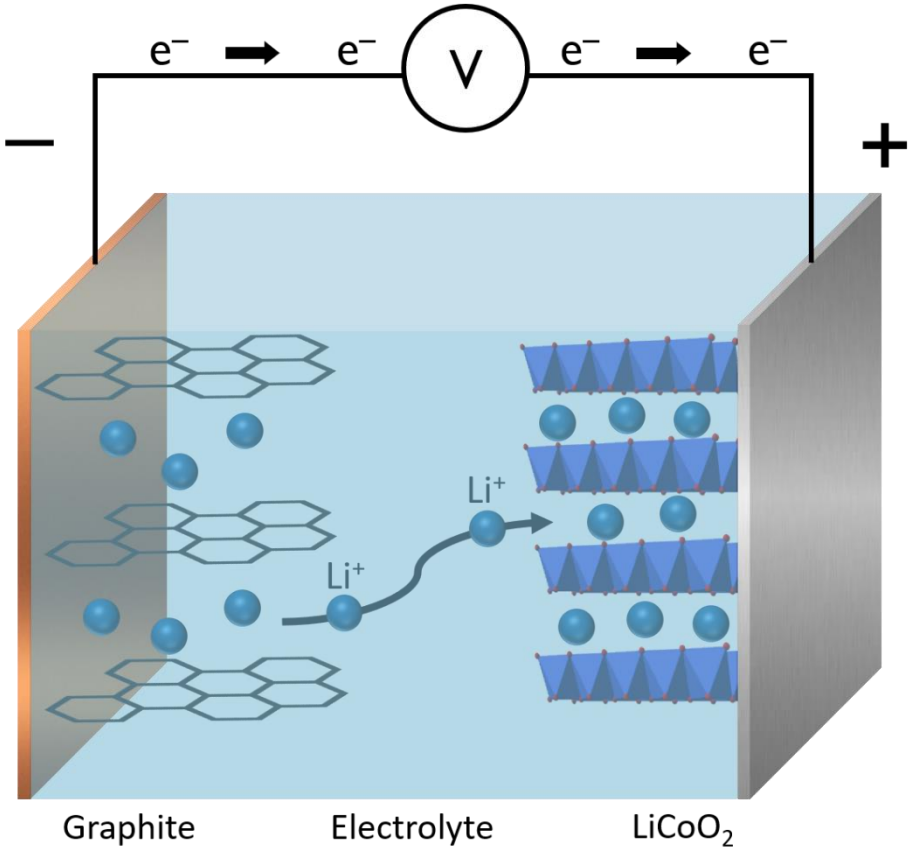


Figure 3 - A schematic illustration of the working principles of a graphite/$LiCoO_2$ lithium-ion cell.

The half – reactions that take place at each electrode during discharge (left to right) and charge (right to left) are as follows:

Negative electrode:

$$Li_n C_6 \leftrightarrow nLi^+ + 6C + ne^-$$

Positive electrode:

$$CoO_2 + nLi^+ + ne^- \leftrightarrow LiCoO_2$$

Overall discharge reaction:

$$Li_n C_6 + CoO_2 \leftrightarrow 6C + Li_n CoO_2$$

1.1.9 Negative Electrode Materials for Li – ion Batteries

Graphite

In order to circumvent safety issues associated with lithium metal electrodes, industry focussed on creating secondary negative electrodes, such as carbonaceous intercalation materials (Figure 4). This is because carbon – based materials are abundant, of low cost and electrically conducting. Graphite electrodes enabled the Li-ion battery to become commercially viable more than 20 years ago and remains the dominant negative electrode of choice today. Electrochemical activity in graphite arises from the intercalation of Li^+ ions between the graphene planes, which offer good 2D mechanical stability and electrical conductivity. One lithium atom can be intercalated per six carbon atoms (LiC_6), yielding a specific capacity of 372 mAh g^{-1}. It also has the combined properties high Li^+ ion diffusivity and low delithiation potential *vs.* Li (0.1 – 0.23 V), meaning graphite exhibits good lithium intercalation and de-intercalation reversibility.[42,43] Its structure can also swell modestly (10%) to accommodate the Li^+ ions with building charge whilst retaining a stable morphology. Lithium dendrites do not grow on graphite, which enhances safety and means that the electrode can be cycled reliably.[44]

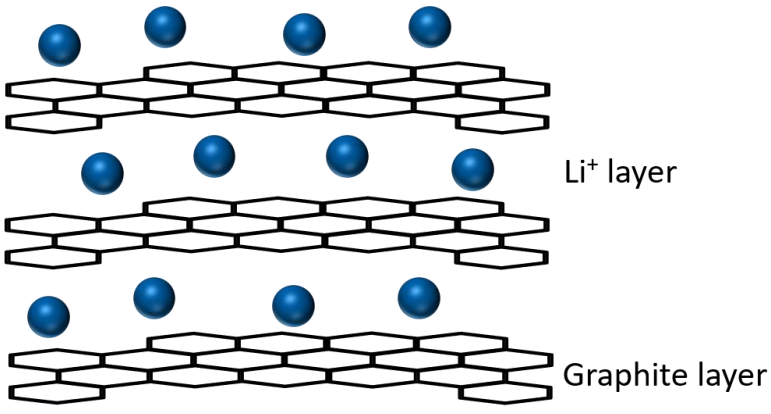


Figure 4 - Structure of lithiated graphite.

Lithium Titanate Oxide – LTO

A second successfully commercialised negative electrode is that of spinel lithium titanium oxide ($Li_4Ti_5O_{12}$, LTO). LTO chemistry is often employed for fast charging applications because LTO can accommodate Li^+ rapidly and reversibly.

Unlike other insertion electrodes, LTO undergoes only an infinitesimal volume change (0.2 %) and its structure remains almost unaltered during lithium intercalation/deintercalation.[42] It is classed as a zero – strain material that cycles extremely well.[43] The lithiation of LTO occurs by insertion of Li^+ into the spinel phase $Li_4Ti_5O_{12}$ to yield the rock salt phase, $Li_7Ti_5O_{12}$ (Figure 5),however both of these phases have poor lithium conductivity. This is paradoxical considering it is a fast – charging electrode. Zhang et al. tracked the real time migration of Li^+ ions in LTO nanoparticles and found that a metastable pathway exists between the two phases which overcomes the kinetic limitations of Li^+ diffusion.[45] The metastable intermediate configurations of LTO have local "polyhedral" distortions which lower the energy barriers, provide a pathway through which lithium ions can travel quickly.[43] Its high operating potential of < 0.8 V (vs. Li/Li^+) means an SEI is seldom formed as electrolyte reduction does not occur whereas SEI formation in graphitic negative electrodes can slow Li^+ insertion and induce lithium losses. LTO is extremely safe because this high potential also prevents lithium dendrite formation. However, LTO is inferior to graphite in terms of its lower specific capacity of 175 mAh g^{-1} and low electronic conductivity in bulk materials ~10^{-13} S cm^{-1}.[46]

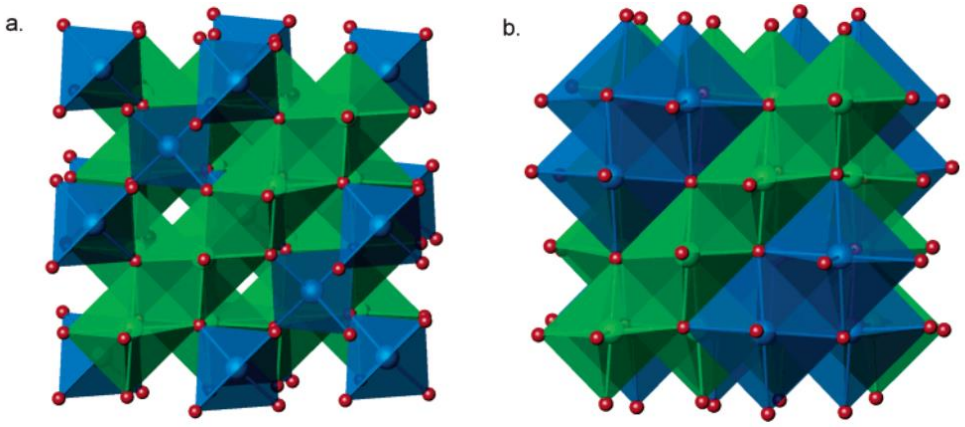


Figure 5 – Structures of $Li_4Ti_5O_{12}$ and $Li_7Ti_5O_{12}$ showing no volume change after charge and discharge. (a) $Li_4Ti_5O_{12}$ spinel structure. Blue tetrahedra represent lithium, and green octahedra represent disordered lithium and titanium. (b) $Li_7Ti_5O_{12}$, rock salt structure. Blue octahedra represent lithium, and green octahedra represent disordered lithium and titanium. Reprinted from[47]. Copyright 2006 American Chemical Society.

1.1.10 Positive Electrode Materials for Li – ion Batteries

The term Lithium-ion does not connote a single technology, but rather a family of technologies. Although they all use lithium as the shuttling ion, different versions of the technology combine the lithium with a variety of other materials to confer different properties. Each type of lithium-ion battery is typically abbreviated to reflect its active cathode materials. For example, Lithium Cobalt Oxide, one of the most successful and common type (used in portable batteries), is called 'LCO', meanwhile Lithium Nickel Manganese Cobalt Oxide is named 'NMC', which is increasingly being used in mobility applications.

$LiCoO_2$ – LCO

The state-of-the-art positive electrode material is represented by Lithium Cobalt Oxide, $LiCoO_2$ (Figure 6). This layered transition metal oxide makes for a very attractive positive electrode material due to its relatively high theoretical specific capacity of 274 mAh g^{-1}, low self-discharge, high discharge voltage, and good cycling performance. [42,48] Self-discharge is an inherent characteristic of all batteries and refers to the loss of useful capacity due to internal chemical reactions whilst the battery is not in use and "on the shelf". A higher discharge voltage results in a reduction of the number of cells needed for a battery module or pack in a battery[49]; a single lithium-ion cell incorporating $LiCoO_2$ can replace three Ni-Cd cells. Cycle performance relates to the number of times a battery can undergo complete charging and discharging processes until permanent capacity loss.[50]

However, there are limitations. Though its theoretical capacity is as high as 274 mAh g^{-1}, when the LCO electrode is cycled between 3 and 4.2 V (measured *vs.* Li/Li^+), its actual reversible capacity is limited to 140 mAh g^{-1} which corresponds to only 50 % extraction of lithium ions during charge.[51] Deep cycling, which means charging above 4.2 V to achieve greater than 50 % lithium ion extraction, induces lattice distortion from hexagonal to monoclinic symmetry.[52] This provokes structural collapse of the $LiCoO_2$ lattice as there is significant electrostatic repulsion between the transition metal polyhedral and in turn, deteriorates cycling performance.[53] Furthermore, LCO electrodes are

expensive because cobalt is less abundant and so has a high cost associated with procuring it.[54] Cobalt also has a risky supply chain as its deposits are located in the Democratic Republic of Congo, sanctioned for human rights abuses.[55] The low thermal stability is also a concern in the large-scale application of Li-ion batteries such as the indefinite grounding of all Boeing 787 aircrafts in 2013.[56] This low thermal stability refers to the exothermic release of oxygen when a transition metal intercalation electrode is heated above a certain temperature resulting in thermal runaway. While this is a general issue for transition metal oxide intercalation electrodes, $LiCoO_2$ has the lowest thermal stability amongst commercialised electrodes of this type (~ 200 °C).[57]

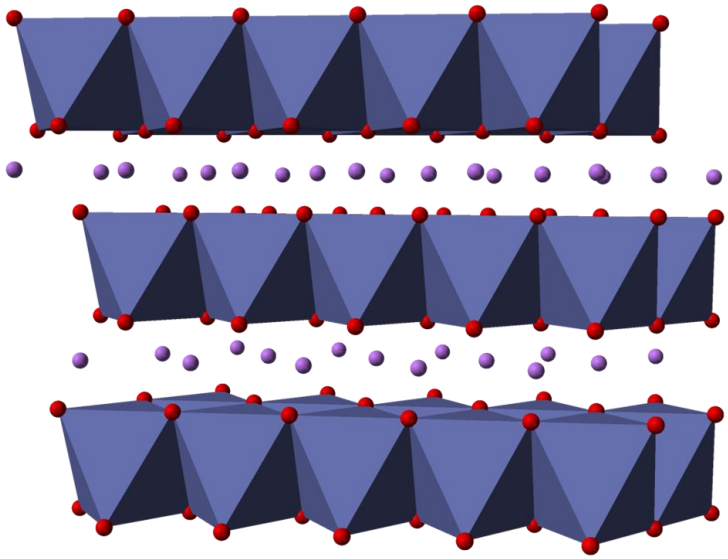


Figure 6 - The solid consists of layers of monovalent Li^+ that lie between extended anion sheets of cobalt and oxygen atoms, arranged as edge – sharing octahedra.[58]

Lithium Nickel Oxide – LNO

Lithium Nickel Oxide, $LiNiO_2$, is isostructural with $LiCoO_2$ and has a similar theoretical specific capacity of 275 mAh g^{-1}. The lower cost of Ni *vs.* Co is the main driver for research into NCO electrodes. However, it is difficult to synthesise stoichiometric $LiNiO_2$ as Ni^{2+} has tendency to occupy the interlayer Li^+ sites. This tendency also extends during the charge process (delithiation), such that the Ni^{2+} blocks Li diffusion pathways.[59]

Lithium Nickel Cobalt Aluminium Oxide – NCA

Partial substitution of Ni with Co was found to be an effective strategy to alleviate cation disorder.[60] The addition of a small amount of aluminium also proved beneficial in improving the thermal stability and electrochemical performance. [61] Thus, $LiNi_{0.8}Co_{0.15}Al_{0.05}O_2$, NCA, found commercial recognition as NCA has a high usable discharge capacity (200 mAh g^{-1}) and a long storage life. The major manufacturer of NCA batteries is Panasonic for some Tesla electric vehicle models.[62] The principal disadvantages associated with NCA electrodes are the high costs associated with cobalt. Variants dubbed 'nickel rich' NCA, $LiNi_xCo_yAl_zO_2$ where $x \geq 0.8$ are more cost effective, however the increase in Ni content also decreases the thermal stability and can cause premature aging of the battery. [63]

Lithium Manganese Oxide – LMO

Another cheaper electrode material is lithium manganese oxide, $LiMn_2O_4$ with a spinel structure (Figure 7). This electrode composition uses abundant, low cost and environmentally benign materials, namely Mn. The manganese occupies the octahedral sites and the lithium predominantly occupies the tetrahedral sites within the Mn_2O_4 poylhedra.[64] This three – dimensional framework lends itself to high rate capability by providing a well – defined 3D network of channels for Li^+ diffusion during lithiation (discharge) and delithiation (charge).[65] However there are surface degradation challenges associated with LMO electrodes arising from the dissolution of manganese during cycling. This phenomenon occurs when Mn^{3+} ions disproportionate to form Mn^{2+} and Mn^{4+}.[66] The Mn^{2+} that is formed is soluble in most electrolytes and its dissolution causes degradation.

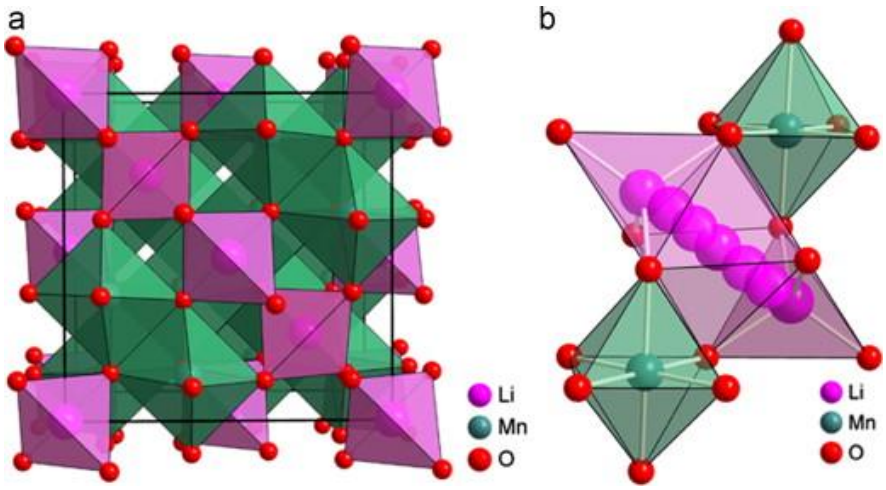


Figure 7 - Crystalline structure of spinel $LiMn_2O_4$ and (b) its corresponding lithium diffusion pathways. Reproduced from[67] with permission from Elsevier.

Lithium Nickel Manganese Cobalt – NMC

Using element substitution strategies outlined above, the combination of all three transition metals, Ni, Mn, and Co, led to a class of electrodes known as NMC (Figure 8). One of the most extensively studied NMC compositions is known as NMC–333, $LiNi_{1/3}Mn_{1/3}Co_{1/3}O_2$, which delivers a practical capacity of 160 mAh g^{-1} between 2.7 – 4.2 V[68]. Different NMC compositions have been extensively studied to optimise the trade – off between the capacity, cycle life and safety of NMC based batteries.

It is generally understood that increasing the Ni content can increase the discharge capacity as Ni can cycle between the $Ni^{2+}/^{3+}$ and $Ni^{3+}/^{4+}$ redox couples without incurring large variations in voltage during the charge/discharge process.[69] However, Ni – rich electrode materials are susceptible to capacity fade during cycling and also have reduced thermal stability. Addition of Mn improves the thermal stability, and its spinel structure is beneficial for enhanced structural integrity[69] and lower internal resistance.[70] However Mn is not an electroactive component and therefore decreases the discharge capacity of NCM.[68,71] Increasing the Co content can reduce the capacity loss during cycling as the smaller radius of Co^{3+} can inhibit the occupation Li^+ sites by Ni^{2+}, thereby stabilising the structure and Li^+ diffusivity.[72] However, this is at the expense of increased material cost. To date, a library of various NMC compositions have

been reported and commercialised for electric vehicles such as the Nissan Leaf, Chevy Volt and BMW i3.[73]

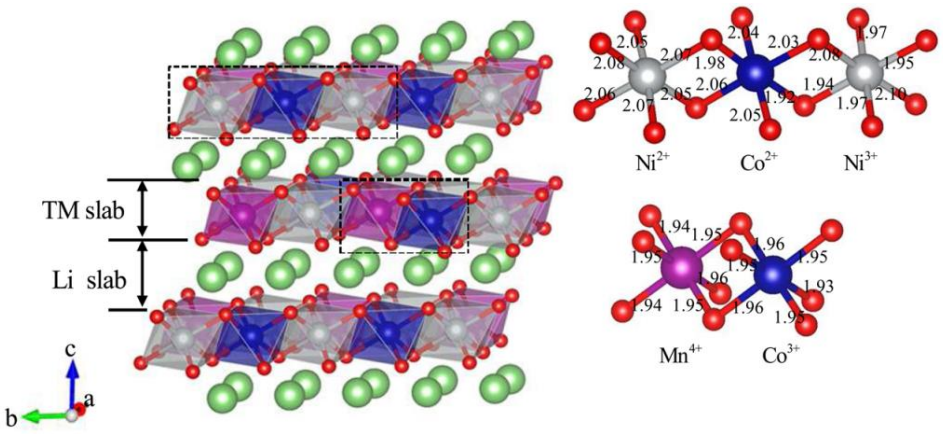


Figure 8 – Transition metal – oxide octahedral complexes in NMC. (a) Ni, Mn, and Co reside at the octahedral site surrounded by six O atoms. (b) Local view of the TM–O octahedral complexes. The grey, blue and purple spheres represent Ni, Co and Mn atoms in the TM layer respectively and red spheres represent O atoms. Reprinted with permission from[74]. Copyright 2017 American Chemical Society.

Lithium Iron Phosphate – LFP

Aside from layered oxides and spinel oxide structures, another class of positive electrode material is polyanion oxides, $Li_xFe_2(XO_4)_3$ (X = S, Mo, W, etc.). The polyanion oxides were found to undergo reversible insertion/extraction of two lithium ions per formula unit.[75,76] The working voltages across the isostructural polyanions such as $Fe_2(MoO_4)_3$ (3.0 V), $Fe_2(WO_4)_3$ (3.0 V), $Fe_2(SO_4)_3$ (3.6 V) are greater than their simple oxide analogues such as Fe_2O_3 and Fe_3O_4 (< 2.5 V) despite the fact they all operated with the same Fe^{2+}/Fe^{3+} redox couple.[77] This elucidated the influence of the counter cations (Mo^{6+}, W^{6+}, S^{6+}) in shifting the redox potential of the Fe^{2+}/Fe^{3+} couple through alteration of the covalency of the Fe – O bond. In the $Li_xFe_2(XO_4)_3$ structure, the FeO_6 octahedra share corners with the XO_4 tetrahedra, such that the linkage is as follows: – O – Fe – O – X – O – Fe – O –. Through the inductive effect, the stronger covalent X – O bond weakens that of the Fe – O bond, thereby lowering the energy of the Fe^{2+}/Fe^{3+} couple and simultaneously increasing the working voltage (Figure 9).[78]

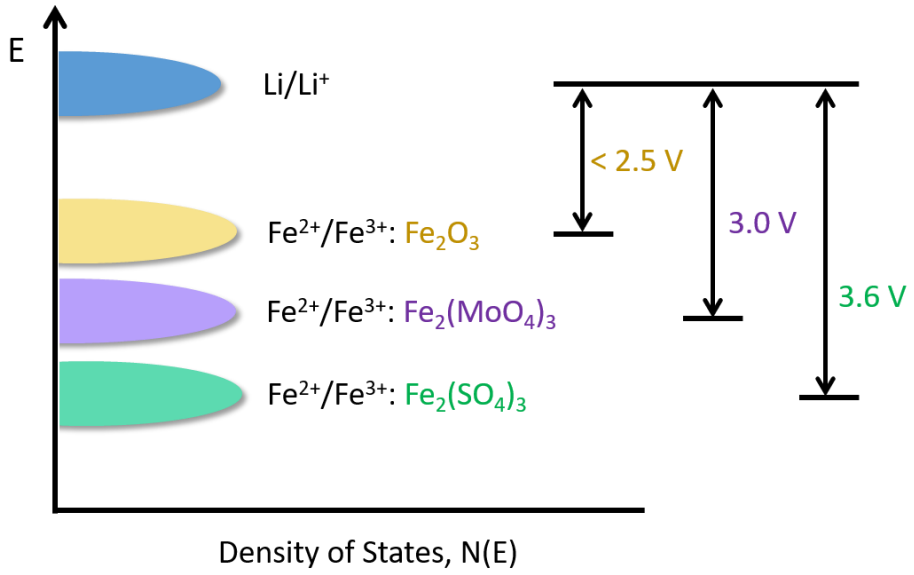


Figure 9 - Role of counter-cations in shifting the redox potentials in polyanion oxides. Lowering the potential of the $Fe^{2+}/^{3+}$ couple results in an increase in the cell voltage, moving from a simple oxide (Fe_2O_3) to a polyanion oxide ($Fe_2(MoO_4)_3$). Adapted from[78] with permission from Springer Nature.

$LiFePO_4$ (LFP) possesses an olivine structure and is the representative material for the polyanions (Figure 10). It presents several advantages over the layered and spinel type electrodes such as cost and safety. A reduction in cost is due to the use of abundant transition metals like Fe and it also contains no Ni or Co.[79] The improved thermal stability (up to 400 °C) and safety stems from the strong covalent bonds between oxygen and P^{5+} to form the PO_4^{3-} polyanion.[80] However, LFP suffers from poor electronic conductivity and therefore requires the synthesis of small particle size[81] and coatings with conductive carbon.[82]

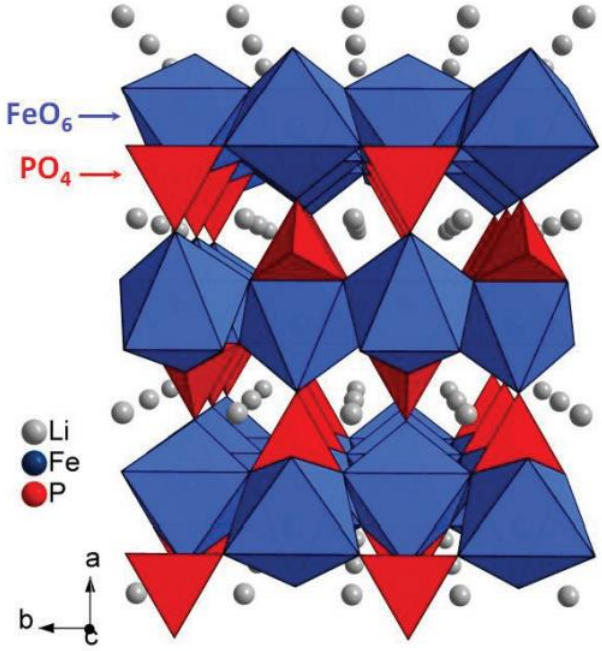


Figure 10 - Olivine structure of $LiFePO_4$. Reprinted from[83] with permission of AIP Publishing.

Next Generation Positive Electrodes

Thus far, we have witnessed the concerted scientific research that has enabled the development of viable, commercialised positive electrode materials. The progression from simple single transition metal oxides such as $LinNiO_2$ and Fe_2O_3 to derivatives substituted with two, or more elements and possessing polyanionic structures, highlights the delicate interplay between composition, structure, and performance.

Moving forward, the projected impact of Li-ion batteries goes beyond portable electronics and extends to sustainability, electrification of transport, rural electrification and large – scale energy storage. To meet the demands for such sectors, continued materials discoveries with game – changing chemistries and unique electrochemical properties are required to evolve the field of energy storage. Attention is now turned towards polyoxometalates as an avenue towards alternative metal oxide materials for electrochemical energy storage.

1.2 Polyoxometalates (POMs)

Polyoxometalates, referred to as POMs, are an extraordinary class of discrete metal oxide clusters.[84] These polyatomic anions are formed from three or more transition metal oxo-anions (typically V, Nb, Ta, Mo and W), in their highest oxidation state which are linked by shared oxygen atoms to form three – dimensional frameworks. This class of metal oxides unveil a range of tuneable properties that are determined in large part by their size, shape and electronic structure. These properties have been exploited for applications such as homogenous catalysis[85], water oxidation[86] and metallodrugs[87]. These promising multi – functional materials have also proven useful for numerous solid – state applications such as heterogeneous catalysis[88,89], single molecule magnets[90], proton conduction materials[91] and energy storage[92,93,94].

1.2.1 Principles of Bonding & Formation

While POMs can adopt a myriad of elaborate structures adopting different shapes and compositions, understanding their structure and formation can be defined using straightforward principles. If we consider an individual $[MO_x]$ polyhedral unit, where M is the central metal atom (addenda atom) coordinated to O^{2-} oxo O – ligands and x = 4 – 7 (Figure 11a). The addenda atoms must satisfy certain criteria in order to form discrete clusters, which include; capable of changing coordination number from 4 – 6 upon polymerisation in solution (usually acidification); possessing a high positive charge and being amongst the smaller of the metal ions to adopt an octahedral arrangement with oxygen atoms; having the ability to form M = O double bonds with terminal oxygens via pπ and dπ orbital interactions.[95] Therefore it follows that early transition metals from groups 6 and 6 such as V, Mo, W and Nb in their highest oxidation states (i.e. d^0 or d^1) are well suited as addenda atoms for POM structures.

Under aqueous acidic conditions, the simple $(MO_x)_n$ units undergo self – assembly, in which they aggregate to form large compounds with specific structures. What is most curious in regard to this POM cluster formation, is the

fact that they can be isolated at all, and do not undergo uncontrolled polymerisation to form extended metal oxides. The O^{2-} oxo ligands which constitute the vertices of each polyhedral unit are responsible for the structural versatility as they are capable of bridging and terminal modes. The oxo ligands facilitate polycondensation through bridging of metal atoms and the stable terminal bonds limit their propagation into infinite metal oxide structures. In the commonly adopted octahedral configuration, the M = O bond shows greater polarisability towards the addenda metal than the bridging M – O bonds and thus the terminal oxo ligands exert a strong thermodynamic *trans* – effect. Traditionally, the *trans* – effect denotes a labilisation of oppositely situated ligands, which are sharing the same metal orbital, to more strongly electron donating groups.[96] With respect to the POM, the *trans* – effect is exerted by the terminal oxo ligand which weakens the bond to the oxygen atom located at the opposite vertex of the octahedron (which shares its orbital). This results in a structural displacement from idealised octahedral geometry as the addenda metal is pulled towards the terminal M = O, resulting in a clear discrepancy in the bond length (Figure 11b). The implication of this distortion is significantly reduced basicity of the oxide surface, reducing the propensity for further protonation and therefore preventing the structure from spiralling into further condensation reactions.

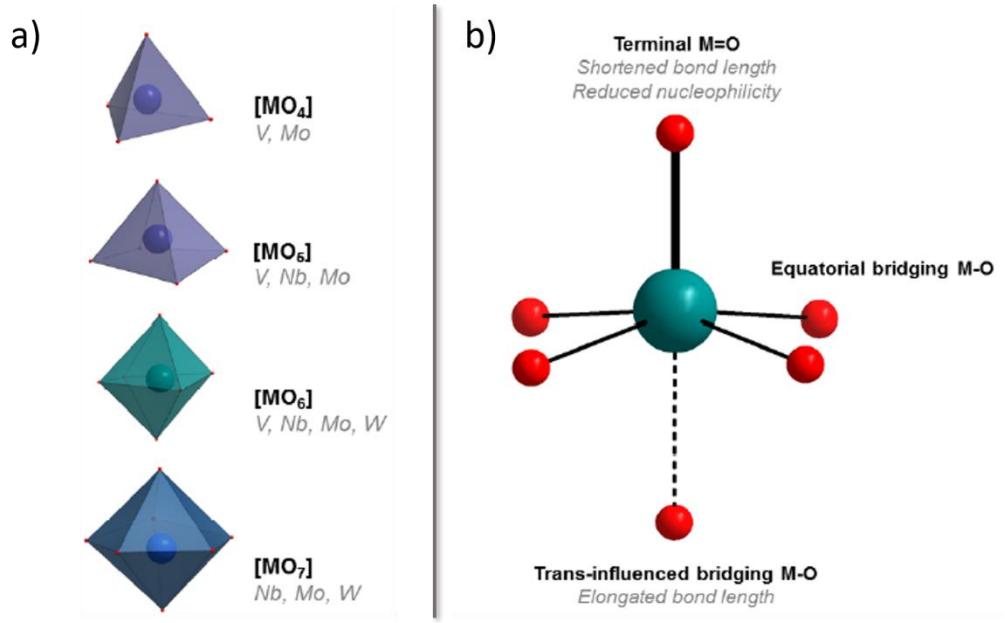


Figure 11 - Left: The main structural features of the primary [MO_6] polyhedral unit common to most POM structures and; right: a comparison of the possible [MOx] polyhedra found in POM structures and the addenda metal species capable of forming them. Reprinted with permission from J.M.Cameron, PhD Thesis, University of Glasgow, 2014.

1.2.2 Synthesis

POMs are typically synthesised under 'one – pot' conditions through pH mediated self – assembly of metal oxyanions in aqueous conditions. The metal oxo-anion is introduced as an oxometalate salt (i.e. Na_2WO_4, Na_2MoO_4, $NaHVO_3$) and for the synthesis of heteropolyoxometalates, a heteroatom source is also added in the form of a mineral acid or alkali metal derivative.

Synthesis of isopolyoxometalate:

$$7WO_4^{2-} + 8H^+ \rightarrow [W_7O_{24}]^{6-} + 4H_2O$$

Synthesis of heteropolyoxometalate:

$$12WO_4^{2-} + H_3PO_4 + 21H^+ \rightarrow [PW_{12}O_{40}]^{3-} + 12H_2O$$

As mentioned previously, the single oxometalate units undergo polycondensation reactions when acidified. Initially, the tetrahedral $[MO]_4^{n-}$ precursors expand their coordination sphere, forming protonated $[MO_x(OH)_y]^{n-y-}$ metal – hydroxide complexes. These are particularly susceptible to condensation reactions due to the increased Lewis acidity of the metal coupled

with the labile water ligands. Indeed, there are several experimental considerations[97] which can influence the self – assembly process to some degree. Most commonly these include temperature, pH, solvent, choice of cation and ratio of M:X (addenda: heteroatom).

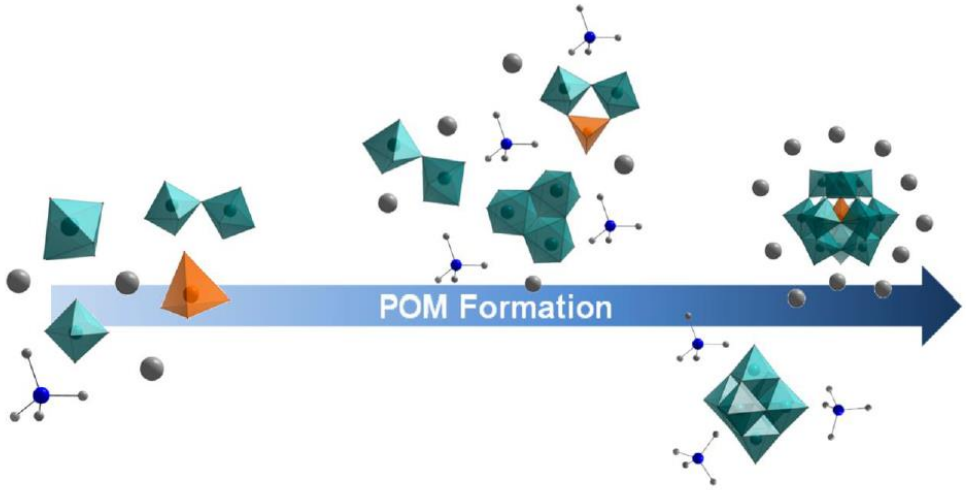


Figure 12 - Schematic representation of the synthesis of POM clusters from monomeric oxo-anions and simple cations (left); through to intermediate, polynuclear secondary building units (centre); and finally, to the polyoxometalate-cation complex itself which forms the isolable product. Reprinted with permission from J.M.Cameron, PhD Thesis, University of Glasgow, 2014.

1.2.3 Structure

POMs can be broadly categorised into isopolyoxometalates and heteropolyoxometalates (Figure 13). The isopolyoxometalates composed of one type of metal and oxide ligand ($[M_xO_y]^{n-}$) and heteropolyoxometalates constitute metal oxide units templated by a heteroatom ($[X_zM_xO_y]^{n-}$). Typically, the heteroatoms are located within the core of the hetero – POM structure and are referred to as the non – addenda atoms. Heteroatoms must be able to form at least three bonds to oxygen atoms and therefore heteroatoms are usually *p* – or *d* – block elements.

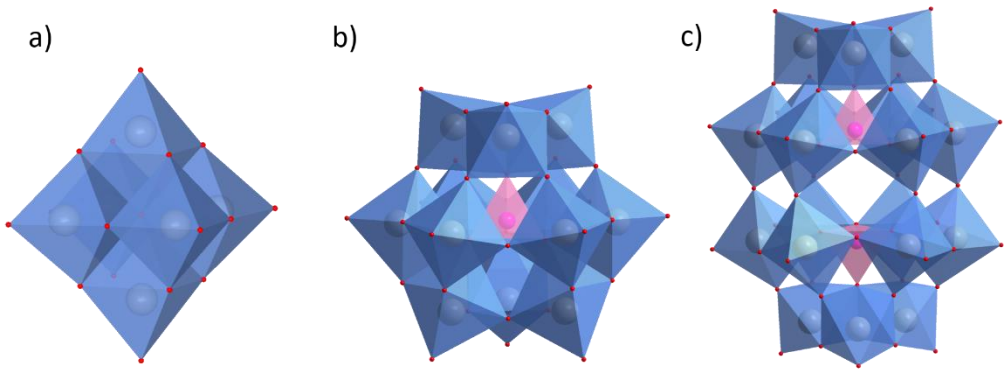


Figure 13 – Representative isopolyoxometalates and heteropolyoxometalates; a) Lindqvist, b) Keggin, c) Wells-Dawson.

While there are thousands of compounds that can be classified as a polyoxometalate, the majority of these are derivatives of archetypal anions. These archetypes have been recognised as general building blocks[98] and their structures are referred to by the name of the crystallographer who first reported or theorised the structure.

Lindqvist Anion

The most representative type of the isopolyoxometalates is the Lindqvist anion $[M_6O_9]^{n-}$ which was first reported in 1950.[99] The structure contains one metal environment and three oxygen ones: central (O_a), bridging (O_b) and terminal (O_c) (Figure 14). It exhibits high point group symmetry (O_h) with six octahedra MO_6 units that share edges. The high stability has been probed using DFT and its stability is thought to originate from the aromaticity of the M_4O_4 rings.[100,101] The Lindqvist structure has been isolated for several of the early transition metals including W, Mo, Ta and Nb but not for V, as the $[V_6O_{19}]^{8-}$ requires additional stabilisation, and is often synthesised as the polyoxoalkoxometalate derivative (POMs incorporating alkoxo ligands).[102] Although the chemistry of the Lindqvist anions may not be as vast as other archetypes, it has been functionalised extensively. Mixed – addenda moieties such as $[VMo_5O_{19}]^{3-}$ have been explored for photocatalysis[103] and some fluoro-functionalised arylimido-substituted hexamolybadates, $(n\text{-}Bu_4N)_2[Mo_6O_{18}(NAr)]$ (Ar = 2-CH_3-4-FC_6H_3) have been tested for herbicidal activity.[104]

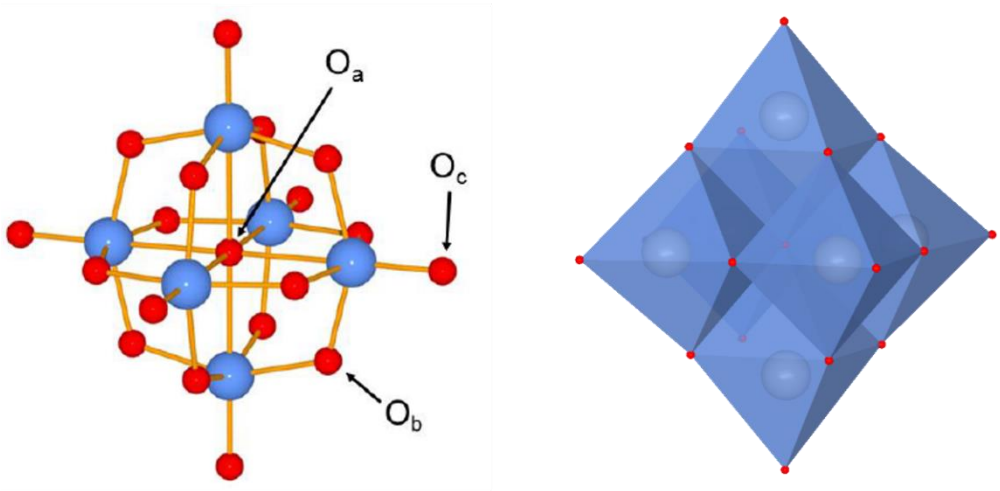


Figure 14 – Ball and stick (left) and polyhedral (right) representation of the Lindqvist polyoxometalate (M_6O_{19}) showing the unique oxygen atom environments within the cluster. Reprinted with permission from A.J.Kibler, PhD Thesis, University of Nottingham, 2019.

Anderson – Evans Anion

The Anderson structure presents an unusual type of heteropolyoxometalate in the sense that the core heteroatom is an octahedral transition metal. The general formula is $[H_yXM_6O_{24}]^{n-}$ (where y = 0 – 6) with a hexameric planar ring of edge sharing $[MO_6]$ units (typically Mo or W) around the central heteroatom (Figure 15). The three oxygen environments are as follows: six O_a atoms link the central heteroatom to a pair of addenda metals, six O_b atoms bridge each pair of addenda metals on the ring periphery and lastly there are six pairs of O_c atoms on each addenda metal. Anderson structures can be further classified into Type A (non – protonated) or Type B (protonated) structures.[105] Type A structures incorporate heteroatoms in a high oxidation state such as Te^{VI} [106] or I^{VII} [107] in the general formula $[X^{n+}M_6O_{24}]^{(12-n)-}$ whereas the B – Type protonated structures have low oxidation state heteroatoms such as Cr^{III} [108] and Fe^{III} [109] in the general formula $[X^{n+}(OH)_6M_6O_{18}]^{(6-n)-}$. The six protons in the B – type structure are located on the six O_a atoms bound to the heteroatom.

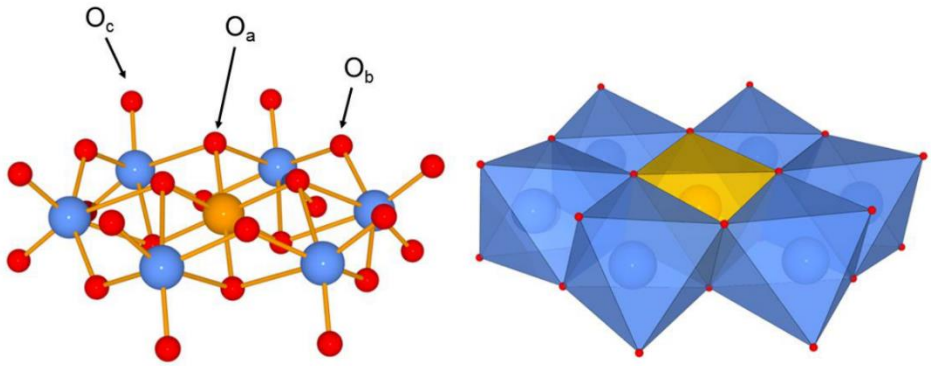


Figure 15 - Ball and stick (left) and polyhedral (right) representation of the Anderson polyoxometalate (XM_6O_{24}) showing the unique oxygen atom environments within the cluster.

The Anderson structure is a prominent example of a Type II POM (vide infra) and consequently does not display any useful redox activity. Nevertheless, the structural diversity of this cluster is extensive given that a wide variety of elements can be used as the heteroatom such as *p* – block and transition metals. Figure 16 exemplifies this diversity and highlights all the elements that have been incorporated into inorganic Anderson structures, with oxidation states spanning II to VII. All first – row transition metals except for Sc, Ti and V have been reported for the molybdate system (element symbol in red) and clearly, the Mo structure has incorporated a greater variety of heteroatoms compared to the tungstate Anderson (element symbol green).[110] The Anderson structure has provided a platform for synthesising a host of unusual, complex and interesting architectures.[111,112]

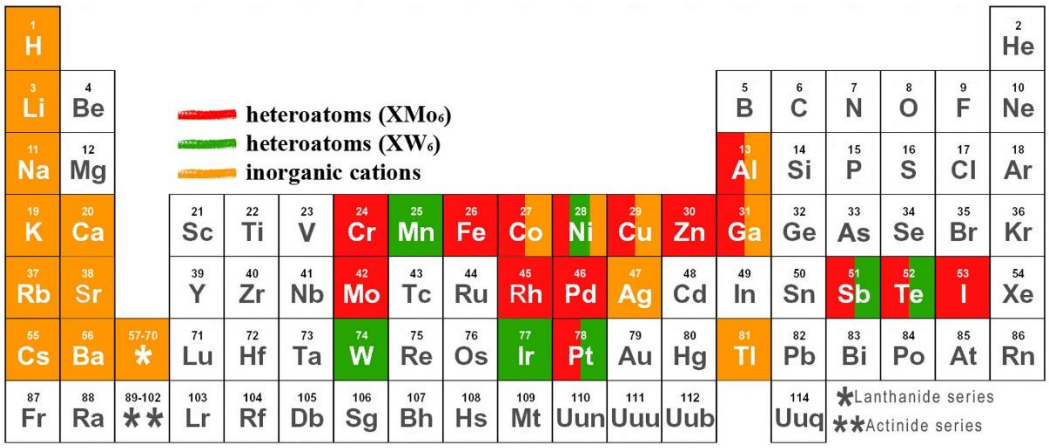


Figure 16 - Periodic table illustrating heteroatoms in XMo_6 and XW_6 systems and the different cations successfully applied. Reprinted from[110] with permission of Elsevier.

Keggin Anion

The first reported Keggin structure was $[H_3PW_{12}O_{40}]$, known as phosphotungstic acid.[113] Since this discovery in 1993, an enormous amount of literature has been devoted to the Keggin moiety and its derivatives. Its structure comprises a tetrahedral $[XO_4]$ heteroatom 'template' surrounded by four groups of $[M_3O_{13}]$ triads, in the general formula $[XM_{12}O_{40}]^{n-}$ (Figure 17). Mo and W are the most prevalent addenda elements, and the most common heteroatoms are P^{5+}, Si^{4+} and B^{3+}. The Keggin motif has four different oxo ligand environments: the central O_a that bridges the heteroatom X and addenda M atoms, O_b (corner) and O_c (edge) which bridge the metal octahedra and lastly the terminal O_d oxo ligands for each metal octahedron.[114]

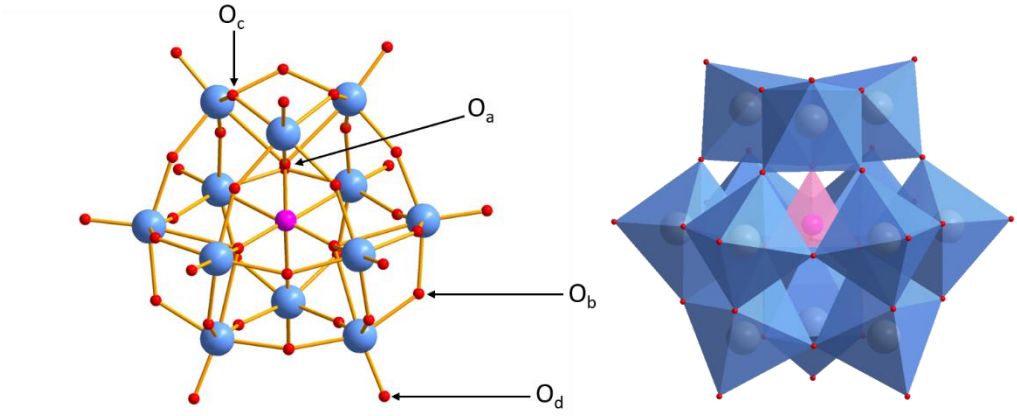


Figure 17 - Ball and stick model (left) and polyhedral (right) representation of the Keggin polyoxometalate ($XM_{12}O_{40}$) highlighting the various oxygen atom environments present in the cluster.

Disparate to the Lindqvist species, Keggin anions can exist as one of five isomers through rotational isomerism (Figure 18), with the original known as the α isomer. Through 60° rotations, the $[M_3O_{13}]$ triads can undergo one, two, three and four rotations to yield the β, γ, δ and ε isomers respectively.[115]

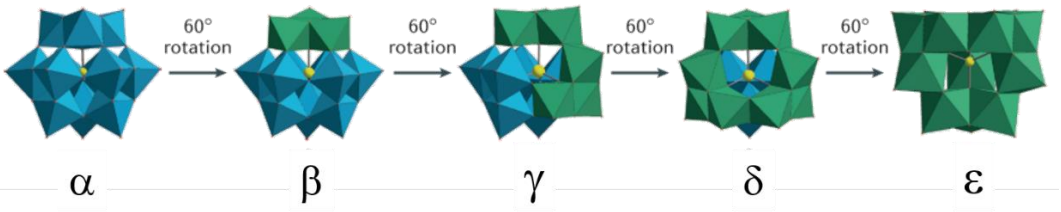


Figure 18 – The five theoretically possible geometric isomers of the Keggin archetype (rotated caps shown in green. Reproduced from[116] with permission from Springer Nature.

Rotation of the triads beyond the β isomer results in a change from corner – sharing to edge – sharing modes between adjacent triads, thereby increasing the intra – cluster coulombic repulsion. Therefore the stability of fully oxidised Keggin anions decreases in the order $\alpha > \beta > \gamma > \delta > \varepsilon$.[117] The α and β isomers are the most stable and have clear literature procedures for their synthesis and isolation of their reduced forms. However, the γ[118], δ[119] and ε[120] isomers are much more scarce, requiring special synthetic procedures for their preparation and the δ and ε can only be isolated in their reduced form when bound to a transition metal ion.[121,122]

Wells – Dawson Anion

Another seminal archetype is known as the Wells – Dawson POM, often referred to as the Dawson cluster, and is just as prolific as the Keggin amongst heteropolyoxometalates. The cluster has the general formula $[X_2W_{18}O_{62}]^{n-}$ which was first proposed in 1945 by Wells[123] and was corroborated by Dawson's x – ray elucidation of the potassium polyoxotungstate, $K_6[P_2W_{18}O_{62}].14H_2O$.[124] This eponymous anion differs from that of the Keggin as it features not one, but two tetrahedral heteroatom cores. Therefore, there are two distinct metal sites known as the 'cap' and 'belt' (Figure 19). There are six cap positions comprising two $[M_3O_{13}]$ triads and twelve equatorial 'belt' positions, created by two dyads $[M_2O_{10}]$ sharing three corners. Additionally, the cap and belt regions give rise to eight different oxygen environments (Figure 19). Two O_{a1} atoms connect the central heteroatoms to the 'cap' metals and six O_{a2} atoms do the same for the 'belt' metals. Six bridging O_{b1} atoms link the 'cap' metals, twelve O_{b2} atoms link the cap region to the belt, another twelve O_{b3} atoms that connect the belt

metals and the six O_{b4} atoms connect the two 'belt' regions. Lastly, there are six terminal O_{c1} atoms at the cap region and twelve terminal O_{c2} located at the equatorial 'belt'.

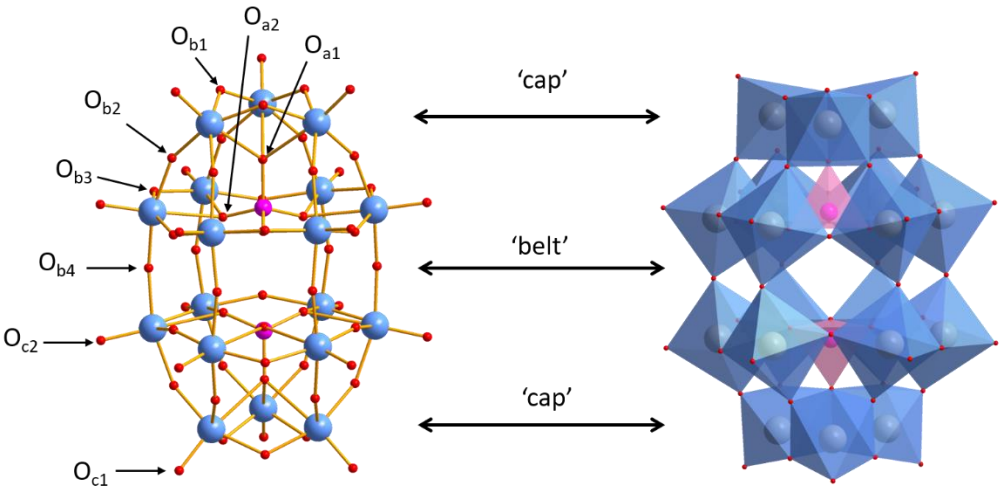


Figure 19 – Ball and stick model (left) and polyhedral (right) representation of the Wells-Dawson cluster (X2M18O62) highlighting the unique oxygen environments within the framework.

Unsurprisingly, the Dawson structure can also experience rotational isomerism differing through orientation of the $[M_3O_{13}]$ triads or the half $[XM_9]$ units (Figure 20). Successive 60° rotations of the triads yield the α, β, and γ isomers and further isomers, α*, β*, and γ*, can be derived from rotations of the 'staggered' form (180° rotation of the $[XM_9]$ unit). However, only four of the isomers, α, β, γ and γ* have been isolated. [125,126]

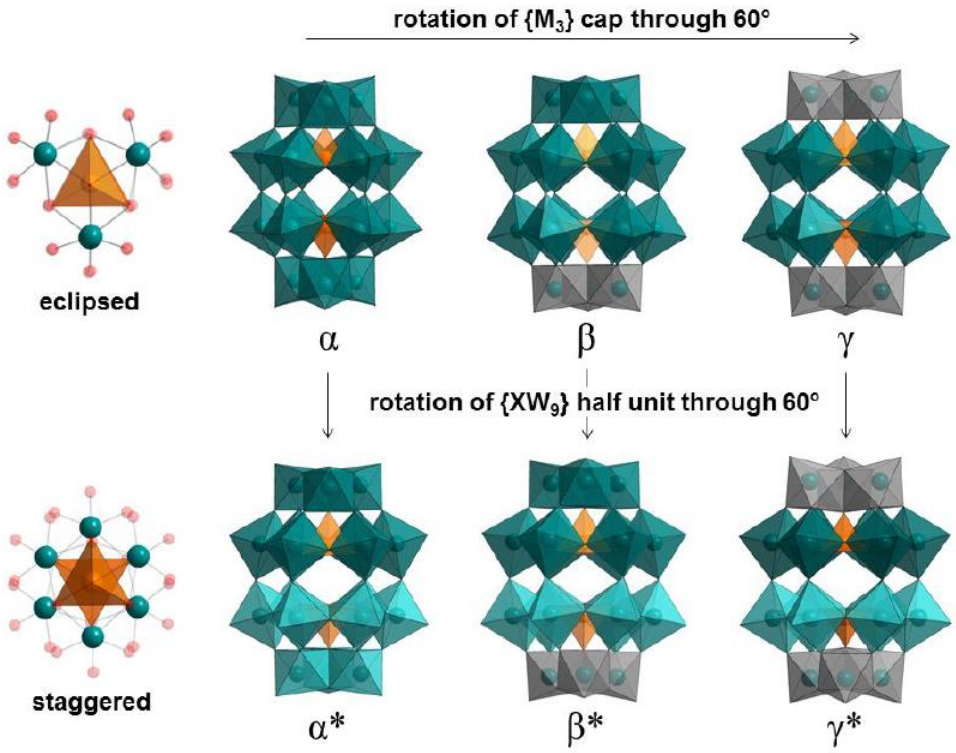


Figure 20 – Depiction of the geometrical isomerism observed in the Dawson cluster showing the six theoretically possible isomers which can be obtained by subsequent rotation of either the {M3} capping triads (top row, rotated triads highlighted in grey) or further ro rotation of an entire {XW_9} half-unit (bottom row, rotated half-units shown in cyan, or a combination of cyan/grey if the {M_3} cap is also rotated). The eclipsed and staggered conformations which are possible between two tetrahedral {XO_4} units in each isomer type (*i.e.* 'standard' or 'starred') is also shown for comparison. Reprinted with permission from J.M.Cameron, PhD Thesis, University of Glasgow, 2014.

1.2.4 Electronic Properties of POMs

POM chemistry is multifaceted but arguably the most fascinating aspect is their unique and complex electrochemical properties. It was discovered early on that certain POMs were readily reduced and produced a deep blue colour, which are referred to as 'heteropoly blues'.[127] The discovery that certain archetypal POMs can exist in electron – rich reduced forms has fuelled research into harnessing and tuning these properties for catalytic[128,129], magnetic[130] and electronic[131,132] properties.

As mentioned previously, the addenda metal atoms in most POM structures are in their highest oxidation state (d^0 or d^1) and thus it follows that these clusters can behave as oxidising agents. However, this property is not

ubiquitous for all POM structures and so POMs can be further classified into Type I, Type II and Type III with respect to the coordination environment of the addenda atom. Type I structures feature one only terminal M = O bond, Type II have two terminal M = O bonds per addendum atom and Type III feature a combination of these sites.

The reducibility of POMs can be rationalised according to molecular orbital theory with respect to the local environment of the addenda atoms. Type I and Type III structures feature octahedral metal oxo units with one terminal M = O bond which has a vacant non – bonding t_{2g} orbital which can be filled upon reduction. Whereas a Type II structure has two terminal M = O bonds and thus lack a non – bonding t_{2g}, since these orbitals are required for π – bonding. Accordingly, amongst the archetypal structures discussed only the Lindqvist, Keggin and Wells – Dawson motifs are capable of reversible reductions. Type II anions such as the Anderson – type POMs experience irreversible reductions leading to fragmentation or rearrangement to other structures.[97]

The number of electrons a particular POM can accept i.e., the degree of reduction depends on its charge to nuclearity ratio. This ratio can be described by q/m where q is the overall negative charge and m is the number of addenda metals in the structure.

Poblet et al. showed that in analysing the redox properties of POMs, the size of the cluster as well as the nuclear charge must be considered.[133] POMs which are large in size with a low negative charge are more readily reduced compared to smaller, more highly charged POMs. For example $[S_2W_{18}O_{62}]^{4-}$ is a powerful oxidant due to its large size bearing a small negative charge whereas $[W_6O_{19}]^{2-}$ is a weaker oxidant.

In comparing isostructural POMs but with differing addenda metal, the LUMO energies of the POM decrease as the electronegativity of the d^0 metal is increased ($W^{6+} < Mo^{6+} < V^{6+}$).[134] As such, in a mixed – addenda Mo/W POM, the Mo sites are preferentially reduced over W. [135] Additionally, polyoxomolybdate have more positive reduction potentials than the corresponding

polyoxotungstate. For example in acetone, the redox couple $[PMo_{12}O_{40}]^{3-}$ /$[PMo_{12}O_{40}]^{4-}$ lies at – 468 mV whereas the $[PW_{12}O_{40}]^{3-}$ /$[PW_{12}O_{40}]^{4-}$ is shifted negative by approximatively 400 mV to – 895 mV.[136]

Lastly, for heteropolyoxometalates, the nature of the templating heteroatom can also influence the electronic properties of the POM. Studies on this phenomenon for Keggin anions are exhaustive. In a study with Keggin polytungstates $[XW_{12}O_{40}]^{n-}$ (where X = B, Al, Ga, Si, Ge, P, As) the internal $[XO_4]$ unit carrying the same charge directly influenced the reduction potential.[137] This phenomenon is consistently observed where the one – electron reduction potential of the Keggin motif decreases linearly with the decreasing valence of the heteroatom.[138] The origin of this has been shown to be a shift in surface charge density: Heteroatoms with lower atomic mass are also smaller in size and so a more negative electrostatic potential is generated, decreasing the ability of the addenda metals to accept electrons.

1.2.5 Merits of POMs as Energy Materials

Though there has been extensive research on new electrode materials for Li-ion batteries, it mostly focuses on a select few, namely the intercalation compounds presented earlier. It is becoming increasingly difficult to discover new lithium intercalation materials and make a breakthrough in battery performance. As such, designing and engineering new materials has been given particular emphasis in the field of energy storage.

POMs provide a spectrum of useful properties that are determined in large part by their size, shape, and electronic structure. Several of these properties can be exploited for battery materials. The structural diversity of POMs goes far beyond the archetypes presented herein, which are steppingstones to thousands of functionalised derivatives. With regards to battery materials, POM derivatives which are redox active are of obvious interest as they contain multiple redox active sites within the three – dimensional framework. The rapid and reversible redox chemistry could potentially assure a high capacity owing the multi – electron redox centres. A

Keggin and bi – capped Keggin structure have been shown to have an initial discharge capacity of 200 mAh g^{-1}.[139,140] The tremendous diversity observed within POMs is particularly desirable as it imparts tuneability with respect to the structure but also the function i.e., tuning the electronic structure through modification of the countercation, heteroatom or addenda metal.

The most prevalent Li-ion positive electrode materials presented so far including layered $LiCoO_2$, spinel $LiMn_2O_4$, and olivine $LiFePO_4$ which all undergo changes in the crystal structure during lithium intercalation and deintercalation, which is expressed as a loss of capacity during prolonged cycling.[141,142,143,144] Therefore, their observed capacities are lower than their theoretical calculated values. However, the open frameworks of POMs consisting of individual molecular units could demonstrate advantages over conventional insertion electrodes with respect to the Li^+ intercalation/deintercalation mechanism. Especially since the multi – electron charge transfer does not induce significant structural changes to the POM cluster.

Conventional lithium intercalation materials involve a relatively arduous synthesis. $LiCoO_2$[145] is synthesised at temperatures exceeding 800 °C over 24 hours and $LiFePO_4$ is synthesised > 550 °C over 6 hours.[146] In contrast, POM synthesis is much more straightforward, economical and less energy demanding. Most POMs can by synthesised by means of self-assembly via pH adjustment, at temperatures below 100 °C.[147]

It is evident that the unique structural properties of these metal oxide clusters show good prospects for application to lithium batteries, but of course, not without challenges. POMs are poor electrical conductors, and they are also soluble in a wide variety of aqueous and organic solvents which can be attributed to their ability to interact with most solutions via electrostatic forces, hydrogen bonding, covalent and non-covalent interactions (Figure 21). Therefore, the use of a pristine POM based electrode would result in low cycling stability and poor rate performance of a Li – POM battery. In order to circumvent these issues, POMs are typically combined with a conductive support such as conductive organic polymers or carbonaceous materials.[148]

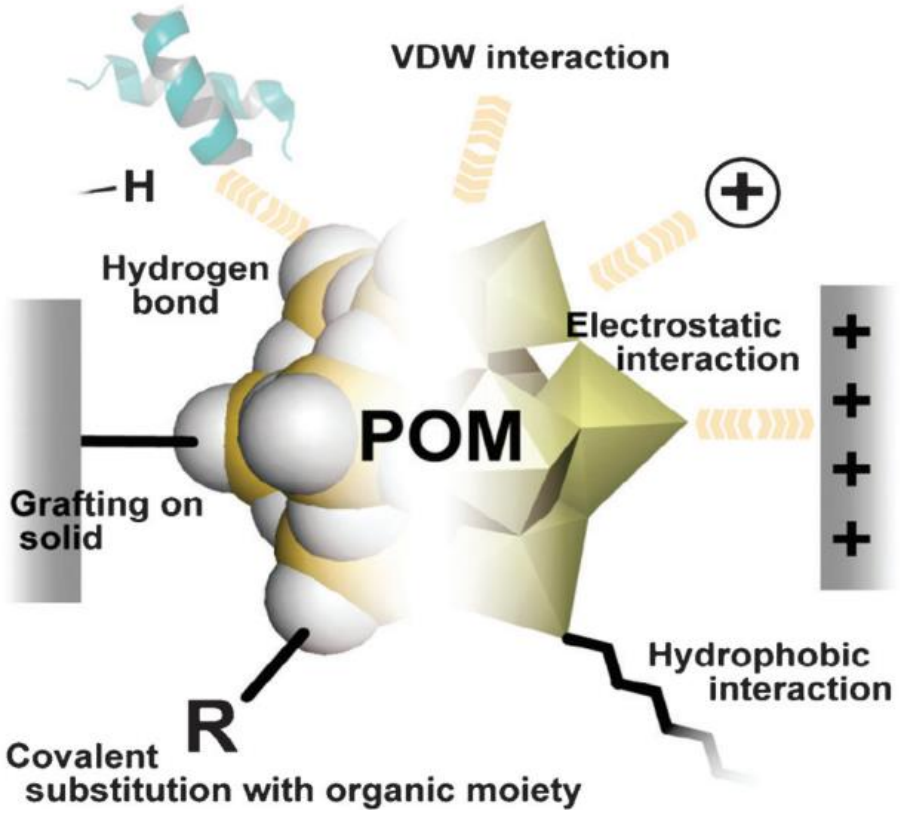


Figure 21 – Various modes of interaction in POM – based materials. Reprinted from[149] with permission from the Royal Society of Chemistry.

1.3 References

1 E. D. Coyle, R. A. Simmons and B. Chapman, *Understanding the Global Energy Crisis*, Purdue University Press, Knowledge., 2014.

2 X. Luo, J. Wang, M. Dooner and J. Clarke, Overview of current development in electrical energy storage technologies and the application potential in power system operation, *Appl. Energy*, 2015, **137**, 511–536.

3 M. S. Whittingham, Lithium Batteries: 50 Years of Advances to Address the Next 20 Years of Climate Issues, *Nano Lett.*, 2020, **20**, 8435–8437.

4 J. Libich, J. Máca, J. Vondrák, O. Čech and M. Sedlaříková, Supercapacitors: Properties and applications, *J. Energy Storage*, 2018, **17**, 224–227.

5 I. Staffell, D. Scamman, A. Velazquez Abad, P. Balcombe, P. E. Dodds, P. Ekins, N. Shah and K. R. Ward, The role of hydrogen and fuel cells in the global energy system, *Energy Environ. Sci.*, 2019, **12**, 463–491.

6 S. Trasatti, 1799-1999: Alessandro Volta's `Electric Pile': Two hundred years, but it doesn't seem like it, *J. Electroanal. Chem.*, 1999, **460**, 1–4.

7 P. Kurzweil, Gaston Planté and his invention of the lead-acid battery-The genesis of the first practical rechargeable battery, *J. Power Sources*, 2010, **195**, 4424–4434.

8 Y. Chang, X. Mao, Y. Zhao, S. Feng, H. Chen and D. Finlow, Lead-acid battery use in the development of renewable energy systems in China, *J. Power Sources*, 2009, **191**, 176–183.

9 R. M. Dell, Batteries - fifty years of materials development, *Solid State Ionics*, 2000, **134**, 139–158.

10 A. K. Shukla, S. Venugopalan and B. Hariprakash, in *Encyclopedia of Electrochemical Power Sources*, Elsevier, 2009, pp. 452–458.

11 D. A. J. Rand and P. T. Moseley, in *Electrochemical Energy Storage for Renewable Sources and Grid Balancing*, 2015, vol. 13, pp. 201–222.

12 F. Putois, Market for nickel-cadmium batteries, *J. Power Sources*, 1995, **57**, 67–70.

13 V. S. Mallela, V. Ilankumaran and S. N. Rao, Trends in cardiac pacemaker batteries, *Indian Pacing Electrophysiol. J.*, 2004, **4**, 201–212.

14 R. S. Treptow, Lithium batteries: A practical application of chemical principles, *J. Chem. Educ.*, 2003, **80**, 1015–1020.

15 T. B. Reddy and D. Linden, *Handbook of Batteries*, McGraw Hill, New York, Third., 2002.

16 C. C. Liang, C. F. Holmes, W. Greatbatch and W. Drive, Performance battery and reliability of the lithium/iodine, *J. Power Sources*, 1980, **5**, 3–13.

17 D. Linden and B. McDonald, The lithium-sulfur dioxide primary battery - its characteristics, performance and applications, *J. Power Sources*, 1980, **5**, 35–55.

18 A. Morita, T. Iijima, T. Fujii and H. Ogawa, Evaluation of cathode materials for the lithium/ carbonmonofluoride battery, *J. Power Sources*, 1980, **5**, 111–125.

19 S. N. H. Ikeda, S. Narukawa, in *'Characteristics of Cylindrical and Rectangular Li /MnO2 Batteries'*, Proc.29th Power Sources Conf., Electrochemical Society, Pennington, N.J., 1980.

20 K. Xu, Nonaqueous liquid electrolytes for lithium-based rechargeable batteries, *Chem. Rev.*, 2004, **104**, 4303–4417.

21 M. Whittingham, The intercalation and hydrothermal chemistry of solid electrodes, *Solid State Ionics*, 1997, **94**, 227–238.

22 M. S. Whittingham, Electrical energy storage and intercalation chemistry, *Science (80-.).*, 1976, **192**, 1126–1127.

23 D. A. J. Rand, Battery systems for electric vehicles — a state-of-the-art review, *J. Power Sources*, 1979, **4**, 101–143.

24 D. Fouchard and J. B. Taylor, The Molicel Rechargeable Lithium System - Multicell Aspects, *J. Power Sources*, 1987, **21**, 195–205.

25 K. Mizushima, P. C. Jones, P. J. Wiseman and J. B. Goodenough, Li_xCoO_2 (0<x<-1): A new cathode material for batteries of high energy density, *Mater. Res. Bull.*, 1980, **15**, 783–789.

26 W. Xu, J. Wang, F. Ding, X. Chen, E. Nasybulin, Y. Zhang and J. G. Zhang, Lithium metal anodes for rechargeable batteries, *Energy Environ. Sci.*, 2014, **7**, 513–537.

27 L. Li, S. Li and Y. Lu, Suppression of dendritic lithium growth in lithium metal-based batteries, *Chem. Commun.*, 2018, **54**, 6648–6661.

28 M. Armand, Polymer Electrolytes, *Annu. Rev. Mater. Sci.*, 1986, **16:1**, 245–61.

29 M. Gauthier, A. Bélanger, P. Bouchard, B. Kapfer, S. Ricard, G. Vassort, M. Armand, J. Y. Sanchez and L. Krause, Large lithium polymer battery development The immobile solvent concept, *J. Power Sources*, 1995, **54**, 163–169.

30 Y. Gofer, M. Ben-Zion and D. Aurbach, Solutions of $LiAsF_6$ in 1,3-dioxolane for secondary lithium batteries, *J. Power Sources*, 1992, **39**, 163–178.

31 D. Aurbach, I. Weissman, A. Zaban, E. Mengeritsky and P. Dan, Safely and Performance of Tadiran TLR-71 03 Rechargeable Balteries, *J. Electrochem. Soc.*, 1996, **143**, 2110–2116.

32 D. Aurbach, A. Zaban, Y. Ein-Eli, I. Weissman, O. Chusid, B. Markovsky, M. Levi, E. Levi, A. Schechter and E. Granot, Recent studies on the correlation between surface chemistry, morphology, three-dimensional structures and performance of Li and Li-C intercalation anodes in several important electrolyte systems, *J. Power Sources*, 1997, **68**, 91–98.

33 D. Aurbach, E. Zinigrad, H. Teller and P. Dan, Factors Which Limit the Cycle Life of Rechargeable Lithium (Metal) Batteries, *J. Electrochem. Soc.*, 2000, **147**, 1274.

34 J. J. Auborn and Y. L. Barberio, Lithium Intercalation Cells Without Metallic Lithium: MoO_2/$LiCoO_2$ and WO_2/$LiCoO_2$, *J. Electrochem. Soc.*, 1987, **134**, 638.

35 M. Lazzari, A Cyclable Lithium Organic Electrolyte Cell Based on Two Intercalation Electrodes, *J. Electrochem. Soc.*, 1980, **127**, 773.

36 B. Scrosati, Lithium Rocking Chair Batteries: An Old Concept?, *J. Electrochem. Soc.*, 1992, **139**, 2776.

37 D. Guerard and A. Herold, Intercalation of lithium into graphite and other carbons, *Carbon N. Y.*, 1975, **13**, 337–345.

38 J. O. Besenhard, The electrochemical preparation and properties of ionic alkali metal-and NR4-graphite intercalation compounds in organic electrolytes, *Carbon N. Y.*, 1976, **14**, 111–115.

39 Yoshino, A., Sanechika, K. & Nakajima, T. Secondary battery. JP patent 1989293 (1985).

40 S. Megahed and B. Scrosati, Lithium-ion rechargeable batteries, *J. Power Sources*, 1994, **51**, 79–104.

41 K. Ozawa, Lithium-ion rechargeable batteries with $LiCoO_2$ and carbon electrodes: the $LiCoO_2$/C system, *Solid State Ionics*, 1994, **69**, 212–221.

42 M. Wang, W. Zhong, S. Zhang, R. Liu, J. Xing and G. Zhang, Li-ion battery materials: present and future, *J. Mater. Chem. A*, 2018, **6**, 9915–9921.

43 N. A. Kaskhedikar and J. Maier, Lithium storage in carbon nanostructures, *Adv. Mater.*, 2009, **21**, 2664–2680.

44 J. Asenbauer, T. Eisenmann, M. Kuenzel, A. Kazzazi, Z. Chen and D. Bresser, The success story of graphite as a lithium-ion anode material – fundamentals, remaining challenges, and recent developments including silicon (oxide) composites, *Sustain. Energy Fuels*, 2020, **4**, 5387–5416.

45 W. Zhang, D.-H. Seo, T. Chen, L. Wu, M. Topsakal, Y. Zhu, D. Lu, G. Ceder and F. Wang, Kinetic pathways of ionic transport in fast-charging lithium titanate, *Science (80-.).*, 2020, **367**, 1030–1034.

46 S. Goriparti, E. Miele, F. De Angelis, E. Di Fabrizio, R. Proietti Zaccaria and C. Capiglia, Review on recent progress of nanostructured anode materials for Li-ion batteries, *J. Power Sources*, 2014, **257**, 421–443.

47 E. M. Sorensen, S. J. Barry, H. K. Jung, J. R. Rondinelli, J. T. Vaughey and K. R. Poeppelmeier, Three-dimensionally ordered macroporous $Li_4Ti_5O_{12}$: Effect of wall structure on electrochemical properties, *Chem. Mater.*, 2006, **18**, 482–489.

48 C. Julien, J. P. Pereira-Ramos and A. Momchilov, *New Trends in Intercalation Compounds for Energy Storage*, Springer Netherlands, Dordrecht, 2002.

49 D. Deng, Li-ion batteries: Basics, progress, and challenges, *Energy Sci. Eng.*, 2015, **3**, 385–418.

50 D. Andrea, *Battery Management Systems for Large Lithium-ion Battery Packs*, Artech House, Boston, 2010.

51 H. Xia, L. Lu, Y. S. Meng and G. Ceder, Phase Transitions and High-Voltage Electrochemical Behavior of $LiCoO_2$ Thin Films Grown by Pulsed Laser Deposition, *J. Electrochem. Soc.*, 2007, **154**, A337.

52 J. N. Reimers and J. R. Dahn, Electrochemical and In Situ X-Ray Diffraction Studies of Lithium Intercalation in Li_xCoO_2, *J. Electrochem. Soc.*, 1992, **139**, 2091–2097.

53 B. C. Melot and J. M. Tarascon, Design and preparation of materials for advanced electrochemical storage, *Acc. Chem. Res.*, 2013, **46**, 1226–1238.

54 J. W. Fergus, Recent developments in cathode materials for lithium ion batteries, *J. Power Sources*, 2010, **195**, 939–954.

55 C. Banza Lubaba Nkulu, L. Casas, V. Haufroid, T. De Putter, N. D. Saenen, T. Kayembe-Kitenge, P. Musa Obadia, D. Kyanika Wa Mukoma, J. M. Lunda Ilunga, T. S. Nawrot, O. Luboya Numbi, E. Smolders and B. Nemery, Sustainability of artisanal mining of cobalt in DR Congo, *Nat. Sustain.*, 2018, **1**, 495–504.

56 N. Williard, W. He, C. Hendricks and M. Pecht, Lessons learned from the 787 dreamliner issue on Lithium-Ion Battery reliability, *Energies*, 2013, **6**, 4682–4695.

57 D. Doughty and E. P. Roth, A general discussion of Li Ion battery safety, *Electrochem. Soc. Interface*, 2012, **21**, 37–44.

58 Y. Shao-Horn, L. Croguennec, C. Delmas, E. C. Nelson and M. A. O'Keefe, Atomic resolution of lithium ions in $LiCoO_2$, *Nat. Mater.*, 2003, **2**, 464–467.

59 A. Rougier, P. Gravereau and C. Delmas, Optimization of the Composition of the $Li_{1-z}Ni_{1+z}O_2$ Electrode Materials: Structural, Magnetic, and Electrochemical Studies, *J. Electrochem. Soc.*, 1996, **143**, 1168–1175.

60 P. Kalyani and N. Kalaiselvi, Various aspects of $LiNiO_2$ chemistry: A review, *Sci. Technol. Adv. Mater.*, 2005, **6**, 689–703.

61 C. H. Chen, J. Liu, M. E. Stoll, G. Henriksen, D. R. Vissers and K. Amine, Aluminum-doped lithium nickel cobalt oxide electrodes for high-power lithium-ion batteries, *J. Power Sources*, 2004, **128**, 278–285.

62 M. Bianchini, M. Roca-Ayats, P. Hartmann, T. Brezesinski and J. Janek, There and Back Again—The Journey of $LiNiO_2$ as a Cathode Active Material, *Angew. Chemie - Int. Ed.*, 2019, **58**, 10434–10458.

63 G. W. Nam, N. Y. Park, K. J. Park, J. Yang, J. Liu, C. S. Yoon and Y. K. Sun, Capacity Fading of Ni-Rich NCA Cathodes: Effect of Microcracking Extent, *ACS Energy Lett.*, 2019, **4**, 2995–3001.

64 M. Thackeray, A. de Kock and W. I. F. David, Synthesis and structural characterization of defect spinels in the lithium-manganese-oxide system, *Mater. Res. Bull.*, 1993, **28**, 1041–1049.

65 H. Uchiyama, E. Hosono, H. Zhou and H. Imai, Three-dimensional architectures of spinel-type $LiMn_2O_4$ prepared from biomimetic porous carbonates and their application to a cathode for lithium-ion batteries, *J. Mater. Chem.*, 2009, **19**, 4012–4016.

66 K. Nishimura, T. Douzono, M. Kasai, H. Andou, Y. Muranaka and Y. Kozono, Spinel-type lithium-manganese oxide cathodes for rechargeable lithium batteries, *J. Power Sources*, 1999, **81–82**, 420–424.

67 Z. Tianran, L. Daixin, Z. Tao and C. Jun, Understanding electrode materials of rechargeable lithium batteries via DFT calculations, *Prog. Nat. Sci. Mater. Int.*, 2013, **23**, 256–272.

68 S. T. Myung, F. Maglia, K. J. Park, C. S. Yoon, P. Lamp, S. J. Kim and Y. K. Sun, Nickel-Rich Layered Cathode Materials for Automotive Lithium-Ion Batteries: Achievements and Perspectives, *ACS Energy Lett.*, 2017, **2**, 196–223.

69 T. Li, X.-Z. Yuan, L. Zhang, D. Song, K. Shi and C. Bock, Degradation Mechanisms and Mitigation Strategies of Nickel-Rich NMC-Based Lithium-Ion Batteries, *Electrochem. Energy Rev.*, 2020, **3**, 43–80.

70 Y. Miao, P. Hynan, A. von Jouanne and A. Yokochi, Current Li-Ion Battery Technologies in Electric Vehicles and Opportunities for Advancements, *Energies*, 2019, **12**, 1074.

71 M. M. Thackeray, W. I. F. David, P. G. Bruce and J. B. Goodenough, Lithium insertion into manganese spinels, *Mater. Res. Bull.*, 1983, **18**, 461–472.

72 Z. Chen, W. Zhang and Z. Yang, A review on cathode materials for advanced lithium ion batteries: Microstructure designs and performance regulations, *Nanotechnology*, 2020, **31**, 012001.

73 M. A. Hannan, M. M. Hoque, A. Hussain, Y. Yusof and P. J. Ker, State-of-the-Art and Energy Management System of Lithium-Ion Batteries in Electric Vehicle Applications: Issues and Recommendations, *IEEE Access*, 2018, **6**, 19362–19378.

74 H. Sun and K. Zhao, Electronic Structure and Comparative Properties of $LiNi_xMn_yCo_zO_2$ Cathode Materials, *J. Phys. Chem. C*, 2017, **121**, 6002–6010.

75 A. Manthiram and J. B. Goodenough, Lithium insertion into $Fe_2(MO_4)_3$ frameworks: Comparison of M = W with M = Mo, *J. Solid State Chem.*, 1987, **71**, 349–360.

76 A. Manthiram and J. B. Goodenough, Lithium insertion into $Fe_2(SO_4)_3$ frameworks, *J. Power Sources*, 1989, **26**, 403–408.

77 M. M. Thackeray, W. I. F. David and J. B. Goodenough, Structural characterization of the lithiated iron oxides $Li_xFe_3O_4$ and $LixFe_2O_3$ (0<x<2), *Mater. Res. Bull.*, 1982, **17**, 785–793.

78 A. Manthiram, A reflection on lithium-ion battery cathode chemistry, *Nat. Commun.*, 2020, **11**, 1550.

79 A. Yamada, S. C. Chung and K. Hinokuma, Optimized $LiFePO_4$ for Lithium Battery Cathodes, *J. Electrochem. Soc.*, 2001, **148**, A224.

80 K. Liu, Y. Liu, D. Lin, A. Pei and Y. Cui, Materials for lithium-ion battery safety, *Sci. Adv.*, 2018, **4**, eaas9820.

81 T. V. S. L. Satyavani, A. Srinivas Kumar and P. S. V. Subba Rao, Methods of synthesis and performance improvement of lithium iron phosphate for high rate Li-ion batteries: A review, *Eng. Sci. Technol. an Int. J.*, 2016, **19**, 178–188.

82 S. Bodoardo, C. Gerbaldi, G. Meligrana, A. Tuel, S. Enzo and N. Penazzi, Optimisation of some parameters for the preparation of nanostructured $LiFePO_4$/C cathode, *Ionics (Kiel).*, 2009, **15**, 19–26.

83 C. Daniel, D. Mohanty, J. Li and D. L. Wood, in *AIP Conference Proceedings*, American Institute of Physics Inc., 2014, vol. 1597, pp. 26–43.

84 M. T. Pope and A. Müller, Polyoxometalate Chemistry, *Angew. Chem. Int. Ed. Engl.*, 1991, **30**, 34–48.

85 K. Nomiya, Y. Murara, Y. Iwasaki, H. Arai, T. Yoshida, N. Chikaraishi Kasuga and T. Matsubara, Highly active, homogeneous catalysis by polyoxometalate-assisted N-heterocyclic carbene gold(I) complexes for hydration of diphenylacetylene, *Mol. Catal.*, 2019, **469**, 144–154.

86 D. Gao, I. Trentin, L. Schwiedrzik, L. González and C. Streb, The Reactivity and Stability of Polyoxometalate Water Oxidation Electrocatalysts, *Molecules*, 2019, **25**, 157.

87 A. Bijelic, M. Aureliano and A. Rompel, Polyoxometalates as Potential Next-Generation Metallodrugs in the Combat Against Cancer, *Angew. Chemie Int. Ed.*, 2019, **58**, 2980–2999.

88 J. J. Ye and C. De Wu, Immobilization of polyoxometalates in crystalline solids for highly efficient heterogeneous catalysis, *Dalt. Trans.*, 2016, **45**, 10101–10112.

89 M. Samaniyan, M. Mirzaei, R. Khajavian, H. Eshtiagh-Hosseini and C. Streb, Heterogeneous Catalysis by Polyoxometalates in Metal–Organic Frameworks, *ACS Catal.*, 2019, **9**, 10174–10191.

90 G. N. Newton, S. Yamashita, K. Hasumi, J. Matsuno, N. Yoshida, M. Nihei, T. Shiga, M. Nakano, H. Nojiri, W. Wernsdorfer and H. Oshio, Redox-controlled magnetic $\{Mn_{13}\}$ Keggin systems, *Angew. Chemie - Int. Ed.*, 2011, **50**, 5716–5720.

91 H. Ma, B. Liu, B. Li, L. Zhang, Y. G. Li, H. Q. Tan, H. Y. Zang and G. Zhu, Cationic Covalent Organic Frameworks: A Simple Platform of Anionic Exchange for Porosity Tuning and Proton Conduction, *J. Am. Chem. Soc.*, 2016, **138**, 5897–5903.

92 Y. Ji, L. Huang, J. Hu, C. Streb and Y. Song, Polyoxometalate-functionalized nanocarbon materials

for energy conversion, energy storage and sensor systems, *Energy Environ. Sci.*, 2015, **8**, 776–789.

93 B. Huang, D. H. Yang and B. H. Han, Application of polyoxometalate derivatives in rechargeable batteries, *J. Mater. Chem. A*, 2020, **8**, 4593–4628.

94 J. Liu, Z. Chen, S. Chen, B. Zhang, J. Wang, H. Wang, B. Tian, M. Chen, X. Fan, Y. Huang, T. C. Sum, J. Lin and Z. X. Shen, 'electron/Ion Sponge'-Like V-Based Polyoxometalate: Toward High-Performance Cathode for Rechargeable Sodium Ion Batteries, *ACS Nano*, 2017, **11**, 6911–6920.

95 L. C. W. Baker and D. C. Glick, Present general status of understanding of heteropoly electrolytes and a tracing of some major highlights in the history of their elucidation, *Chem. Rev.*, 1998, **98**, 3–49.

96 R. G. Pearson, C. R. Boston and F. Basolo, Mechanism of Substitution Reactions in Complex Ions. III. Kinetics of Aquation of Some Cobalt(III) Complex Ions, *J. Am. Chem. Soc.*, 1953, **75**, 3089–3092.

97 J. Borrás-Almenar, E. Coronado, A. Müller and M. T. Pope, *Polyoxometalate Molecular Science*, Kluwer Academic Publishers, 2003, vol. 35.

98 D. L. Long, R. Tsunashima and L. Cronin, Polyoxometalates: Building blocks for functional nanoscale systems, *Angew. Chemie - Int. Ed.*, 2010, **49**, 1736–1758.

99 I.Lindqvist, The Structure of the Tetramolybdate Ion, *Ark. Kemi*, 1950, **2**, 349–355.

100 A. J. Bridgeman and G. Cavigliasso, Structure and bonding in $[M_6O_{19}]^{n-}$ isopolyanions, *Inorg. Chem.*, 2002, **41**, 1761–1770.

101 J. Li, Electronic structures, (d-p)π conjugation effects, and spectroscopic properties of polyoxometalates: $M_6O_{19}^{2-}$ (M=Cr, Mo, W), *J. Clust. Sci.*, 2002, **13**, 137–163.

102 C. Daniel and H. Hartl, Neutral and cationic VIV/VV mixed-valence alkoxo-polyoxovanadium clusters $[V_6O_7(OR)_{12}]^{n+}$ (R = $-CH_3$, $-C_2H_5$): Structural, cyclovoltammetric and IR-spectroscopic investigations on mixed valency in a hexanuclear core, *J. Am. Chem. Soc.*, 2005, **127**, 13978–13987.

103 W. Deng, Q. Zhang and Y. Wang, Polyoxometalates as efficient catalysts for transformations of cellulose into platform chemicals, *Dalt. Trans.*, 2012, **41**, 9817–9831.

104 S. Xue, C. Xiang, Y. Wei, Z. Tao, A. Chai, W. Bian and Z. Xu, Synthesis, crystal structure, spectroscopic, and herbicidal activity studies of a series of designed fluoro-functionalized phenylimido derivatives of hexametalate cluster, *Cryst. Growth Des.*, 2008, **8**, 2437–2443.

105 M. T. Pope, *Heteropoly & Isopoly Polyoxometalates*, Springer-Verlag Berlin Heidelberg, 1st edn., 1983.

106 K. J. Schmidt, G. J. Schrobilgen and J. F. Sawyer, Hexasodium hexatungstotellurate(VI) 22-hydrate, *Acta Crystallogr. Sect. C Cryst. Struct. Commun.*, 1986, **42**, 1115–1118.

107 H. Kondo, A. Kobayashi and Y. Sasaki, The structure of the hexamolybdoperiodate anion in its potassium salt, *Acta Crystallogr. Sect. B Struct. Crystallogr. Cryst. Chem.*, 1980, **36**, 661–664.

108 A. Perloff, The Crystal Structure of Sodium Hexamolybdochromate(III) Octahydrate, $Na_3(CrMo_6O_{24}H_6)\cdot 8H_2O$, *Inorg. Chem.*, 1970, **9**, 2228–2239.

109 C. Wu, X. Lin, R. Yu, W. Yang, C. Lu and H. Zhuang, $[Na_4(H_2O)_7][Fe(OH)_6\ Mo_6O_{18}]$: A new [12] metallacrown-6 structure with an octahedrally coordinated iron at the center, *Sci. China, Ser. B Chem.*, 2001, **44**, 49–54.

110 A. Blazevic and A. Rompel, The Anderson-Evans polyoxometalate: From inorganic building blocks via hybrid organic-inorganic structures to tomorrows 'Bio-POM', *Coord. Chem. Rev.*, 2016, **307**, 42–64.

111 B. Artetxe, S. Reinoso, L. San Felices, L. Lezama, J. M. Gutiérrez-Zorrilla, C. Vicent, F. Haso and T. Liu, New Perspectives for Old Clusters: Anderson-Evans Anions as Building Blocks of Large Polyoxometalate Frameworks in a Series of Heterometallic 3d-4f Species, *Chem. - A Eur. J.*, 2016, **22**, 4616–4625.

112 Q. Li and Y. Wei, A series of unprecedented triol-stabilized $[H_3MW_6O_{24}]^{n-}$: The missing piece between A- and B-type Anderson-Evans polyoxometalates, *Chem. Commun.*, 2018, **54**, 1375–1378.

113 J. F. Keggin, Structure of the molecule of 12-phosphotungstic acid [2], *Nature*, 1933, **131**, 908–909.

114 J. Canny, A. Tézé, R. Thouvenot and G. Hervé, Disubstituted Tungstosilicates. 1. Synthesis, Stability, and Structure of the Lacunary Precursor Polyanion γ-$SiW_{10}O_{36}^{8-}$, *Inorg. Chem.*, 1986, **25**, 2114–2119.

115 U. B. Mioc and Z. P. Nedić, in *Encyclopedia of Membranes*, Springer Berlin Heidelberg, 2014, pp. 1–3.

116 N. I. Gumerova and A. Rompel, Synthesis, structures and applications of electron-rich polyoxometalates, *Nat. Rev. Chem.*, 2018, **2**, 0112.

117 X. López, J. M. Maestre, C. Bo and J. M. Poblet, Electronic properties of polyoxometalates: A DFT study of α/β-$[XM_{12}O_{40}]^{n-}$ relative stability (M=W, Mo and X a main group element), *J. Am. Chem. Soc.*, 2001, **123**, 9571–9576.

118 A. Tézé, E. Cadot, V. Béreau and G. Hervé, About the Keggin Isomers: Crystal Structure of $[N(C_4H_9)_4]_4$ -γ-$[SiW_{12}O_{40}]$, the γ-Isomer of the Keggin Ion. Synthesis and ^{183}W NMR Characterization of the Mixed γ-$[SiMo_2W_{10}O_{40}]^{n-}$ (n = 4 or 6), *Inorg. Chem.*, 2001, **40**, 2000–2004.

119 J. Rowsell and L. F. Nazar, Speciation and thermal transformation in alumina sols: Structures of the polyhydroxyoxoaluminum cluster $[Al_{30}O_8(OH)_{56}(H_2O)_{26}]^{18+}$ and its δ-keggin moiete [4], *J. Am. Chem. Soc.*, 2000, **122**, 3777–3778.

120 D. Sloboda-Rozner, K. Neimann and R. Neumann, Aerobic oxidation of aldehydes catalyzed by ε-Keggin type polyoxometalates $[Mo_{12}VO_{39}(\mu_2\text{-}OH)10H_2\{XII(H_2O)_3\}_4]$ (X = Ni, Co, Mn and Cu) as heterogeneous catalysts, *J. Mol. Catal. A Chem.*, 2007, **262**, 109–113.

121 X. López and J. M. Poblet, DFT study on the five isomers of $PW_{12}O_{40}^{3-}$: Relative stabilization upon reduction, *Inorg. Chem.*, 2004, **43**, 6863–6865.

122 X. López, J. J. Carbó, C. Bo and J. M. Poblet, Structure, properties and reactivity of polyoxometalates: A theoretical perspective, *Chem. Soc. Rev.*, 2012, **41**, 7537–7571.

123 F. A. Wells, *Structural Inorganic Chemistry*, Oxford University Press, Oxford, 1st Ed., 1945.

124 B. Dawson, The structure of the 9(18)-heteropoly anion in potassium 9(18)-tungstophosphate, $K_6(P_2W_{18}O_{62}).14H_2O$, *Acta Crystallogr.*, 1953, **6**, 113–126.

125 F. Q. Zhang, W. Guan, L. K. Yan, Y. T. Zhang, M. T. Xu, E. Hayfron-Benjamin and Z. M. Su, On the origin of the relative stability of wells-dawson isomers: A DFT study of α-, β-, γ-, α*-, β*-, and γ*-$[(PO_4)_2W_{18}O_{54}]^{6-}$ anions, *Inorg. Chem.*, 2011, **50**, 4967–4977.

126 L. Vilà-Nadal, S. G. Mitchell, D. L. Long, A. Rodríguez-Fortea, X. López, J. M. Poblet and L. Cronin, Exploring the rotational isomerism in non-classical Wells-Dawson anions $\{W_{18}X\}$: A combined theoretical and mass spectrometry study, *Dalt. Trans.*, 2012, **41**, 2264–2271.

127 A. Müller, J. Meyer, E. Krickemeyer and E. Diemann, Molybdenum Blue: A 200 Year Old Mystery Unveiled, *Angew. Chemie (International Ed. English)*, 1996, **35**, 1206–1208.

128 Q. Chen, C. Shen and L. He, Recent advances of polyoxometalate-catalyzed selective oxidation based on structural classification, *Acta Crystallogr. Sect. C Struct. Chem.*, 2018, **74**, 1182–1201.

129 D. Voß, R. Dietrich, M. Stuckart and J. Albert, Switchable Catalytic Polyoxometalate-Based Systems for Biomass Conversion to Carboxylic Acids, *ACS Omega*, 2020, **5**, 19082–19091.

130 U. Kortz, A. Müller, J. van Slageren, J. Schnack, N. S. Dalal and M. Dressel, Polyoxometalates: Fascinating structures, unique magnetic properties, *Coord. Chem. Rev.*, 2009, **253**, 2315–2327.

131 A. J. Kibler and G. N. Newton, Tuning the electronic structure of organic–inorganic hybrid polyoxometalates: The crucial role of the covalent linkage, *Polyhedron*, 2018, **154**, 1–20.

132 M. R. Horn, A. Singh, S. Alomari, S. Goberna-Ferrón, R. Benages-Vilau, N. Chodankar, N. Motta, K. (Ken) Ostrikov, J. MacLeod, P. Sonar, P. Gomez-Romero and D. Dubal, Polyoxometalates (POMs): from electroactive clusters to energy materials, *Energy Environ. Sci.*, 2021, **14**, 1652–1700.

133 X. López, J. A. Fernández and J. M. Poblet, Redox properties of polyoxometalates: New insights on the anion charge effect, *J. Chem. Soc. Dalt. Trans.*, 2005, **6**, 1162–1167.

134 X. López, C. Bo and J. M. Poblet, Electronic properties of polyoxometalates: Electron and proton affinity of mixed-addenda Keggin and wells-dawson anions, *J. Am. Chem. Soc.*, 2002, **124**, 12574–12582.

135 P. A. Aparicio, J. M. Poblet and X. Lõpez, Tungsten redox waves in $[XMW_{11}O_{40}]^{n-}$ (X = P, Si, Al and M = W, Mo, V, Nb, Ti) keggin compounds - Effect of localised/delocalised charges, *Eur. J. Inorg.*

Chem., 2013, **2013**, 1910–1916.

136 K. Maeda, H. Katano, T. Osakai, S. Himeno and A. Saito, Charge dependence of one-electron redox potentials of Keggin-type heteropolyoxometalate anions, *J. Electroanal. Chem.*, 1995, **389**, 167–173.

137 I. M. Mbomekallé, X. López, J. M. Poblet, F. Sécheresse, B. Keita and L. Nadjo, Influence of the heteroatom size on the redox potentials of selected polyoxoanions, *Inorg. Chem.*, 2010, **49**, 7001–7006.

138 J. J. J. Chen and M. A. Barteau, Electrochemical Properties of Keggin-Structure Polyoxometalates in Acetonitrile: Effects of Countercation, Heteroatom, and Framework Metal Exchange, *Ind. Eng. Chem. Res.*, 2016, **55**, 9857–9864.

139 N. Sonoyama, Y. Suganuma, T. Kume and Z. Quan, Lithium intercalation reaction into the Keggin type polyoxomolybdates, *J. Power Sources*, 2011, **196**, 6822–6827.

140 S. Uematsu, Z. Quan, Y. Suganuma and N. Sonoyama, Reversible lithium charge-discharge property of bi-capped Keggin-type polyoxovanadates, *J. Power Sources*, 2012, **217**, 13–20.

141 S. Hwang, S. M. Kim, S. M. Bak, K. Y. Chung and W. Chang, Investigating the Reversibility of Structural Modifications of $Li_xNi_yMn_zCo_{1-y-z}O_2$ Cathode Materials during Initial Charge/Discharge, at Multiple Length Scales, *Chem. Mater.*, 2015, **27**, 6044–6052.

142 A. Yoshino, in *Lithium-Ion Batteries: Advances and Applications*, Elsevier B.V., 2014, pp. 1–20.

143 E. Hu, X. Wang, X. Yu and X. Q. Yang, Probing the Complexities of Structural Changes in Layered Oxide Cathode Materials for Li-Ion Batteries during Fast Charge-Discharge Cycling and Heating, *Acc. Chem. Res.*, 2018, **51**, 290–298.

144 N. Mohamed and N. K. Allam, Recent advances in the design of cathode materials for Li-ion batteries, *RSC Adv.*, 2020, **10**, 21662–21685.

145 A. Ueda and T. Ohzuku, Solid-State Redox Reactions of $LiCoO_2$ (R3m) for 4 Volt Secondary Lithium Cells, *J. Electrochem. Soc.*, 1994, **141**, 2972–2977.

146 A. Yamada, H. Koizumi, S.-I. Nishimura, N. Sonoyama, R. Kanno, M. Yonemura, T. Nakamura and Y. Kobayashi, Room-temperature miscibility gap in LixFePO4., *Nat. Mater.*, 2006, **5**, 357–60.

147 A. P. Ginsberg, Ed., *Inorganic Syntheses*, John Wiley & Sons, Inc, 1990, vol. 27.

148 M. Genovese and K. Lian, Polyoxometalate modified inorganic–organic nanocomposite materials for energy storage applications: A review, *Curr. Opin. Solid State Mater. Sci.*, 2015, **19**, 126–137.

149 Y.-F. Song and R. Tsunashima, Recent advances on polyoxometalate-based molecular and composite materials, *Chem. Soc. Rev.*, 2012, **41**, 7384–7402.

2. Solution Phase Voltammetry of Polyoxometalates in Non-Aqueous & Aqueous Solvents

2.1 Introduction

As alluded to previously, polyoxometalates (POMs) represent a class of early transition metal oxide clusters that possess an unparalleled range of physical and chemical properties. Owing to their multitudinous architectures, POMs are prolific in several research disciplines, including medicine[1,2], nanotechnology[3,4], macromolecular crystallography[5,6], catalysis[7,8], molecular magnetism, electrochemistry[9,10], and materials chemistry[11]. Arguably, perhaps the most intriguing feature of POMs is their rich electrochemistry. These species have been identified as powerful electron reservoirs due to their propensity to participate in multi – electron redox reactions rapidly, reversibly and under marginal structural rearrangement. [9,12] Moreover, these redox properties are tuneable via substitution of the framework metals, central heteroatoms and countercations.[13] Different solvents can also influence the redox properties of POMs which provides scope for tailoring and engineering these redox – active materials for a specified application.

Of course, this electrochemical tuneability means that the electrochemical behaviour of POMs in solution can be complicated and this behaviour must therefore be interpreted with respect to the particular set of conditions. POMs can undergo several rapid one- and two- electron reversible reductions and sometimes further irreversible multi – electron reductions with concomitant decomposition. It is well known that the position of POM redox couples can be influenced by pH, namely that the redox peaks can converge and shift to more positive potentials with decreasing pH. This is because POMs can be regarded as weak Lewis bases due to their surface oxo ligands. When reduction occurs, the charge density of the POM anion is increased, and

consequently its basicity. With each subsequent reduction, the anion acquires an increasing negative charge, thereby encouraging protonation. This results in the negative charge being lowered and allowing further reductions to proceed. However, in neutral aqueous or organic solutions where no protonation can occur, both Keggin and Dawson-type anions may undergo several one-electron reductions. Many studies exist in the literature which corroborate these types of observations.[14–17] A particularly comprehensive compilation of electrochemical studies of redox-active POMs in aqueous and organic solvent systems can be found in the review by Sadakane and Steckhan.[18]

2.2 Approach

Cyclic Voltammetry (CV) is the electroanalytical technique of choice to reveal the redox properties of an active species in solution. This technique is used here to probe the electrochemical behaviour of a selected library of POMs. A classic three – electrode cell setup is used as illustrated in Figure 1.

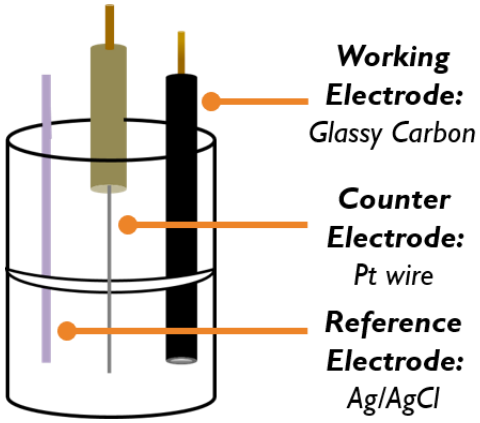


Figure 1 - Three electrode cell setup for solution phase cyclic voltammetry consisting of a glassy carbon working electrode, platinum wire counter electrode and Ag/AgCl reference electrode.

During a CV experiment, a potential is applied to the working electrode and is scanned over a potential range of interest, as a function of time. The potential scan is then reversed at a set potential (switching potential) and scanned back in the direction of the initial potential. The current response is recorded, providing a current *vs.* potential graph, known as a voltammogram.

This current results from the active species of interest being reduced or oxidised, giving rise to a reduction (E_{pc}) and oxidation peak (E_{pa}). Figure 2 depicts a typical simplified voltammogram for a reversible one – electron redox process. The reduction process is initiated by scanning negatively from point A until the switching potential, point C. The corresponding reduction peak occurs at point B which is called the 'cathodic' peak potential (E_{pc}) and the resulting current is the 'cathodic' current (i_{pc}). The E_{pc} represents the point at which all of the substrate at the working electrode has been reduced. After point C, the potential is reversed to the positive region, until point E, the final potential. The positive scan results in a parallel oxidation peak at point D with the anodic peak potential (E_{pa}) and anodic current. Accordingly, the E_{pa} represents the point at which the substrate at the working electrode surface has been oxidised.

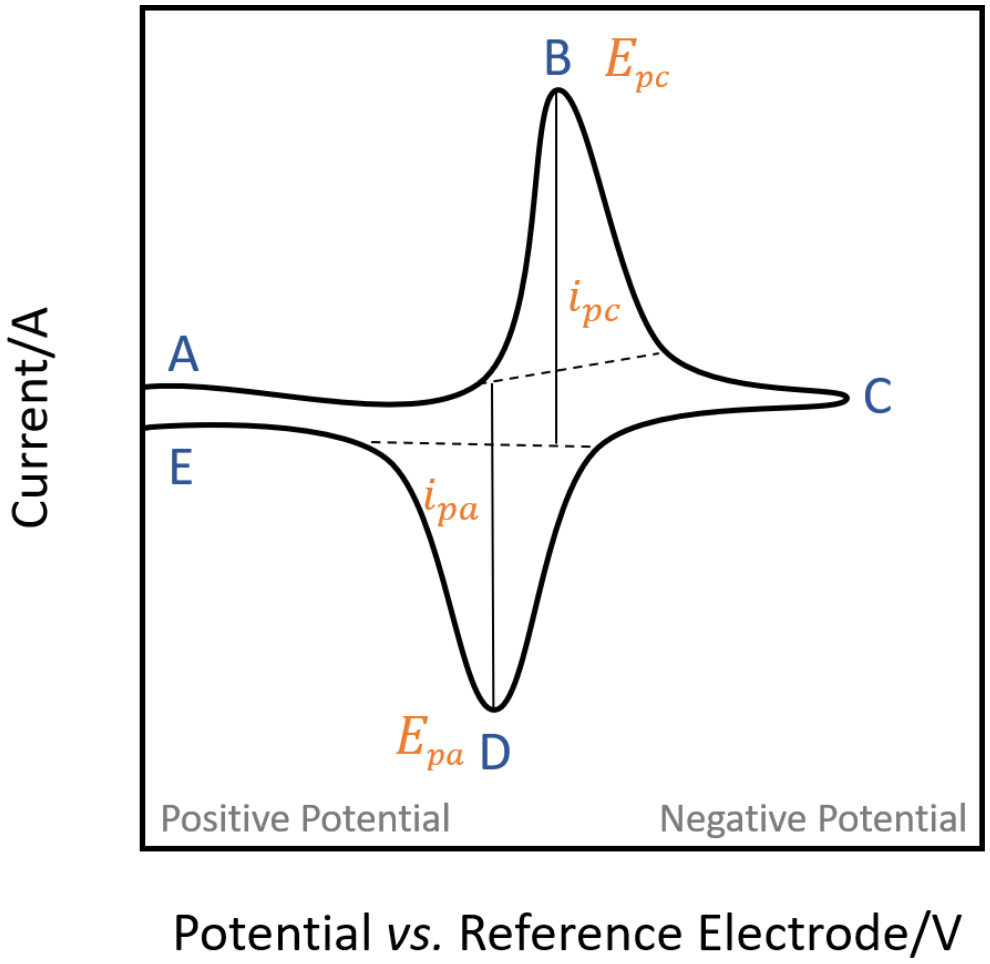


Figure 2 - Cylic voltammogram depicting the US convention to report CV data: potential axis moves from positive potential to negative potential.

The term 'reversible' is an ambiguous and often misused term in electrochemistry. The following passage serves to clarify the ways in which a reaction can be defined as 'reversible'.

The reduction of an oxidised form of a solution species at a solid electrode interface can be represented by the following equation:

$$Ox + ne^- \leftrightarrow Red \quad (1)$$

where n represents the stoichiometric number of electrons for the process and Red signifies the reduced form of the solution species, Ox. This is the reaction for the forward scan (toward negative potentials). The oxidised form of the solution species can be regenerated from the reduced form if the product is stable on the time scale of the voltammetric experiment, thus demonstrating *chemical reversibility* of the solution species.

Electron transfer is a heterogenous process occurring between a solid working electrode and a solution species close to, or at the surface of the electrode. *Electrochemical reversibility* describes the rate of electron transfer and a reversible wave arises when the rate of electron transfer is very fast. It is important to note that this rate is related to the ease of electron transfer, meaning it occurs facilely and frequently whenever an analyte molecule approaches the electrode, as opposed to the speed of the electron transfer (smaller ΔE_p values). When there is a high barrier to electron transfer (*electrochemical irreversibility*), electron transfer reactions are slower and thus more negative potentials are required to facilitate reduction reactions, giving rise to larger ΔE_p values (vide infra).

There are several important parameters to note when conducting data analysis of cyclic voltammograms and determining electrochemical reversibility:

1. The peak potentials of the forward and reverse peaks (E_{pc} and E_{pa}), allowing for calculation of the peak-to-peak separation ΔE_p

2. The ratio of the peak current (i_p) of the reverse scan and forward scan ($\frac{i_{pa}}{i_{pc}}$)
3. The dependence of peak current on the scan rate (ν)

For a chemically and electrochemically reversible process, the peak potentials at which the current reaches a maximum or minimum during the electron transfer event are referred to as E_{pc} and E_{pa}. These E_p values do not change with scan rate for reversible waves, whereas the E_p values of an irreversible wave will tend to shift with increasing scan rates. A voltammogram that features a forward and a reverse wave, regardless of whether it is reversible or irreversible, should be defined by its midpoint potential, E_{mid} , which is the potential exactly in the middle of the two peaks as defined by Equation 2:

$$E_{mid} = \frac{E_{pc} + E_{pa}}{2} \quad (2)$$

The difference of the two peak potentials, ΔE_p, can also be used to ascertain the electrochemical reversibility of a redox couple with Equation 3[19]:

$$\Delta E_p = \frac{59\ mV}{n} \quad (3)$$

for the case of a reversible single electron transfer. This value is independent of the scan rate for fast electron transfer. Increasing values of ΔE_p as a function of increasing scan rate indicates the presence of a quasi-reversible process or electrochemical irreversibility as well as uncompensated solution resistance. The ΔE_p is also useful in determining n, as a reversible two-electron transfer (where $n = 2$) will give an approximate ΔE_p of 29 mV. However, in reality, this value of ΔE_p is seldom observed as it is an ideal theoretical value only equal to 59 mV at exactly 25 °C. Thus, processes with ΔE_p values close to the ideal value can be deemed reversible, but larger deviations can warrant further inquiry.

The stability of an electrochemically generated product can be assessed by observing the current ratio for the forward and reverse scan. If the product is stable during the timescale of the experiment, then the peak observed for the

return wave should be of a similar magnitude to that of the forward scan. This indicates that electron transfer is reversible in both directions, such that the peak current ratio is at unity:

$$\frac{i_{pa}}{i_{pc}} = 1 \tag{4}$$

However, the measurement of peak current comes with the caveat that more complicated voltammograms present difficulties in locating a proper baseline from which to define the magnitude of a peak.

Using the Randles-Ševčík equation (Equation 5), the scan rate dependence of the peak current can be a useful diagnostic tool for the characterisation of an electrochemically reversible process. The equation is as follows:

$$i_p = 0.446nFAC\left(\frac{nF\nu D}{RT}\right)^{\frac{1}{2}} \tag{5}$$

where i_p = peak current in amps, n = number of electrons transferred in the redox event, A = electrode area in cm^2, F= Faraday's Constant in C mol^{-1}, D = diffusion coefficient of the analyte cm^2 s^{-1}, C = bulk concentration in mol cm^{-3}, ν = scan rate in V s^{-1}, R = gas constant in J K^{-1} mol^{-1} and T = temperature in K. For an electrochemically reversible electron transfer process, that involves freely diffusing redox species, a plot of i_p *vs.* $\nu^{\frac{1}{2}}$ should be linear. Deviations from linearity are indicative of complications in the kinetics of the observed electron transfer or that the reaction is in the quasi-reversible or irreversible regime.

In some instances, throughout this chapter, differential pulse voltammetry (DPV) has been used to determine the number of electrons involved for a given redox process. DPV is a voltammetric technique which is the first derivative of linear sweep voltammetry (LSV), a method where the current at the working electrode is measured as the potential between the working and references electrodes is swept linearly over time. DPV offers an enhanced discrimination of Faradaic currents (i.e. electron transfer to and from an electrode) where the current is measured immediately before the potential

pulse is applied and then again after a predetermined time. This current variation is then plotted as a function of potential, giving rise to peaks. DPV is mainly useful in separating closely overlapped redox couples, although it can also be used as a diagnostic tool to help determine the number of electrons in a redox couple. For a reversible process at 25 °C the width of the peak at half height (full width at half maximum, FWHM) is given by Equation 6[20]:

$$FWHM = \frac{3.52RT}{nF} = \frac{90.4}{n}\ (mV) \qquad (6)$$

Where the widths for n = 1, 2, 3 are 90.4, 45.2 and 30.1 mV respectively. Nevertheless, it must be taken into account that DPV presents two limitations[20]:

1. Even though DPV works well with solid working electrodes under stationary conditions, in principle, it requires the use of the dropping mercury electrode (since by definition, polarographic measurements such as LSV from which DPV is derived, use dropping mercury working electrodes). Therefore, the reliability of DPV can vary with the use of alternative working electrodes;
2. It employs rather low scan rates (lower than 0.02 V s^{-1}), which can lead to difficulty in interpreting responses in those cases in which the electrogenerated species are not stable (i.e., they undergo chemical reactions).

Of course, the relationship described above can be used in principle to determine the number of electrons, but taking into account the limitations, discrepancies in reversibility and the fact that real peaks are wider (for example experiments that are conducted under non – standard conditions), experimental variation in FWHM values is to be expected.

2.3 Aims

This chapter seeks to evaluate the electrochemical properties of selected Keggin and Wells-Dawson type POMs, presented with a view toward their potential application in rechargeable lithium batteries. The redox properties of POMs with different countercations (H^+, K^+, $[N(C_4H_9)_4]^+$ (tetra-n-

butylammonium,TBA)) and different framework metals (W and Mo) are compared in N, N – dimethylformamide (DMF) with a tetra-n-butylammonium heaxafluroophosphate ($TBAPF_6$) supporting electrolyte. Other structural variations include a lacunary structure, an inorganic-organic hybrid POM and a transition metal-substituted POM. DMF was the solvent of choice due to its relatively wide potential window (+1.4 to -4 V *vs.* Fc/Fc^+) and more importantly, all the POM materials showed good solubility in DMF.

Additionally, the redox properties of three plenary POM motifs are studied in aqueous solvents, namely sulphuric acid and perchlorate – based (perchlorates ($HClO_4$, $LiClO_4$, $NaClO_4$, $Mg(ClO_4)_2$) supporting electrolytes. Here we observe how the differing cations present in the electrolyte dictates the electrochemical behaviour of the POM.

2.4 Results & Discussion

2.4.1 Voltammetry in Organic Solvents – N, N-Dimethylformamide

2.4.1.1 Wells-Dawson Polyoxotungstates $[P_2W_{18}O_{62}]^{6-}$

The voltammetry of the following polyoxotungstates $H_6[P_2W_{18}O_{62}]$, $TBA_6[P_2W_{18}O_{62}]$ and $K_6[P_2W_{18}O_{62}]$ was studied in an aprotic solvent system of DMF containing 0.1M tetrabutylammonium hexafluorophosphate ($TBAPF_6$) as the supporting electrolyte. The cyclic voltammogram of $H_6[P_2W_{18}O_{62}]$, denoted $\{H_6W_{18}\}$, shows four one – electron redox couples; I/I', II/II', III/III', IV/IV' (Equations 1 – 4). These appear from positive to negative potentials with reduction occurring at the 'cathodic' current (positive current) and the corresponding oxidation at the 'anodic' peak current (negative current) (Figure 3). The first three pairs are more well-defined than the fourth. The mid-point potentials E_{mid} and peak-to-peak separations, ΔE_p of each redox couple are in Table 1. The ΔE_p values indicate that these processes are indeed reversible as they are close to the theoretical value of 59 mV for a reversible freely diffusing redox species.

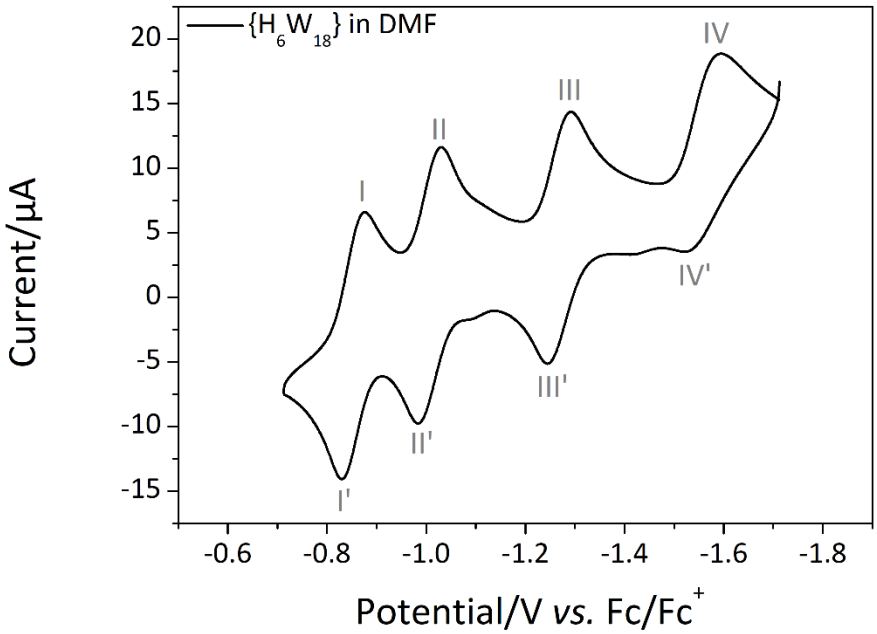


Figure 3 - CV of $\{H_6W_{18}\}$ in 1M $TBAPF_6$ in DMF, performed using a 3 mm GC WE, Pt CE, Ag wire pseudoreference electrode and Fc/Fc^+ internal reference electrode. The scan rate was 100 mV s^{-1}.

Equations 1 – 4: Redox couples for $\{H_6W_{18}\}$ in 1M $TBAPF_6$ in DMF.

$$\text{I/I'}: [P_2W_{18}O_{62}]^{6-} + e^- \leftrightarrow [P_2W_{18}O_{62}]^{7-} \quad (1)$$

$$\text{II/II'}: [P_2W_{18}O_{62}]^{7-} + e^- \leftrightarrow [P_2W_{18}O_{62}]^{8-} \quad (2)$$

$$\text{III/III'}: [P_2W_{18}O_{62}]^{8-} + e^- \leftrightarrow [P_2W_{18}O_{62}]^{9-} \quad (3)$$

$$\text{IV/IV'}: [P_2W_{18}O_{62}]^{9-} + e^- \leftrightarrow [P_2W_{18}O_{62}]^{10-} \quad (4)$$

Table 1 - Observed Midpoint Potentials (E_{mid}) and Peak-to- Peak Separations (ΔE_p) for $\{H_6W_{18}\}$ in 1M $TBAPF_6$ in DMF.

Process	E_{mid}/V	ΔE_p/mV
I/I'	– 0.85	37
II/II'	–1.01	39
III/III'	–1.27	41
IV/IV'	–1.56	62

In contrast, when TBA is the countercation, different redox behaviour is observed. Three successive redox couples appear for $\{(TBA_6)W_{18}\}$ which correspond to three one-electron waves (processes I – III, equations 4 – 6, Figure 4). The ΔE_p values for all three processes indicate they are reversible as they are very close to the ideal value of 59 mV.

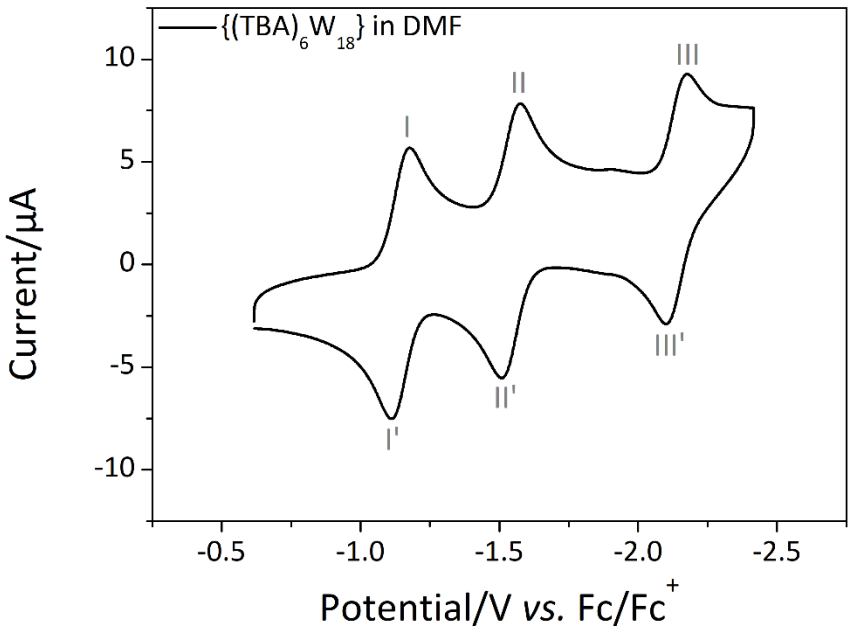


Figure 4 - CV of $\{(TBA)_6W_{18}\}$ in 1M $TBAPF_6$ in DMF, performed using a 3 mm GC WE, Pt CE, Ag wire pseudoreference electrode and Fc/Fc^+ internal reference electrode. The scan rate was 100 mV s^{-1}.

Equations 4 – 6: Redox couples for $\{(TBA)_6W_{18}\}$ in 1M $TBAPF_6$ in DMF.

$$\mathbf{I/I'}: [P_2W_{18}O_{62}]^{6-} + e^- \longleftrightarrow [P_2W_{18}O_{62}]^{7-} \quad (4)$$

$$\mathbf{II/II'}: [P_2W_{18}O_{62}]^{7-} + e^- \longleftrightarrow [P_2W_{18}O_{62}]^{8-} \quad (5)$$

$$\mathbf{III/III'}: [P_2W_{18}O_{62}]^{8-} + e^- \longleftrightarrow [P_2W_{18}O_{62}]^{9-} \quad (6)$$

Table 2 - Observed Midpoint Potentials (E_{mid}) and Peak-to- Peak Separations (ΔE_p) for $\{(TBA)_6W_{18}\}$ in 1M $TBAPF_6$ in DMF.

Process	E_{mid}/V	ΔE_p/mV
I/I'	–1.14	62
II/II'	–1.54	62
III/III'	–2.14	72

The electrochemical behaviour of $\{K_6W_{18}\}$ in DMF is different yet again. Four reduction processes up to –2.2 V *vs.* Fc/Fc^+ are observed, however only two corresponding oxidations are discernible (Figure 5). The first two waves are monoelectronic (equations 4 – 5 above). A sharp irreversible oxidation is observed shortly after the II/II' redox couple. This is likely due to a degradative process that occurs in solution at more negative potentials, resulting in a deposition of degraded POM on the working electrode, thereby obscuring the return waves for reductions III and IV. The ΔE_p values calculated for processes I and II indicate reversibility. This degradation process does not appear in aqueous conditions, most likely a consequence of the increased solubility of the potassium salt POM in aqueous solvent.

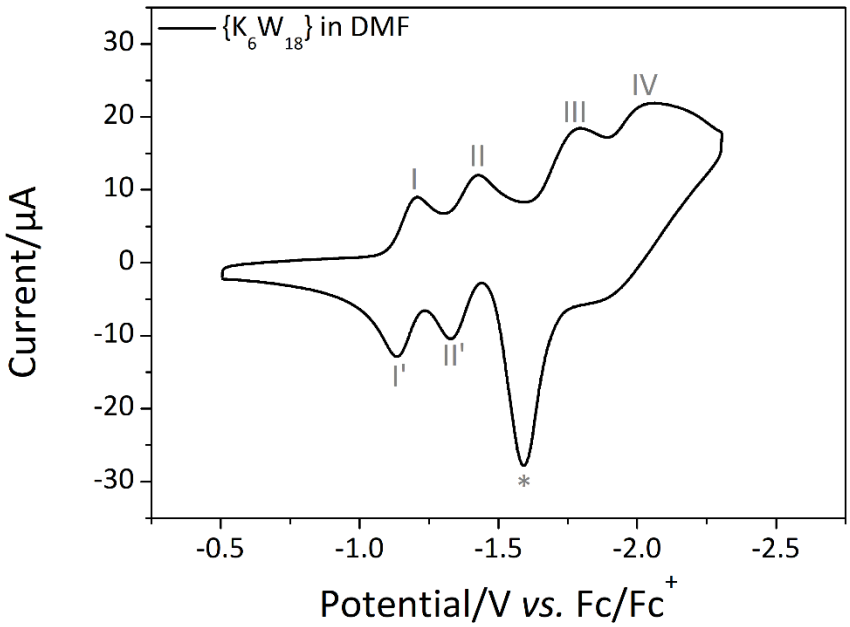


Figure 5 - CV of $\{K_6W_{18}\}$ in 1M $TBAPF_6$ in DMF, performed using a 3 mm GC WE, Pt CE, Ag wire pseudoreference electrode and Fc/Fc^+ internal reference electrode. The scan rate was 100 mV s^{-1}.

Table 3 - Observed Midpoint Potentials (E_{mid}) and Peak-to- Peak Separations (ΔE_p) for $\{K_6W_{18}\}$ in 1M $TBAPF_6$ in DMF.

Process	E_{mid}/V	ΔE_p/mV
I/I'	–1.17	69
II/II'	–1.34	91

All four redox processes I—IV for $\{H_6W_{18}\}$ have the most positive E_{mid} values *vs.* Fc/Fc^+. The midpoint potentials for processes I and II for $\{K_6W_{18}\}$ are shifted by approximately 320 mV and 376 mV negative of processes I and II for $\{H_6W_{18}\}$. This negative shift coupled with the larger ΔE_p value (91 mV for process II) indicates that process II for $\{K_6W_{18}\}$ has a higher barrier to electron transfer and the processes are quasi-reversible as opposed to the reversible waves observed for $\{H_6W_{18}\}$. Process I for $\{(TBA_6)W_{18}\}$ which is a one – electron process has a midpoint potential that is 290 mV more negative than the mean E_{mid} values of the monoelectronic processes I and II for $\{H_6W_{18}\}$; but is at a very

similar potential to the mean E_{mid} values for I and II of {(TBA$_6$)W$_{18}$} (Figure 6). Lastly the final two-electron process for {(TBA$_6$)W$_{18}$} is centred at –2.14 V and occurs at the most negative potential *vs.* Fc/Fc$^+$.

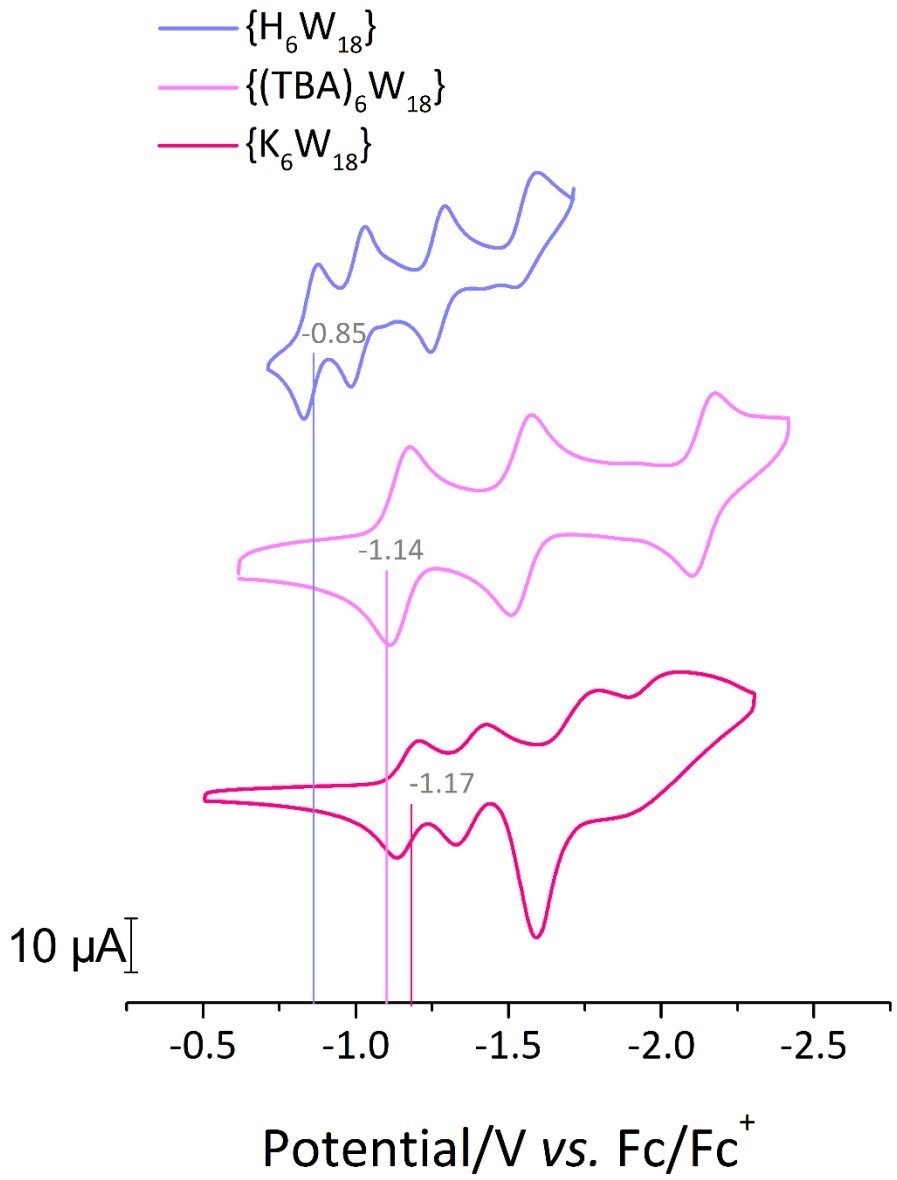


Figure 6 – Stacked solution phase CVs of {H$_6$W$_{18}$}, {(TBA)$_6$W$_{18}$} and {K$_6$W$_{18}$} highlighting shifts in E_{mid} values.

2.4.1.2 Keggin Polyoxotungstates/Polyoxomolybdate $[PW_{12}O_{40}]^{3-}$ /$[PMo_{12}O_{40}]^{3-}$ in DMF

Phosphotungstic acid, H$_3$[PW$_{12}$O$_{40}$], abbreviated {H$_3$W$_{12}$}, has the strongest acidity among Keggin-type heteropoly acids. Due to their strong

acidity and redox properties, they have been applied as homogenous catalysts and prompted investigation into their use as heterogenous catalysts.[21–23] Solid phosphotungstic acid has also been explored as a potential solid acid to supplant corrosive and environmentally toxic liquid acid catalysts that are currently used by industry.[24] Investigations into the proton positions and acid strength of phosphotungstic acid have led to the consideration of $\{H_3W_{12}\}$ as a superacid.[25,26]

Keggin-type heteropolyanions can accept a limited number of electrons without decomposition, and in some cases the reduced compounds have been isolated.[18] The voltammetry of the following Keggin moieties $H_3[PW_{12}O_{40}]$, $TBA_3[PW_{12}O_{40}]$ and $H_3[PMo_{12}O_{40}]$ was studied in an aprotic solvent system of DMF containing 0.1M tetrabutylammonium hexafluorophosphate ($TBAPF_6$) as the supporting electrolyte. $K_3[PW_{12}O_{40}]$ only partially dissolved in DMF and did not exhibit any redox activity.

The CV of $\{H_3W_{12}\}$ shows three well-defined redox waves which are all monoelectronic processes (processes I-III Figure 7, equations 7 – 9).

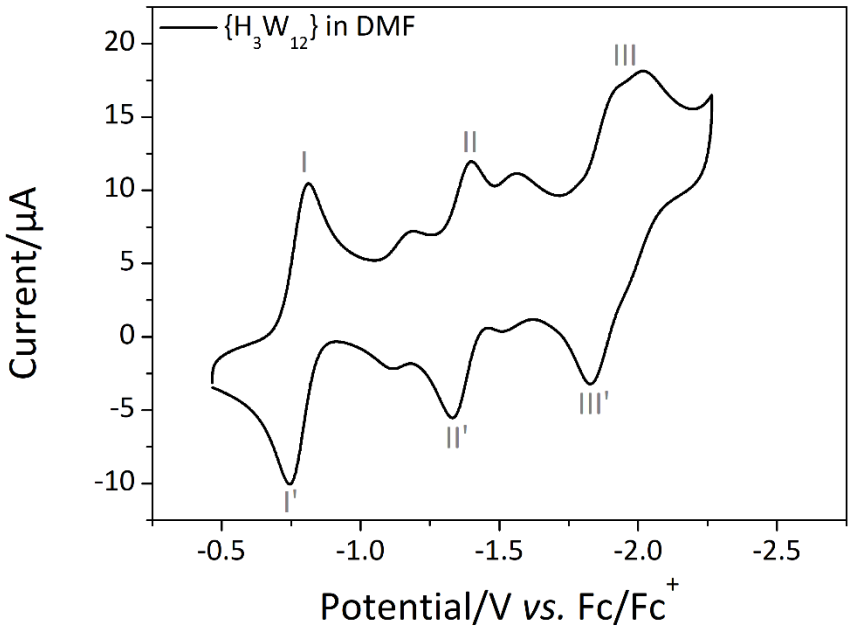


Figure 7 - CV of $\{H_3W_{12}\}$ in 1M $TBAPF_6$ in DMF, performed using a 3 mm GC WE, Pt CE, Ag wire pseudoreference electrode and Fc/Fc^+ internal reference electrode. The scan rate was 100 mV s^{-1}.

Equations 7 – 9 - Redox couples for $\{H_3W_{12}\}$ in 1M $TBAPF_6$ in DMF.

I/I': $[PW_{12}O_{40}]^{3-} + e^- \longleftrightarrow [PW_{12}O_{40}]^{4-}$ (7)

II/II': $[PW_{12}O_{40}]^{4-} + e^- \longleftrightarrow [PW_{12}O_{40}]^{5-}$ (8)

III/III': $[PW_{12}O_{40}]^{5-} + e^- \longleftrightarrow [PW_{12}O_{40}]^{6-}$ (9)

Table 4 - Observed Midpoint Potentials (E_{mid}) and Peak-to- Peak Separations (ΔE_p) for $\{H_3W_{12}\}$ in 1M $TBAPF_6$ in DMF.

Process	E_{mid}/V	ΔE_p/mV
I/I'	–0.7	63
II/II'	–1.37	59
III/III'	–1.91	165

The ΔE_p values for process I and II are 63 and 59 mV respectively, signifying their reversible nature. However, process III has a much greater value of 165 mV, and is therefore quasi – reversible. Interestingly, shoulders in the voltammogram can be observed close to process II. Typically, these can be associated with protonation events. Since the solvent is aprotic, it may be possible that the acidic Keggin introduces adventitious water into the electrolyte system, potentially allowing for 'self-protonation' or proton – coupled charge transfer. This hypothesis would require further investigation.

$\{(TBA)_3W_{12}\}$ has an almost identical voltammogram, with three monoelectronic waves and with no major shifts in midpoint potentials (Figure 8 Equations 10 – 12). The ΔE_p values follow the same trend as $\{H_3W_{12}\}$ with process I and II being reversible but process III being irreversible (Table 5).

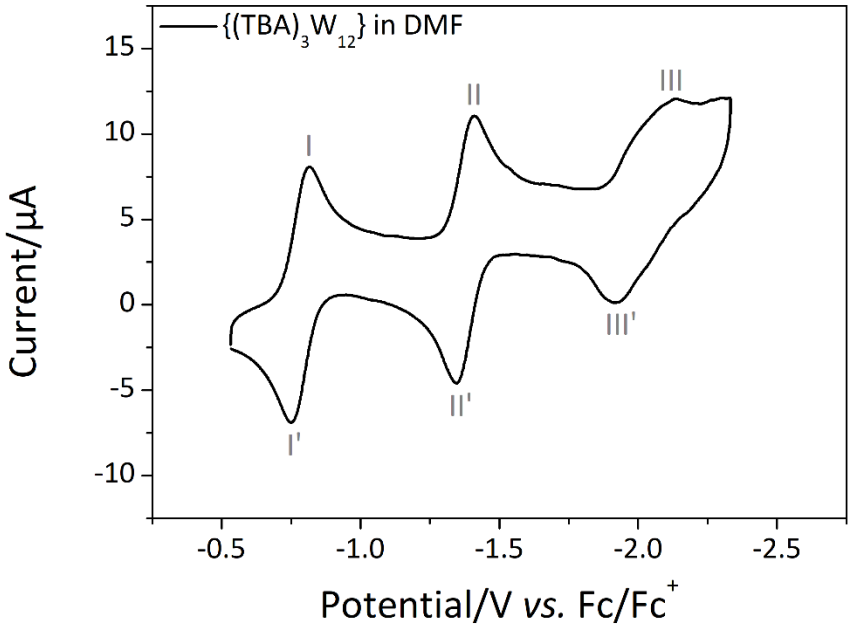


Figure 8 - CV of $\{(TBA)_3W_{12}\}$ in 1M $TBAPF_6$ in DMF, performed using a 3 mm GC WE, Pt CE, Ag wire pseudoreference electrode and Fc/Fc^+ internal reference electrode. The scan rate was 100 mV s^{-1}.

Equations 10 – 12 - Redox couples for $\{(TBA)_3W_{12}\}$ in 1M $TBAPF_6$ in DMF.

I/I': $[PW_{12}O_{40}]^{3-} + e^- \leftrightarrow [PW_{12}O_{40}]^{4-}$ (10)

II/II': $[PW_{12}O_{40}]^{4-} + e^- \leftrightarrow [PW_{12}O_{40}]^{5-}$ (11)

III/III': $[PW_{12}O_{40}]^{5-} + e^- \leftrightarrow [PW_{12}O_{40}]^{6-}$ (12)

Table 5 - Observed Midpoint Potentials (E_{mid}) and Peak-to- Peak Separations (ΔE_p) for $\{(TBA)_3W_{12}\}$ in 1M $TBAPF_6$ in DMF.

Process	E_{mid}/V	ΔE_p/mV
I/I'	–0.78	59
II/II'	–1.38	59
III/III'	–2.02	202

Due to the facile hydrolysis of $[PMo_{12}O_{40}]^{3-}$, it is difficult to obtain well-defined redox waves in aqueous electrolytes and so much of the literature is centred on voltammetry in organic solvents to stabilise the polymolybdate anion.[18] In the experimental conditions of this study, $\{(TBA)_3Mo_{12}\}$ undergoes

three one-electron reductions, similar to $\{H_3W_{12}\}$ and $\{(TBA)_3W_{12}\}$ (Figure 9). Polyoxomolybdates are more readily reduced than polyoxotungstates.[18] This is confirmed by all three redox waves appearing at much more positive potentials than those of their tungsten analogues. The ΔE_p values show that all three processes are reversible (Table 6), different from the irreversibility observed for the third processes of $\{H_3W_{12}\}$ and $\{(TBA)_3W_{12}\}$.

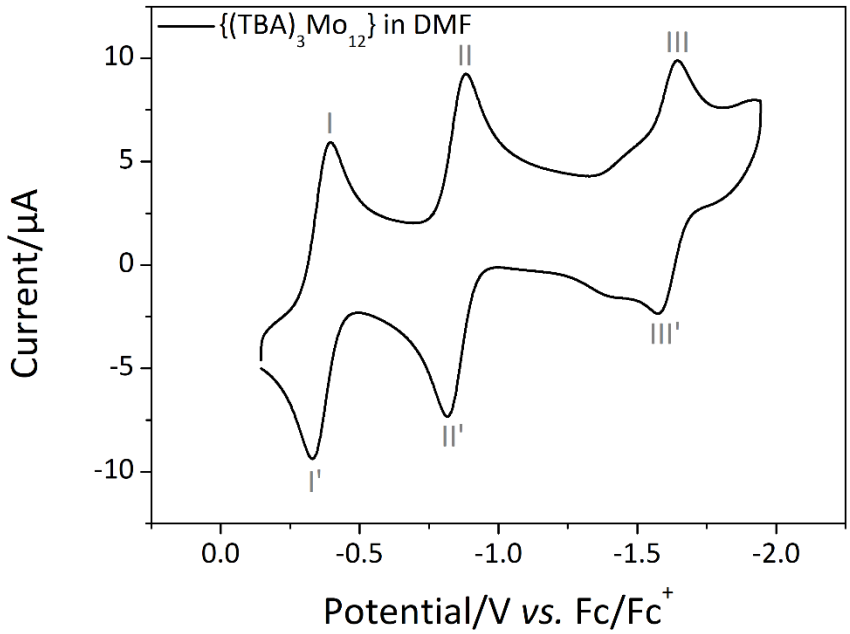


Figure 9 - CV of $\{(TBA)_3Mo_{12}\}$ in 1M $TBAPF_6$ in DMF, performed using a 3 mm GC WE, Pt CE, Ag wire pseudoreference electrode and Fc/Fc^+ internal reference electrode. The scan rate was 100 mV s^{-1}.

Equations 13 – 15 - Redox couples for $\{(TBA)_3Mo_{12}\}$ in 1M $TBAPF_6$ in DMF.

$$\mathbf{I/I'}: [PMo_{12}O_{40}]^{3-} + e^- \longleftrightarrow [PMo_{12}O_{40}]^{4-} \quad (13)$$

$$\mathbf{II/II'}: [PMo_{12}O_{40}]^{4-} + e^- \longleftrightarrow [PMo_{12}O_{40}]^{5-} \quad (14)$$

$$\mathbf{III/III'}: [PMo_{12}O_{40}]^{5-} + e^- \longleftrightarrow [PMo_{12}O_{40}]^{6-} \quad (15)$$

Table 6 - Observed Midpoint Potentials (E_{mid}) and Peak-to- Peak Separations (ΔE_p) for $\{(TBA)_3Mo_{12}\}$ in 1M $TBAPF_6$ in DMF.

Process	E_{mid}/V	ΔE_p/mV
I/I'	–0.36	55
II/II'	–0.85	63
III/III'	–1.61	64

The ΔE_p values of processes I – III for $\{H_3W_{12}\}$ and $\{(TBA)_3W_{12}\}$ fall at very similar potentials, with process III for $\{(TBA)_3W_{12}\}$ being shifted approximately 100 mV more negative than for process III of $\{H_3W_{12}\}$. All three redox processes for $\{(TBA)_3Mo_{12}\}$ occur at much more positive potentials than both tungsten analogues and this trend agrees with the literature. Processes I – III for $\{(TBA)_3Mo_{12}\}$ are positively shifted by approximately 424 mV, 525 mV and 408 mV respectively, in relation to $\{(TBA)_3W_{12}\}$. Figure 10 highlights these differences among the different cation-substituted and addenda metal-substituted Keggin species.

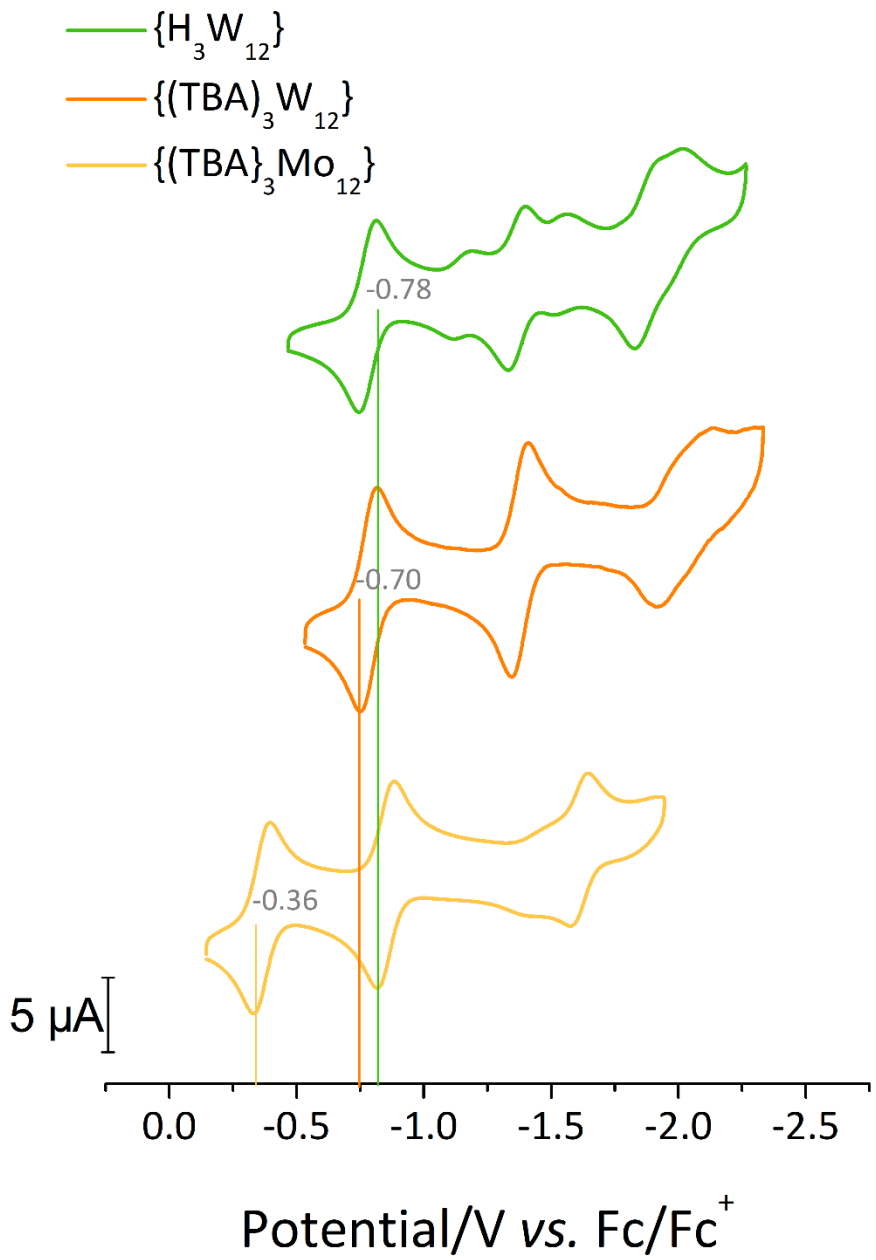


Figure 10 - Stacked solution phase CVs of $\{H_3W_{12}\}$, $\{(TBA)_3W_{12}\}$ and $\{(TBA)_3Mo_{12}\}$ highlighting shifts in E_{mid} values.

2.4.2 Modified Polyoxometalates

2.4.2.1 Hybridised POMs

The definition of hybrid polyoxometalates is very broad, as it is an umbrella term for functionalisation through the addition of inorganic or organic components to design composite materials. Hybridisation is a means of synergising the intrinsic properties of the organic and inorganic moieties, to directly influence the physiochemical properties of the POM such as photo(electro)chemistry, catalytic activity, and solubility.

Hybrid POMs can be classified based on the nature of the component and how it is integrated into the plenary POM structure. [27] Inorganic hybrids pertain to the addition of transition metals or f-block metals to the POM. This strategy affords a convenient platform for the stabilisation of unusually high oxidation state metal oxo species, as the POM can coordinate and electrostatically stabilise the highly charged cationic centre.[28–30] These polynuclear complexes are important building blocks for the construction of highly connected coordination frameworks.[31,32] Additionally, transition metal substituted POMs have demonstrated multifaceted bioactivity that encompasses anti-viral, anti-cancer and anti-bacterial properties.[33,34]

Organic hybrids can be separated into two distinct categories with respect to the nature of the interaction between the organic components: class I and class II hybrids. Class I hybrids refer to a system where the association between the POM and organic component is dictated by non-covalent interactions such as electrostatics where the anionic POM pairs with organic cations.[35] Other examples include hydrogen bonding and host-guest interactions.[36,37] On the contrary, the organic and inorganic moieties in class II hybrids are linked by covalent bonds. Organic chemistry allows for a multitude of possibilities of hybrid structural diversity tailored to a given application. Accordingly, organofunctionalisation of POMs is represented by an exhaustive literature precedent. [38–40]

2.4.2.2 Organic-Inorganic Hybrid

While it is possible to directly graft organic groups onto plenary polyoxovanadate and polyoxomolybdate anions, this is not the case for polyoxotungstates. Covalent functionalisation of Keggin and Dawson anions must proceed via the lacunary species. POMs are synthesised via condensation reactions in acidic solution, and they can be partially disassembled in controlled basic conditions. The removal of one or more addenda atoms from the plenary POM results in a subclass of POMs with vacancies in their structure, known as lacunary POMs.

Condensation of phenyl phosphonic acid with the mono-lacunary Dawson anion $[P_2W_{17}O_{61}]^{10-}$, yielded the hybrid POM $K_6[P_2W_{17}O_{59}(PO_3C_6H_5)_2]$ (referred to as $\{K_6W_{17}\}$hybrid, Figure 11). The nature of the grafted organic groups is known to have a major effect on the redox behaviour of hybrid-POMs.[41–43]

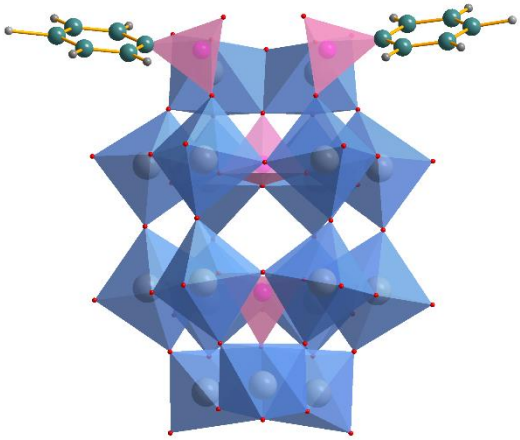


Figure 11 - Polyhedral representation of the hybrid POM $K_6[P_2W_{17}O_{59}(PO_3C_6H_5)_2]$, referred to as $\{K_6W_{17}\}$hybrid.

CV experiments can be used to determine the magnitude of the effect of the organophosphonate moieties on the electronic properties of the POM core. The hybrid shows three quasi-reversible peaks compared to its equivalently charged plenary parent anion $[P_2W_{18}O_{62}]^{6-}$ (Figure 12). Each peak

corresponds to a one-electron process (equations 1–3). All three processes occur at more positive potentials than the processes observed for the plenary POM $\{K_6W_{18}\}$. Processes I and II for the hybrid $\{K_6W_{17}\}$ are positively shifted by 410 mV and 330 mV respectively when compared to processes I and II for $\{K_6W_{18}\}$. This positive shift is suggestive of a change in the electronic structure of the POM framework upon modification with organic moieties. It also indicates a lowering of the LUMO energy relative to its parent structure $\{K_6W_{18}\}$, which is in good agreement with a previous report on band gap manipulation of this species.[44]

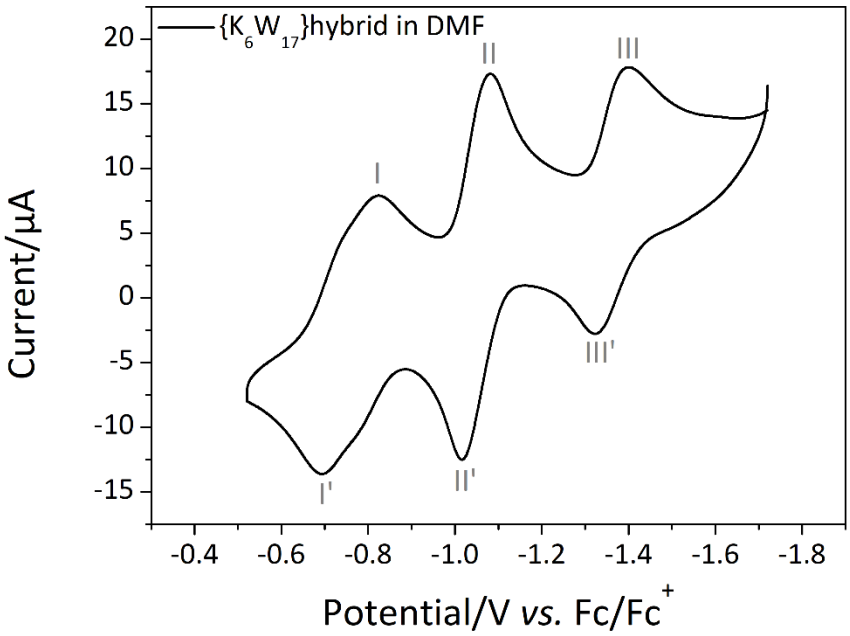


Figure 12 - CV of $\{K_6W_{17}\}$hybrid in 1M $TBAPF_6$ in DMF, performed using a 3 mm GC WE, Pt CE, Ag wire pseudoreference electrode and Fc/Fc^+ internal reference electrode. The scan rate was 100 mV s^{-1}.

Equations 16 – 18 - Redox couples for $\{K_6W_{17}\}$hybrid in 1M $TBAPF_6$ in DMF.

I/I': $[P_2W_{17}O_{59}(PO_3C_6H_5)_2]^{6-} + e^- \leftrightarrow [P_2W_{17}O_{59}(PO_3C_6H_5)_2]^{7-}$ (16)

II/II': $[P_2W_{17}O_{59}(PO_3C_6H_5)_2]^{7-} + e^- \leftrightarrow [P_2W_{17}O_{59}(PO_3C_6H_5)_2]^{8-}$ (17)

III/III': $[P_2W_{17}O_{59}(PO_3C_6H_5)_2]^{8-} + e^- \leftrightarrow [P_2W_{17}O_{59}(PO_3C_6H_5)_2]^{9-}$ (18)

Table 7 - Observed Midpoint Potentials (E_{mid}) and Peak-to- Peak Separations (ΔE_p) for $\{K_6W_{17}\}$hybrid in 1M $TBAPF_6$ in DMF.

Process	E_{mid}/V	ΔE_p/mV
I/I'	–0.76	120
II/II'	–1.05	64
III/III'	–1.36	71

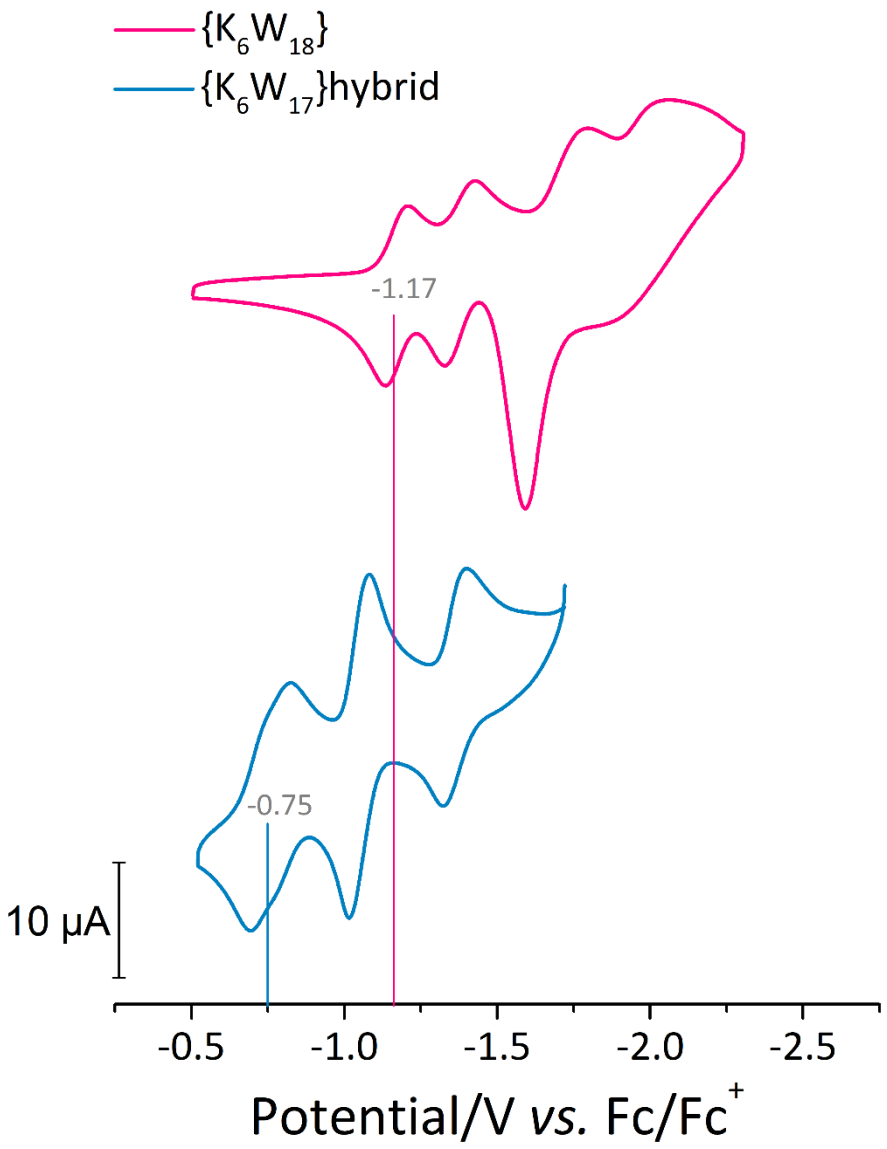


Figure 13 - Stacked solution phase CVs of plenary anion $\{K_6W_{18}\}$ and the derived $\{K_6W_{17}\}$hybrid, highlighting shifts in E_{mid} values.

2.4.2.3 Inorganic-Organic Hybrid

Among different families of transition metal-substituted POMs, mono-substituted Keggin derivatives have been studied extensively because they can be systematically modified on the molecular scale; on the basis of size, shape, charge density, acidity, redox activity, stability, solubility, and so forth, thus, these properties lead to diverse catalytic platforms.[45] The transition metals which are substituted into the POM may also be involved in reversible redox processes. Previous electrochemical studies have been carried out in aqueous media of mono-substituted Keggin structures $[XM_{11}M'O_{39}]^{n-}$ (***X*** *= P, Si, B;* ***M*** *= W, Mo;* ***M'*** *= Cr, Mn, Fe, Co, and Ni*).[46]

In this study, the CV of the anion $[PW_{11}Fe(H_2O)O_{39}]^{4-}$ showed two redox processes which are both monoelectronic. Interestingly, the first wave corresponds to a one-electron transfer at the substituting metal iron centre and Fe^{III} is reduced to Fe^{II}. The second wave corresponds to the tungsten reduction process W^{VI}/W^{V}, however at a much more negative potential (< 1 V) than the first reduction process of the acid and TBA salt Keggin anions (Figure 14).

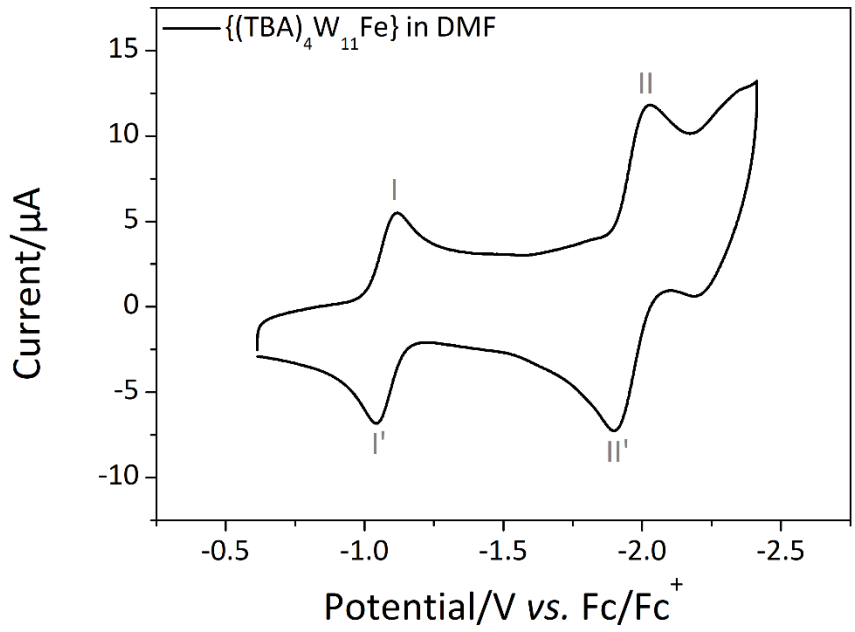


Figure 14 - CV of $\{(TBA)_4W_{11}Fe\}$ in 1M $TBAPF_6$ in DMF, performed using a 3 mm GC WE, Pt CE, Ag wire pseudoreference electrode and Fc/Fc^+ internal reference electrode. The scan rate was 100 mV s^{-1}.

Equations 19 – 20 - Redox couples for $\{(TBA)_4W_{11}Fe\}$ in 1M $TBAPF_6$ in DMF.

I/I': $(TBA)_4[PW^{VI}_{11}Fe^{III}(H_2O)O_{39}] + e^- \leftrightarrow (TBA)_5[PW^{VI}_{11}Fe^{II}(H_2O)O_{39}]$ (19)

II/II': $(TBA)_4[PW^{VI}_{11}Fe^{II}(H_2O)O_{39}] + e^- \leftrightarrow (TBA)_6[PW^{VI}_{10}W^{V}Fe^{II}(H_2O)O_{39}]$ (20)

Table 8 - Observed Midpoint Potentials (E_{mid}) and Peak-to- Peak Separations (ΔE_p) for $\{(TBA)_4W_{11}Fe\}$ in 1M $TBAPF_6$ in DMF.

Process	E_{mid}/V	ΔE_p/mV
I/I'	–1.08	75
II/II'	–1.96	116

Figure 15 highlights the extremely negative shift (< 1V) observed for the tungsten redox process (W^{VI}/W^{V}) in the Fe-substituted Keggin compared to the equivalent process for the acid and TBA salt clusters.

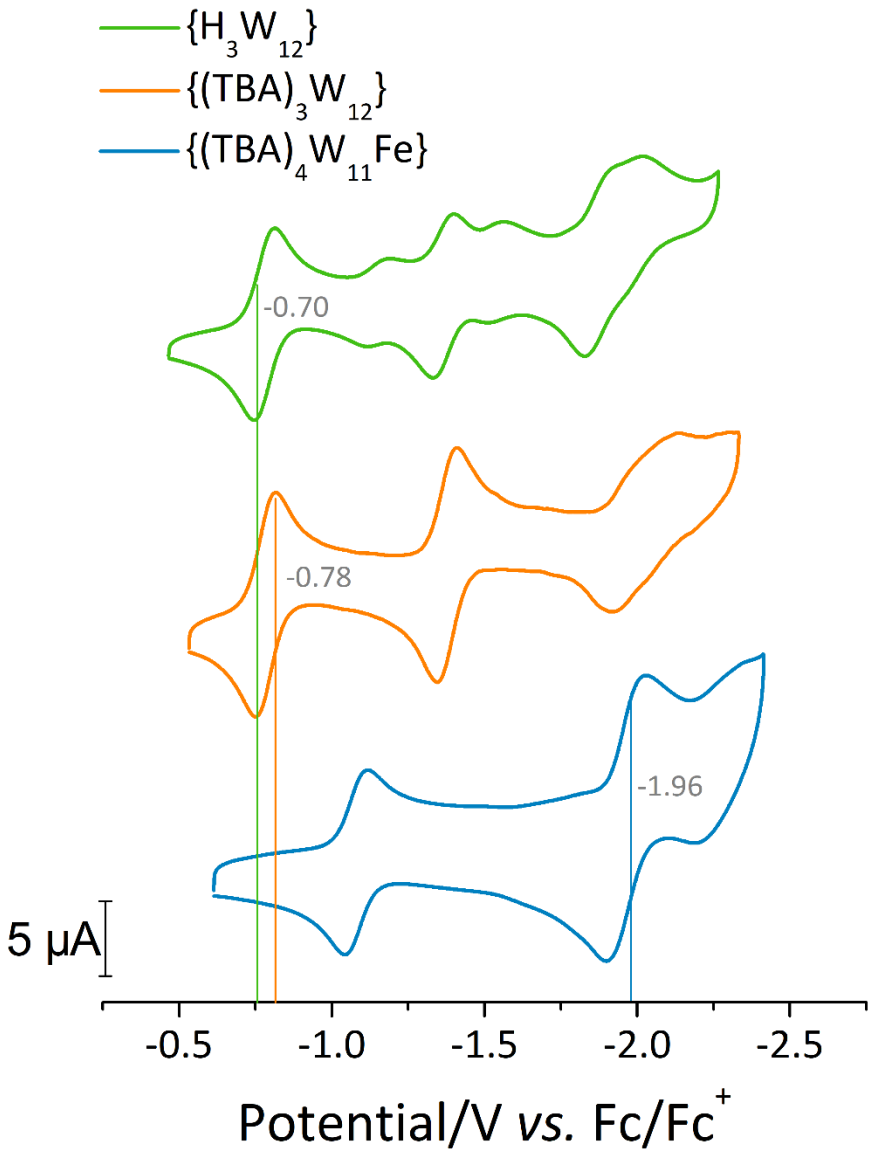


Figure 15 – Negative shift of the first one-electron redox couple observed for the Fe-substituted Keggin in comparison to $\{H_3W_{12}\}$ and $\{(TBA)_3W_{12}\}$.

2.4.3 Voltammetry in Organic Battery Solvent

With a view towards energy storage applications, it is useful to assess the electrochemical behaviour of POMs within a typical battery solvent. 1M lithium hexafluorophosphate ($LiPF_6$) dissolved in a 50/50 (v/v) solution of ethylene carbonate (EC) and ethyl methyl carbonate (EMC) was used as the electrolyte. The CV measurements were performed in a glovebox under an argon atmosphere, using a standard three-electrode cell setup: glassy carbon working electrode, platinum counter electrode and a lithium iron phosphate ($LiFePO_4$) reference electrode, which was then referenced to Li/Li^+. Moving forward, the following POMs are the subject of further electrochemical studies: $H_3[PW_{12}O_{40}]$, $H_6[P_2W_{18}O_{62}]$, $K_6[P_2W_{18}O_{62}]$, denoted $\{H_3W_{12}\}$, $\{H_6W_{18}\}$ and $\{K_6W_{18}\}$.

The CV of $\{H_3W_{12}\}$ in 1M $LiPF_6$ EC/EMC shows two redox processes within the potential range 3.6 – 2.6 V *vs.* Li/Li^+ (Figure 16). Both processes are monoelectronic and possess ΔE_p values close to 59 mV, indicating reversibility. Looking at Figure 17, the effect of increasing the potential range to more negative values in order to access additional processes can be seen. The top CV (grey) shows that the Keggin is 'stable' between 3.6 – 2.6 V and the two redox processes are visible. When the range is extended further to 2.4 V, a third process starts to form at approximately 2.7 V, however the return waves for all three processes are now indiscernible (middle, navy). When the potential range is reverted to 3.6 - 2.6 V, the two original redox processes are not recovered (bottom, pink), indicating irreversible chemical decomposition of the Keggin anion.

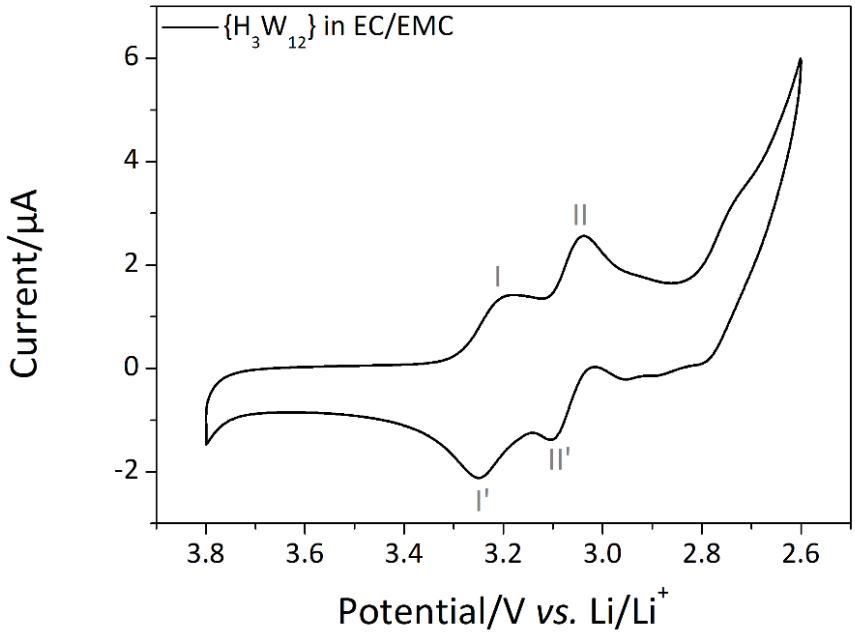


Figure 16 - CV of $\{H_3W_{12}\}$ in 1M $LiPF_6$ in EC/EMC, performed in the glovebox, using a 3 mm GC WE, Pt CE, LFP reference electrode which was then converted to Li/Li^+. The scan rate was 50 mV s^{-1}.

Equations 21 – 22 – Redox couples for $\{H_3W_{12}\}$ in 1M $LiPF_6$ in EC/EMC.

I/I': $[PW_{12}O_{40}]^{3-} + e^- \longleftrightarrow [PW_{12}O_{40}]^{4-}$ (21)

II/II': $[PW_{12}O_{40}]^{4-} + e^- \longleftrightarrow [PW_{12}O_{40}]^{5-}$ (22)

Table 9 - Observed Midpoint Potentials (E_{mid}) and Peak-to- Peak Separations (ΔE_p) for $\{H_3W_{12}\}$ in 1M $LiPF_6$ in EC/EMC.

Process	E_{mid}/V	ΔE_p/mV
I/I'	3.22	48
II/II'	3.07	51

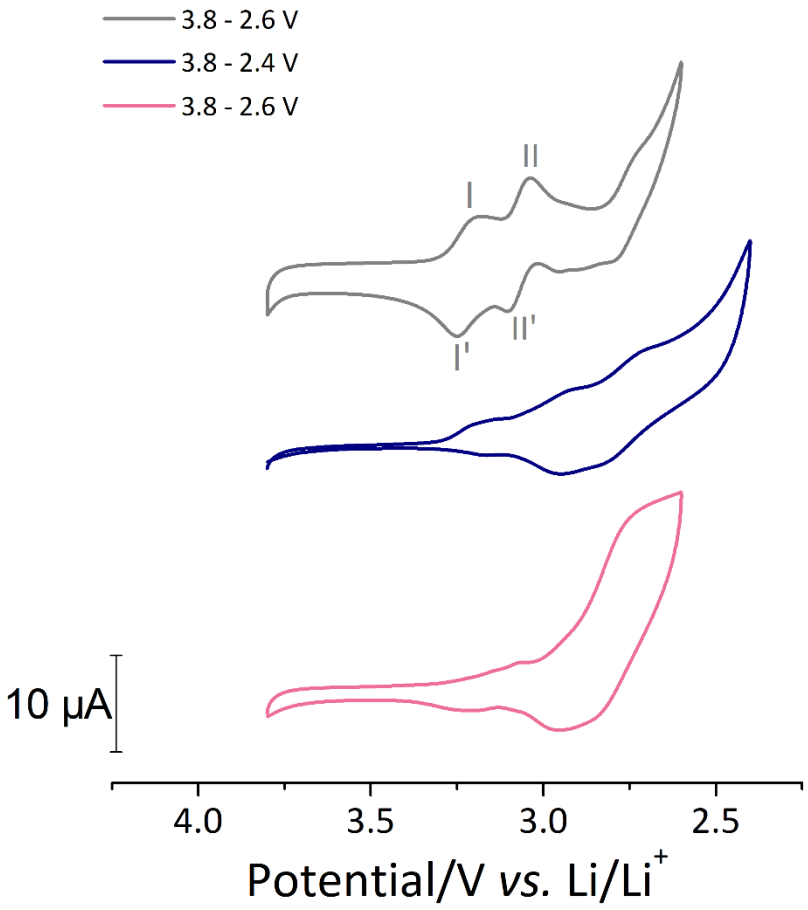


Figure 17 – Solution phase CVs for $\{H_3W_{12}\}$ in 1M $LiPF_6$ in EC/EMC showing the changes observed in the redox profile as the potential window is increased.

The CV of $\{H_6W_{18}\}$ shows three well-defined redox peaks between the potential range of 4 – 3 V *vs.* Li/Li^+ (Figure 18). Each process corresponds to a one-electron transfer and the ΔE_p values (Table 10) indicate that the first two processes are reversible (75 and 85 mV) and the third is quasi-reversible in nature (109 mV). The potential range was extended to lower potentials (4 – 2.6 V) and a fourth reduction process arises at approximately 2.76 V (marked by *, olive trace), with no corresponding oxidation. This caused the peak-to-peak separations to widen for the first three redox waves (86, 124 and 135 mV), shifting the second reversible wave into the quasi-reversible regime. By increasing the potential window further by 0.2 V (4 – 2.4 V), the formation of a

fifth reduction process (marked *, orange trace) is observed. Process I still has a well-defined reoxidation wave, however the reoxidation waves for processes II and III have consolidated into a single peak and also diminished in intensity. Further increasing the potential window to 4 – 2.2 V shows a flatlining of reoxidation peaks for processes II and III and miscellaneous processes IV and V (marked by *, purple trace). Additionally, the ΔE_p value for process I sees a drastic increase to 175 mV, transitioning from reversible to irreversible. Reverting the potential range back to 4 – 3 V (not shown) does not reintroduce any semblance of reversibility to processes I – III, which means the chemical changes that occur at lower potentials are destructive to the Dawson's electrochemistry and is also irretrievable.

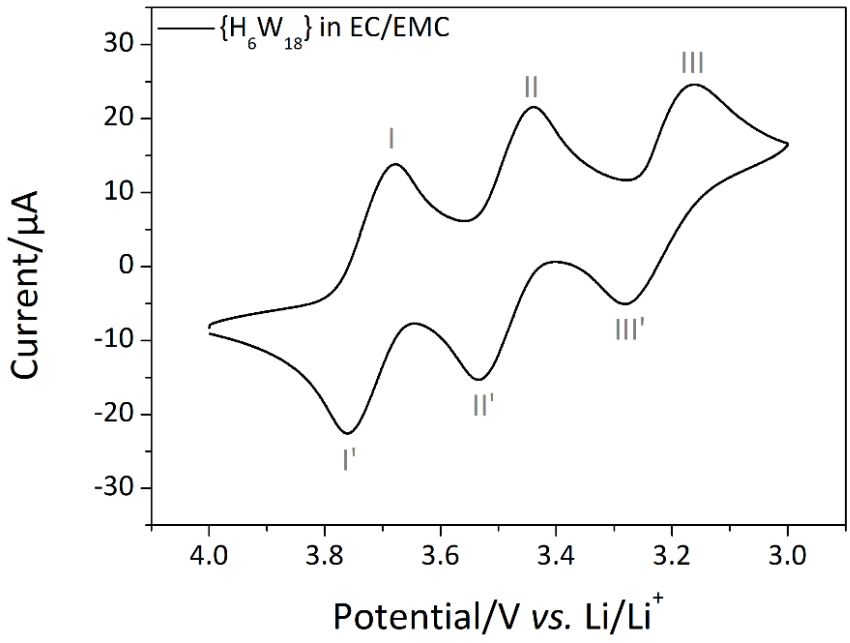


Figure 18 - CV of $\{H_6W_{18}\}$ in 1M $LiPF_6$ in EC/EMC, performed in the glovebox, using a 3 mm GC WE, Pt CE, LFP reference electrode which was then converted to Li/Li^+. The scan rate was 50 mV s^{-1}.

Equations 23 – 25 - Redox couples for $\{H_6W_{18}\}$ in 1M $LiPF_6$ in EC/EMC.

I/I': $[P_2W_{18}O_{62}]^{6-} + e^- \longleftrightarrow [P_2W_{18}O_{62}]^{7-}$ (23)

II/II': $[P_2W_{18}O_{62}]^{7-} + e^- \longleftrightarrow [P_2W_{18}O_{62}]^{8-}$ (24)

III/III': $[P_2W_{18}O_{62}]^{8-} + e^- \longleftrightarrow [P_2W_{18}O_{62}]^{9-}$ (25)

Table 10 - Observed Midpoint Potentials (E_{mid}) and Peak-to- Peak Separations (ΔE_p) for $\{H_6W_{18}\}$ in 1M $LiPF_6$ in EC/EMC.

Process	E_{mid}/V	ΔE_p/mV
I/I'	3.72	75
II/II'	3.48	87
III/III'	3.22	109

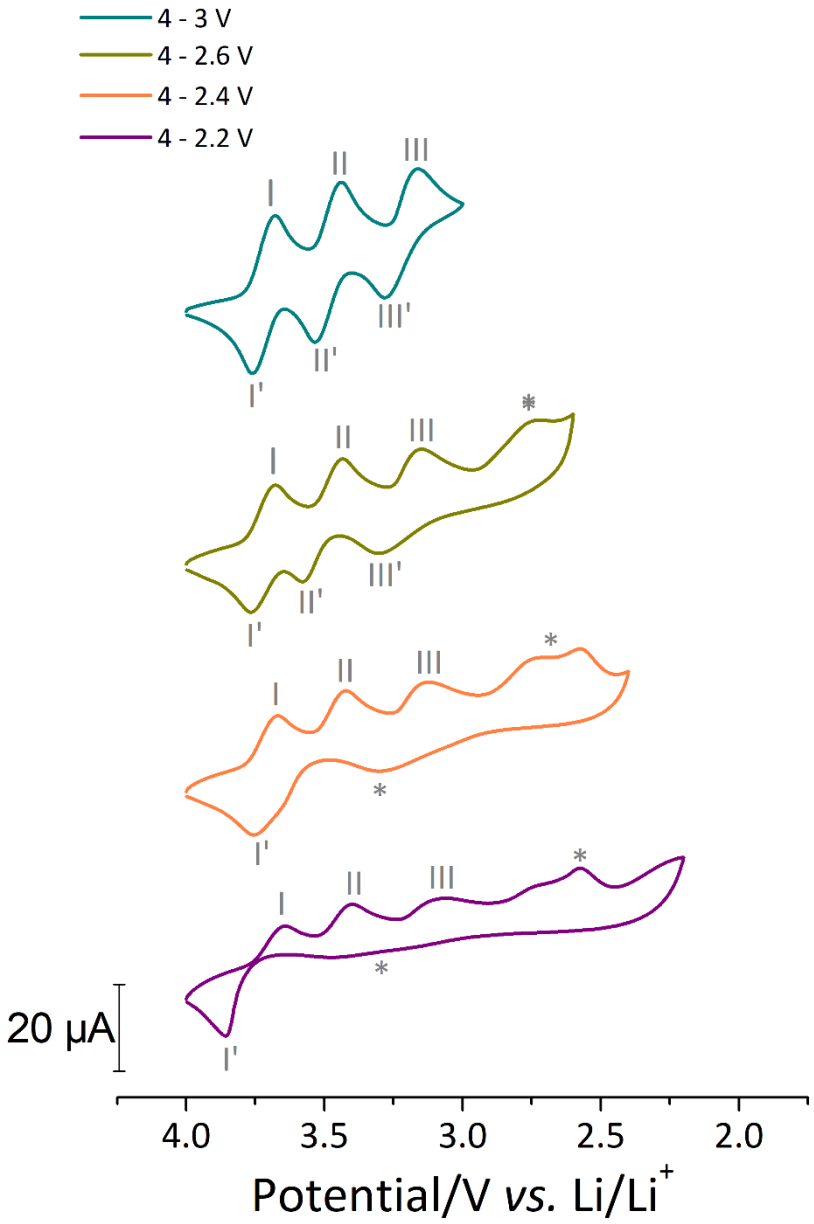


Figure 19 - Solution phase CVs for $\{H_6W_{18}\}$ in 1M $LiPF_6$ in EC/EMC showing the irreverble changes that are induced in rensponse to the potential window being increased.

Table 11 - Observed Midpoint Potentials (E_{mid}) and Peak-to- Peak Separations (ΔE_p) for $\{H_6W_{18}\}$ in 1M $LiPF_6$ in EC/EMC in response to the potential window being increased.

Potential Range/V	Process	E_{mid}/V	ΔE_p/mV
4 – 2.6	I/I'	3.72	86
4 – 2.6	II/II'	3.50	124
4 – 2.6	III/III'	3.22	135
4 – 2.4	I/I'	3.72	86
4 – 2.2	I/'	3.75	175

Lastly, the CV of $\{K_6W_{18}\}$ (Figure 20) in the battery solvent exhibits similar behaviour to that of $\{H_6W_{18}\}$. Three redox processes are observed in the potential range 4.2 – 2.75 V *vs.* Li/Li^+, each corresponding to a one-electron transfer and the ΔE_p values indicate that the first process is reversible (75 mV) whereas the second and third processes are in the quasi-reversible regime (117 and 142 mV). Continuing the examination of the stability of the electrochemical window, the potential was lowered (4.2 – 2.4 V) and a fourth reduction process is observed, centred at approximately 2.55 V (marked with *, green trace). This is likely to be a two-electron reduction, given that the magnitude of the peak is much larger than the preceding peaks. However, this fourth process does not have a corresponding oxidation and its appearance causes the oxidation waves for II and III to coalesce into a single ill-defined peak. Additionally, the ΔE_p value for process I increased to 141 mV, becoming quasi-reversible. Reducing the potential further still (4.2 – 2.2 V, lilac trace), results in an even larger separation between the reduction and oxidation peaks for process I, driving the process into the irreversible regime (ΔE_p = 302 mV). Reverting the potential range back to 4.2 – 2.6 V (not shown) does not reintroduce reversibility to process I and processes II and III do not recover their reoxidation waves, meaning the chemical changes that occur at lower potentials are irreversible and destructive to the Dawson's electrochemistry. These results signify that the potential window in which the POM is subject to redox reactions must be chosen

judiciously to maximise cycling and rate capability within a POM – Lithium test battery.

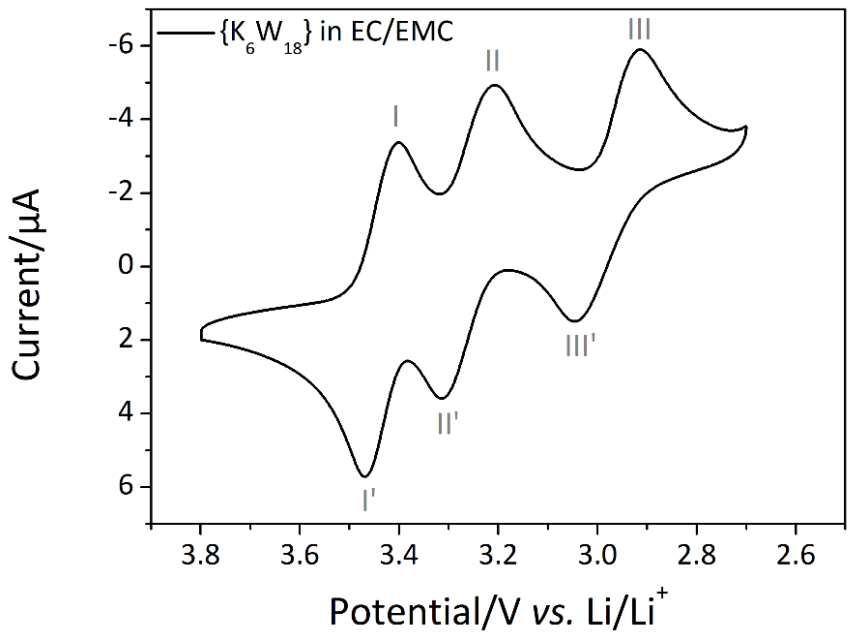


Figure 20 - CV of $\{K_6W_{18}\}$ in 1M $LiPF_6$ in EC/EMC, performed in the glovebox, using a 3 mm GC WE, Pt CE, LFP reference electrode which was then converted to Li/Li^+. The scan rate was 50 mV s^{-1}.

Equations 26 – 28 - Redox couples for $\{K_6W_{18}\}$ in 1M $LiPF_6$ in EC/EMC.

$$\text{I/I'}: [P_2W_{18}O_{62}]^{6-} + e^- \leftrightarrow [P_2W_{18}O_{62}]^{7-} \quad (26)$$

$$\text{II/II'}: [P_2W_{18}O_{62}]^{7-} + e^- \leftrightarrow [P_2W_{18}O_{62}]^{8-} \quad (27)$$

$$\text{III/III'}: [P_2W_{18}O_{62}]^{8-} + e^- \leftrightarrow [P_2W_{18}O_{62}]^{9-} \quad (28)$$

Table 12 - Observed Midpoint Potentials (E_{mid}) and Peak-to- Peak Separations (ΔE_p) for $\{K_6W_{18}\}$ in 1M $LiPF_6$ in EC/EMC.

Process	E_{mid}/V	ΔE_p/mV
I/I'	3.43	68
II/II'	3.35	103
III/III'	2.98	124

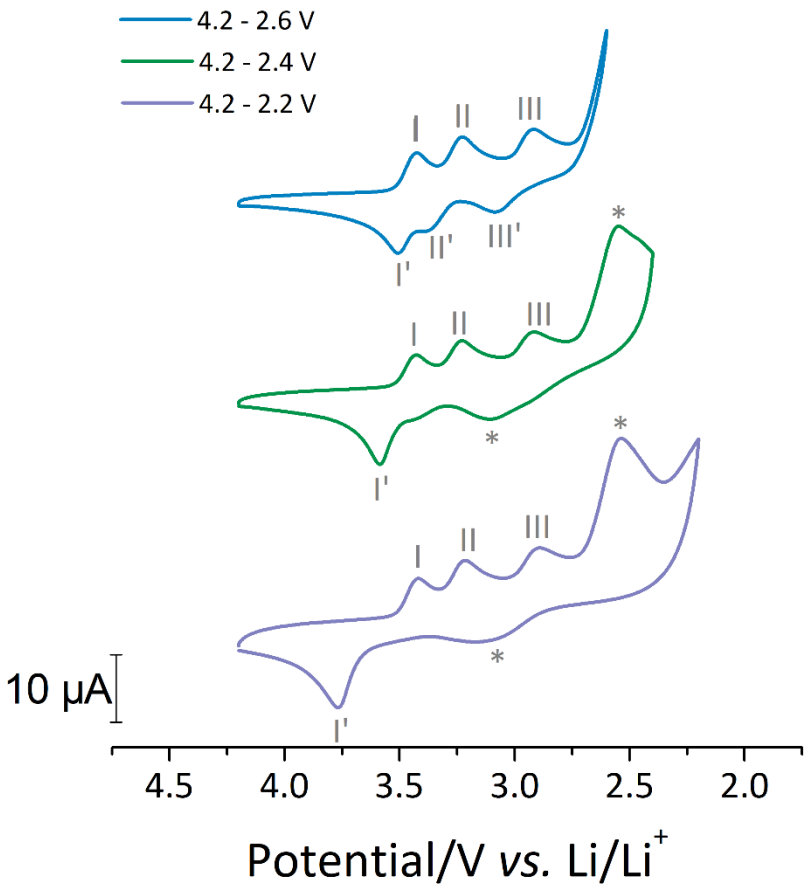


Figure 21 - Solution phase CVs for $\{K_6W_{18}\}$ in 1M $LiPF_6$ in EC/EMC showing the irreverble changes that are induced in rensponse to the potential window being increased.

Table 13 - Observed Midpoint Potentials (E_{mid}) and Peak-to- Peak Separations (ΔE_p) for process I of $\{K_6W_{18}\}$ in 1M $LiPF_6$ in EC/EMC in response to the potential window being increased.

Potential Range	Process	E_{mid}/V	ΔE_p/mV
4.2 – 2.6 V	I/I’	3.47	75
4.2 – 2.4 V	I/I’	3.50	141

2.4.4 Voltammetry in Aqueous Solvent - 1M Sulphuric Acid (H_2SO_4)

As alluded to previously, the electrochemical behaviour of POMs in aqueous electrolytes is greatly influenced by the pH of the solvent and the presence of protons. In this section, the electrochemistry of $\{H_3W_{12}\}$, $\{H_6W_{18}\}$ and $\{K_6W_{18}\}$ are characterised in a protic environment, using 1M H_2SO_4 as the electrolyte.

The CV of $\{H_3W_{12}\}$ in 1M H_2SO_4 shows three redox processes within the potential range of 0.2 – -0.8 V *vs*. Ag/AgCl (Figure 22). The first two process are monoelectronic and the third comprises a two-electron transfer which is also accompanied by protonation (Equations 1 – 3). The ΔE_p values for processes I (44 mV) and II (42 mV) are close to 59 mV and the ΔE_p for process III is 28 mV, close to the theoretical value of 29 mV for a two-electron process, therefore indicating that all three processes are reversible (Table 14). From the DPV trace (Figure 23), it can be seen that peaks I – 3 have a ratio of 1:1:2 based on current intensity. Additionally, the full width at half maximum (FWHM) values (Table 14) are close to the theoretical values of 90.4 mV for a one-electron process and 45.2 mV for a two-electron process, further confirming the correct electron assignment for each process as well as their reversible nature.

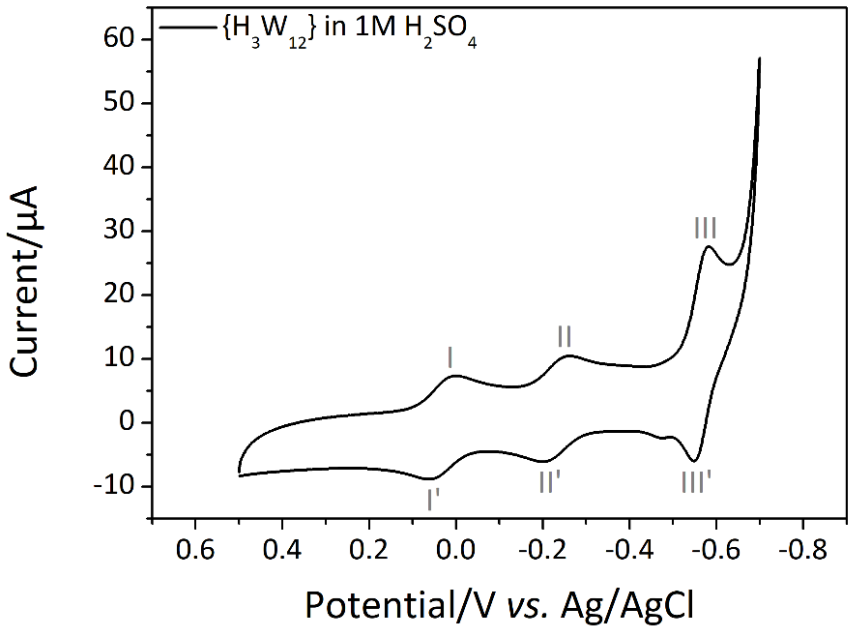


Figure 22 - CV of $\{H_3W_{12}\}$ in 1M H_2SO_4 performed using a 3 mm diameter GC working electrode, a Pt counter electrode, and a Ag/AgCl reference electrode. The scan rate was 100 mV s^{-1}.

Equations 29 – 30 - Redox couples for $\{H_3W_{12}\}$ in 1M H_2SO_4.

I/I': $[PW_{12}O_{40}]^{3-} + e^- \leftrightarrow [PW_{12}O_{40}]^{4-}$ (29)

II/II': $[PW_{12}O_{40}]^{4-} + e^- \leftrightarrow [PW_{12}O_{40}]^{5-}$ (30)

III/III': $[PW_{12}O_{40}]^{5-} + 2e^- + 2H^+ \leftrightarrow [H_2PW_{12}O_{40}]^{5-}$ (31)

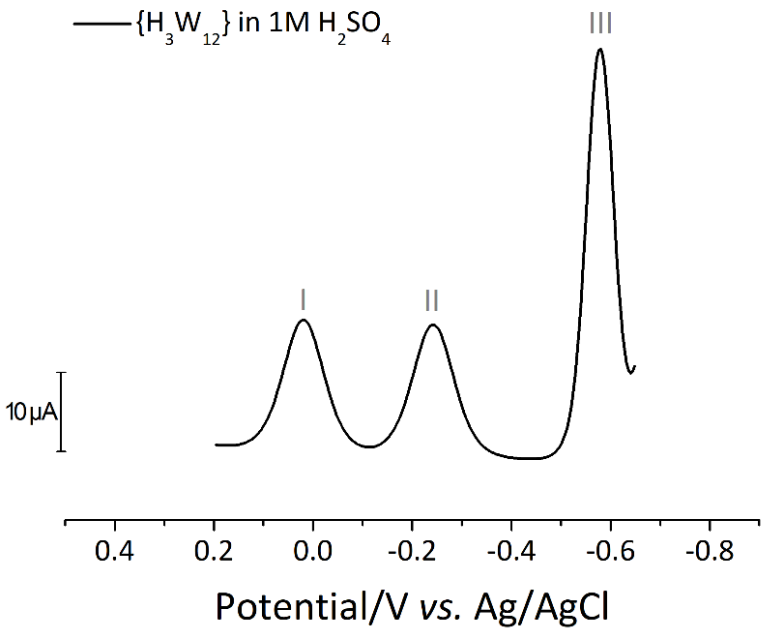


Figure 23 – DPV trace of $\{H_3W_{12}\}$ in 1M H_2SO_4 performed using a 3 mm diameter GC working electrode, a Pt counter electrode, and a Ag/AgCl reference electrode. The scan rate was 100 mV s^{-1}.

Table 14 - Observed Midpoint Potentials (E_{mid}), Peak-to- Peak Separations (ΔE_p), Full Width at Half Maximum (FWHM) and number of electrons (n) for $\{H_3W_{12}\}$ in 1M H_2SO_4.

Process	E_{mid}/V	ΔE_p/mV	FWHM/mV	n (no. of electrons)
I/I'	0.032	44	86	1.1 (1)
II/II'	-0.23	42	82	1.1 (1)
III/III'	-0.56	28	58	1.6 (2)

The CV of $\{H_6W_{18}\}$ shows four redox processes between the potential range of 0.2 – -0.8 V *vs.* Ag/AgCl (Figure 24). The first two peaks are one-electron processes and the third and fourth peaks are two-electron processes, both involving protonation (Equations 32 – 35). The ΔE_p values suggest that all four processes are reversible with respect to the number of electrons involved for each peak (1, 1, 2, 2, Table 15). Though the DPV trace (Figure 25) shows a clear ratio of 1:1:2:2 for the peak current intensity, the FWHM values for processes III

and IV deviate from the theoretical value of 45.2 for a two-electron transfer, giving *n* values lower than 2. This exemplifies that experimental variation is not uncommon and that some caution must be exercised when interpreting FWHM values.

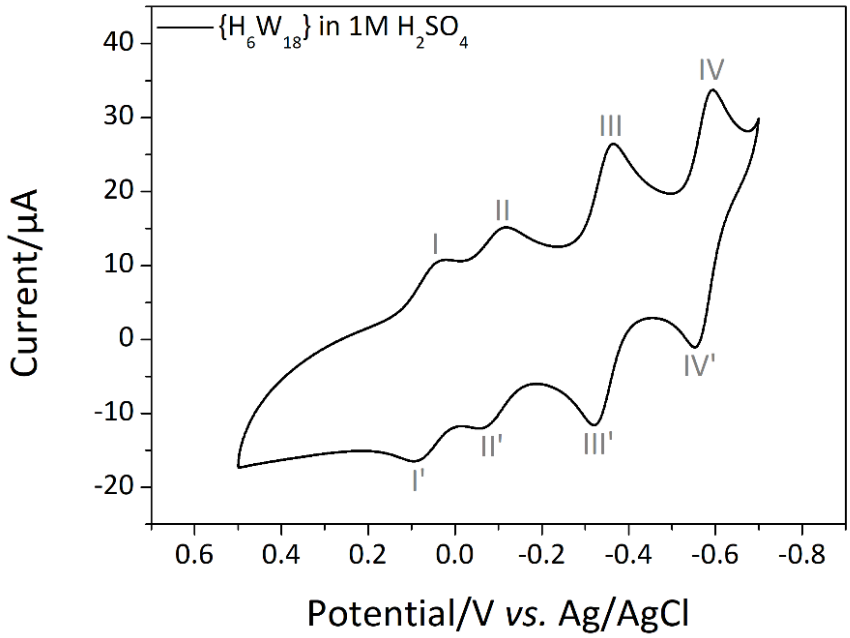


Figure 24 - CV of $\{H_6W_{18}\}$ in 1M H_2SO_4 performed using a 3 mm diameter GC working electrode, a Pt counter electrode, and a Ag/AgCl reference electrode. The scan rate was 100 mV s^{-1}.

Equations 32 – 35 - Redox couples for $\{H_6W_{18}\}$ in 1M H_2SO_4.

I/I': $[P_2W_{18}O_{62}]^{6-} + e^- \longleftrightarrow [P_2W_{18}O_{62}]^{7-}$ (32)

II/II': $[P_2W_{18}O_{62}]^{7-} + e^- \longleftrightarrow [P_2W_{18}O_{62}]^{8-}$ (33)

III/III': $[P_2W_{18}O_{62}]^{8-} + 2e^- + 2H^+ \longleftrightarrow [H_2P_2W_{18}O_{62}]^{8-}$ (34)

IV/IV': $[H_2P_2W_{18}O_{62}]^{8-} + 2e^- + 2H^+ \longleftrightarrow [H_4P_2W_{18}O_{62}]^{8-}$ (35)

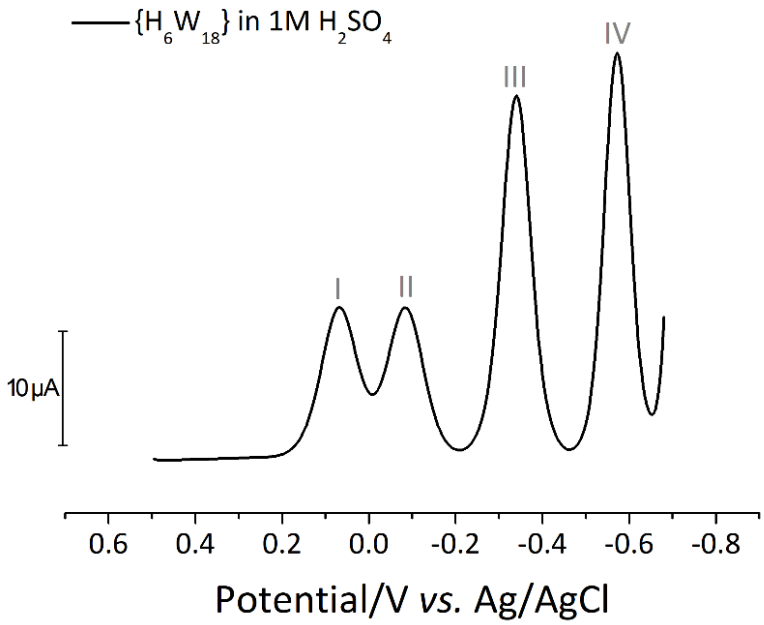


Figure 25 - DPV trace of $\{H_6W_{18}\}$ in 1M H_2SO_4 performed using a 3 mm diameter GC working electrode, a Pt counter electrode, and a Ag/AgCl reference electrode. The scan rate was 100 mV s^{-1}.

Table 15 - Observed Midpoint Potentials (E_{mid}), Peak-to- Peak Separations (ΔE_p), Full Width at Half Maximum (FWHM) and number of electrons (n) for $\{H_6W_{18}\}$ in 1M H_2SO_4.

Process	E_{mid}/V	ΔE_p/mV	FWHM/mV	n (no. of electrons)
I/I'	0.065	42	82	1.1 (1)
II/III	-0.095	39	83	1.1 (1)
III/III'	-0.34	36	69	1.3 (~2)
IV/IV'	-0.57	34	62	1.5 (~2)

Lastly, the CV of $\{K_6W_{18}\}$ exhibits similar behaviour to that of $\{H_6W_{18}\}$ in 1M H_2SO_4. Four redox processes are observed in the potential range of 0.2 – -0.8 V *vs.* Ag/AgCl (Figure 26), corresponding to two one-electron and two two-electron transfers, with the latter being accompanied by protonation. The E_{mid} values show infinitesimal shifts of no more than 10 mV for each redox process when compared to the midpoint potentials of $\{H_6W_{18}\}$. The ΔE_p values indicate

that all four processes are indeed reversible. The DPV trace (Figure 27) and FWHM values show a similar trend to that of $\{H_6W_{18}\}$, where the redox peaks are present in a 1:1:2:2 ratio but the FWHM values for the last two processes deviate from the theoretical value of 45.2 for a two-electron transfer, thus giving *n* values lower than 2. This does not mean that the electron assignment is incorrect, it simply reiterates that FWHM values are a complementary source of information, combined with what is already known about the system of study.

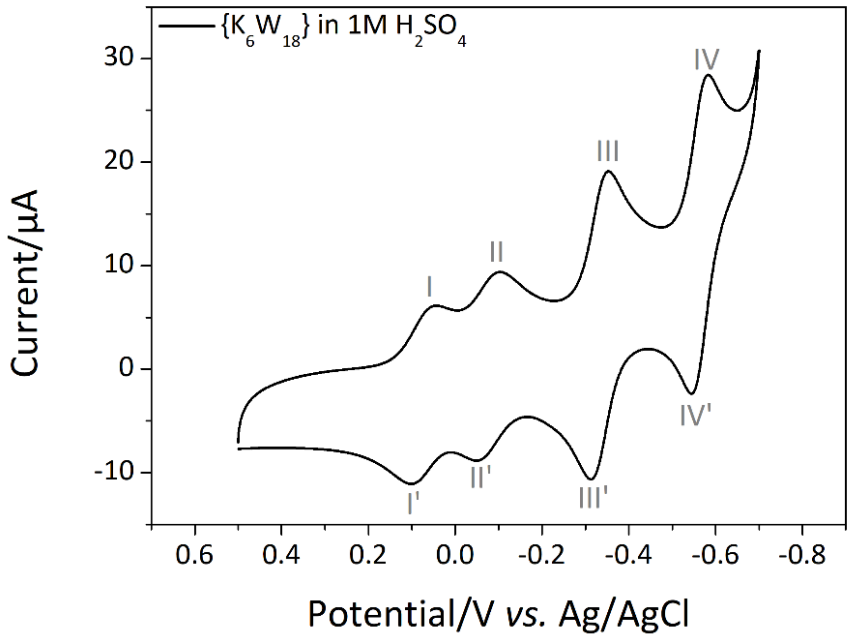


Figure 26 - CV of $\{K_6W_{18}\}$ in 1M H_2SO_4 performed using a 3 mm diameter GC working electrode, a Pt counter electrode, and a Ag/AgCl reference electrode. The scan rate was 100 mV s^{-1}.

Equations 36 – 39 - Redox couples for $\{K_6W_{18}\}$ in 1M H_2SO_4.

I/I': $[P_2W_{18}O_{62}]^{6-} + e^- \longleftrightarrow [P_2W_{18}O_{62}]^{7-}$ (36)

II/II': $[P_2W_{18}O_{62}]^{7-} + e^- \longleftrightarrow [P_2W_{18}O_{62}]^{8-}$ (37)

III/III': $[P_2W_{18}O_{62}]^{8-} + 2e^- + 2H^+ \longleftrightarrow [H_2P_2W_{18}O_{62}]^{8-}$ (38)

IV/IV': $[H_2P_2W_{18}O_{62}]^{8-} + 2e^- + 2H^+ \longleftrightarrow [H_4P_2W_{18}O_{62}]^{8-}$ (39)

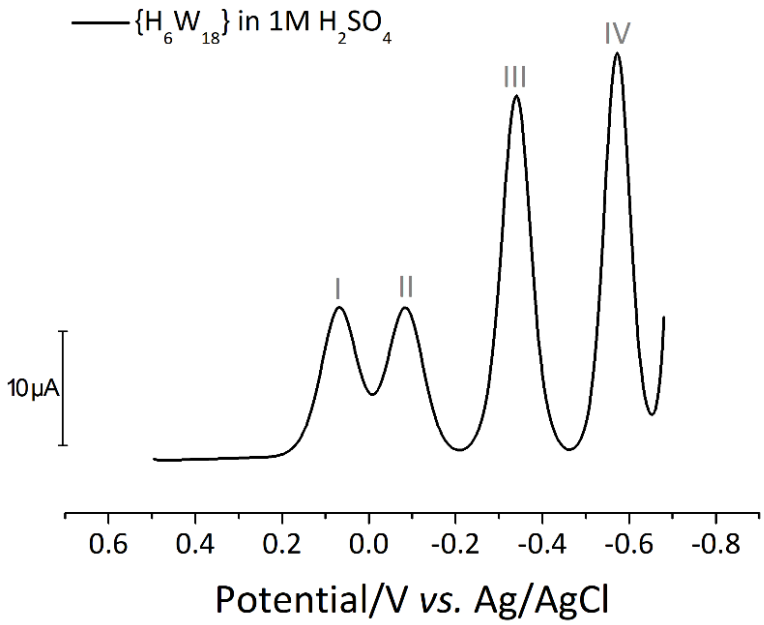


Figure 27 - DPV trace of $\{K_6W_{18}\}$ in 1M H_2SO_4 performed using a 3 mm diameter GC working electrode, a Pt counter electrode, and a Ag/AgCl reference electrode. The scan rate was 100 mV s^{-1}.

Table 16 - Observed Midpoint Potentials (E_{mid}), Peak-to- Peak Separations (ΔE_p), Full Width at Half Maximum (FWHM) and number of electrons (n) for $\{K_6W_{18}\}$ in 1M H_2SO_4.

Process	E_{mid}/V	ΔE_p/mV	FWHM/mV	n (no. of electrons)
I/I'	0.075	50	86	1.1 (1)
II/II'	-0.081	42	85	1.1 (1)
III/III'	-0.33	34	70	1.3 (~2)
IV/IV'	-0.56	32	64	1.2 (~2)

2.4.5 Cation-dependent Electrochemistry

Recently, interactions between redox-active molecules and alkali ions have been investigated for the modulation of the electrochemical properties of energy storage materials, for the purpose of influencing the potentials at which redox events occur, without incurring significant changes to the molecular structure of the system.[47–51] Abruña et al. reported that the coordination of small alkali cations (Li^+ and Mg^{2+}) to the Lewis basic oxygen atoms of carbonyl entities of 1,2-di(thiophen-2-yl)ethane-1,2-dione (DTED) resulted in a positive shift of the redox potential of the analyte. In turn this increased the cell voltage, thereby increasing the overall gravimetric energy density in the context of electrochemical energy storage.[52] The voltammograms of DTED were conducted in DMF containing different perchlorate supporting electrolytes. In TBAP (tetra-*n*-butylammonium perchlorate), DTED showed two well-defined one-electron processes. In the presence of $LiClO_4$, a positive shift of 400 mV for the second reduction process was observed, which reflects the ionic stabilisation of the dianion by Li^+. A similar effect was observed in the presence of $NaClO_4$ but to a lesser extent, which was ascribed to a difference in cation size and ionic interaction. However, when applying the same experimental conditions using $Mg(ClO_4)_2$, the changes were significant. In the presence of Mg^{2+}, the shift of the second wave is such that rather than observing two one-electron processes (as for TBA^+, Li^+ and Na^+), a single two-electron process is obtained at a much more positive potential. Computational studies allowed for estimation of the binding energy between the carbonyl moiety and the cation which quantifies the ionic coupling. In the case of TBA^+, the binding was found to be negligible, whereas Li^+ and Mg^{2+} were found to be strongly interacting, with the latter having the highest binding energy.[52]

Over the past few decades, several studies have been performed to further understand different factors that may govern the redox chemistry of POMs such as pH, transition metal substitutions and organofunctionalisation.[53–55] Additionally, one of the most fundamental roles of cations in POM chemistry is controlling solubility. While many studies rely on moderating solubility in

various solvents, other applications require insolubility, to prevent leaching from a material or device for example. Indeed, the electrostatic interactions between polyoxoanions and their countercations in aqueous and organic media have been noted to significantly influence their redox behaviour and electrocatalytic activity.[56,18] Cation pairing interactions as shown by Abruña et al. have also been shown to induce similar stabilising effects on the electrochemical profiles of POM anions, causing positive shifts of redox events corresponding to the formation of reduced polyoxoanions in solution.[57,58] A comprehensive review that highlights the role of cations in POM chemistry going beyond simple electrostatic charge-balancing can be found by Streb et al.[56]

Several studies have sought to explore the effect of cations other than H^+, including the non-coordinating tetrabutylammonium and tetramethylammonium cations (TBA^+, TMA^+), alkali metal cations (Li^+ and Na^+) as well as small radius multivalent cations (Mg^{2+}). Maeda et al. conducted studies in acetonitrile with the addition of different concentrations of triflic acid (CF_3SO_3H) to observe changes in electrochemical behaviour of $[PMo_{12}O_{40}]^{3-}$ and $[SiMo_{12}O_{40}]^{4-}$. They found that when the proton concentration was varied independently such that the ratio of H^+ to POM increased, the redox peaks shifted to more positive potentials and the one-electron processes converged to form a series of three two-electron waves.[59]

Himeno et al. examined the effect of Li^+ on $[PMo_{12}O_{40}]^{3-}$ and $[PW_{12}O_{40}]^{3-}$ in acetonitrile via the addition of different concentrations of lithium perchlorate ($LiClO_4$).[60] Generally, the effect was qualitatively similar to that of increasing H^+ concentration but specific changes depend on the identity of the cation and the POM anion. As the H^+ concentration increased, the three successive one-electron peaks for $[PMo_{12}O_{40}]^{3-}$ changed to three two-electron processes but consolidated into two peaks in the presence of Li^+. For $[PW_{12}O_{40}]^{3-}$, the four one-electron processes merged into two two-electron processes. Whereas in the presence of Li^+, the first one electron peak was unaffected and did not merge with the second one-electron process. This second process had also shifted to a

more positive potential and the third peak became a two-electron process, also occurring at more positive potentials than in the absence of Li^+.[60]

Matson et al. reported the ion-pairing interactions of the Lindqvist-type polyoxovanadate alkoxide (POV alkoxide) cluster, $[V_6O_7(OCH_3)_{12}]^{2-}$, with alkylammonium, lithium, sodium and potassium cations.[61] In all cases, the presence of alkali cations positively shifts the mid-point potentials of the first two redox processes of the POV alkoxide cluster relative to alkylammonium. The magnitude of these shifts increases as the size of the alkali metal decreases (in the order $K^+ < Na^+ \ll Li^+$). They concluded that the relatively small shift in E_{mid} values for the first redox process across all supporting electrolytes indicated that only a very weak interaction exists between the alkali cations and the singly reduced form of the cluster. In contrast, the 2nd redox process was much more sensitive to the identity of the compensating cation, suggesting that the alkali cations have a higher affinity for the dianionic form of the POV alkoxide cluster. However, these positive shifts are also accompanied by an increase in ΔE_p values, meaning that the stabilisation using alkali cations is accompanied by a loss of electrochemical reversibility.[61]

Previous ion-pairing studies of POMs and metal cations have taken place in organic solvents. Our studies have been conducted in aqueous solutions of perchlorate salts. In aqueous media, the metal cations are hydrated, and thus their binding affinity to anions is more likely to be dictated by the charge density of the hydrated ion (hydrated radii) as opposed to the bare ion (ionic radii).[62] For instance, although the bare ion of Li^+ has the highest charge density (smallest ionic radius) among the alkali metal cations, the charge density of a hydrated Li^+ ion is the lowest (largest hydrated radius), rendering it the weakest alkali metal cation for the anion–cation interaction. Therefore, the common trends of binding affinity follow as $Li^+ < Na^+ < K^+ < Rb^+ < Cs^+$ for monovalent cations and $Mg^{2+} < Ca^{2+} < Sr^{2+} < Ba^{2+}$ for divalent cations.[63–66]

2.4.5.1 Electrochemistry of {H_6W_{18}} in Perchlorate-based Electrolytes

The electrochemical behaviour of the {H_6W_{18}} Dawson motifs observed in the various perchlorate electrolyte systems (1M $HClO_4$/$LiClO_4$/$NaClO_4$/$Mg(ClO_4)_2$) is described below.

In all cases, {H_6W_{18}} shows four redox waves, corresponding to two one-electron processes, followed by two two-electron processes (Figures 27, 30, 32, 34 and Equations 40 – 43 apply in all cases). Small shifts in E_{mid} values towards more positive potentials are observed for process I in the presence of Li^+, Na^+ and Mg^{2+} compared to $HClO_4$ (38, 54, 65 mV respectively), indicating ion-association effects between the metal cations and the singly reduced $[P_2W_{18}O_{62}]^{7-}$ anion (Table 21). Process II also experiences positive shifts in E_{mid} values in the presence of the metal cations but to a lesser extent.

In contrast, processes III and IV, are shifted into the negative regime, meaning that these processes are more difficult to access in the presence of the metal cations (Table 21: process III shifts Li^+/Na^+/Mg^{2+} *vs*. H^+ = -100/-84/-75 mV; process IV shifts Li^+/Na^+/Mg^{2+} *vs.* H^+ = -124/-109/-105 mV). In the highly acidic medium of 1M $HClO_4$, the redox couples III/III' and IV/IV' arise at more positive potentials. Interestingly, the processes experience a greater negative shift in the presence of Li^+ whereas the smallest negative shifts occur in the presence of Mg^{2+}. Since processes III and IV are proton-coupled and therefore pH dependent, these results can be explained by examining the pH of each electrolyte system; 1M $HClO_4$ = pH 0, $LiClO_4$ = pH 9, $NaClO_4$ = pH 8 and $Mg(ClO_4)_2$ = pH 7. For every change in one pH unit, a shift of approximately 59 mV is expected. Our results are consistent with this; as the pH increases, consequently the proton concentration decreases and so processes III and IV all experience negative shifts in the presence of the metal cations. The largest negative shift is observed for the most basic solution of $LiClO_4$ and the smallest shift is observed for the least basic of the metal cation electrolytes, $Mg(ClO_4)_2$. Figure 36 highlights the aforementioned shifts in E_{mid} values.

The ΔE_p values for processes I and II of $\{H_6W_{18}\}$ in the presence of $H^+/Li^+/Na^+/Mg^{2+}$ all correlate to a one-electron process (Table 21). Conversely, the ΔE_p values for processes III and IV in the presence of $Li^+/Na^+/Mg^{2+}$ are much higher than the theoretical value of 29 mV for a reversible two-electron transfer as opposed to the ΔE_p values in 1M $HClO_4$, suggesting these processes are quasi-reversible in the presence of the metal cations (Table 21).

In the four electrolytes, the DPV traces for $\{H_6W_{18}\}$ show four peaks in the ratio of 1:1:2:2 for the peak current intensity (Figures 29, 31, 33 and 35). In all instances, the FWHM values for processes I and II relate to a one-electron transfer. The FWHM values in the presence of the metal cations are in better agreement with the theoretical value of 90.4 mV for a one-electron transfer, attesting to the more reversible nature of these peaks *vs.* in IM $HClO_4$. However, the FWHM values for processes III and IV in the presence of $Li^+/Na^+/Mg^{2+}$ are much larger than expected for a two-electron transfer (> 45.2 mV), giving *n* values lower than 2 (Tables 17 – 20). This deviation can be ascribed to the quasi-reversible nature of the redox peaks as observed in the corresponding CVs.

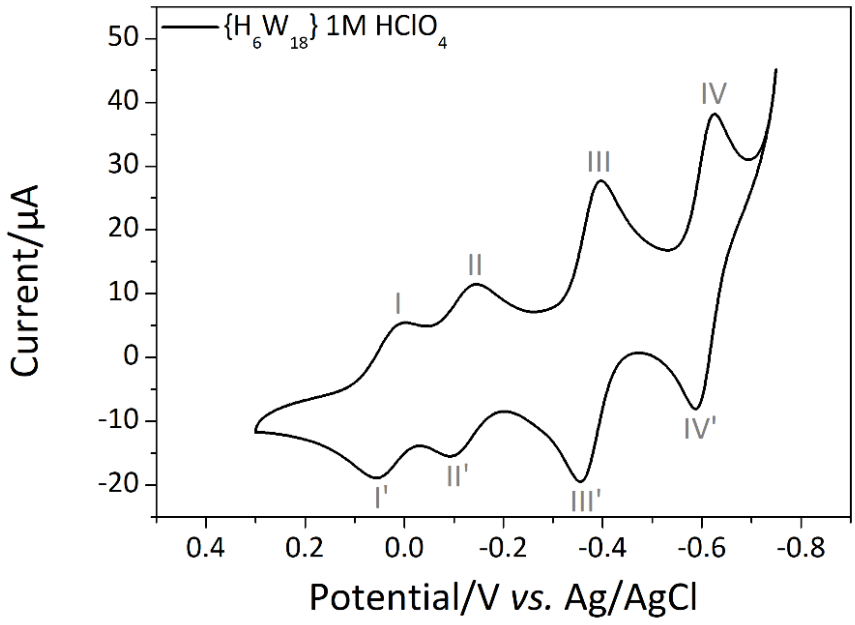


Figure 28 - CV of $\{H_6W_{18}\}$ in 1M $HClO_4$ performed using a 3 mm diameter GC working electrode, a Pt counter electrode, and a Ag/AgCl reference electrode. The scan rate was 100 mV s^{-1}.

Equations 40 – 43 - Redox couples for $\{H_6W_{18}\}$ in all 1M Perchlorate electrolytes.

I/I': $[P_2W_{18}O_{62}]^{6-} + e^- \leftrightarrow [P_2W_{18}O_{62}]^{7-}$ (40)

II/II': $[P_2W_{18}O_{62}]^{7-} + e^- \leftrightarrow [P_2W_{18}O_{62}]^{8-}$ (41)

III/III': $[P_2W_{18}O_{62}]^{8-} + 2e^- + 2H^+ \leftrightarrow [H_2P_2W_{18}O_{62}]^{8-}$ (42)

IV/IV': $[H_2P_2W_{18}O_{62}]^{8-} + 2e^- + 2H^+ \leftrightarrow [H_4P_2W_{18}O_{62}]^{8-}$ (43)

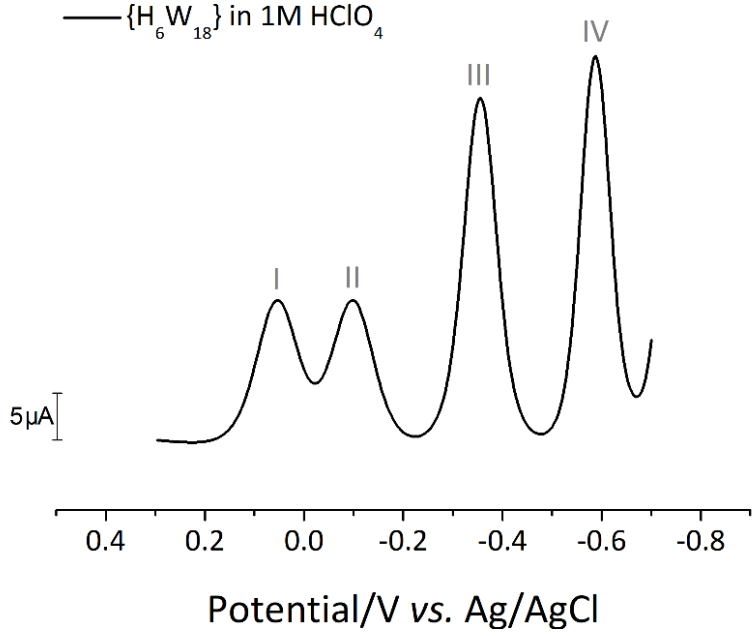


Figure 29 - DPV trace of $\{H_6W_{18}\}$ in 1M $HClO_4$ performed using a 3 mm diameter GC working electrode, a Pt counter electrode, and a Ag/AgCl reference electrode. The scan rate was 100 mV s^{-1}.

Table 17 - Observed Midpoint Potentials (E_{mid}), Peak-to- Peak Separations (ΔE_p), Full Width at Half Maximum (FWHM) and number of electrons (n) for $\{H_6W_{18}\}$ in 1M $HClO_4$.

Process	E_{mid}/V	ΔE_p/mV	FWHM/mV	n (no. of electrons)
I/I'	0.034	47	79	1.1 (1)
II/II'	-0.12	41	73	1.2 (1)
III/III'	-0.38	35	66	1.4 (~2)
IV/IV'	-0.61	31	61	1.5 (~2)

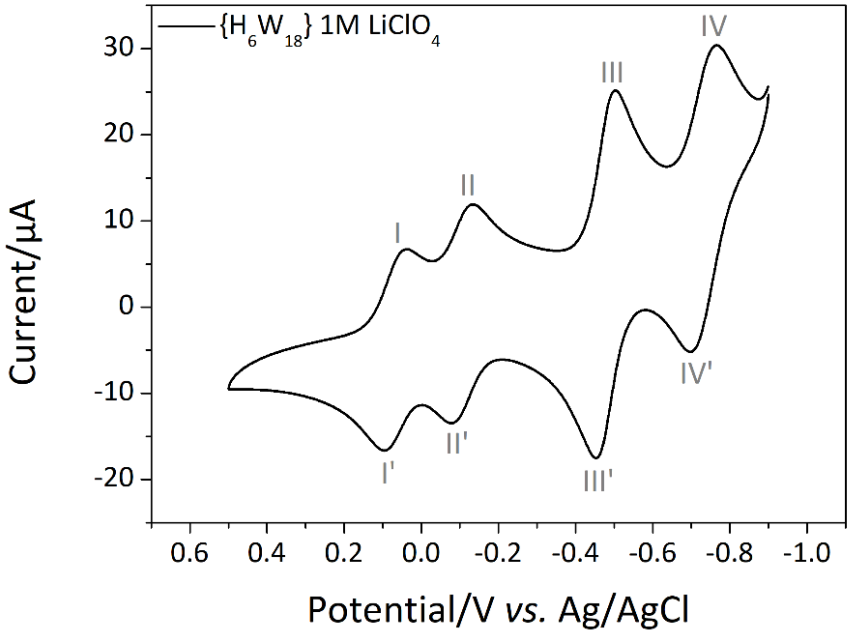


Figure 30 - CV of $\{H_6W_{18}\}$ in 1M $LiClO_4$ performed using a 3 mm diameter GC working electrode, a Pt counter electrode, and a Ag/AgCl reference electrode. The scan rate was 100 mV s^{-1}.

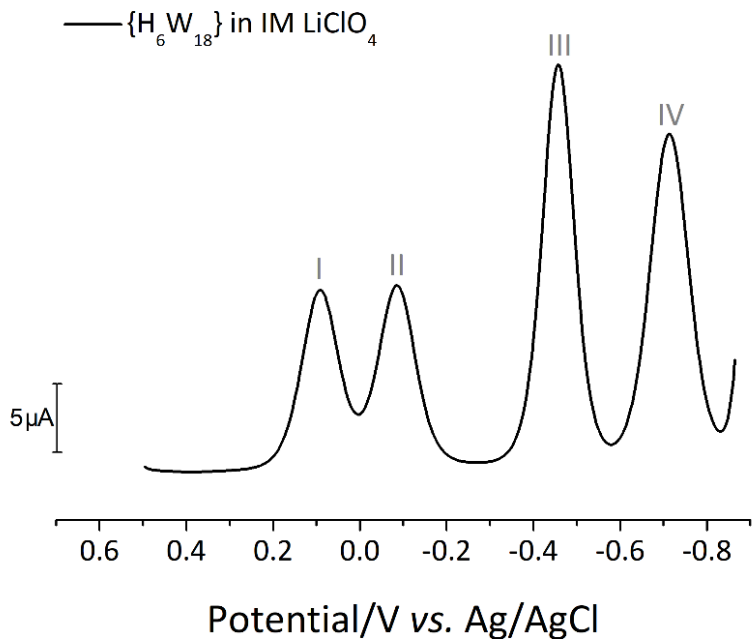


Figure 31 - DPV trace of $\{H_6W_{18}\}$ in 1M $LiClO_4$ performed using a 3 mm diameter GC working electrode, a Pt counter electrode, and a Ag/AgCl reference electrode. The scan rate was 100 mV s^{-1}.

Table 18 - Observed Midpoint Potentials (E_{mid}), Peak-to- Peak Separations (ΔE_p), Full Width at Half Maximum (FWHM) and number of electrons (n) for $\{H_6W_{18}\}$ in 1M $LiClO_4$.

Process	E_{mid}/V	ΔE_p/mV	FWHM/mV	n (no. of electrons)
I/I'	0.072	50	85	1.1 (1)
II/II'	-0.11	46	87	1 (1)
III/III'	-0.48	46	76	1.2 (2)
IV/IV'	-0.73	60	93	0.97 (2)

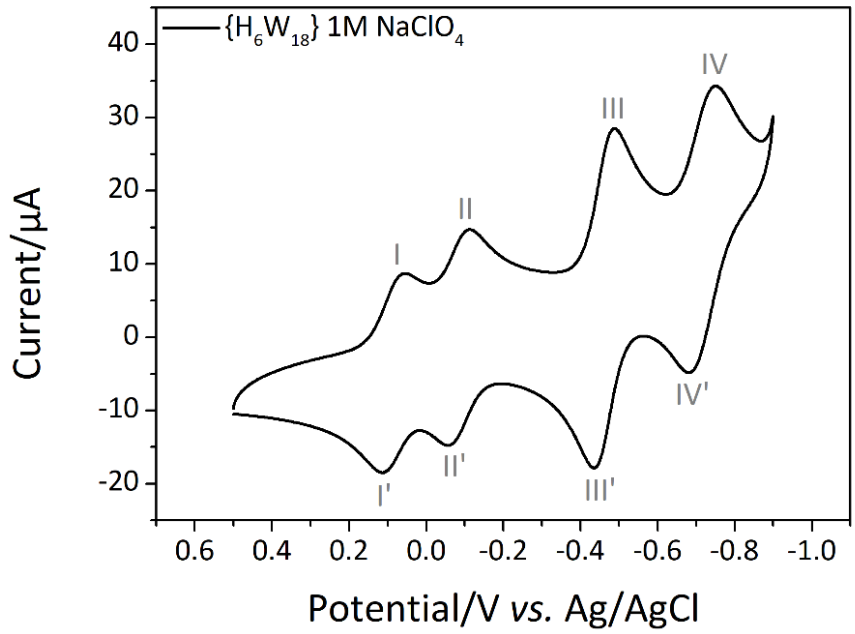


Figure 32 - CV of $\{H_6W_{18}\}$ in 1M $NaClO_4$ performed using a 3 mm diameter GC working electrode, a Pt counter electrode, and a Ag/AgCl reference electrode. The scan rate was 100 mV s^{-1}.

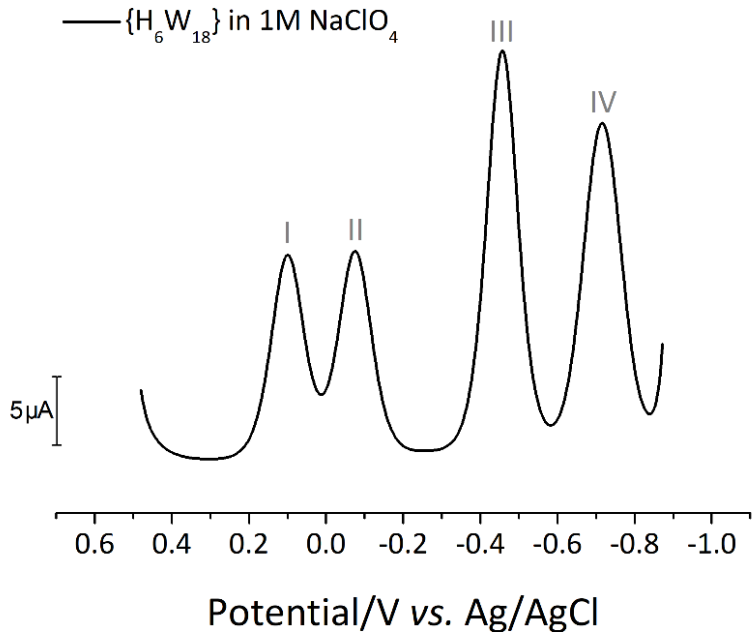


Figure 33 - DPV trace of $\{H_6W_{18}\}$ in 1M $NaClO_4$ performed using a 3 mm diameter GC working electrode, a Pt counter electrode, and a Ag/AgCl reference electrode. The scan rate was 100 mV s^{-1}.

Table 19 - Observed Midpoint Potentials (E_{mid}), Peak-to- Peak Separations (ΔE_p), Full Width at Half Maximum (FWHM) and number of electrons (n) for $\{H_6W_{18}\}$ in 1M $NaClO_4$.

Process	E_{mid}/V	ΔE_p/mV	FWHM/mV	n (no. of electrons)
I/I'	0.087	45	82	1.1 (1)
II/II'	-0.087	43	84	1 (1)
III/III'	-0.46	49	83	1.1 (~2)
IV/IV'	-0.72	59	100	0.9 (~2)

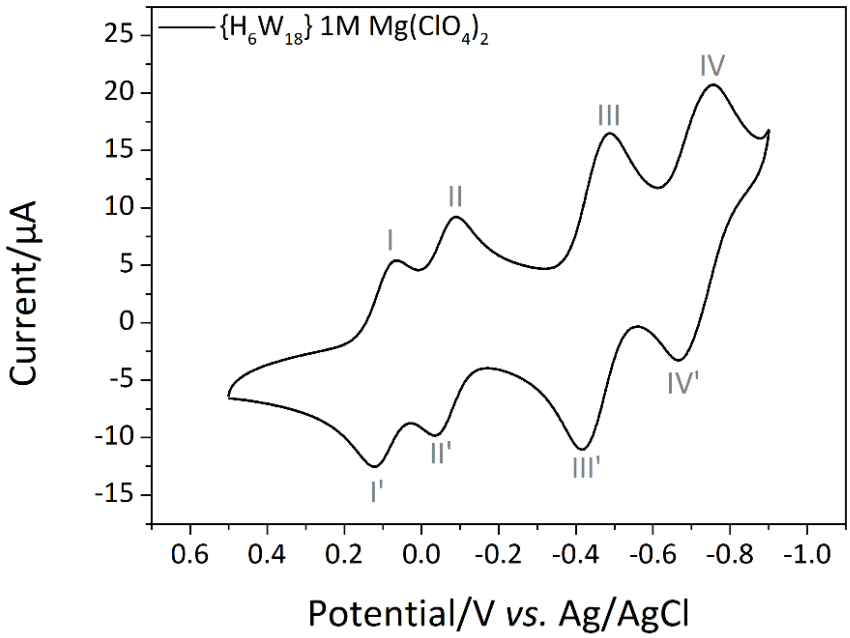


Figure 34 - CV of $\{H_6W_{18}\}$ in 1M $Mg(ClO_4)_2$ performed using a 3 mm diameter GC working electrode, a Pt counter electrode, and a Ag/AgCl reference electrode. The scan rate was 100 mV s^{-1}.

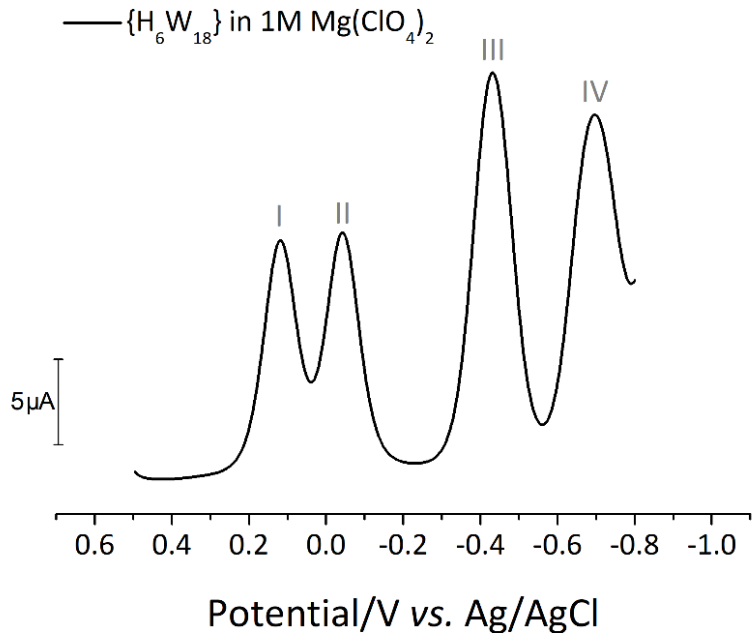


Figure 35 - DPV trace of $\{H_6W_{18}\}$ in 1M $Mg(ClO_4)_2$ performed using a 3 mm diameter GC working electrode, a Pt counter electrode, and a Ag/AgCl reference electrode. The scan rate was 100 mV s^{-1}.

Table 20 - Observed Midpoint Potentials (E_{mid}), Peak-to- Peak Separations (ΔE_p), Full Width at Half Maximum (FWHM) and number of electrons (n) for $\{H_6W_{18}\}$ in 1M $Mg(ClO_4)_2$.

Process	E_{mid}/V	ΔE_p/mV	FWHM/mV	n (no. of electrons)
I/I'	0.098	48	86	1.1 (1)
II/II'	-0.065	42	90	1 (1)
III/III'	-0.45	65	100	0.9 (~2)
IV/IV'	-0.71	77	132	0.7 (~2)

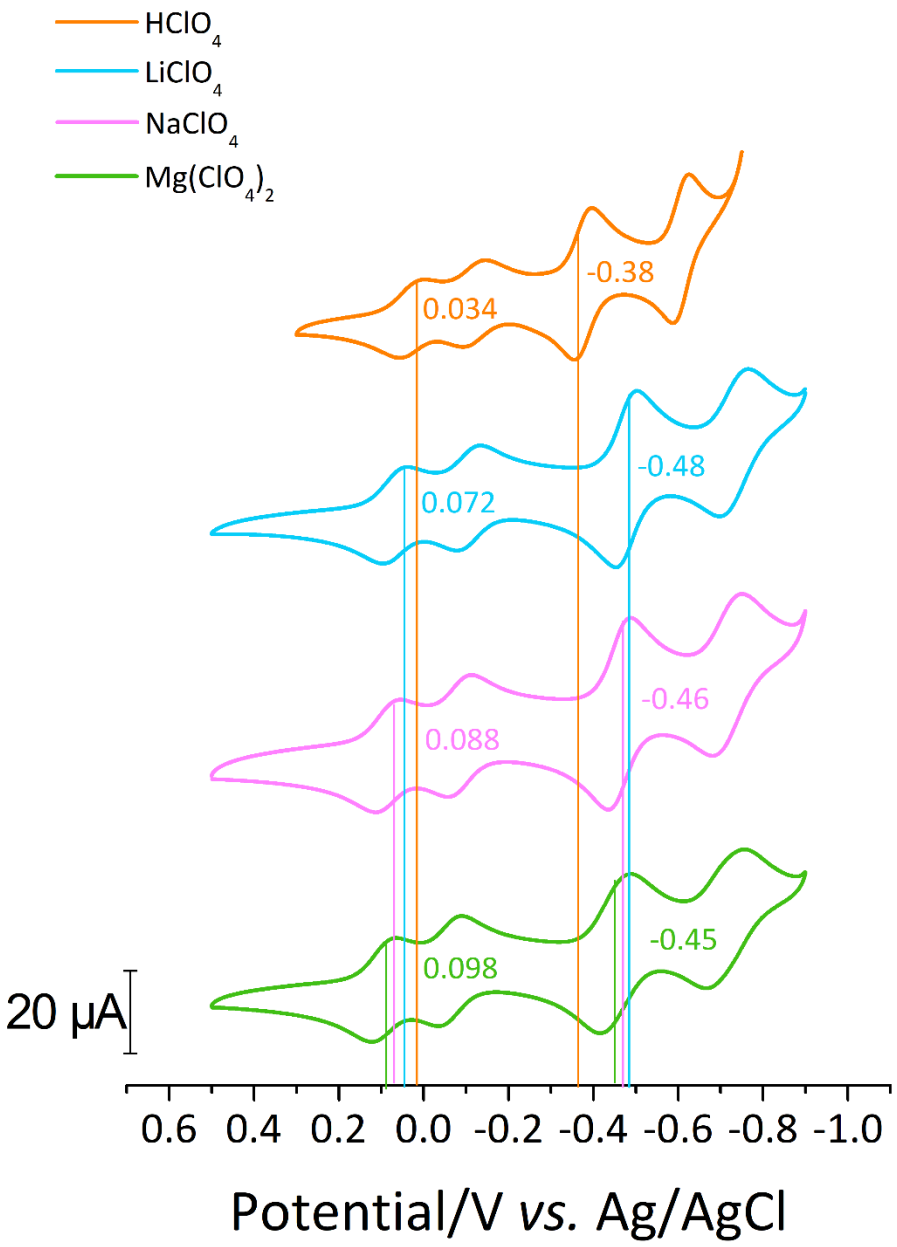


Figure 36 – Stacked solution phase CVs of $\{H_6W_{18}\}$ in the studied perchlorate systems, highlighting the metal cation association effects *vs.* H^+.

Table 21 – Comparison of E_{mid} and ΔE_p values for $\{H_6W_{18}\}$ in 1M perchlorate electrolytes.

Process	$HClO_4$		$LiClO_4$		$NaClO_4$		$Mg(ClO_4)_2$	
	E_{mid}/V	ΔE_p/mV	E_{mid}/V	ΔE_p/mV	E_{mid}/V	ΔE_p/mV	E_{mid}/V	ΔE_p/mV
I/I'	0.0335	47	0.072 (+38 mV shift *vs.* H^+)	50	0.0875 (+54 mV shift *vs.* H^+)	45	0.098 (+65 mV shift *vs.* H^+)	48
II/II'	-0.1215	41	-0.11 (+11 mV shift *vs.* H^+)	46	-0.0875 (+34 mV shift *vs.* H^+)	43	-0.065 (+57 mV shift *vs.* H^+)	42
III/III'	-0.3765	35	-0.477 (-100 mV shift *vs.* H^+)	46	-0.4605 (-84 mV shift *vs.* H^+)	49	-0.4515 (-75 mV shift *vs.* H^+)	65
IV/IV'	-0.6065	31	-0.73 (-124 mV shift *vs.* H^+)	60	-0.7155 (-109 mV shift *vs.* H^+)	59	-0.7115 (-105 mV shift *vs.* H^+)	77

2.4.5.2 Electrochemistry of $\{K_6W_{18}\}$ in Perchlorate-based Electrolytes

The most striking difference between the electrochemical behaviour of $\{K_6W_{18}\}$ and $\{H_6W_{18}\}$ is that in the presence of $Li^+/Na^+/Mg^{2+}$, six redox peaks are observed instead of four. Analogous to $\{H_6W_{18}\}$, $\{K_6W_{18}\}$ exhibits the canonical voltammogram of four redox waves in 1M $HClO_4$, corresponding to two one-electron processes, proceeded by the two proton-coupled two-electron processes (Figure 37, Equations 44 – 47). Upon changing the electrolyte, the last two processes separate such that they convert from two two-electron processes to four one-electron redox waves which are no longer proton-coupled (Figures 39, 40, 42 and Equations 48 – 53 apply to 1M $LiClO_4$/$NaClO_4$/$Mg(ClO_4)_2$).

Similar to $\{H_6W_{18}\}$, process I and II for $\{K_6W_{18}\}$ experience shifts in E_{mid} values towards more positive potentials in the presence of $Li^+/Na^+/Mg^{2+}$ compared to $HClO_4$ (Table 26: process I shifts $Li^+/Na^+/Mg^{2+}$ *vs.* H^+ = +30/+48/+64 mV; process II shifts $Li^+/Na^+/Mg^{2+}$ *vs.* H^+ = +10/+27/+58 mV respectively). These shifts indicate ion-association effects between the alkali metal cations and the singly and doubly reduced $[P_2W_{18}O_{62}]^{7-}$ and $[P_2W_{18}O_{62}]^{8-}$ anions. Considering the hydrated radii of the cations in decreasing order $Mg^{2+} > Li^+ > Na^+$ and the trend

in charge density Mg^{2+} > Li^{+} > Na^{+}, it appears that the larger but doubly charged Mg^{2+} cation is the most stabilising compared to the smaller, singly charged cations which is a rather interesting observation.

The next four one-electron process III – VI that arise in the presence of Li^{+}/Na^{+}/Mg^{2+} all occur at potentials negative (in the range of -0.5 – -1 V) of the two two-electron processes exclusive to {K_6W_{18}} in IM $HClO_4$ (E_{mid} III/III' = -0.38 V; E_{mid} IV/IV' = -0.61 V). It is remarkable that these processes are no longer proton-coupled. Though speculative on our part, these differences are likely due to differences in pH. In the case of {H_6W_{18}}, the POM can be considered as a superacid as we have 6 H^{+} countercations per POM. Whereas for {K_6W_{18}}, we have an overall more basic solution, simply due to a change in the countercation. Looking at processes V and VI, the reduction occurs at more positive potentials moving from Li^{+} to Na^{+} to Mg^{2+}. As seen with {H_6W_{18}}, the greatest negative shifts occur in the presence of Li^{+} whereas the opposite is observed in the presence of Mg^{2+}. It is clear that this phenomenon is linked to decreasing the pH.

The ΔE_p values for processes I and II of {K_6W_{18}} in the presence of H^{+}/Li^{+}/Na^{+}/Mg^{2+} correlate to a one-electron process (Table 26). Additionally, these ΔE_p values are very close to the theoretical value of 59 mV for a one-electron transfer, suggesting that these processes are highly reversible in the presence of the metal cations and in 1M $HClO_4$. The ΔE_p values for processes III and IV in the presence of H^{+} both correspond to two-electron transfers. In the presence of Li^{+}, the ΔE_p values for the subsequent four one-electron processes (III – VI) steadily increase (ΔE_p > 59 mV), indicating these processes become less reversible in the lithium medium. The deviations in ΔE_p values observed for processes III – VI in Na^{+} and Mg^{2+} are not as significant. Though it is clear an interaction between the metal cations and POM anions exists, the fundamental nature of the interaction is unknown. However, we can hypothesise that the interaction between the metal cations and POMs does lead to a perturbation in the electron transfer processes, by making them slower or less favourable.

Figure 43 showcases the different redox profiles in the presence of H^+ and metal cations as well as shifts in E_{mid} values.

The DPV trace for $\{K_6W_{18}\}$ in 1M $HClO_4$ shows four peaks in the ratio of 1:1:2:2 for the peak current intensity (Figure 38). The FWHM values for processes I and II are in good agreement with the theoretical value of 90.4 mV for a one-electron transfer. Though the FWHM values for processes III and IV are larger than expected for a two-electron transfer (> 45.2 mV, Table 22), this is likely due to errors in peak fitting. In the presence of Na^+ (Figure 41) and Mg^{2+} (Figure 43), the DPV trace shows six peaks in a 1:1:1:1:1:1 ratio, albeit the last two peaks in both electrolytes being asymmetrical (DPV trace in 1M $LiClO_4$ not recorded). These asymmetric peaks complicate the peak fitting process as false FWHM values can be derived from an ill-fitting baseline. This is reflected in the large deviations in FWHM values obtained for processes V and IV in the presence of Na^+ and Mg^{2+}, giving *n* values less than 1 (Tables 24 and 25).

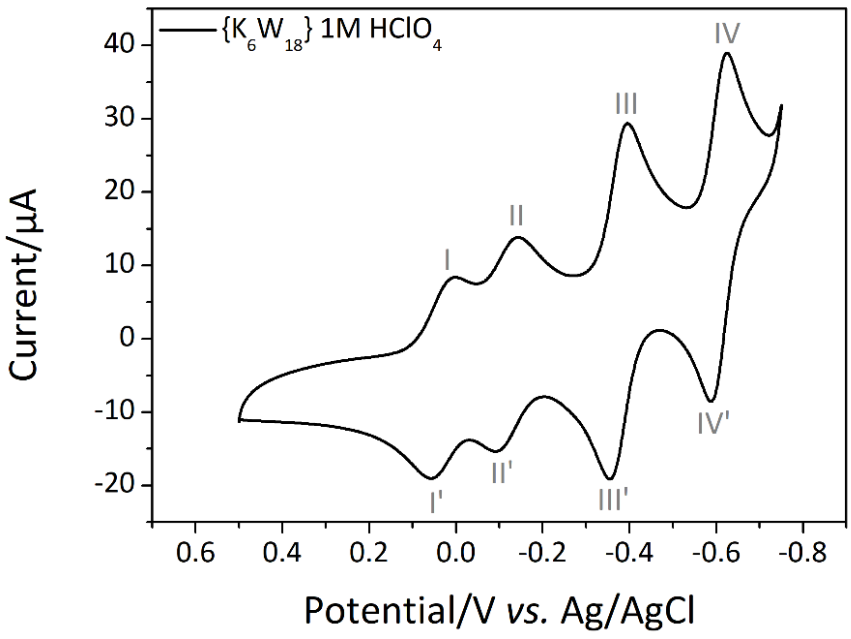


Figure 37 - CV of $\{K_6W_{18}\}$ in 1M $HClO_4$ performed using a 3 mm diameter GC working electrode, a Pt counter electrode, and a Ag/AgCl reference electrode. The scan rate was 100 mV s^{-1}.

Equations 44 – 47 - Redox couples for $\{K_6W_{18}\}$ in 1M $HClO_4$.

I/I': $[P_2W_{18}O_{62}]^{6-} + e^- \longleftrightarrow [P_2W_{18}O_{62}]^{7-}$ (44)

II/II': $[P_2W_{18}O_{62}]^{7-} + e^- \longleftrightarrow [P_2W_{18}O_{62}]^{8-}$ (45)

III/III': $[P_2W_{18}O_{62}]^{8-} + 2e^- + 2H^+ \longleftrightarrow [H_2P_2W_{18}O_{62}]^{10-}$ (46)

IV/IV': $[H_2P_2W_{18}O_{62}]^{10-} + e^- + 2H^+ \longleftrightarrow [H_4P_2W_{18}O_{62}]^{12-}$ (47)

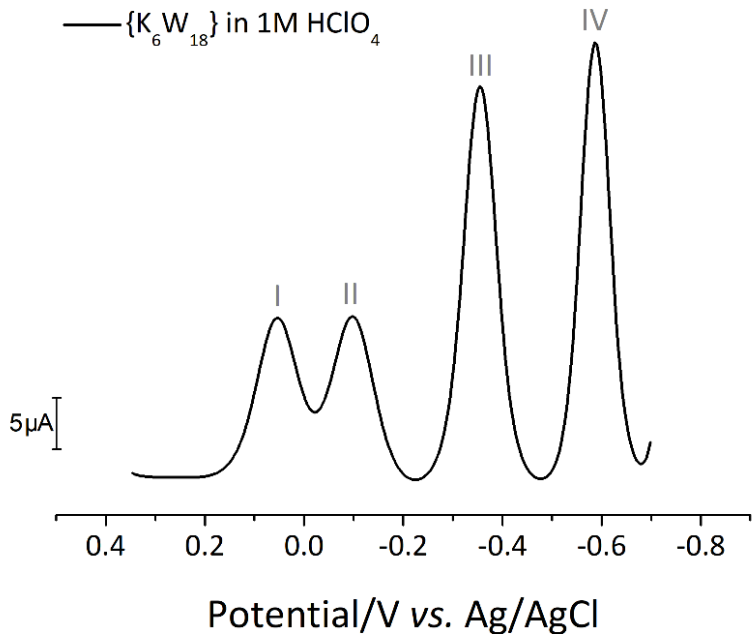


Figure 38 - DPV trace of $\{K_6W_{18}\}$ in 1M $HClO_4$ performed using a 3 mm diameter GC working electrode, a Pt counter electrode, and a Ag/AgCl reference electrode. The scan rate was 100 mV s^{-1}.

Table 22 - Observed Midpoint Potentials (E_{mid}), Peak-to- Peak Separations (ΔE_p), Full Width at Half Maximum (FWHM) and number of electrons (n) for $\{K_6W_{18}\}$ in 1M $HClO_4$.

Process	E_{mid}/V	ΔE_p/mV	FWHM/mV	n (no. of electrons)
I/I'	0.035	45	85	1.1 (1)
II/II'	-0.12	38	80	1.1 (1)
III/III'	-0.38	38	67	1.3 (2)
IV/IV'	-0.61	34	60	1.5 (2)

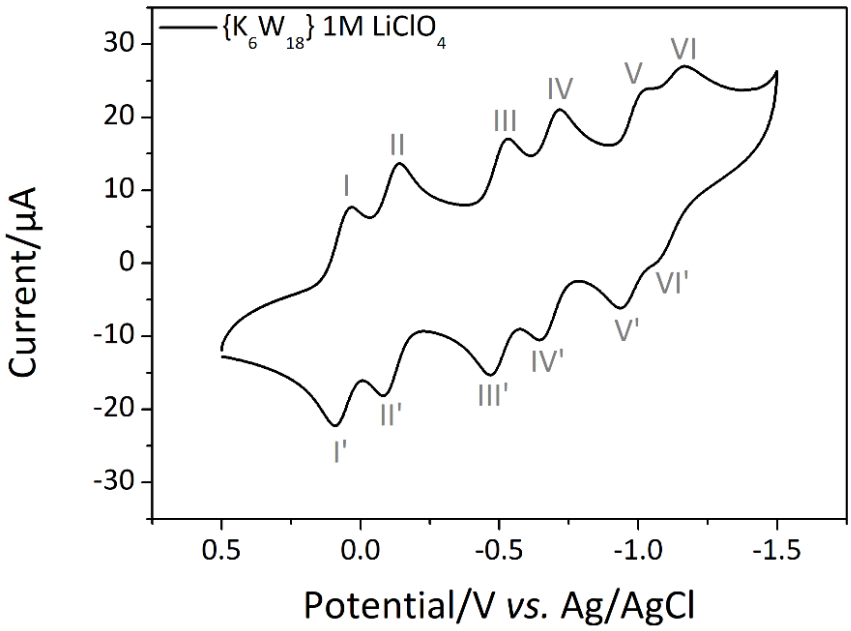


Figure 39 - CV of $\{K_6W_{18}\}$ in 1M $LiClO_4$ performed using a 3 mm diameter GC working electrode, a Pt counter electrode, and a Ag/AgCl reference electrode. The scan rate was 100 mV s^{-1}.

Equations 48 – 53 – Redox couples for $\{K_6W_{18}\}$ in 1M $LiClO_4$/$NaClO_4$/$Mg(ClO_4)_2$

I/I': $[P_2W_{18}O_{62}]^{6-} + e^- \leftrightarrow [P_2W_{18}O_{62}]^{7-}$ (48)

II/II': $[P_2W_{18}O_{62}]^{7-} + e^- \leftrightarrow [P_2W_{18}O_{62}]^{8-}$ (49)

III/III': $[P_2W_{18}O_{62}]^{8-} + e^- \leftrightarrow [P_2W_{18}O_{62}]^{9-}$ (50)

IV/IV': $[P_2W_{18}O_{62}]^{9-} + e^- \leftrightarrow [P_2W_{18}O_{62}]^{10-}$ (51)

V/V': $[P_2W_{18}O_{62}]^{10-} + e^- \leftrightarrow [P_2W_{18}O_{62}]^{11-}$ (52)

VI/VI': $[P_2W_{18}O_{62}]^{11-} + e^- \leftrightarrow [P_2W_{18}O_{62}]^{12-}$ (53)

Table 23 - Observed Midpoint Potentials (E_{mid}) and Peak-to- Peak Separations (ΔE_p) for $\{K_6W_{18}\}$ in 1M $LiClO_4$.

Process	E_{mid}/V	ΔE_p/mV
I/I'	0.064	50
II/II'	-0.11	49
III/III'	-0.50	57
IV/IV'	-0.68	65
V/V'	-0.98	88
VI/VI'	-1.07	87

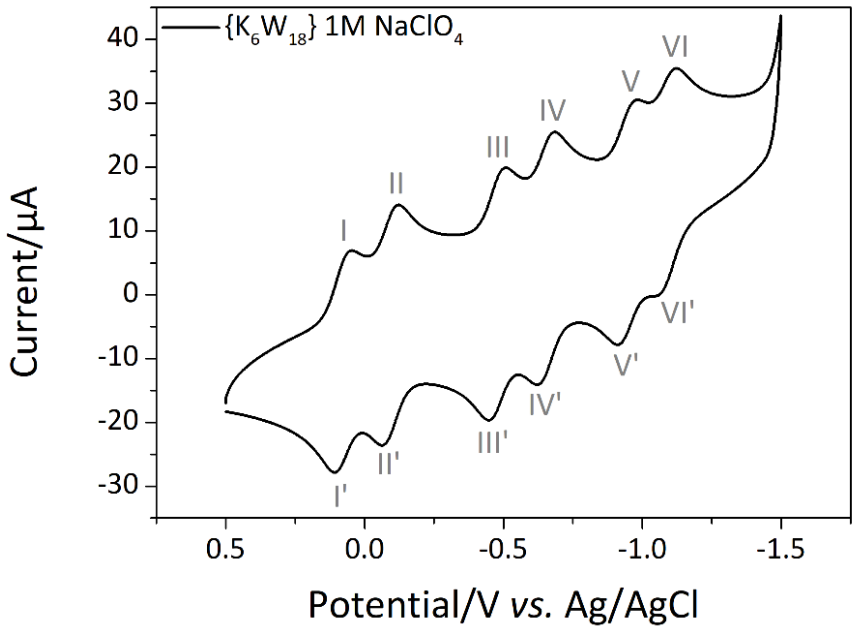


Figure 40 - CV of $\{K_6W_{18}\}$ in 1M $NaClO_4$ performed using a 3 mm diameter GC working electrode, a Pt counter electrode, and a Ag/AgCl reference electrode. The scan rate was 100 mV s^{-1}.

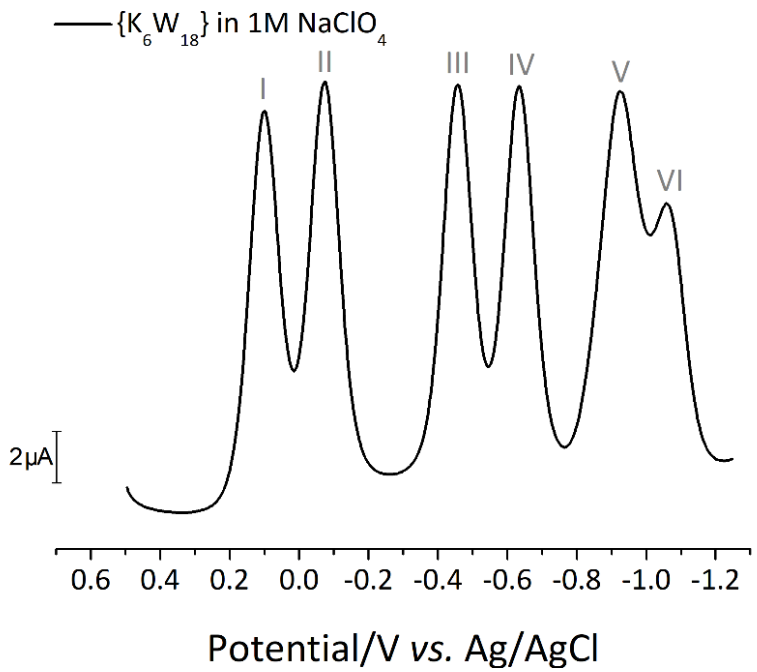


Figure 41 - DPV trace of $\{K_6W_{18}\}$ in 1M $NaClO_4$ performed using a 3 mm diameter GC working electrode, a Pt counter electrode, and a Ag/AgCl reference electrode. The scan rate was 100 mV s^{-1}.

Table 24 - Observed Midpoint Potentials (E_{mid}), Peak-to- Peak Separations (ΔE_p), Full Width at Half Maximum (FWHM) and number of electrons (n) for $\{K_6W_{18}\}$ in 1M $NaClO_4$.

Process	E_{mid}/V	ΔE_p/mV	FWHM/mV	n (no. of electrons)
I/I'	0.082	52	84	1.1 (1)
II/II'	-0.094	47	91	1.0 (1)
III/III'	-0.48	52	90	1.0 (1)
IV/IV'	-0.65	52	92	0.98 (1)
V/V'	-0.94	56	123	0.7 (1)
VI/VI'	-1.09	50	96	0.94 (1)

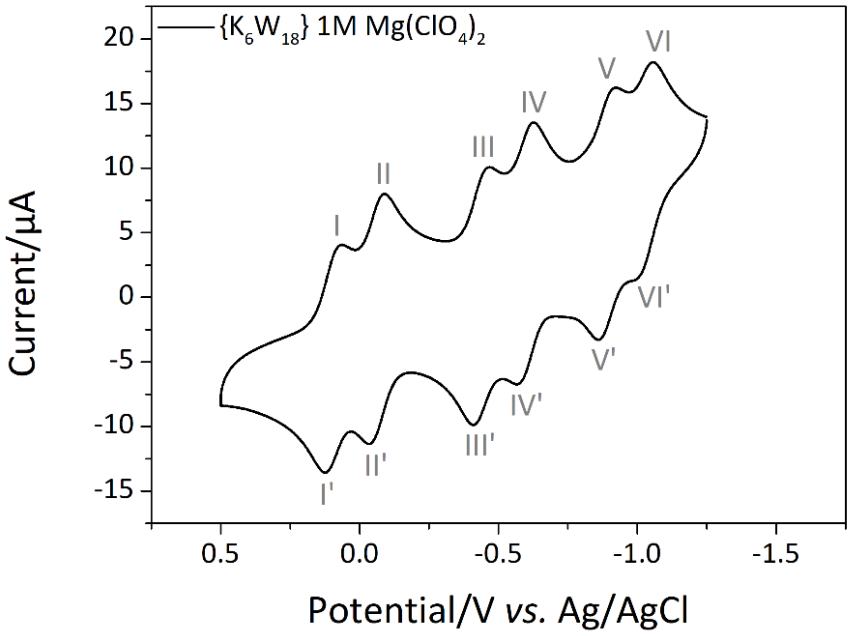


Figure 42 - CV of $\{K_6W_{18}\}$ in 1M $Mg(ClO_4)_2$ performed using a 3 mm diameter GC working electrode, a Pt counter electrode, and a Ag/AgCl reference electrode. The scan rate was 100 mV s^{-1}.

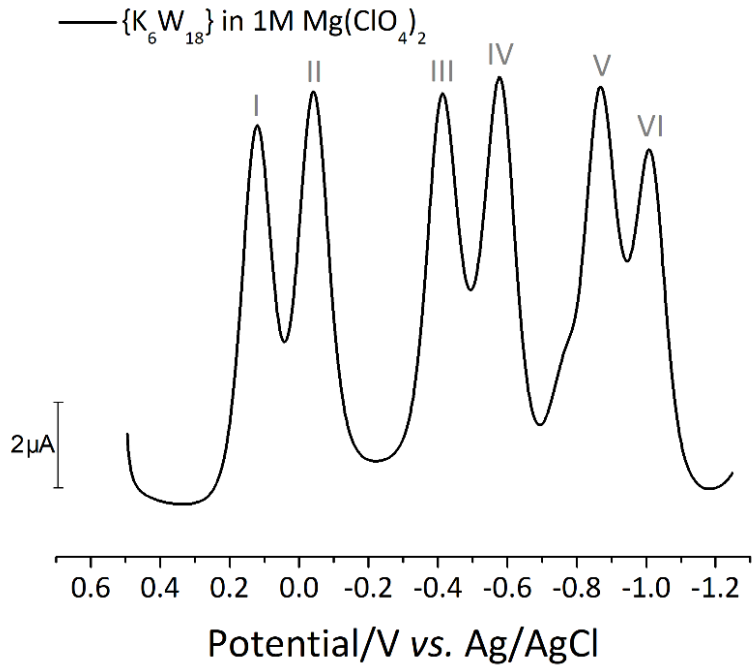


Figure 43 - DPV trace of $\{K_6W_{18}\}$ in 1M $Mg(ClO_4)_2$ performed using a 3 mm diameter GC working electrode, a Pt counter electrode, and a Ag/AgCl reference electrode. The scan rate was 100 mV s^{-1}.

Table 25 - Observed Midpoint Potentials (E_{mid}), Peak-to- Peak Separations (ΔE_p), Full Width at Half Maximum (FWHM) and number of electrons (n) for $\{K_6W_{18}\}$ in 1M $Mg(ClO_4)_2$.

Process	E_{mid}/V	ΔE_p/mV	FWHM/mV	n (no. of electrons)
I/I'	0.098	49	83	1.1 (1)
II/II'	-0.064	45	93	0.97 (1)
III/III'	-0.44	52	97	0.93 (1)
IV/IV'	-0.60	49	96	0.94 (1)
V/V'	-0.89	51	137	0.66 (1)
VI/VI'	-1.03	45	75	1.2 (1)

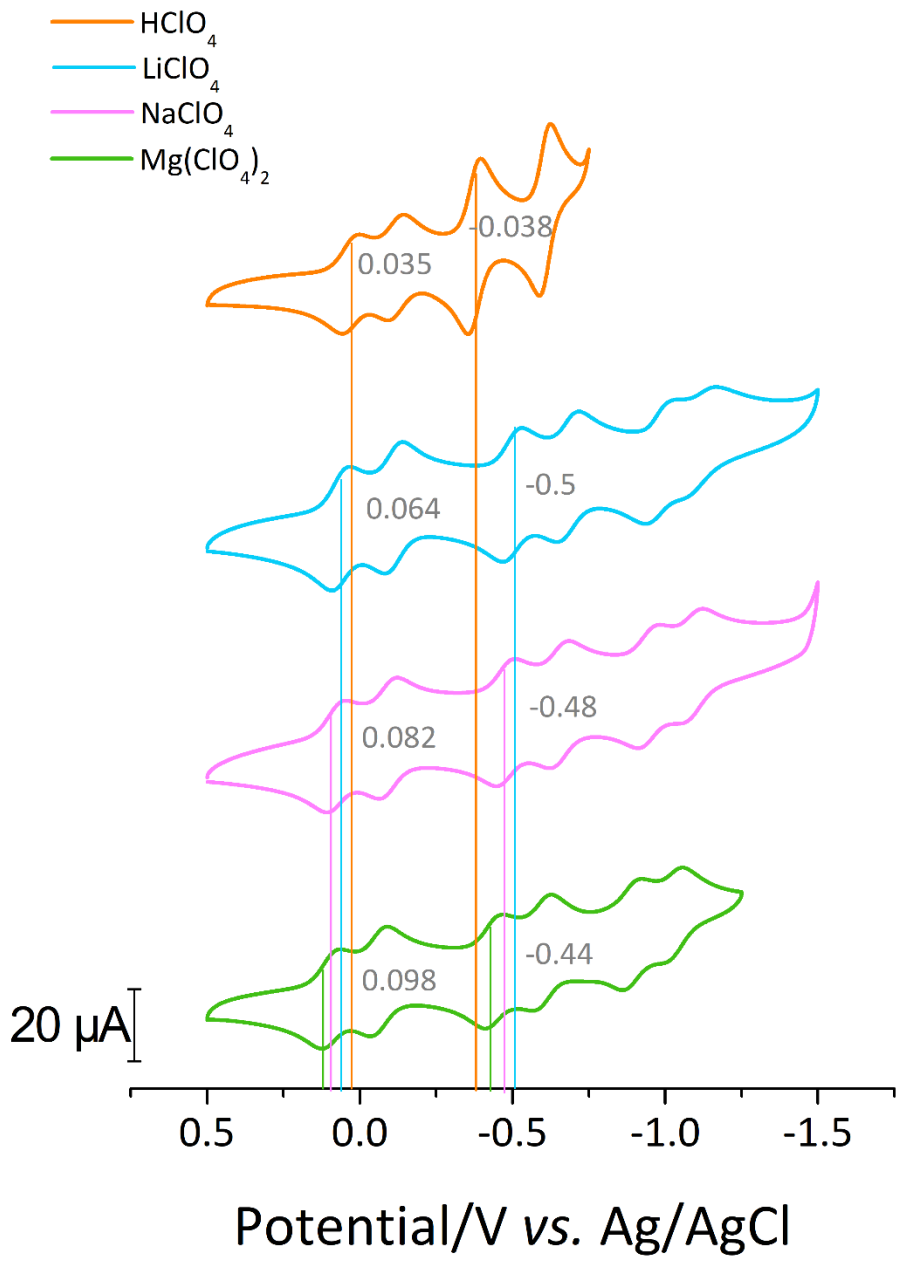


Figure 44 - Stacked solution phase CVs of $\{K_6W_{18}\}$ in the studied perchlorate systems, highlighting the metal cation association effects *vs.* H^+.

Table 26 - Comparison of E_{mid} and ΔE_p values for $\{H_6W_{18}\}$ in 1M perchlorate electrolytes.

Process	$HClO_4$		$LiClO_4$		$NaClO_4$		$Mg(ClO_4)_2$	
	E_{mid}/V	ΔE_p/mV	E_{mid}/V	ΔE_p/mV	E_{mid}/V	ΔE_p/mV	E_{mid}/V	ΔE_p/mV
I/I'	0.035	45	0.064 (+30 mV shift *vs.* H^+)	50	0.082 (+48 mV shift *vs.* H^+)	52	0.099 (+64 mV shift *vs.* H^+)	49
II/II'	-0.121	38	-0.11 (+9.5 mV shift *vs.* H^+)	49	-0.095 (+27 mV shift *vs.* H^+)	47	-0.064 (+58 mV shift *vs.* H^+)	45
III/III'	-0.375	38	-0.50 (-125 mV shift *vs.* H^+)	57	-0.475 (-100 mV shift *vs.* H^+)	52	-0.44 (-60 mV shift *vs.* H^+)	52
IV/IV'	-0.605	34	-0.68 (-75 mV shift *vs.* H^+)	65	-0.65 (-49 mV shift *vs.* H^+)	52	-0.60 (+4.5 mV shift *vs.* H^+)	49
V/V'	-	-	-0.98	88	-0.94	56	-0.89	51
VI/VI'	-	-	-1.11	87	-1.1	50	-1.03	45

2.4.5.3 Electrochemistry of $\{H_3W_{12}\}$ in Perchlorate-based Electrolytes

The redox profiles obtained for $\{H_3W_{12}\}$ in the presence of metal cations exhibit much more complicated behaviour. The CV of $\{H_3W_{12}\}$ in 1M $HClO_4$ shows the typical redox profile of the tungstate Keggin in acidic media as seen with 1M H_2SO_4, where three reversible redox waves are obtained, corresponding to two one-electron processes and one two-electron process (Figure 45). The latter is accompanied by protonation (Equations 54 – 56). The ΔE_p and FWHM values are in good agreement with the electron assignment.

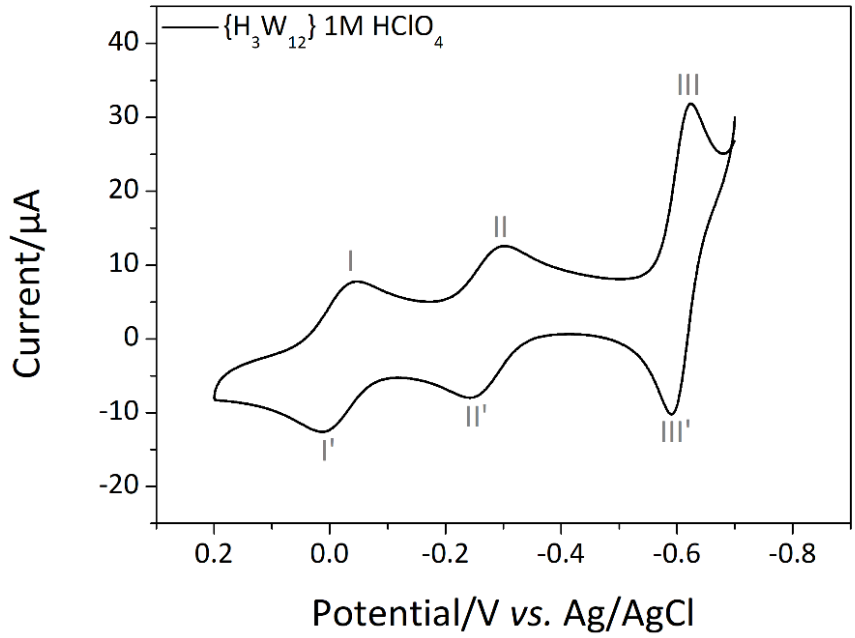


Figure 45 - CV of $\{H_3W_{12}\}$ in 1M $HClO_4$ performed using a 3 mm diameter GC working electrode, a Pt counter electrode, and a Ag/AgCl reference electrode. The scan rate was 100 mV s^{-1}.

Equations 54 – 56 – Redox couples of $\{H_3W_{12}\}$ in 1M $HClO_4$.

I/I': $[PW_{12}O_{40}]^{3-} + e^- \leftrightarrow [PW_{12}O_{40}]^{4-}$ (54)

II/II': $[PW_{12}O_{40}]^{4-} + e^- \leftrightarrow [PW_{12}O_{40}]^{5-}$ (55)

III/III': $[PW_{12}O_{40}]^{5-} + 2e^- + 2H^+ \leftrightarrow [H_2PW_{12}O_{40}]^{7-}$ (56)

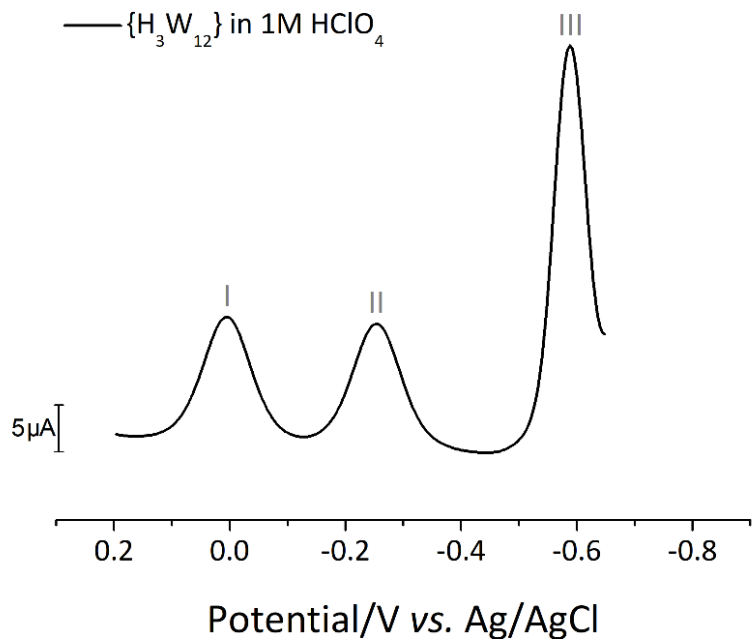


Figure 46 - DPV trace of $\{H_3W_{12}\}$ in 1M $HClO_4$ performed using a 3 mm diameter GC working electrode, a Pt counter electrode, and a Ag/AgCl reference electrode. The scan rate was 100 mV s^{-1}.

Table 27 - Observed Midpoint Potentials (E_{mid}), Peak-to- Peak Separations (ΔE_p), Full Width at Half Maximum (FWHM) and number of electrons (n) for $\{H_3W_{12}\}$ in 1M $HClO_4$.

Process	E_{mid}/V	ΔE_p/mV	FWHM/mV	n (no. of electrons)
I/I'	-0.014	46	89	1.0 (1)
II/II'	-0.27	48	82	1.1 (1)
III/III'	-0.61	32	59	1.5 (2)

In the presence of Li^+, four redox process are observed, and the potential window in which these processes appear narrows, due to the occurrence of both positive and negative shifts (Figure 47). Process I for $\{H_3W_{12}\}$ in 1M $LiClO_4$ is negatively shifted by 186 mV in relation to process I of $\{H_3W_{12}\}$ in 1M $HClO_4$, whereas process IV is positively shifted by 170 mV with respect to process III in 1M $HClO_4$. Lacunary POMs are generated by treating the parent POM with a weak base. In this instance, it is very possible that the Keggin is undergoing

partial hydrolysis in the alkaline conditions of 1M $LiClO_4$. The electrolyte is pH 9 which constitutes the regime of POM degradation and lacunary POM generation, thus there is a combination of factors that complicate the electrochemical behaviour. The DPV trace is included below, but due to the ill-defined peaks for processes I – III and subsequent probable peak fitting errors, it is difficult to declare with certainty the electron assignment for the redox processes.

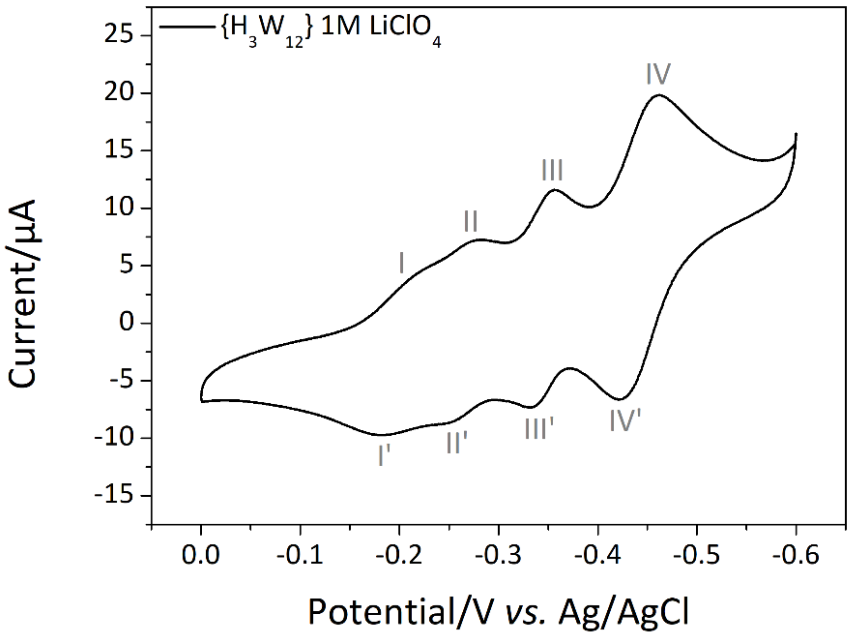


Figure 47 - CV of $\{H_3W_{12}\}$ in 1M $LiClO_4$ performed using a 3 mm diameter GC working electrode, a Pt counter electrode, and a Ag/AgCl reference electrode. The scan rate was 100 mV s^{-1}.

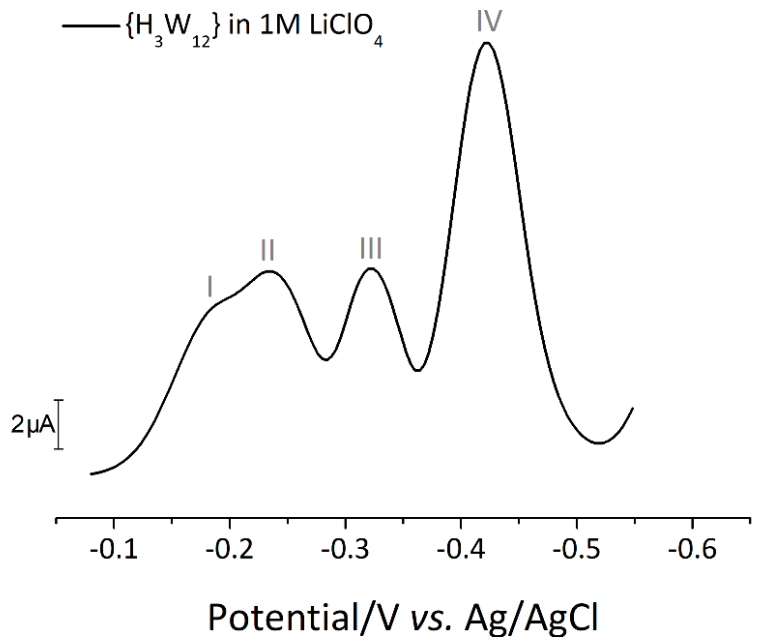


Figure 48 - DPV trace of $\{H_3W_{12}\}$ in 1M $LiClO_4$ performed using a 3 mm diameter GC working electrode, a Pt counter electrode, and a Ag/AgCl reference electrode. The scan rate was 100 mV s^{-1}.

Table 28 - Observed Midpoint Potentials (E_{mid}), Peak-to- Peak Separations (ΔE_p), Full Width at Half Maximum (FWHM) and number of electrons (n) for $\{H_3W_{12}\}$ in 1M $LiClO_4$.

Process	E_{mid}/V	ΔE_p/mV	FWHM/mV	n (no. of electrons)
I/I'	-0.2	35	46	1.0
II/II'	-0.26	28	65	1.1
III/III'	-0.35	18	42	1.5
IV/IV'	-0.44	29	58	1.6

In the presence of Na^+, five redox process are observed in the range of 0.05 – -0.7 V *vs.* Ag/AgCl (Figure 49). The very small currents for each process coupled with the larger background capacitive current suggests a loss of concentration of the POM within the electrolyte as well as deposition occurring on the surface of the working electrode. During the electrochemical measurements, a white precipitate was also observed in the analyte. Typically,

potassium hydrogen carbonate ($KHCO_3$) or sodium hydrogen carbonate ($NaHCO_3$) are used to generate lacunary POMs as K^+ and Na^+ are considered as ideal stabilising cations. Once again, it is possible that the Keggin is being hydrolysed in the alkaline conditions of 1M $NaClO_4$ and is precipitating out of solution on to the electrode surface. The DPV trace is included below (Figure 50), however the complicated redox profile leads to a false baseline in the peak fitting. This means the FWHM values are overestimates and as such will not be used to assign electron counts for the redox waves.

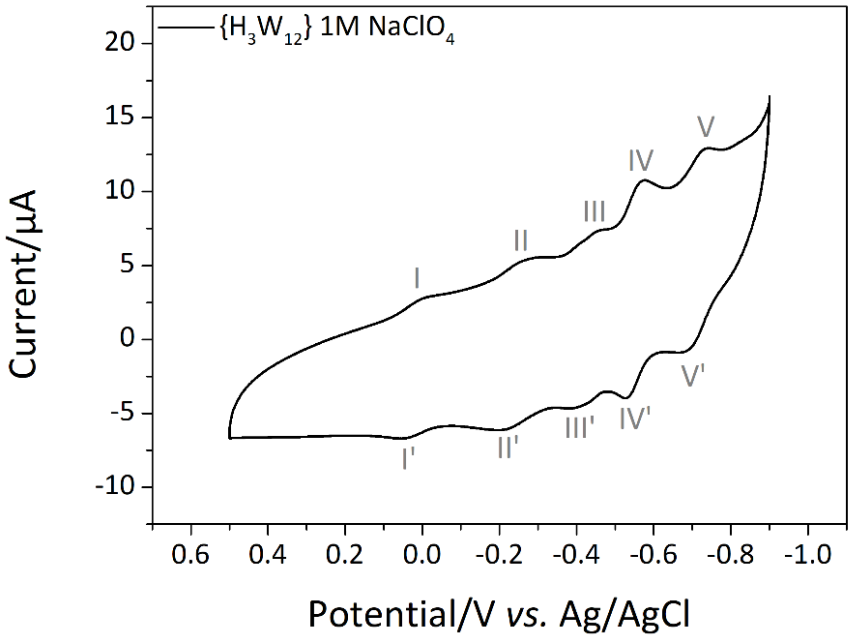


Figure 49 - CV of $\{H_3W_{12}\}$ in 1M $NaClO_4$ performed using a 3 mm diameter GC working electrode, a Pt counter electrode, and a Ag/AgCl reference electrode. The scan rate was 100 mV s^{-1}.

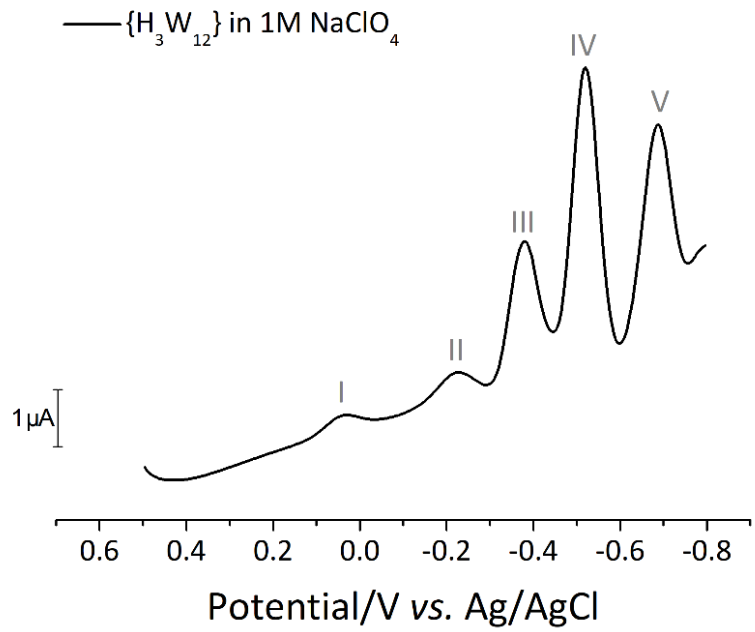


Figure 50 - DPV trace of $\{H_3W_{12}\}$ in 1M $NaClO_4$ performed using a 3 mm diameter GC working electrode, a Pt counter electrode, and a Ag/AgCl reference electrode. The scan rate was 100 mV s^{-1}.

Table 29 - Observed Midpoint Potentials (E_{mid}), Peak-to- Peak Separations (ΔE_p), Full Width at Half Maximum (FWHM) and number of electrons (n) for $\{H_3W_{12}\}$ in 1M $NaClO_4$.

Process	E_{mid}/V	ΔE_p/mV	FWHM/mV	n (no. of electrons)
I/I'	0.023	45	333	0.27
II/II'	-0.24	51	119	0.76
III/III'	-0.43	35	92	0.98
IV/IV'	-0.55	35	66	1.4
V/v'	-0.71	41	155	0.6

The redox profile of $\{H_3W_{12}\}$ in the presence of Mg^{2+} is very interesting as four redox waves are observed (Figure 51). The intensity of the redox waves coupled with the peak height ratio observed in the DPV (Figure 52), indicate that these processes correspond to two one-electron processes and two two-electron processes. This would be a total of six electrons, two more than for

$\{H_3W_{12}\}$ in acidic media. It is not unheard of for Keggin anions to undergo reductions greater than four electrons[67] but it is interesting to observe this in aqueous media in the presence of Mg^{2+}.

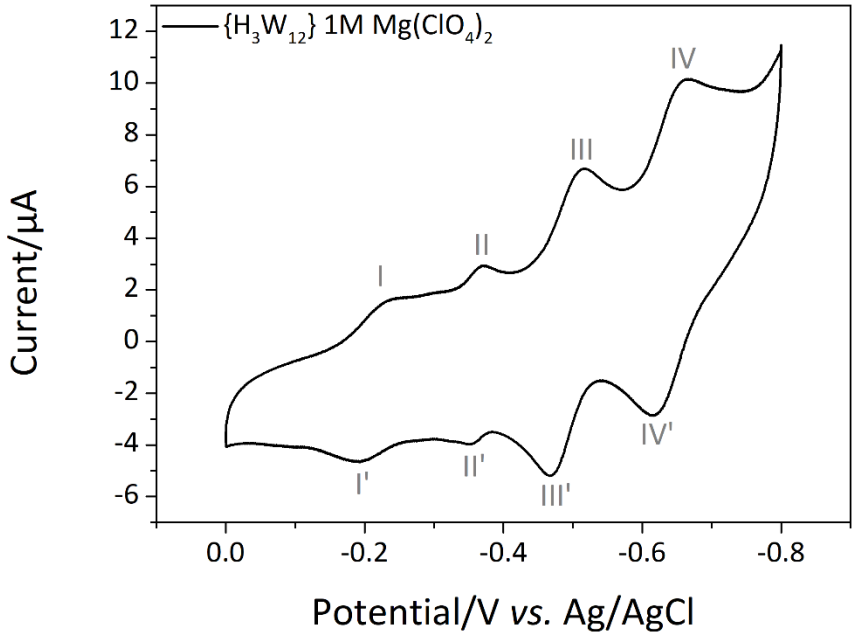


Figure 51 - CV of $\{H_3W_{12}\}$ in 1M $Mg(ClO_4)_2$ performed using a 3 mm diameter GC working electrode, a Pt counter electrode, and a Ag/AgCl reference electrode. The scan rate was 100 mV s^{-1}.

However, the electron assignments from the DPV trace (Figure 52, Table 30) do not reconcile a six-electron reduction. With $Mg(ClO_4)_2$ being a weak base, the possibility of POM degradation occurring cannot be completely eliminated.

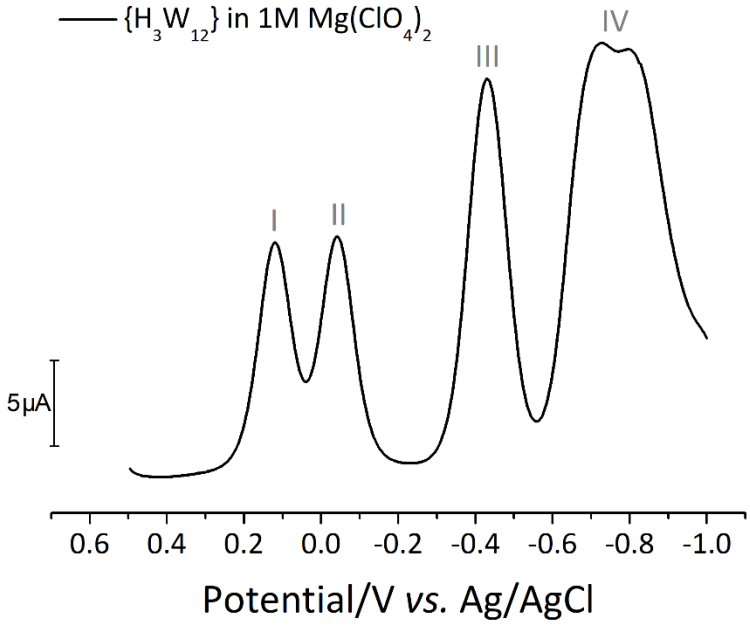


Figure 52 - DPV trace of $\{H_3W_{12}\}$ in 1M $Mg(ClO_4)_2$ performed using a 3 mm diameter GC working electrode, a Pt counter electrode, and a Ag/AgCl reference electrode. The scan rate was 100 mV s^{-1}.

Table 30 - Observed Midpoint Potentials (E_{mid}), Peak-to- Peak Separations (ΔE_p), Full Width at Half Maximum (FWHM) and number of electrons (n) for $\{H_3W_{12}\}$ in 1M $Mg(ClO_4)_2$.

Process	E_{mid}/V	ΔE_p/mV	FWHM/mV	n (no. of electrons)
I/I'	-0.21	45	83	1.1
II/II'	-0.36	51	90	1
III/III'	-0.49	35	94	0.96
IV/IV'	-0.64	35	235	0.38

Evidence from the Dawson motifs show that the most positive redox processes are observed in the presence of Mg^{2+}, which suggests that there might be an inherently stronger affinity between the POM and Mg^{2+}. It can be hypothesised that with the Keggin, there is a possibility that the Mg^{2+} in fact protects the Keggin from hydrolysis and stabilises the polyanionic structure. Whereas the weaker affinities of Li^+ and Na^+ for the Keggin means it is more susceptible to decomposition in their presence. It is noteworthy that neither

Dawson motif shows evidence of decomposition in the basic electrolytes, presumably due to the greater thermodynamic stability of the Dawson archetype. For $\{H_3W_{12}\}$, the ΔE_p and FWHM values for process I and II are in good agreement with one-electron processes. The ΔE_p values for processes III (65 mV) and IV (77 mV) are higher than expected a for a reversible two-electron process (expected 29 mV), and concomitantly so are the FWHM values (process III = 100 mV, process IV = 132 mV, expected 45.2 mV), indicating these final two processes are quasi-reversible.

Magnesium-ion batteries are a key contender in battery chemistries going beyond Li-ion, owing to their prospective benefits including operational safety, high theoretical capacity, and abundance of raw materials.[68,69] Very few examples on the use of POM precursors for Mg-ion batteries exist, however recently Jacobson and co-workers showed that the microporous molybdenum-vanadium oxide can be used as an intercalation cathode not only for Li^+ ions but also for Mg^{2+}.[70] The 3D mixed metal microporous framework $Mo_{2.5+y}VO_{9+\delta}$ (containing $Mo^{5+/6+}$ and $V^{4+/5+}$) contains large open tunnels which can overcome the problem of sluggish Mg^{2+} diffusion kinetics present in traditional electrodes. Additionally, all of the metal ions with mixed-valences (including V^{4+}, V^{5+}, Mo^{5+}, and Mo^{6+}) actively participated in the electrochemical reaction processes during the insertion of Mg^{2+}, massively enhancing the electrochemical performance of the Mg-ion battery.[70] The fascinating electrochemistry of the $K_6[P_2W_{18}O_{62}]$ POM in the presence of Mg^{2+} could be further investigated for multivalent batteries.

2.5 Conclusion & Future Work

Cyclic voltammetry was used to evaluate the electrochemical properties of a library of different POMs, including the plenary Dawson and Keggin motifs as well as a handful of their derivatives. Differential pulse voltammetry clarified the electron stoichiometry of the couples where appropriate.

The redox properties of the Keggin and Dawson POMs were examined in organic DMF solvent which showed that the same anion can have a different electrochemical profile depending on the featured countercation (H^+, K^+, TBA). The identity of the countercation also influences the solubility and subsequent electrochemical behaviour as seen with the degradation of the $K_6[P_2W_{18}O_{62}]$ motif. Amongst the Keggin and Dawson tungstates, the most positive redox potentials (E_{mid}) were observed for the H^+ countercation. The Keggin molybdate showed the most positive E_{mid} values compared to its tungsten counterpart. This is a result of the inherent difference in electronegativity between tungsten and molybdenum ($W^{6+} > Mo^{5+}$) resulting in a lowering of the LUMO energies and facilitating reduction.

A similar phenomenon was observed for the organic – inorganic hybrid $K_6[P_2W_{17}O_{59}(PO_3C_6H_5)_2]$ electrochemistry in DMF. The LUMO energy was lowered through hybridisation with electron – withdrawing moieties which manifested as more positive E_{mid} values in comparison to its purely inorganic counterpart ($K_6[P_2W_{18}O_{62}]$). The Fe-substituted Keggin showed drastically different electrochemistry to the acid Keggin ($H_3[PW_{12}O_{40}]$) and its TBA salt ($(N(C_4H_9)_4)_3[PW_{12}O_{40}]$. The Fe^{3+}/Fe^{2+} redox event occurred first and the W^{6+}/W^{5+} redox couple was shifted negatively by over 1 V, which exemplifies the tuneabilty that can be imparted onto POMs.

The acid Keggin $H_3[PW_{12}O_{40}]$, acid Dawson $H_6[P_2W_{18}O_{62}]$, and potassium salt $K_6[P_2W_{18}O_{62}]$ were analysed in a classic battery solvent. This fundamental study showed that the Keggin did not display well – defined or reversible electrochemistry, contrary to the Dawson motifs. The stability studies in increasingly wider potential windows showed complex and irreversible redox

behaviour, emphasising that the potential window must be taken into account for the operational design of a POM – Lithium battery.

The aqueous electrolyte studies highlighted the pH sensitive behaviour (pH) of POMs in solution and how protons can act as a countercation to induce proton – coupled behaviour, depending on the anionic charge of the POM (degree of reduction).

1M H_2SO_4 and 1M $HClO_4$ induced proton – coupled redox behaviour across all three POM motifs ($H_3[PW_{12}O_{40}]$, $H_6[P_2W_{18}O_{62}]$, $K_6[P_2W_{18}O_{62}]$). Striking differences were observed between the electrochemical profiles of $H_6[P_2W_{18}O_{62}]$ and $K_6[P_2W_{18}O_{62}]$. Both showed positive shifts of the first two one-electron processes upon association with an alkali metal cation. However, the potassium Dawson did not show any proton – coupled behaviour in the presence of metal ions and six one-electron processes were observed as opposed to four processes for the acid Dawson (two one-electron, two two-electron). In particular, the behaviour of $K_6[P_2W_{18}O_{62}]$ in the presence of Mg^{2+} presents an intriguing proposition with respect to multivalent POM – based batteries, either as an active material or electrolyte component. The redox profiles of the acid Keggin were more complicated to assign the number of electrons transferred due to potential stability issues, arising from insolubility and structural perturbation given the basic nature of the electrolytes. Future studies on the cycling behaviour of the Dawson and Keggin POMs using titration experiments to progressively alter the basicity of the electrolyte solutions could be useful in elucidating the tolerance limits in basic electrolytes. Through progressive measurements, it could be possible to see the redox waves transition from stable and well-defined redox couples to more complicated quasi and irreversible peaks as observed in this chapter.

2.6 Experimental

Solvents and reagents were purchased from either Sigma Aldrich, Acros Organics, Fischer scientific or VWR and were used without further purification.

^{1}H and ^{31}P NMR spectra were obtained using a Bruker DPX 300 spectrometer or AV400. Infra-red spectra were measured using a Bruker Alpha FTIR spectrometer with a platinum ATR module.

Synthesis of $K_6[P_2W_{18}O_{62}].9H_20$

$K_6[P_2W_{18}O_{62}].9H_20$ was synthesised according to Graham and Finke.[71] $Na_2WO_4.2H_2O$ (100 g, 0.303 mol) was dissolved in deionised water (120 ml) and stirred vigorously. After 5 minutes, 4M HCl (83 ml, 0.332 mol) was added dropwise at a rate of 2 drops per second. A milky white precipitate appeared and then dissolved with continued stirring, leaving a colourless solution. Immediately after, 4M H_3PO_4 (83 ml, 0.332 mol) was added dropwise at a rate of 4 drops per second, resulting in a pale yellow solution. This was then refluxed at 100 °C for 24 hours, forming a bright yellow solution. The solution was cooled to room temperature before adding KCl (50 g, 0.671 mol), resulting in the formation of a chalky yellow precipitate. Buchner filtration gave the crude product as a pale yellow powder. Following recrystallisation from a minimum amount of boiling water, the final product was obtained as yellow crystals.

Yield: 80.93 g, 99 %. ^{31}P NMR (δ, D_2O): -13.01. IR (ATR) cm^{-1}: 1085 (P-O, s), 954 (W=Od, s), 906 (W-Ob-W, s), 735 (W-Oc-W, s).

Synthesis of $H_6[P_2W_{18}O_{62}].6H_20$

$K_6[P_2W_{18}O_{62}].9H_20$ (10 g, 2.57 mmol) was dissolved in deionised water (150 ml). Diethyl ether (200 ml) was then added and the flask placed in an ice bath. 12M HCl (100 ml, 400 mmol) was added slowly before sealing the flask and leaving to stir overnight. The solution formed three layers; diethyl ether (top), aqueous (middle), etherate (bottom). The etherate was isolated using a separating funnel and resembled a golden yellow oil. The etherate was left to dry at 50 °C on a hotplate, resulting in a pale yellow-green powder.

Yield: 4.06 g. ^{31}P NMR (δ, D_2O): -13.01. IR (ATR) cm^{-1}: 1085 (P-O, s), 956 (W=Od, s), 904 (W-Ob-W, s), 727 (W-Oc-W, s).

Cation Exchange $K_6[P_2W_{18}O_{62}].9H_20 \rightarrow TBA_6[P_2W_{18}O_{62}].9H_20$

$K_6P_2W_{18}O_{62}$ (1.9 g, 0.49 mmol) was dissolved in distilled water (90 ml) to form a clear yellow solution. To this an aqueous solution of TBAB (1.25 g) in water (10 ml) was added dropwise, resulting in the immediate formation of a milky white precipitate. After stirring for an hour, the solvent volume was reduced, and the precipitate was filtered and air dried.

Yield: 2.41 g. ^{31}P NMR (δ, D_2O): -13.01. IR (ATR) cm^{-1}: 1085 (P-O, s), 955 (W=Od, s), 905 (W-Ob-W, s), 730 (W-Oc-W, s).

Synthesis of $H_3[PW_{12}O_{40}].3H_20$

$Na_2WO_4.2H_2O$ (100 g, 0.303 mol) and $Na_2HPO_4.2H_2O$ (50 g, 0.281 mol) were added to deionised water (160 ml) and dissolved with vigorous stirring. The solution was refluxed at 80 °C for 1 hour. 12M HCl (100 ml, 0.4 mol) was added slowly and the solution became yellow. It was then left to reflux overnight at 80 °C. A white precipitate formed which was filtered and washed with diethyl ether. The white powder was recrystallised from a minimum amount of boiling water, yielding large white crystals.

Yield: 54.32 g, 70 %. ^{31}P NMR (δ, D_2O): -15.27. IR (ATR) cm^{-1}: 1072 (P-O, s), 973 (W=Od, s), 904 (W-Ob-W, s), 770 (W-Oc-W, s).

Synthesis of $TBA_3[PMo_{12}O_{40}].3H_20$

1 M H_3PO_4 (10 ml, 0.01 mol) was added to a mixture of $Na_2.MoO_4$ (120 ml, 1M), 13M HNO_3 (18 ml, 0.234 mol) and 1, 4-dioxane (100 ml). The resulting bright yellow solution was precipitated by adding TBAB (10 g, 0.031 mol) in water (10 ml). The mixture was stirred for 30 mins before filtering. After filtration, the yellow solid was treated by boiling water (100 ml), filtered again and washed with water, ethanol and ether. A yellow powder was obtained and recrystallised in hot acetone.

Yield: 13.38 g, 74 %. ^{31}P NMR (δ, DMSO): -4.11. IR (ATR) cm^{-1}: 1059 (P-O, s), 948 (Mo=Od, s), 880 (Mo-Ob-Mo, s), 783 (Mo-Oc-Mo, s).

Synthesis of $K_{10}[P_2W_{17}O_{61}].9H20$ (lacunary POM)

$K_6[P_2W_{18}O_{62}].9H_20$ (40 g, 0.01 mol) was dissolved in deionised water (100 ml). To this was added a solution of $KHCO_3$ (10 g, 0.099 mol) in water (100 ml) whilst stirring. The reaction was complete after 1 hour and the white precipitate was filtered. It was then redissolved in hot water (250 ml, 95°C). After cooling to room temperature, the snow like crystals were filtered after 3 hours, dried under suction for 5 hours and then air-dried for 2 days.

Yield: 30.61 g, 62 %. ^{31}P NMR (δ, D2O): -7.23, -14.37. IR (ATR) cm^{-1}:1084 (P-O, s), 1050 (W=Od, s), 1012 (W-Ob-W, s).

Synthesis of $K_6[P_2W_{17}O_{57}(PO_3H_5C_6)_2].6C_4H_9NO$

$K_{10}[P_2W_{17}O_{61}].9H_20$ (125.0 mg, 0.025 mmol), phenylphosphonic acid (17.8 mg, 0.113 mmol) and KCl (39.9 mg, 535 mmol) were suspended in N,N'-dimethylacetamide (6 ml) before adding 12 M HCl (20 µL). The reaction mixture was then heated at 90 °C for 24 hours. After cooling to room temperature, the reaction mixture was filtered to give a green solution. Subsequent centrifugation with diethyl ether, then ethanol and again with diethyl ether gave a green solid which dried to a green powder.

Yield: 88.34 mg, 75%. ^{31}P NMR (δ, DMSO): 15.27, -10.92, -12.54. IR (ATR) cm^{-1}:1614 (C=C, m), 1402 (C=C, m), 1190 (W=Od, s).

Synthesis of $TBA_4[PW_{11}Fe(H_2O)O_{39}].4H_20$

$Na_2WO_4.2H_2O$ (3.29 g, 10 mmol) was dissolved in distilled water (20 ml). Na2HPO4 (0.13 g, 0.91 mmol) and $Fe(NO_3)_3.9H_2O$ (0.49 g, 1.2 mmol) were added to this solution. The pH was adjusted to 4.5 under stirring and the mixture was heated to 85 °C. following this, an aqueous solution of TBAB (1.45 g) in distilled water (5 ml) was added dropwise to the above solution. The mixture was stirred and a white-yellow precipitate formed. The precipitate was recovered by filtration, washed with ether, and air-dried.

Yield: 3.67 g, 92%. ^{31}P NMR (δ, DMSO): -11.55. IR (ATR) cm^{-1}:1068 (P-O, s), 962 (W=Od, s), 887 (W-Ob-W, s), 793 (W-Oc-W, s).

Solution Phase Cyclic Voltammetry – DMF

A 0.01 M concentration of POM was dissolved in 5 mL DMF (supporting electrolyte 0.1 M $TBAPF_6$) or. All experiments were performed using a CH Instrument 600E potentiostat with a three-electrode electrochemical cell configuration. A 3 mm glassy carbon (GC) working electrode was used with a platinum (Pt) wire counter electrode and a silver (Ag) wire as the pseudo-reference electrode. Ferrocene (Fc/Fc^+) was used an internal reference and added at the end of the measurements. The GC surface was polished successively using a slurry of 0.3 µm, 0.1 µm, and 0.05 µm alumina, and then washed with water and acetone before gently drying. Analyte solutions were purged with argon for at least 10 minutes before CV experiments. The CV experiments were controlled with CHI software and were typically carried out at a scan rate of 100 mV s $^{-1}$.

Solution Phase Cyclic Voltammetry – Battery Solvent

A 0.01 M concentration of POM was dissolved in 5 mL battery solvent: 1M $LiPF_6$ in ethylene carbonate (EC) + ethyl methyl carbonate (EMC) (1:1 v/v). All experiments were conductive in an air and moisture-free environment inside an argon-filled glovebox. All experiments were performed using a CH Instrument 600E potentiostat with a three-electrode electrochemical cell configuration. A 3 mm glassy carbon (GC) working electrode was used with a platinum (Pt) wire counter electrode and a lithium iron phosphate (LFP) reference electrode was used to reference the potentials *vs.* Li/Li^+. The LFP electrode is stored in the glovebox at all times. The GC surface was polished successively using a slurry of 0.3 µm, 0.1 µm, and 0.05 µm alumina, and then washed with water and acetone before gently drying. The WE, CE, glassware and POM were purged in the antechamber for at least 45 mins prior to the CV experiments. The CV experiments were controlled with CHI software and were typically carried out at a scan rate of 50 mV s $^{-1}$.

Solution Phase Cyclic Voltammetry – Aqueous Electrolytes

A 0.01 M concentration of POM was dissolved in 10 mL of a 1M concentration of the aqueous electrolyte: 1M H_2SO_4/$HClO_4$/$LiClO_4$/$NaClO_4$/$Mg(ClO_4)_2$. All experiments were performed using a CH Instrument 600E potentiostat with a three-electrode electrochemical cell configuration. A 3 mm glassy carbon (GC) working electrode was used with a platinum (Pt) wire counter electrode and a glass frit containing a silver/silver chloride (Ag/Ag^+) reference electrode. The GC surface was polished successively using a slurry of 0.3 μm, 0.1 μm, and 0.05 μm alumina, and then washed with water and acetone before gently drying. Analyte solutions were purged with argon for at least 10 minutes before CV experiments. The CV experiments were controlled with CHI software and were typically carried out at a scan rate of 100 $mV\ s^{-1}$.

2.7 References

1 A. Bijelic, M. Aureliano and A. Rompel, Polyoxometalates as Potential Next-Generation Metallodrugs in the Combat Against Cancer, *Angew. Chemie - Int. Ed.*, 2019, **58**, 2980–2999.

2 A. Bijelic, M. Aureliano and A. Rompel, The antibacterial activity of polyoxometalates: Structures, antibiotic effects and future perspectives, *Chem. Commun.*, 2018, **54**, 1153–1169.

3 Y. Wang and I. A. Weinstock, Polyoxometalate-decorated nanoparticles, *Chem. Soc. Rev.*, 2012, **41**, 7479–7496.

4 S. Martín, Y. Takashima, C. G. Lin, Y. F. Song, H. N. Miras and L. Cronin, Integrated Synthesis of Gold Nanoparticles Coated with Polyoxometalate Clusters, *Inorg. Chem.*, 2019, **58**, 4110–4116.

5 A. Bijelic and A. Rompel, The use of polyoxometalates in protein crystallography - An attempt to widen a well-known bottleneck, *Coord. Chem. Rev.*, 2015, **299**, 22–38.

6 A. Bijelic and A. Rompel, Ten Good Reasons for the Use of the Tellurium-Centered Anderson-Evans Polyoxotungstate in Protein Crystallography, *Acc. Chem. Res.*, 2017, **50**, 1441–1448.

7 M. Wang, W. Zhong, S. Zhang, R. Liu, J. Xing and G. Zhang, An overall water-splitting polyoxometalate catalyst for the electromicrobial conversion of CO_2 in neutral water, *J. Mater. Chem. A*, 2018, **6**, 9915–9921.

8 S.-S. Wang and G.-Y. Yang, Recent Advances in Polyoxometalate-Catalyzed Reactions, *Chem. Rev.*, 2015, **115**, 4893–4962.

9 T. Ueda, Electrochemistry of Polyoxometalates: From Fundamental Aspects to Applications, *ChemElectroChem*, 2018, **5**, 823–838.

10 N. I. Gumerova and A. Rompel, Synthesis, structures and applications of electron-rich polyoxometalates, *Nat. Rev. Chem.*, 2018, **2**, 0112.

11 A. Proust, R. Thouvenot and P. Gouzerh, Functionalization of polyoxometalates: towards advanced applications in catalysis and materials science, *Chem. Commun.*, 2008, 1837.

12 I. A. Weinstock, Homogeneous-phase electron-transfer reactions of polyoxometalates, *Chem. Rev.*, 1998, **98**, 113–170.

13 D. L. Long, R. Tsunashima and L. Cronin, Polyoxometalates: Building blocks for functional nanoscale systems, *Angew. Chemie - Int. Ed.*, 2010, **49**, 1736–1758.

14 S. Himeno, K. Maeda, T. Osakai, A. Saito and T. Hori, A Voltammetric Study on the One-Electron Redox Processes of the Dawson-Type Heteropolymolybdate Complexes., *Bull. Chem. Soc. Jpn.*, 1993, **66**, 109–113.

15 K. Maeda, S. Himeno, T. Osakai, A. Saito and T. Hori, A voltammetric study of Keggin-type heteropolymolybdate anions, *J. Electroanal. Chem.*, 1994, **364**, 149–154.

16 K. Maeda, H. Katano, T. Osakai, S. Himeno and A. Saito, Charge dependence of one-electron redox potentials of Keggin-type heteropolyoxometalate anions, *J. Electroanal. Chem.*, 1995, **389**, 167–173.

17 L. Parent, P. A. Aparicio, P. De Oliveira, A. L. Teillout, J. M. Poblet, X. López and I. M. Mbomekallé, Effect of electron (De)localization and pairing in the electrochemistry of polyoxometalates: Study of Wells-Dawson molybdotungstophosphate derivatives, *Inorg. Chem.*, 2014, **53**, 5941–5949.

18 M. Sadakane and E. Steckhan, Electrochemical Properties of Polyoxometalates as Electrocatalysts, *Chem. Rev.*, 1998, **98**, 219–238.

19 L. R. Bard, A. J.; Faulkner, *Electrochemical Methods: Fundamentals and Applications*, John Wiley & Sons, Inc, 2nd edn., 2001.

20 P. Zanello, *Inorganic Electrochemistry: Theory, Practice, and Application*, Royal Society of Chemistry, 1st edn., 2003.

21 S. Javanshir, A. Ohanian, M. M. Heravi, M. R. Naimi-Jamal and F. F. Bamoharram, Ultrasound-

promoted, rapid, green, one-pot synthesis of 2'-aminobenzothiazolomethylnaphthols via a multi-component reaction, catalyzed by heteropolyacid in aqueous media, *J. Saudi Chem. Soc.*, 2014, **18**, 502–506.

22 M. Misono, Unique acid catalysis of heteropoly compounds (heteropolyoxometalates) in the solid state, *Chem. Commun.*, 2001, **1**, 1141–1153.

23 M. Masteri-Farahani and M. Modarres, Encapsulation of Keggin-type phosphotungstic acid into the mesopores of SBA-16 as a reusable heterogeneous catalyst for the epoxidation of olefins, *Sci. Iran.*, 2017, **24**, 0–0.

24 M. M. Heravi, M. Vazin Fard and Z. Faghihi, Heteropoly acids-catalyzed organic reactions in water: doubly green reactions, *Green Chem. Lett. Rev.*, 2013, **6**, 282–300.

25 N. Mizuno and M. Misnnot, Heteropolyacid catalysts, *Curr. Opin. Solid State Mater. Sci.*, 1997, **2**, 84–89.

26 J. Yang, M. J. Janik, D. Ma, A. Zheng, M. Zhang, M. Neurock, R. J. Davis, C. Ye and F. Deng, Location, acid strength, and mobility of the acidic protons in Keggin 12-$H_3PW_{12}O_{40}$: A combined solid-state NMR spectroscopy and DFT quantum chemical calculation study, *J. Am. Chem. Soc.*, 2005, **127**, 18274–18280.

27 G. Kickelbick, *Introduction to Hybrid Materials*, Wiley-VCH Verlag, 2007.

28 C. Rong and F. C. Anson, Simplified Preparations and Electrochemical Behavior of Two Chromium-Substituted Heteropolytungstate Anions, *Inorg. Chem.*, 1994, **33**, 1064–1070.

29 A. Müller, L. Dloczik, E. Diemann and M. T. Pope, A cyclic voltammetric study of mangano(II)undecatungstosilicate: An illustrative example of the reduction, protonation and disproportionation pathways of transition metal substituted heteropolytungstates in aqueous solution, *Inorganica Chim. Acta*, 1997, **257**, 231–239.

30 M. Sadakane, D. Tsukuma, M. H. Dickman, B. Bassil, U. Kortz, M. Higashijima and W. Ueda, Structural characterization of mono-ruthenium substituted Keggin-type silicotungstates, *Dalt. Trans.*, 2006, 4271.

31 S. Li, W. Zhu, H. Ma, H. Pang, H. Liu and T. Yu, Structure and bifunctional electrocatalytic activity of a novel 3D framework based on dimeric monocopper-substituted polyoxoanions as ten-connected linkages, *RSC Adv.*, 2013, **3**, 9770–9777.

32 X. L. Wang, C. Qin, E. B. Wang, Z. M. Su, Y. G. Li and L. Xu, Self-assembly of nanometer-scale $[Cu_{24}I_{10}L_{12}]^{14+}$ cages and ball-shaped keggin clusters into a (4,12)-connected 3D framework with photoluminescent and electrochemical properties, *Angew. Chemie - Int. Ed.*, 2006, **45**, 7411–7414.

33 N. Gao, H. Sun, K. Dong, J. Ren, T. Duan, C. Xu and X. Qu, Transition-metal-substituted polyoxometalate derivatives as functional anti-amyloid agents for Alzheimer's disease, *Nat. Commun.*, 2014, **5**, 1–9.

34 J. J. Hu, L. Wang, B. N. Chen, G. X. Chi, M. J. Zhao and Y. Li, Transition Metal Substituted Polyoxometalates as α-Glucosidase Inhibitors, *Eur. J. Inorg. Chem.*, 2019, **2019**, 3270–3276.

35 S. Ivanova, Hybrid Organic-Inorganic Materials Based on Polyoxometalates and Ionic Liquids and Their Application in Catalysis, *ISRN Chem. Eng.*, 2014, **2014**, 1–13.

36 M. Stuckart and K. Y. Monakhov, Polyoxometalate encapsulation into metal-organic frameworks: The way towards functional nanomaterials for water splitting, *J. Mater. Chem. A*, 2018, **6**, 17849–17853.

37 M. Stuckart and K. Y. Monakhov, Polyoxometalates as components of supramolecular assemblies, *Chem. Sci.*, 2019, **10**, 4364–4376.

38 A. J. Kibler and G. N. Newton, Tuning the electronic structure of organic–inorganic hybrid polyoxometalates: The crucial role of the covalent linkage, *Polyhedron*, 2018, **154**, 1–20.

39 A. V Anyushin, A. Kondinski and T. N. Parac-Vogt, Hybrid polyoxometalates as post-functionalization platforms: From fundamentals to emerging applications, *Chem. Soc. Rev.*, 2020, **49**, 382–432.

40 A. Dolbecq, E. Dumas, C. R. Mayer and P. Mialane, Hybrid Organic–Inorganic Polyoxometalate Compounds: From Structural Diversity to Applications, *Chem. Rev.*, 2010, **110**, 6009–6048.

41 J. M. Cameron, S. Fujimoto, K. Kastner, R. Wei, D. Robinson, V. Sans, G. N. Newton and H. H. Oshio, Orbital Engineering: Photoactivation of an Organofunctionalized Polyoxotungstate, *Chem. - A Eur. J.*, 2017, **23**, 47–50.

42 B. Matt, C. Coudret, C. Viala, D. Jouvenot, F. Loiseau, G. Izzet and A. Proust, Elaboration of covalently linked polyoxometalates with ruthenium and pyrene chromophores and characteriation of their photophysical properties, *Inorg. Chem.*, 2011, **50**, 7761–7768.

43 Z. M. Zhang, T. Zhang, C. Wang, Z. Lin, L. S. Long and W. Lin, Photosensitizing metal-organic framework enabling visible-light-driven proton reduction by a wells-dawson-type polyoxometalate, *J. Am. Chem. Soc.*, 2015, **137**, 3197–3200.

44 J. M. Cameron, S. Fujimoto, K. Kastner, R. J. Wei, D. Robinson, V. Sans, G. N. Newton and H. H. Oshio, Orbital Engineering: Photoactivation of an Organofunctionalized Polyoxotungstate, *Chem. - A Eur. J.*, 2017, **23**, 47–50.

45 F. M. Zonoz, Electrochemistry Investigation of the Monolacunary and Their Transition Metal Substituent Keggin-Type Polyoxometalates, *Electrocatalysis*, 2016, **7**, 215–225.

46 F. a. R. S. Couto, A. M. V. Cavaleiro, J. D. Pedrosa de Jesus and J. E. J. Simão, Study of polyoxotungstates with the Keggin structure by cyclic voltammetry, *Inorganica Chim. Acta*, 1998, **281**, 225–228.

47 A. J. Wain, G. G. Wildgoose, C. G. R. Heald, L. Jiang, T. G. J. Jones and R. G. Compton, Electrochemical ESR and voltammetric studies of lithium ion pairing with electrogenerated 9,10-anthraquinone radical anions either free in acetonitrile solution or covalently bound to multiwalled carbon nanotubes, *J. Phys. Chem. B*, 2005, **109**, 3971–3978.

48 H. Chen, M. Armand, M. Courty, M. Jiang, C. P. Grey, F. Dolhem, J. M. Tarascon and P. Poizot, Lithium salt of tetrahydroxybenzoquinone: Toward the development of a sustainable Li-ion battery, *J. Am. Chem. Soc.*, 2009, **131**, 8984–8988.

49 W. Walker, S. Grugeon, O. Mentre, S. Laruelle, J. M. Tarascon and F. Wudl, Ethoxycarbonyl-based organic electrode for Li-batteries, *J. Am. Chem. Soc.*, 2010, **132**, 6517–6523.

50 Z. Song, H. Zhan and Y. Zhou, Polyimides: Promising energy-storage materials, *Angew. Chemie - Int. Ed.*, 2010, **49**, 8444–8448.

51 Q. Li, C. Batchelor-Mcauley, N. S. Lawrence, R. S. Hartshorne and R. G. Compton, Electrolyte tuning of electrode potentials: The one electron vs. two electron reduction of anthraquinone-2-sulfonate in aqueous media, *Chem. Commun.*, 2011, **47**, 11426–11428.

52 K. Hernández-Burgos, G. G. Rodríguez-Calero, W. Zhou, S. E. Burkhardt and H. D. Abruña, Increasing the gravimetric energy density of organic based secondary battery cathodes using small radius cations (Li^+ and Mg^{2+}), *J. Am. Chem. Soc.*, 2013, **135**, 14532–14535.

53 M. T. Pope and E. Papaconstantinou, Heteropoly Blues. II. Reduction of 2:18-Tungstates, *Inorg. Chem*, 1967, **6**, 1147–1152.

54 M. S. Balulla, J. A. Gamelas, H. M. Carapuça, A. M. V Cavaleiro and W. Schlindwein, Electrochemical behaviour of first row transition metal substituted polyoxotungstates: A comparative study in acetonitrile, *Eur. J. Inorg. Chem.*, 2004, **4**, 619–628.

55 S. Amin, J. M. Cameron, J. A. Watts, D. A. Walsh, V. Sans and G. N. Newton, Effects of chain length on the size, stability, and electronic structure of redox-Active organic-inorganic hybrid polyoxometalate micelles, *Mol. Syst. Des. Eng.*, 2019, **4**, 995–999.

56 A. Misra, K. Kozma, C. Streb and M. Nyman, Beyond Charge Balance: Counter-Cations in Polyoxometalate Chemistry, *Angew. Chemie Int. Ed.*, 2020, **59**, 596–612.

57 V. A. Grigoriev, D. Cheng, C. L. Hill and I. A. Weinstock, Role of alkali metal cation size in the energy and rate of electron transfer to solvent-separated 1:1 [(M^+) (acceptor)] (M^+ = Li^+, Na^+, K^+) ion pairs, *J. Am. Chem. Soc.*, 2001, **123**, 5292–5307.

58 J. M. Gómez-Gil, E. Laborda, J. Gonzalez, A. Molina and R. G. Compton, Electrochemical and

Computational Study of Ion Association in the Electroreduction of $PW_{12}O_{40}^{3-}$, *J. Phys. Chem. C*, 2017, **121**, 26751–26763.

59 K. Maeda, S. Himeno, T. Osakai, A. Saito and T. Hori, A voltammetric study of Keggin-type heteropolymolybdate anions, *J. Electroanal. Chem.*, 1994, **364**, 149–154.

60 S. Himeno and M. Takamoto, Difference in voltammetric properties between the Keggin-type $[XW_{12}O_{40}]^{n-}$ and $[XMo_{12}O_{40}]^{n-}$ complexes, *J. Electroanal. Chem.*, 2002, **528**, 170–174.

61 E. Schreiber, N. A. Hartley, W. W. Brennessel, T. R. Cook, J. R. McKone and E. M. Matson, An Organofunctionalized Polyoxovanadium Cluster as a Molecular Model of Interfacial Pseudocapacitance, *ACS Appl. Energy Mater.*, 2019, **2**, 8985–8993.

62 J. Luo, S. Ye, T. Li, E. Sarnello, H. Li and T. Liu, Distinctive Trend of Metal Binding Affinity via Hydration Shell Breakage in Nanoconfined Cavity, *J. Phys. Chem. C*, 2019, **123**, 14825–14833.

63 M. R. Antonio, M. Nyman and T. M. Anderson, Direct observation of contact ion-pair formation in aqueous solution, *Angew. Chemie - Int. Ed.*, 2009, **48**, 6136–6140.

64 J. He, H. Li, P. Yang, F. Haso, J. Wu, T. Li, U. Kortz and T. Liu, Tuning of Polyoxopalladate Macroanionic Hydration Shell via Countercation Interaction, *Chem. - A Eur. J.*, 2018, **24**, 3052–3057.

65 J. M. Pigga, J. A. Teprovich, R. A. Flowers, M. R. Antonio and T. Liu, Selective monovalent cation association and exchange around keplerate polyoxometalate macroanions in dilute aqueous solutions, *Langmuir*, 2010, **26**, 9449–9456.

66 Y. Chu, J. Chen, F. Haso, Y. Gao, J. E. S. Szymanowski, P. C. Burns and T. Liu, Expanding the Schulze–Hardy Rule and the Hofmeister Series to Nanometer-Scaled Hydrophilic Macroions, *Chem. - A Eur. J.*, 2018, **24**, 5479–5483.

67 H. Wang, S. Hamanaka, Y. Nishimoto, S. Irle, T. Yokoyama, H. Yoshikawa and K. Awaga, In operando X-ray absorption fine structure studies of polyoxometalate molecular cluster batteries: Polyoxometalates as electron sponges, *J. Am. Chem. Soc.*, 2012, **134**, 4918–4924.

68 M. Mao, T. Gao, S. Hou and C. Wang, A critical review of cathodes for rechargeable Mg batteries, *Chem. Soc. Rev.*, 2018, **47**, 8804–8841.

69 D. Aurbach, I. Weissman, Y. Gofer and E. Levi, Nonaqueous magnesium electrochemistry and its application in secondary batteries, *Chem. Rec.*, 2003, **3**, 61–73.

70 W. Kaveevivitchai and A. J. Jacobson, High Capacity Rechargeable Magnesium-Ion Batteries Based on a Microporous Molybdenum-Vanadium Oxide Cathode, *Chem. Mater.*, 2016, **28**, 4593–4601.

71 C. R.Graham and R. G.Finke, The Classic Wells-Dawson Polyoxometalate, $K_6[r\text{-}P_2W_{18}O_{62}]\cdot 14H_2O$. Answering an 88 Year-Old Question: What Is Its Preferred, Optimum Synthesis?, *Inorg. Chem.*, 2008, **47**, 3679–3686.

3. Preparation & Characterisation of Polyoxometalates Supported on Vulcan Carbon

3.1 Introduction

As outlined previously, one of the most prominent features of POMs is their unique redox behaviour. POMs are stable in a variety of oxidation states, which span a wide potential range, and can participate in rapid and reversible multi-electron transfer processes. Their structural diversity and tuneable chemical properties make them particularly useful building blocks for functional nanomaterials.[1–4] Consequently, POMs have been used as the active redox species in a range of devices and systems, such as batteries[5], supercapacitors[6], dye-sensitized solar cells[6], electrocatalysis[7], water-splitting[8] and proton conductors[9]. As solid-state electrode materials are often preferred in such systems, and POMs exhibit relatively little electronic conductivity, the development of methods for attaching POMs to conductive (often carbon) supports is a very active area of research.[10,11]

Aside from the negligible conductivity, their high solubility is another reason to heterogenise POMs to prevent leaching and enhance the long-term stability of the proposed composite system. It is also important to understand how this stability is affected by the operating conditions. For example, Singh et al. reported the synthesis of Ru- and Ir- functionalized octamolybdate clusters, deposited on Ni-foam electrodes as model catalysts. However, under the harsh hydrogen evolution reaction conditions, the POMs experienced significant chemical changes, resulting in the formation of nanocomposites with much higher electrocatalytic activity than the POM precursors.[12]

Another approach to circumvent structural evolution and leaching of POMs is to use protective coatings such as Al_2O_3.[13] This would be particularly

beneficial for water oxidation catalysts, which are susceptible to degradation via detachment of the catalyst during prolonged (photo)electrochemical operation.[14] Care must be taken in the thickness of the coating; too thick and it will hinder catalyst accessibility, resulting in poor performance. Numerous strategies also exist to trap and stabilize POMs in porous structures such as metal-organic frameworks (MOFs)[15], covalent-organic frameworks (COFs)[16] and zeolitic imidazolate frameworks (ZIFs)[17]. Here, principles of size matching the POM moiety to pore size, organic functionalisation with linker groups as well as exchanging the POM counteractions for larger MOF/ZIF framework clusters are applied. However, these composites are generally not electrically conductive and synthetically challenging.

With this in mind, carbons are the material of choice which have the desired conductivity, strong affinity for POMs and structural versatility owing to a considerable number of allotropes. High-surface-area carbons such as activated carbons (ACs), carbon blacks (CBs), and carbon nanotubes (CNTs) are increasingly popular catalyst supports, due to their chemical, electrochemical and mechanical properties and their chemical flexibility.

CBs such as Vulcan XC-72R are especially promising due to their low cost and high conductivity, and have been used as supports for Pt-based electrocatalysts in fuel cells.[18,19] Though its hydrophobic nature may affect how readily an active phase can be supported, the advantage with CBs is that their surface chemistry can be readily modified. Most carbons contain an intrinsic level of native oxygen and by using oxidative treatments, this oxygen content can be increased. This occurs through the introduction of surface oxides and polar functional groups, promoting hydrophilic binding sites on a hydrophobic surface. In the field of polymer electrolyte membrane fuel cells (PEMFC), the electrocatalyst is typically platinum supported on carbon black.[19] It has been shown that surface chemistry governed by oxygen containing functional groups serve as nucleation points for depositing the platinum.[20,21] This means a greater number of oxygenated sites facilitates better metal dispersion.[22]

The properties of carbon supports, including their ability to interact with adsorbates, can be chemically tuned using acid treatments[23,24] and gaseous/vapor phase reactions,[25,26] which can introduce carboxylic acid, carbonyl, quinone and ether groups to the carbon surface.[27,28] These treatments also increase the hydrophilicity, dispersion stability and wettability of the carbon surface.

A range of non-covalent strategies is available for forming POM/carbon composites, which exploit electrostatic interactions,[29,30] π-π interactions,[31] and layer-by-layer assembly (LbL).[32] However, these strategies must often be used in conjunction with one another to ensure a stable composite. Often for LbL, extra conductive linkers which exhibit their own redox activity may need to be added to the system, as many common polyelectrolytes have limited electrical activity and conductivity, thereby limiting the performance of the composite. This type of multi-component layered assembly renders the translation to industrial application challenging, with respect to generating these systems at sufficiently high throughput and low cost.

Electrostatic interactions between POMs and carbon supports are particularly favoured at microporous and hydrophilic carbons, and are encouraged by the presence of oxygen-based functional groups.[33,34] Hydrophilic supports can offer a platform for hydrogen bonding with the POM and micropores (< 2 nm) are the ideal size for trapping POM clusters (Keggin 1 nm, Dawson 1.2 nm). Chemisorption of POM motifs onto carbon surfaces is a popular covalent strategy to preparing POM-carbon composites. It has been applied to a spectrum of different carbon substrates including activated carbons[35], carbon nanotubes[36], and graphene[37].

The importance of carbon oxidation for chemisorption was illustrated in a study by Kang on $[P_2W_{18}O_{62}]^{6-}$-CNT composites.[38] Kang found that post-sonication in a POM solution, CNTs that had been oxidised using HNO_3 yielded POM-CNT composites with a well-dispersed surface decoration of POM particles, whereas the unoxidised CNTs showed little to no POM tethering.[38] Cuentas-Gallegos *et al.* also explored the role of carbon oxidation for the

preparation of POM-CNT composites. They showed that treatment using 2M H_2SO_4 led to a high concentration of surface carboxylic acid groups, and resulted in the most homogeneous dispersion of POM particles on the carbon surface.[39] In both of these instances, the POM tethering has been attributed to surface carboxylic acid groups and a mechanism for the covalent chemisorption binding mode has been proposed (Scheme 1).[39] However, no electrochemical studies were performed on these composite systems.

Scheme 1 - Proposed reaction scheme which suggests POM-chemisorption through the hydroxyl group and electron transfer appearing as the reduction of Mo^{VI}. Reproduced from[39] with permission from Elsevier.



Using a different approach, Cuentas-Gallegos *et al.* employed a multi-step procedure to graft diazonium derivatives to introduce -NH_2 and -OH groups onto the Vulcan carbon surface and found that greater POM loading was observed on the matrix rich in -OH groups compared to the -NH_2 rich matrix or unmodified Vulcan.[40] However, upon electrochemical cycling in aqueous conditions, they observed that a higher percentage of POM is lost from the OH- and -NH_2 modified Vulcan supports compared to its unmodified counterpart. Despite the higher loadings on the modified matrices, the unmodified Vulcan showed better electrochemical stability in aqueous conditions, thus no discernible electrochemical benefit to the chemical modification of Vulcan carbon was observed.[40] These results were surprising considering the literature precedent which generally favours oxidised supports for adsorbates.

Herein we explored a simple and scalable route to carbon modification. We employ a single-step oxidation procedure in order to introduce carboxylic acid groups onto the Vulcan carbon matrix and synthesise a more electrochemically stable redox-active POM-carbon composite.

3.2 Aims

The aim of this chapter is to explore the influence of oxidation on the Vulcan XC-72R carbon surfaces and how it alters the surface chemistry. The plenary POMs $H_3[PW_{12}O_{40}]$, $K_6[P_2W_{18}O_{62}]$ and $H_6[P_2W_{18}O_{62}]$ were loaded onto the oxidised Vulcan and unmodified Vulcan matrices to form a library of POM/Vulcan composites. The POMs will be referred to as $\{H_3W_{12}\}$, $\{K_6W_{18}\}$ and $\{H_6W_{18}\}$ respectively. Using voltammetric analysis, the electrochemical cycling capability, stability and electrochemical accessibility of the POM/Vulcan composites were established.

Extensive structural characterisation has only been completed for the $\{K_6W_{18}\}$@V and $\{K_6W_{18}\}$@[O]V composites. The electrochemistry of these composites was studied in aqueous systems (1M H_2SO_4 and 1M perchlorates) as well as organic battery solvent (1M $LiPF_6$ in 50/50 (v/v) ethylene carbonate (EC) and ethyl methyl carbonate (EMC)).

We also hypothesised that the acid Dawson and acid Keggin, which can be considered as superacids, could perform an in-situ oxidation and simultaneous adsorption when added to the Vulcan matrix. This hypothesis is explored herein.

These results have significant implications for the development of composite electrode materials based on POMs and could lead to new approaches to the development of long-lived devices using these materials.

3.3 Results & Discussion

3.3.1 Preparation

Oxidised Vulcan XC-72R, denoted as [O]V, was prepared using an adapted procedure, by refluxing Vulcan XC-72R in 2M H_2SO_4 for 5 h, followed by filtration and drying overnight.[39] The POM-Vulcan composites were formed by stirring 100 mg of Vulcan or 100 mg of [O]Vulcan in a 20 mM aqueous solution of the respective POM (Figure 1). The POMs studied include $K_6P_2W_{18}O_{62}$ denoted as $\{K_6W_{18}\}$, $H_6P_2W_{18}O_{62}$ denoted $\{H_6W_{18}\}$ and $H_3PW_{12}O_{40}$ denoted

$\{H_3W_{12}\}$. The solid products, $\{K_6W_{18}\}$@V, $\{H_6W_{18}\}$@V, $\{H_3W_{12}\}$@V, $\{K_6W_{18}\}$@[O]V, $\{H_6W_{18}\}$@[O]V and $\{H_3W_{12}\}$@[O]V were then filtered and dried overnight at 70 °C.

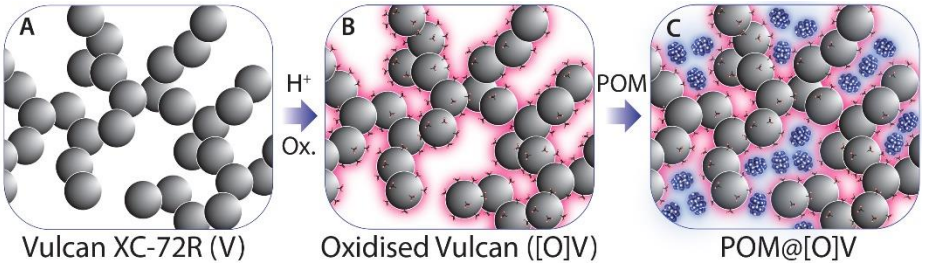


Figure 1 - A to B: Chemical oxidation of Vulcan XC-72R; B to C: Incorporation of POM with Oxidised Vulcan to form POM@[O]V.

3.3.2 Structural Characterisation

Thermogravimetric analysis of Vulcan and [O]V was used to determine the influence of oxygen functionalisation on the thermal stability of the carbon black (Figure 2). Vulcan exhibits a high resistance to air oxidation and shows little mass loss up until the onset of its oxidation at 646 °C. The thermogram of [O]V shows a two mass loss events, with the onset of the first at 172 °C and the second at 629.5 °C. The first mass loss event corresponds to the loss of the surface functional groups which were generated by chemical oxidation. This is then followed by air oxidation of the [O]V matrix at a lower temperature than Vulcan, indicating that [O]V shows less resistance to air oxidation compared to its unmodified counterpart. This decrease in thermal stability following chemical oxidation can be ascribed to the destabilisation of the carbon structure, caused by an increase in the concentration of oxygenic groups on the carbon surface.[41]

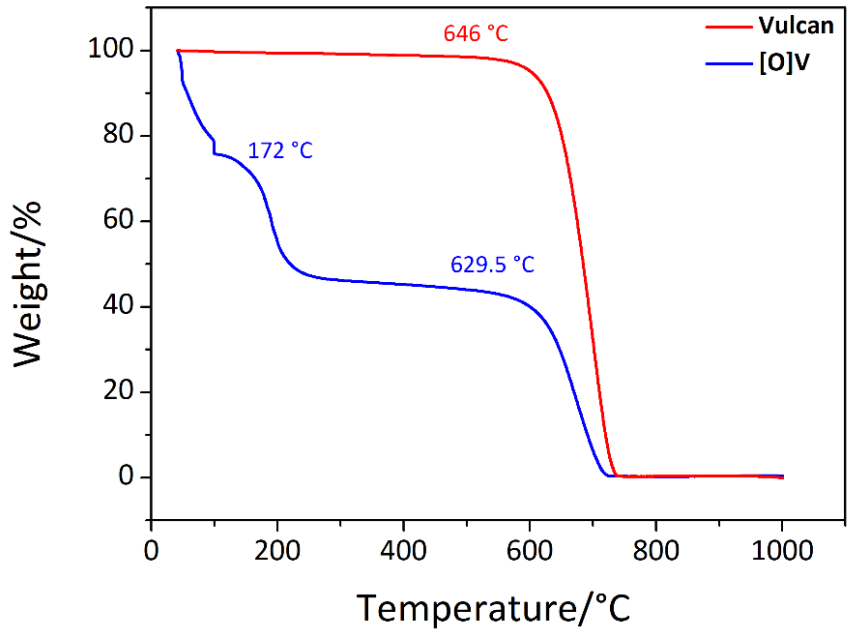


Figure 2 - TG curves for Vulcan and Oxidised Vulcan, showing the onset temperature of their mass loss events.

Figure 3 shows the thermogravimetric curves for the POM/Vulcan composites. $\{K_6W_{18}\}$@Vulcan shows a reduction in its thermal stability compared to its parent carbon matrix. The onset of its decomposition occurs at 570 °C which is due to the presence of the inorganic POM. $\{K_6W_{18}\}$@[O]V also shows a reduction in thermal stability compared to the [O]V matrix, with the onset of its decomposition at 580 °C. Interestingly there is no significant mass loss below 200 °C, which was previously ascribed to desorption of surface functional groups. This indicates that there is an interaction between the POM and these surface functional groups such that they are not oxidised in air as early as they are in [O]V.

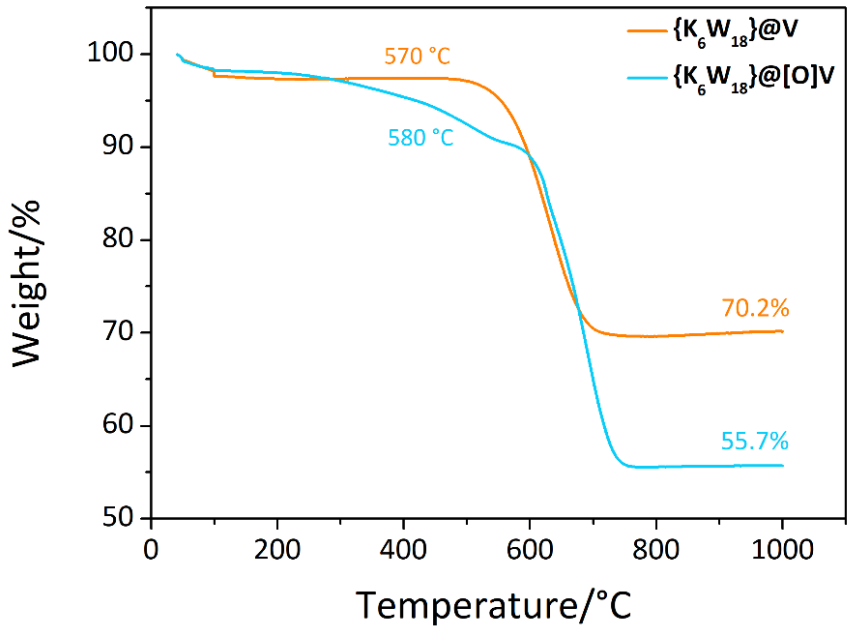


Figure 3 - TG curves for $\{K_6W_{18}\}$@Vulcan and $\{K_6W_{18}\}$@ Oxidised Vulcan, showing the onset temperature of their mass loss events and the approximate weight percent loading of POM within each composite.

As the organic carbonaceous material is completely combusted, the weight of the residual inorganic material can be used to estimate the percentage weight loading of POM within the Vulcan and [O]V composites. The loadings are 70.2 wt% and 55.7 wt% for $\{K_6W_{18}\}$@Vulcan and $\{K_6W_{18}\}$@[O]V, respectively. The discrepancy in loadings will be addressed later.

3.3.3. Surface Characterisation

X-ray photoelectron spectroscopy (XPS) is a highly sensitive technique used to analyse the surface chemistry of a material. XPS of Vulcan, [O]V, $\{K_6W_{18}\}$@Vulcan, and $\{K_6W_{18}\}$@[O]V was used to probe the concentrations, chemical environments and oxidation states of the components of the composite materials. The atomic concentrations of elements present in each sample are presented in Table 1 and show that the oxygen concentrations of the carbons increased after treatment with H_2SO_4. The presence of tungsten in the composite materials confirms that the POMs were incorporated into both matrices.

Table 1 – Elemental atomic concentrations as determined by XPS.

Sample	Atomic Concentration %			
	C 1s	O 1s	S 2p	W 4f
Vulcan	94.2	4.6	0.6	0
[O]V	68.2	22	5	0
$\{K_6W_{18}\}$@V	87	9.6	0.3	1
$\{K_6W_{18}\}$@[O]V	80	15.1	0.7	1

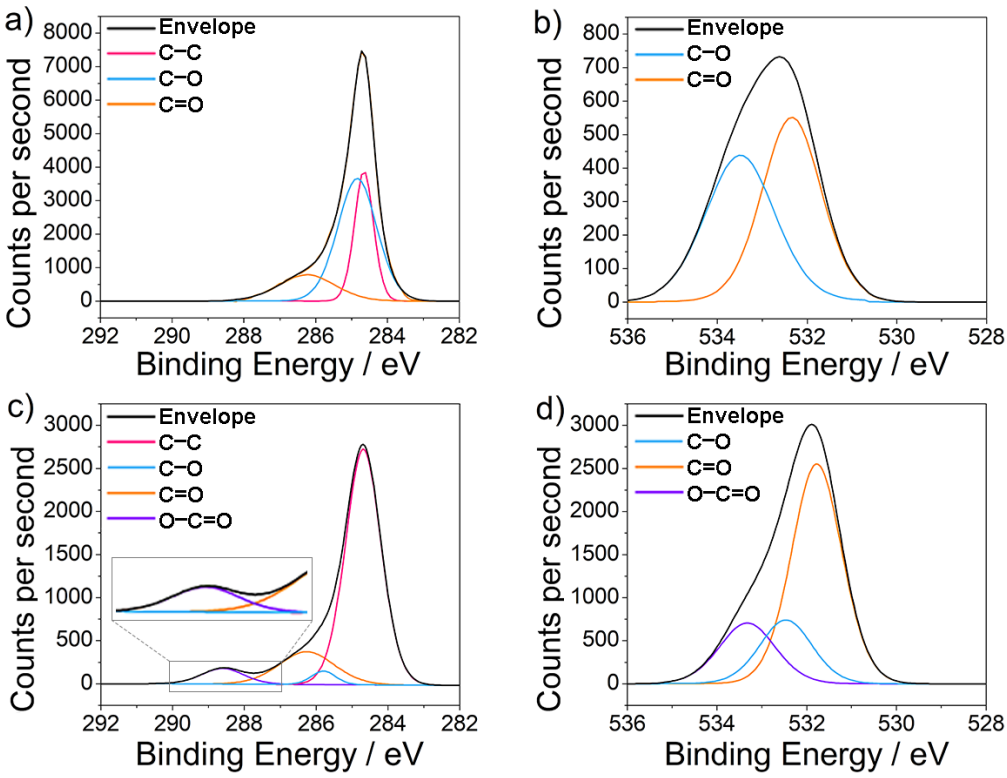


Figure 4 - High-resolution XP spectra of the carbon matrices: (a) C 1s and (b) O 1s spectra of Vulcan and (c) C 1s and (d) O 1s spectra of [O]V. Note that the purple O–C=O fit in (c) overlaps with the experimental envelope peak centered at 288.7 eV.

Analysis of the high-resolution XP spectra of the materials in the carbon regions (Figure 4a and 4c) reveals peaks at 284.7 eV due to the graphitic carbon in the Vulcan and [O]V, respectively. The peaks at 285.0 eV and 285.8 eV are due to the presence of C-O functionalities in Vulcan and [O]V, respectively, while those at 286.2 eV are due to C=O functionalities. The peak at 288.6 eV in Figure 1C is due to the presence of carboxylic acid functionalities (O-C=O) in [O]V.[28,42–45] Analysis of the O 1s region of the high-resolution XP spectra reveals the

presence of C-O (532.5 – 533 eV), C=O (531 – 532.2 eV) and O-C=O (533.3 eV) functionalities in each material (Figure 4b and 4d).[42]

High-resolution W4f XP spectra of $\{K_6W_{18}\}$, $\{K_6W_{18}\}$@Vulcan, and $\{K_6W_{18}\}$@[O]V are shown in Figures 5, 6 and 7 respectively. Deconvolution of the W 4f photoemission signal in the spectrum of $\{K_6W_{18}\}$ reveals a doublet with peaks at 35.6 eV and 37.7 eV, due to the W $4f_{7/2}$ and W $4f_{5/2}$ signals, respectively, as expected for W^{6+}.[46] The spectra of $\{K_6W_{18}\}$@Vulcan and $\{K_6W_{18}\}$@[O]V exhibit peaks centered at 36.2 eV 38.3 eV; the position and the shape of these peaks are again representative of W atoms with an oxidation state of +6.[46] The O 1s peak for the POM-containing samples is in the range of 532 - 533 eV which is expected for the oxo ligands of the POMs.[47]

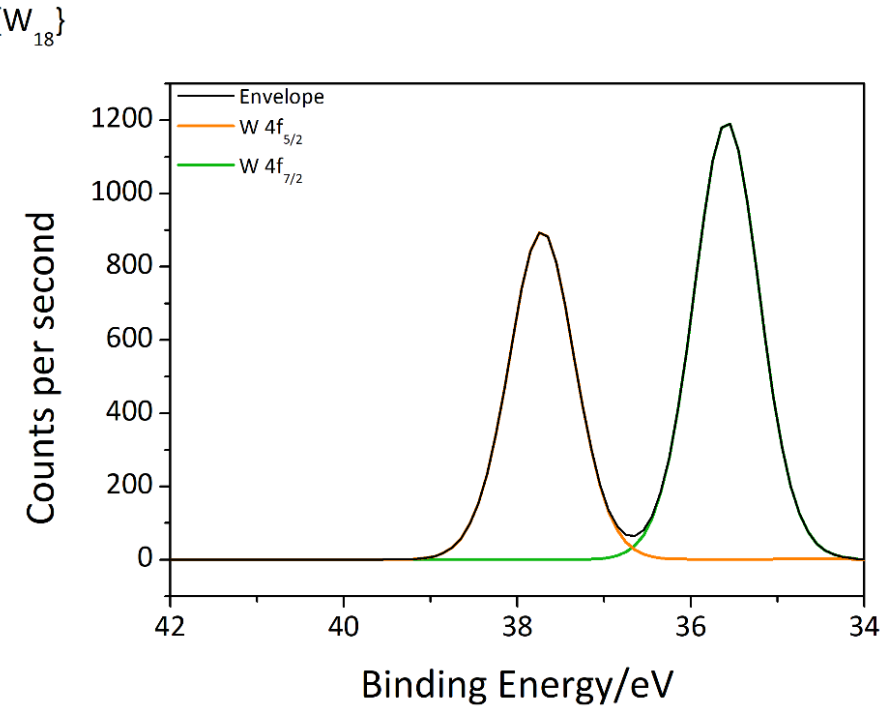


Figure 5 - Deconvoluted W4f XPS spectra of $\{K_6W_{18}\}$.

{W$_{18}$}@V

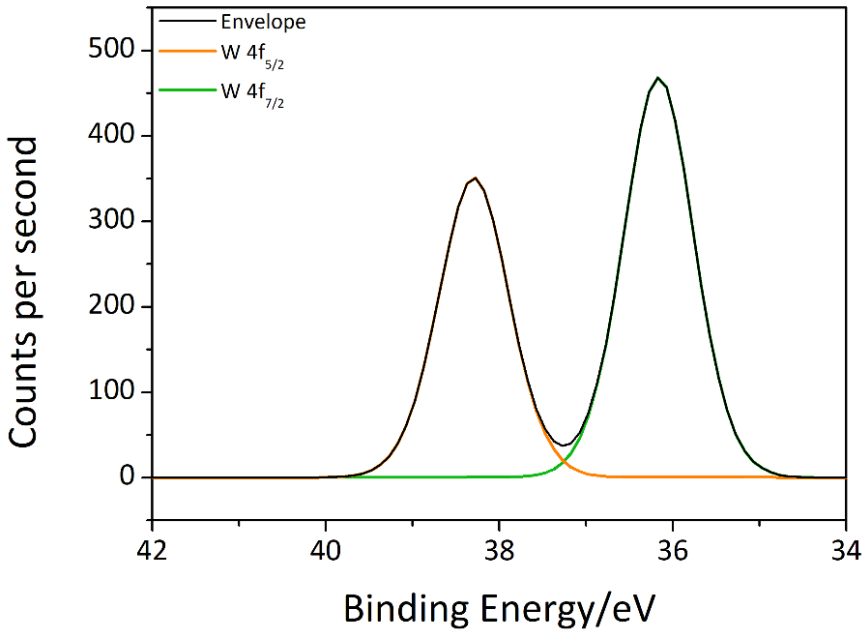


Figure 6 - Deconvoluted W4f XPS spectra of {K_6W_{18}}@V.

{W$_{18}$}@[O]V

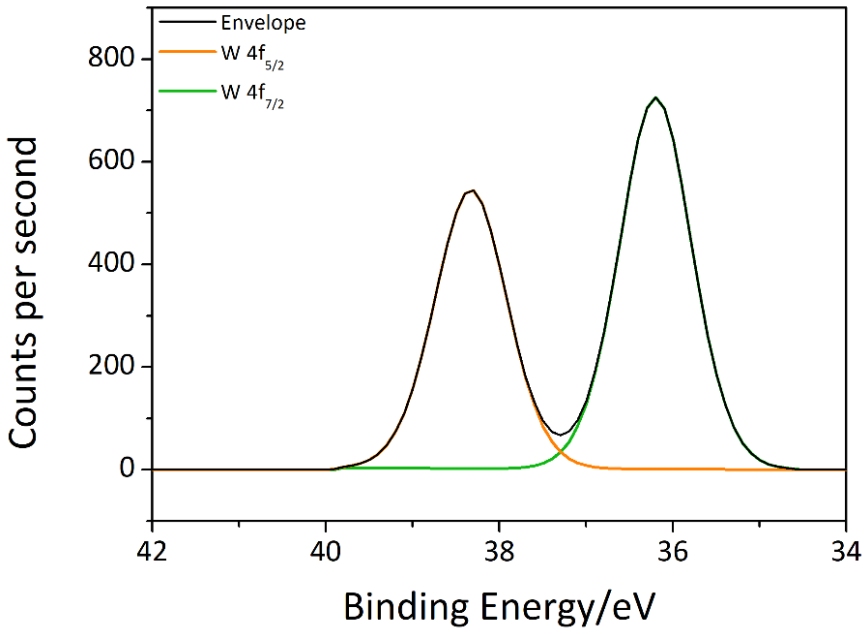


Figure 7 - Deconvoluted W4f XPS spectra of {K_6W_{18}}@[O]V.

Overall, the XPS analysis indicates that the chemical oxidation of Vulcan leads to the introduction of hydrophilic carboxylic acid groups onto the carbon support and that both the pristine and oxidised Vulcan act as supports for the adsorption of POMs.

3.3.4 Textural Characterisation

SEM-EDX analysis was used to elucidate the morphology of the samples and study the homogeneity of the composite materials. Figure 8 offers a direct comparison of the morphologies of Vulcan and [O]V, illustrating the stark difference in their structure. Vulcan is quite 'fluffy' and dominated by loosely-packed spherical aggregates, whereas [O]V has a much more compacted structure, with an apparently lower surface area. BET analysis of the materials revealed that the specific surface area (S_{BET}) of Vulcan is 234 $m^2\ g^{-1}$, while that of [O]V is lower at 108 $m^2\ g^{-1}$. This finding is in line with previous studies that have shown that oxidation of Vulcan reduces porosity, leading to a decrease in specific surface area.[27,41] The discrepancy in POM-loadings of the composites seen in the TGA data is likely to arise from a combination of the differences in surface area (high surface area favouring high loading) and chemistry of the carbons (oxidation improves tethering). Despite increasing the surface concentration of oxygenic groups which should have a higher affinity for POMs, the concomitant reduction in total surface areas leads to an overall lower loading of POMs onto Oxidised Vulcan.

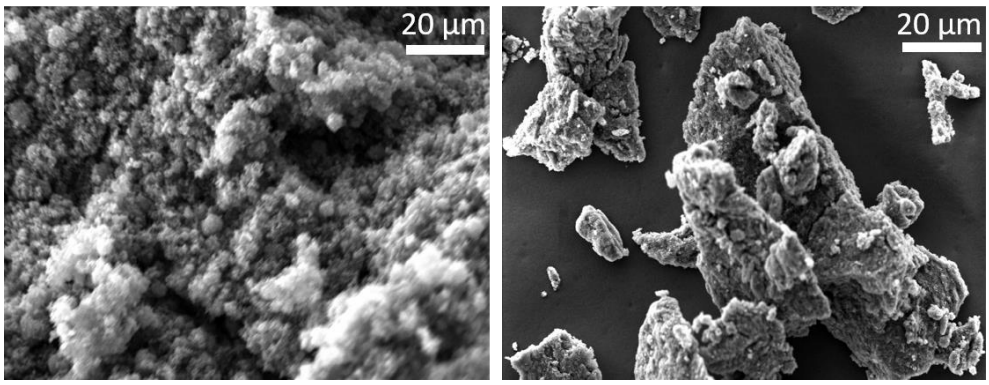


Figure 8 - SEM images of unmodified Vulcan (left) and [O]V (right).

Figure 9a shows an SEM image and the corresponding overall elemental map of $\{K_6W_{18}\}$@Vulcan. The image suggests that the deposition of the hydrophilic POMs onto the hydrophobic carbon results in a scattering of POM microcrystal agglomerates over the surface. This is in contrast to the SEM image and elemental map obtained for $\{K_6W_{18}\}$@[O]V, where a much more homogenous distribution of POM is achieved across the surface of [O]V (Figure 9b).

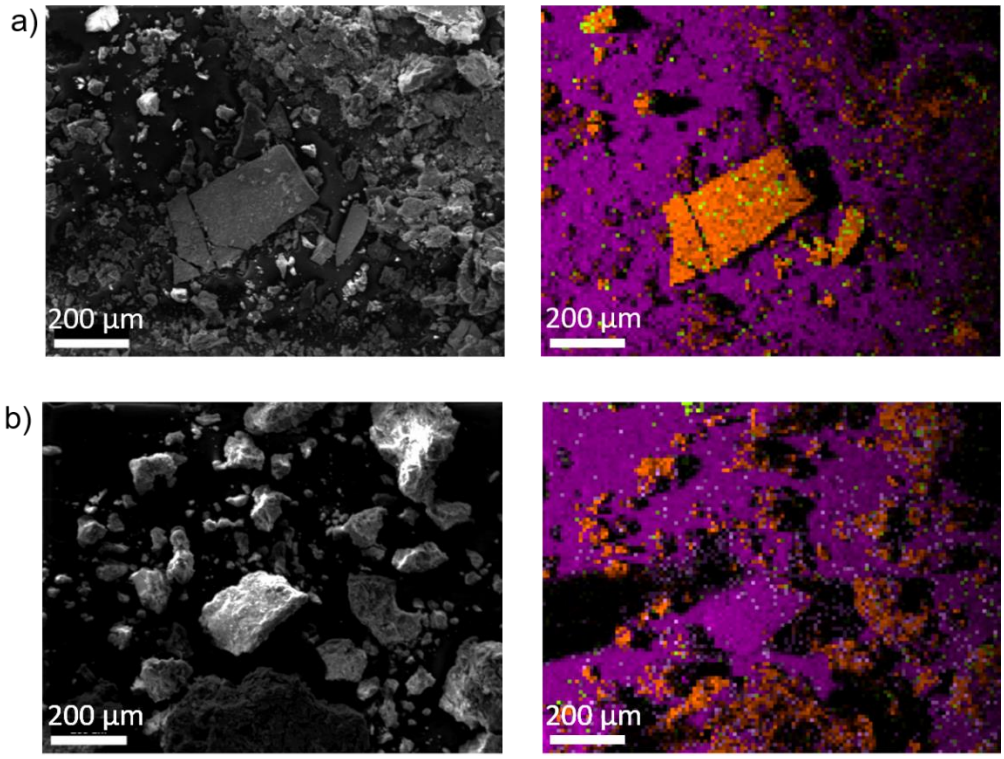


Figure 9 - SEM images and the corresponding overall element map of the POM/Vulcan composites: (a) $\{K_6W_{18}\}$@Vulcan and (b) $\{K_6W_{18}\}$@[O]V; *orange* (tungsten), *purple* (carbon), and *green* (oxygen).

3.3.5 Electrochemical Characterisation in 1M Sulphuric Acid

The electrochemical properties of Vulcan and [O]V were analysed by dropcasting GC electrodes with suspensions of both materials. This dropcast method is depicted in Figure 10.

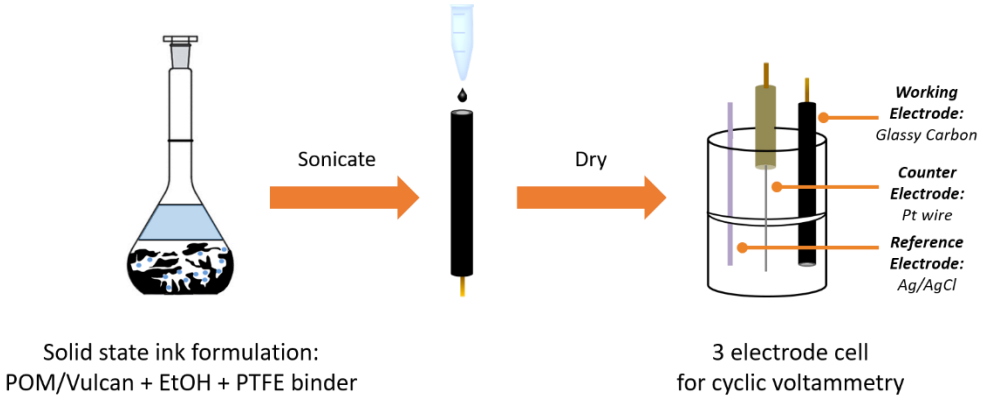


Figure 10 - Preparation of POM/Vulcan ink with binder and ethanol. Subsequent dropcasting and drying prior to use in a three electrode cell for solid state cyclic voltammetry.

Largely featureless voltammograms, which are characteristic of a capacitive material such as conductive carbon, were observed (Figure 11). A small oxidation peak is seen for Vulcan at approximately 0.2 V *vs.* Ag/AgCl which can be ascribed to oxidation of the Vulcan surface, given that the experiment was conducted in 1M H_2SO_4.

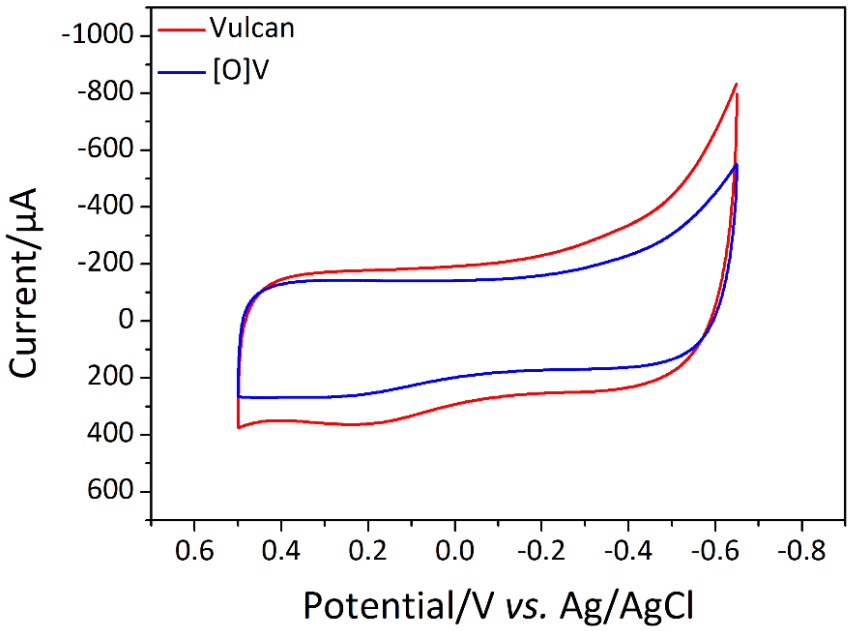


Figure 11 - Solid state CVs of Vulcan and Oxidised Vulcan in 1M H_2SO_4, recorded using a 3 mm diameter glassy carbon working electrode, a Pt counter electrode, and a Ag/AgCl reference electrode. The scan rate was 100 mv s^{-1}.

Solid-state voltammetry of the POM/Vulcan composites was performed to ascertain POM-induced redox activity. The electrodes were prepared as per Figure 10. For reference, the solution phase CV of $\{K_6W_{18}\}$ dissolved in 1M aqueous H_2SO_4 is shown in Figure 12. Four redox couples I - IV (from positive to negative potentials) were observed which correspond two consecutive 1-electron processes followed by two 2-electron processes (equations 1 – 4). The latter are proton-coupled as seen in the literature and discussed in Chapter 2. The mid-point potential, E_{mid}, and peak-to-peak separation, ΔE_p, values of each redox couple are provided in Table 2. These are in good agreement with the values found in the literature.[48]

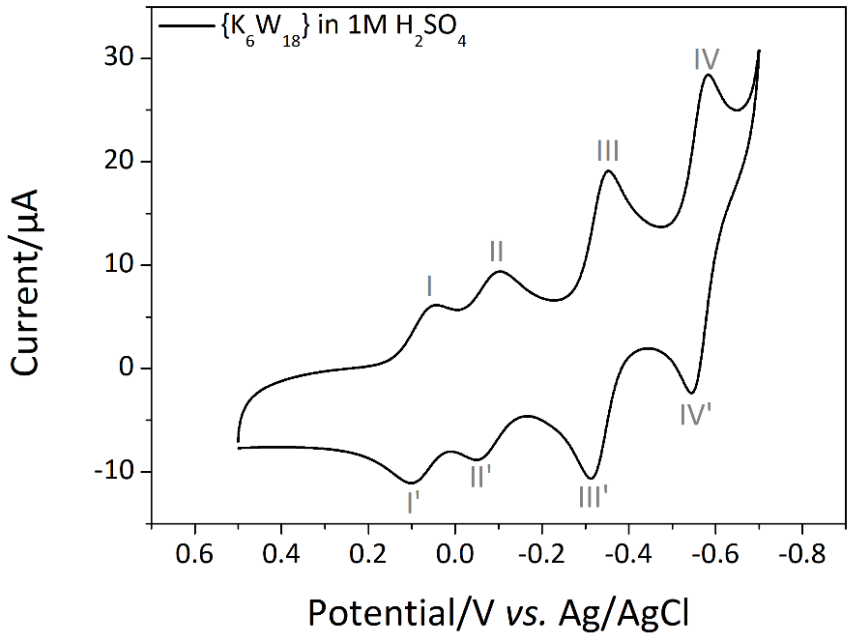


Figure 12 - Solution phase CV of $\{K_6W_{18}\}$ in 1M H_2SO_4, recorded using a 3 mm diameter glassy carbon working electrode, a Pt counter electrode, and a Ag/AgCl reference electrode. The scan rate was 100 mv s^{-1}.

Equations 1 – 4 - Redox couples for $\{K_6W_{18}\}$ in 1M H_2SO_4.

$$\textbf{I/I'}: [P_2W_{18}O_{62}]^{6-} + e^- \longleftrightarrow [P_2W_{18}O_{62}]^{7-} \quad (1)$$

$$\textbf{II/II'}: [P_2W_{18}O_{62}]^{7-} + e^- \longleftrightarrow [P_2W_{18}O_{62}]^{8-} \quad (2)$$

$$\textbf{III/III'}: [P_2W_{18}O_{62}]^{8-} + 2e^- + 2H^+ \longleftrightarrow [H_2P_2W_{18}O_{62}]^{8-} \quad (3)$$

$$\textbf{IV/IV'}: [H_2P_2W_{18}O_{62}]^{8-} + 2e^- + 2H^+ \longleftrightarrow [H_4P_2W_{18}O_{62}]^{8-} \quad (4)$$

Table 2 - Observed Midpoint Potentials (E_{mid}) and Peak-to-Peak Separations (ΔE_p) for $\{K_6W_{18}\}$ in 1M H_2SO_4.

Process	E_{mid}/V	ΔE_p/mV
I/I'	0.075	50
II/II'	-0.08	42
III/III'	-0.33	34
IV/IV'	-0.56	32

$E_{mid} = (E_c + E_a)/2$; E_c = cathodic peak potential and E_a = anodic peak potential.

Solid-state voltammetry of the POM/Vulcan composites revealed well-defined redox waves, demonstrating that the POMs within each composite material were still electrochemically accessible. The CV of $\{K_6W_{18}\}$@V exhibits three reduction/oxidation couples; A/A', B/B' and C/C' (Figure 13) whereas $\{K_6W_{18}\}$@[O]V exhibits four redox couples labelled I/I', II/II', III/III', IV/IV' (Figure 14).

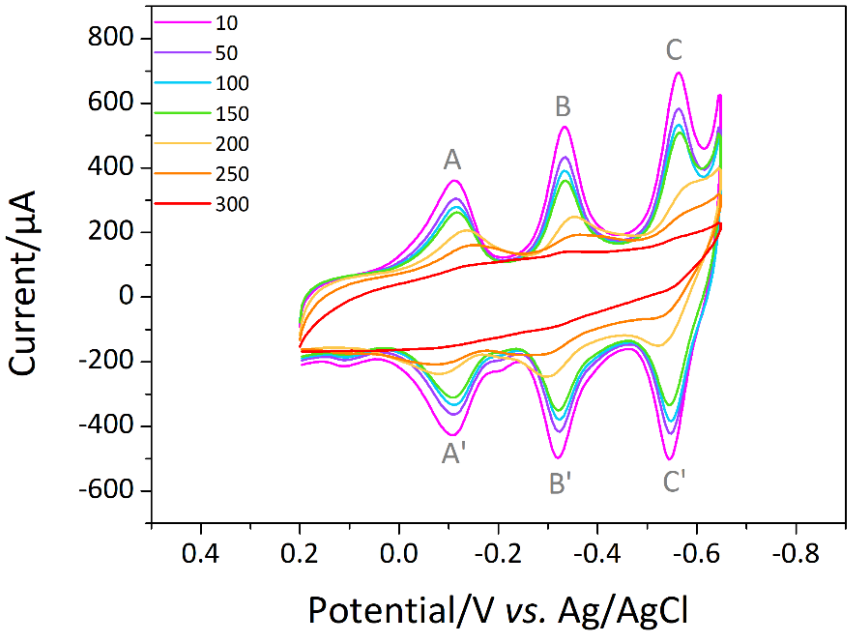


Figure 13 – Solid state CV of $\{K_6W_{18}\}$@Vulcan in 1M H_2SO_4, recorded at a scan rate of 100 mv s^{-1}, showing cycles 10 – 300.

Equations 5 – 7 - Redox couples for $\{K_6W_{18}\}$@Vulcan in 1M H_2SO_4.

$$\textbf{A/A'}: [P_2W_{18}O_{62}]^{6-} + 2e^- \longleftrightarrow [P_2W_{18}O_{62}]^{8-} \quad (5)$$

$$\textbf{B/B'}: [P_2W_{18}O_{62}]^{8-} + 2e^- + 2H^+ \longleftrightarrow [H_2P_2W_{18}O_{62}]^{8-} \quad (6)$$

$$\textbf{C/C'}: [H_2P_2W_{18}O_{62}]^{8-} + 2e^- + 2H^+ \longleftrightarrow [H_4P_2W_{18}O_{62}]^{8-} \quad (7)$$

Table 3 - Observed Midpoint Potentials (E_{mid}) and Peak-to-Peak Separations (ΔE_p) for $\{K_6W_{18}\}$@Vulcan in 1M H_2SO_4.

Process	E_{mid} /V	ΔE_p/mV
A/A'	-0.11	9
B/B'	-0.33	19
C/C'	-0.55	23

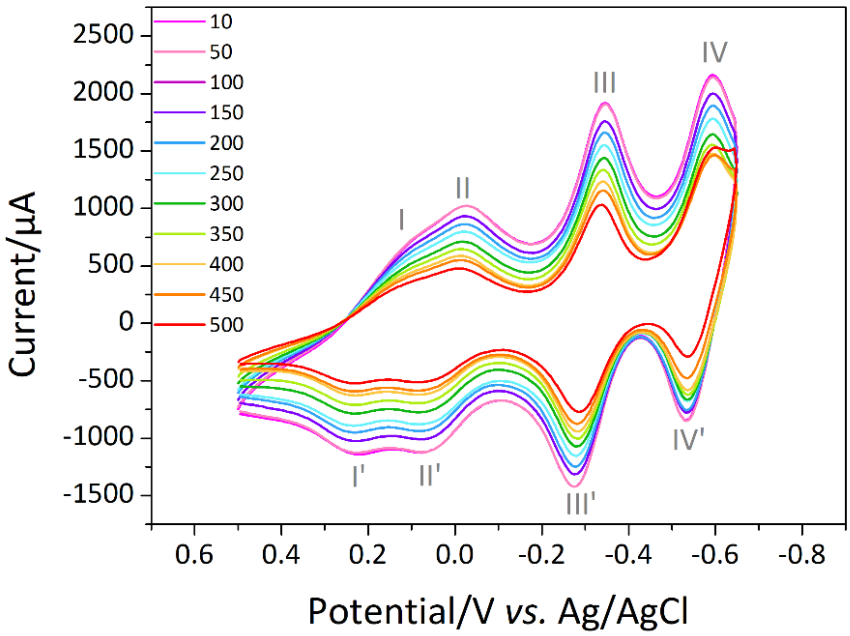


Figure 14 – Solid state CV of $\{K_6W_{18}\}$@Oxidised Vulcan in 1M H_2SO_4, recorded at a scan rate of 100 mv s^{-1}, showing cycles 10 – 500.

Equations 8 – 11 - Redox couples for $\{K_6W_{18}\}$@Oxidised Vulcan in 1M H_2SO_4.

I/I': $[P_2W_{18}O_{62}]^{6-} + e^- \longleftrightarrow [P_2W_{18}O_{62}]^{7-}$ (8)

II/II': $[P_2W_{18}O_{62}]^{7-} + e^- \longleftrightarrow [P_2W_{18}O_{62}]^{8-}$ (9)

III/III': $[P_2W_{18}O_{62}]^{8-} + 2e^- + 2H^+ \longleftrightarrow [H_2P_2W_{18}O_{62}]^{8-}$ (10)

IV/IV': $[H_2P_2W_{18}O_{62}]^{8-} + 2e^- + 2H^+ \longleftrightarrow [H_4P_2W_{18}O_{62}]^{8-}$ (11)

Table 4 - Observed Midpoint Potentials (E_{mid}) and Peak-to-Peak Separations (ΔE_p) for $\{K_6W_{18}\}$@Oxidised Vulcan in 1M H_2SO_4.

Process	E_{mid} /V	ΔE_p/mV
I/I'	0.182	77
II/II'	0.021	41
III/III'	-0.31	70
IV/IV'	-0.56	62

Interestingly, processes I/I' and II/II' from the voltammogram of $\{K_6W_{18}\}$@[O]V appear to have coalesced to yield a single process (A/A') in the voltammogram of $\{K_6W_{18}\}$@V. Moreover, processes I/I' and II/II' are shifted by approximately 292 mV and 131 mV positive of process A/A' (Figure 15). Indeed, they are even positively shifted relative to their redox potentials in the solution phase voltammogram (Figure 12, Table 2). These data demonstrate that reduction of POMs at the oxidised carbon surface was more thermodynamically favourable than at the unoxidised surface, most likely due to interactions between the POM clusters and surface carboxylic acid groups. Processes B/B' and C/C' and processes III/III' and IV/IV' occur at the same potentials are remain largely unaffected by the nature of the Vulcan matrices.

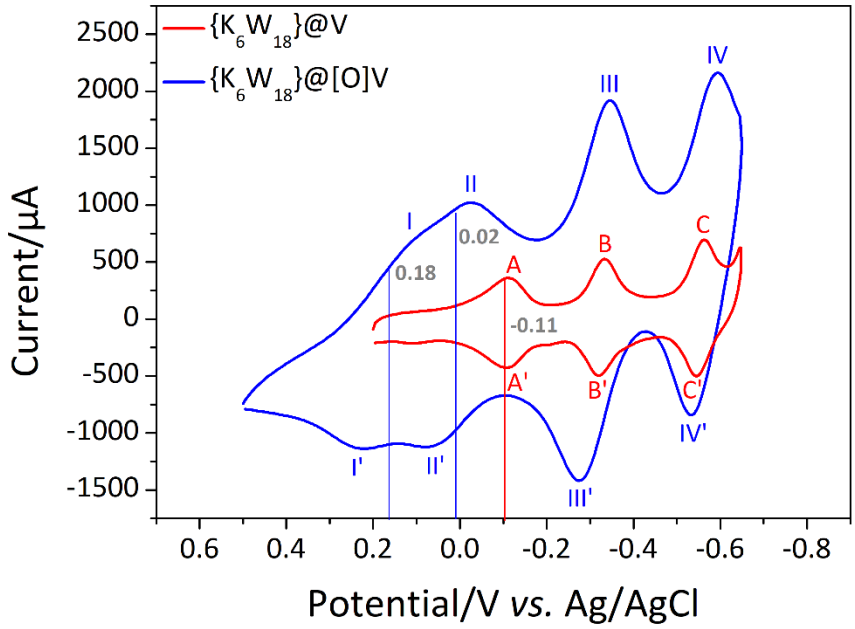


Figure 15 - Overlay of second cycles of $\{K_6W_{18}\}$@Vulcan and $\{K_6W_{18}\}$@[O]V showing the positive shift in the midpoint potentials of processes I/I′ and II/II′ compared to process A/A′.

It is interesting to note that the peaks for $\{K_6W_{18}\}$@V appear to be more symmetrical whereas those of $\{K_6W_{18}\}$@[O]V are slightly offset. Symmetrical peaks are expected for a surface-confined heterogenous process, but the offset in the redox peaks for $\{K_6W_{18}\}$@[O]V could be indicative that the processes are slightly diffusional in nature. This could allude to the presence of a combination of homogeneous and heterogenous electron-transfer states, where the POM remains tethered to the oxidised Vulcan surface while also participating in solution phase redox reactions.

For a fully reversible surface-confined process, the peak-to-peak separation of a redox couple is expected to be 0 mV. For $\{K_6W_{18}\}$@V, the ΔE_p values for processes A, B and C are much lower than for the $[P_2W_{18}O_{32}]^{6-}$ anion dissolved in a solution of 1M H_2SO_4. The values were found to be 9, 19 and 23 mV respectively, approaching the value of 0 mV, confirming that the processes are surface confined but quasi-reversible. The ΔE_p values for processes I, II, III and IV of $\{K_6W_{18}\}$@[O]V are further away from 0 mV and closer to the values

observed for $[P_2W_{18}O_{32}]^{6-}$ dissolved in 1M H_2SO_4. We can surmise that discrepancies in these values arise from the complicated electron transfer mechanisms at play (combination of diffusion and surface confined electrochemistry), coupled with reduced reversibility.

Analysis of the effects of increasing the voltammetric scan rate revealed that the peak heights for each redox couple in each composite material increased in direct proportion to the increasing scan rate (Figures 16 and 17), as expected for a surface-immobilised redox species.[49]

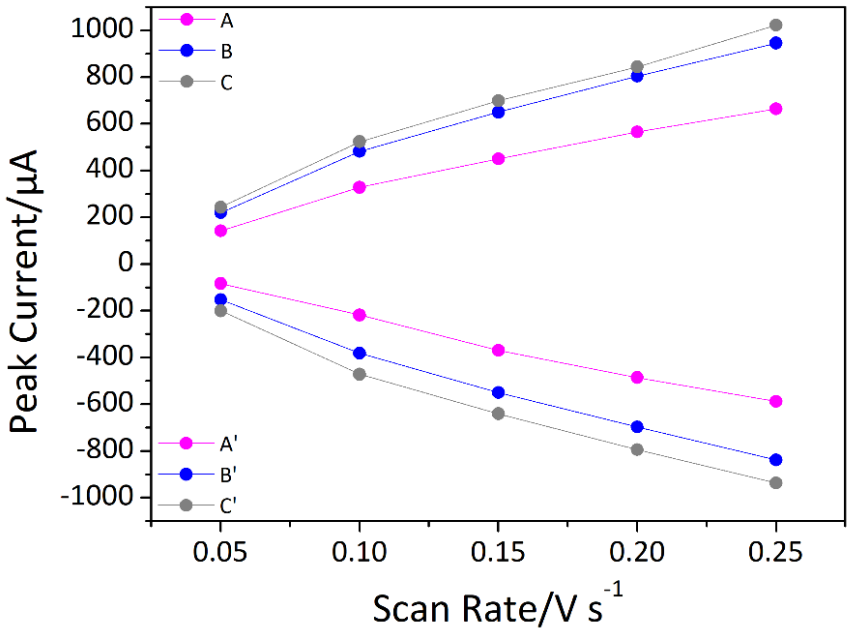


Figure 16 - Peak currents of redox processes A – C for $\{K_6W_{18}\}$@Vulcan plotted against increasing scan rate.

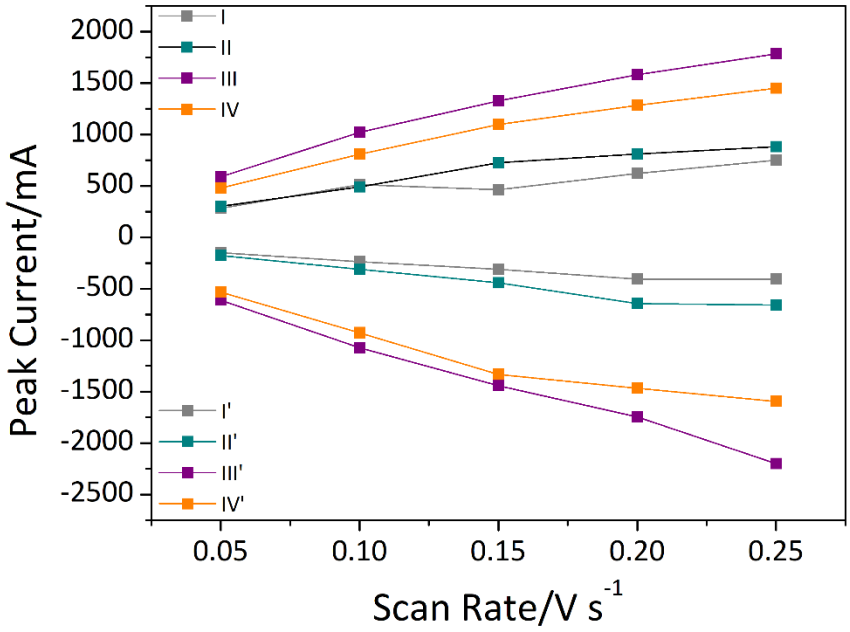


Figure 17 - Peak currents of redox processes I – IV for $\{K_6W_{18}\}$@Oxidised Vulcan plotted against increasing scan rate.

The composite materials were then subjected to electrochemical cycling tests to compare their POM retention over multiple charge-discharge cycles. In both experiments the currents observed in the initial scan decreased upon cycling, indicating that the molecular redox species were slowly lost from the electrode surface. The currents decreased more rapidly over time for $\{K_6W_{18}\}$@V and the redox processes observed in the voltammogram were almost entirely lost by the 250th cycle (Figure 13). In contrast, the currents decreased much more gradually over repeated cycling for the $\{K_6W_{18}\}$@[O]V sample, and the redox activity was clearly retained beyond the 500th cycle (Figure 14). These results demonstrate that the electrochemical stability of $\{K_6W_{18}\}$@[O]V is significantly enhanced compared to the non-oxidised analogue. Indeed, Figure 18 shows the impact of electrochemical cycling on the voltammogram peak current (processes III and B) and highlights the significant enhancement in POM retention induced by oxidation of the Vulcan.

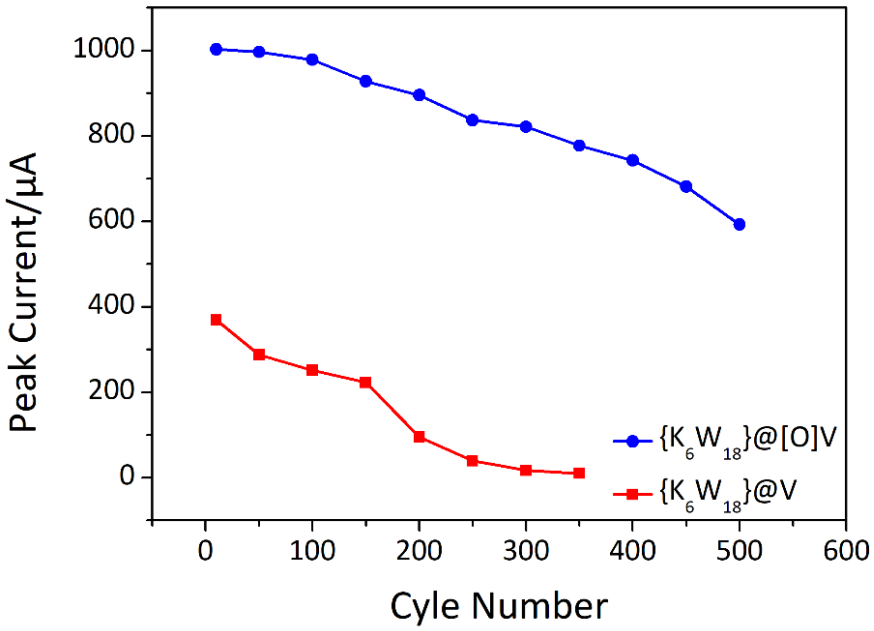


Figure 18 - Peak current of processes III and B in the voltammograms of $\{K_6W_{18}\}$@[O]V and $\{K_6W_{18}\}$@Vulcan, respectively, over multiple charge–discharge cycles. The plots demonstrate the rapid loss of redox species from the unmodified carbon (V) compared to the effective retention of the POMs on the Oxidised Vulcan ([O]V).

$\{K_6W_{18}\}$ readily dissolves in 1M aqueous H_2SO_4, so the fact that the POM remained anchored to [O]V for hundreds of cycles is a validation of our experimental strategy. We propose that this stability stems from the carboxylic acid sites of [O]V providing anchorage points for the POMs via electrostatic interactions such as hydrogen bonding. This interaction hinders leaching of the electroactive material and translates to enhanced cycling stability.

Though the redox processes observed for $\{K_6W_{18}\}$@V display the characteristics of surface-confined electrochemistry, the limited cycling performance of $\{K_6W_{18}\}$@Vulcan indicates that the redox species readily desorb from the surface; an unsurprising consequence of the relatively weak interaction between the POMs and the Vulcan support. As shown by the SEM and EDX, the POMs appear to sit on the carbon surface as block microcrystals, effectively minimizing the contact between the active species and the support.

The percentage of POMs that were electrochemically accessible on the different matrices was calculated using the equation $n_E = Q/zF$, where n_E is the number of moles electrolysed, Q = the area under a CV peak (in this case, process III or process B), z = number of electrons transferred (2 e^-) and F is Faraday's constant. The nominal number of moles of POM present on the electrode was estimated using the mass difference before and after drop-casting the slurry, combined with the percentage POM loading determined by thermal gravimetry (vide supra). The results of these calculations are shown in Table 5.

Table 5 – Percentage of POMs electrochemically accessible over repeated cycling.

Cycle no.	{K_6W_{18}}@V (%)	{K_6W_{18}}@[O]V (%)
2	3.9	19
10	3.4	16.5
300	0.13	15
500	-	10.3

The two matrices exhibit significant differences in this regard; 19% of the POMs are reduced in the second reduction scan of {K_6W_{18}}@[O]V, while only 3.9% are reduced in the voltammogram of {K_6W_{18}}@Vulcan. Upon electrochemical cycling, the accessibility values drop for both materials with {K_6W_{18}}@[O]V reaching 10.3% by the 500th cycle and {K_6W_{18}}@Vulcan falling to 0.13% by the 300th cycle. Despite the gravimetrically-determined POM loadings of 70.2% and 55.7% for {K_6W_{18}}@Vulcan and {K_6W_{18}}@[O]V, respectively, the material with the higher POM content ({K_6W_{18}}@Vulcan) has significantly fewer electrochemically-accessible sites than {K_6W_{18}}@[O]V. As evidenced from the SEM images, the presence of large microcrystals on the surface of Vulcan, which are electrically insulating mean that not all of the POMs in the crystals will be able to participate in redox reactions. In contrast, the better dispersion of POMs on the Oxidised Vulcan surface means that more POMs are in contact with the conductive support. This is reflected in the enhanced cycling stability of

{K_6W_{18}}@[O]V compared to {K_6W_{18}}@V. These findings render the {K_6W_{18}}@[O]V system a more efficient and stable composite redox material, and more promising for energy storage applications, than the unmodified analogue, {K_6W_{18}}@Vulcan.

3.3.6 Electrochemical Characterisation in Perchlorate-based Electrolytes

Having already tested the solution phase voltammetry of the {K_6W_{18}} POM in perchlorate-based electrolytes in chapter 2, this next section is a complementary assessment of the electrochemical stability of the corresponding Vulcan and [O]V {K_6W_{18}} based composites in 1M $HClO_4$, 1M $LiClO_4$, 1M $NaClO_4$ and 1M $Mg(ClO_4)_2$.

1M $HClO_4$

Starting with 1M $HClO_4$, the observed voltammograms for POM/Vulcan composites are parallel to those in 1M H_2SO_4. Four distinct processes are seen for {K_6W_{18}}@[O]V (processes I – IV) (Figure 19) analogous to {K_6W_{18}} in 1M $HClO_4$ solution (Figure 20), corresponding to two one-electron transfers proceeded by two two-electron proton-coupled processes.

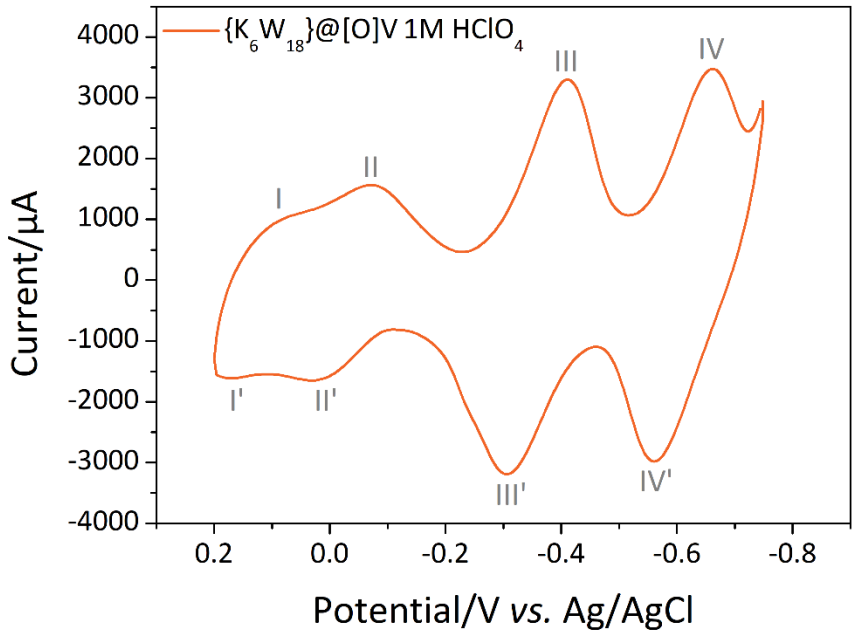


Figure 19 – Solid state CV of $\{K_6W_{18}\}$@[O]V in 1M $HClO_4$ recorded using a 3 mm diameter glassy carbon working electrode, a Pt counter electrode, and a Ag/AgCl reference electrode. The scan rate was 100 mv s^{-1}.

Equations 12 – 15 - Redox couples for $\{K_6W_{18}\}$@[O]V in 1M $HClO_4$.

I/I': $[P_2W_{18}O_{62}]^{6-} + e^- \leftrightarrow [P_2W_{18}O_{62}]^{7-}$ (12)

II/II': $[P_2W_{18}O_{62}]^{7-} + e^- \leftrightarrow [P_2W_{18}O_{62}]^{8-}$ (13)

III/III': $[P_2W_{18}O_{62}]^{8-} + 2e^- + 2H^+ \leftrightarrow [H_2P_2W_{18}O_{62}]^{8-}$ (14)

IV/IV': $[H_2P_2W_{18}O_{62}]^{8-} + 2e^- + 2H^+ \leftrightarrow [H_4P_2W_{18}O_{62}]^{8-}$ (15)

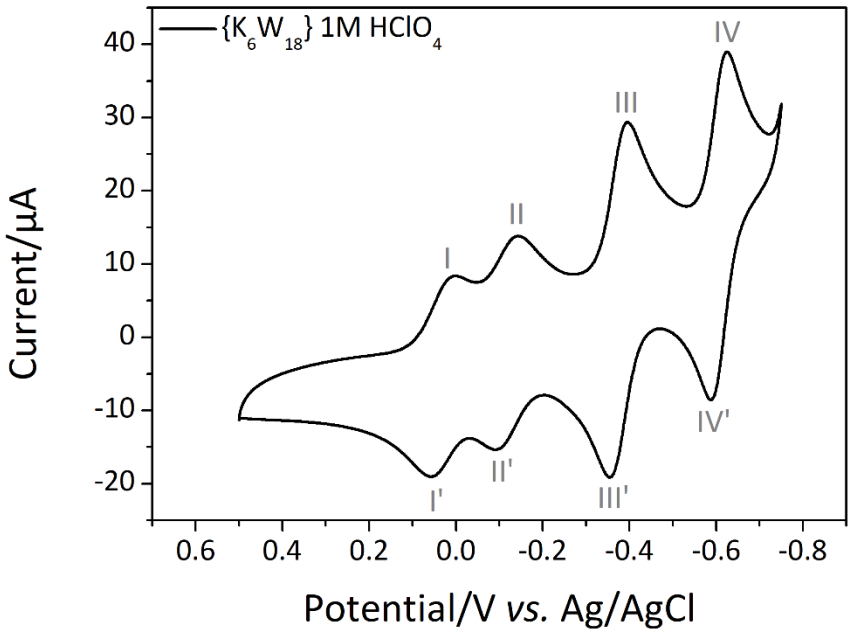


Figure 20 – Solution phase CV of $\{K_6W_{18}\}$ in 1M $HClO_4$, recorded using a 3 mm diameter glassy carbon working electrode, a Pt counter electrode, and a Ag/AgCl reference electrode. The scan rate was 100 mv s^{-1}.

$\{K_6W_{18}\}$@V has three redox waves (A – C) corresponding to three two-electron processes. Once again, the one-electron processes, I and II, present for $\{K_6W_{18}\}$ in solution and $\{K_6W_{18}\}$@[O]V in the solid state, have consolidated to form a single two-electron process, A, for $\{K_6W_{18}\}$@V (Figure 20).

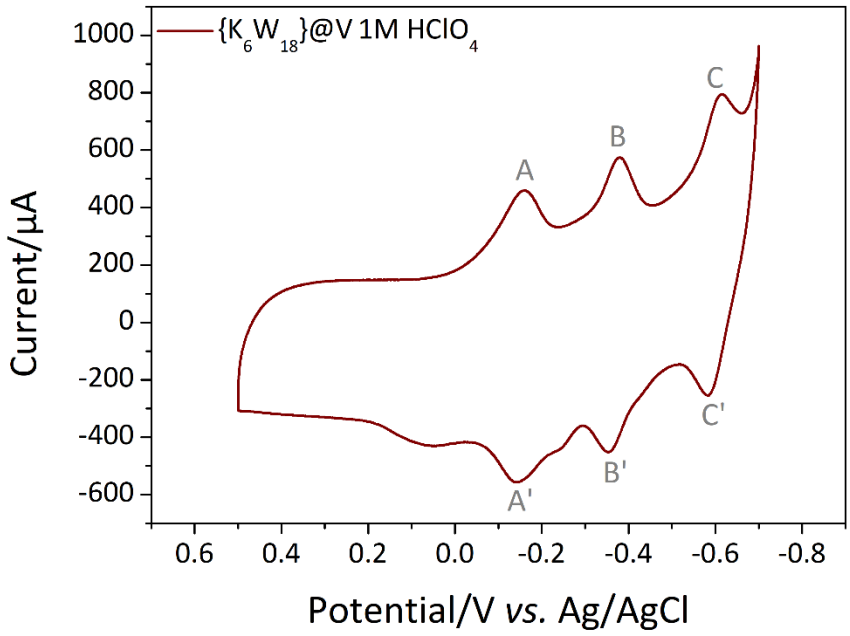


Figure 21 – Solid state CV of $\{K_6W_{18}\}$@V in 1M $HClO_4$ recorded using a 3 mm diameter glassy carbon working electrode, a Pt counter electrode, and a Ag/AgCl reference electrode. The scan rate was 100 mv s^{-1}.

Equations 16 – 18 - Redox couples for $\{K_6W_{18}\}$@V in 1M $HClO_4$.

$$\textbf{A/A'}: [P_2W_{18}O_{62}]^{6-} + 2e^- \longleftrightarrow [P_2W_{18}O_{62}]^{8-} \quad (16)$$

$$\textbf{B/B'}: [P_2W_{18}O_{62}]^{8-} + 2e^- + 2H^+ \longleftrightarrow [H_2P_2W_{18}O_{62}]^{8-} \quad (17)$$

$$\textbf{C/C'}: [H_2P_2W_{18}O_{62}]^{8-} + 2e^- + 2H^+ \longleftrightarrow [H_4P_2W_{18}O_{62}]^{8-} \quad (18)$$

Moreover, processes I/I' and II/II' of $\{K_6W_{18}\}$@[O]V are shifted by approximately 267 mV and 125 mV positive of process A/A' for $\{K_6W_{18}\}$@V (Figure 21). In fact, processes I/I' and II/II' for $\{K_6W_{18}\}$@[O]V are even positively shifted relative to their redox potentials in the solution phase voltammogram, by 81 mV and 95 mV respectively (Table 6). Process A/A' is negatively shifted by 186 mV and 30 mV with respect to process I/I' and II/II' of $\{K_6W_{18}\}$. These positive and negative shifts indicate that the reduction of $\{K_6W_{18}\}$ is more thermodynamically favourable at the oxidised carbon surface, than at the unoxidised surface, most likely facilitated by the surface carboxylic acid groups. The potentials at which processes B/B' and C/C' for $\{K_6W_{18}\}$@V and processes

III/III' and IV/IV' for $\{K_6W_{18}\}$@[O]V remain unchanged and occur at the same potentials observed for $\{K_6W_{18}\}$ in solution (Table 6).

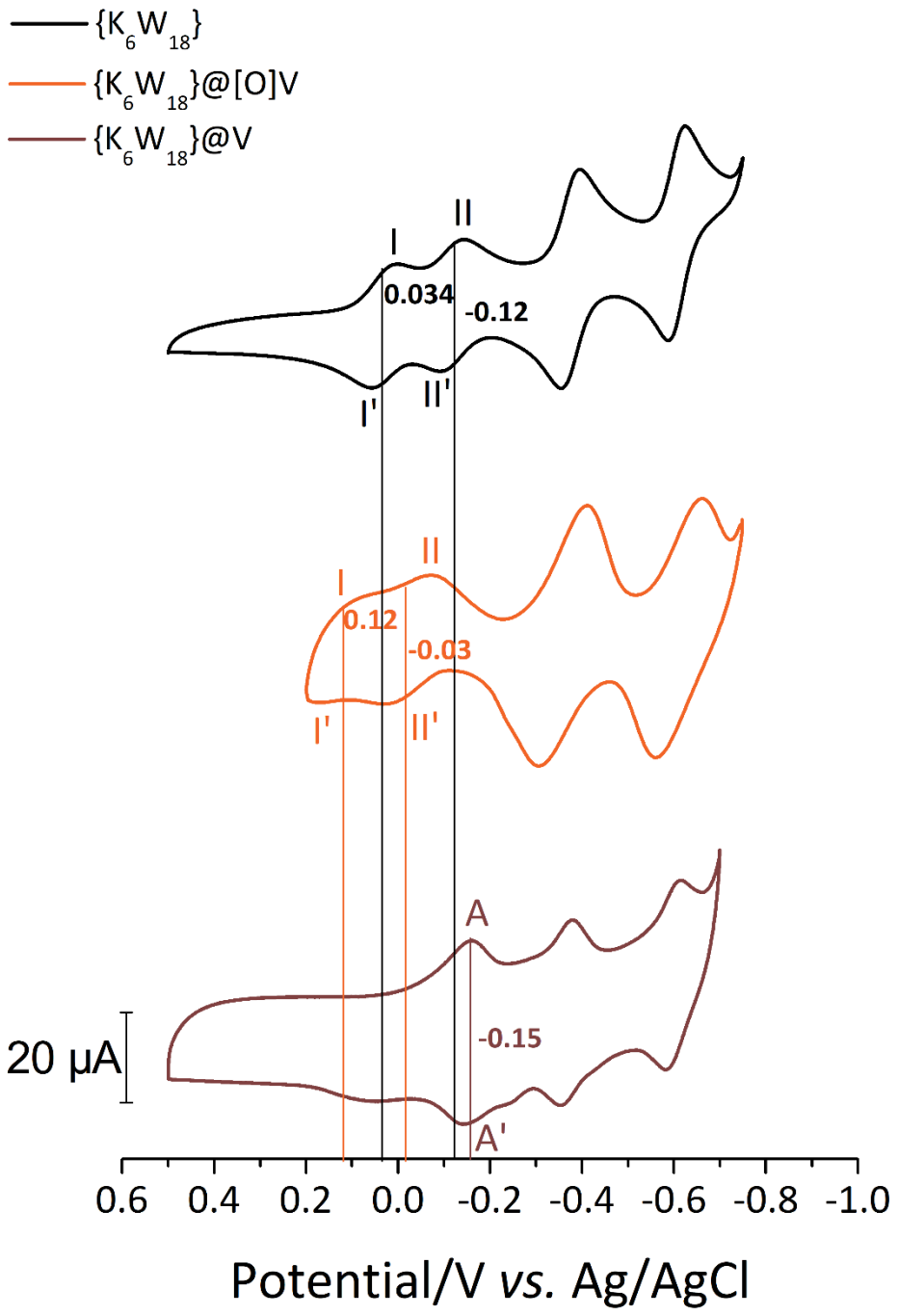


Figure 22 - Stacked CVs featuring the solution phase CV of $\{K_6W_{18}\}$ and the solid state voltammograms of $\{K_6W_{18}\}$@[O]V and $\{K_6W_{18}\}$@V to compare the redox profiles and peak shifts in 1M $HClO_4$.

For $\{K_6W_{18}\}$@V, the ΔE_p values for processes A, B and C are lower than for the $[P_2W_{18}O_{32}]^{6-}$ anion dissolved in a solution of 1M H_2SO_4. The values were found to be 12, 24 and 30 mV respectively, approaching the value of 0 mV, confirming that the processes are surface confined but quasi-reversible. The ΔE_p values $\{K_6W_{18}\}$@[O]V are less straightforward in their interpretation due to the mix of homogenous and heterogeneous electron transfer mechanisms, but as they are larger than expected for either surface-confined or diffusional processes, we can deduce they are less reversible in nature.

Table 6 - Comparison of E_{mid} and ΔE_p values for $\{K_6W_{18}\}$ dissolved in 1M $HClO_4$ and for the $\{K_6W_{18}\}$@[O]V and $\{K_6W_{18}\}$@V solid state CVs in 1M $HClO_4$.

Process	$\{K_6W_{18}\}$		Process	$\{K_6W_{18}\}$@V		Process	$\{K_6W_{18}\}$@[O]V	
	E_{mid}/V	ΔE_p/mV		E_{mid}/V	ΔE_p/mV		E_{mid}/V	ΔE_p/mV
I	0.034	45	A	-0.15	12	I	0.12	77
II	-0.12	38	B	-0.38	24	II	-0.03	107
III	-0.37	38	C	-0.60	30	III	-0.35	113
IV	-0.60	34	-	-	-	IV	-0.60	107

With regards to cyclability, there is a clear difference between the composites $\{K_6W_{18}\}$@V and $\{K_6W_{18}\}$@[O]V. The former shows a rapid loss in peak currents for the POM redox processes, indicating that the POMs are readily desorbed form the Vulcan surface over repeated cycling (Figure 23). Its stability does not persist beyond 100 cycles, after which only a capacitive current from the conductive Vulcan remains. For $\{K_6W_{18}\}$@[O]V, it is clear that the signature POM peaks are still accessible beyond 200 cycles (Figure 24). Cycling data after 250 cycles was not included due to the onset of hydrogen evolution, obscuring the POM redox processes.

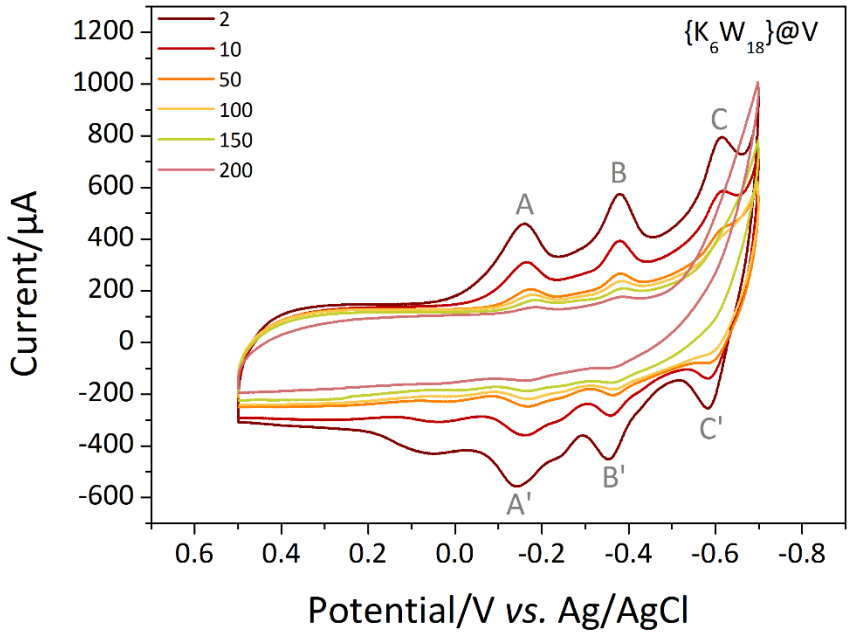


Figure 23 – Solid state CV of $\{K_6W_{18}\}$@Vulcan in 1M $HClO_4$, recorded at a scan rate of 100 mv s^{-1}, showing cycles 2 – 200.

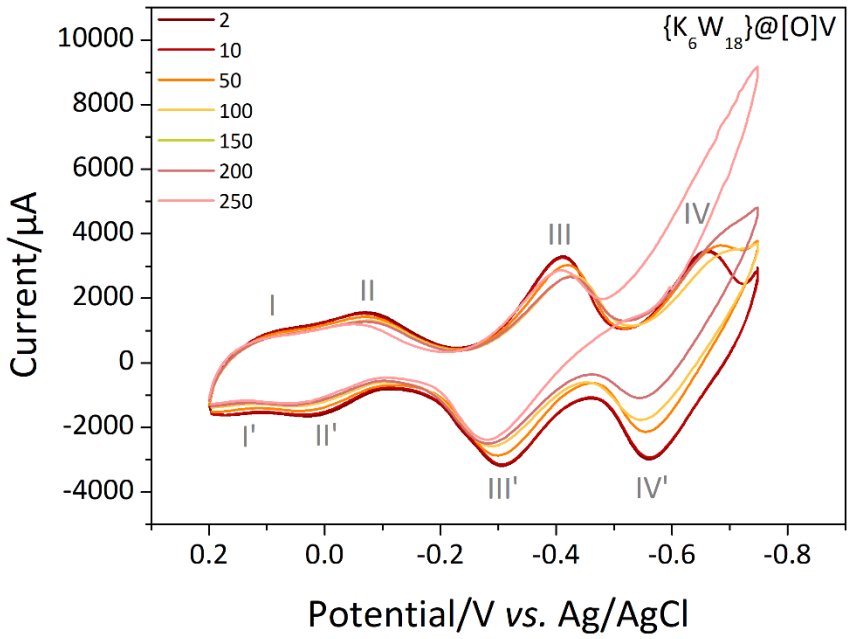


Figure 24 - Solid state CV of $\{K_6W_{18}\}$@[O]V in 1M $HClO_4$, recorded at a scan rate of 100 mv s^{-1}, showing cycles 2 – 250.

1M $LiClO_4$

In the presence of the metal cations $Li^+/Na^+/Mg^{2+}$, very interesting electrochemical behaviour is observed. In 1M $LiClO_4$, the voltammogram for $\{K_6W_{18}\}$@[O]V (Figure 25) shows six distinct one-electron processes (I – VI), which are proton-decoupled, as previously seen for $\{K_6W_{18}\}$ dissolved in 1M $LiClO_4$ (Figure 26). In the presence of H^+, these processes coalesce to produce two two-electron redox waves. All six one-electron redox processes for $\{K_6W_{18}\}$@[O]V occur at similar potentials to those of the solution phase voltammogram, albeit at slightly more positive potentials with the positive shifts ranging between 20 – 62 mV (Table 7).

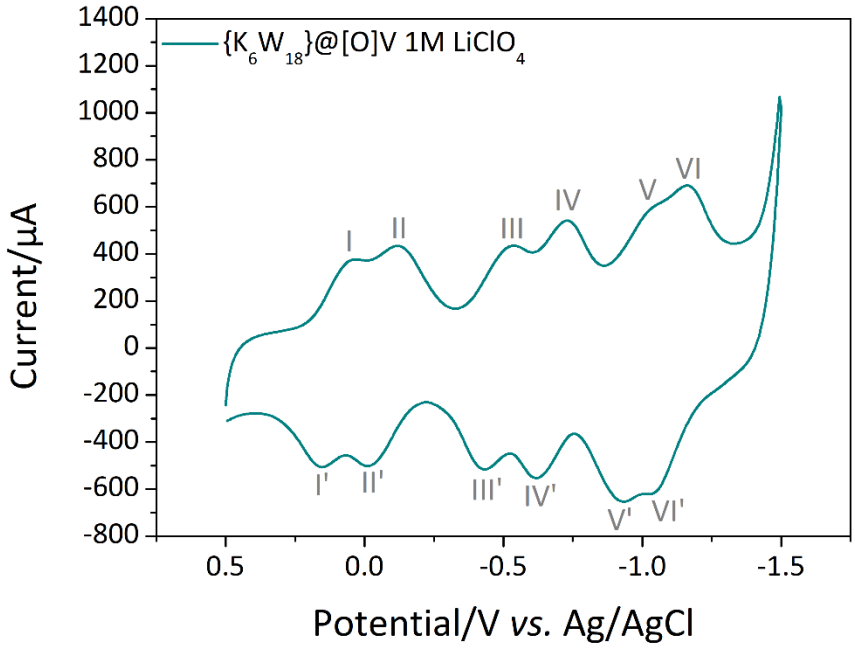


Figure 25 - Solid state CV of $\{K_6W_{18}\}$@[O]V in 1M $LiClO_4$ recorded using a 3 mm diameter glassy carbon working electrode, a Pt counter electrode, and a Ag/AgCl reference electrode. The scan rate was 100 mv s^{-1}.

Equations 19 – 24 - Redox couples for $\{K_6W_{18}\}$@[O]V in 1M $LiClO_4$.

$$\textbf{I/I'}: [P_2W_{18}O_{62}]^{6-} + e^- \longleftrightarrow [P_2W_{18}O_{62}]^{7-} \quad (19)$$

$$\textbf{II/II'}: [P_2W_{18}O_{62}]^{7-} + e^- \longleftrightarrow [P_2W_{18}O_{62}]^{8-} \quad (20)$$

$$\textbf{III/III'}: [P_2W_{18}O_{62}]^{8-} + e^- \longleftrightarrow [P_2W_{18}O_{62}]^{9-} \quad (21)$$

$$\textbf{IV/IV'}: [P_2W_{18}O_{62}]^{9-} + e^- \longleftrightarrow [P_2W_{18}O_{62}]^{10-} \quad (22)$$

$$\textbf{V/V'}: [P_2W_{18}O_{62}]^{10-} + e^- \longleftrightarrow [P_2W_{18}O_{62}]^{11-} \quad (23)$$

$$\textbf{VI/VI'}: [P_2W_{18}O_{62}]^{11-} + e^- \longleftrightarrow [P_2W_{18}O_{62}]^{12-} \quad (24)$$

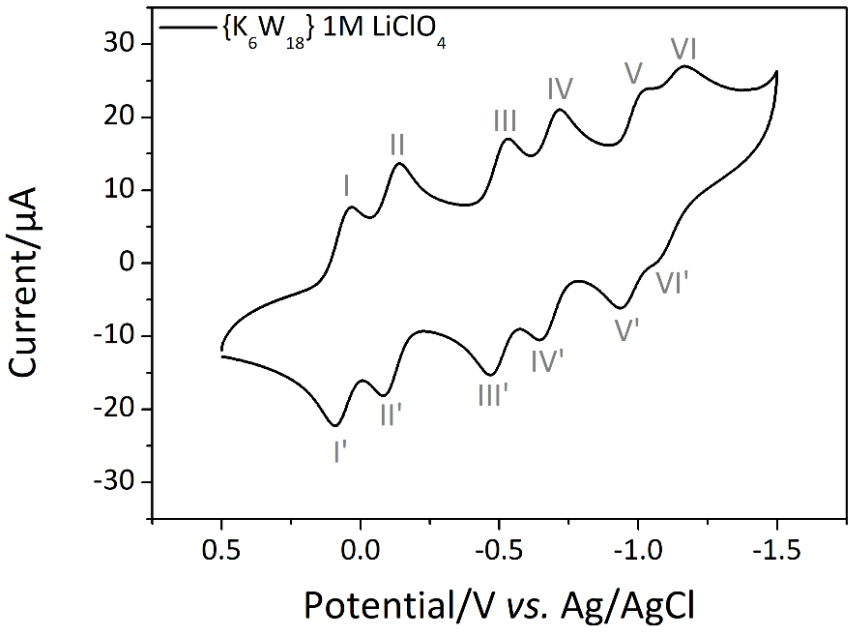


Figure 26 - Solution phase CV of $\{K_6W_{18}\}$ in 1M $LiClO_4$, recorded using a 3 mm diameter glassy carbon working electrode, a Pt counter electrode, and a Ag/AgCl reference electrode. The scan rate was 100 mv s^{-1}.

$\{K_6W_{18}\}$@V has five redox waves (A – E) corresponding to one two-electron process followed by four one-electron processes. As seen previously in the presence of 1M H_2SO_4 and 1M $HClO_4$, the first two one-electron processes, I and II, present for $\{K_6W_{18}\}$ in solution and $\{K_6W_{18}\}$@[O]V in the solid state, have coalesced to form a single two-electron process, A, for $\{K_6W_{18}\}$@V (Figure 27).

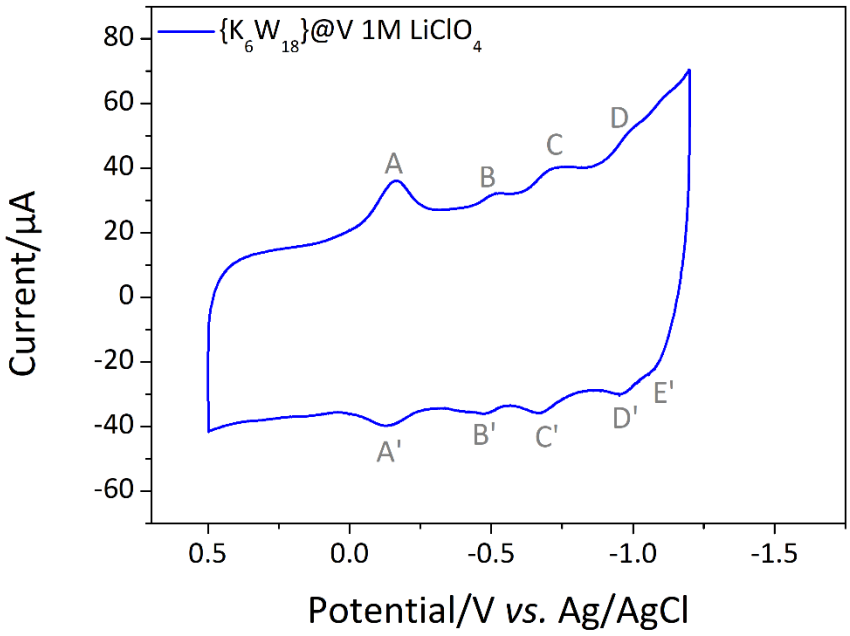


Figure 27 - Solid state CV of $\{K_6W_{18}\}$@V in 1M $LiClO_4$ recorded using a 3 mm diameter glassy carbon working electrode, a Pt counter electrode, and a Ag/AgCl reference electrode. The scan rate was 100 mv s^{-1}.

Equations 25 – 29 - Redox couples for $\{K_6W_{18}\}$@V in 1M $LiClO_4$.

$$\textbf{A/A'}: [P_2W_{18}O_{62}]^{6-} + 2e^- \longleftrightarrow [P_2W_{18}O_{62}]^{8-} \quad (25)$$

$$\textbf{B/B'}: [P_2W_{18}O_{62}]^{8-} + e^- \longleftrightarrow [P_2W_{18}O_{62}]^{9-} \quad (26)$$

$$\textbf{C/C'}: [P_2W_{18}O_{62}]^{9-} + e^- \longleftrightarrow [P_2W_{18}O_{62}]^{10-} \quad (27)$$

$$\textbf{D/D'}: [P_2W_{18}O_{62}]^{10-} + e^- \longleftrightarrow [P_2W_{18}O_{62}]^{11-} \quad (28)$$

$$\textbf{E/E'}: [P_2W_{18}O_{62}]^{11-} + e^- \longleftrightarrow [P_2W_{18}O_{62}]^{12-} \quad (29)$$

The mid-point potential for process A/A' is negatively shifted from processes I/I' and II/II' for $\{K_6W_{18}\}$ in 1M $LiClO_4$ by 205 mV and 30 mV respectively (Figure 28). Process A/A' is 243 mV and 91 mV more negative than processes I/I' and II/II' of $\{K_6W_{18}\}$@[O]V. Processes I/I' and II/II' for $\{K_6W_{18}\}$@[O]V are positively shifted by 38 mV and 62 mV with respect to processes I/I' and II/II' for $\{K_6W_{18}\}$ dissolved in 1M $LiClO_4$. Processes B – E for $\{K_6W_{18}\}$@V and processes III – VI for $\{K_6W_{18}\}$@[O]V occur at comparable potentials to $\{K_6W_{18}\}$ dissolved in solution. These results signify that process A of $\{K_6W_{18}\}$@V and processes I and

II of $\{K_6W_{18}\}$@[O]V are the most influenced by the presence of Li^+. However, the surface chemistry of the oxidised Vulcan support plays some cooperative role in rendering the redox processes more thermodynamically favourable as the general trend is that positive potential shifts occur on the oxidised Vulcan support and negative potential shifts are associated with the unmodified Vulcan (Table 7). The rest of the processes (B – E of $\{K_6W_{18}\}$@V and III – VI $\{K_6W_{18}\}$@[O]V) remain largely unaffected by the presence of Li^+ or the environment of the conductive carbon support, as evidenced by their very small shifts in E_{mid} values when compared to the potentials observed for $\{K_6W_{18}\}$ dissolved in solution (Table 7). This finding is in line with what was previously observed in Chapter 2 where only the first two processes of $\{K_6W_{18}\}$ experienced a positive shift when moving from the acidic electrolytes to the basic metal cation-based electrolytes.

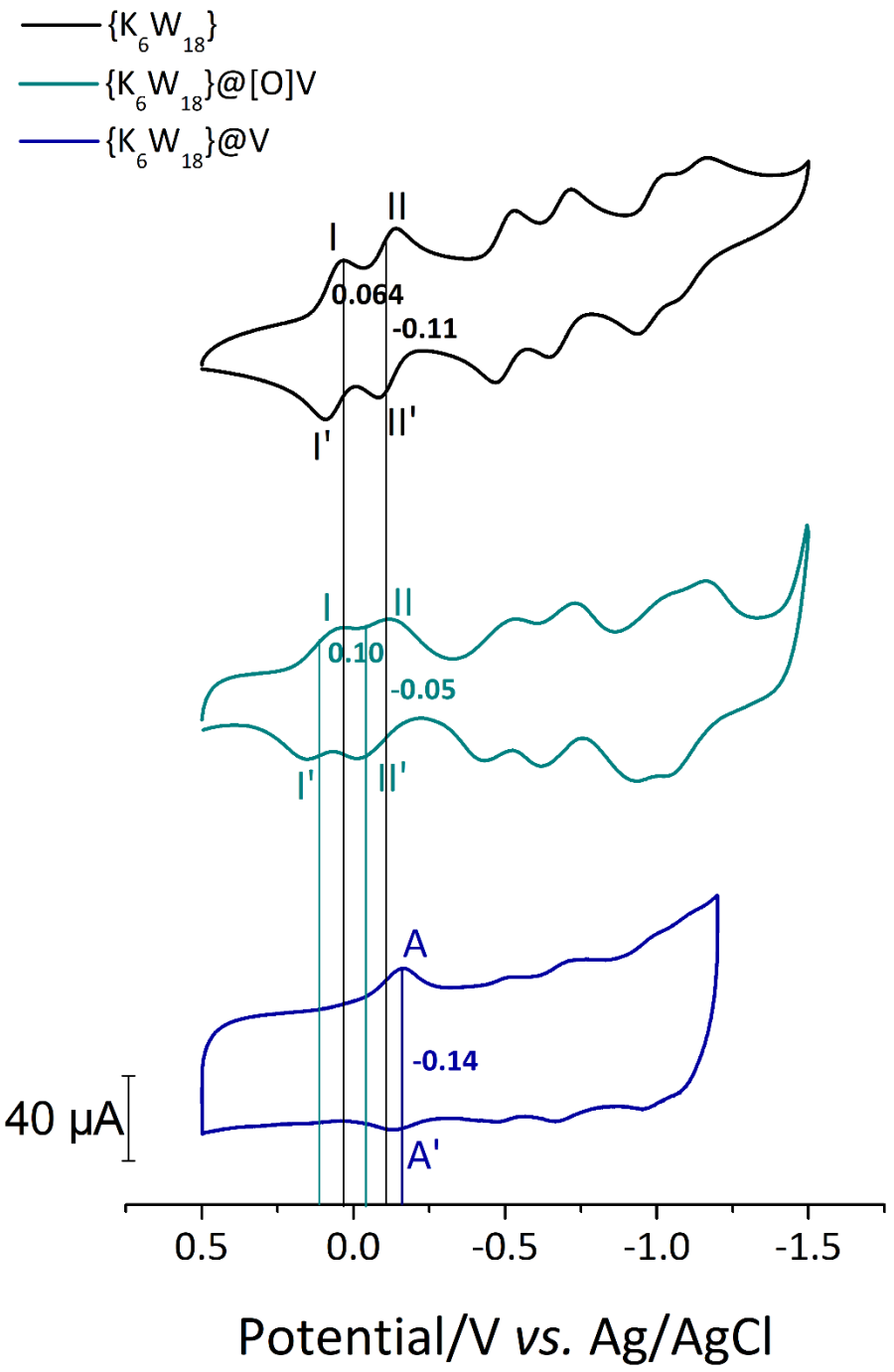


Figure 28 - Stacked CVs featuring the solution phase CV of $\{K_6W_{18}\}$ and the solid state voltammograms of $\{K_6W_{18}\}$@[O]V and $\{K_6W_{18}\}$@V to compare the redox profiles and peak shifts in 1M $LiClO_4$.

Table 7 - Comparison of E_{mid} and ΔE_p values for $\{K_6W_{18}\}$ dissolved in 1M $LiClO_4$ and for the $\{K_6W_{18}\}$@[O]V and $\{K_6W_{18}\}$@V solid state CVs in 1M $LiClO_4$.

Process	$\{K_6W_{18}\}$		Process	$\{K_6W_{18}\}$@V		Process	$\{K_6W_{18}\}$@[O]V	
	E_{mid}/V	ΔE_p/mV		E_{mid}/V	ΔE_p/mV		E_{mid}/V	ΔE_p/mV
I	0.064	50	A	-0.14	26	I	0.10	104
II	-0.11	49	B	-0.49	36	II	-0.05	100
III	-0.50	57	C	-0.69	34	III	-0.47	84
IV	-0.68	65	D	-0.96	28	IV	-0.65	83
V	-0.98	88	E	-1.09	60	V	-0.96	97
VI	-1.11	87	-	-	-	VI	-1.10	98

Electrochemical cycling revealed a stark contrast in stability between the composites $\{K_6W_{18}\}$@V and $\{K_6W_{18}\}$@[O]V. $\{K_6W_{18}\}$@V shows significantly reduced stability in the presence of Li^+, than when in the presence of H^+. In 1M $LiClO_4$, the signature POM redox processes are lost in between cycles 2 and 10 (Figure 29). For $\{K_6W_{18}\}$@[O]V, the loss of redox active material from the oxidised Vulcan surface is much more gradual, and can be cycled 250 times before the complete loss of POM is seen (Figure 30).

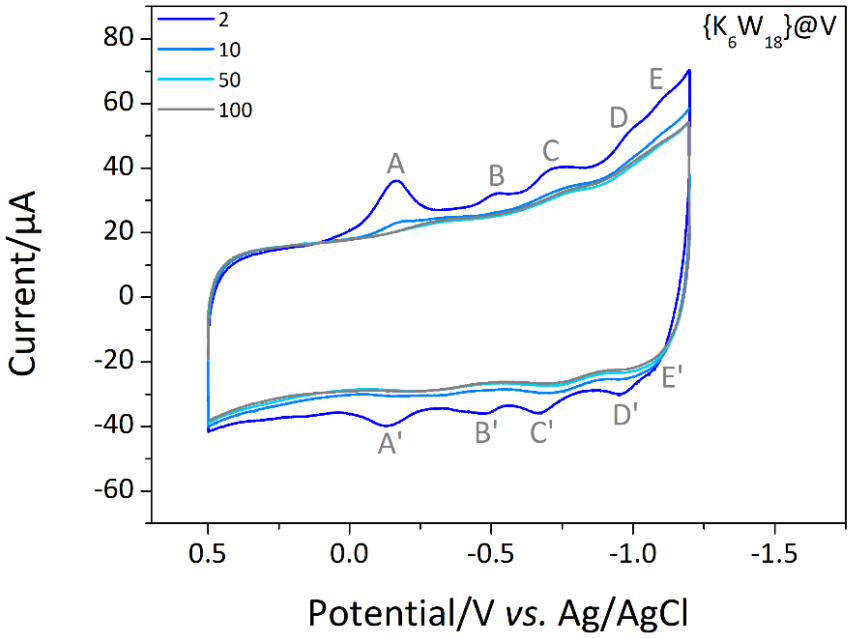


Figure 29 - Solid state CV of $\{K_6W_{18}\}$@Vulcan in 1M $LiClO_4$, recorded at a scan rate of 100 mv s^{-1}, showing cycles 2 – 100.

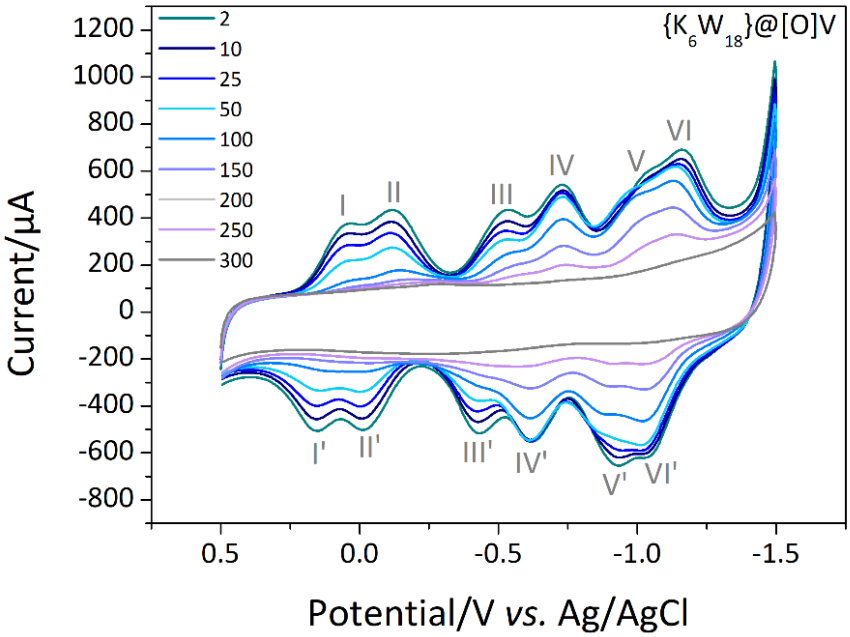


Figure 30 - Solid state CV of $\{K_6W_{18}\}$@[O]V in 1M $LiClO_4$, recorded at a scan rate of 100 mv s^{-1}, showing cycles 2 – 300.

The ΔE_p values for processes A – E of {K_6W_{18}}@V and I – VI of {K_6W_{18}}@[O]V are larger than expected for their respective electronic assignments (two-electron or one-electron processes). Coupled with the fact that some of the processes are ill-defined, namely E/E' and V/V – VI/VI', it is clear that both systems operate in a quasi-reversible regime. Whether the processes are surface-confined or diffusion controlled cannot be ascertained so easily either, as particularly for the {K_6W_{18}}@V material, scan rate studies were not possible due to the rapid dissolution of POM in the time-frame of the experiment.

1M $NaClO_4$

The electrochemical behaviour in the presence of Na^+ is akin to the behaviour witnessed in the presence of Li^+. In 1M $NaClO_4$, the voltammogram for {K_6W_{18}}@[O]V (Figure 31) shows six distinct one-electron processes (I – VI), as previously seen for {K_6W_{18}} dissolved in 1M $NaClO_4$ (Figure 32). Following the trend thus far, all six of these redox processes for {K_6W_{18}}@[O]V occur at comparable potentials to those of the solution phase voltammogram. Positive shifts ranging between 6 – 50 mV are observed (Table 8).

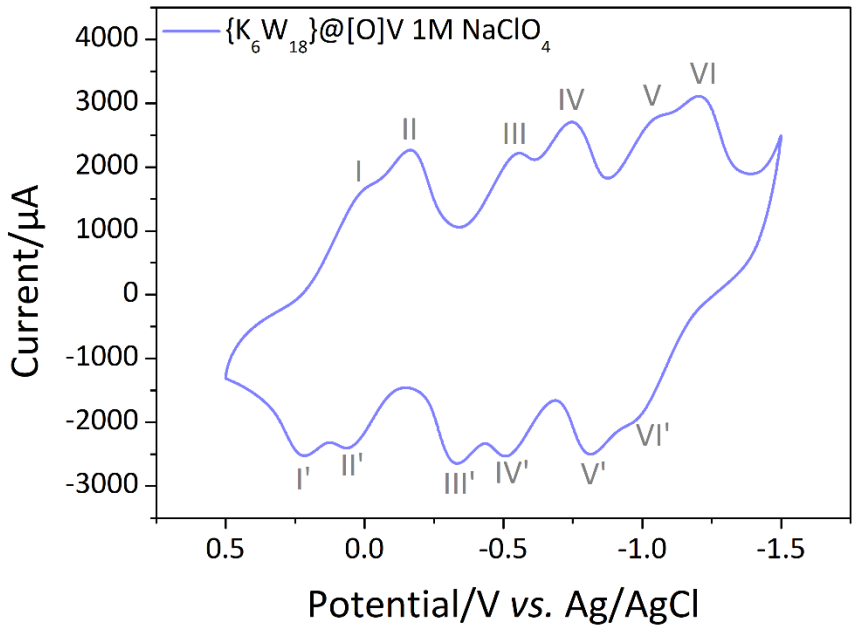


Figure 31 - Solid state CV of $\{K_6W_{18}\}$@[O]V in 1M $NaClO_4$ recorded using a 3 mm diameter glassy carbon working electrode, a Pt counter electrode, and a Ag/AgCl reference electrode. The scan rate was 100 mv s^{-1}.

Equations 30 – 35 - Redox couples for $\{K_6W_{18}\}$@[O]V in 1M $NaClO_4$.

$$\text{I/I'}: [P_2W_{18}O_{62}]^{6-} + e^- \longleftrightarrow [P_2W_{18}O_{62}]^{7-} \quad (30)$$

$$\text{II/II'}: [P_2W_{18}O_{62}]^{7-} + e^- \longleftrightarrow [P_2W_{18}O_{62}]^{8-} \quad (31)$$

$$\text{III/III'}: [P_2W_{18}O_{62}]^{8-} + e^- \longleftrightarrow [P_2W_{18}O_{62}]^{9-} \quad (32)$$

$$\text{IV/IV'}: [P_2W_{18}O_{62}]^{9-} + e^- \longleftrightarrow [P_2W_{18}O_{62}]^{10-} \quad (33)$$

$$\text{V/V'}: [P_2W_{18}O_{62}]^{10-} + e^- \longleftrightarrow [P_2W_{18}O_{62}]^{11-} \quad (34)$$

$$\text{VI/VI'}: [P_2W_{18}O_{62}]^{11-} + e^- \longleftrightarrow [P_2W_{18}O_{62}]^{12-} \quad (35)$$

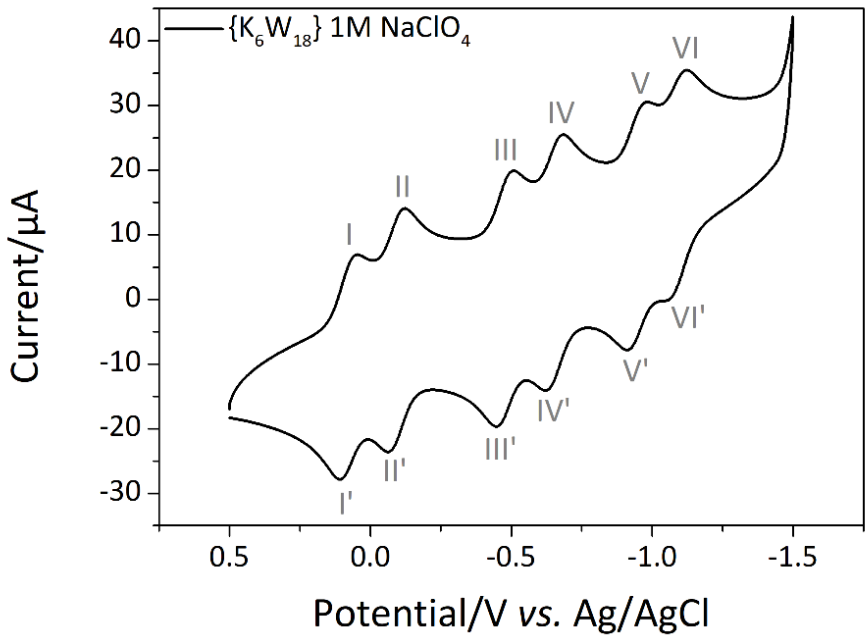


Figure 32 - Solution phase CV of $\{K_6W_{18}\}$ in 1M $NaClO_4$, recorded using a 3 mm diameter glassy carbon working electrode, a Pt counter electrode, and a Ag/AgCl reference electrode. The scan rate was 100 mv s^{-1}.

$\{K_6W_{18}\}$@V has five redox waves (A – E) corresponding to one two-electron process followed by four one-electron processes. As seen previously in the presence of 1M H_2SO_4, 1M $HClO_4$ and 1M $LiClO_4$, the first two one-electron processes, I and II, present for $\{K_6W_{18}\}$ in solution and $\{K_6W_{18}\}$@[O]V in the solid state, have coalesced to form a single two-electron process, A, for $\{K_6W_{18}\}$@V (Figure 33).

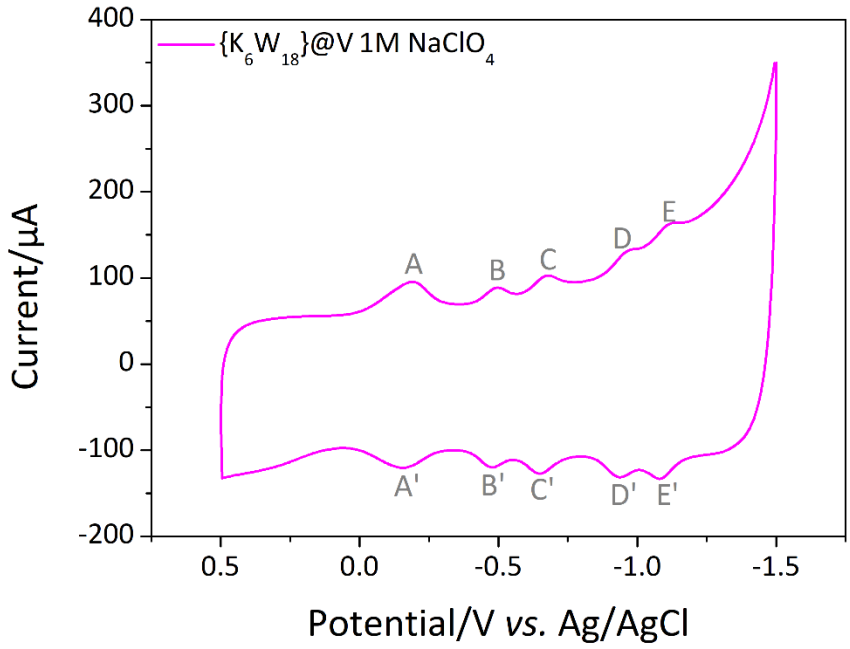


Figure 33 - Solid state CV of $\{K_6W_{18}\}$@V in 1M $NaClO_4$ recorded using a 3 mm diameter glassy carbon working electrode, a Pt counter electrode, and a Ag/AgCl reference electrode. The scan rate was 100 mv s^{-1}.

Equations 36 – 40 - Redox couples for $\{K_6W_{18}\}$@V in 1M $NaClO_4$.

$$\textbf{A/A'}: [P_2W_{18}O_{62}]^{6-} + 2e^- \leftrightarrow [P_2W_{18}O_{62}]^{8-} \quad (36)$$

$$\textbf{B/B'}: [P_2W_{18}O_{62}]^{8-} + e^- \leftrightarrow [P_2W_{18}O_{62}]^{9-} \quad (37)$$

$$\textbf{C/C'}: [P_2W_{18}O_{62}]^{9-} + e^- \leftrightarrow [P_2W_{18}O_{62}]^{10-} \quad (38)$$

$$\textbf{D/D'}: [P_2W_{18}O_{62}]^{10-} + e^- \leftrightarrow [P_2W_{18}O_{62}]^{11-} \quad (39)$$

$$\textbf{E/E'}: [P_2W_{18}O_{62}]^{11-} + e^- \leftrightarrow [P_2W_{18}O_{62}]^{12-} \quad (40)$$

The mid-point potential for process A/A' is negatively shifted from processes I/I' and II/II' for $\{K_6W_{18}\}$ in 1M $NaClO_4$ by 247 mV and 70 mV respectively. Process A/A' is 280 mV and 120 mV more negative than processes I/I' and II/II' of $\{K_6W_{18}\}$@[O]V. Processes I/I' and II/II' for $\{K_6W_{18}\}$@[O]V are positively shifted by 33 mV and 50 mV with respect to processes I/I' and II/II' for $\{K_6W_{18}\}$ dissolved in 1M $NaClO_4$. The E_{mid} values for processes B – E for $\{K_6W_{18}\}$@V and processes III – VI for $\{K_6W_{18}\}$@[O]V occur at comparable potentials to $\{K_6W_{18}\}$ dissolved in solution, with the general trend being that

positive potential shifts occur on the oxidised Vulcan support and negative shifts are associated with the unmodified Vulcan (Table 8).

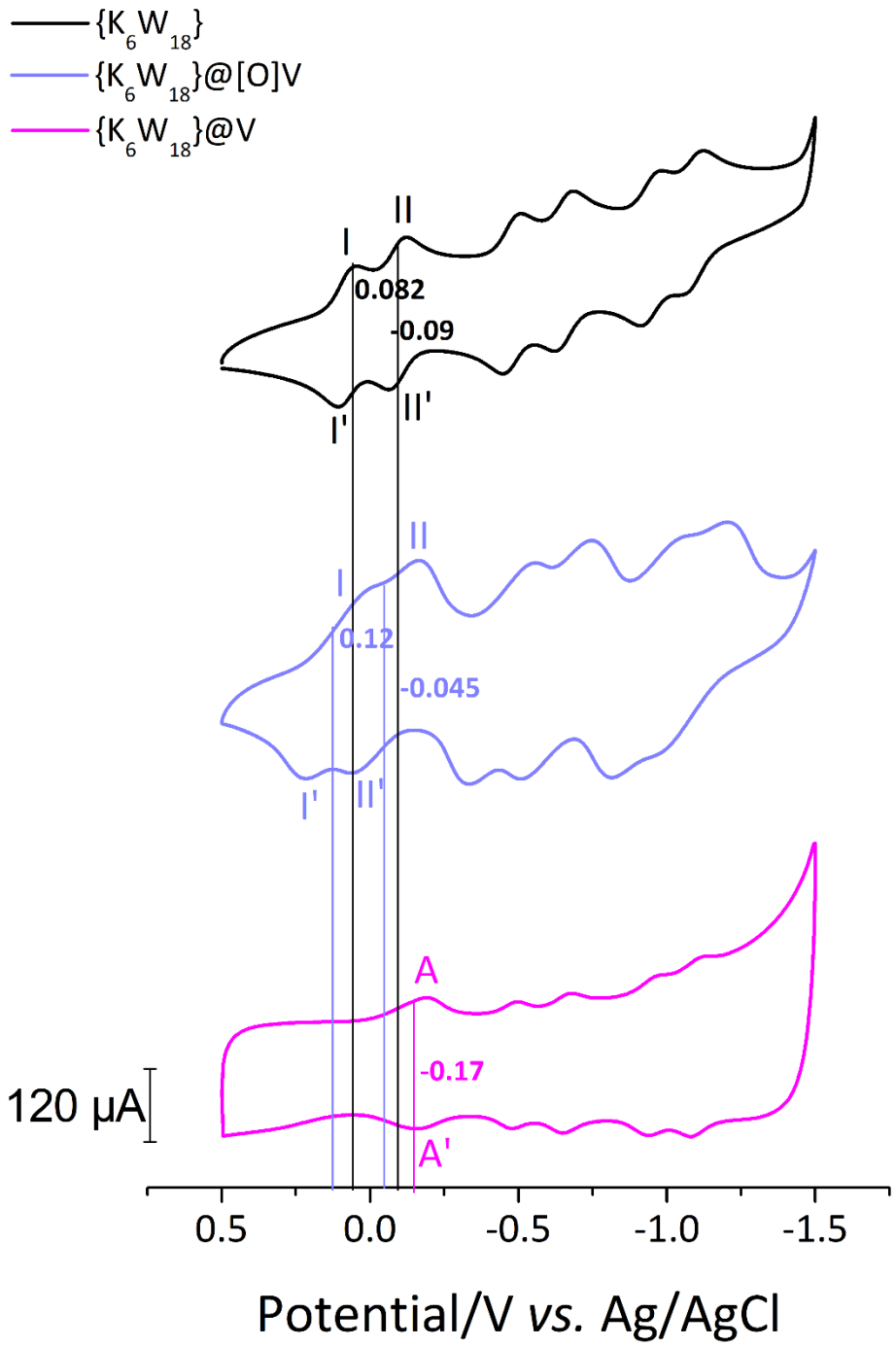


Figure 34 - Stacked CVs featuring the solution phase CV of $\{K_6W_{18}\}$ and the solid state voltammograms of $\{K_6W_{18}\}$@[O]V and $\{K_6W_{18}\}$@V to compare the redox profiles and peak shifts in 1M $NaClO_4$.

Table 8 - Comparison of E_{mid} and ΔE_p values for $\{K_6W_{18}\}$ dissolved in 1M $NaClO_4$ and for the $\{K_6W_{18}\}$@[O]V and $\{K_6W_{18}\}$@V solid state CVs in 1M $NaClO_4$.

Process	$\{K_6W_{18}\}$		Process	$\{K_6W_{18}\}$@V		Process	$\{K_6W_{18}\}$@[O]V	
	E_{mid}/V	ΔE_p/mV		E_{mid}/V	ΔE_p/mV		E_{mid}/V	ΔE_p/mV
I	0.082	52	A	-0.17	20	I	0.12	200
II	-0.09	47	B	-0.49	20	II	-0.045	220
III	-0.47	52	C	-0.66	25	III	-0.44	218
IV	-0.65	52	D	-0.95	35	IV	-0.62	231
V	-0.94	56	E	-1.1	30	V	-0.94	246
VI	-1.09	50	-	-	-	VI	-1.09	226

Electrochemical cycling yielded similar voltammograms to those of the composites in 1M $LiClO_4$. In the presence of Na^+, $\{K_6W_{18}\}$@V shows poor cycling stability, as the signature POM redox processes are rapidly lost in between cycles 2 and 10, beyond which only the capacitive current of Vulcan is observed (Figure 35). However this loss of redox active material from the oxidised Vulcan surface is much more steady and it can be seen that $\{K_6W_{18}\}$@[O]V can be cycled 250 times before the complete loss of POM redox activity is observed (Figure 36).

The ΔE_p values for processes A – E of $\{K_6W_{18}\}$@V in 1M $NaClO_4$ are smaller and closer to 0 mV than the ΔE_p values for processes A – E of $\{K_6W_{18}\}$@V in 1M $LiClO_4$. Additionally, the forward and reverse waves are better resolved in $NaClO_4$ than $LiClO_4$. This suggests that the surface-confined redox processes are more reversible in the presence of Na^+ than Li^+, even though this reversibility is only short-lived. In contrast, the ΔE_p values for processes I – VI of $\{K_6W_{18}\}$@[O]V are much larger (> 200 mV) than expected for a one-electron surface-confined or diffusion-controlled processes, meaning the redox activity of $\{K_6W_{18}\}$@[O]V operates in the quasi-reversible/irreversible regime. Scan rate studies were not possible due to the rapid dissolution of POM in the time-frame of the experiment, especially for $\{K_6W_{18}\}$@V.

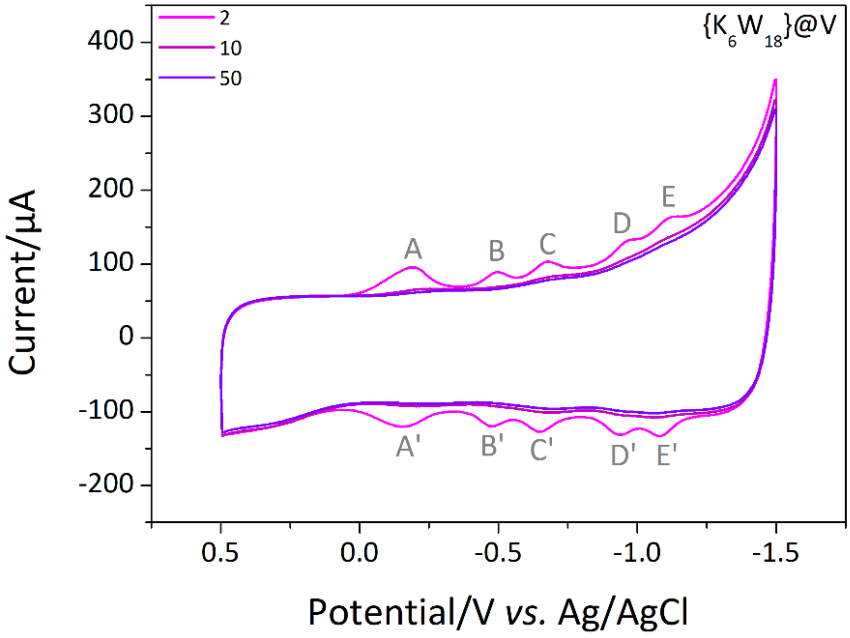


Figure 35 - Solid state CV of $\{K_6W_{18}\}$@Vulcan in 1M $NaClO_4$, recorded at a scan rate of 100 mv s^{-1}, showing cycles 2 – 50.

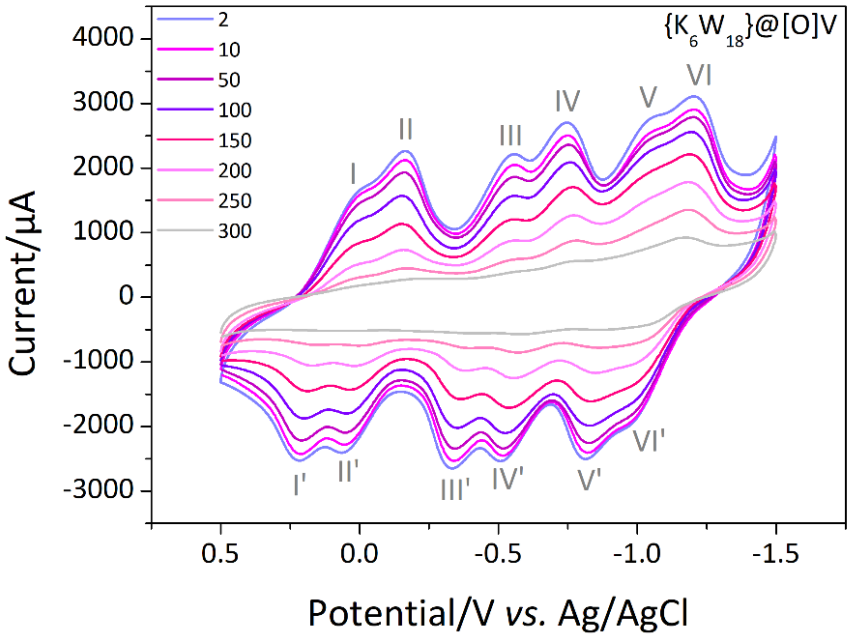


Figure 36 - Solid state CV of $\{K_6W_{18}\}$@[O]V in 1M $NaClO_4$, recorded at a scan rate of 100 mv s^{-1}, showing cycles 2 – 300.

IM $Mg(ClO_4)_2$

Finally, in the case of $Mg(ClO_4)_2$, the redox profiles for $\{K_6W_{18}\}$@V and $\{K_6W_{18}\}$@[O]V follow the same general trends as seen for $LiClO_4$ and $NaClO_4$, but with some notable differences in the cycling. In the presence of Mg^{2+}, the voltammogram for $\{K_6W_{18}\}$@[O]V (Figure 37) shows six distinct one-electron processes (I – VI), analogous to the solution phase voltammogram of $\{K_6W_{18}\}$ (Figure 38). The E_{mid} values for the six redox processes of $\{K_6W_{18}\}$@[O]V are similar to those of the dissolved moiety with some small positive shifts ranging between 15 – 53 mV (Table 9).

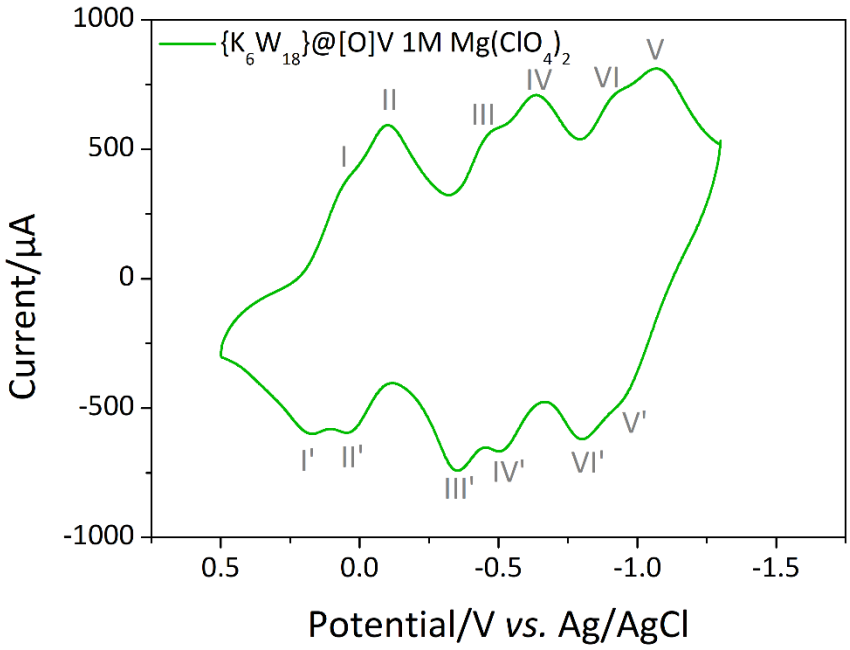


Figure 37 - Solid state CV of $\{K_6W_{18}\}$@[O]V in 1M $Mg(ClO_4)_2$ recorded using a 3 mm diameter glassy carbon working electrode, a Pt counter electrode, and a Ag/AgCl reference electrode. The scan rate was 100 mv s^{-1}.

Equations 41 – 46 - Redox couples for $\{K_6W_{18}\}$@[O]V in 1M $Mg(ClO_4)_2$.

$$\text{I/I'}: [P_2W_{18}O_{62}]^{6-} + e^- \leftrightarrow [P_2W_{18}O_{62}]^{7-} \quad (41)$$

$$\text{II/II'}: [P_2W_{18}O_{62}]^{7-} + e^- \leftrightarrow [P_2W_{18}O_{62}]^{8-} \quad (42)$$

$$\text{III/III'}: [P_2W_{18}O_{62}]^{8-} + e^- \leftrightarrow [P_2W_{18}O_{62}]^{9-} \quad (43)$$

$$\text{IV/IV'}: [P_2W_{18}O_{62}]^{9-} + e^- \leftrightarrow [P_2W_{18}O_{62}]^{10-} \quad (44)$$

$$\text{V/V'}: [P_2W_{18}O_{62}]^{10-} + e^- \leftrightarrow [P_2W_{18}O_{62}]^{11-} \quad (45)$$

$$\text{VI/VI'}: [P_2W_{18}O_{62}]^{11-} + e^- \leftrightarrow [P_2W_{18}O_{62}]^{12-} \quad (46)$$

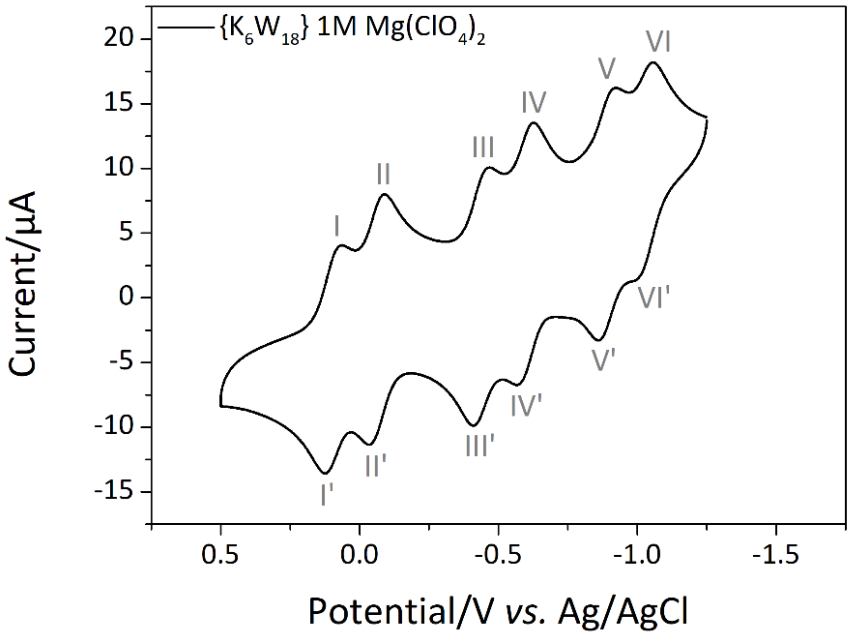


Figure 38 - Solution phase CV of $\{K_6W_{18}\}$ in 1M $Mg(ClO_4)_2$, recorded using a 3 mm diameter glassy carbon working electrode, a Pt counter electrode, and a Ag/AgCl reference electrode. The scan rate was 100 mv s^{-1}.

Figure 39 shows that $\{K_6W_{18}\}$@V exhibits five redox waves (A – E) in line with results observed with the other metal salts. Process A is a two-electron process which is the product of the first two one-electron processes I and II merging (I and II for $\{K_6W_{18}\}$ in solution and $\{K_6W_{18}\}$@[O]V in the solid state). Process A is followed by four successive one-electron processes (B – E).

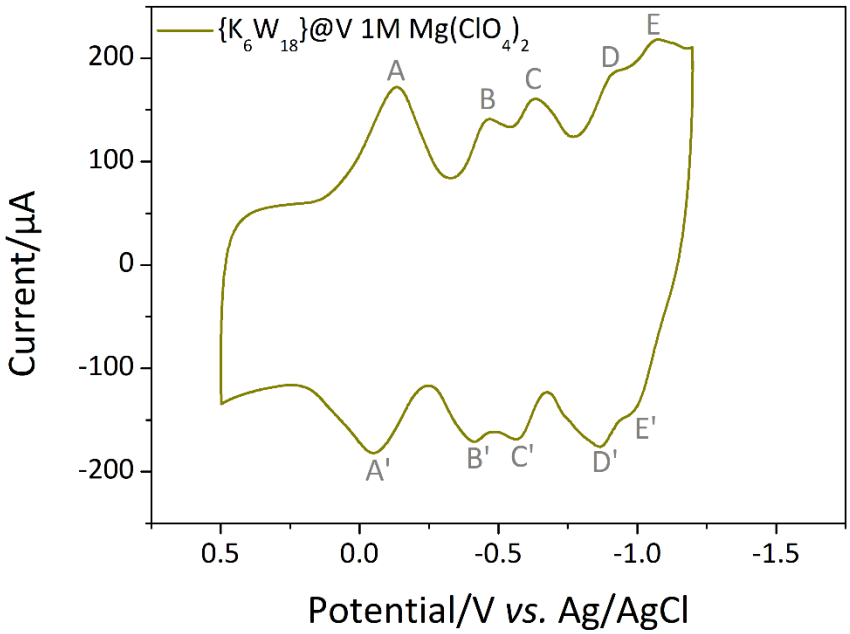


Figure 39 - Solid state CV of $\{K_6W_{18}\}$@Vulcan in 1M $Mg(ClO_4)_2$ recorded using a 3 mm diameter glassy carbon working electrode, a Pt counter electrode, and a Ag/AgCl reference electrode. The scan rate was 100 mv s^{-1}.

Equations 47 – 51 - Redox couples for $\{K_6W_{18}\}$@V in 1M $Mg(ClO_4)_2$.

$$\textbf{A/A'}: [P_2W_{18}O_{62}]^{6-} + 2e^- \longleftrightarrow [P_2W_{18}O_{62}]^{8-} \quad (47)$$

$$\textbf{B/B'}: [P_2W_{18}O_{62}]^{8-} + e^- \longleftrightarrow [P_2W_{18}O_{62}]^{9-} \quad (48)$$

$$\textbf{C/C'}: [P_2W_{18}O_{62}]^{9-} + e^- \longleftrightarrow [P_2W_{18}O_{62}]^{10-} \quad (49)$$

$$\textbf{D/D'}: [P_2W_{18}O_{62}]^{10-} + e^- \longleftrightarrow [P_2W_{18}O_{62}]^{11-} \quad (50)$$

$$\textbf{E/E'}: [P_2W_{18}O_{62}]^{11-} + e^- \longleftrightarrow [P_2W_{18}O_{62}]^{12-} \quad (51)$$

The mid-point potential for process A/A' is negatively shifted from processes I/I' and II/II' for $\{K_6W_{18}\}$ in 1M $Mg(ClO_4)_2$ by 183 mV and 21 mV respectively. Process A/A' is 198 mV and 102 mV more negative than processes I/I' and II/II' of $\{K_6W_{18}\}$@[O]V. Processes I/I' and II/II' for $\{K_6W_{18}\}$@[O]V are positively shifted by 15 mV and 46 mV with respect to processes I/I' and II/II' for $\{K_6W_{18}\}$ dissolved in 1M $Mg(ClO_4)_2$. The E_{mid} values for processes B – E for $\{K_6W_{18}\}$@V and processes III – VI for $\{K_6W_{18}\}$@[O]V occur at similar potentials to the parent anion $\{K_6W_{18}\}$ dissolved in solution. The general trend has persisted

whereby positive potential shifts occur on the oxidised Vulcan support, but negative shifts are linked to the unmodified Vulcan (Table 9).

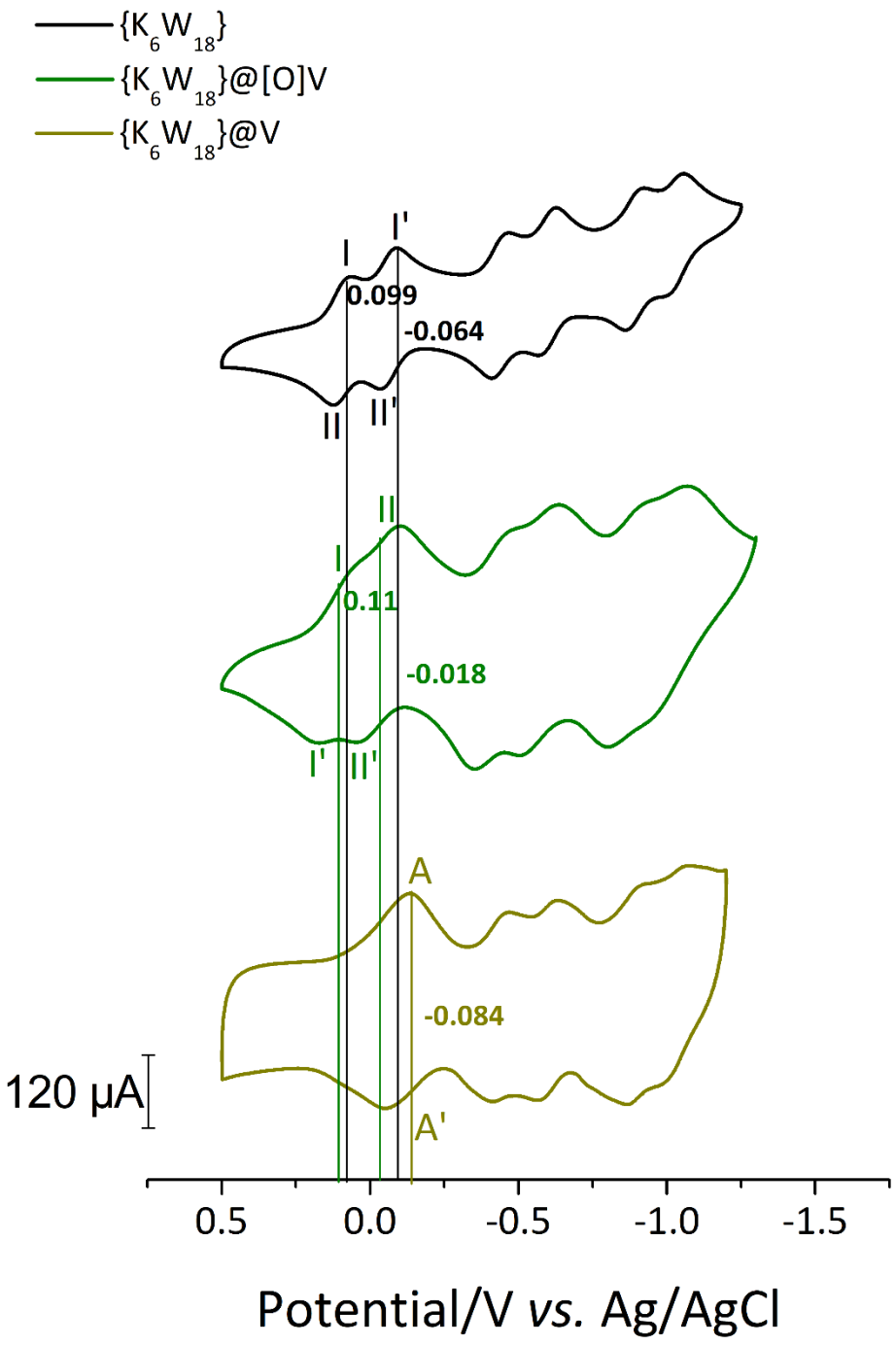


Figure 40 - Stacked CVs featuring the solution phase CV of $\{K_6W_{18}\}$ and the solid state voltammograms of $\{K_6W_{18}\}$@[O]V and $\{K_6W_{18}\}$@V to compare the redox profiles and peak shifts in 1M $Mg(ClO_4)_2$.

Table 9 - Comparison of E_{mid} and ΔE_p values for $\{K_6W_{18}\}$ dissolved in 1M $Mg(ClO_4)_2$ and for the $\{K_6W_{18}\}$@[O]V and $\{K_6W_{18}\}$@V solid state CVs in 1M $Mg(ClO_4)_2$.

Process	$\{K_6W_{18}\}$		Process	$\{K_6W_{18}\}$@V		Process	$\{K_6W_{18}\}$@[O]V	
	E_{mid}/V	ΔE_p/mV		E_{mid}/V	ΔE_p/mV		E_{mid}/V	ΔE_p/mV
I	0.099	49	A	-0.084	68	I	0.11	131
II	-0.064	45	B	-0.43	46	II	-0.018	132
III	-0.44	52	C	-0.60	46	III	-0.40	142
IV	-0.60	49	D	-0.89	46	IV	-0.56	152
V	-0.89	51	E	-1.03	54	V	-0.84	177
VI	-1.03	45	-	-	-	VI	-1.00	122

In the presence of Mg^{2+}, $\{K_6W_{18}\}$@V still shows poor cycling stability (Figure 41). However the loss of redox processes attributed to the POM does not commence until after the 25th cycle, as opposed to the Li^+ and Na^+ environments where this loss occurs between cycles 2 and 10. The most remarkable difference in the cycling data for $\{K_6W_{18}\}$@[O]V in the presence of Mg^{2+} is that the loss of POM from the oxidised Vulcan is much less pronounced, such that the signature POM peaks are retained at 500 cycles (Figure 42). This is in contrast to the cycling data for $\{K_6W_{18}\}$@[O]V in 1M $LiClO_4$ and $NaClO_4$ where the POM redox profile was not discernible beyond 250 cycles.

The ΔE_p values for processes A – E of $\{K_6W_{18}\}$@V and I – VI of $\{K_6W_{18}\}$@[O]V are difficult to interpret due to a combination of factors such as ill-defined peaks, interplay of surface-confined or diffusion controlled processes and a lack of scan rate studies. From what we know about the solution phase voltammogram of $\{K_6W_{18}\}$, it is reasonable to suggest the composites $\{K_6W_{18}\}$@V and $\{K_6W_{18}\}$@[O]V also display quasi-reversible behaviour.

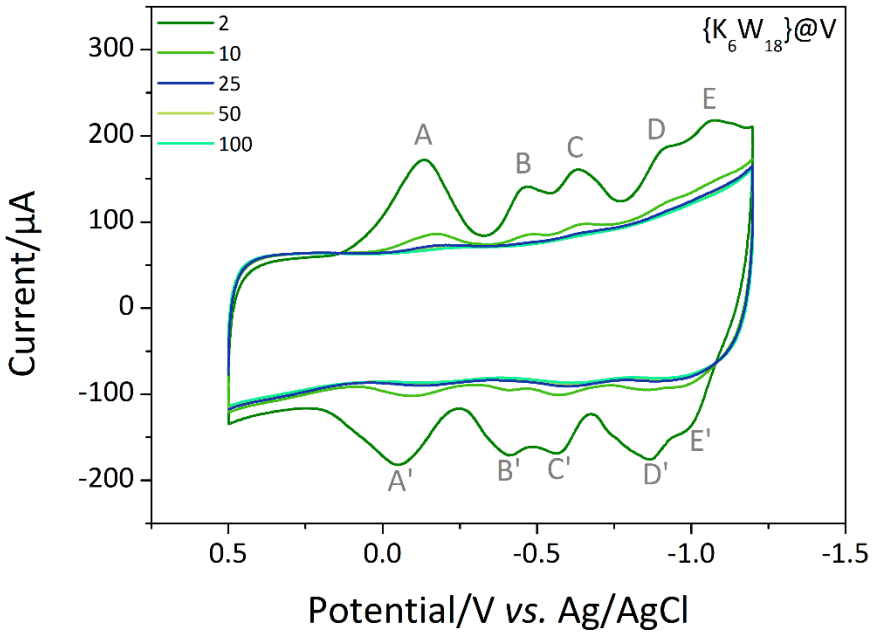


Figure 41 - Solid state CV of $\{K_6W_{18}\}$@V in 1M $Mg(ClO_4)_2$, recorded at a scan rate of 100 mv s^{-1}, showing cycles 2 – 100.

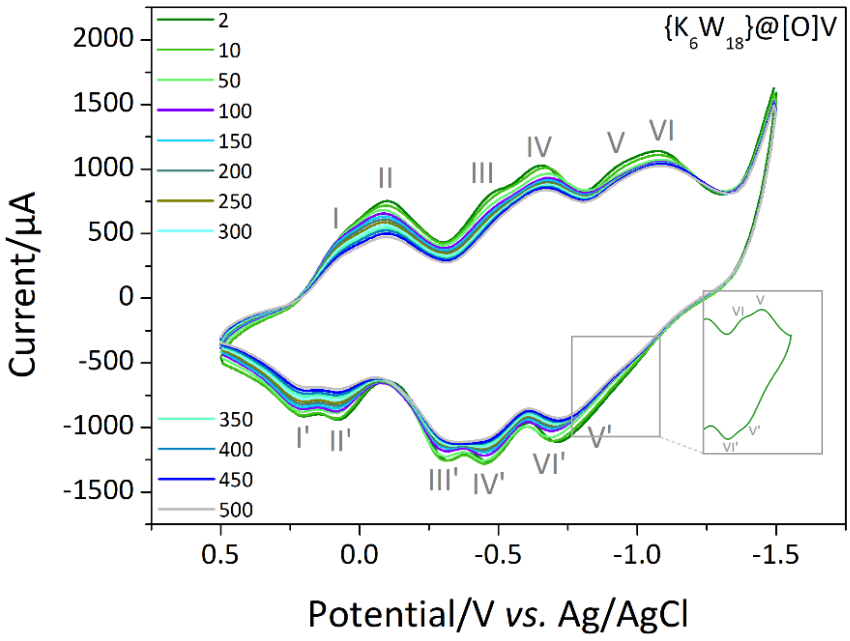


Figure 42 - Solid state CV of $\{K_6W_{18}\}$@[O]V in 1M $Mg(ClO_4)_2$, recorded at a scan rate of 100 mv s^{-1}, showing cycles 2 – 500.

Summary

In all cases, it was observed that the oxidised Vulcan support exhibited enhanced POM retention during electrochemical cycling *vs.* the unmodified Vulcan. In the presence of the metal cations $Li^+/Na^+/Mg^{2+}$, additional interesting electrochemical behaviour is observed. As we know from the solution phase voltammograms, pH plays a substantial part in dictating the redox profiles of POMs. However, from the solution phase experiments, we also know that the $\{K_6W_{18}\}$ moiety is fundamentally stable in the perchlorate electrolytes and thus changes in the solid-state are induced by the nature of the Vulcan support.

Regarding the solution phase voltammograms, positive shifts in the first two processes, I and II, for $\{K_6W_{18}\}$ dissolved in the metal-based electrolytes was indicative of ion-pairing between the $Li^+/Na^+/Mg^{2+}$ cations with the singly and doubly reduced $\{K_6W_{18}\}$ anion. In the case of the composites, the first two processes, I and II for $\{K_6W_{18}\}$@[O]V remain as one-electron processes as seen in the solution CVs and it also retains proton decoupled behaviour in the presence of $Li^+/Na^+/Mg^{2+}$ with six sequential monoelectronic processes. But in the case of the $\{K_6W_{18}\}$@V composite, the first two one-electron processes always coalesce to produce a single two-electron redox process, A/A'. Additionally, I and II for $\{K_6W_{18}\}$@[O]V are always positively shifted in relation to process A. This would imply that the difference in surface chemistry between the oxidised Vulcan and unmodified Vulcan impacts the nature of the cation association interaction.

$\{K_6W_{18}\}$@V shows better cycling stability in presence of H^+ (100 cycles) when compared to $Li^+/Na^+/Mg^{2+}$ (< 25 cycles). It is possible that metal cation association exacerbates the dissolution of the POMs adhered ono the hydrophobic Vulcan surface. The destabilisation of the redox active species (POM) on the surface is effectively brought about by the relatively strong interactions between the solvated cations in solution and the POM. In the case of protons, the steric component contributing to the destabilisation of POMs from the Vulcan surfaces is inconsequential. Whereas in the case of the metal

cations, which possess larger hydrated radii, a steric factor is introduced with respect to charge balancing which is no longer trivial.

The oxidised Vulcan support has a surface decorated with carboxylic acid groups, providing anchorage points for POM tethering during electrochemical cycling. As such, it is likely that during charge balancing, the metal cations can associate with the reduced POMs via an interaction with the weakly acidic carboxylic acid groups. The combined effect of the surface chemistry and effective metal cation association could explain the prominent differences in electrochemical cyclability between the unmodified Vulcan and oxidised Vulcan composites. This synergy is most pronounced for the $\{K_6W_{18}\}$@[O]V composite in $Mg(ClO_4)_2$, which is the least basic (pH 7) and has double the cycling capability compared to $LiClO_4$ and $NaClO_4$. Interestingly, no 'penalty' is incurred for ion-pairing with a divalent cation. The Mg^{2+} cation could be bound to both the POM and the carboxylic acid sites on the oxidised Vulcan surface. This charge balancing conundrum is very intriguing for energy storage applications, as effectively half the number of cations is needed to charge balance the $\{K_6W_{18}\}$ anion reduced by six electrons. Certainly, this phenomenon warrants further work for investigation.

3.3.7 Electrochemical Characterisation in Battery Solvent

The electrochemical behaviour of the $\{K_6W_{18}\}$@V and $\{K_6W_{18}\}$@[O]V composites were tested in non-aqueous battery solvent (1M lithium hexafluorophosphate ($LiPF_6$) in 50/50 (v/v) ethylene carbonate (EC):ethyl methyl carbonate (EMC)). This study was conducted to further explore the effect of surface oxidation of Vulcan in a traditional battery solvent with a view towards energy storage applications. The solution phase voltammogram of $\{K_6W_{18}\}$ dissolved in the battery solvent from Chapter 2 is shown in Figure 43.

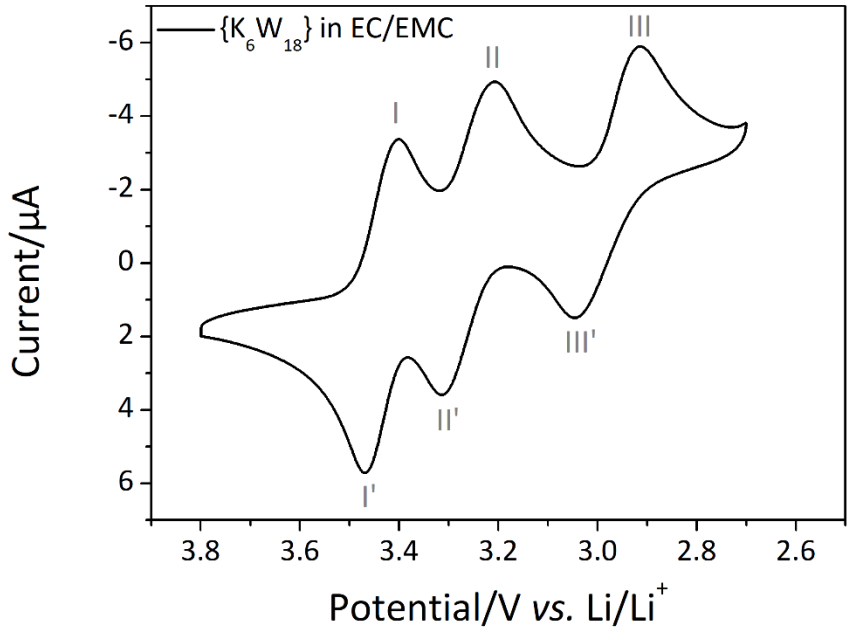


Figure 43 – Solution phase CV of $\{K_6W_{18}\}$ in 1M $LiPF_6$ in EC/EMC, performed in the glovebox, using a 3 mm GC WE, Pt CE, LFP reference electrode which was then converted to Li/Li^+. The scan rate was 50 mV s^{-1}.

Equations 52 – 54 - Redox couples for $\{K_6W_{18}\}$ in battery solvent.

$$\textbf{I/I'}: [P_2W_{18}O_{62}]^{6-} + e^- \longleftrightarrow [P_2W_{18}O_{62}]^{7-} \quad (52)$$

$$\textbf{II/II'}: [P_2W_{18}O_{62}]^{7-} + e^- \longleftrightarrow [P_2W_{18}O_{62}]^{8-} \quad (53)$$

$$\textbf{III/III'}: [P_2W_{18}O_{62}]^{8-} + e^- \longleftrightarrow [P_2W_{18}O_{62}]^{9-} \quad (54)$$

Solid-state voltammetry of the composites revealed three redox waves, demonstrating that the POMs within each composite material were still electrochemically accessible in the organic battery solvent. Both CVs exhibit three monoelectronic reduction/oxidation couples; A/A', B/B', C/C' for $\{K_6W_{18}\}$@V (Figure 44, Equations 55 – 57) and I/I', II/II', III/III' for $\{K_6W_{18}\}$@[O]V (Figure 45, Equations 58 – 60). Contrary to what was previously observed in the aqueous electrolytes, the E_{mid} values for all three processes in each composite are close to the E_{mid} values for $\{K_6W_{18}\}$ dissolved in the battery solvent. As such, no large positive or negative shifts were observed. The differences in the Vulcan

and [O]V surface chemistry also have little influence over the E_{mid} values as generally the [O]V support induced positive shifts in aqueous environments.

Table 10 - Comparison of E_{mid} and ΔE_p values for $\{K_6W_{18}\}$ dissolved in battery solvent and for the $\{K_6W_{18}\}$@[O]V and $\{K_6W_{18}\}$@V solid state CVs in battery solvent.

Process	$\{K_6W_{18}\}$		Process	$\{K_6W_{18}\}$@V		Process	$\{K_6W_{18}\}$@[O]V	
	E_{mid}/V	ΔE_p/mV		E_{mid}/V	ΔE_p/mV		E_{mid}/V	ΔE_p/mV
I	3.47	75	A	3.54	227	I	3.49	149
II	3.30	117	B	3.34	217	II	3.29	171
III	3.01	142	C	3.07	244	III	3.03	191

However, looking at the cycling data, there is an undeniable difference in cyclability, arising from the chemical differences of the supports. For the $\{K_6W_{18}\}$@V composite, a very rapid desorption of POM from the surface of Vulcan is observed (cycles 10 – 15).

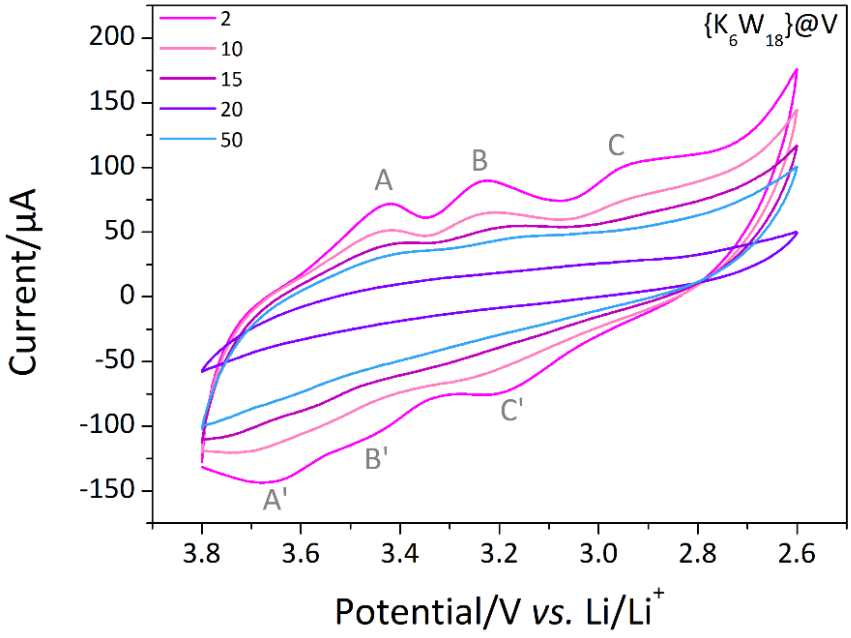


Figure 44 - Solid state CV of $\{K_6W_{18}\}$@Vulcan in 1M $LiPF_6$ in EC/EMC, performed in the glovebox, using a 3 mm GC WE, Pt CE, LFP reference electrode which was then converted to Li/Li^+. The scan rate was 50 mV s^{-1}.

Equations 55 – 57 - Redox couples for $\{K_6W_{18}\}$@V in battery solvent.

$$\textbf{A/A'}: [P_2W_{18}O_{62}]^{6-} + e^- \longleftrightarrow [P_2W_{18}O_{62}]^{7-} \quad (55)$$

$$\textbf{B/B'}: [P_2W_{18}O_{62}]^{7-} + e^- \longleftrightarrow [P_2W_{18}O_{62}]^{8-} \quad (56)$$

$$\textbf{C/C'}: [P_2W_{18}O_{62}]^{8-} + e^- \longleftrightarrow [P_2W_{18}O_{62}]^{9-} \quad (57)$$

In contrast, the $\{K_6W_{18}\}$@[O]V demonstrates enhanced cyclability with redox activity still being observed at 400 cycles. This is impressive given the highly polar nature of the solvent, though the processes do become less reversible over time (ΔE_p > 59 mV). It is very interesting that the dissolution of POM off the Vulcan surface happens so quickly, given that the $\{K_6W_{18}\}$ does not readily dissolve in the organic battery solvent without agitation. Thus, immobilisation on the oxidised Vulcan provides a superior platform for Li^+ cation exchange. The driving force for the POM dissolution from the Vulcan *vs.* [O]V is undoubtedly due to the mode of attachment of the POM on each support. The carboxylic acid groups provide efficient anchorage sites for the POM to remain 'docked' at the oxidised Vulcan surface, this supportive interaction is absent for the unmodified Vulcan surface. As seen from the SEM images, POM agglomerates are adhered to the surface of the unmodified Vulcan, and these are readily lost during electrochemical characterisation and cycling.

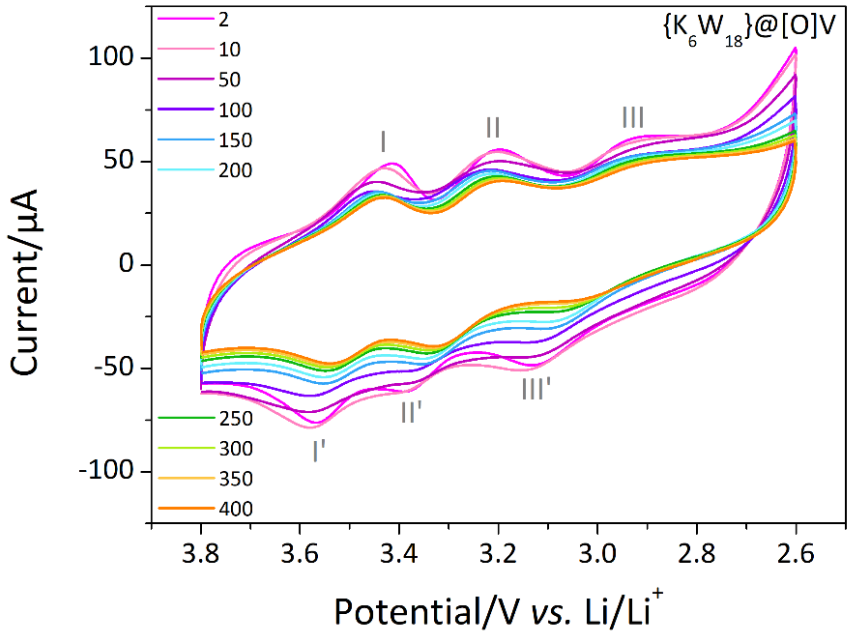


Figure 45 - Solid state CV of $\{K_6W_{18}\}$@[O]Vulcan in 1M $LiPF_6$ in EC/EMC, performed in the glovebox, using a 3 mm GC WE, Pt CE, LFP reference electrode which was then converted to Li/Li^+. The scan rate was 50 mV s^{-1}.

Equations 58 – 60 - Redox couples for $\{K_6W_{18}\}$@[O]V in battery solvent.

$$\textbf{I/I'}: [P_2W_{18}O_{62}]^{6-} + e^- \longleftrightarrow [P_2W_{18}O_{62}]^{7-} \quad (58)$$

$$\textbf{II/II'}: [P_2W_{18}O_{62}]^{7-} + e^- \longleftrightarrow [P_2W_{18}O_{62}]^{8-} \quad (59)$$

$$\textbf{III/III'}: [P_2W_{18}O_{62}]^{8-} + e^- \longleftrightarrow [P_2W_{18}O_{62}]^{9-} \quad (60)$$

3.38 Oxidation Using Acidic Polyoxometalates

As evidenced from the findings above, oxidation of the Vulcan surface has a clear benefit with respect to POM retention during electrochemical cycling. We hypothesised that the superacid Wells-Dawson $H_6[P_2W_{18}O_{62}]$, and the free acid Keggin motif $H_3[PW_{12}O_{40}]$ could be used to perform a simultaneous in-situ oxidation and adsorption to the Vulcan surface. In this sense, Vulcan was stirred in solutions of either $\{H_3W_{12}\}$ or $\{H_6W_{18}\}$ and the composites are denoted as $\{H_3W_{12}\}$@V and $\{H_6W_{18}\}$@V. The properties of these composites were compared to the composites $\{H_3W_{12}\}$@[O]V and $\{H_6W_{18}\}$@[O]V which were prepared by adding already Oxidised Vulcan (by 2M H_2SO_4 as detailed in

experimental section) to solution of the $\{H_3W_{12}\}$ or $\{H_6W_{18}\}$ POM. This study was done to explore the difference in countercation (K^+ vs. H^+) and its influence on the preparation of such Vulcan based composites.

Keggin/Vulcan Composites

Starting with the TGA data for the Keggin/Vulcan composites, the onset of their decomposition events occurs at similar temperatures (Figure 46). With respect to the approximate POM loading, we see a parallel with the $\{K_6W_{18}\}$ composites whereby the unmodified Vulcan has a higher POM loading vs. the oxidised support: 46.7% loading for $\{H_3W_{12}\}$@V is and 29.5% for $\{H_3W_{12}\}$@[O]V.

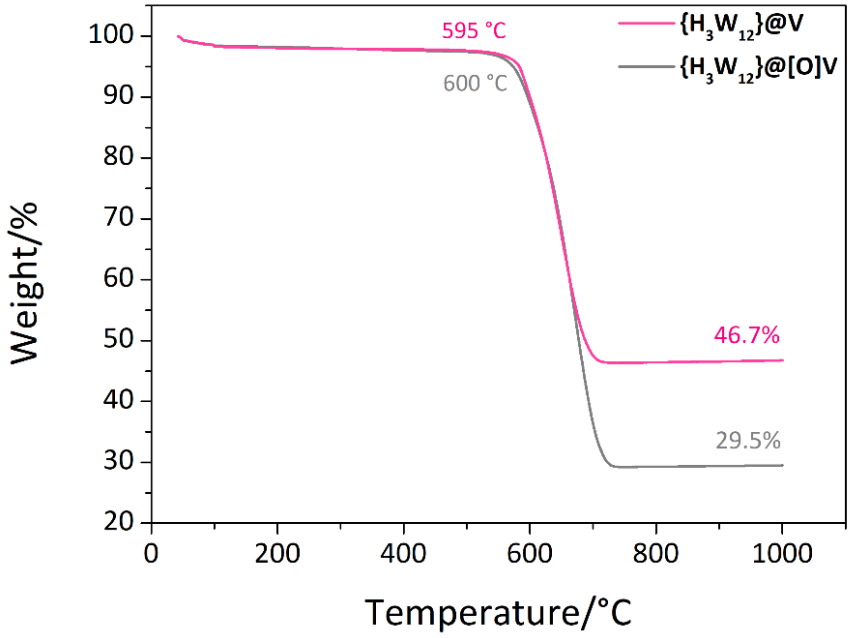


Figure 46 – TG curves for $\{H_3W_{12}\}$@Vulcan and $\{H_3W_{12}\}$@ Oxidised Vulcan, showing the onset temperature of their mass loss events and the approximate weight percent loading of POM within each composite.

The electrochemical behaviour of the Keggin/Vulcan composites in 1M H_2SO_4 presents some similarities and some differences to what was previously observed for the $\{K_6W_{18}\}$/Vulcan composites. $\{H_3W_{12}\}$@V and $\{H_3W_{12}\}$@[O]V retain the same redox profile as $\{H_3W_{12}\}$ dissolved in 1M H_2SO_4 (Figure 47).

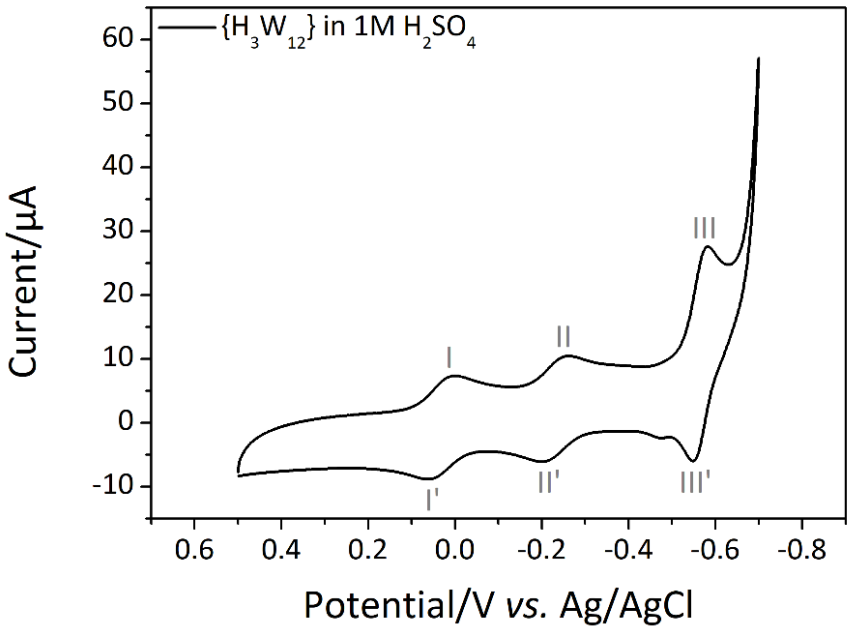


Figure 47 – Solution phase CV of $\{H_3W_{12}\}$ in 1M H_2SO_4 performed using a 3 mm diameter GC working electrode, a Pt counter electrode, and a Ag/AgCl reference electrode. The scan rate was 100 mV s^{-1}.

Equations 61 – 63 - Redox couples for $\{H_3W_{12}\}$ in 1M H_2SO_4.

$$\textbf{I/I'}: [PW_{12}O_{40}]^{3-} + e^- \longleftrightarrow [PW_{12}O_{40}]^{4-} \quad (61)$$

$$\textbf{II/II'}: [PW_{12}O_{40}]^{4-} + e^- \longleftrightarrow [PW_{12}O_{40}]^{5-} \quad (62)$$

$$\textbf{III/III'}: [PW_{12}O_{40}]^{5-} + 2e^- + 2H^+ \longleftrightarrow [H_2PW_{12}O_{40}]^{5-} \quad (63)$$

Both voltammograms show three redox waves corresponding to two one-electron processes, followed by a proton-coupled two-electron process.[50] No merging of the one-electron processes is observed: the first two processes I and II for $\{H_3W_{12}\}$ in solution remain as I and II for $\{H_3W_{12}\}$@[O]V (Figure 48) and correspond to A and B for $\{H_3W_{12}\}$@V (Figure 49) in the solid state.

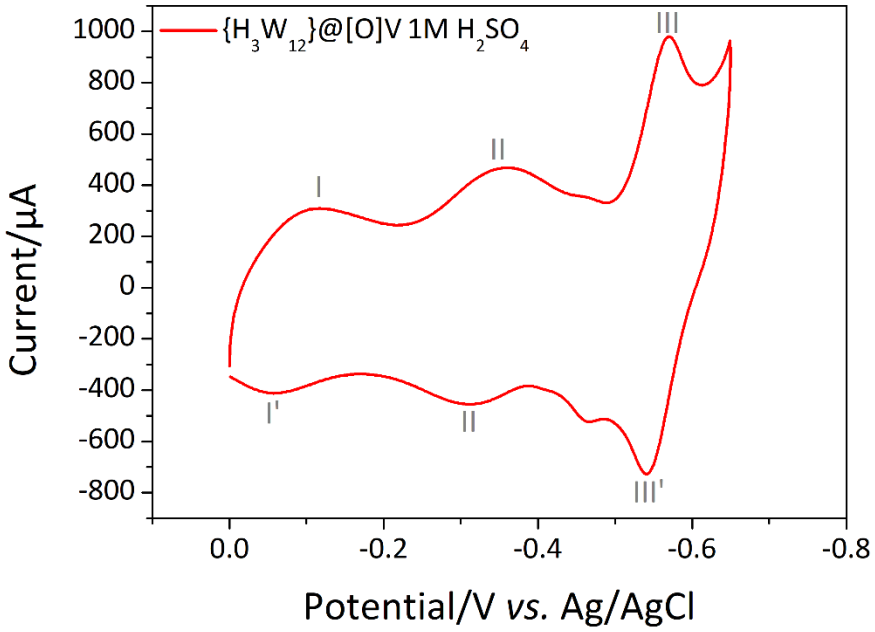


Figure 48 - Solid state CV of $\{K_6W_{18}\}$@[O]V in 1M H_2SO_4 recorded using a 3 mm diameter glassy carbon working electrode, a Pt counter electrode, and a Ag/AgCl reference electrode. The scan rate was 100 mv s^{-1}.

Equations 64 – 66 - Redox couples for $\{H_3W_{12}\}$@[O]V in 1M H_2SO_4.

I/I': $[PW_{12}O_{40}]^{3-} + e^- \leftrightarrow [PW_{12}O_{40}]^{4-}$ (64)

II/II': $[PW_{12}O_{40}]^{4-} + e^- \leftrightarrow [PW_{12}O_{40}]^{5-}$ (65)

III/III': $[PW_{12}O_{40}]^{5-} + 2e^- + 2H^+ \leftrightarrow [H_2PW_{12}O_{40}]^{5-}$ (66)

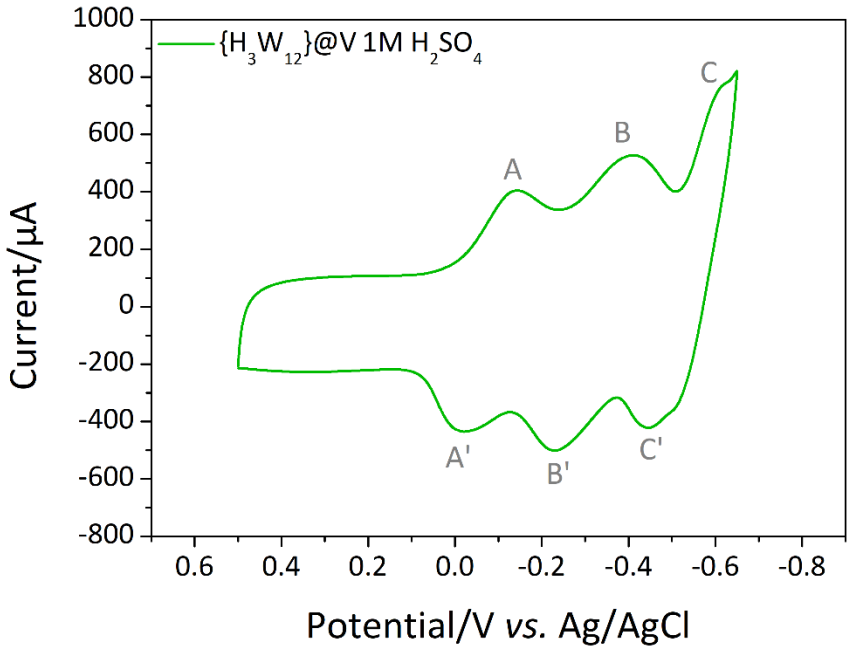


Figure 49 - Solid state CV of $\{K_6W_{18}\}$@[O]V in 1M H_2SO_4 recorded using a 3 mm diameter glassy carbon working electrode, a Pt counter electrode, and a Ag/AgCl reference electrode. The scan rate was 100 mv s^{-1}.

Equations 67 – 69 - Redox couples for $\{H_3W_{12}\}$@V in 1M H_2SO_4.

$$\textbf{A/A'}: [PW_{12}O_{40}]^{3-} + e^- \longleftrightarrow [PW_{12}O_{40}]^{4-} \quad (67)$$

$$\textbf{B/B'}: [PW_{12}O_{40}]^{4-} + e^- \longleftrightarrow [PW_{12}O_{40}]^{5-} \quad (68)$$

$$\textbf{C/C'}\ [PW_{12}O_{40}]^{5-} + 2e^- + 2H^+ \longleftrightarrow [H_2PW_{12}O_{40}]^{5-} \quad (69)$$

Processes A and B and processes I and II for $\{H_3W_{12}\}$@[O]V are negatively shifted compared to processes I and II $\{H_3W_{12}\}$ in solution (negative shifts *vs.* I and II in solution: A = 103 mV B = 88 mV, I = 111 mV, II = 113 mV). Processes C and III for $\{H_3W_{12}\}$@V and $\{H_3W_{12}\}$@[O]V respectively, occur at similar potentials to III in solution (Figure 50, Table 11). More interestingly, the E_{mid} values for processes A, B and C of $\{H_3W_{12}\}$@V are very close to the E_{mid} values for processes I, II and III for $\{H_3W_{12}\}$@[O]V. This is in contrast to the $\{K_6W_{18}\}$/Vulcan composites where an obvious positive shift for the first two processes was always observed on the oxidised surface, demonstrating the oxidised support provided a more favourable environment for reduction to occur. The fact that the E_{mid} values for the Keggin/Vulcan composites are so comparable indicates

that the Keggin was able to oxidise the Vulcan support to some extent (though unlikely to the same chemical extent as the oxidation method to produce [O]Vulcan). However, control experiments with the potassium salt of the Keggin are needed to further support this conclusion.

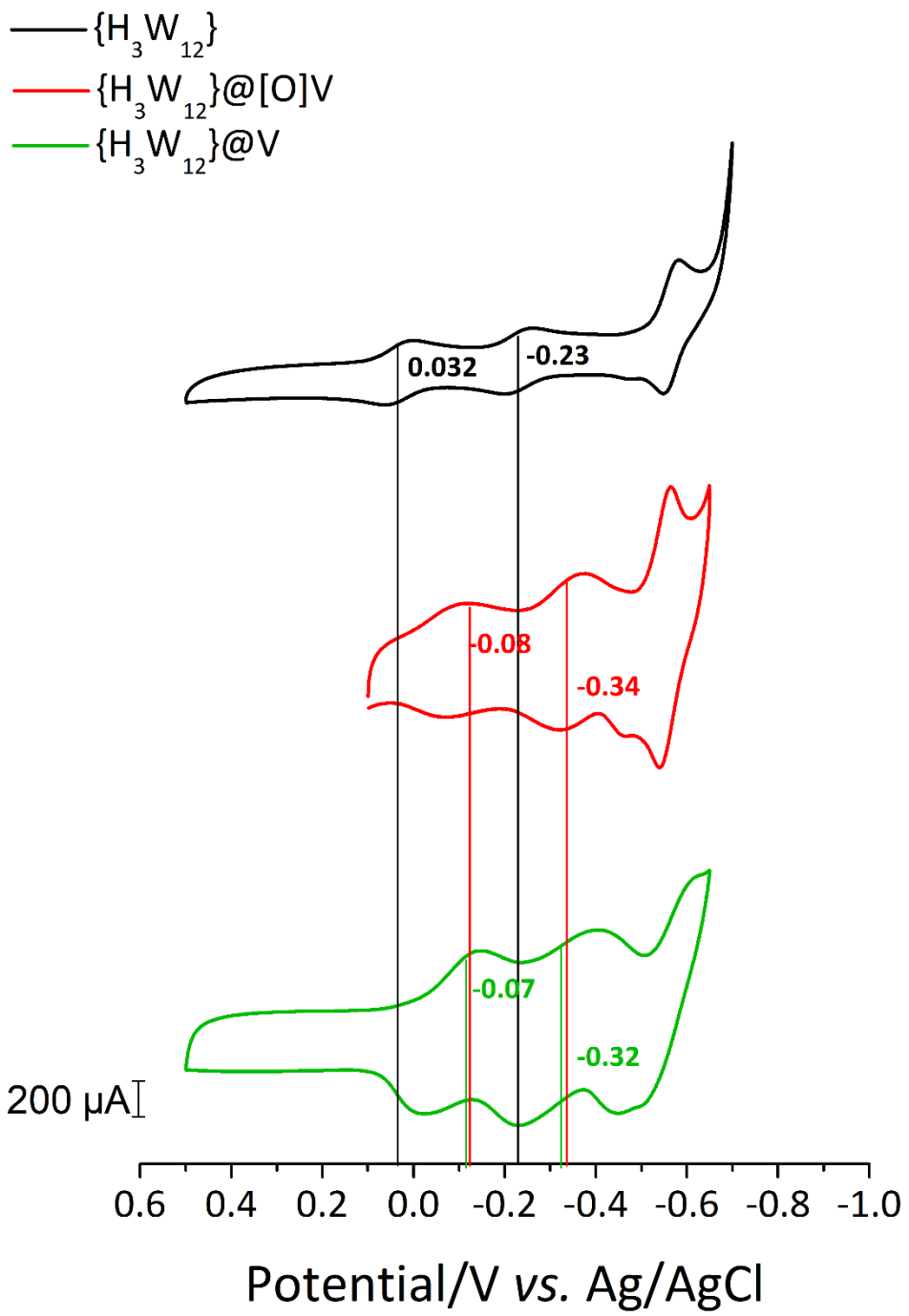


Figure 50 - Stacked CVs featuring the solution phase CV of $\{H_3W_{12}\}$ and the solid state voltammograms of $\{H_3W_{12}\}$@[O]V and $\{H_3W_{12}\}$@V to compare the redox profiles and peak shifts in 1M H_2SO_4.

Table 11 - Comparison of E_{mid} and ΔE_p values for $\{H_3W_{12}\}$ dissolved in 1M H_2SO_4 and for the $\{H_3W_{12}\}$@[O]V and $\{H_3W_{12}\}$@V solid state CVs in 1M H_2SO_4.

Process	$\{H_3W_{12}\}$		Process	$\{H_3W_{12}\}$@V		Process	$\{H_3W_{12}\}$@[O]V	
	E_{mid}/V	ΔE_p/mV		E_{mid}/V	ΔE_p/mV		E_{mid}/V	ΔE_p/mV
I	0.032	44	A	-0.07	123	I	-0.08	37
II	-0.23	42	B	-0.32	171	II	-0.34	51
III	-0.56	28	C	-0.53	166	III	-0.55	23

For a fully reversible surface-confined process, the peak-to-peak separation of a redox couple is expected to be 0 mV. The ΔE_p values for $\{H_3W_{12}\}$@V are much larger than 0 mV and the peaks are not symmetrical, so it is clear the $\{H_3W_{12}\}$@V composite operates in the quasi-reversible/irreversible regime. The ΔE_p values for $\{H_3W_{12}\}$@[O]V are approaching the value of 0 mV, confirming that the processes are surface-confined but quasi-reversible. Process III seems to be the most reversible (ΔE_p = 23 mV).

With regards to electrochemical cyclability, the $\{H_3W_{12}\}$@[O]V still outperformed the $\{H_3W_{12}\}$@V composite, though the cyclability is poorer overall when directly compared to the $\{K_6W_{18}\}$ composites. The intensity in peak current for $\{H_3W_{12}\}$@V diminished quickly with cycling and was only stable up until 50 cycles (Figure 51), whereas $\{H_3W_{12}\}$@[O]V showed a more gradual loss of $\{H_3W_{12}\}$ from the surface, and was stable to approximately 200 cycles (Figure 52).

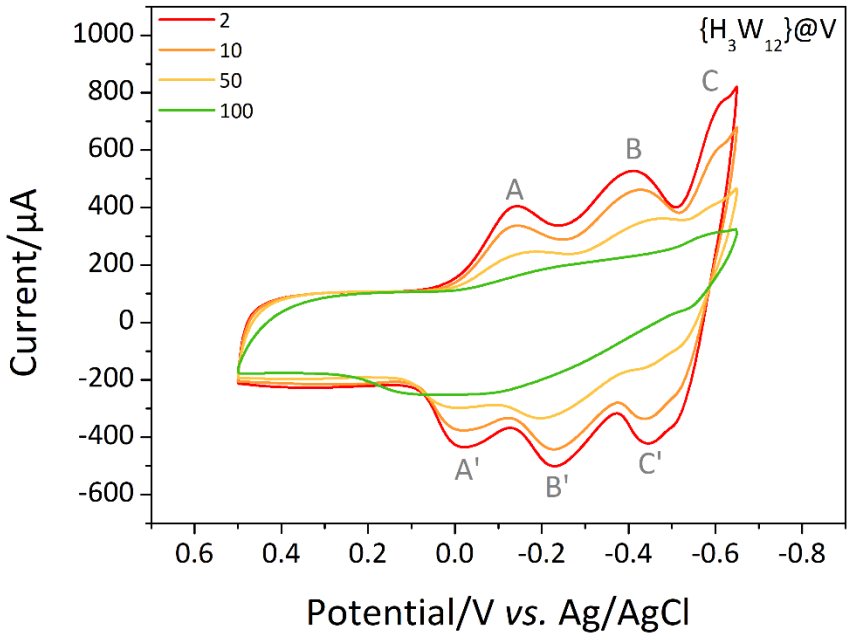


Figure 51 - Solid state CV of $\{H_3W_{12}\}$@V in 1M H_2SO_4, recorded at a scan rate of 100 mv s^{-1}, showing cycles 2 – 100.

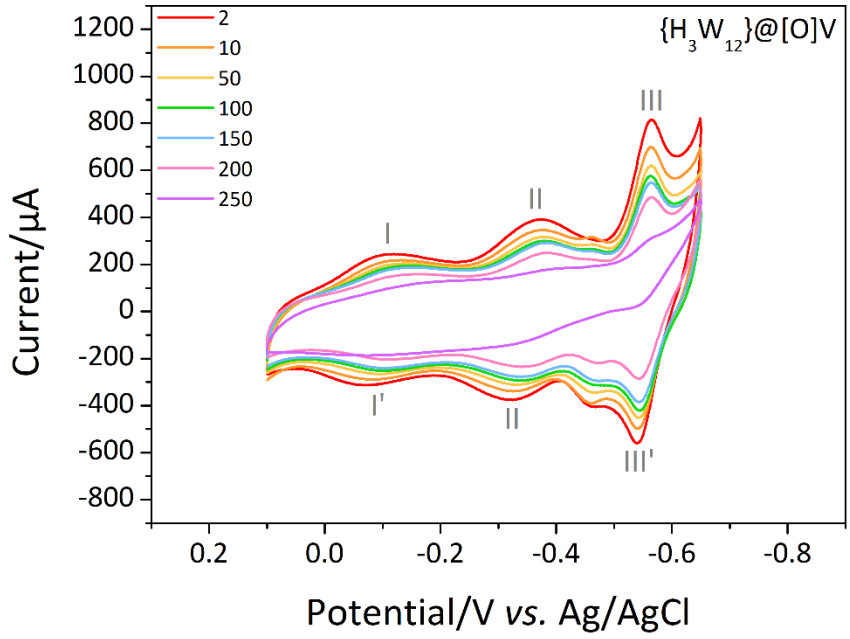


Figure 52 - Solid state CV of $\{H_3W_{12}\}$@[O]V in 1M H_2SO_4, recorded at a scan rate of 100 mv s^{-1}, showing cycles 2 – 250.

Acid Dawson/Vulcan Composites

For the acidic Dawson/Vulcan composites, the TGA data shows that the onset of their decomposition events occurs at similar temperatures (Figure 53). As seen previously, the unmodified Vulcan bears a much higher POM loading *vs.* the oxidised support: 82% loading for $\{H_6W_{18}\}$@V and 54% for $\{H_6W_{18}\}$@[O]V. Higher loadings on the Vulcan support have been consistently observed for the different POMs. As we saw from the SEM images, large POM crystallites aggregate on the Vulcan surface, in contrast to the more uniform deposition for the Oxidised Vulcan.

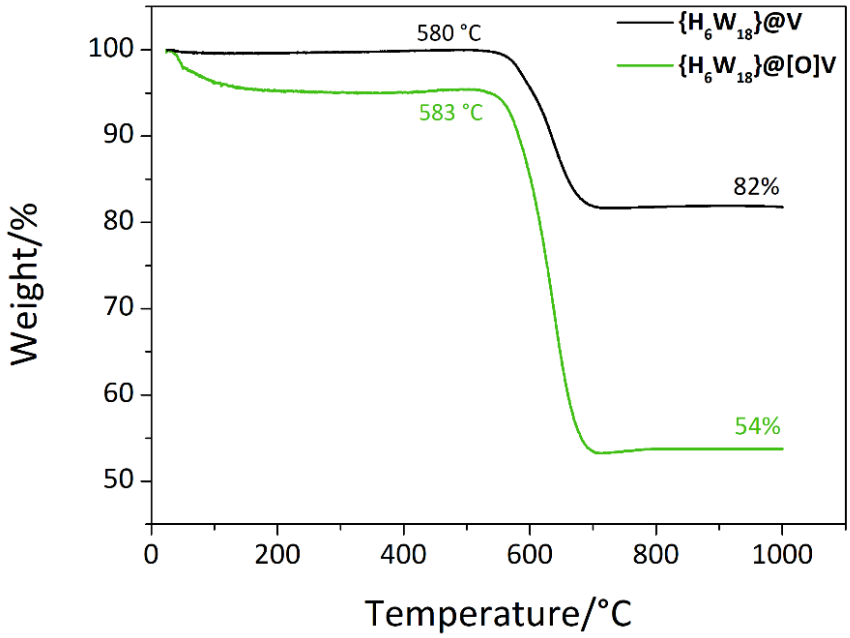


Figure 53 - TG curves for $\{H_6W_{18}\}$@Vulcan and $\{H_6W_{18}\}$@ Oxidised Vulcan, showing the onset temperature of their mass loss events and the approximate weight percent loading of POM within each composite.

The electrochemical behaviour for $\{H_6W_{18}\}$/Vulcan composites displays additional interesting deviations from its potassium analogue. $\{H_6W_{18}\}$@V and $\{H_6W_{18}\}$@[O]V display a similar redox profile to one another, both having three redox waves, which is in contrast to $\{H_6W_{18}\}$ dissolved in 1M H_2SO_4, possessing four redox waves (Figure 54).

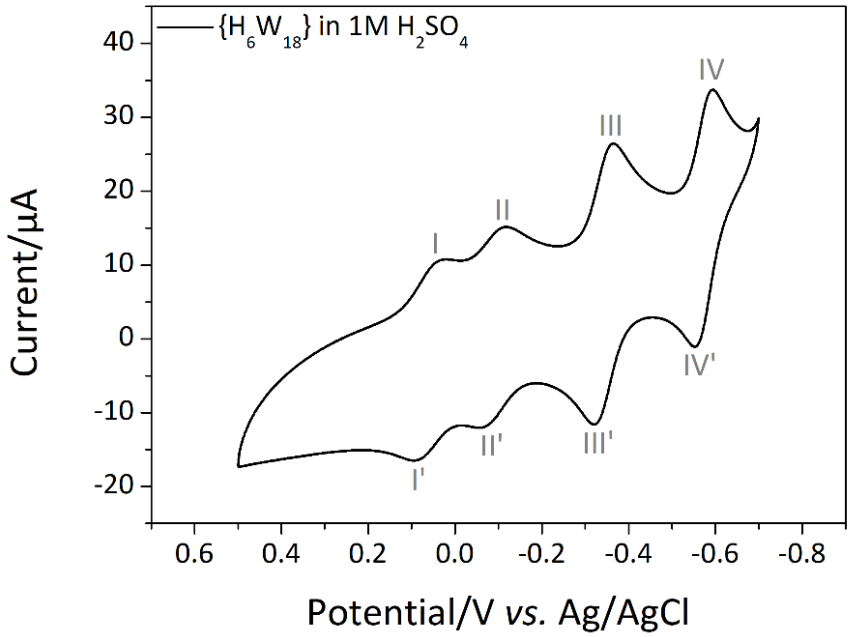


Figure 54 - Solution phase CV of $\{H_6W_{18}\}$ in 1M H_2SO_4 performed using a 3 mm diameter GC working electrode, a Pt counter electrode, and a Ag/AgCl reference electrode. The scan rate was 100 mV s^{-1}.

The solid state voltammograms for $\{H_6W_{18}\}$@V and $\{H_6W_{18}\}$@[O]V are shown in Figures 55 and 56.

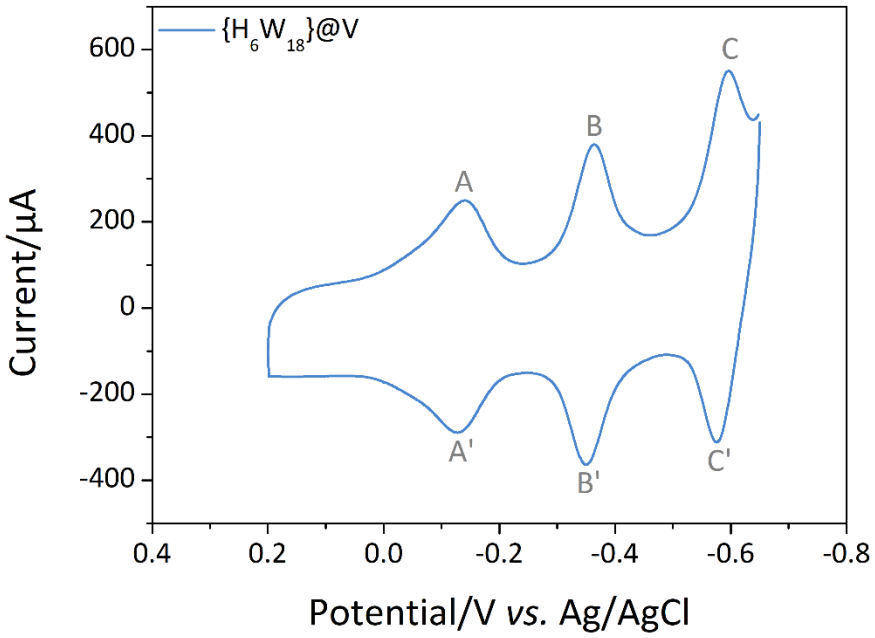


Figure 55 - Solid state CV of $\{H_6W_{18}\}$@V in 1M H_2SO_4 recorded using a 3 mm diameter glassy carbon working electrode, a Pt counter electrode, and a Ag/AgCl reference electrode. The scan rate was 100 mv s^{-1}.

Equations 70 – 72 - Redox couples for $\{H_6W_{18}\}$@V in 1M H_2SO_4.

$$\textbf{A/A'}: [P_2W_{18}O_{62}]^{6-} + 2e^- \longleftrightarrow [P_2W_{18}O_{62}]^{8-} \quad (70)$$

$$\textbf{B/B'}: [P_2W_{18}O_{62}]^{8-} + 2e^- + 2H^+ \longleftrightarrow [H_2P_2W_{18}O_{62}]^{10-} \quad (71)$$

$$\textbf{C/C'}: [H_2P_2W_{18}O_{62}]^{10-} + 2e^- + 2H^+ \longleftrightarrow [H_4P_2W_{18}O_{62}]^{12-} \quad (72)$$

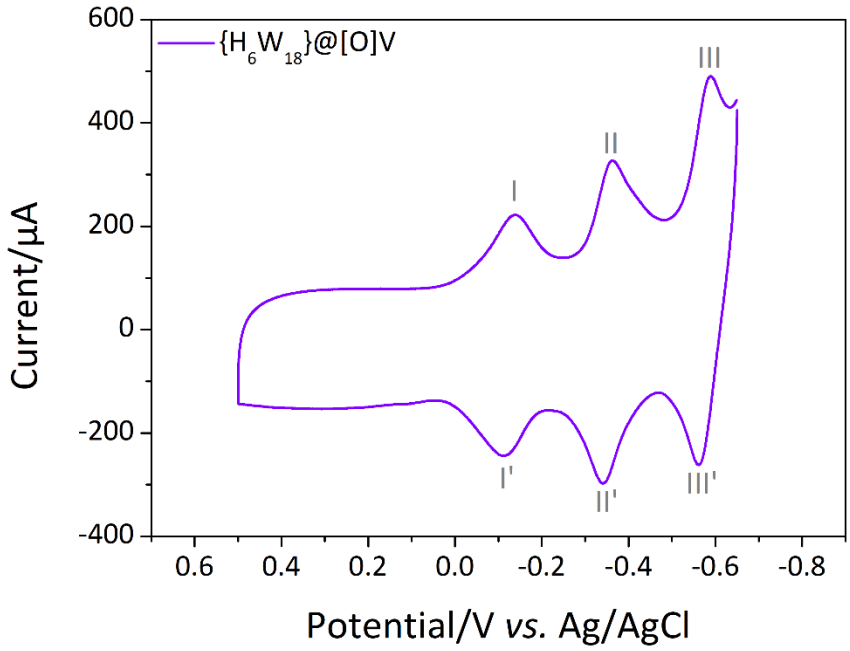


Figure 56 - Solid state CV of $\{H_6W_{18}\}$@[O]V in 1M H_2SO_4 recorded using a 3 mm diameter glassy carbon working electrode, a Pt counter electrode, and a Ag/AgCl reference electrode. The scan rate was 100 mv s^{-1}.

Equations 73 – 75 - Redox couples for $\{H_6W_{18}\}$@[O]V in 1M H_2SO_4.

$$\textbf{I/I'}: [P_2W_{18}O_{62}]^{6-} + 2e^- \longleftrightarrow [P_2W_{18}O_{62}]^{8-} \quad (73)$$

$$\textbf{II/II'}: [P_2W_{18}O_{62}]^{8-} + 2e^- + 2H^+ \longleftrightarrow [H_2P_2W_{18}O_{62}]^{8-} \quad (74)$$

$$\textbf{III/III'}: [H_2P_2W_{18}O_{62}]^{8-} + 2e^- + 2H^+ \longleftrightarrow [H_4P_2W_{18}O_{62}]^{8-} \quad (75)$$

The three redox processes for the composites correspond to three two-electron processes, with the last two being proton-coupled[48]. In both instances, $\{H_6W_{18}\}$@V and $\{H_6W_{18}\}$@[O]V, the first two-electron redox process (A/A' and I/I'), is a product of the two one-electron processes I/I' and II/II' merging for $\{H_6W_{18}\}$ in solution. This is in contrast to the $\{K_6W_{18}\}$/Vulcan composites where merging of the first two one-electron processes was only observed for the Vulcan support, and $\{K_6W_{18}\}$@[O]V retained the same redox profile as $\{K_6W_{18}\}$ in solution. Figure 57 shows the shifts in E_{mid} values between the composites and in relation to the parent anion dissolved in solution. Process A/A' for $\{H_6W_{18}\}$@V and process I/I' $\{H_6W_{18}\}$@[O]V are negatively shifted compared to

processes I and II $\{H_6W_{18}\}$ in solution (negative shifts *vs.* I in solution: A = 197 mV, I = 183 mV; negative shifts *vs.* II in solution: A = 37 mV, I = 23 mV). The E_{mid} values for B/B', C/C and III/III', IV/IV' for $\{H_6W_{18}\}$@V and $\{H_6W_{18}\}$@[O]V respectively, are very close to the E_{mid} values for processes III/III' and IV/IV' in solution, and so appear to be largely unaffected by the nature of the conductive support (Table 12).

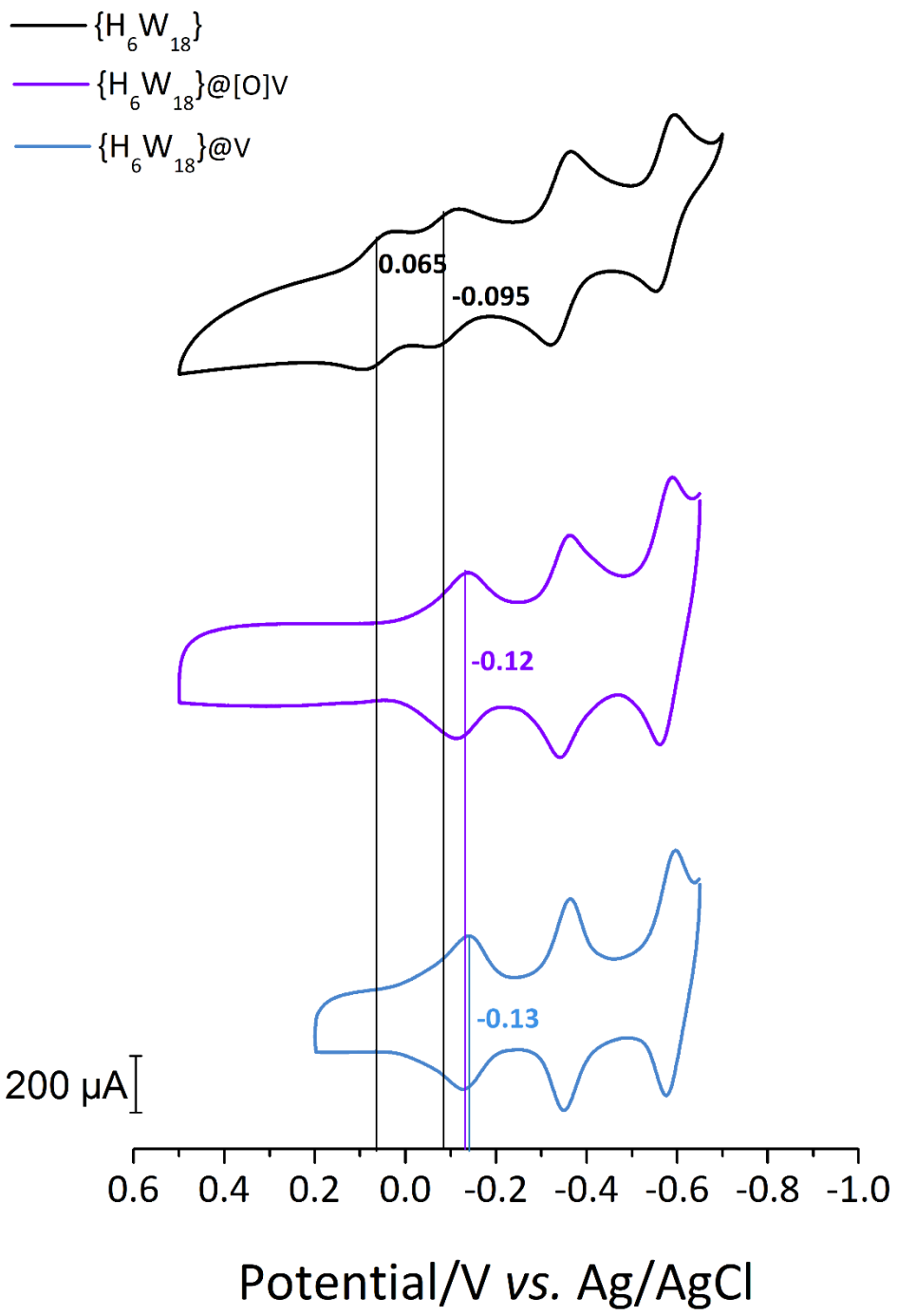


Figure 57 - Stacked CVs featuring the solution phase CV of $\{H_6W_{18}\}$ and the solid state voltammograms of $\{H_6W_{18}\}$@[O]V and $\{H_6W_{18}\}$@V to compare the redox profiles and peak shifts in 1M H_2SO_4.

Table 12 - Comparison of E_{mid} and ΔE_p values for $\{H_6W_{18}\}$ dissolved in 1M H_2SO_4 and for the $\{H_6W_{18}\}$@[O]V and $\{H_6W_{18}\}$@V solid state CVs in 1M H_2SO_4.

Process	$\{H_6W_{18}\}$		Process	$\{H_6W_{18}\}$@V		Process	$\{H_6W_{18}\}$@[O]V	
	E_{mid}/V	ΔE_p/mV		E_{mid}/V	ΔE_p/mV		E_{mid}/V	ΔE_p/mV
I	0.065	42	A	-0.13	23	I	-0.12	33
II	-0.095	39	B	-0.36	24	II	-0.35	24
III	-0.34	36	C	-0.59	29	III	-0.58	25
IV	-0.57	34						

Additionally, the E_{mid} values for processes A, B and C of $\{H_6W_{18}\}$@V are comparable to the E_{mid} values for processes I, II and III for $\{H_6W_{18}\}$@[O]V. This is in contrast to the $\{K_6W_{18}\}$/Vulcan composites where an obvious positive shift for the first two processes was always observed on the oxidised surface, demonstrating the oxidised support provided a more favourable environment for reduction to occur *vs.* the Vulcan matrix. The ΔE_p values for processes A – C and I – III are approaching the value of 0 mV, confirming that the processes are surface-confined but quasi-reversible (Table 12).

The similarity in E_{mid} values for the $(H_6W_{18}\}$/Vulcan composites coupled with their parallel redox profiles suggests that the unmodified Vulcan, having been in contact with $\{H_6W_{18}\}$ in solution during composite preparation, is not so dissimilar in nature to the oxidised Vulcan support. The hypothesis that the superacidic $\{H_6W_{18}\}$ POM could perform a simultaneous oxidation of Vulcan and adsorption to the surface is certainly plausible. However further structural characterisation such as XPS is needed to clarify the nature of this oxidation.

With regards to electrochemical cyclability, the trend thus far has been that the oxidised Vulcan enhances the cyclability in all tested electrolytes. However in this instance, the $\{H_6W_{18}\}$@V (Figure 58) and $\{H_6W_{18}\}$@[O]V (Figure 59) have very similar cyclability but more interestingly, the $\{H_6W_{18}\}$@V composite appears to be more stable. The first two redox processes for

$\{H_6W_{18}\}$@V are still visible even after 300 cycles whereas the cyclability for $\{H_6W_{18}\}$@[O]V does not extend past 200 cycles.

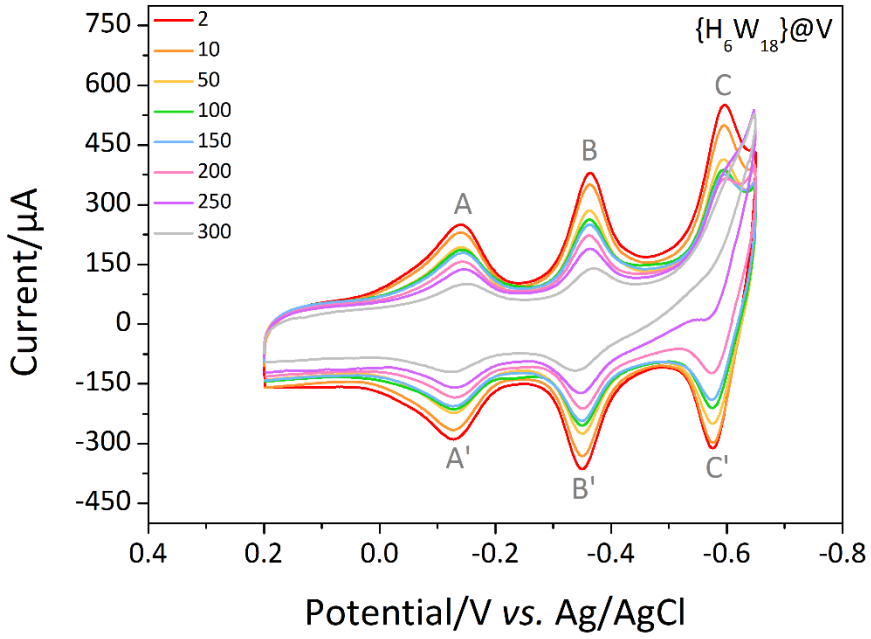


Figure 58 - Solid state CV of $\{H_6W_{18}\}$@V in 1M H_2SO_4, recorded at a scan rate of 100 mv s^{-1}, showing cycles 2 – 300.

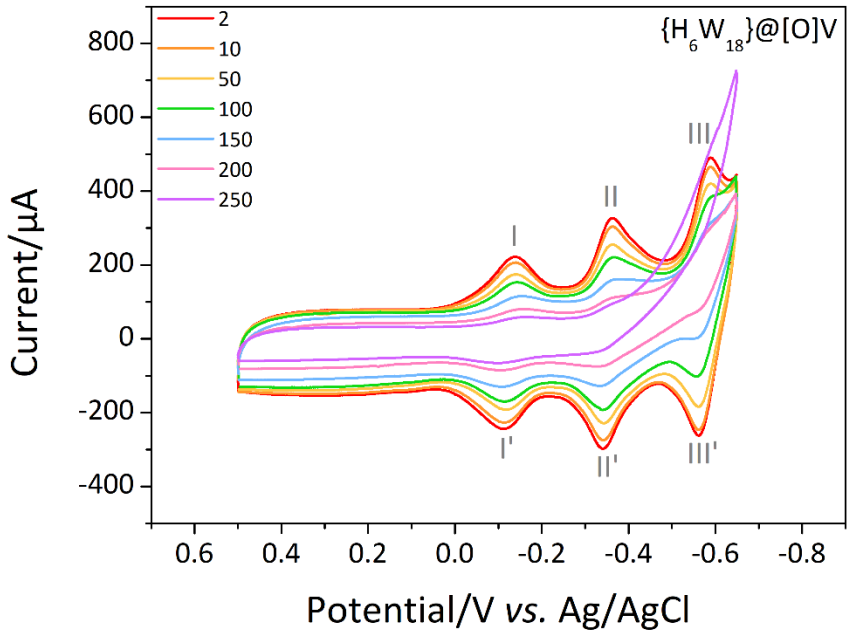


Figure 59 - Solid state CV of $\{H_6W_{18}\}$@[O]V in 1M H_2SO_4, recorded at a scan rate of 100 mv s^{-1}, showing cycles 2 – 250.

Overall, the intensity in peak currents for $\{H_6W_{18}\}$@V and $\{H_6W_{18}\}$@[O]V declined steadily with increased cycling but beyond 100 cycles, the peak current for $\{H_6W_{18}\}$@[O]V decreased more quickly. This trend is depicted for process II of $\{H_6W_{18}\}$@[O]V and process B of $\{H_6W_{18}\}$@V (Figure 60).

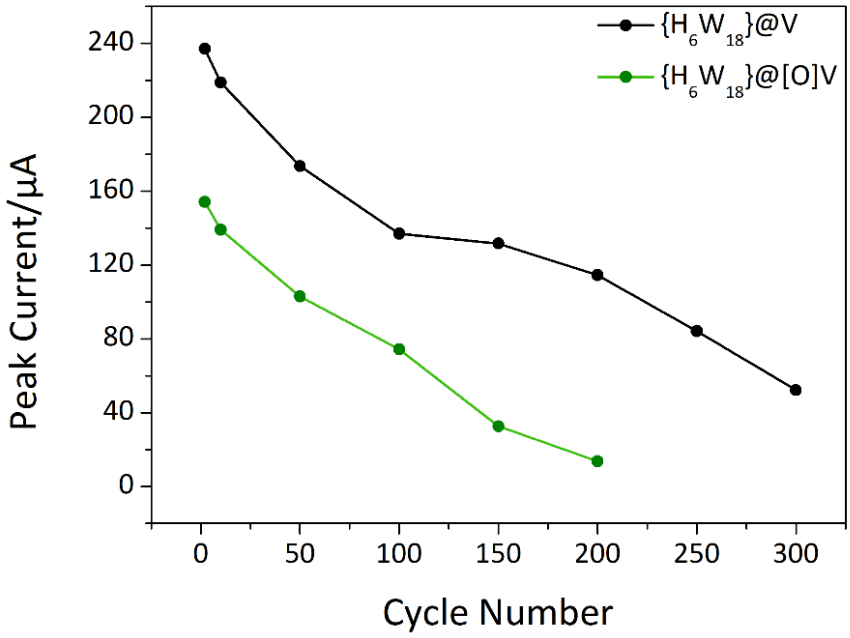


Figure 60 - Peak current of processes II and B in the voltammograms of $\{H_6W_{18}\}$@[O]V and $\{H_6W_{18}\}$@Vulcan, respectively, over multiple charge–discharge cycles.

Analysis of the effects of increasing the voltammetric scan rate revealed that the peak heights for each redox couple in each composite material increased in direct proportion to the increasing scan rate (Figures 61 and 62), as expected for a surface-confined redox process.

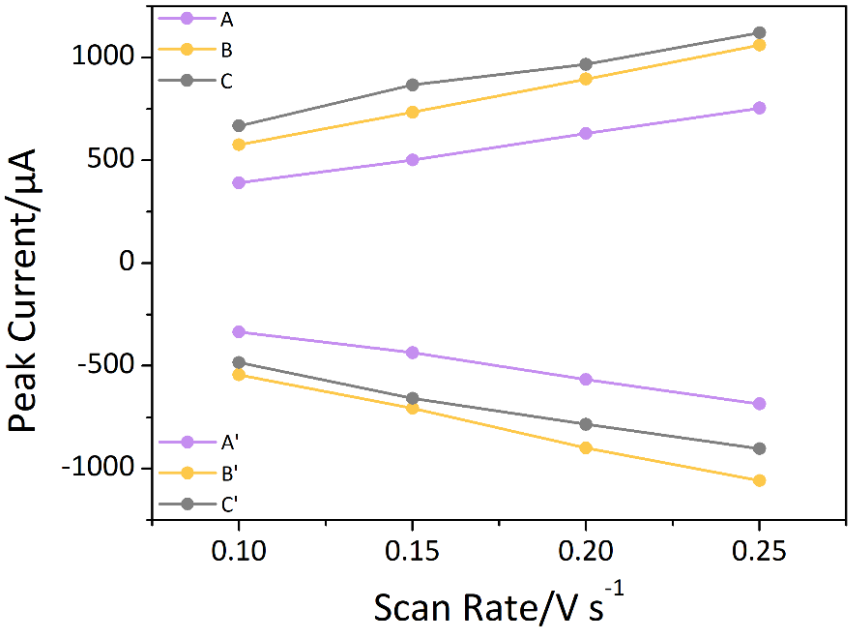


Figure 61 - Peak currents of redox processes A – C for $\{H_6W_{18}\}$@Vulcan plotted against increasing scan rate.

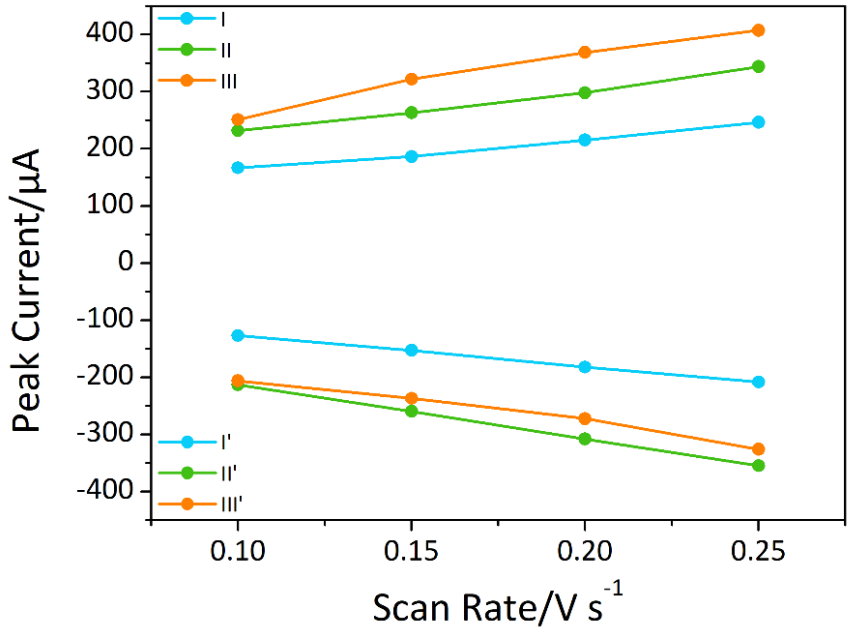


Figure 62 - Peak currents of redox processes I – III for $\{H_6W_{18}\}$@Vulcan plotted against increasing scan rate.

The percentage of POMs that were electrochemically accessible on the different matrices was calculated using the equation $n_E = Q/zF$, where n_E is the number of moles electrolysed, Q = the area under a CV peak (in this case, process II or process B), z = number of electrons transferred (2 e^-) and F is Faraday's constant. The nominal number of moles of POM present on the electrode was estimated using the mass difference before and after drop-casting the slurry, combined with the percentage POM loading determined by thermal gravimetry (vide supra). The results of these calculations are shown in Table 13. The percentages listed reflect the trend seen in peak current intensity, where a more accelerated loss of electrochemically accessible POMs is seen beyond 100 cycles for $\{H_6W_{18}\}$@[O]V. This is in stark contrast to the values obtained for the $\{K_6W_{18}\}$@[O]V analogue which displayed significantly enhanced electrochemical accessibility *vs.* $\{K_6W_{18}\}$@[O]V. Additionally, the percentage of electrochemically accessible POMs for $\{H_6W_{18}\}$@[O]V is far lower than the potassium analogue (2.3% at cycle 2 *vs.* 19%) which raises questions about the verity of an in-situ oxidation and adsorption.

Table 13 - Percentage of POMs electrochemically accessible over repeated cycling.

Cycle no.	$\{H_6W_{18}\}$@V (%)	$\{H_6W_{18}\}$@[O]V (%)
2	3.8	2.3
10	3.5	2.1
50	2.8	1.5
100	2.1	1.2
150	2	0.55
200	1.7	0.21
250	1.3	-

3.4 Conclusion

A comparative study encompassing several different POM@Carbon nanocomposites was conducted. Vulcan XC-72R was oxidised with H_2SO_4 in order to impart surface functional groups that could serve as binding sites for POM incorporation. We show that our approach increases the accessibility and stability of redox sites within the composite material compared to those within a composite formed using unoxidised Vulcan XC-72R.

For $\{K_6W_{18}\}$, we observe that the oxidised substrate showed enhanced POM retention during electrochemical cycling (over 500 cycles) compared to its unoxidised counterpart. Surface oxidation of the conductive Vulcan support is demonstrated to be an effective technique to anchor POMs onto the material, not just within aqueous acidic media but also in the presence of metal cations ($Li^+/Na^+/Mg^{2+}$) and in an organic battery solvent. In all cases, it was observed that the oxidised Vulcan support exhibited enhanced POM retention during electrochemical cycling (250 – 500 cycles) *vs.* the unmodified Vulcan (> 25 cycles). The longevity of the electrochemical performance of $\{K_6W_{18}\}$@[O]V in the presence of Mg^{2+} poses a fascinating avenue to explore for the reversible intercalation of Mg^{2+} cations in the context of batteries beyond Li-ion.

Using these findings, we hypothesised that the free acid analogues, $\{H_3W_{12}\}$ and $\{H_6W_{18}\}$, could be combined with Vulcan to perform an in-situ

oxidation and simultaneous adsorption to the surface. This approach worked better with the Wells-Dawson motif given that it is more strongly acidic in nature than the Keggin moiety. Though the study is preliminary, the voltammograms of the $\{H_6W_{18}\}$-Vulcan composites are not vastly different and does confirm that the acidic POM is able to oxidise the Vulcan in-situ. This requires further work to explore the effectiveness of this method, but it does present another easy method to prepare such composite materials in the future.

As it has been ascertained that the acid Dawson can oxidise the Vulcan support, it is also likely that it further oxidises the already oxidised Vulcan support as well. However, this additional oxidation is disadvantageous to the overall cycling performance. This could be induced by a further loss of surface area and consequently a loss of electrochemically accessible POMs on the surface.

Our work is a focused attempt to tune and understand the surface chemistry of potential energy materials. This method of simple carbon surface oxidation can be used to improve the performance and efficiency of POM@Carbon systems. The results thus far in aqueous and organic battery solvents have been very promising and indicates that such an approach could be used design POM-composite electrodes for lithium batteries.

3.5 Experimental

Oxidation of Vulcan XC-72R

500 mg of Vulcan was dispersed into 300 ml of 2M H_2SO_4 and left to reflux for 4 hours. The resulting suspension was filtered under vacuum and the solid was dried overnight at 80 °C.

POM Incorporation to form POM@Vulcan and POM@[O]V

100 mg of each carbon matrix, Vulcan and Oxidised Vulcan, was stirred into 15 mL of a 20 mM aqueous solution of the desired POM ($K_6[P_2W_{18}O_{62}]$/$H_6[P_2W_{18}O_{62}]$/$H_3[PW_{12}O_{40}]$) at room temperature for 1 hour. The resulting suspension was washed with deionised water to remove any excess, unbound POMs. Following this, the solution was centrifuged, decanted and finally dried overnight at 80 °C to yield the POM/Vulcan composites.

Thermogravimetric Analysis

TG analysis was carried out with a Discovery TGA (TA instruments) analyser. A small quantity of sample (3 – 5 mg) was added to a platinum pan of known weight and analysed under a constant air flow. Samples were heated from room temperature to 1000 °C at a ramp rate of 10 °C min^{-1} including a 10-minute isothermal step at 100 °C.

X-ray Photoelectron Spectroscopy

Samples were analysed using the Kratos AXIS ULTRA with a mono-chromated Al kα X-ray source (1486.6eV) operated at 10 mA emission current and 12 kV anode potential (120 W). Spectra were acquired with the Kratos VISION II software. A charge neutralizer filament was used to prevent surface charging. Hybrid –slot mode was used measuring a sample area of approximately 300 x 700 µm. The analysis chamber pressure was better than 5 x 10^{-9} mbar. Three areas per sample were analysed. A wide scan at low resolution (Binding energy range 1400 eV to -5 eV, with pass energy 80 eV, step 0.5 eV, sweep time 20 minutes). The wide scan spectra were used to estimate the total atomic % of the detected elements. High resolution spectra at pass

energy 20 eV, step of 0.1 eV, and sweep times of 10 minutes each were also acquired for photoelectron peaks from the detected elements, and these were used to model the chemical composition. The spectra were charge corrected to the C 1s peak (adventitious carbon or a known polymer CH_2 or CH_3 peak) set to 285 eV.

Scanning Electron Microscopy

SEM images were taken using a ZEISS EVO MA10 SEM with an EDAX Element, at a working distance of 8.50 mm, an accelerating voltage of 8.00 kV and a beam current of 50.0 pA.

Gas Adsorption – Brunauer-Emmett-Teller (BET)

Approximately 40-80 mg of each sample was added to a measurement tube of a precisely known weight. The sample was degassed for 16 h at 230 °C and the weight of the sample and tube was measured accurately. The outgassed sample was characterised using a Micrometrics Physisorption Analyser (3Flex) at 77 K with N_2 as the adsorptive gas.

Cyclic Voltammetry – Dropcasting

Carbon inks were prepared by dispersing 10 mg of the desired carbon sample into 200 µL of ethanol and 20 µL of an aqueous 3 wt % polytetrafluoroethylene (PTFE) binder. The mixture was sonicated for 10 minutes to ensure adequate dispersion. Blank CVs of the bare glassy carbon working electrodes were taken prior to ink addition on to the surface. 5.5 µl of carbon ink was dropcast on the GC surface and left to dry for a minimum of 2 hours. Aqueous CVs were performed in 1 M H_2SO_4 with a Pt wire counter electrode and Ag/AgCl reference electrode. Aqueous CVs were carried out at a scan rate of 100 mv s^{-1} unless otherwise stated. Organic battery solvent CVs were conducted in an argon-filled glovebox using 1M $LiPF_6$ in 50/50 (by volume) ethylene carbonate and ethyl methyl carbonate, using a lithium iron phosphate (LFP) reference electrode and Pt wire counter electrode. CVs performed int he glovebox were conducted at a scan rate of 100 mv s^{-1}.

3.6 References

1 D. J. Wales, Q. Cao, K. Kastner, E. Karjalainen, G. N. Newton and V. Sans, 3D-Printable Photochromic Molecular Materials for Reversible Information Storage, *Adv. Mater.*, 2018, **30**, 1800159.

2 S. Amin, J. M. Cameron, J. A. Watts, D. A. Walsh, V. Sans and G. N. Newton, Effects of chain length on the size, stability, and electronic structure of redox-Active organic-inorganic hybrid polyoxometalate micelles, *Mol. Syst. Des. Eng.*, 2019, **4**, 995–999.

3 E. Hampson, J. M. Cameron, S. Amin, J. Kyo, J. A. Watts, H. Oshio and G. N. Newton, Asymmetric Hybrid Polyoxometalates: A Platform for Multifunctional Redox-Active Nanomaterials, *Angew. Chemie - Int. Ed.*, 2019, **58**, 18281–18285.

4 C. Martin, K. Kastner, J. M. Cameron, E. Hampson, J. Alves Fernandes, E. K. Gibson, D. A. Walsh, V. Sans and G. N. Newton, Redox-Active Hybrid Polyoxometalate-Stabilised Gold Nanoparticles, *Angew. Chemie Int. Ed.*, 2020, **59**, 14331–14335.

5 H. Wang, S. Hamanaka, Y. Nishimoto, S. Irle, T. Yokoyama, H. Yoshikawa and K. Awaga, In operando X-ray absorption fine structure studies of polyoxometalate molecular cluster batteries: Polyoxometalates as electron sponges, *J. Am. Chem. Soc.*, 2012, **134**, 4918–4924.

6 A. Mu, J. Li, W. Chen, X. Sang, Z. Su and E. Wang, The composite material based on Dawson-type polyoxometalate and activated carbon as the supercapacitor electrode, *Inorg. Chem. Commun.*, 2015, **55**, 149–152.

7 D. M. Fernandes, M. P. Araújo, A. Haider, A. S. Mougharbel, A. J. S. Fernandes, U. Kortz and C. Freire, Polyoxometalate-graphene Electrocatalysts for the Hydrogen Evolution Reaction, *ChemElectroChem*, 2018, **5**, 273–283.

8 M. Wang, W. Zhong, S. Zhang, R. Liu, J. Xing and G. Zhang, An overall water-splitting polyoxometalate catalyst for the electromicrobial conversion of CO_2 in neutral water, *J. Mater. Chem. A*, 2018, **6**, 9915–9921.

9 H. Ma, B. Liu, B. Li, L. Zhang, Y. G. Li, H. Q. Tan, H. Y. Zang and G. Zhu, Cationic Covalent Organic Frameworks: A Simple Platform of Anionic Exchange for Porosity Tuning and Proton Conduction, *J. Am. Chem. Soc.*, 2016, **138**, 5897–5903.

10 Y. Ji, L. Huang, J. Hu, C. Streb and Y. Song, Polyoxometalate-functionalized nanocarbon materials for energy conversion, energy storage and sensor systems, *Energy Environ. Sci.*, 2015, **8**, 776–789.

11 A. S. Cherevan, S. P. Nandan, I. Roger, R. Liu, C. Streb and D. Eder, Polyoxometalates on Functional Substrates: Concepts, Synergies, and Future Perspectives, *Adv. Sci.*, 2020, **7**, 1903511.

12 V. Singh, P. Ma, M. G. B. Drew, J. Niu, J. Wang and G. X. Jin, Heterooctamolybdate-Based Clusters $H_3[(Cp*Rh)_4PMo_8O_{32}]$ and $H_5[Na2_(Cp*Ir)_4PMo_8O_{34}]$ and Derived Hybrid Nanomaterials with Efficient Electrocatalytic Hydrogen Evolution Reaction Activity, *Inorg. Chem.*, 2017, **56**, 12520–12528.

13 A. K. Cuentas-Gallegos, R. Martínez-Rosales, M. Baibarac, P. Gómez-Romero and M. E. Rincón, Electrochemical supercapacitors based on novel hybrid materials made of carbon nanotubes and polyoxometalates, *Electrochem. commun.*, 2007, **9**, 2088–2092.

14 K. Hanson, M. K. Brennaman, H. Luo, C. R. K. Glasson, J. J. Concepcion, W. Song and T. J. Meyer, Photostability of phosphonate-derivatized, Ru II polypyridyl complexes on metal oxide surfaces, *ACS Appl. Mater. Interfaces*, 2012, **4**, 1462–1469.

15 M. Stuckart and K. Y. Monakhov, Polyoxometalate encapsulation into metal-organic frameworks: The way towards functional nanomaterials for water splitting, *J. Mater. Chem. A*, 2018, **6**, 17849–17853.

16 R. Ma, N. Liu, T. T. Lin, T. Zhao, S. L. Huang and G. Y. Yang, Anderson polyoxometalate built-in covalent organic frameworks for enhancing catalytic performances, *J. Mater. Chem. A*, 2020, **8**, 8548–8553.

17 S. Mukhopadhyay, J. Debgupta, C. Singh, A. Kar and S. K. Das, A Keggin Polyoxometalate Shows Water Oxidation Activity at Neutral pH: POM@ZIF-8, an Efficient and Robust Electrocatalyst, *Angew. Chemie - Int. Ed.*, 2018, **57**, 1918–1923.

18 S. Tang, G. Sun, J. Qi, S. Sun, J. Guo, Q. Xin and G. M. Haarberg, Review of New Carbon Materials as Catalyst Supports in Direct Alcohol Fuel Cells, *Chinese J. Catal.*, 2010, **31**, 12–17.

19 M. Kim, J. N. Park, H. Kim, S. Song and W. H. Lee, The preparation of Pt/C catalysts using various carbon materials for the cathode of PEMFC, *J. Power Sources*, 2006, **163**, 93–97.

20 E. Antolini, Formation, microstructural characteristics and stability of carbon supported platinum catalysts for low temperature fuel cells, *J. Mater. Sci.*, 2003, **38**, 2995–3005.

21 F. Rodríguez-reinoso, The role of carbon materials in heterogeneous catalysis, *Carbon N. Y.*, 1998, **36**, 159–175.

22 Dong Jin Suh, P. Tae-Jin and I. Son-Ki, Effect of surface oxygen groups of carbon supports on the characteristics of Pd/C catalysts, *Carbon N. Y.*, 1993, **31**, 427–435.

23 V. Datsyuk, M. Kalyva, K. Papagelis, J. Parthenios, D. Tasis, A. Siokou, I. Kallitsis and C. Galiotis, Chemical oxidation of multiwalled carbon nanotubes, *Carbon N. Y.*, 2008, **46**, 833–840.

24 H. ShamsiJazeyi and T. Kaghazchi, Investigation of nitric acid treatment of activated carbon for enhanced aqueous mercury removal, *J. Ind. Eng. Chem.*, 2010, **16**, 852–858.

25 I. Sutherland, E. Sheng, R. H. Bradley and P. K. Freakley, Effects of ozone oxidation on carbon black surfaces, *J. Mater. Sci.*, 1996, **31**, 5651–5655.

26 C. M. Chang and Y. L. Liu, Functionalization of multi-walled carbon nanotubes with non-reactive polymers through an ozone-mediated process for the preparation of a wide range of high performance polymer/carbon nanotube composites, *Carbon N. Y.*, 2010, **48**, 1289–1297.

27 S. Pérez-Rodríguez, E. Pastor and M. J. Lázaro, Electrochemical behavior of the carbon black Vulcan XC-72R: Influence of the surface chemistry, *Int. J. Hydrogen Energy*, 2018, **43**, 7911–7922.

28 S. M. Senthil Kumar, J. Soler Herrero, S. Irusta and K. Scott, The effect of pretreatment of Vulcan XC-72R carbon on morphology and electrochemical oxygen reduction kinetics of supported Pd nano-particle in acidic electrolyte, *J. Electroanal. Chem.*, 2010, **647**, 211–221.

29 J. W. Jordan, G. A. Lowe, R. L. McSweeney, C. T. Stoppiello, R. W. Lodge, S. T. Skowron, J. Biskupek, G. A. Rance, U. Kaiser, D. A. Walsh, G. N. Newton and A. N. Khlobystov, Host–Guest Hybrid Redox Materials Self-Assembled from Polyoxometalates and Single-Walled Carbon Nanotubes, *Adv. Mater.*, 2019, **31**, 1904182.

30 J. P. Tessonnier, S. Goubert-Renaudin, S. Alia, Y. Yan and M. A. Barteau, Structure, stability, and electronic interactions of polyoxometalates on functionalized graphene sheets, *Langmuir*, 2013, **29**, 393–402.

31 D. Ma, L. Liang, W. Chen, H. Liu and Y. F. Song, Covalently tethered polyoxometalate-pyrene hybrids for noncovalent sidewall functionalization of single-walled carbon nanotubes as high-performance anode material, *Adv. Funct. Mater.*, 2013, **23**, 6100–6105.

32 M. Genovese, Y. W. Foong and K. Lian, Designing Polyoxometalate based Layer-by-Layer Thin Films on Carbon Nanomaterials for Pseudocapacitive Electrodes, *J. Electrochem. Soc.*, 2015, **162**, A5041–A5046.

33 M. Genovese and K. Lian, Polyoxometalate modified inorganic–organic nanocomposite materials for energy storage applications: A review, *Curr. Opin. Solid State Mater. Sci.*, 2015, **19**, 126–137.

34 J. Alcañiz-Monge, G. Trautwein, S. Parres-Esclapez and J. A. Maciá-Agulló, Influence of microporosity of activated carbons as a support of polyoxometalates, *Microporous Mesoporous Mater.*, 2008, **115**, 440–446.

35 J. Suárez-Guevara, V. Ruiz and P. Gomez-Romero, Hybrid energy storage: High voltage aqueous supercapacitors based on activated carbon-phosphotungstate hybrid materials, *J. Mater. Chem. A*, 2014, **2**, 1014–1021.

36 N. Kawasaki, H. Wang, R. Nakanishi, S. Hamanaka, R. Kitaura, H. Shinohara, T. Yokoyama, H. Yoshikawa and K. Awaga, Nanohybridization of polyoxometalate clusters and single-wall carbon nanotubes: Applications in molecular cluster batteries, *Angew. Chemie - Int. Ed.*, 2011, **50**, 3471–3474.

37 H. Li, S. Pang, X. Feng, K. Müllen and C. Bubeck, Polyoxometalate assisted photoreduction of graphene oxide and its nanocomposite formation, *Chem. Commun.*, 2010, **46**, 6243–6245.

38 Z. Kang, Y. Wang, E. Wang, S. Lian, L. Gao, W. You, C. Hu and L. Xu, Polyoxometalates nanoparticles:

Synthesis, characterization and carbon nanotube modification, *Solid State Commun.*, 2004, **129**, 559–564.

39 A. K. Cuentas-Gallegos, R. Martínez-Rosales, M. E. Rincón, G. A. Hirata and G. Orozco, Design of hybrid materials based on carbon nanotubes and polyoxometalates, *Opt. Mater. (Amst).*, 2006, **29**, 126–133.

40 A. K. Cuentas-Gallegos, S. López-Cortina, T. Brousse, D. Pacheco-Catalán, E. Fuentes-Quezada, H. Mosqueda and G. Orozco-Gamboa, Electrochemical study of H_3PMo_{12} retention on Vulcan carbon grafted with NH2 and OH groups, *J. Solid State Electrochem.*, 2016, **20**, 67–79.

41 M. J. Lázaro, L. Calvillo, V. Celorrio, J. I. Pardo, S. Perathoner and R. Moliner, in *Carbon Black: Production, Properties and Uses*, 2011, pp. 41–68.

42 K. H. Kangasniemi, D. A. Condit and T. D. Jarvi, Characterization of Vulcan Electrochemically Oxidized under Simulated PEM Fuel Cell Conditions, *J. Electrochem. Soc.*, 2004, **151**, E125.

43 V. Alderucci, L. Pino, P. L. Antonucci, W. Roh, J. Cho, H. Kim, D. L. Cocke and V. Antonucci, XPS study of surface oxidation of carbon-supported Pt catalysts, *Mater. Chem. Phys.*, 1995, **41**, 9–14.

44 J. P. Chen and S. Wu, Acid/Base-Treated Activated Carbons: Characterization of Functional Groups and Metal Adsorptive Properties, *Langmuir*, 2004, **20**, 2233–2242.

45 A.-L. Teillout, P. de Oliveira, J. Marrot, R. Howell, N. Vilà, A. Walcarius and I. Mbomekallé, Synthesis, Crystal Structure, Electrochemistry and Electro-Catalytic Properties of the Manganese-Containing Polyoxotungstate, $[(Mn(H_2O)_3)_2(H_2W_{12}O_{42})]^{6-}$, *Inorganics*, 2019, **7**, 15.

46 S. D. Ponja, S. Sathasivam, H. O. Davies, I. P. Parkin and C. J. Carmalt, Polyoxometalate Complexes as Precursors to Vanadium-Doped Molybdenum or Tungsten Oxide Thin Films by Means of Aerosol-Assisted Chemical Vapour Deposition, *Chempluschem*, 2016, **81**, 307–314.

47 E. Hryha, E. Rutqvist and L. Nyborg, Stoichiometric vanadium oxides studied by XPS, *Surf. Interface Anal.*, 2012, **44**, 1022–1025.

48 M. Sadakane and E. Steckhan, Electrochemical Properties of Polyoxometalates as Electrocatalysts, *Chem. Rev.*, 1998, **98**, 219–238.

49 L. R. Bard, A. J.; Faulkner, *Electrochemical Methods: Fundamental and Applications*, John Wiley & Sons, Hoboken, 2nd edn., 2001.

50 S. Himeno, M. Takamoto, R. Santo and A. Ichimura, Redox properties and basicity of Keggin-type polyoxometalate complexes, *Bull. Chem. Soc. Jpn.*, 2005, **78**, 95–100.

4. Evaluation of POM/Vulcan Electrodes in Lithium Batteries

4.1 Introduction

Li-ion batteries are the pinnacle of battery development since the 1990s and remain the leading commercial battery of choice, especially for electric vehicles.[1] As discussed in detail in Chapter 1, batteries are an established form of energy storage, both for stationary and portable applications. Current positive electrode materials for secondary Li-ion batteries include an array of bulk transition metal oxides ($LiCoO_2$)[2], spinel structures ($LiMn_2O_4$)[3] and olivine structures ($LiFePO_4$)[4]. However, many of these materials suffer from either limited electrical conductivity, slow Li-ion transport, low thermal stability or dissolution.[5]

Figure 1 depicts the working principle of a commercialised Li-ion battery employing a dual – intercalation mechanism during discharge. Li-ion batteries are distinguished from Li-metal batteries as the former only uses lithiated compounds/electrolytes as a source of Li^+ with no metallic lithium source, whereas the latter employs a lithium metal negative electrode. The negative electrode is constructed of graphite and the positive electrode is $LiCoO_2$. Intercalation refers to the process of reversibly inserting and removing lithium ions within host structures without incurring significant structural changes. During discharge, the Li^+ ions de-intercalate from the negative electrode, graphite, and migrate towards the positive electrode, $LiCoO_2$, and intercalate into the lattice. The electrons travel in an external circuit simultaneously, in the same direction as the Li^+ ions, whereas current moves in the opposite direction to the Li^+ ions. During charge, the reverse occurs: Li^+ ions are de-intercalated from the ordered lattice of $LiCoO_2$ and move to become re-intercalated between the graphite layers.

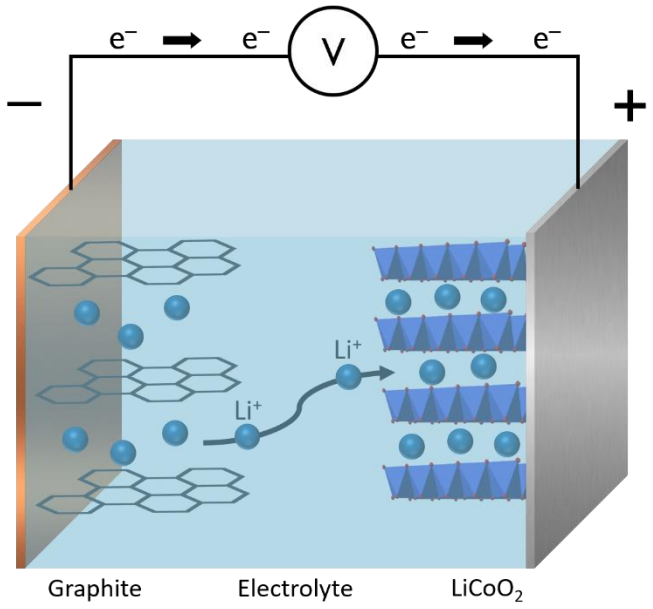


Figure 1 - A schematic illustration of the working principles of a graphite/$LiCoO_2$ lithium-ion cell.

A great advantage of the Li-ion battery is its versatility with respect to the combination of positive and negative electrodes that can be used. This offers many possibilities in designing new high-performance electrodes based on low-cost elements. New positive electrode materials that are capable of multi-electron redox reactions that enable rapid Li-ion transportation whilst still maintaining stable cycling performance are required.[6] Layered $LiCoO_2$ has long been the benchmark and research on alternative positive electrode materials is presently divided between improving layered oxides and designing new polyanionic compounds.[7,8] Among these materials, composites based on polyoxometalates have received significant attention in the field of energy storage.[9] Polyoxometalates (POMs) are polyanionic molecular metal oxides based on high valent transition metals (e.g., W^{VI}, Mo^{VI}, V^{V}) are promising multi-functional materials which have proven useful for numerous solid-state applications such as catalysis[10], water-splitting[11], single molecule magnets[12] and as proton conduction materials[13].

As discussed in Chapter 1, POMs present several merits as an electrode material;

1- The rapid and reversible redox chemistry could potentially assure a high capacity due to the multiple metal addenda atoms all capable of undergoing multi – electron redox reactions simultaneously;
2- POMs constitute a whole library of extremely tuneable metal oxides, which not only imparts tuneability with respect to the physical structure but also the functional properties i.e., tuning the photochemistry or electrochemistry through modification of the countercation, hybridisation with organic linkers and substitution of the heteroatom or addenda metal;
3- Conventional intercalation electrodes undergo structural changes with prolonged cycling (Li^+ intercalation/deintercalation) resulting in capacity fade. However, POMs do not consist of extended crystal structures, but rather of isolated, discrete polyanions, leveraging them with unique structural characteristics over typical intercalation electrodes. For example, the stability of the POM based electrode is dependent on the stability of the cluster ion unit and not on the recoverability of its crystal structure;
4- Conventional lithium intercalation materials employ harsh synthetic procedures, for example $LiCoO_2$ is synthesised at temperatures exceeding 800 °C over 24 hours. In contrast, POM synthesis is relatively straightforward, using a one-pot approach by means of self-assembly via pH adjustment, typically at temperatures below 100 °C.

Sonoyama et al. studied the electrochemical properties of a Keggin type heteropolyoxomolybdate crystal $K_3[PMo_{12}O_{40}]$ (KPM) as a positive electrode material for lithium metal batteries.[14] It showed charge–discharge performance in the potential region from 4.2 to 1.5 V with an initial capacity of over 200 mAh g^{-1}. Reversible expansion and contraction of the crystalline KPM lattice was confirmed via XRD. However, the main discharge voltage (2.1 V average) was lower than usual positive electrode material in lithium batteries and low cycle stability was observed. Capacity fade is a phenomenon observed in rechargeable batteries where the amount of charge a battery can deliver at the rated voltage decreases with use. In highly reducing conditions, the $[PMo_{12}O_{40}]^{3-}$ anion in

solution experienced a structural change as one of the $[Mo_3O_9]$ units of $[PMo_{12}O_{40}]^{3-}$ rotated by 60°. Though it was not clearly determined as to whether the same change occurs within the solid crystal, the low cycle stability and capacity fade of KPM was attributed to this α - β isomerisation.

Building upon these findings, Sonoyama et al. synthesised a new molecular cluster $K_{5.72}H_{3.28}[PV_{14}O_{42}]$ (KPV); a heteropolyoxovanadate possessing a bi-capped Keggin structure.[15] The most improved property of KPV compared with the previously synthesised KPM was greater cycle stability. KPV retained 95% of its initial discharge capacity (370 mAh g^{-1}) after 50 discharge-charge cycles whereas KPM retained only 35%. To account for the difference in cycle capability, ex-situ XRD and X-ray absorption fine structure (XAFS) measurements were carried out on KPV. It was found that a structural change occurred during the first discharge-charge process; the KPV crystal became amorphous. However, the cluster ion that is formed, $[PV_{14}O_{42}]^{9-}$, which is no longer a regular crystal structure, was stable during the subsequent discharge-charge processes and continued to cycle. The authors suggest that the amporphisation could be due to the release of crystal water as a drying process and not by isomerisation as seen with KPM. They concluded that the stability of this KPV positive electrode material is mainly dependent on the stability of the cluster ion unit, not on the recoverability of its crystal structure.

Following this work, Sonoyama et al. turned their attention to an Anderson type polyoxomolybdate, $Na_3[AlMo_6O_{24}H_6]$ (NAM) as a positive electrode material.[16] This structure was expected to be stable during redox reactions due to the presence of strong covalent bonds. Furthermore, the crystal structure of NAM has a 3D framework in which lithium ions can diffuse. POMs possess poor electrical conductivity and so to overcome this, NAM was mixed with conductive carbon additives such as acetylene black (AB) and ketjen black (KB) by hand-grinding and ball-milling. The discharge capacity and cycle performance of the NAM positive electrode varied according to the type of conductive additive and the mixing method used. The capacities of each system were investigated and it was found that NAM ball-milled with ketjen black (KB)

showed very high initial discharge capacity of 437 mAh g^{-1} as well as the most stable cycle performance; it retained 91.2% of its capacity after 50 cycles. The reaction mechanism was also investigated. XRD showed lattice expansion upon Li^+ ion insertion and also amporphisation over the discharge-process; NAM was irreversibly amorphised after 5 cycles. This is similar to the KPV electrode reported previously. However, the molecular cluster ion $[AlMo_6O_{24}H_6]^{3-}$ was found to be stable, confirmed by *ex-situ* Raman spectroscopy. Despite this structural change, the stable cluster unit continued to interact reversibly with lithium ions giving rise to good cycle stability. This is in contrast to conventional lithium intercalation materials where the amount of usable lithium for intercalation and de-intercalation is dependent on the recoverability of crystal structure. Insertion and extraction of Li^+ ions in NAM proceeded despite amporphisation.

In 2007, researchers in Japan designed a new battery concept called the molecular cluster battery (MCB).[17] Molecular metal clusters are small aggregates of metal ions connected by (organic) ligands which are used as the positive electrode material and lithium metal is the negative electrode. Wang et al. have explored POM-carbon composites as potential materials for lithium batteries.[18] Once again, the Keggin type POM anion $[PMo_{12}O_{40}]^{3-}$ was explored as a positive electrode material but this time for a molecular cluster battery. $TBA_3[PMo_{12}O_{40}]$ (TBA = $[N(CH_2CH_2CH_2CH_3)_4]^+$ was mixed with carbon black to form the positive electrode and lithium metal was used as the negative electrode. The POM-MCB exhibited a large capacity of up to 270 mAh g^{-1} in a voltage range of 4 – 1.5 V. Operando X-ray absorption near edge structure (XANES) disclosed that all 12 Mo^{6+} ions in the PMo_{12} cluster were reduced to Mo^{4+} during discharge, yielding a super-reduced state of the POM; $[PMo_{12}O_{40}]^{27-}$, which stores 24 electrons. This is different from typical lithium-ion batteries where only 50% of the Co ions of $LiCoO_2$ are reduced but for the PMo_{12}-MCB, all of the Mo ions contribute to the battery capacity. Additionally, the PMo_{12}-MCB presented reasonably good stability with a capacity of 210 mAh g^{-1} after the tenth discharge cycle. This so called “electron sponge” behaviour is

a newly unveiled feature as a promising positive electrode material for high-performance rechargeable batteries.

4.2 Approach

One of the most prominent features of POMs is the ability to tailor their redox properties for the desired output.[19] However it is necessary to address the drawbacks associated with the use of POMs such as their negligible electronic conductivity and high solubility in a wide variety of solvents. Heterogenising POMs to a conductive host matrix is mandatory in order to overcome their intrinsic insulating nature and avoid leaching or dissolution. As discussed in Chapter 3, POMs have previously been integrated into a diverse range of carbon matrices including activated carbon[20], carbon nanotubes[21] and graphene[22].

Our own studies from Chapter 3 saw the anchoring of the Dawson POM ($K_6[P_2W_{18}O_{62}]$) onto a surface modified carbon black, known as Vulcan.[23] The surface was oxidised using 2M H_2SO_4, which introduced carboxylic acid functionalities on to the Vulcan surface. The $\{K_6W_{18}\}$@[O]V composite was formed by stirring the Oxidised Vulcan in a solution of the $\{K_6W_{18}\}$ POM. Compared to the unmodified Vulcan analogue ($\{K_6W_{18}\}$@V), the $\{K_6W_{18}\}$@[O]V composite exhibited homogeneous dispersion of $\{K_6W_{18}\}$ on the surface, enhanced cycling stability in both aqueous and non-aqueous solvents, more efficient POM retention as well as higher electrochemical accessibility of the redox-active POMs.

The use of lithium metal electrodes to enable rechargeable lithium batteries is paramount to significantly advance developments in grid energy storage and electrification of transport. Current Li-ion batteries typically use graphite as the negative electrode, paired with a metal oxide intercalation compound as the positive electrode ($LiCoO_2$, $LiFePO_4$, $LiNi_{1/3}Mn_{1/3}Co_{1/3}O_2$ (NMC) etc). This dual intercalation mechanism is responsible for its high cyclability. The specific capacity of these materials is usually below 400 mAh g^{-1} for graphite[24] and 200 mAh g^{-1} for $LiNi_xCo_yAl_zO_2$ (NCA where $x + y + z = 1$)[25], a positive electrode

with one of the highest capacities. Thus, it would appear that the cathode is the limiting factor in the achievable capacities of current Li-ion technologies. However, Albertus et al. discussed the impact on specific capacity by replacing graphite electrodes with lithium metal and argue that it is in fact the weight and volume of graphite which imposes the upper limit on the energy content of Li-ion cells.[26] Li metal has an ultrahigh specific capacity of 3861 mAh g^{-1} which would assure much higher energy dense batteries in the future. Of course, this is subject to materials optimisation and addressing operational difficulties with the use of metal anodes, which is not within the scope of this thesis.

A two-electrode cell can be used for galvanostatic cycling experiments, which are classed as half cells or full cells. A half cell constitutes the electrode of interest paired with an electrode with a well-known potential as the counter electrode.[27] A half cell is typically used in the earlier stages of research where the reactions and chemistry are studied for only one electrode at a time. Full cells, as the name suggests, contain both battery electrodes. Half cells provide explicit information about the reactions and performance of an individual electrode, whereas a full cell shows how the two electrodes perform in conjunction.[27] However, for the purposes of this study, the cell will be considered as a full cell, with a Li metal negative electrode and a POM/Vulcan composite positive electrode.

4.2.1 Galvanostatic Charge-Discharge Cycling

As described in this thesis, cyclic voltammetry is useful in determining the electrochemical behaviour of a system with respect to but not limited to, its stable potential window, redox activity, cycle stability and the effect of scan rate. Cyclic voltammetry shows the variation in current in a specified fixed potential window. Galvanostatic charge-discharge cycling is conducted by applying a constant current between designated voltage cut-off points. Voltage profiles (potential *vs.* capacity) are the output of a galvanostatic experiment, which show the changes in the electrochemical cell performance during charge and discharge over time. A repetitive loop of charging and discharging constitutes a cycle and the charge i.e. capacity, is measured for each procedure. It is one of

the most commonly used methods to evaluate battery performance, both at new material discovery level, and advanced long-term degradation studies.

4.2.2 Differential Capacity Analysis

Understanding how Li-ion batteries degrade and lose capacity has been the topic of much research and one approach is to use the Differential Capacity.[28,29,30,31,32] The first derivative of the obtained galvanostatic curve $\left(\frac{dQ}{dV}\right)$ is known as the Differential Capacity (DC).

The steep increase of charge in a narrow voltage region results in plateaus on a potential *vs.* capacity profile. Therefore, where potential plateaus are observed on the voltage profile, a corresponding series of peaks are visible on a $\frac{dQ}{dV}$ *vs*. potential curve. DC plots are complementary to the voltage profiles of a given cell as the plateaus can be related to clearly identifiable peaks. In turn, these peaks can provide information about the phase transitions of an electrode material, the reversibility of the electrode reactions and information about Li^+ diffusion kinetics[33]. Changes in peak heights relating to these characteristic features can provide insight to the processing occurring in the battery over long-term cycling.

4.2.3 Battery Specifications

To understand the performance characteristics of a given battery there are several terms that need to be defined first such as specific capacity, rate capability, cyclability and coulombic efficiency.

The specific capacity of a material is defined as the amount of energy that can be stored in a given amount of mass of active material, and it is measured in terms of Ampere-hour per gram (Ah g^{-1}).

When describing batteries, the rate capability can be better expressed as C-rate. The C-rate of a battery can be defined as a measure of the rate at which a battery is discharged relative to its maximum achievable capacity. This is done to normalise against battery capacity which can vary greatly between different battery configurations. The C-rate is the capacity of the battery divided

by the hourly charging rate. A 1C rate means that the discharge current applied will discharge the entire battery in 1 hour. A 2C rate means it would discharge twice as fast (30 mins). For example, when a 4 Ah battery is being charged at 2 A then it is said to be being charged at a rate of C/2.

Put simply, the cyclability of a battery can be defined as the number of charging cycles a battery can undergo in its lifetime. Commercialised Li-ion batteries have a long cycle life, allowing them to operate continuously for long periods of time for portable applications.

The capacity, C-rate and cyclability are all important factors to consider for a battery, especially as they are interrelated. The C-rate has a direct effect on the cyclability of a battery. If the current is charged or discharged at higher C-rates i.e., faster, then this is a source of stress on the battery. This stress can exacerbate degradation and decrease the cyclability of the battery when compared to lower C-rates.[34] Likewise, the capacity of a battery tends to continuously decrease with an increasing number of cycles. This results from structural changes in the positive electrode material during charging and discharging, as not all the lithium that moves toward the negative side of the battery (during charge) will make it back to the positive electrode during discharge.[35] As such, the capacity of a Li-ion battery is directly related to the amount of Li^+ ions that can be shuttled back and forth during charge and discharge. As we have already seen, intercalation type electrodes make this shuttling possible. However, as the battery is cycled, these Li^+ ions can be consumed in other reactions not pertaining to the redox chemistry of the battery, for example the formation of a solid electrolyte interphase (SEI).[36] This interphase is the product of reactions between the highly reactive negative electrode (graphite) and the liquid electrolyte that is the transport medium for Li^+ ions. The SEI is a protective passivation layer on the graphite surface which impedes further electrolyte degradation and affords longer shelf life. However, the SEI remains poorly understood. For every electrolyte molecule that reacts and becomes decomposed during reduction, a lithium ion gets trapped in the

interphase. Thus, the capacity of the battery diminishes with increasing amounts of trapped lithium.

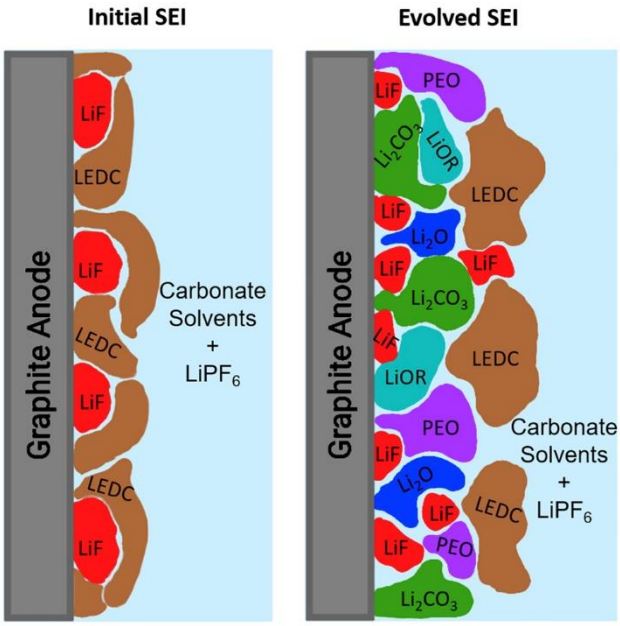


Figure 2 – Depiction of the initial and evolved SEI formed on the graphite anode (negative electrode). Reprinted from[36] with permission from Elsevier.

Coulombic Efficiency (CE) is widely used as a quantifiable indicator of reversibility within a given battery. It can be useful in assessing the lifespan of Li-ion batteries but not necessarily Li-metal batteries, which create a high energy environment, complicating lifespan prediction.[37] CE is defined as the ratio of discharge capacity over the charge capacity of a specific electrode as per Equation (1).

$$Coulombic\ Efficiency = \frac{Discharge\ capacity}{Charge\ capacity} * 100 \quad (1)$$

In an ideal cell, the flow of Li^+ ion and electrons are purely from reversible electrochemical reactions with no side reactions, and therefore the CE is equal to 100%. Realistically, side reactions between electrolyte and electrode

materials are ubiquitous. These side reactions could be chemical or electrochemical. Parasitic chemical reactions which generate electrons may or may not be detected by the current collectors. Electrochemical side reactions involving the loss and acceptance of electrons still takes place on the current collectors but are likely to be irreversible. For example, electrolyte decomposition such as electrolyte polymerisation incite the formation of electrochemically inactive by-products.[38,39,40] Electrons generated from these types of side reactions could subsequently be accounted for in the calculated CE, which adds a degree of complexity to the true meaning of the CE with respect to the system in study.

4.3 Aims

The aim of this chapter is to appraise a POM-based positive electrode material in a Li-metal battery. In addition to this, any differences in the support, Vulcan *vs.* Oxidised Vulcan, will be assessed and whether there is a direct influence on the composite stability at device level. As this is a preliminary study of an unoptimised material, some experimental parameters are varied i.e., potential window of study, post-drying processing and electrode composition. The results of these studies will help to optimise experimental design for the fabrication and testing of POM based Vulcan materials.

4.4 Results & Discussion

4.4.1 Preliminary Characterisation

As discussed previously, the Wells-Dawson POM, $K_6P_2W_{18}O_{62}$, shows redox activity within the battery solvent, 1M lithium hexafluorophosphate ($LiPF_6$) dissolved in a 50/50 (v/v) solution of ethylene carbonate (EC) and ethyl methyl carbonate (EMC). Three redox processes are observed in the potential range 4.2 – 2.6 V *vs.* Li/Li^+, each corresponding to a one-electron transfer (Figure 3, Equations 1 – 3).

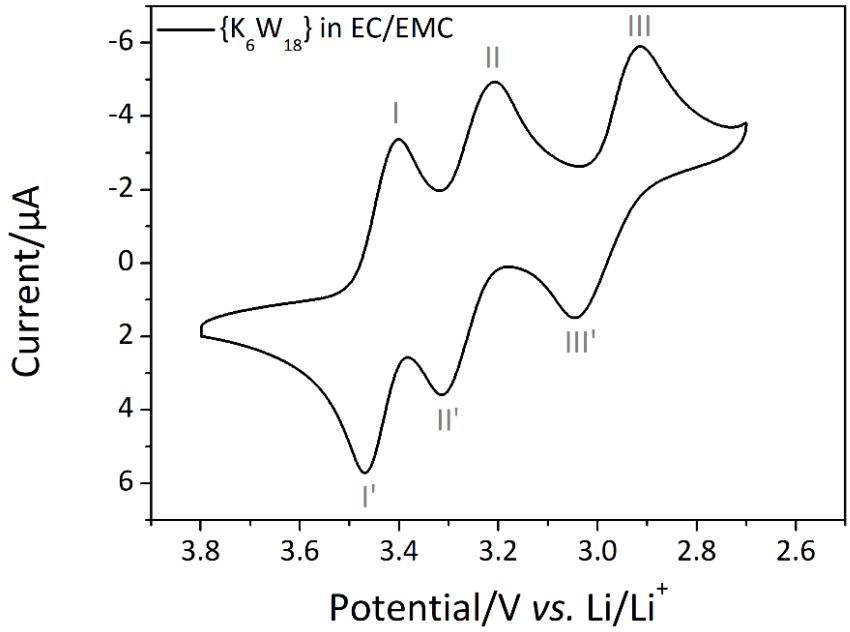


Figure 3 - CV of $\{K_6W_{18}\}$ in 1M $LiPF_6$ in EC/EMC, performed in the glovebox, using a 3 mm GC WE, Pt CE, LFP reference electrode which was then converted to Li/Li^+. The scan rate was 50 mV s^{-1}.

Equations 1 – 3: Redox couples for $\{K_6W_{18}\}$ in 1M $LiPF_6$ in EC/EMC.

I/I': $[P_2W_{18}O_{62}]^{6-} + e^- \longleftrightarrow [P_2W_{18}O_{62}]^{7-}$ (1)

II/II': $[P_2W_{18}O_{62}]^{7-} + e^- \longleftrightarrow [P_2W_{18}O_{62}]^{8-}$ (2)

III/III': $[P_2W_{18}O_{62}]^{8-} + e^- \longleftrightarrow [P_2W_{18}O_{62}]^{9-}$ (3)

Table 1 - Observed Midpoint Potentials (E_{mid}) and Peak-to- Peak Separations (ΔE_p) for $\{K_6W_{18}\}$ in 1M $LiPF_6$ in EC/EMC.

Process	E_{mid}/V	ΔE_p/mV
I/I'	3.43	68
II/II'	3.25	103
III/III'	2.98	124

Solid state voltammograms were obtained by dropcasting an ink of the material on a glassy carbon electrode followed by subsequent testing in a three-electrode cell, as shown in Figure 4.

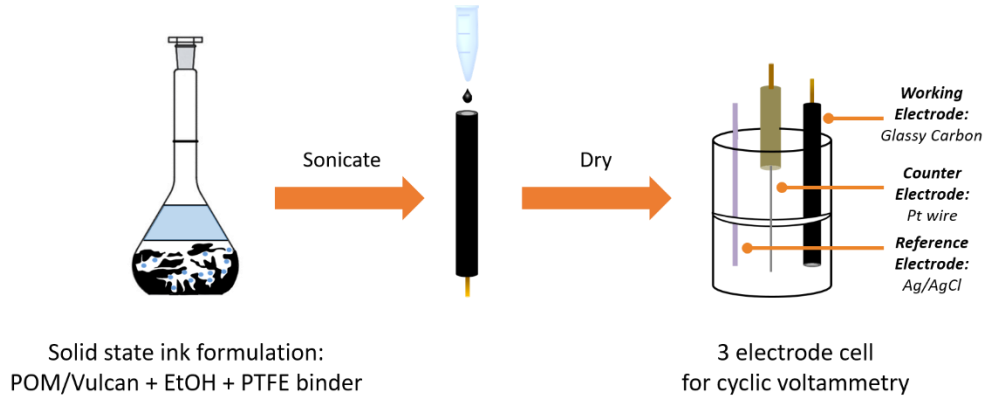


Figure 4 - Preparation of POM/Vulcan ink with binder and ethanol. Subsequent dropcasting and drying prior to use in a three electrode cell for solid state cyclic voltammetry.

When the redox active POM is combined with Vulcan and Oxidised Vulcan to form the composites, $\{K_6W_{18}\}$@V and $\{K_6W_{18}\}$@[O]V respectively, the electrochemistry is retained (Figures 5 and 6). Indeed, $\{K_6W_{18}\}$@[O]V shows significantly better cyclability than the $\{K_6W_{18}\}$@V material (400 cycles *vs.* 20 cycles).

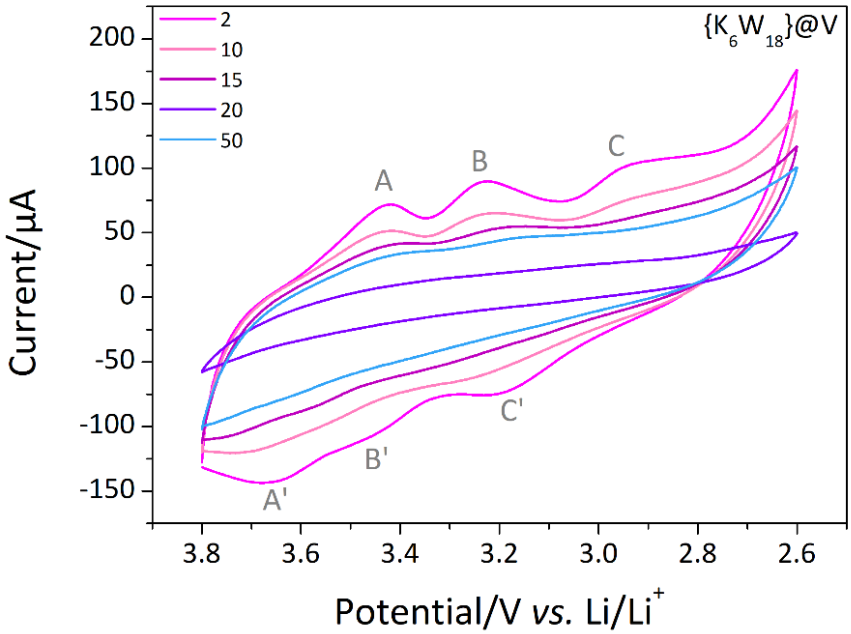


Figure 5 - Solid state CV of $\{K_6W_{18}\}$@Vulcan in 1M $LiPF_6$ in EC/EMC, performed in the glovebox, using a 3 mm GC WE, Pt CE, LFP reference electrode which was then converted to Li/Li^+. The scan rate was 50 mV s^{-1}.

Equations 4 – 6 - Redox couples for $\{K_6W_{18}\}$@V in battery solvent.

A/A': $[P_2W_{18}O_{62}]^{6-} + e^- \leftrightarrow [P_2W_{18}O_{62}]^{7-}$ (4)

B/B': $[P_2W_{18}O_{62}]^{7-} + e^- \leftrightarrow [P_2W_{18}O_{62}]^{8-}$ (5)

C/C': $[P_2W_{18}O_{62}]^{8-} + e^- \leftrightarrow [P_2W_{18}O_{62}]^{9-}$ (6)

Table 2 - Observed E_{mid} and ΔE_p values for $\{K_6W_{18}\}$@V solid state CV in battery solvent.

Process	E_{mid}/V	ΔE_p/mV
A/A'	3.54	227
B/B'	3.34	217
C/C'	3.07	244

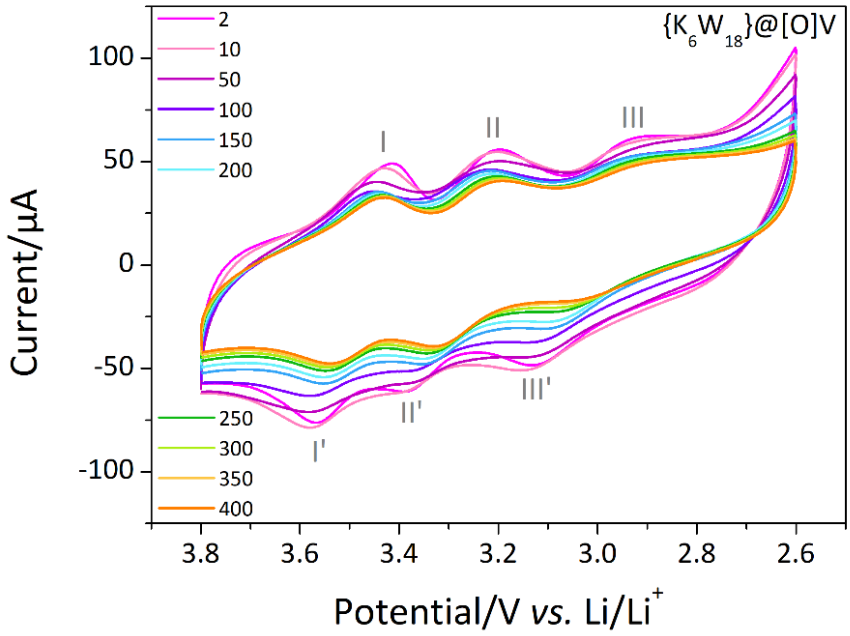


Figure 6 - Solid state CV of $\{K_6W_{18}\}$@[O]Vulcan in 1M $LiPF_6$ in EC/EMC, performed in the glovebox, using a 3 mm GC WE, Pt CE, LFP reference electrode which was then converted to Li/Li^+. The scan rate was 50 mV s^{-1}.

Equations 7 – 9 - Redox couples for $\{K_6W_{18}\}$@V in battery solvent.

$$\text{I/I'}: [P_2W_{18}O_{62}]^{6-} + e^- \leftrightarrow [P_2W_{18}O_{62}]^{7-} \quad (7)$$

$$\text{II/II'}: [P_2W_{18}O_{62}]^{7-} + e^- \leftrightarrow [P_2W_{18}O_{62}]^{8-} \quad (8)$$

$$\text{III/III'}: [P_2W_{18}O_{62}]^{8-} + e^- \leftrightarrow [P_2W_{18}O_{62}]^{9-} \quad (9)$$

Table 3 - Observed E_{mid} and ΔE_p values for $\{K_6W_{18}\}$@[O]V solid state CV in battery solvent.

Process	E_{mid}/V	ΔE_p/mV
I/I'	3.49	149
II/II'	3.29	171
III/III'	3.03	191

The chemical differences between Oxidised Vulcan and Vulcan clearly play a role in the cyclability of the composite materials and retention of the

POM's redox activity. This is a very promising result and certainly merits further investigation into their use as an energy material for Lithium batteries.

4.4.2 Prediction of Galvanostatic Behaviour of POM/Vulcan Electrodes

As we know the number of electrons we expect to be involved in the redox reactions of $\{K_6W_{18}\}$ in the battery solvent, the theoretical specific capacity with respect to the active material can be calculated, as per Equation (2). For clarity, the term 'active material' pertains to the $\{K_6W_{18}\}$ POM *only* and not to the Vulcan-based carbon supports.

$$Theoretical\ Specific\ Capacity\ mAh\ g^{-1} = \frac{n_e F}{3600 * MW} = 17.94\ mAh\ g^{-1} \quad (2)$$

The equation terms are as follows: n_e = number of electrons transferred ($3e^-$), F = Faraday's constant (96485.3 C mol^{-1}), 3600 is the conversion factor for C to Ah and finally $\mathbf{MW}$ = molecular weight of the active material ($K_6P_2W_{18}O_{62}$ = 4597.6 g mol^{-1}). Given that the POM has a high mass, it is not surprising that the theoretical capacity is so low. However, it will be interesting to see how this compares to the observed capacities from galvanostatic charge-discharge cycling. In all the presented voltage profiles, the capacities are reported as specific capacities. These have been normalised with respect to the specific active material mass on the given electrode, to allow for easier comparison across the different sets.

Knowing the expected redox reactions, from the solution phase and solid state dropcasted voltammograms allows the prediction of a voltage profile as shown in Figure 7. Three voltage plateaus are anticipated, corresponding to the three one-electron reductions and oxidations associated with $\{K_6W_{18}\}$. Given that lithium metal is used as the negative electrode, we would expect the potential plateaus to be complementary to the reduction/oxidation potentials from the solution phase and solid state voltammograms, at approximately 3.5 V, 3.2 V and 3 V.

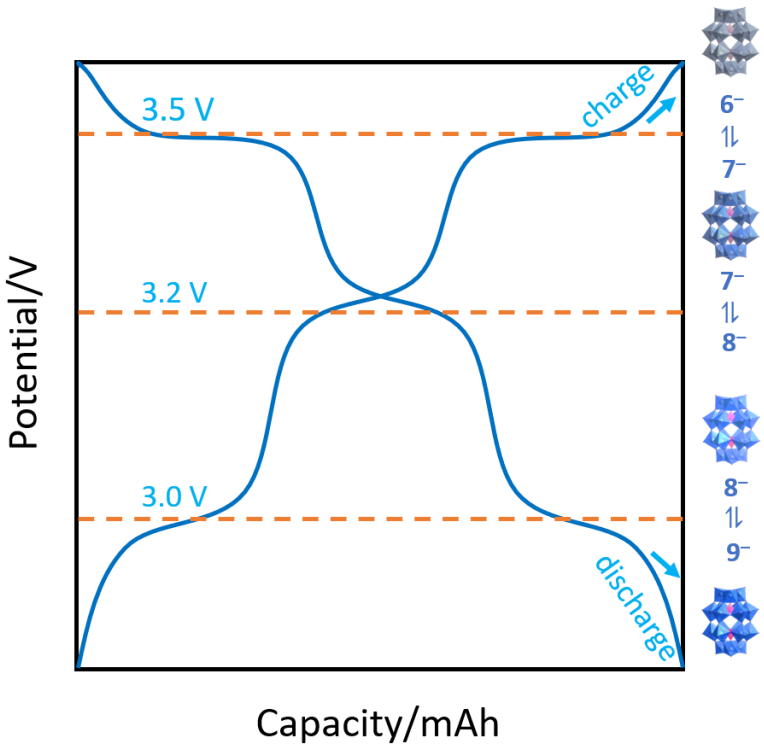


Figure 7 – Predicted potential profile showing expected voltage plateaus for a $\{K_6W_{18}\}$/Vulcan lithium metal battery.

Additionally, the complementary, predicted $\frac{dQ}{dV}$ *vs.* potential profile is shown in Figure 8. Three peaks corresponding to the three potential plateaus would be expected. The POMs are reduced during discharge (right to left, bottom trace) and oxidised during charge (left to right, top trace).

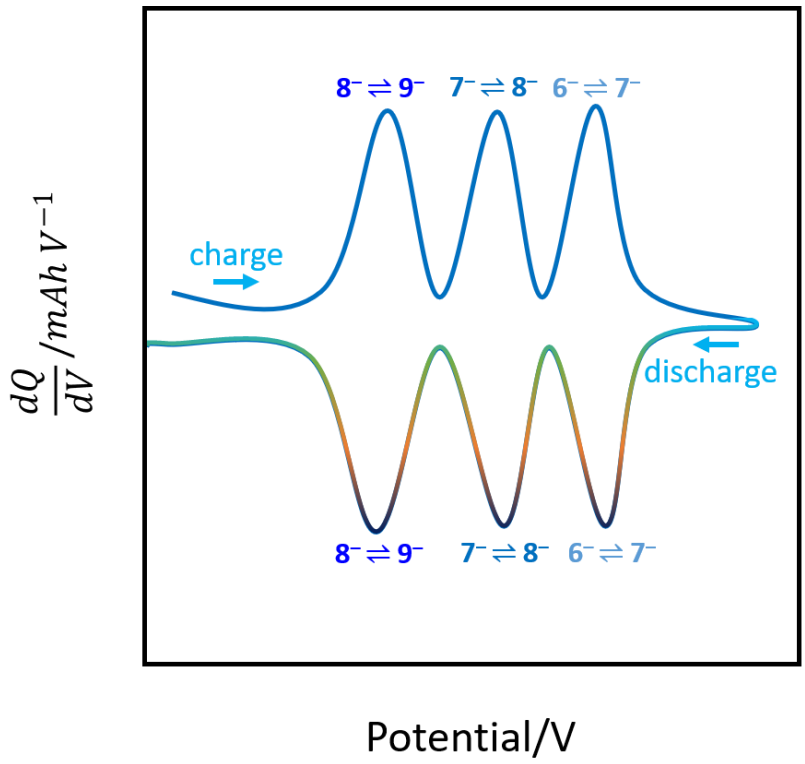


Figure 8 – Predicted $\frac{dQ}{dV}$ *vs.* potential profile for a $\{K_6W_{18}\}$/Vulcan lithium metal battery.

Figure 9 shows the design concept of a lithium metal cell undergoing discharge. For lithium metal batteries, the lithium metal electrode is conventionally termed the anode. However, it is important to reiterate that the terms anode and cathode refer to the *function* of the electrode and not its structure. During discharge, oxidation occurs at the anode, liberating electrons, which travel in an external circuit to the cathode, where reduction takes place. A conventional current describes the direction in which positive electronic charges move. As electrons have a negative charge, the flow of electrons is opposite to current flow. Thus, the cathode is the positive terminal since negative electrons flowing in constitutes a positive current going out. Therefore, during discharge, the anode is the negative terminal, and the opposite holds true during charge.

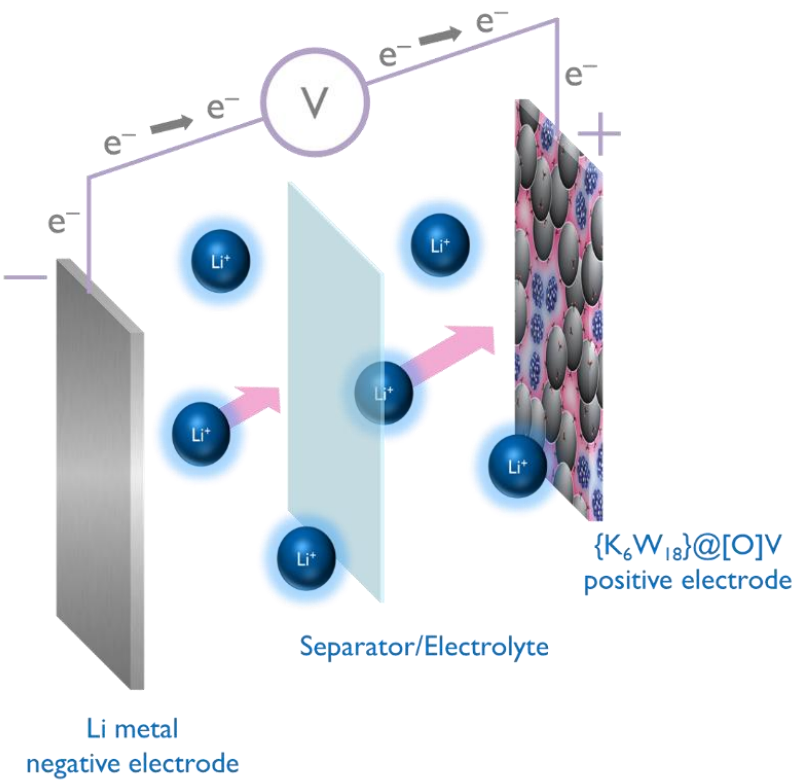


Figure 9 – Working cell schematic comprising a lithium metal negative electrode, Li^+ conducting separator and $\{K_6W_{18}\}$/Vulcan positive electrode. The electron and ion flow depicts discharge.

The expected oxidation and reduction half-reactions during discharge and charge are as follows:

Discharge (left to right); Charge (right to left)

Negative Electrode:

$Li \longleftrightarrow Li^+ + e^-$

Positive Electrode:

$Li_6[P_2W_{18}O_{62}]^{6-} + e^- \longleftrightarrow Li_7[P_2W_{18}O_{62}]$

$Li_7[P_2W_{18}O_{62}]^{7-} + e^- \longleftrightarrow Li_8[P_2W_{18}O_{62}]$

$Li_8[P_2W_{18}O_{62}]^{8-} + e^- \longleftrightarrow Li_9[P_2W_{18}O_{62}]$

4.4.3 Preparation & Cell Assembly

Electrodes using $\{K_6W_{18}\}$@V and $\{K_6W_{18}\}$@[O]V as the cathode material were fabricated as detailed in the experimental section. Briefly, the composite materials were combined with Super P conductive carbon (not in all sets) and polyvinylidene fluoride (PVDF) binder in the desired weight ratio. Following successful coating and drying, the electrodes were punched to the required size (12 mm) and transferred to an argon-filled glovebox.

Lithium cells were built using Swagelok fittings. The Swagelok cells were composed of stainless steel, including the nuts and body, and the stainless steel rods were secured with PTFE ferrules on either side. The cell comprised of lithium foil as the counter/reference electrode, $\{K_6W_{18}\}$@V or $\{K_6W_{18}\}$@[O]V as the working electrode, and two glass fibre separators (all 12 mm diameter) as shown in Figure 10. The electrolyte used was a typical battery solvent (1M $LiPF_6$ in 50/50 EC/EMC) and the cells were left to rest for two hours before cycling measurements to allow for adequate electrolyte penetration of the electrodes.

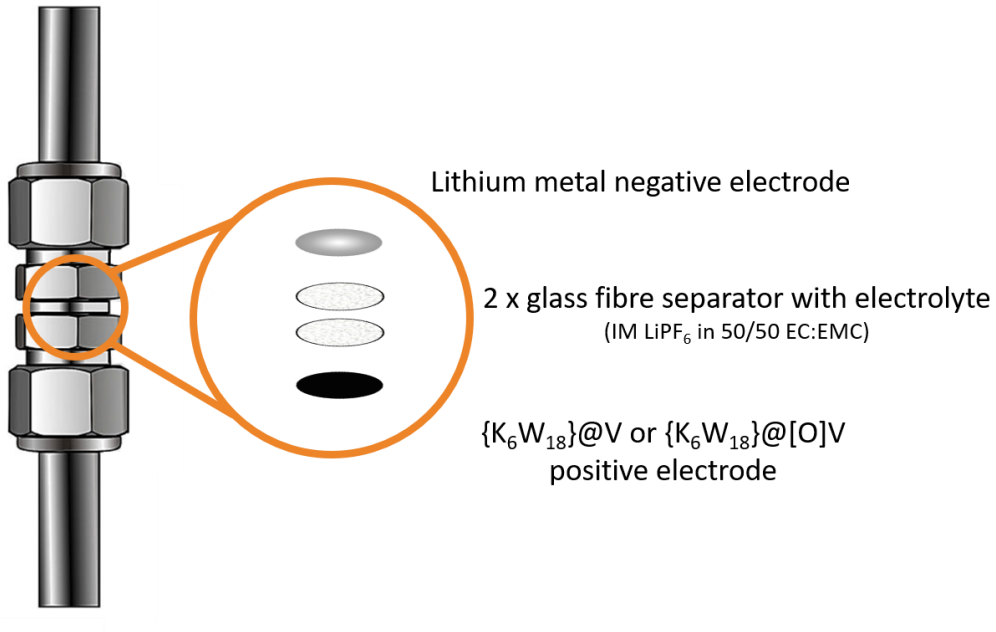


Figure 10 – Swagelok cell design and components used in this study.

4.4.4 Battery Components

In order to assess the electrochemical performance of $\{K_6W_{18}\}$@Vulcan and $\{K_6W_{18}\}$@[O]Vulcan as positive electrode materials, six different sets of electrodes were fabricated. Each set differs by composite material, electrode composition and processing techniques. These are tabulated in Table 4.

Table 4 – Electrode compositions and the approximate weight percent loading as determined by TGA.

Electrode	Composition	Processing	TGA wt % $\{K_6W_{18}\}$
A	8:1:1 $\{K_6W_{18}\}$@[O]V:Super P:PVDF	N/A	55.7
B	8:1:1 $\{K_6W_{18}\}$@V:Super P:PVDF	N/A	70.0
C	8:1:1 $\{K_6W_{18}\}$@[O]V:Super P:PVDF	Calendaring	48.8
D	8:1:1 $\{K_6W_{18}\}$@V:Super P:PVDF	Calendaring	42.8
E	95:5 $\{K_6W_{18}\}$@[O]V:PVDF	Calendaring	34.5
F	95:5 $\{K_6W_{18}\}$@V:PVDF	Calendaring	39.7

Prior to cell assembly, each electrode was accurately weighed. The specific charging/discharging capacities were calculated on the basis of the weight of $\{K_6W_{18}\}$ within that particular positive electrode. Depending on the electrode composition, either 80% or 95% of the weight of the cathode is $\{K_6W_{18}\}$@[O]V or $\{K_6W_{18}\}$@V and then the subsequent TGA weight % loading of $\{K_6W_{18}\}$ is taken into account for the respective electrode set. The capacities are normalised to the active material mass to allow for easier comparison of specific capacities across the different batteries, irrespective of the electrode composition.

4.4.5 Performance of $\{K_6W_{18}\}$@[O]V versus $\{K_6W_{18}\}$@V as a Positive Electrode

4.4.5.1 Solid State Voltammograms

The first set of electrodes studied were made of either $\{K_6W_{18}\}$@[O]V (Set A) or $\{K_6W_{18}\}$@V (Set B) as the positive electrode material in an 8:1:1 weight ratio with conductive Super P carbon and PVDF binder. Prior to charge-discharge cycling, the solid state voltammetry of an electrode from Set A and Set B were tested in a three-electrode setup. This was done according to Figure 11 with a Set A or Set B positive electrode disc as the working electrode, Lithium Iron Phosphate (LFP) as the reference electrode, and a platinum wire counter electrode. The electrolyte used was the battery solvent (1M $LiPF_6$ in EC/EMC) and the CV was collected in an argon-filled glovebox, with a scan rate of 50 mv s^{-1}.

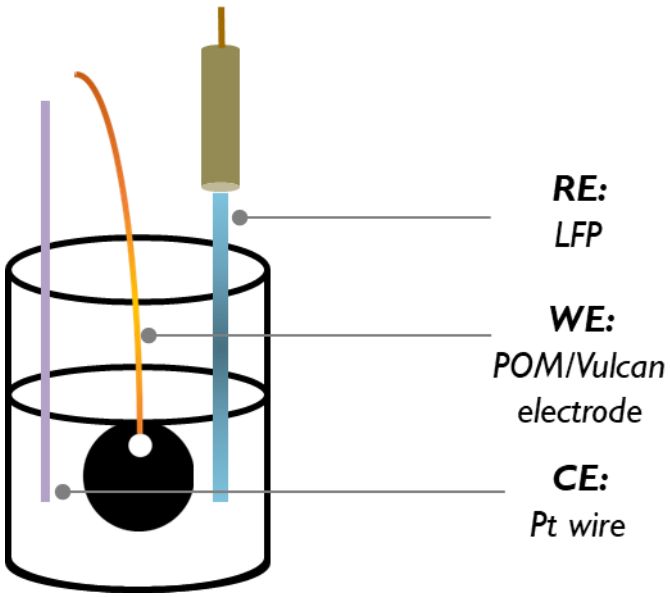


Figure 11 - Three electrode cell setup for solid state disc cyclic voltammetry consisting of a POM/Vulcan working electrode, platinum wire counter electrode and Lithium Iron Phosphate reference electrode (which is then converted to Li/Li^+).

The solid state voltammogram for Set A ($\{K_6W_{18}\}$@[O]V) shows three one-electron reduction/oxidation peaks labelled as I/I', II/II', III/III' (Figure 12). The E_{mid} values are converted from the LFP reference electrode to be reported

vs. Li/Li^+.[36] These are centred at E_{mid} values close to 3.5 V, 3.2 V and 3.0 V *vs.* Li/Li^+ (Table 5), as expected from the $\{K_6W_{18}\}$ solution phase E_{mid} values. The large deviation in ΔE_p values from the theoretical value of 0 mV expected for surface-confined process, indicate that the processes are not very reversible. Additionally, it is interesting to note that moving from the dropcasted GC style solid state study to this disc electrode 'solid state' study has resulted in differences in the cycling stability. Previously, the dropcast method shows that the $\{K_6W_{18}\}$@[O]V material could be cycled at least 400 times. Whereas when $\{K_6W_{18}\}$@[O]V is incorporated into an electrode material, the POM redox peaks are lost between the 15th and 20th cycle. This could be due to fundamental differences in sample preparation, with respect to the binder used as well as air/moisture exposure.

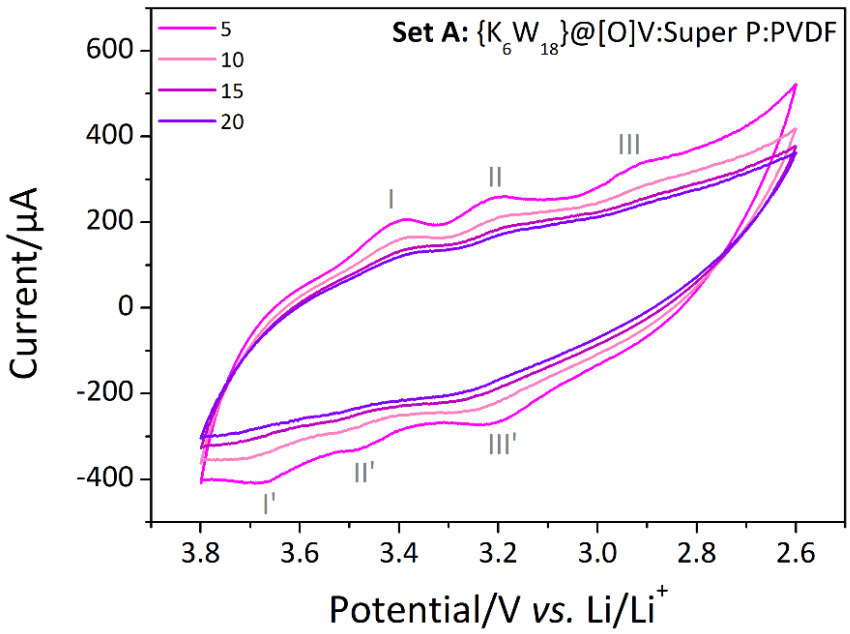


Figure 12 - Solid state disc CV of $\{K_6W_{18}\}$@[O]V Set A electrode in battery solvent, recorded in a glovebox at a scan rate of 50 mv s^{-1}, showing cycles 5 – 20.

Table 5 - Observed E_{mid} and ΔE_p values for $\{K_6W_{18}\}$@[O]V Set A electrode in battery solvent.

Process	E_{mid}/V	ΔE_p/mV
I/I'	3.49	149
II/II'	3.29	171
III/III'	3.03	191

The solid state voltammogram for the Set B electrode ($\{K_6W_{18}\}$@V) is shown in Figure 13. Three one-electron reduction/oxidation peaks labelled as A/A', B/B', C/C' are observed, which are centred at the expected E_{mid} values close to 3.5 V, 3.2 V and 3.0 V (Table 6). Similar to Set A, the very large ΔE_p values indicate the processes are not very reversible in nature. After 20 cycles, the POM redox peaks in the Set B electrode are still discernible. This is in contrast to the dropcasted GC style 'solid state' voltammogram obtained for $\{K_6W_{18}\}$@V, where no POM redox activity was observed beyond the 20th cycle (Figure 13).

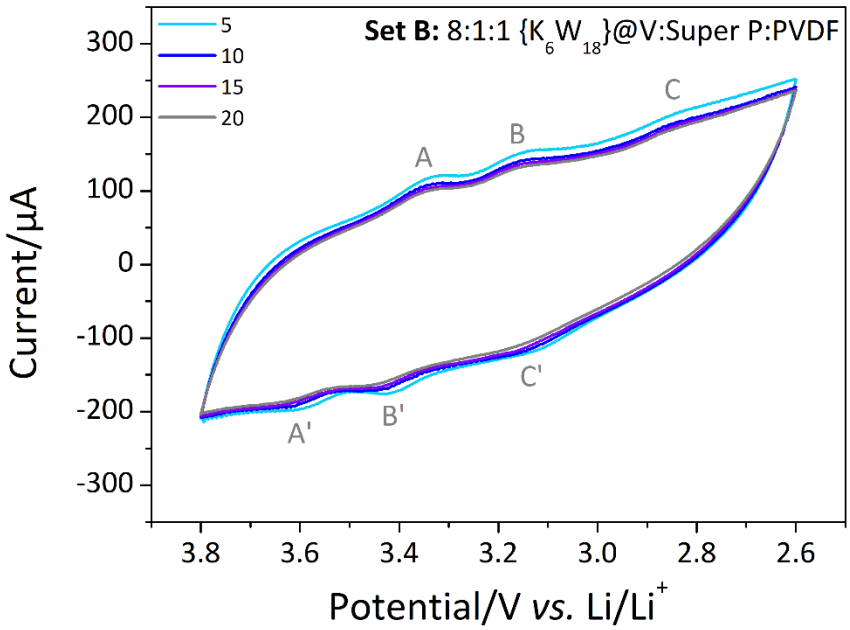


Figure 13 - Solid state disc CV of $\{K_6W_{18}\}$@V Set B electrode in battery solvent, recorded in a glovebox at a scan rate of 50 mv s^{-1}, showing cycles 5 – 20.

Table 6 - Observed E_{mid} and ΔE_p values for $\{K_6W_{18}\}$@V Set B electrode in battery solvent.

Process	E_{mid}/V	ΔE_p/mV
A/A'	3.40	286
B/B'	3.21	310
C/C'	2.88	284

This result for the Set B electrode is also in contrast to the analogous voltammogram for Set A ($\{K_6W_{18}\}$@[O]V, Figure 12). For Set A, the flattening of POM redox peaks had occurred by the 20th cycle. Until now, the Oxidised Vulcan matrix outperformed the Vulcan matrix with respect to cyclability and POM retention in the battery solvent. However, the difference in voltammograms for the Set A and Set B electrodes presents an interesting proposition, whereby the Vulcan matrix may actually be a more favourable support for the POM during battery cycling.

4.4.5.2 Charge – Discharge Cycling for Set A: $\{K_6W_{18}\}$@[O]V Positive Electrode

The first set of charge – discharge curves for Set A were measured at a constant current of 50 μA in the voltage range of 1.5 – 3 V. During the discharge process, the POM reduction is accompanied by lithium oxidation. The difference in potential (V) between these two processes occurring manifests as a voltage plateau on the charge/discharge curve. From the CV experiments, the potential range in which we expect these reactions to happen is known. Figure 14 shows the 1st and 2nd charge/discharge curve obtained for Set A, using $\{K_6W_{18}\}$@[O]V as the positive electrode. Interestingly, four voltage plateaus are observed (dashed lines) instead of the anticipated three. Additionally, the four redox events take place at lower potentials, shifted by approximately 1 V lower when compared to the $\{K_6W_{18}\}$@[O]V solid state voltammogram (Figure 6).

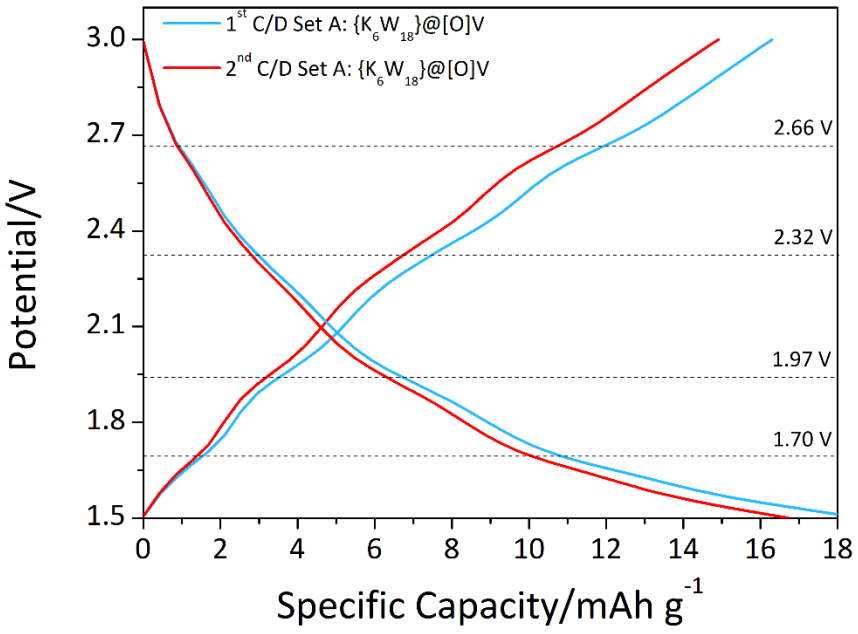


Figure 14 – 1st and 2nd charge-discharge profile for Set A in the voltage range 1.5 – 3 V.

The initial charge/discharge capacities are 16.3 mAh g^{-1} and 18.7 mAh g^{-1} respectively (Figure 15). These capacities are very close to the theoretical specific capacity of 17.94 mAh g^{-1}. This is a very good result considering that this is an unoptimised material using a very standard electrode composition, with no additional processing or modifications.

The CE values are greater than 100%, suggesting that the cell chemistry does have some irreversible or parasitic side reactions. The observed capacities steadily decrease with repetitive charge – discharge cycling, levelling off at approximately 8 mAh g^{-1} (Figure 15). The discharge process corresponds to lithiation of the $\{K_6W_{18}\}$@[O]V electrode and the charge process is delithiation. As the charge – discharge cycling continues, some lithium is irreversibly consumed for additional processes such as the formation of a solid electrolyte interface (SEI)[41] or side reactions with the electrolyte.[42] This lithium cannot be recovered in the following charge – discharge cycles, resulting in a loss of capacity. This capacity loss is apparent from the 2nd charge/discharge curve and continues to fade quite dramatically in the first 10 cycles as seen in Figure 15.

We also know from the cyclic voltammetric cycling studies of the $\{K_6W_{18}\}$@[O]V material in various aqueous and organic solvents that POM leaching over time does occur. Within a lithium cell, this POM leaching phenomenon is likely to persist, which is a trigger for irreversible capacity loss.

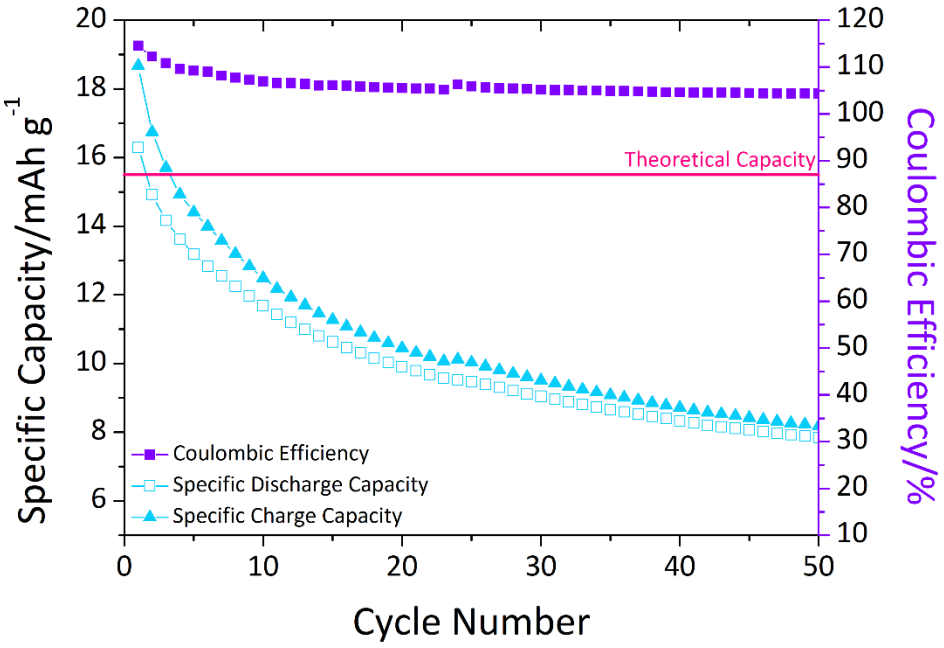


Figure 15 – Specific charge/discharge capacity and coulombic efficiency values per cycle.

Figure 16 shows the first ten charge – discharge cycles, as well as the 15th, 20th, 30th and 50th cycles. The capacity loss can be clearly seen from the 1st charge/discharge (light blue trace) curve to the 50th (dark green trace). Looking more closely at the curves, they become increasingly linear which indicates less redox activity with repetitive cycling. As seen in Figure 16, the voltage plateaus are still visible beyond the 10th cycle, and linearity of the curves occurs beyond the 30th cycle (dark blue trace). This would suggest that most of the POM leaching occurs in the first 20 cycles.

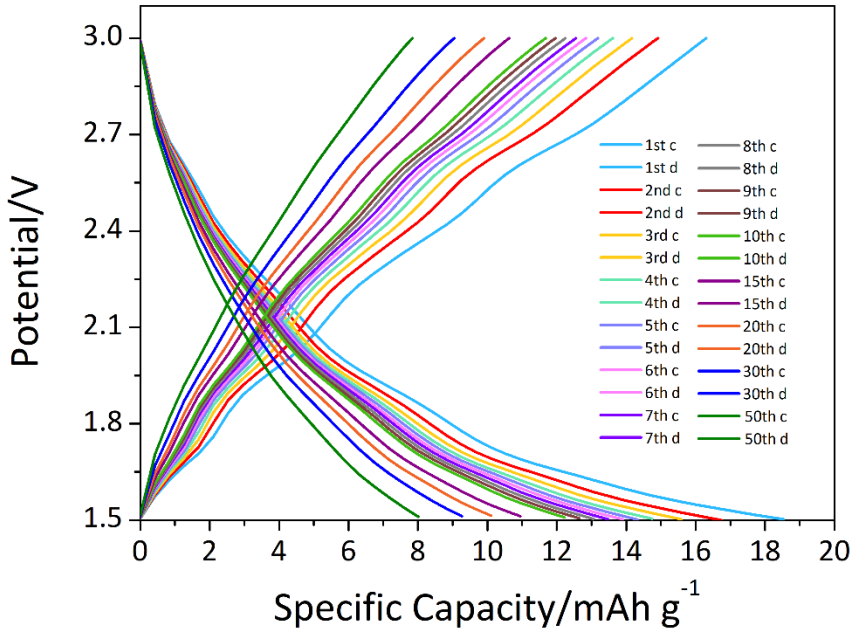


Figure 16 – First ten charge/discharge cycles as well as the 15th, 20th, 30th and 50th cycles.

The differential capacity plot for the 1st charge/discharge curve is shown in Figure 17 with an inset of the 30th and 50th charge/discharge cycles. The DC curve for the 1st cycle shows four peaks which correspond well to the four plateaus observed in the voltage profile. Though the charge – discharge curves in Figure 16 for the 30th and 50th cycles look linear, the DC curve for each respective cycle shows that redox chemistry is in fact still happening. The intensity and magnitude of these four peaks is greatly reduced compared the peaks for the 1st charge/discharge cycle, which is likely due to a loss of active material, however some POM is still present which continues to participate in reduction – oxidation reactions.

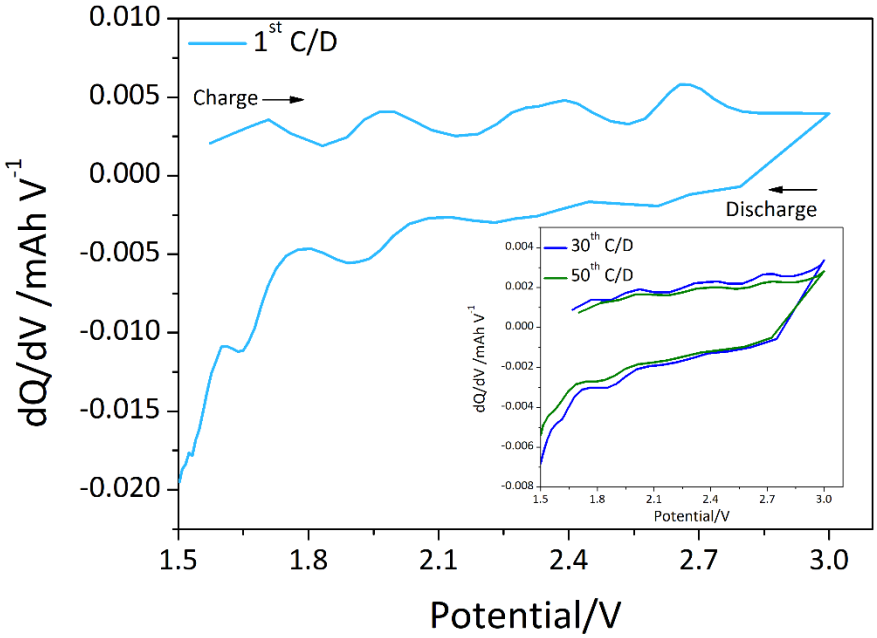


Figure 17 – Differential capacity plot, $\frac{dQ}{dV}$ *vs.* potential for the 1st charge-discharge cycle and an inset for the 30th and 50th cycle.

4.4.5.3 Charge – Discharge Cycling for Set B: $\{K_6W_{18}\}$@V Positive Electrode

Like Set A, the first set of charge – discharge curves for Set B were measured at a constant current of 50 µA in the voltage range of 1.5 – 3 V. Figure 18 shows four ill-defined potential plateaus which can be discerned at similar to potentials to the Set A plateaus (between 1.70 – 2.70 V).

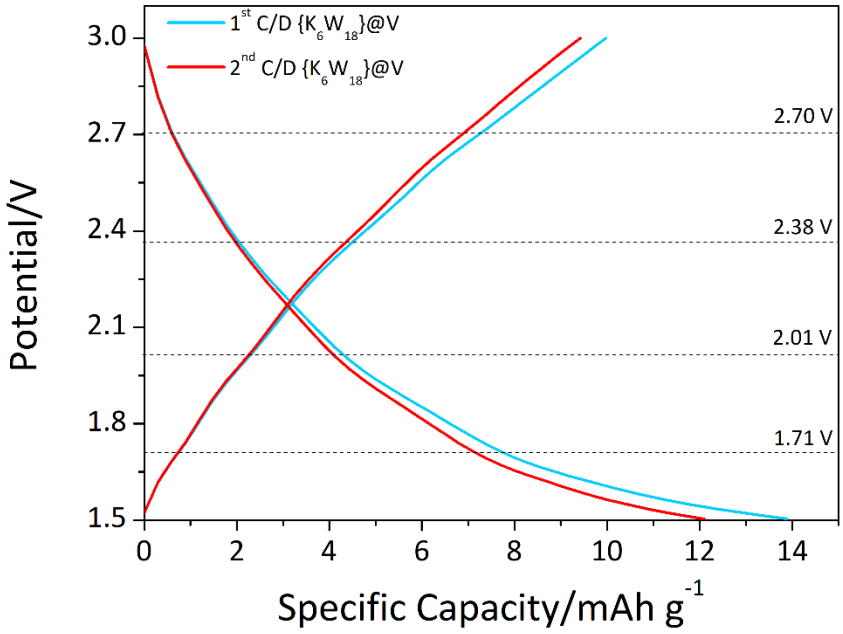


Figure 18 - 1st and 2nd charge-discharge profile for Set B in the voltage range 1.5 – 3 V.

Figure 19 shows the capacity fade over 50 cycles. The initial charge and discharge capacities are 10 mAh g^{-1} and 14.13 mAh g^{-1} respectively, which are lower than the theoretical capacity. The capacities decline rapidly in the first five cycles and then plateau to a capacity between 6 – 8 mAh g^{-1}. The initial CE of 141 % is very high and attests to unusual behaviour occurring inside the cell, besides the chemistry of interest. Further anomalous behaviour in the CE is observed between cycles 20 – 35 where the CE suddenly drops but then steadily recovers itself. This behaviour may be unrelated to conventional charge – discharge characteristics and rather pertains to the evolution of parasitic pathways dependent on the cell's electrode/electrolyte chemistries, which is beyond the scope of this thesis.

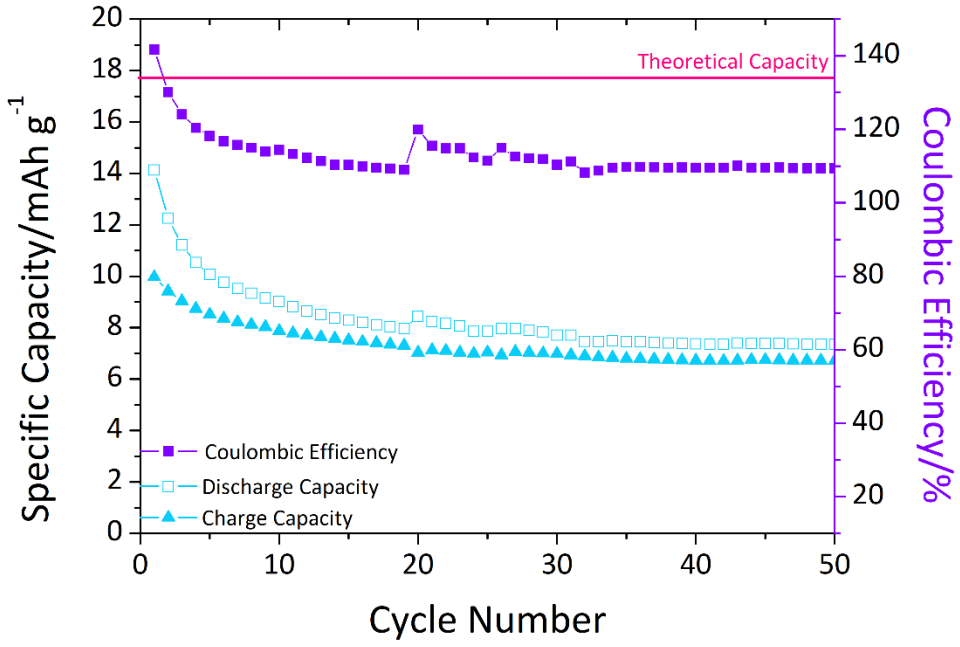


Figure 19 - Specific charge/discharge capacity and coulombic efficiency values per cycle.

Figure 20 shows the first ten charge/discharge curves, with ill – defined plateaus which rapidly become linear in appearance. The plateaus observed in cycles 1 and 2 do not persist beyond the 4th cycle.

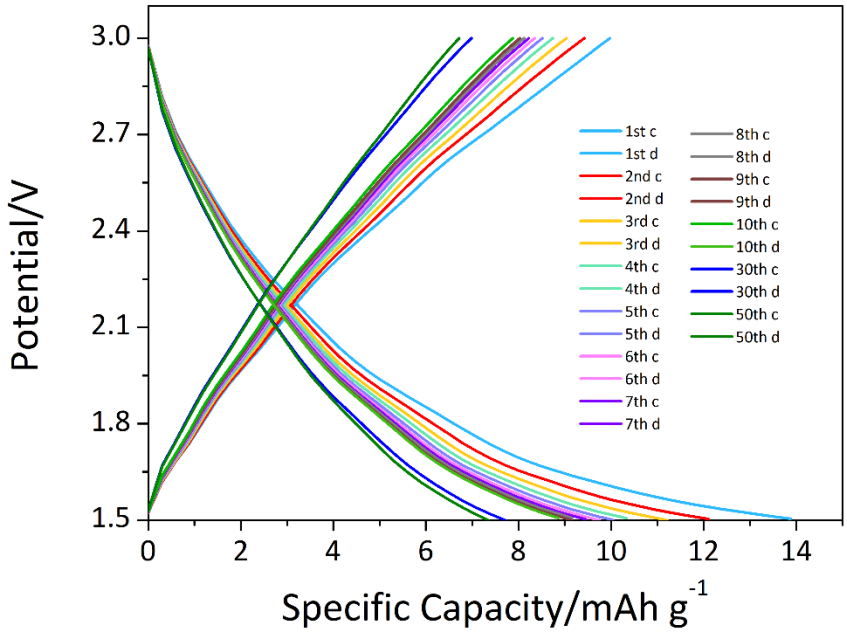


Figure 20 - First ten charge/discharge cycles as well as the 15th, 20th, 30th and 50th cycles.

The differential capacity plot for the 1st charge/discharge curve is shown in Figure 21 with an inset of the 30th and 50th charge/discharge cycles. The DC curve for the 1st cycle shows four peaks corresponding to the four observed plateaus, however the peaks are much lower in intensity in comparison to the analogous plot for Set A. Furthermore, the peaks corresponding to the last two charge processes around 2.4 V and 2.7 V have very poorly resolved corresponding discharge peaks, which look very flat from the 1st charge/discharge. The increasing linearity of the charge – discharge curves coupled with the ill – defined $\frac{dQ}{dV}$ peaks certainly allude to the reduced reversibility of the POM redox chemistry in this system.

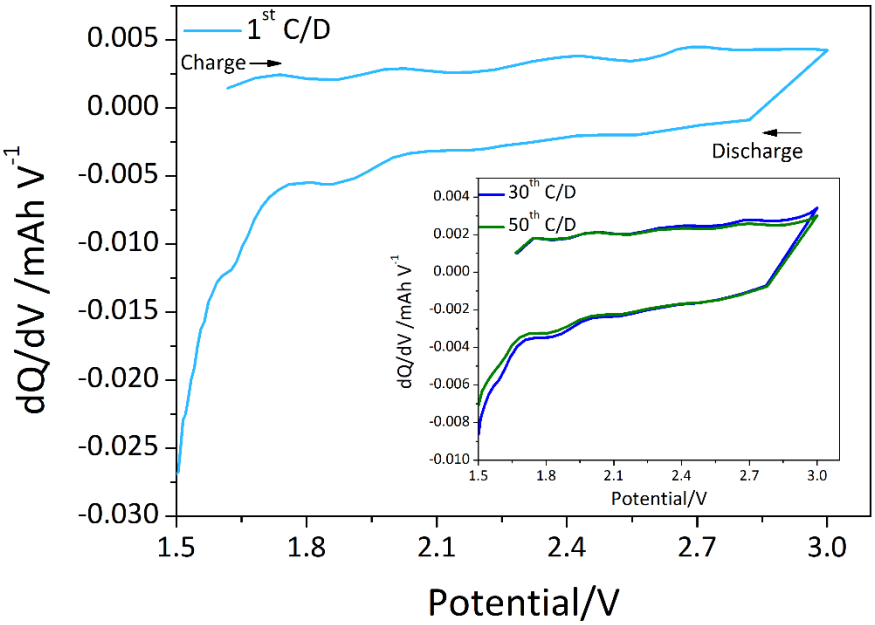


Figure 21 - Differential capacity plot, $\frac{dQ}{dV}$ *vs.* potential for the 1st charge-discharge cycle and an inset for the 30th and 50th cycle.

Despite the promising solid state disc electrode voltammogram (Figure 13) for Set B, which hinted at good cyclability of the material within the battery solvent, the respective lithium cells do not come close to this performance. Voltage plateaus between 1.5 – 3 V are not well-defined but their presence was confirmed using dQ/dV analysis.

The results from Set A and Set B are very interesting because firstly, there is a clear difference between the nature of the voltage profiles of $\{K_6W_{18}\}$@[O]V and $\{K_6W_{18}\}$@V. This is in line with our previous studies which acknowledge the enhanced POM retention capability of the Oxidised Vulcan support *vs.* unmodified Vulcan in several electrolyte systems. It is interesting though that the potentials at which the redox processes occur in the cell are lower than where we would expect them to be, according to the voltammograms. This allows for a 4th redox event to take place in the cell, which is not observed in the voltammograms due to the instability of the POM in

battery solvent at lower potentials. However, the $\frac{dQ}{dV}$ curves do show that the first two discharge processes lose intensity over time and appear flat.

Prior to the charge – discharge cycling, the cells were allowed to rest for 2 hours. Given that the solid state GC dropcast study for $\{K_6W_{18}\}$@V (Figure 5) in battery solvent showed very rapid dissolution of the POM from the Vulcan surface, it is likely that a large proportion of the POM leached out of the Vulcan matrix during the resting period. Whereas the Oxidised Vulcan matrix with its carboxylic acid anchorage points, displays superior POM redox chemistry. Thus far, the $\{K_6W_{18}\}$@[O]V composite shows greater promise as a positive electrode material than the $\{K_6W_{18}\}$@V composite.

4.4.6 Investigating the Effect of Calendaring on Electrode Performance $\{K_6W_{18}\}$@[O]V versus $\{K_6W_{18}\}$@V

Following the coating and drying of electrodes, they can be 'processed' by way of calendaring. This is a common compaction technique whereby the electrodes are passed through two rollers, at a set thickness, as shown in Figure 22. This technique can eliminate structural deformations on the surface. Calendaring has been shown to improve electrode adhesion and rate capability of the battery.[43] Lu et al. analysed calendared $LiFePO_4$ electrodes and found that the improvement in rate capability was a result of enhanced contact between the active material and the conductive carbon additives.[44]

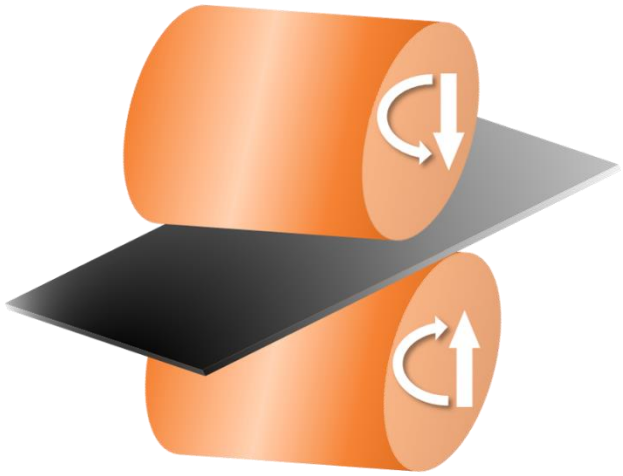


Figure 22 – Aluminium foil coated and dried with electrode material is passed through calendar rollers at a specified thickness.

Set C uses $\{K_6W_{18}\}$@[O]V as the positive electrode material and Set D uses $\{K_6W_{18}\}$@V. They are fabricated in the weight ratio of 8:1:1 with Super P and PVDF binder, akin to Set A and Set B. However, Set C and Set D differ from Set A and B with respect to post – drying processing via calendaring.

4.4.6.1 Solid State Voltammograms

Solid state voltammograms of an electrode from Set C and Set D were collected using the same three electrode setup as described earlier in Figure 11. Both solid state voltammogram for Set C and Set D show three one-electron reduction/oxidation processes which are labelled as I/I', II/II', III/III' and A/A', B/'B, C/C' respectively (Figures 23 and 24). Once again, the E_{mid} values lie in the expected potential range (Tables 7 and 8). The ΔE_p values deviate greatly from the theoretical value of 0 mV expected for surface-confined processes, indicating the low reversibility of the redox reactions. This deviation is twice as large for the Vulcan based Set D electrode compared to the Oxidised Vulcan Set C electrode. Additionally, the cycling stability differs between the two sets where flattening of the POM redox peaks is observed earlier for Set D, within the first 20 cycles. Set C shows better cyclability where loss of POM redox activity is observed around the 75 cycles mark, however this is still inferior to the cycling

stability previous observed for $\{K_6W_{18}\}$@[O]V in the dropcasted solid state voltammogram (minimum 400 cycles).

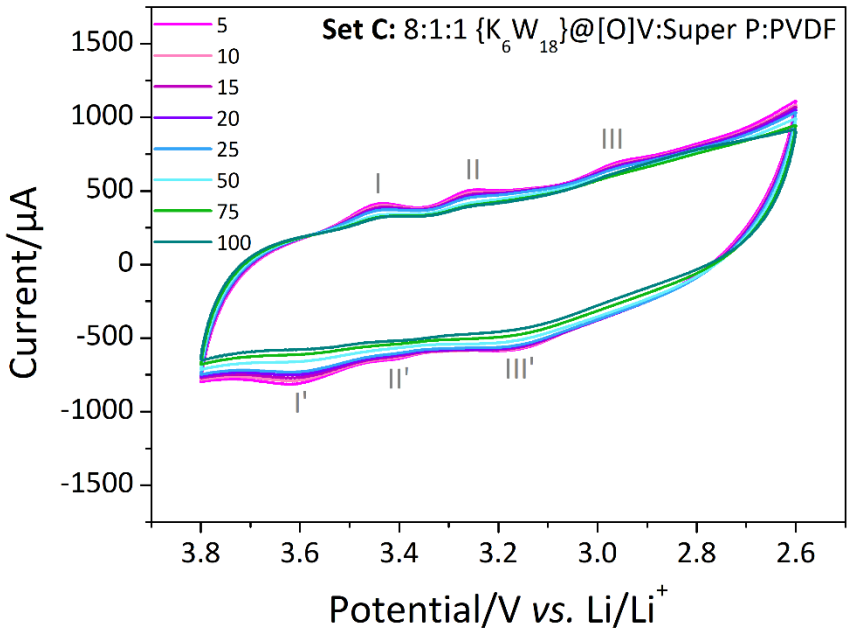


Figure 23 - Solid state disc CV of $\{K_6W_{18}\}$@[O]V Set C electrode in battery solvent, recorded in a glovebox at a scan rate of 50 mv s^{-1}, showing cycles 5 – 100.

Table 7 - Observed E_{mid} and ΔE_p values for $\{K_6W_{18}\}$@[O]V Set C electrode in battery solvent.

Process	E_{mid}/V	ΔE_p/mV
I/I'	3.52	168
II/II'	3.32	160
III/III'	3.04	199

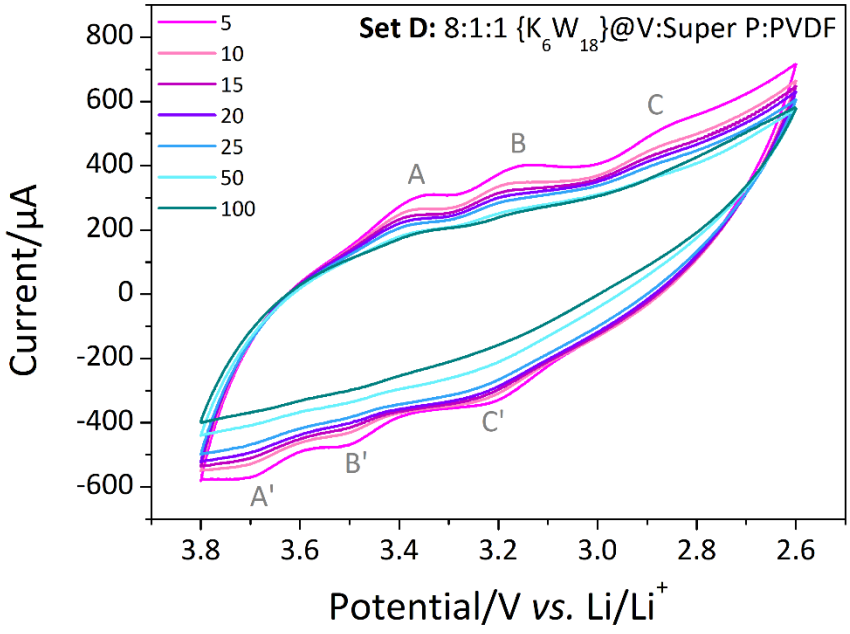


Figure 24 - Solid state disc CV of $\{K_6W_{18}\}$@V Set D electrode in battery solvent, recorded in a glovebox at a scan rate of 50 mv s^{-1}, showing cycles 5 – 100.

Table 8 - Observed E_{mid} and ΔE_p values for $\{K_6W_{18}\}$@V Set D electrode in battery solvent.

Process	E_{mid}/V	ΔE_p/mV
A/A'	3.46	376
B/B'	3.22	408
C/C'	2.90	357

4.4.6.2 Charge – Discharge Cycling for Set C: $\{K_6W_{18}\}$@[O]V

Figure 25 shows the 1st and 2nd charge/discharge curve obtained for Set C, using $\{K_6W_{18}\}$@[O]V as the positive electrode in the potential range of 1.5 – 3 V. Four very well – defined charge and discharge plateaus are observed (dashed lines). These four redox events take place between 1.7 – 2.7 V, at least 1 V lower than anticipated form the voltammetric studies.

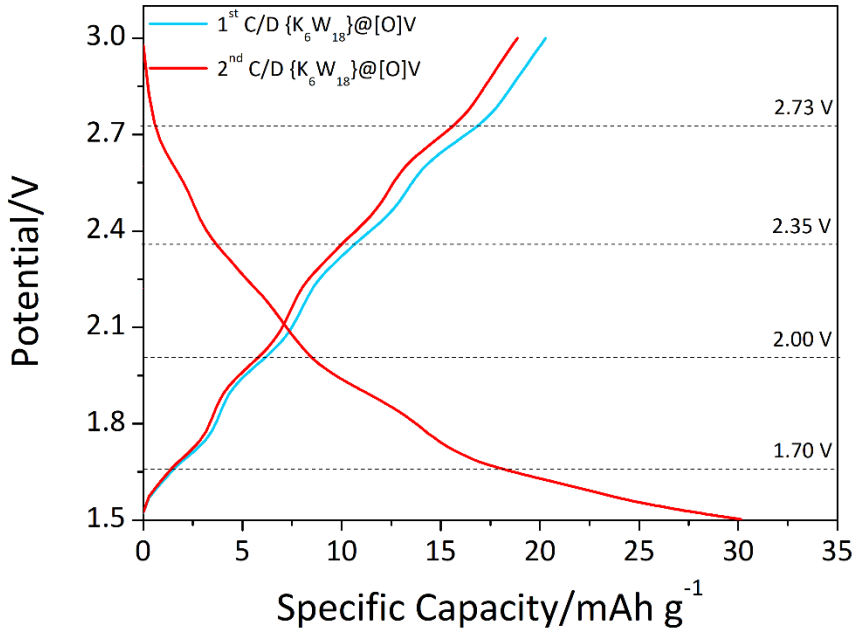


Figure 25 - 1st and 2nd charge-discharge profile for Set C in the voltage range 1.5 – 3 V.

The initial charge/discharge capacities are 20.3 mAh g^{-1} and 30.4 mAh g^{-1} respectively (Figure 26). These capacities are higher than expected in relation to the theoretical specific capacity of 17.94 mAh g^{-1} but they are also higher than the observed capacities for the uncalendared electrode of Set A. The charge and discharge capacity falls below the theoretical capacity (pink line) within the first few cycles, and slowly decline to a final capacity between 9 – 11 mAh g^{-1}. The high CE value starts at 149 % and steadily declines to 120 %. At this early stage of study, the CE cannot be interpreted as a literal reflection of the stability of the cell with regards to electrochemical reversibility of the POM-lithium redox reactions or the nature of SEI formation. Firstly, the observed redox activity in the charge – discharge profiles is already more than what we expected. Secondly, how long a lithium metal cell can cycle stably is determined by several factors[45] such as the depletion rate of lithium metal and electrolyte as well as the build-up rate of cell impedance, which have not been measured in this study.

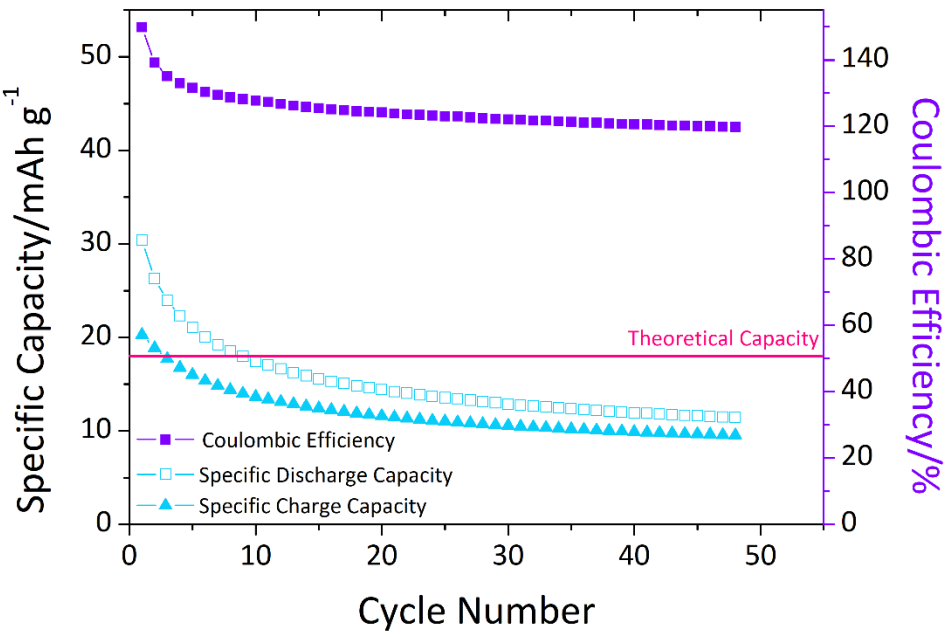


Figure 26 - Specific charge/discharge capacity and coulombic efficiency values per cycle.

Figure 27 shows the first ten charge – discharge cycles, as well as the 15th, 20th, 30th, 40th and 50th cycles. The reduction in capacity with repetitive cycling can be seen from the 1st charge/discharge curve (light blue trace) to the 50th (dark green trace). The curves with the lowest capacity values are more linear in appearance (beyond 30 cycles). The principal cause of this is likely to be a deficiency of active material over time, including both loss of the active positive electrode material {K_6W_{18}} through leaching and loss of active lithium through inefficient lithiation and delithiation (as described for the SEI formation process, vide supra).

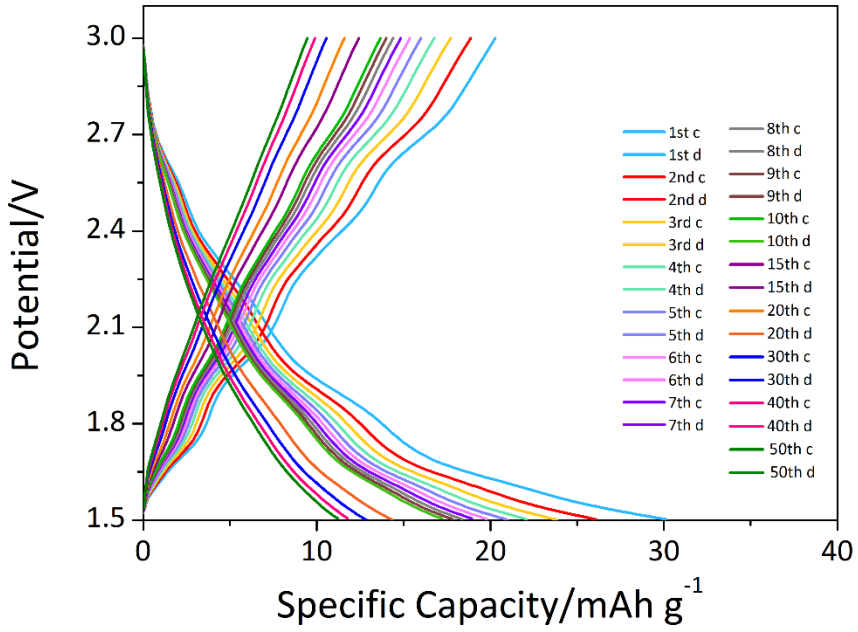


Figure 27 - First ten charge/discharge cycles as well as the 15th, 20th, 30th, 40th and 50th cycles.

The differential capacity curve for the 1st charge/discharge curve is shown in Figure 28 with an inset of the 30th and 50th charge/discharge cycles. The DC curve for the 1st cycle shows four broad peaks which correspond to the four plateaus observed in the voltage profile. However, it is interesting to note that the peaks between 1.5 – 1.8 V and 2.2 – 2.5 V have double humps which certainly prompts further investigation into the working mechanism of the cell with regards to the lithiation and delithiation of the $\{K_6W_{18}\}$@[O]V electrode. The first double hump between 1.5 – 1.8 V very quickly smoothens to just one peak whereas the double humped peak between 2.2 – 2.5 V persists until at least the 30th cycle.

Despite the linear appearance of the 30th and 50th charge/discharge curves in Figure 27, the DC curve for each respective cycle shows that redox chemistry continues to take place. The intensity and magnitude of these $\frac{dQ}{dV}$ peaks do diminish over time which is echoed the loss of capacity over time.

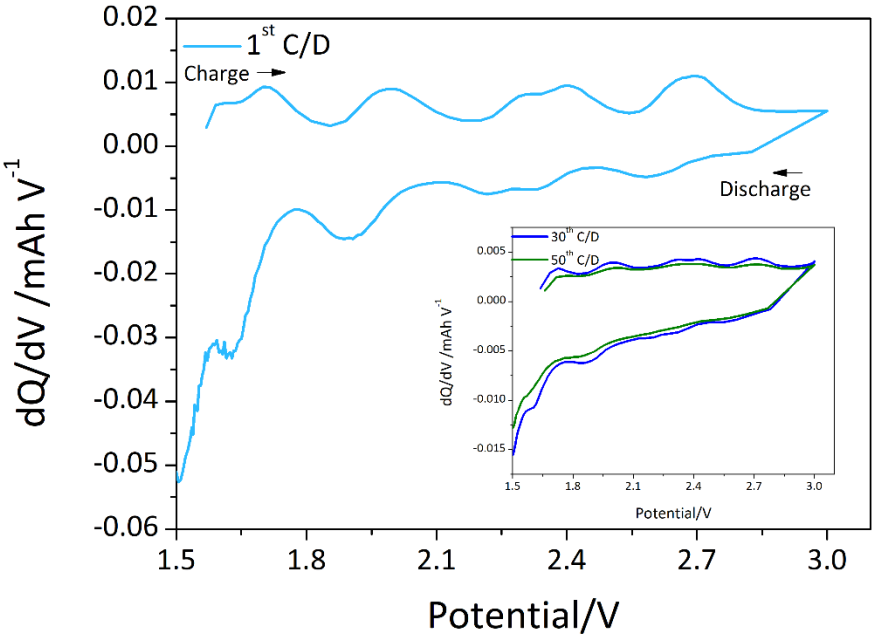


Figure 28 - Differential capacity plot, $\frac{dQ}{dV}$ *vs.* potential for the 1st charge-discharge cycle and an inset for the 30th and 50th cycle.

4.4.6.3 Charge – Discharge Cycling for Set D: $\{K_6W_{18}\}$@V

Figure 29 shows the 1st and 2nd charge/discharge curve obtained for the Set D electrode where $\{K_6W_{18}\}$@V is the positive electrode. Four charge and discharge plateaus are observed between 1.5 – 3 V (dashed lines) which are better defined than the uncalendared analogue (Set B). These four redox events also take place between 1.7 – 2.7 V as seen with all the charge – discharge curves so far.

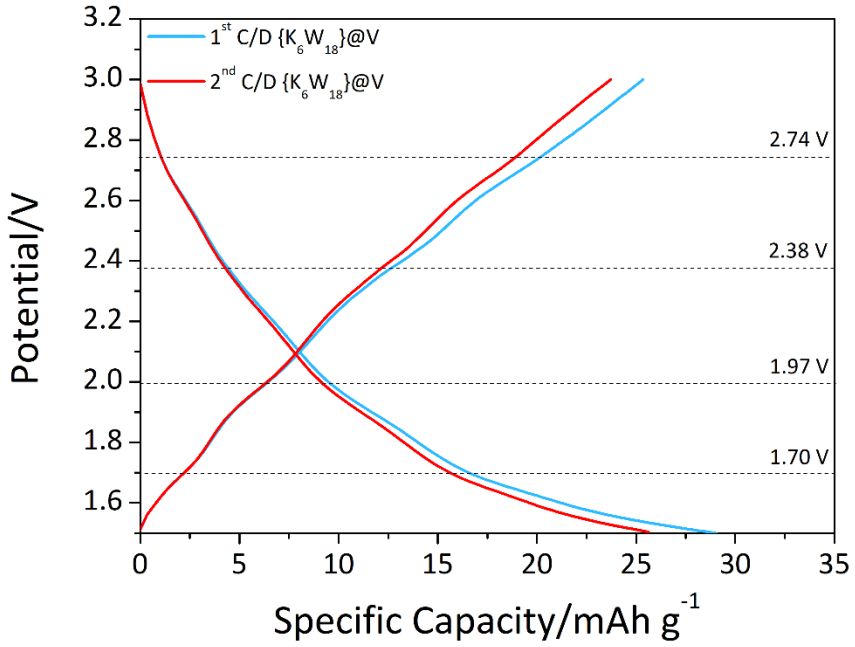


Figure 29 - 1st and 2nd charge-discharge profile for Set D in the voltage range 1.5 – 3 V.

The initial charge/discharge capacities are 25.3 mAh g^{-1} and 29.1 mAh g^{-1} respectively (Figure 30). These capacities are both higher than the theoretical specific capacity and the initial capacities observed for the uncalendared analogue (Set B). A steep decline in the initial capacities occurs within the first ten cycles before they reach the theoretical capacity (pink line). The final charge and discharge capacities are approximately 14 mAh g^{-1}. The CE values start at 114 % and steadily decrease to 102 %. These results are interesting because the calendaring process has clearly had a marked effect on the performance of the $\{K_6W_{18}\}$@V composite. The calendaring has improved the contact between the POM and the Vulcan surface which is evidenced by the better-defined plateaus compared to Set B. Better contact has resulted in capacities more comparable to the theoretical specific capacity as well as the capacities exhibited by the Oxidised Vulcan composites (Set A and C).

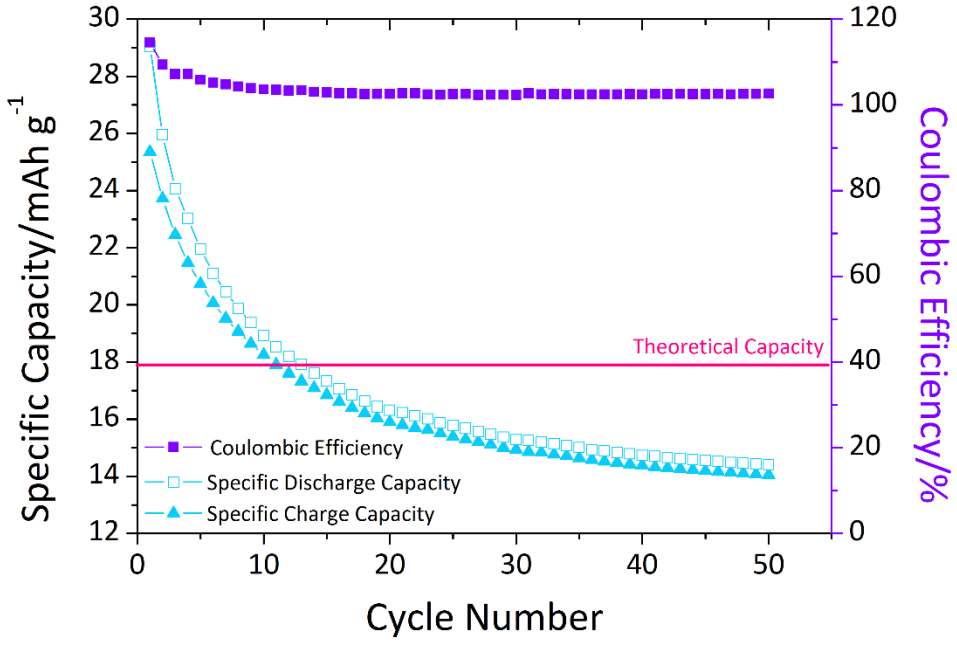


Figure 30 - Specific charge/discharge capacity and coulombic efficiency values per cycle.

The first ten charge – discharge cycles as well as the 15th, 20th, 30th, and 50th cycles are shown in Figure 31. The capacity fade with increasing cycles can be seen from the 1st charge/discharge curve (light blue trace) to the final 50th (dark green trace). Though the plateaus are better defined in this set of electrodes compared to Set B, the curves still assume a linear appearance beyond 20 cycles.

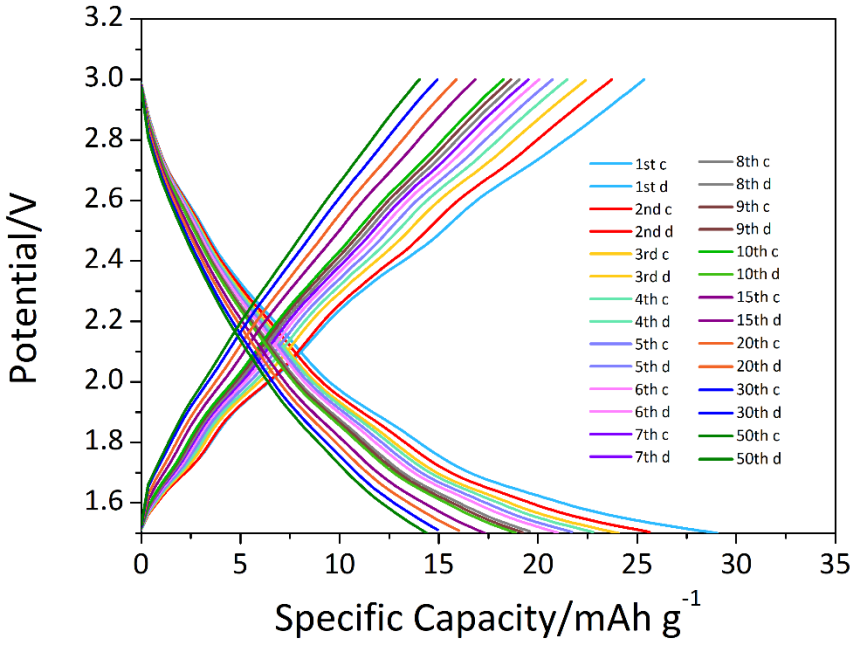


Figure 31 - First ten charge/discharge cycles as well as the 15th, 20th, 30th and 50th cycles.

Figure 32 shows the DC curve for the 1st charge/discharge curve alongside an inset for the 30th and 50th charge/discharge cycles. In the 1st charge/discharge cycle, four broad peaks can be seen. Once again, the peak between 2.2 – 2.5 V has a double hump, raising questions about the number of electrons we think are being transferred versus what is actually observed. Additionally, the corresponding discharge $\frac{dQ}{dV}$ peak in the later cycles has a drastic reduction in intensity as well as the preceding discharge $\frac{dQ}{dV}$ peak (~ 2.7 V), which looks flat (Figure 32). This indicates that the redox reactions become increasingly irreversible through progressive cycling.

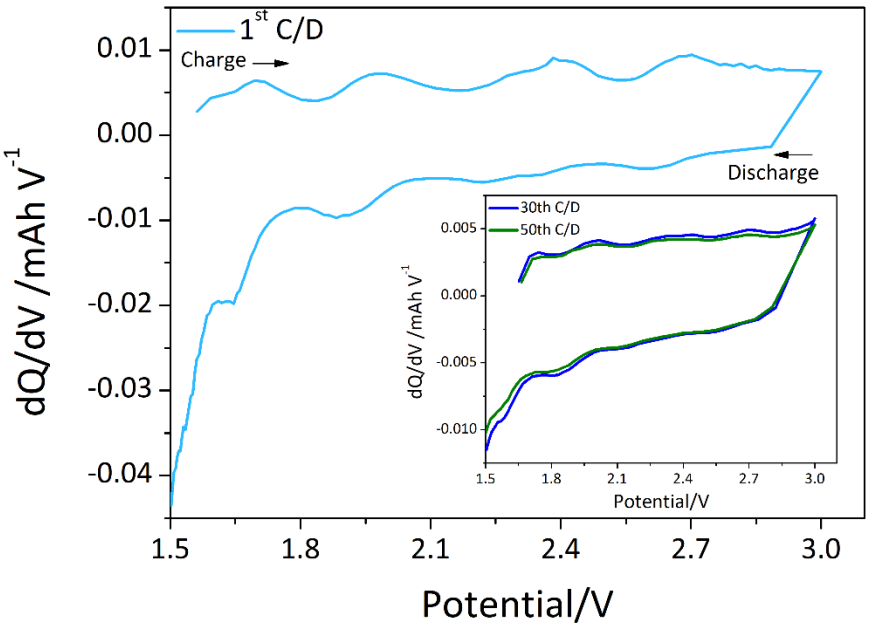


Figure 32 - Differential capacity plot, $\frac{dQ}{dV}$ *vs.* potential for the 1st charge-discharge cycle and an inset for the 30th and 50th cycle.

The effect of calendaring is evident for both Set C and Set D as their potential plateaus are much more well-defined than their uncalendared counterparts, Set A and B. Additionally the increase in capacity, particularly for Set B ({K_6W_{18}}@V), attests to the advantage of calendaring, which increases the contact between the redox active POM and its conductive support ([O]V or V) as well as the Super P additive. Calendaring can also help to eliminate any structural deformations on the surface as well as increasing contact between the coating and aluminium foil current collector. These have positive knock-on effects during the galvanostatic cycling and therefore this form of post-drying processing should be taken into consideration for future preparation of such electrodes.

Generally, for the electrodes studied, the discharge capacity is higher than the charge capacity. The discharge process involves lithiation of the POM/Vulcan materials and charge is the reverse. This means more energy is being released from the material than it has when it is charged. Therefore,

alongside the lithiation, current is likely being passed through additional processes which contribute to the discharge capacity. We hypothesise that when the POM/Vulcan electrodes are lithiated, it becomes an unstable electrode. The implication of this is that there are now several competing factors preventing all the lithium to return to the negative electrode side i.e., lithium leaching into the system, the formation of an unstable interface on the electrode which consumes lithium or parasitic side reactions. It would not be unsurprising to see these phenomena occurring in an unoptimised material and battery. Further investigation using in-situ monitoring and post-mortem analyses would be beneficial.

4.4.7 Effect of Increasing the Potential Window

Between the range of 1.5 – 3V, extra redox chemistry was accessed than predicted. Of course, experimental parameters will have an influence over the cell chemistry and cell performance. In the next set of galvanostatic measurements, electrodes from Set A and B were subjected to a constant current of 50 µA in a wider potential window between 1.5 – 4.2 V. This voltage range has previously been reported for POM-based battery systems using similar electrolyte composition.[15,18,6,46] Using a wider potential window will allow us to garner behavioural characteristics of the POM/Vulcan electrodes under conditions reported in the literature.

4.4.7.1 Charge – Discharge Cycling for Set A: $\{K_6W_{18}\}$@[O]V

Figure 33 shows the 1st and 2nd charge/discharge curve obtained for $\{K_6W_{18}\}$@[O]V as the positive electrode. Four potential plateaus are observed, in line with our observations between 1.5 – 3V. However, the fourth charge plateau (2.8 V) and 1st discharge plateau (4.1 V) are much longer than all the other plateaus and are accompanied by a sharp climb (during charge) or steep drop (during discharge) in potential. This suggests the presence of other charge storage mechanisms, not related to the active material $\{K_6W_{18}\}$.

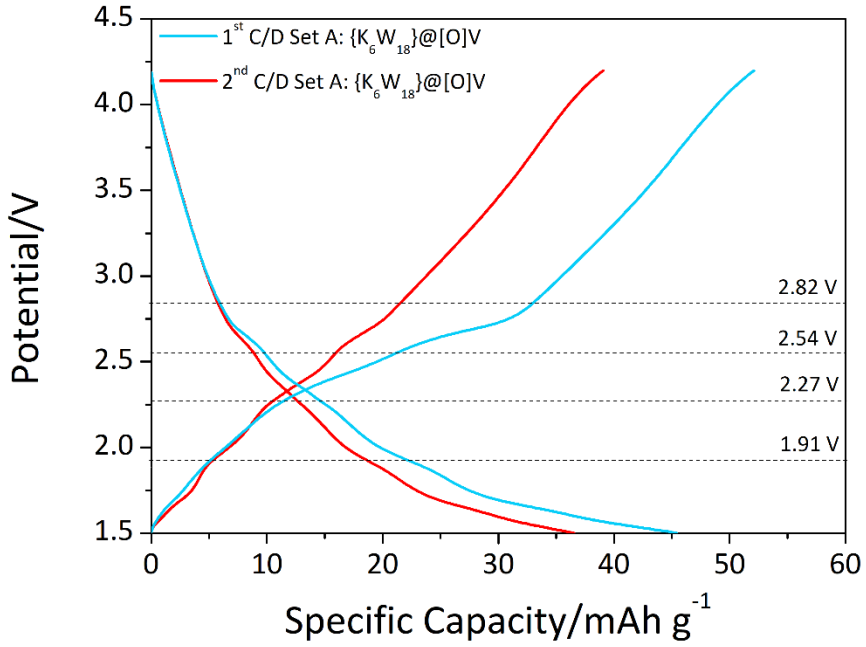


Figure 33 - 1st and 2nd charge-discharge profile for Set A in the voltage range 1.5 – 4.2 V.

If we compare this voltage profile to its corresponding $\frac{dQ}{dV}$ profile which is shown in Figure 34, we see that the chemistry occurring during the first charge does not resemble POM redox chemistry. Though this does stabilise on the 2nd charge/discharge curve, a level of complexity has been introduced following the literature protocol of increasing the potential window. By the 50th cycle, these peaks reduce into a rectangular shaped curve and so the capacity that is being recorded is not due to POM redox chemistry.

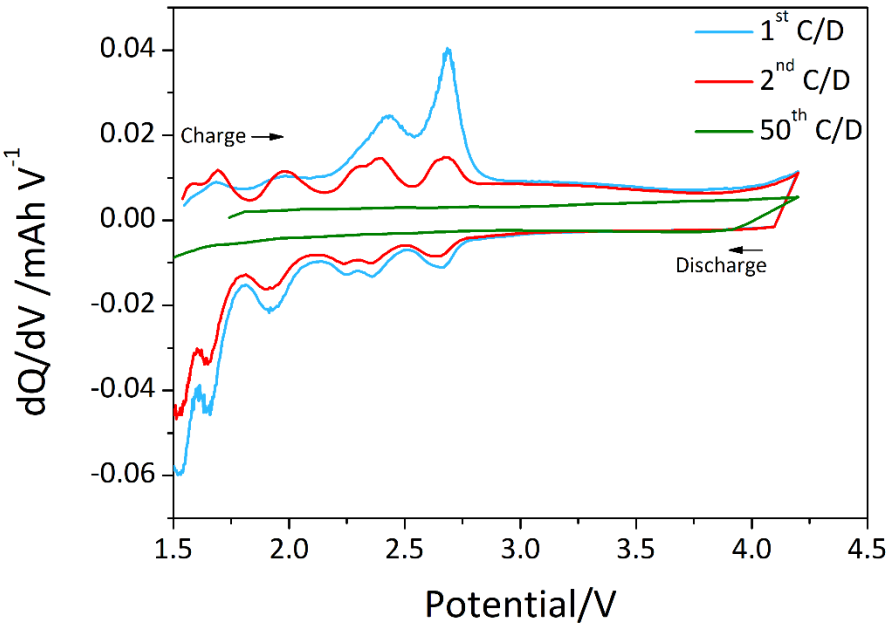


Figure 34 - Differential capacity plot, $\frac{dQ}{dV}$ *vs.* potential for the 1st, 2nd and 50th charge-discharge cycles.

The initial charge and discharge capacities are quite high, 52.1 mAh g^{-1} and 45.5 mAh g^{-1} respectively, much higher than what we have observed thus far (Figure 35). In fact, the observed capacity in these first 10 cycles is also much higher than the calculated theoretical specific capacity of 17.94 mAh g^{-1}. There are a number of caveats which concern the validity of these capacity values. Increasing the potential window has taken the system outside the realm of POM redox chemistry. The wide window has allowed for a large amount of charge to be stored on the Oxidised Vulcan support and subsequently discharged. The charge storage capabilities of the carbon support are not accounted for in the theoretical capacity calculation.

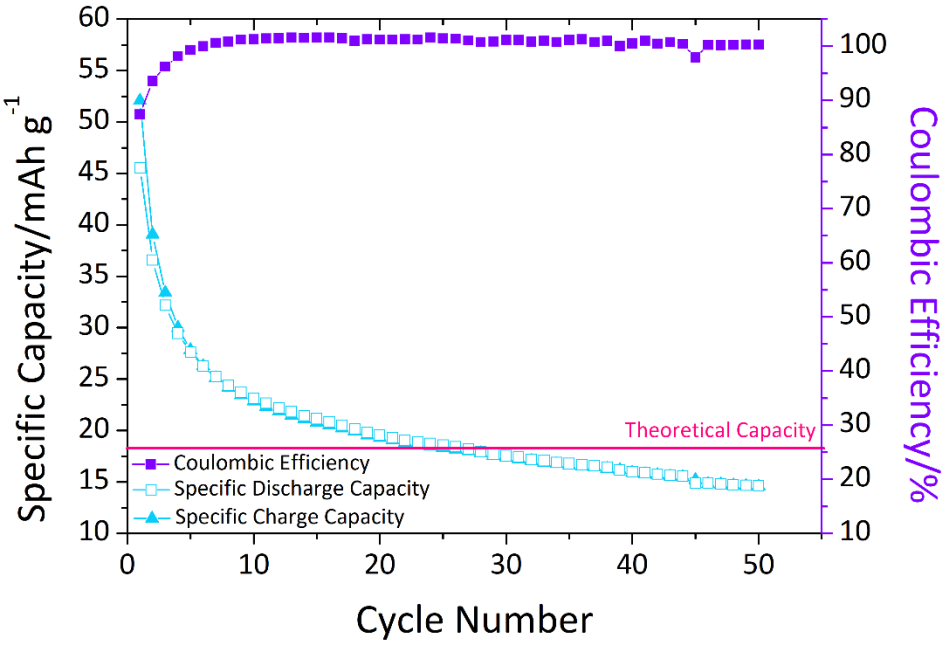


Figure 35 - Specific charge/discharge capacity and coulombic efficiency values per cycle.

Moreover, a wide potential window is desirable for the development of high energy batteries as it allows for greater flexibility with respect to bespoke and novel battery chemistries. A wide electrochemical window is an important criterion, such that electrolyte degradation should not occur within the range of the redox chemistry of interest at the positive and negative electrodes.[47] Our previous studies of the solution phase behaviour of the $\{K_6W_{18}\}$ POM in the battery solvent show that between 2.2 – 4.2 V, complex electrochemistry is observed (Figure 36). The POM redox chemistry becomes irreversible with the appearance of new peaks (marked with *), birthed from solvent induced POM degradation. At cell level, there is no evidence to suggest that the addition of Oxidised Vulcan remedies the POM stability within the region of 2.2 – 4.2 V. Thus, the observed capacity values are likely not attributable to the desired POM redox chemistry. Instead, electrons which are liberated from electrolyte degradation mechanisms or from charge stored on the Oxidised Vulcan support all contribute to the observed capacity, providing misleadingly high values. The high coulombic efficiency for the cell between 90 – 100% would suggest that

the redox reactions are reversible and stable, but as per the reasons outlined above, these values are not a true reflection of the cell performance in this case.

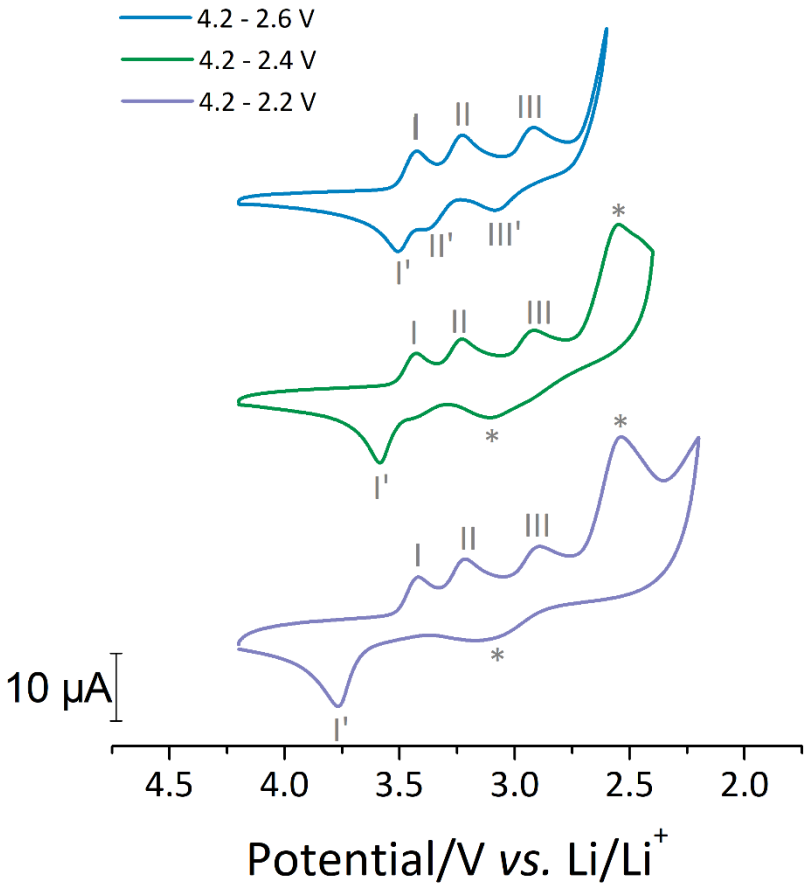


Figure 36 - Solution phase CVs for $\{K_6W_{18}\}$ in 1M $LiPF_6$ in EC/EMC showing the irreverble changes that are induced in rensponse to the potential window being increased.

The region in which the chemistry of interest is actually happening is between 1.5 V and 2.7 V, which is marked with a green dashed trace in Figure 37.

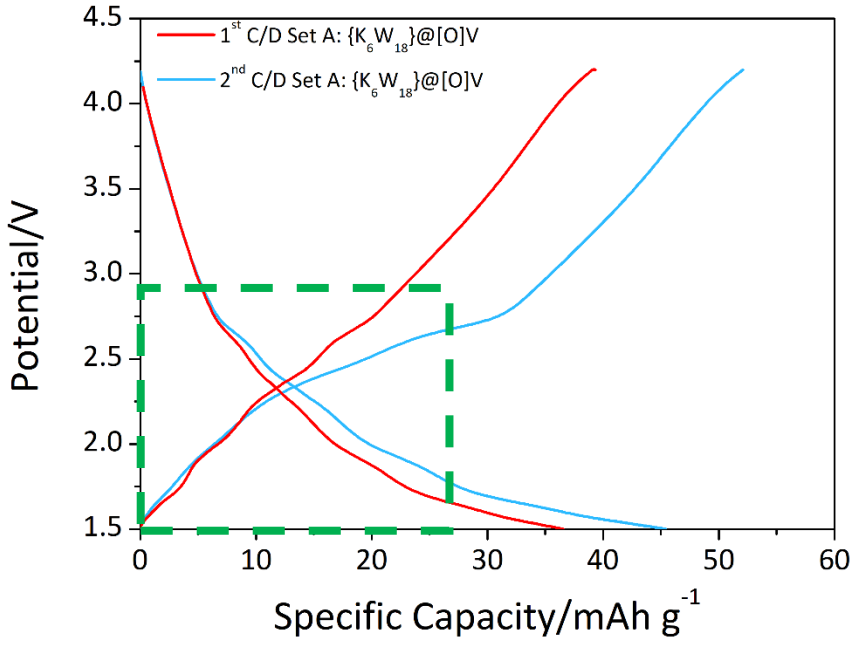


Figure 37 – Green line marks region of interest for battery testing experiments, with respect to observing clear POM redox chemistry.

4.4.7.2 Charge – Discharge Cycling for Set B

The 1st and 2nd charge/discharge curves for the Set B electrode ({K_6W_{18}@V) between 1.5 – 4.2 V are shown in Figure 38. No discernible voltage plateaus are observed, and the curves are highly linear in appearance. This is in stark contrast to the 1st charge/discharge curve for the Set B electrode cycled in the potential range of 1.5 – 3 V, where four plateaus could be detected. The linear appearance of the curves indicates low accessibility of the POMs.

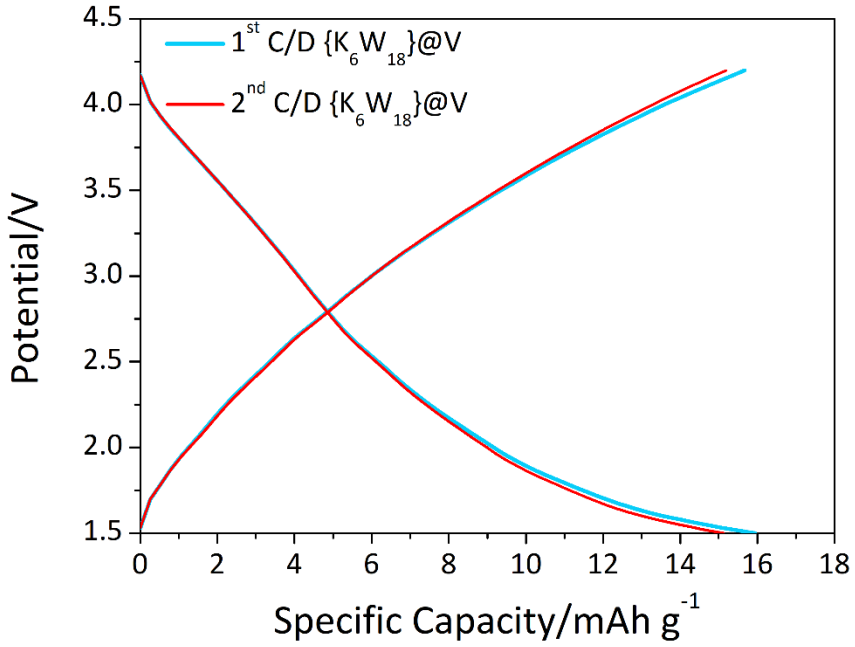


Figure 38 - 1st and 2nd charge-discharge profile for Set B in the voltage range 1.5 – 4.2 V.

The $\frac{dQ}{dV}$ show three very small peaks which quickly diminish in intensity by the final 20th cycle (Figure 39). Between 2.7 V and 4.2 V capacitive charging and discharging of the Vulcan support is occurring.

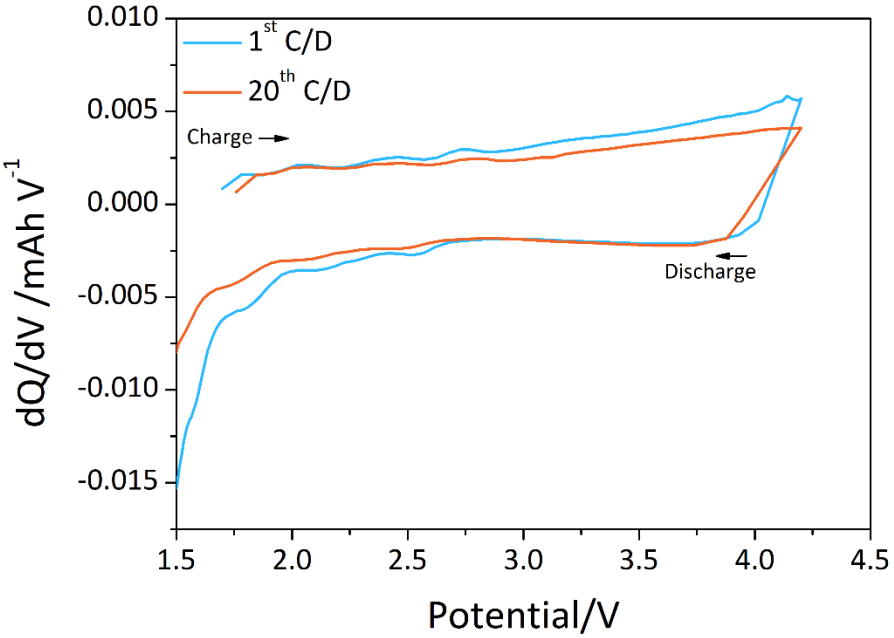


Figure 39 - Differential capacity plot, $\frac{dQ}{dV}$ *vs.* potential for the 1st and 20th charge-discharge cycle.

The maximum observed charge – discharge capacity for this system was 15.7 mAh g^{-1}/15.9 mAh g^{-1} (Figure 40). The poor performance for electrode B is multifaceted. We already know that the Vulcan support has a greater tendency to succumb to POM leaching, which is very likely to have transpired in the 2 hours resting period to galvanostatic measurements. This was alleviated to some extent by way of calendaring. We also know that within this wider potential window of study, the POMs are susceptible to degradation, introducing complexity and irreversibility to the system. This degradation coupled with the wider potential window allows capacitive charging and discharging of the Vulcan carbon support, which renders the measured capacity values ineffectual.

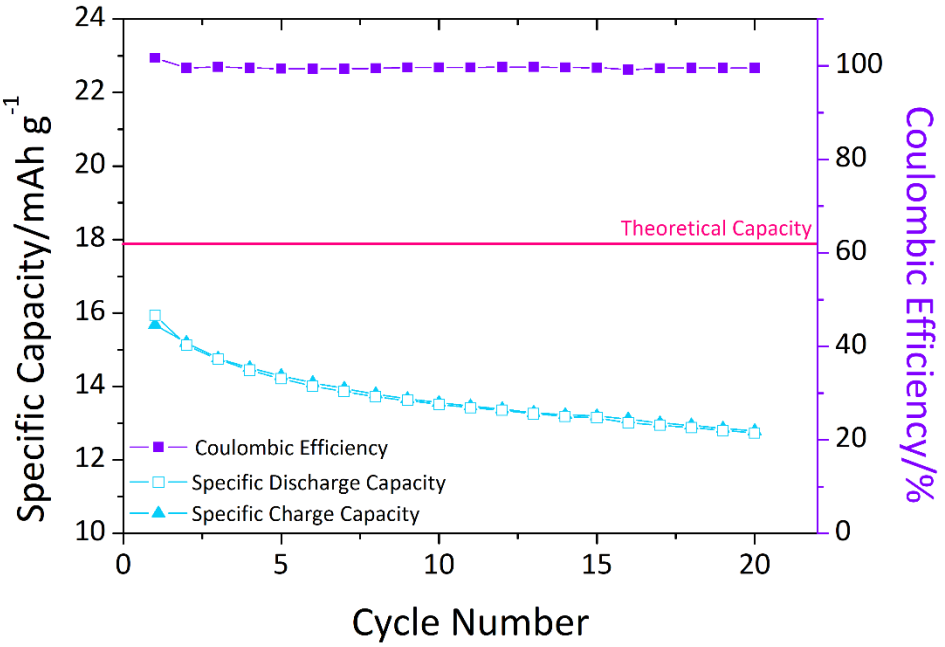


Figure 40 - Specific charge/discharge capacity and coulombic efficiency values per cycle.

4.4.8 Effect of Narrowing the Potential Window

The next set of charge – discharge curves were recorded in a narrower potential window between 2.6 – 3.8 V. This is the range in which the POM redox peaks appear in the solution phase voltammogram (Figure 3).

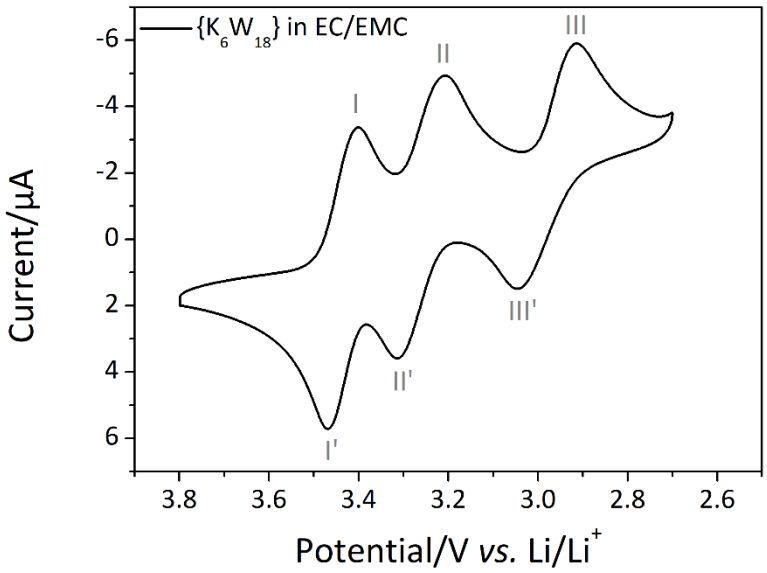


Figure 3 - CV of $\{K_6W_{18}\}$ in 1M $LiPF_6$ in EC/EMC, performed in the glovebox, using a 3 mm GC WE, Pt CE, LFP reference electrode which was then converted to Li/Li^+. The scan rate was 50 mV s^{-1}.

The charge – discharge profiles of Set A, B, C and D are shown below in Figures 41 – 44 . An inset of the $\frac{dQ}{dV}$ curves is also shown for each set of charge – discharge curves. Interestingly, no POM redox chemistry is detected in any of the sets, which is confirmed by the featureless $\frac{dQ}{dV}$ curves. As a result, the capacities observed are very low and are due to the capacitive charging and discharging of the Vulcan and Oxidised Vulcan supports. Interestingly, the calendared electrode of Set D which has $\{K_6W_{18}\}$@V as the positive electrode material exhibits the highest initial discharge capacity of 36 mAh g^{-1}. This study reiterates that it is important to choose an appropriate potential window with respect to the system of interest. In this case, it may be necessary to extend the window to lower potentials starting at 1.5 V to instigate the POM redox reactions.

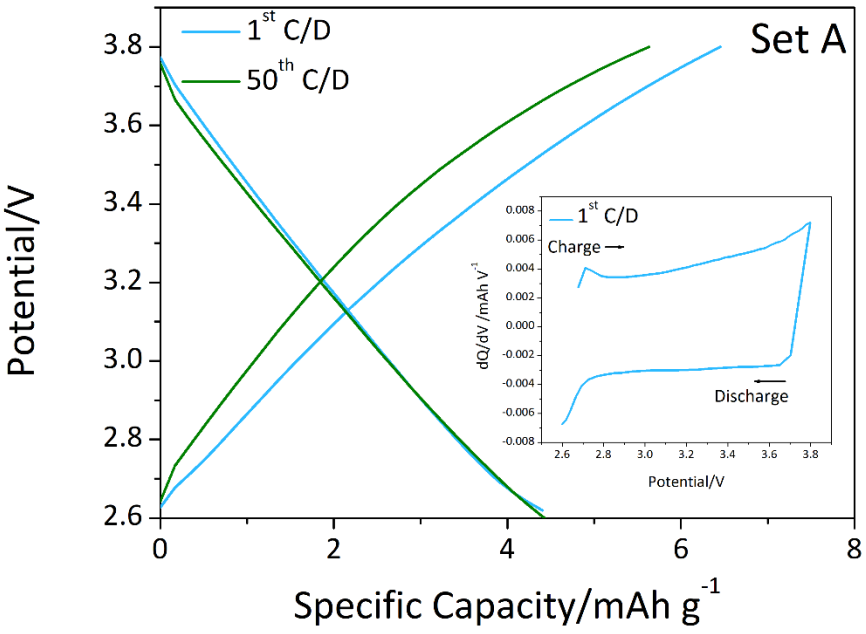


Figure 41 - 1st and 50th charge-discharge curves for Set A in the voltage range 2.6 – 3.8 V with an inset of the $\frac{dQ}{dV}$ curve for the 1st charge-discharge cycle.

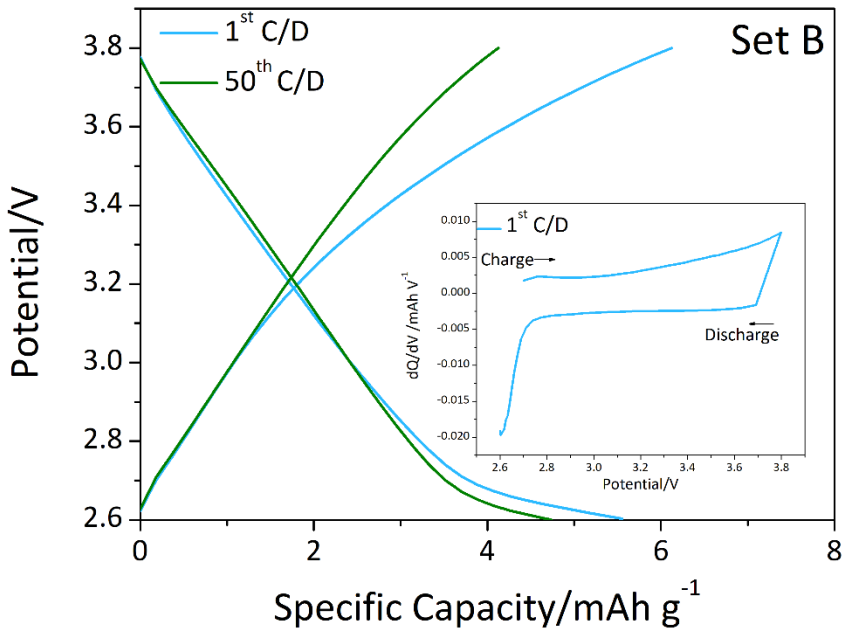


Figure 42 - 1st and 50th charge-discharge curves for Set B in the voltage range 2.6 – 3.8 V with an inset of the $\frac{dQ}{dV}$ curve for the 1st charge-discharge cycle.

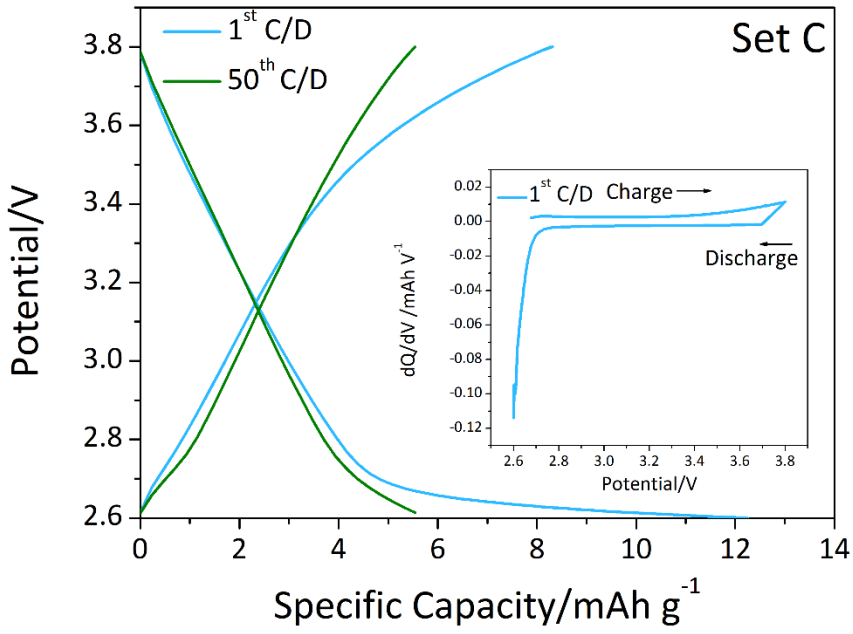


Figure 43 - 1st and 50th charge-discharge curves for Set C in the voltage range 2.6 – 3.8 V with an inset of the $\frac{dQ}{dV}$ curve for the 1st charge-discharge cycle.

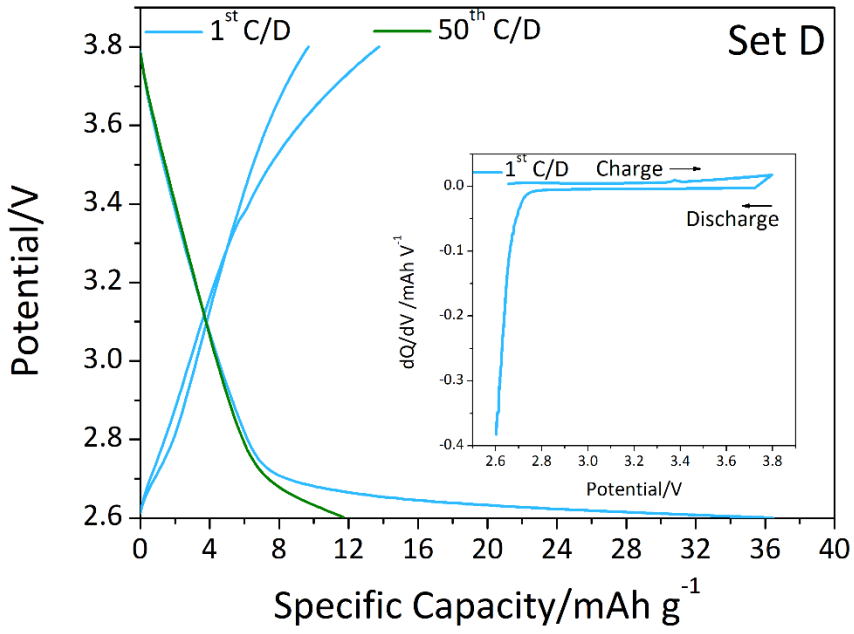


Figure 44 - 1st and 50th charge-discharge curves for Set A in the voltage range 2.6 – 3.8 V with an inset of the $\frac{dQ}{dV}$ curve for the 1st charge-discharge cycle.

4.4.9 Effect of Removing Super P

Set E and Set F electrodes were fabricated with either $\{K_6W_{18}\}$@[O]V or $\{K_6W_{18}\}$@V and PVDF binder in a weight ratio of 95:5. The electrodes were also calendared post drying. This study was conducted in order to make an assessment on the effect of removing extra additives, which will inform decisions about tailoring the electrode composition.

Solid state voltammograms were collected using the three-electrode setup as described in Figure 11. Figure 45 shows the voltammogram for Set E and Figure 46 shows the voltammogram for Set F. There does not appear to be any obvious differences between the nature of the support, as their voltammetric profiles look very similar and both show a distinct absence of well-defined POM redox peaks.

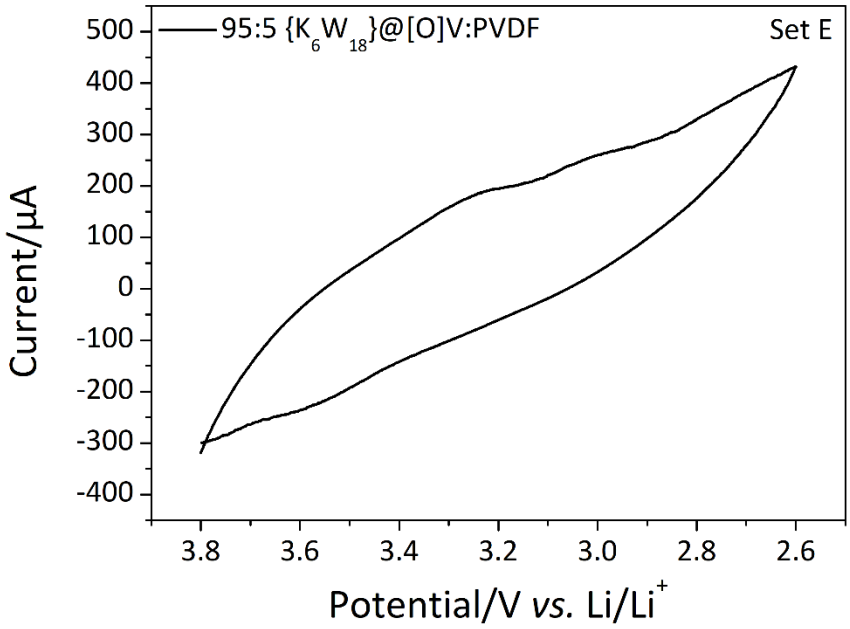


Figure 45 - Solid state disc CV of $\{K_6W_{18}\}$@[O]V Set E electrode in battery solvent, recorded in a glovebox at a scan rate of 50 mv s^{-1}.

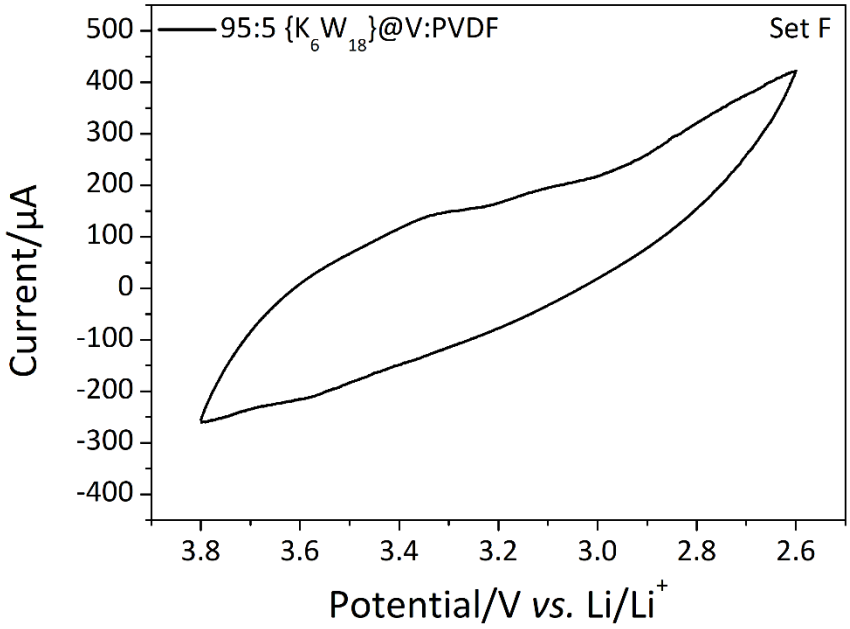


Figure 46 - Solid state disc CV of $\{K_6W_{18}\}$@V Set F electrode in battery solvent, recorded in a glovebox at a scan rate of 50 mv s^{-1}.

The corresponding 1st and 2nd charge/discharge cycles for Set E and F are shown in Figure 47 and Figure 48 respectively. Four plateaus can be discerned for each voltage profile between the range of 1.8 – 2.8 V. Due to the wider potential window used to measure these profiles, we once again see the long, continuous charge – discharge plateaus, especially beyond 2.7 V.

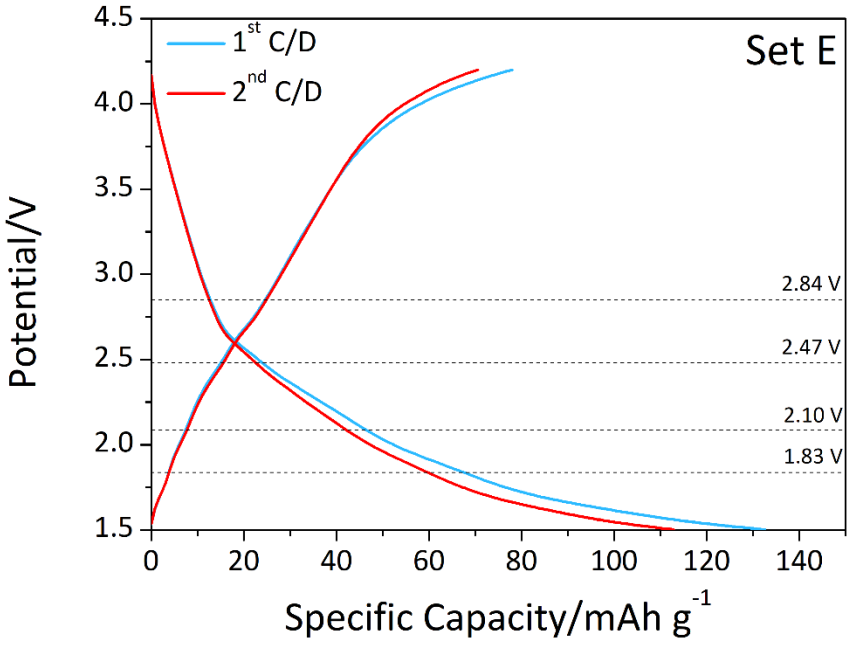


Figure 47 - 1st and 2nd charge-discharge profile for Set E in the voltage range 1.5 – 4.2 V.

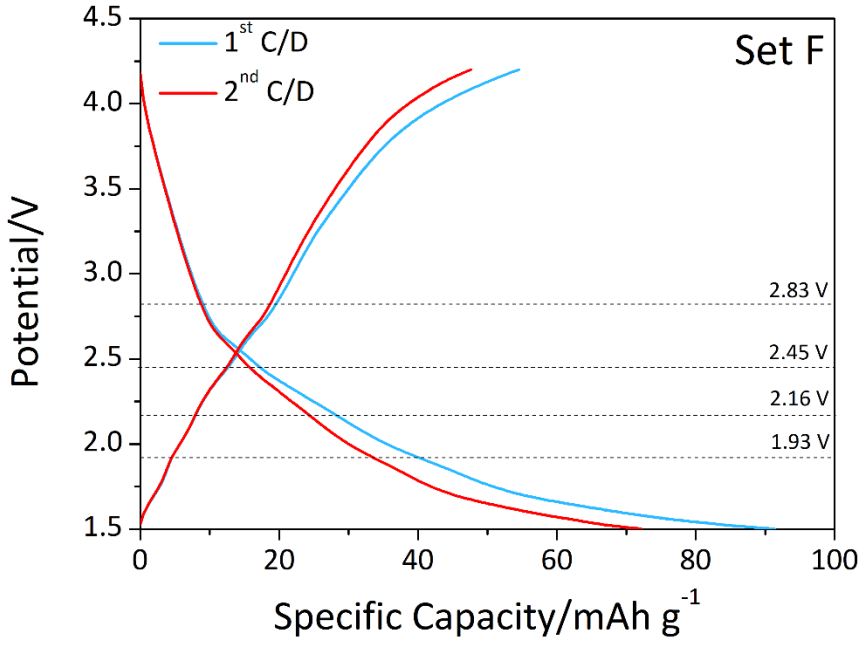


Figure 48 - 1st and 2nd charge-discharge profile for Set F in the voltage range 1.5 – 4.2 V.

What is most interesting about this electrode composition is the resultant extremely high observed capacities. The Set E electrode has an initial charge and discharge capacity of 77 mAh g^{-1} and 133 mAh $^{-1}$ (Figure 49) which is more than four and seven times greater than the theoretical specific capacity. The Set F electrode also exhibits a very large initial charge and discharge capacity of 54 mAh g^{-1} and 95 mAh g^{-1} (Figure 50). The capacities for each electrode do not decline so much that they reach the theoretical capacity, in fact the final capacity values remain at least twice as high as the theoretical capacity.

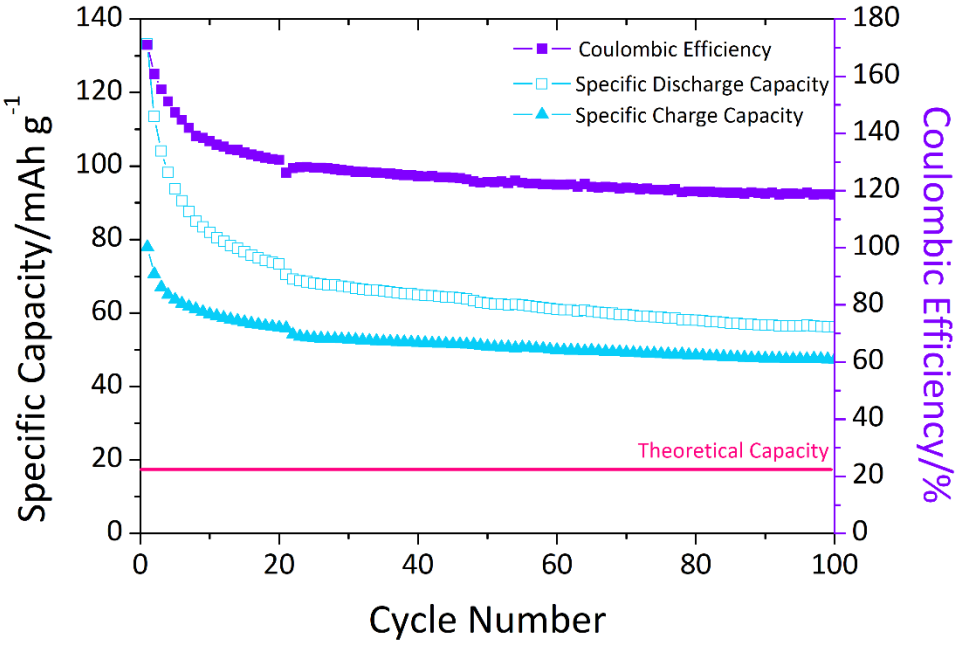


Figure 49 - Specific charge/discharge capacity and coulombic efficiency values per cycle.

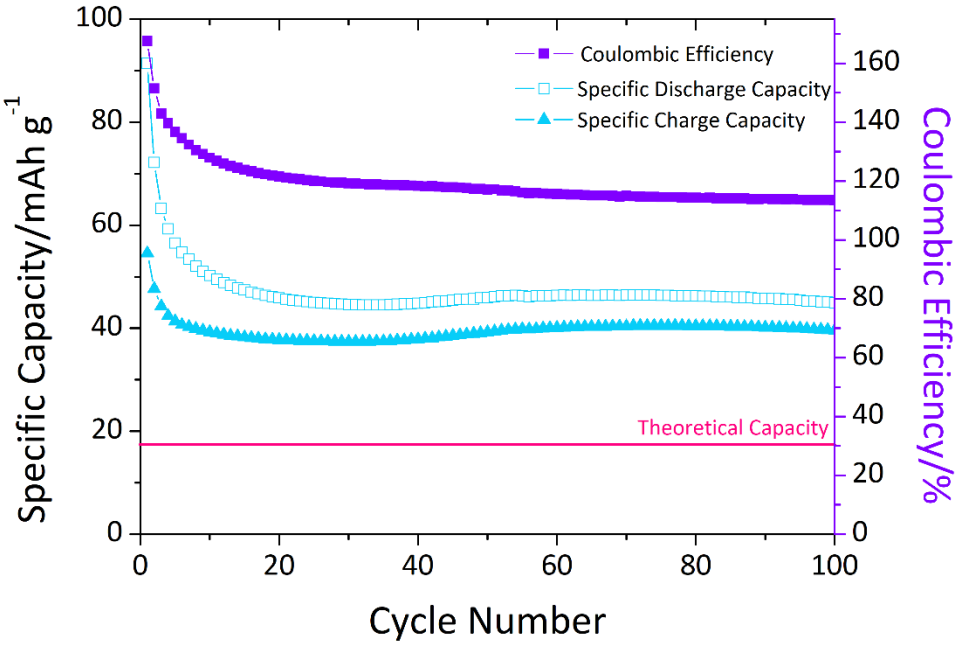


Figure 50 - Specific charge/discharge capacity and coulombic efficiency values per cycle.

Additionally, the coulombic efficiencies are consistently above 100 % which certainly demonstrates the irregular behaviour of the system. Clearly, these capacities are not related to the POM redox chemistry. Since POMs are insulating in nature, it may be predicted that the absence of a conductive additive would result in very low capacities. It appears that the absence of Super P does quash the POM redox chemistry, which is surprising as it would be expected that the Vulcan and Oxidised Vulcan supports are sufficiently conductive to relay the charge from the POM redox processes. Indeed, the suppression of the POM redox chemistry results in the capacitive characteristics of the Vulcan and Oxidised Vulcan dominating the charge – discharge measurements, thereby massively increasing the observed capacity. As we have already ascertained, the wide potential window is also a gateway to undesirable side reactions, which also contribute to the erroneous capacity and CE values. This study highlights the importance of the conductive additive to ensure the redox chemistry of interest prevails. The results pair well with the studies conducted in wide and narrow potential windows to inform future experimental design.

4.5 Conclusions & Future Work

In this chapter, a series of electrodes made from the materials of interest, $\{K_6W_{18}\}$@[O]V and $\{K_6W_{18}\}$@V were tested for their potential as positive electrodes for lithium batteries. Using a standard electrode composition and Swagelok assembly, a clear difference in the electrochemical performance was observed between Set A and Set B, continuing the trend that the Oxidised Vulcan support shows enhanced POM retention *vs.* Vulcan. This trend extends to the calendared analogues, Set C and Set D. This processing technique proved to be advantageous as it allowed for an increase in the observed capacities, making them closer to the theoretical value, most likely by enhancing the contact between the active material and its conductive support.

Between the potential window of 1.5 – 3V, from the voltage profiles and $\frac{dQ}{dV}$ curves, we see that the POM redox chemistry is reversible, achieves

capacities close to the theoretical value and generally fits the trends observed from the voltammetric studies. Interestingly, the potential plateaus occur at lower potentials than the redox waves observed from the solution phase and solid state voltammograms. This discrepancy allows for a 4th reversible redox event to take place in the cell, which was not observed in the voltammograms due to the instability of the POM in battery solvent at lower potentials, giving rise to irreversible peaks. Although the $\frac{dQ}{dV}$ curves do show that this 4th plateau in the voltage profile (1st discharge plateau and 4th charge plateau) loses intensity over time and appears flat at later cycles. The 2nd discharge process also reduces in intensity over time. Thus, it would be valuable to shorten the window further, to perhaps 1.5 – 2.7 V to investigate this phenomenon and see whether the reduced reversibility of the 2nd discharge process is coupled to that of the 1st discharge process. Additional measurements such as cyclic voltammetry of the Swagelok cell within different potential windows may provide more clarity. The use of a 'control' battery setup where only Vulcan and Oxidised Vulcan are used as the positive electrode material would provide insight to the capacities achieved in relation to the lithiation and delithiation of the carbon in the absence of POM.

Studies conducted in the potential range of 1.5 – 4.2 V show that a level of complexity is introduced into the system, stemming from a combination of the Oxidised Vulcan and Vulcan supports being charged and discharged as well as undesirable side reactions (POM degradation). The effect of narrowing the potential window to match that of the CV experiments did not show that POM redox chemistry was happening in the cell but rather capacitive charging and discharging of the Vulcan based supports was observed. These potential window studies will inform the design of future experiments of this nature.

Lastly, the plateaus on the charge curve tend to be more well – defined than their corresponding partners on the discharge curve i.e., when the POM/Vulcan material is being delithiated. This could be due to the potential window used as mentioned earlier, however the interplay between the redox chemistry of the POM and lithium has not been well characterised in the

literature. $K_6[P_2W_{18}O_{62}]$ is an open-framework material consisting of multiple individual clusters, each of which has multiple tungsten centres capable of participating in redox reactions. As such, it may have a rather different Li-ion transportation mechanism to that of conventional bulk metal oxides which poses a very interesting premise for future study.

Future work will involve investigations into enhancing the capacity by optimising the loading of POM on [O]V. For example, instead of stirring the two materials in an aqueous solution of POM, the two materials could be ball-milled instead. Ball-milling is a widely used mechanical grinding technique which does not require solvent. By controlling the particle size morphology, the POM could be even more well distributed within the [O]V matrix which may help in maintaining stable, consistently high capacities. The experiments conducted thus far provide a proof of concept that POM/Vulcan based systems can be applied as a positive electrode material for Li-metal batteries.

4.6 Experimental

Preparation of POM/Vulcan electrodes – Set A and Set B

The electrodes were prepared by mixing an 80 wt % mass of the composite material ({K_6W_{18}}@V or {K_6W_{18}@[O]V) with 10 wt % conductive Super P carbon, and 10 wt% polyvinilidenefluoride (PVDF) binder. Slurries were made by adding N-methyl-2-pyrrolidone (NMP) solvent and subsequently casted on to aluminium foil using a doctor blade. The coated Al foils were then dried at 80 °C overnight in a vacuum oven before being punched into circular electrodes, 12 mm in diameter. The electrodes were dried again in a vacuum oven at 80 °C overnight before being transferred to a dry, argon-filled glovebox.

Preparation of POM/Vulcan electrodes – Set C and Set D

The electrodes were prepared in exactly the same way as Set A and Set B, with the addition of a calendaring step prior to punching circular electrodes.

Preparation of POM/Vulcan electrodes – Set E and F

The electrodes were prepared by mixing a 95 wt % mass of the composite material ({K_6W_{18}}@V or {K_6W_{18}@[O]V) with 5 wt % of polyvinilidenefluoride (PVDF) binder with the exclusion of Super P carbon. Slurries were made by adding N-methyl-2-pyrrolidone (NMP) solvent and subsequently casted on to aluminium foil using a doctor blade. The coated Al foils were then dried at 80 °C overnight in a vacuum oven before being calendared and punched into circular electrodes, 12 mm in diameter. The electrodes were dried again in a vacuum oven at 80 °C overnight before being transferred to a dry, argon-filled glovebox.

Swagelok cell assembly

The electrochemical performance of the Set A, B, C and D positive electrodes was tested using Swagelok type cells in an argon-filled dry glovebox. Li metal foil was used as the negative electrode (also known as counter or reference electrode in a ‘half cell’). Two glass fibre discs were used as the separator. All electrodes/discs were punched to 12 mm in diameter. 120 μL of

the commercially available battery electrolyte (Merck) was used, which consisted of 1M $LiPF_6$ in a 50/50 by volume ethylene carbonate/ethyl methyl carbonate (EC/DMC, 1:1, v/v). The cells were allowed to rest for 2 hours at room temperature after assembly, in order to ensure adequate wettability of the electrodes and separation with electrolyte.

Galvanostatic Cycling

The cell cycling experiments were performed by galvanostatic charge – discharge cycling over the desired potential range at a constant applied current of 50 μA. The measurements were conducted using a computerised multi-channel battery-testing instrument from BioLogic.

4.7 References

1 Y. Miao, P. Hynan, A. Von Jouanne and A. Yokochi, Current li-ion battery technologies in electric vehicles and opportunities for advancements, *Energies*, 2019, **12**, 1074.

2 V. Etacheri, R. Marom, R. Elazari, G. Salitra and D. Aurbach, Challenges in the development of advanced Li-ion batteries: A review, *Energy Environ. Sci.*, 2011, **4**, 3243–3262.

3 M. J. Lee, S. Lee, P. Oh, Y. Kim and J. Cho, High performance $LiMn_2O_4$ cathode materials grown with epitaxial layered nanostructure for Li-Ion batteries, *Nano Lett.*, 2014, **14**, 993–999.

4 A. Yamada, S. C. Chung and K. Hinokuma, Optimized $LiFePO_4$ for Lithium Battery Cathodes, *J. Electrochem. Soc.*, 2001, **148**, A224.

5 M. Wang, W. Zhong, S. Zhang, R. Liu, J. Xing and G. Zhang, Li-ion battery materials: present and future, *J. Mater. Chem. A*, 2018, **6**, 9915–9921.

6 J.-J. Chen, M. D. Symes, S.-C. Fan, M.-S. Zheng, H. N. Miras, Q.-F. Dong and L. Cronin, High-Performance Polyoxometalate-Based Cathode Materials for Rechargeable Lithium-Ion Batteries, *Adv. Mater.*, 2015, **27**, 4649–4654.

7 K. Redel, A. Kulka, A. Plewa and J. Molenda, High-Performance Li-Rich Layered Transition Metal Oxide Cathode Materials for Li-Ion Batteries, *J. Electrochem. Soc.*, 2019, **166**, A5333–A5342.

8 Z. Gong and Y. Yang, Recent advances in the research of polyanion-type cathode materials for Li-ion batteries, *Energy Environ. Sci.*, 2011, **4**, 3223–3242.

9 Q. Li, L. Zhang, J. Dai, H. Tang, Q. Li, H. Xue and H. Pang, Polyoxometalate-based materials for advanced electrochemical energy conversion and storage, *Chem. Eng. J.*, 2018, **351**, 441–461.

10 S.-S. Wang and G.-Y. Yang, Recent Advances in Polyoxometalate-Catalyzed Reactions, *Chem. Rev.*, 2015, **115**, 4893–4962.

11 M. Wang, W. Zhong, S. Zhang, R. Liu, J. Xing and G. Zhang, An overall water-splitting polyoxometalate catalyst for the electromicrobial conversion of CO_2 in neutral water, *J. Mater. Chem. A*, 2018, **6**, 9915–9921.

12 G. N. Newton, S. Yamashita, K. Hasumi, J. Matsuno, N. Yoshida, M. Nihei, T. Shiga, M. Nakano, H. Nojiri, W. Wernsdorfer and H. Oshio, Redox-controlled magnetic $\{Mn_{13}\}$ Keggin systems, *Angew. Chemie - Int. Ed.*, 2011, **50**, 5716–5720.

13 H. Ma, B. Liu, B. Li, L. Zhang, Y. G. Li, H. Q. Tan, H. Y. Zang and G. Zhu, Cationic Covalent Organic Frameworks: A Simple Platform of Anionic Exchange for Porosity Tuning and Proton Conduction, *J. Am. Chem. Soc.*, 2016, **138**, 5897–5903.

14 N. Sonoyama, Y. Suganuma, T. Kume and Z. Quan, Lithium intercalation reaction into the Keggin type polyoxomolybdates, *J. Power Sources*, 2011, **196**, 6822–6827.

15 S. Uematsu, Z. Quan, Y. Suganuma and N. Sonoyama, Reversible lithium charge-discharge property of bi-capped Keggin-type polyoxovanadates, *J. Power Sources*, 2012, **217**, 13–20.

16 E. Ni, S. Uematsu and N. Sonoyama, Anderson type polyoxomolybdate as cathode material of lithium battery and its reaction mechanism, *J. Power Sources*, 2014, **267**, 673–681.

17 H. Yoshikawa, C. Kazama, K. Awaga, M. Satoh and J. Wada, Rechargeable molecular cluster batteries, *Chem. Commun.*, 2007, 3169.

18 H. Wang, S. Hamanaka, Y. Nishimoto, S. Irle, T. Yokoyama, H. Yoshikawa and K. Awaga, In operando X-ray absorption fine structure studies of polyoxometalate molecular cluster batteries: Polyoxometalates as electron sponges, *J. Am. Chem. Soc.*, 2012, **134**, 4918–4924.

19 A. J. Kibler and G. N. Newton, Tuning the electronic structure of organic–inorganic hybrid polyoxometalates: The crucial role of the covalent linkage, *Polyhedron*, 2018, **154**, 1–20.

20 J. Suárez-Guevara, V. Ruiz and P. Gomez-Romero, Hybrid energy storage: High voltage aqueous supercapacitors based on activated carbon-phosphotungstate hybrid materials, *J. Mater. Chem. A*, 2014, **2**, 1014–1021.

21 C. G. Lin, J. Hu and Y. F. Song, in *Advances in Inorganic Chemistry*, 2017, vol. 69, pp. 181–212.

22 J. P. Tessonnier, S. Goubert-Renaudin, S. Alia, Y. Yan and M. A. Barteau, Structure, stability, and

electronic interactions of polyoxometalates on functionalized graphene sheets, *Langmuir*, 2013, **29**, 393–402.

23 N. S. Mughal, D. A. Walsh and G. N. Newton, Functionalization of Carbon Surfaces Tunes the Redox Stability of Polyoxometalate@Carbon Electrodes, *ACS Appl. Energy Mater.*, 2020, **3**, 12308–12315.

24 J. Asenbauer, T. Eisenmann, M. Kuenzel, A. Kazzazi, Z. Chen and D. Bresser, The success story of graphite as a lithium-ion anode material-fundamentals, remaining challenges, and recent developments including silicon (oxide) composites, *Sustain. Energy Fuels*, 2020, **4**, 5387–5416.

25 C. M. Julien and A. Mauger, NCA, NCM811, and the Route to Ni-Richer Lithium-Ion Batteries, *Energies*, 2020, **13**, 6363.

26 P. Albertus, S. Babinec, S. Litzelman and A. Newman, Status and challenges in enabling the lithium metal electrode for high-energy and low-cost rechargeable batteries, *Nat. Energy*, 2018, **3**, 16–21.

27 H. Berg, *Batteries for electric vehicles: Materials and electrochemistry*, Cambridge University Press, 2015.

28 A. J. Smith and J. R. Dahn, Delta Differential Capacity Analysis, *J. Electrochem. Soc.*, 2012, **159**, A290–A293.

29 M. Safari and C. Delacourt, Aging of a Commercial Graphite/$LiFePO_4$ Cell, *J. Electrochem. Soc.*, 2011, **158**, A1123.

30 L. Zheng, J. Zhu, D. D. C. Lu, G. Wang and T. He, Incremental capacity analysis and differential voltage analysis based state of charge and capacity estimation for lithium-ion batteries, *Energy*, 2018, **150**, 759–769.

31 J. Zhu, M. S. Dewi Darma, M. Knapp, D. R. Sørensen, M. Heere, Q. Fang, X. Wang, H. Dai, L. Mereacre, A. Senyshyn, X. Wei and H. Ehrenberg, Investigation of lithium-ion battery degradation mechanisms by combining differential voltage analysis and alternating current impedance, *J. Power Sources*, 2020, **448**, 227575.

32 D. Guo, G. Yang, G. Zhao, M. Yi, X. Feng, X. Han, L. Lu and M. Ouyang, Determination of the differential capacity of lithium-ion batteries by the deconvolution of electrochemical impedance spectra, *Energies*, 2020, **13**, 915.

33 J. Li, J. Harlow, N. Stakheiko, N. Zhang, J. Paulsen and J. Dahn, Dependence of Cell Failure on Cut-Off Voltage Ranges and Observation of Kinetic Hindrance in $LiNi_{0.8}Co_{0.15}Al_{0.05}O_2$, *J. Electrochem. Soc.*, 2018, **165**, A2682–A2695.

34 A. Tomaszewska, Z. Chu, X. Feng, S. O'Kane, X. Liu, J. Chen, C. Ji, E. Endler, R. Li, L. Liu, Y. Li, S. Zheng, S. Vetterlein, M. Gao, J. Du, M. Parkes, M. Ouyang, M. Marinescu, G. Offer and B. Wu, Lithium-ion battery fast charging: A review, *eTransportation*, 2019, **1**, 100011.

35 J. Cabana, B. J. Kwon and L. Hu, Mechanisms of Degradation and Strategies for the Stabilization of Cathode-Electrolyte Interfaces in Li-Ion Batteries, *Acc. Chem. Res.*, 2018, **51**, 299–308.

36 S. K. Heiskanen, J. Kim and B. L. Lucht, Generation and Evolution of the Solid Electrolyte Interphase of Lithium-Ion Batteries, *Joule*, 2019, **3**, 2322–2333.

37 J. Xiao, Q. Li, Y. Bi, M. Cai, B. Dunn, T. Glossmann, J. Liu, T. Osaka, R. Sugiura, B. Wu, J. Yang, J. G. Zhang and M. S. Whittingham, Understanding and applying coulombic efficiency in lithium metal batteries, *Nat. Energy*, 2020, **5**, 561–568.

38 D. Aurbach, B. Markovsky, I. Weissman, E. Levi and Y. Ein-Eli, On the correlation between surface chemistry and performance of graphite negative electrodes for Li ion batteries, *Electrochim. Acta*, 1999, **45**, 67–86.

39 P. Verma, P. Maire and P. Novák, A review of the features and analyses of the solid electrolyte interphase in Li-ion batteries, *Electrochim. Acta*, 2010, **55**, 6332–6341.

40 J. Henschel, C. Peschel, S. Klein, F. Horsthemke, M. Winter and S. Nowak, Clarification of Decomposition Pathways in a State-of-the-Art Lithium Ion Battery Electrolyte through ^{13}C-Labeling of Electrolyte Components, *Angew. Chemie - Int. Ed.*, 2020, **59**, 6128–6137.

41 N. L. Hamidah, F. M. Wang and G. Nugroho, The understanding of solid electrolyte interface (SEI) formation and mechanism as the effect of flouro-o-phenylenedimaleimaide (F-MI) additive on lithium-ion battery, *Surf. Interface Anal.*, 2019, **51**, 345–352.

42 W. Xu, J. Wang, F. Ding, X. Chen, E. Nasybulin, Y. Zhang and J. G. Zhang, Lithium metal anodes for rechargeable batteries, *Energy Environ. Sci.*, 2014, **7**, 513–537.

43 A. van Bommel and R. Divigalpitiya, Effect of Calendering $LiFePO_4$ Electrodes, *J. Electrochem. Soc.*, 2012, **159**, A1791–A1795.

44 W. Lu, A. Jansen, D. Dees and G. Henriksen, Olivine electrode engineering impact on the electrochemical performance of lithium-ion batteries, *J. Mater. Res.*, 2010, **25**, 1656–1660.

45 S. Chen, C. Niu, H. Lee, Q. Li, L. Yu, W. Xu, J. G. Zhang, E. J. Dufek, M. S. Whittingham, S. Meng, J. Xiao and J. Liu, Critical Parameters for Evaluating Coin Cells and Pouch Cells of Rechargeable Li-Metal Batteries, *Joule*, 2019, **3**, 1094–1105.

46 M. Priyadarshini, S. Shanmugan, K. P. Kirubakaran, A. Thomas, M. Prakash, C. Senthil, C. W. Lee and K. Vediappan, High energy storage of Li-ions on keggin-type polyoxometalate as electrodes for rechargeable lithium batteries, *J. Phys. Chem. Solids*, 2020, **142**, 109468.

47 Q. Li, J. Chen, L. Fan, X. Kong and Y. Lu, Progress in electrolytes for rechargeable Li-based batteries and beyond, *Green Energy Environ.*, 2016, **1**, 18–42.

5. Dimensionally Controlled Polyoxometalate Impregnated Activated Carbons

5.1 Introduction

Polyoxometalates are at the crux of many application-driven material design strategies and so, the heterogenisation of POMs has been reported using a whole host of immobilisation techniques on a variety of functional substrates.[1,2,3] This is because POMs possess a unique range of physiochemical properties including cation-controlled solubility in aqueous and organic solvents, high redox activity, photoactivity in the UV and near-visible region, high Bronsted acidity, oxygen transfer capability and chemical tunability via structural modification.[4,5] Though early research was focused on homogeneous catalysis, the heterogenisation of POMs allows for their unique properties to be incorporated into a functional substrate to create a synergistic material specifically tailored for the application, for example catalyst recoverability.

In the context of electrochemical energy storage, it is necessary to anchor POMs onto a conductive surface to hone their electrochemical properties, as they are intrinsically insulating. Additionally, POMs are soluble in a wide variety of solvents and so leaching of the redox active material must be prevented by immobilisation. The development of hybrid nanocomposite materials which could combine faradaic and double-layer capacities are favoured for future devices with improved energy and power densities. As such, combinations of carbon and oxides seem especially well-suited to the task since they could provide the right mixture of double-layer and faradaic activities.

Electrochemical Capacitors (EC) are one such avenue for the aforementioned materials. ECs have emerged as attractive electrochemical energy storage devices, owing to their high-power capability, long cycle life, and

simple operation. There are two primary categories of ECs, (i) Electrochemical Double Layer Capacitors (EDLCs) which store charge through reversible adsorption of ions from the electrolyte and (ii) pseudocapacitors which store charge through reversible surface redox reactions which occur at the interface between the electrode and the electrolyte. For the former, different kinds of (nano)carbon species e.g. activated carbon, carbon nanotubes, and graphene have been used due to their high electrical conductivities, wide availability and tuneable morphologies.[6,7,8,9] Regarding the latter, pseudocapacitive materials include but are not limited to transition metal oxides[10] or chalcogenides[10] (RuO_2 and MoS_2) or conductive polymers such as polyaniline[11] and polypyrrole[12].

However, if used individually, each of these components suffers from particular disadvantages that preclude their optimal implementation into supercapacitive devices. For example, porous carbon materials exhibit a wide pore size distribution, and it is important that the pores of the electrode material match the size of the electrolyte ions to avoid ion-sieving effects. Whereas metal oxides suffer from low electronic conductivity. Therefore, a practical way to overcome these limitations lies in the synergistic combination of two or more of the above components. This hybrid material can combine both the EDL and the pseudocapacitive energy storage mechanisms to form an enhanced supercapacitor. The rapid and reversible multi-electron transfer demonstrated by POMs makes them well-suited for pseudocapacitance and consequently there have been several reports on the use of POMs for EC applications.[13,14,15,16]

Porous carbon materials have long been of scientific interest as they can interact with atoms, ions, molecules and supramolecules.[17] Activated carbons are perhaps the most widely explored class of porous carbons, due to their array of advantageous properties. These include high specific surface area, chemical inertness, high conductivity and capacitance, good thermal stability and low cost of starting materials. Typically, activated carbons have been employed for use as catalyst supports and adsorbents. However they have now burgeoned for use in energy storage, especially for applications that require constrained space or pores for ion access such as electrode materials.[18]

Several examples of POMs supported on ACs exist in the literature, with a view towards catalysis and capacitor electrodes. Frenzel et al. prepared a series of transition metal substituted Keggins supported on activated carbon using the incipient wetness method. The Keggin anion, ($[PW_{11}O_{39}M(H_2O)]^{5-}$, where M= Ni^{2+},Co^{2+},Cu^{2+}, Zn^{2+}) served as the catalyst for the sulfoxidation of 2-(methylthio)-benzothiazole (2-MTBT), an emerging environmental pollutant. They showed that the activated carbon efficiently entrapped the Keggin moieties such that the Keggin-AC catalyst could be used for the liquid phase sulfoxidation of 2-MTBT. Due to the heterogeneous nature of the system, they found that the Keggin-AC catalyst could be easily separated and reused without appreciable loss of the catalytic activity at least three times.[19]

Gomez Romero et al. explored the use of phosphotungstic acid $H_3PW_{12}O_{40}$ supported on activated carbon to form hybrid supercapacitor electrodes.[20,21] Their approach involved a 24-hour sonication of a 10mM aqueous solution of $H_3PW_{12}O_{40}$ with a commercial activated carbon (DLC Super 30) to form a hybrid material. The POMs adsorbed onto the activated carbon surface was found to be beneficial in several ways; increased capacitance and operating voltage of the symmetrical supercapacitor cells when compared to just the commercial activated carbon. The hybrid material also proved to be robust as the presence of the adsorbed POMs provided protection towards irreversible oxidation of the carbon matrix, leading to longer-lasting cells with excellent cyclability.[21]

Genovese et al. used a similar adsorption technique however they prepared their own activated carbons using pinecone biochar. Biochar activated carbon which is produced from the pyrolysis of inexpensive biomass feedstock such as rice husk, wood, agricultural residues, etc. has been studied as an EDLC material.[22,23,24] The parent biomass material imparts a natural porous template to the biochar carbon and this can be further modified via chemical activation.[25,26] They found that POM adsorption was greatly favoured within the carbon matrix that had micropores in the 1-2 nm range. Additionally, the POM

was homogeneously dispersed within the material resulting in a high POM loading, such that the areal capacitance of the hybrid material was 2.5 times greater than that of just the activated carbon.

Additional hybrid materials, which involve the entrapment of POM moieties in metal organic frameworks (MOFs)[27] and CNT networks with molecular cages[28] have also been reported. This chapter will explore the possibility of entrapment of POM clusters within the pores of activated carbon. This strategy is discussed further below.

5.2 Approach

Many different feedstocks can be used in the production of activated carbons and the properties of the resultant activated carbon can be influenced by the nature of the precursor used. Structurally, the AC can be classified into microporous, mesoporous and macroporous solids with pore sizes of <20 Å, between 20-500 Å and larger than 500 Å, respectively. Synthetic pathways to porous solids are manifold and often depend strongly on the targeted product.

Traditionally, two different methods can be used to prepare activated carbons; physical or chemical activation. Physical activation involves different oxidising gases such as air, O_2, CO_2, steam or a mixture. A two-step heating process is implemented where the first step is pyrolysis of the precursor in an inert atmosphere between 400-900 ºC. The porosity and surface area are developed during the second step with a flow of oxidising gas over the sample at the activation temperature (350-1000 ºC). In contrast, chemical activation is a one-step heating process where the precursor is mixed with an activating agent (an acid, strong base or a salt) and then heated to the activation temperature (450-900 ºC).[18] The main advantage of chemical activation over physical activation is that there is only one heating step and the temperature required is typically lower. Additionally, the ratio of activating agent to precursor and the activation temperature can both be altered to tailor the properties of the activated carbon.

Hydrothermal Carbonisation (HTC) is also a well-recognised alternative thermochemical synthetic route to produce functional activated carbon materials with a tuneable chemical structure and ultra-high surface area.[29] HTC involves heating an aqueous mixture of the precursor in an autoclave between 200-250 ºC. The autoclave allows the solution to undergo an autogenous increase in pressure as the temperature rises. The resulting carbonaceous material (hydrochar) is not typically porous, however chemical activation of the hydrochar can often elicit the formation of activated carbons with greater porosity than those formed by direct chemical activation.[30]

The approach used in this study was to introduce the POM during the chemical activation process of the cellulose acetate derived hydrochar. Knowing that the dimensions of the Keggin and Wells-Dawson anions are between 1 – 1.2 nm respectively, we hypothesised that the presence of POMs during the activation process would force the pore formation around the POM moieties, creating a network of POM-occupied pores. Additionally as we saw from the preliminary study in Chapter 3, the acid analogues of the Keggin and Dawson do have some oxidative influence on to the Vulcan support.

The design of the chemical activation experiment implemented in this study was rationalised with various conditions. Instead of direct chemical activation, the activation would proceed via hydrothermal carbonisation (HTC) prior to chemical activation to maximise porosity. Among the potential precursors that can be employed for HTC, cellulosic materials are the most promising as they are by far the most abundant and inexpensive saccharides available.[30] The chosen starting material was cellulose acetate to produce hydrochar prior to chemical activation.

With respect to the chemical activating agent, KOH is the leading choice for the production of highly porous carbons, routinely achieving BET surface areas in excess of 2500–3000 $m^2 g^{-1}$, along with a relatively well-controlled pore size distribution (PSD).[31] Despite these favourable properties, the fact remains that it is highly corrosive and toxic. Additionally, POMs are subject to degradation under strongly basic conditions. Therefore, potassium oxalate

($K_2C_2O_4$) was chosen as a mildly basic and less corrosive chemical activating agent.[32] The ratio of activating agent to hydrochar is also an important consideration. Generally, as the amount of activating agent increases, the surface area and pore volume also increase but at the expense of a widened PSD.

Using hydrochar can enable the design of ultra-high surface area activated carbons, with pore structures that can be customised to accommodate molecular modifiers such as POMs. The manipulation of preparation parameters also allows for versatility in the design of the desired porous solid. A notable concept of this can be referred to as template synthesis. Many templating strategies have already been developed for producing porous materials such as microporous zeolites[33], ordered mesoporous silicas[34] and nanoparticle templates for mesoporous carbons.[35]

The synthesis of activated carbons is manifold and thus ideally only one experimental parameter should be modified each time in order to observe clear trends. Several ratios and parameters were tested but for the sake of clarity and completeness, only a few examples are detailed in this chapter. Ratios of activating agent (AA) to hydrochar (HC) to polyoxometalate (POM) included 4.5:1:0.5 and 2:1:1. Potassium oxalate ($K_2C_2O_4$) was the primary activating agent and activation temperatures of 750 °C and 500 °C were explored.

5.3 Aims

This study will look at whether the principles of template synthesis can be applied to design polyoxometalate-activated carbon composite materials. This is a novel approach for the preparation of structurally-sound electrode materials, with confinement of redox active moieties. Such an approach could assure materials with high cycling capacity due to reduced dissolution of active material.

Two different POMs ($H_3PW_{12}O_{40}$ and $H_6P_2W_{18}O_{62}$) were introduced as an additional component in the chemical activation process of cellulose-derived hydrochar. The presence of the POM could either be co-activating or inhibitive.

The POM-activated carbon materials will be characterised and compared to the parent activated carbon and to see whether the electrochemical properties of the POM are retained within the composite POM-activated carbon material. The principal aim of this study is to investigate the in-situ carbonisation of POMs as a potential methodology for the synthesis of dimensionally controlled AC frameworks impregnated with a redox-active species with its electrochemistry intact. Figure 1 depicts the two-step synthetic procedure.

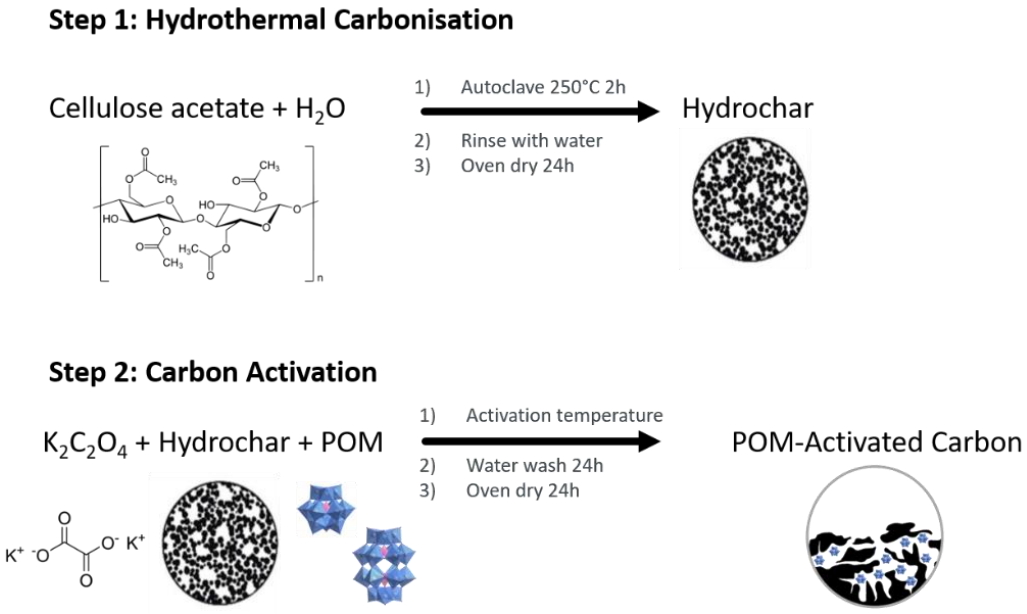


Figure 1- Synthetic approach to making dimensionally – controlled POM@AC composites using hydrothermal carbonisation as a precursor.

5.4 Results & Discussion

5.4.1 Preliminary Characterisation

5.4.1.1 Thermal Characterisation of $\{H_3W_{12}\}$ and $\{H_6W_{18}\}$

The thermogravimetric analyses of the two POMs indicate that their thermal decomposition is a multi-step process (Figure 2). At first, the Keggin and Dawson phosphotungstates lose water molecules below 200 °C. No significant mass losses are observed beyond 200 °C and the final weight % residues for the Keggin and Dawson is 93.6 % and 96.4 % respectively. However, beyond 600 °C, the POMs could also undergo structural rearrangement to generate new phases

that would not necessarily constitute a weight loss. The assignment of these last structures is difficult, since WO_3 and P_2O_5 are able to combine in multiple proportions.[36] It is important to note that WO_3 is not redox active and so experimental parameters must be chosen judiciously to retain the redox activity of the plenary structure.

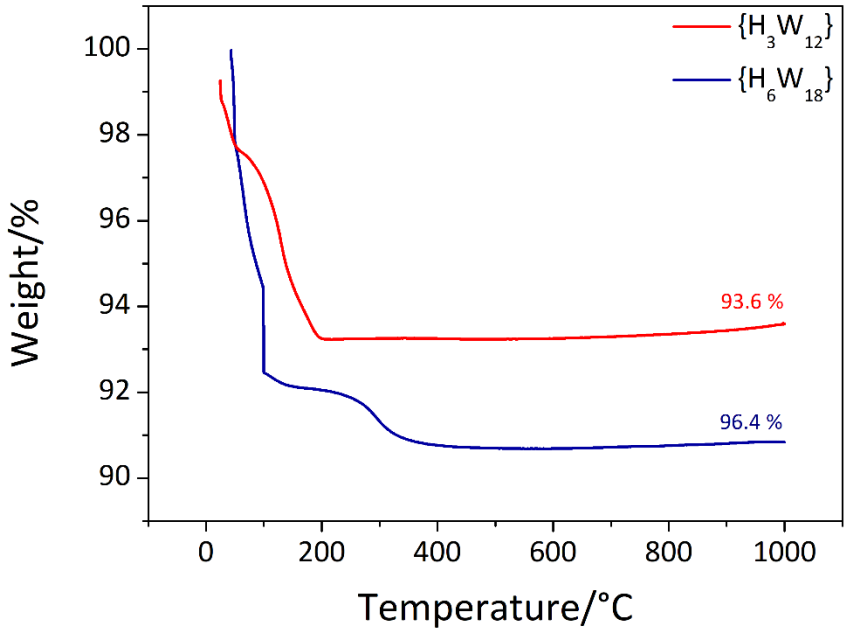


Figure 2 – TG curves for $\{H_3W_{12}\}$ and $\{H_6W_{18}\}$, showing the onset temperature of their mass loss events and the approximate weight percent residue.

These analyses state that the Keggin and Dawson phosphotungstates remain intact until around 600 °C. It was hypothesised that if the carbon pores formed around the POMs during the ramp up to the activation temperature of 750 °C, they would be somewhat shielded, causing a delay in the onset of their degradation to their corresponding metal oxides.

5.4.1.2 Infrared Spectroscopy of $\{H_3W_{12}\}$, $\{H_6W_{18}\}$ and Hydrochar

Sidgwick[37] describes four types of addendum-oxygen connections that are responsible for the appearance of peaks in polyoxometalates:

- O_a – oxygen atoms which bridge the heteroatom, X and the addendum metal, M;

- O_b – oxygen atoms which bridge two addenda metal atoms, M, located in two different sets of triplets M_3O_{13};
- O_c – oxygen atoms which bridge two addenda atoms within the same triplet M_3O_{13};
- O_d – terminal double bond oxygen atoms belonging to the MO_6 octahedron.

The IR spectra of POMs shows several characteristic metal–oxygen vibrational modes in the 1100 – 700 cm^{-1} range: terminal W = O_d bonds, 955 – 970 cm^{-1}; W-O-W bridge bonds appear on a wider range, 735 – 970 cm^{-1}, as there are several types of such bonds; P-O bond in tungsten complexes appear around 1080 cm^{-1}. The spectra of $\{H_3W_{12}\}$ and $\{H_6W_{18}\}$ are shown below.

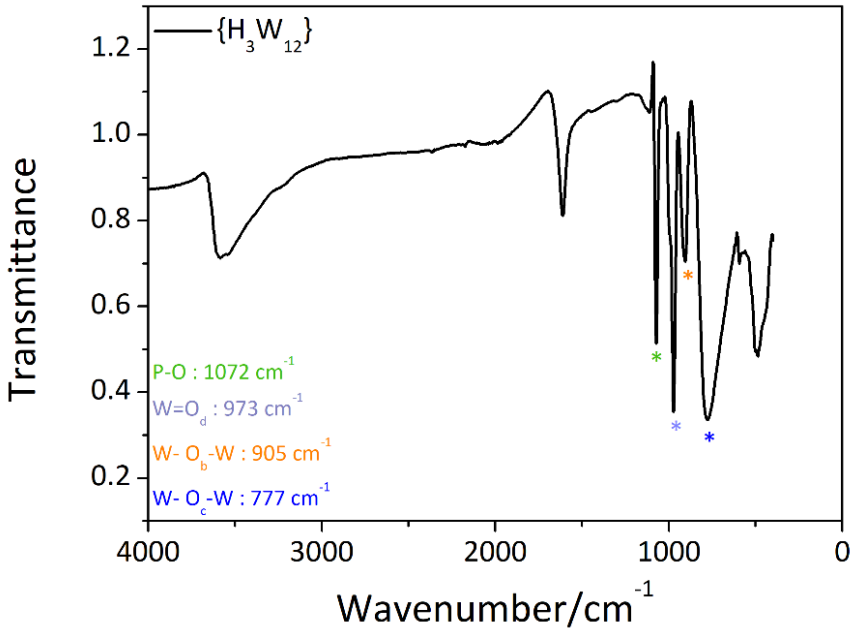


Figure 3 – IR spectrum showing the characteristic absorption signals of $\{H_3W_{12}\}$.

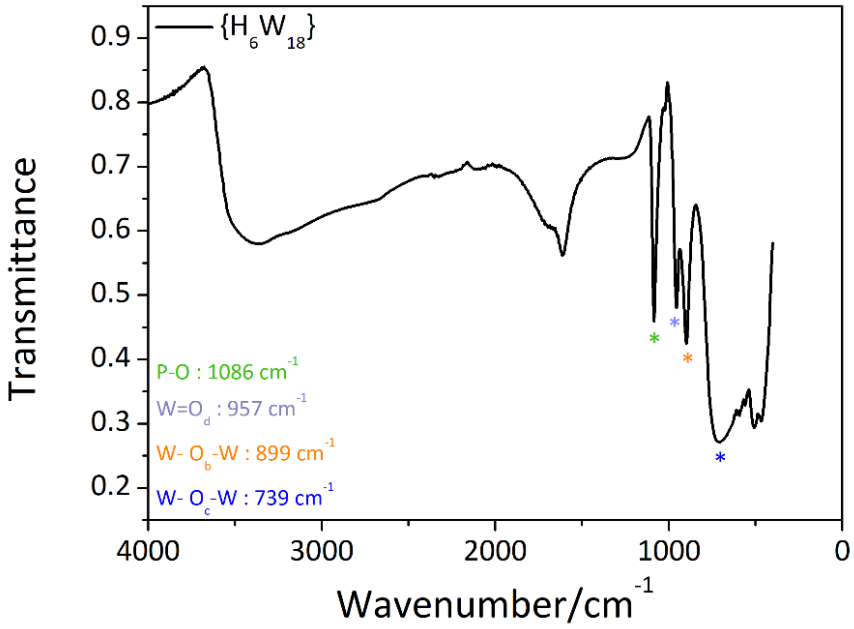


Figure 4 - IR spectrum showing the characteristic absorption signals of $\{H_6W_{18}\}$.

The IR spectrum for the cellulose acetate derived hydrochar prepared at 250 °C shows a variety of functional groups and evidence for aromatisation (Figure 5). The assignments of these groups is based on previous studies.[38,39] The broad peak between 3600 and 3000 cm^{-1} (section 1) corresponds to the stretching vibration of O–H hydroxyl and carboxyl groups. The peaks between 3000 and 2800 cm^{-1} are due to stretching vibrations of aliphatic C–H bonds, indicating the presence of aliphatic structures (section 2). The peaks between 1800 and 1650 cm^{-1} present in the hydrochar result from C=O carbonyl stretches of esters, carboxylic acids, aldehydes or ketones as well as C=C vibrations (section 3). Meanwhile the peaks between 1500 and 1000 cm^{-1} correspond to C–O vibrations from esters, ethers, phenols, and aliphatic alcohols (section 4). The well-defined peak below 1000 cm^{-1} (section 5) arises from the deformation of C–H out-of-plane bending vibrations in aromatic compounds. Overall, the spectrum is complex and has a variety of functional groups.

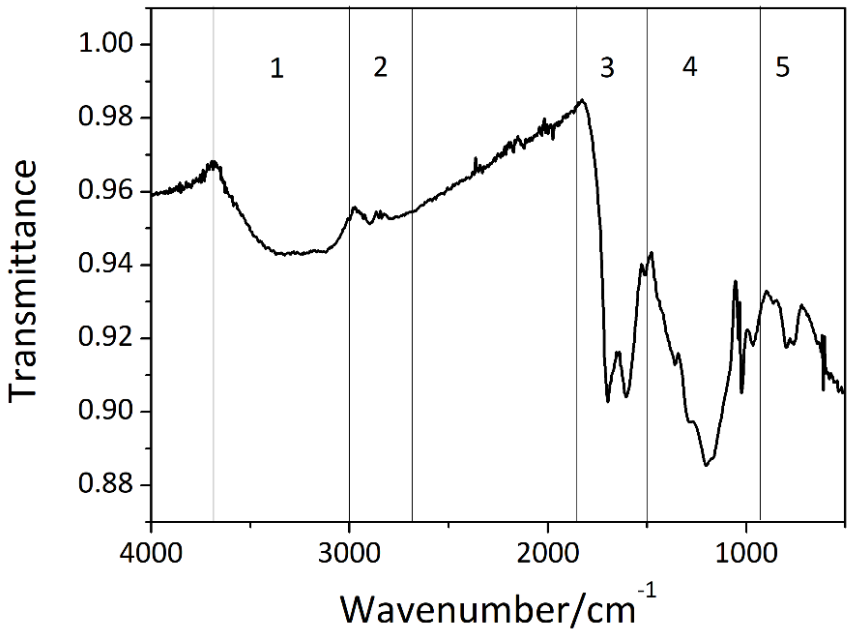


Figure 5 - IR spectrum showing the characteristic absorption signals observed for hydrochar.

5.4.1.3 Powder X-ray Diffraction of $\{H_3W_{12}\}$, $\{H_6W_{18}\}$, WO_3 and Hydrochar

Powder X-ray Diffraction is a non-destructive characterisation technique for nanoscale materials. The diffraction pattern can be used to assess the degree of crystallinity or amporphisation within a material as well as phase identification and sample purity. PXRD has also been used to detect the formation of new crystalline metal oxide phases, for example, due to degradation of POMs under operational conditions.[40,41,42] For $H_3PW_{12}O_{40}$, the most significant peaks are observed between 8 – 10°, 17 – 20°, 26 – 30° and 32 – 35° according to previous literature reports.[43,44,45] For $H_6P_2W_{18}O_{62}$, the peaks at 2Θ = 7 – 10° , 14 – 19°, and 24 – 30° have been used to confirm the presence of the Wells-Dawson anion within various salts.[46,47,48]

The PXRD patterns obtained for $\{H_3W_{12}\}$ and $\{H_6W_{18}\}$ are shown below (Figures 6 and 7). $\{H_3W_{12}\}$ shows the following notable peaks: 7.9°, 8.8°, 17.6°, 27.4°, 29.8°, 35.5° which match well with the literature. The Dawson contains the following: 9.2°, 24.6°, 25.3°, 27.1°, 29.8° which also correspond well with

previously reported values. The ranges in which these peaks fall are marked with an asterisk for each pattern.

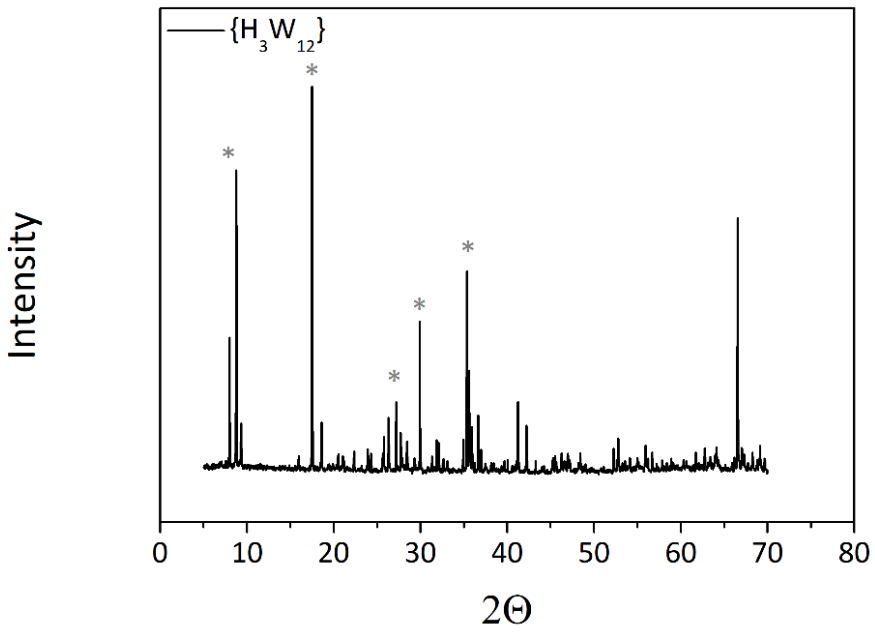


Figure 6 – PXRD pattern for $\{H_3W_{12}\}$ with characteristic peaks marked with a (*).

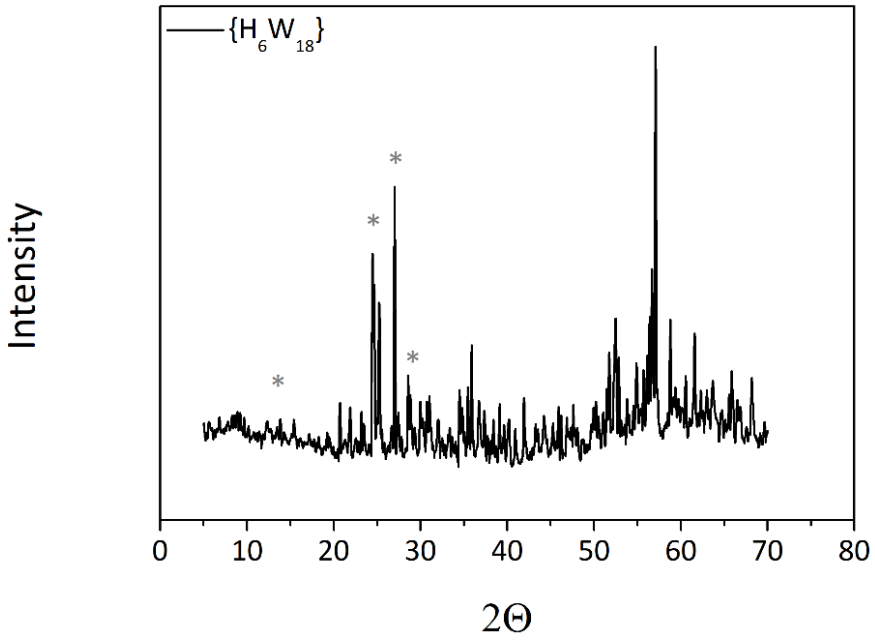


Figure 7- PXRD pattern for $\{H_3W_{12}\}$ with characteristic peaks marked with a (*).

A possible degradation product of polyoxotungstates at high temperatures is tungsten oxide (WO_3). The monoclinic structure of WO_3 possesses three distinct XRD peaks that have been previously reported as 2θ = 23.14°, 23.60°, and 24.40°.[49] A diffraction pattern was obtained for WO_3 and the following peaks were observed: 22.9°, 23.5° and 24.3° which match well with the literature. The range in which these peaks occur is marked with an asterisk (Figure 8).

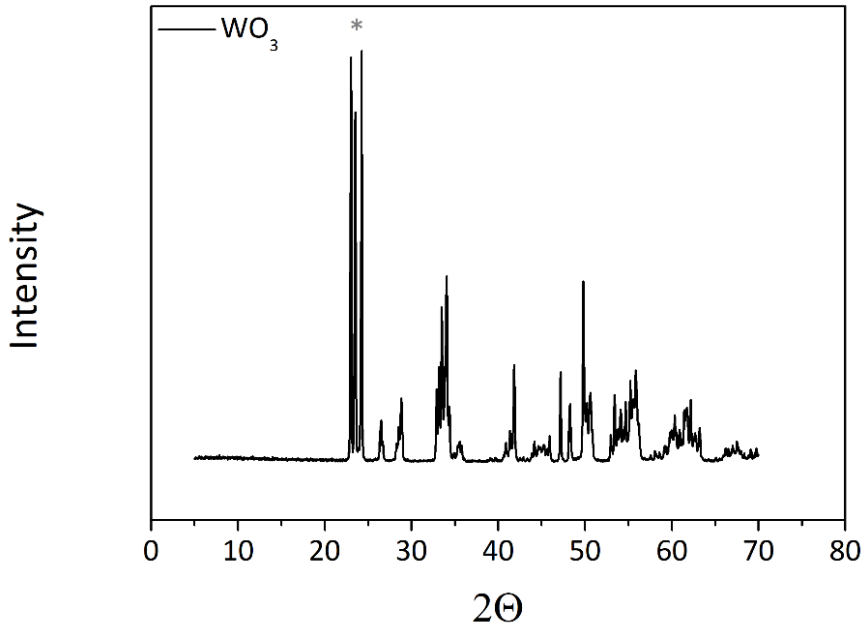


Figure 8 - PXRD pattern for WO_3 with characteristic peaks marked with a (*).

Lastly, PXRD analysis was carried out on the cellulose acetate derived hydrochar. The absence of sharp diffraction peaks in the pattern for the hydrochar confirms that it is indeed amorphous in nature (Figure 9). Two distinct broad peaks centered at a 2θ angle of 21.8° and 42.3° are visible, which are characteristic of carbon materials and specifically correspond to the (002) and (001) planes of graphene, respectively.[50]

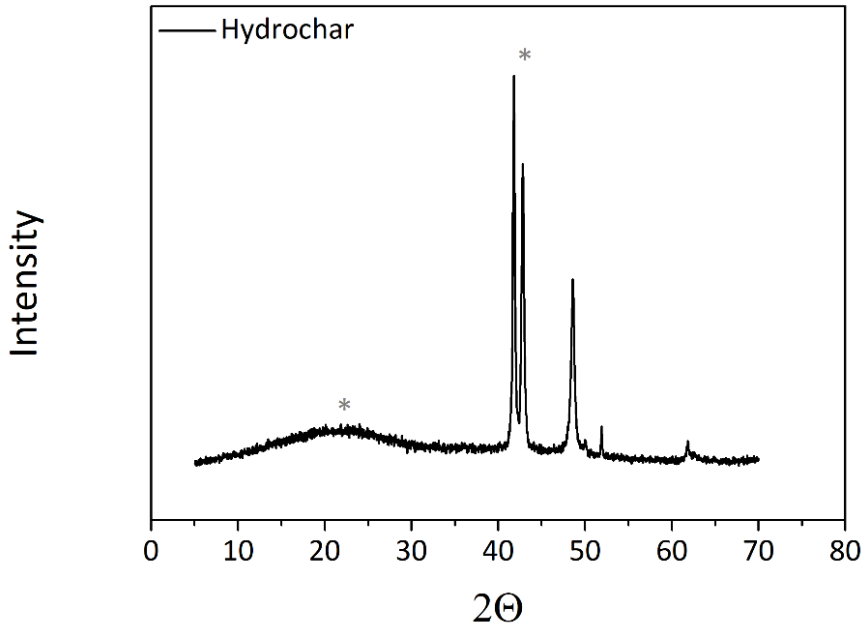


Figure 9 - PXRD pattern for hydrochar with characteristic graphitic peaks marked with a (*).

5.4.1.4 Electrochemistry of $\{H_3W_{12}\}$ and $\{H_6W_{18}\}$

The electrochemistry of the acidic POMs $\{H_3W_{12}\}$ and $\{H_6W_{18}\}$ in 1M H_2SO_4 has already been discussed in detail in Chapter 2 but the key aspects are reiterated here. The CV of $\{H_3W_{12}\}$ in 1M H_2SO_4 shows three redox processes within the potential range of 0.2 – -0.8 V *vs.* Ag/AgCl (Figure 10). The first two process are monoelectronic and the third comprises a two-electron transfer which is also accompanied by protonation (Equations 1 – 3). The E_{mid} and ΔE_p values are reported in Table 1.

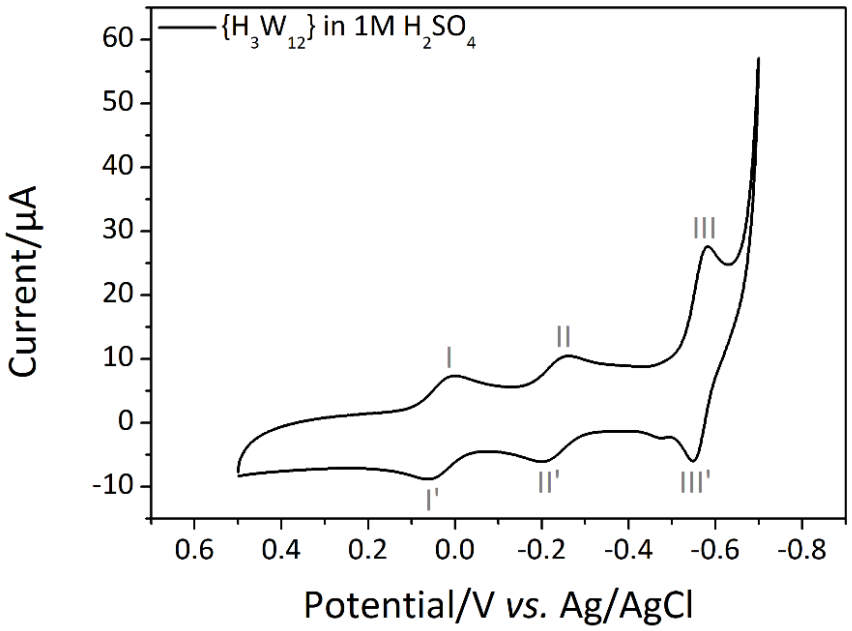


Figure 10 - Solution phase CV of $\{H_3W_{12}\}$ in 1M H_2SO_4 performed using a 3 mm diameter GC working electrode, a Pt counter electrode, and a Ag/AgCl reference electrode. The scan rate was 100 mV s^{-1}.

Equations 1 – 3 - Redox couples for $\{H_3W_{12}\}$ in 1M H_2SO_4.

I/I': $[PW_{12}O_{40}]^{3-} + e^- \leftrightarrow [PW_{12}O_{40}]^{4-}$ (1)

II/II': $[PW_{12}O_{40}]^{4-} + e^- \leftrightarrow [PW_{12}O_{40}]^{5-}$ (2)

III/III': $[PW_{12}O_{40}]^{5-} + 2e^- + 2H^+ \leftrightarrow [H_2PW_{12}O_{40}]^{5-}$ (3)

Table 1 - Observed Midpoint Potentials (E_{mid}) and Peak-to- Peak Separations (ΔE_p) for $\{H_3W_{12}\}$ in 1M H_2SO_4.

Process	E_{mid}/V	ΔE_p/mV
I	0.032	44
II	-0.23	42
III	-0.56	28

The CV of $\{H_6W_{18}\}$ shows four redox processes between the potential range of 0.2 – -0.8 V *vs.* Ag/AgCl (Figure 11). The first two peaks are one-electron processes and the third and fourth peaks are two-electron processes, both

involving protonation (Equations 4 – 7). The corresponding E_{mid} and ΔE_p values are reported in Table 1.

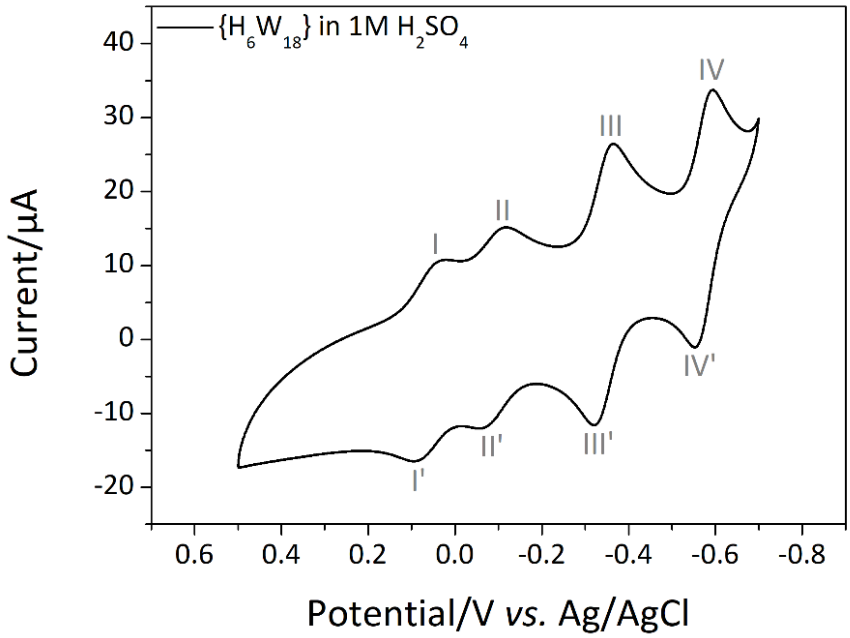


Figure 11 - CV of $\{H_6W_{18}\}$ in 1M H_2SO_4 performed using a 3 mm diameter GC working electrode, a Pt counter electrode, and a Ag/AgCl reference electrode. The scan rate was 100 mV s^{-1}.

Equations 4 – 7 - Redox couples for $\{H_6W_{18}\}$ in 1M H_2SO_4.

I/I': $[P_2W_{18}O_{62}]^{6-} + e^- \leftrightarrow [P_2W_{18}O_{62}]^{7-}$ (4)

II/II': $[P_2W_{18}O_{62}]^{7-} + e^- \leftrightarrow [P_2W_{18}O_{62}]^{8-}$ (5)

III/III': $[P_2W_{18}O_{62}]^{8-} + 2e^- + 2H^+ \leftrightarrow [H_2P_2W_{18}O_{62}]^{8-}$ (6)

IV/IV': $[H_2P_2W_{18}O_{62}]^{8-} + 2e^- + 2H^+ \leftrightarrow [H_4P_2W_{18}O_{62}]^{8-}$ (7)

Table 2 - Observed Midpoint Potentials (E_{mid}) and Peak-to- Peak Separations (ΔE_p) for $\{H_6W_{18}\}$ in 1M H_2SO_4.

Process	E_{mid}/V	ΔE_p/mV
I/I'	0.065	42
II/III	-0.095	39
III/III'	-0.34	36
IV/IV'	-0.57	34

5.4.1.5 Electrochemical Accessibility of POMs in the Solid State

To assess the electrochemical accessibility of POMs adsorbed onto activated carbon, a rudimentary experiment was first carried out (Figure 12). The microcrystalline attachment of POM to an already activated carbon was as follows: 1 – 2 mg of $\{H_6W_{18}\}$ was ground with 10 mg of activated carbon. A sample amount of this $\{H_6W_{18}\}$@AC composite were placed on coarse grade filter paper and the glassy carbon electrode was gently rubbed over the material, causing some of the compound to adhere to the electrode surface. The only driving force here for the POM adsorption onto the carbon surface is mechanical grinding. Previous studies have shown this method to be a convenient and simple method to probing the redox properties of solids.[51,52]

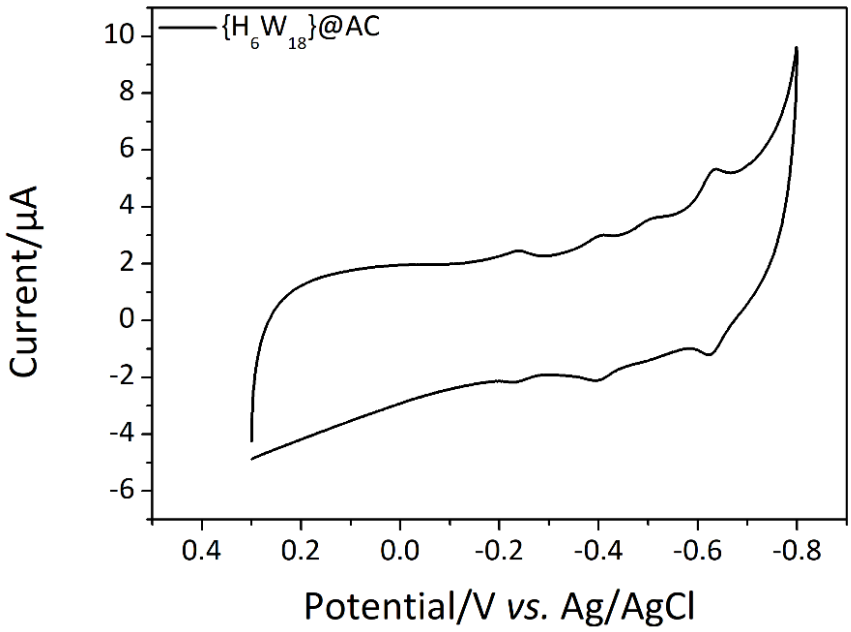


Figure 12 – Solid state CV of $\{H_6W_{18}\}$ mechanically ground with pre-activated carbon and subsequently tested for POM-induced redox activity. CV was conducted in 1M H_2SO_4 using a 3 mm diameter GC working electrode, a Pt counter electrode, and a Ag/AgCl reference electrode. The scan rate was 100 mV s^{-1}.

The glassy carbon electrode was then tested in 1M H_2S0_4 electrolyte with a classic three-electrode cell using a platinum counter electrode and Ag/AgCl reference electrode. Three redox couples of $\{H_6W_{18}\}$ are discerned in the voltammogram of $\{H_6W_{18}\}$@AC. This preliminary test shows that even in the absence of a major driving force to attach POMs to a given carbon surface, the electrochemistry is still accessible.

5.4.2 In-situ Carbonisations – Set 1

5.4.2.1 Preparation of POM-AC Composites - Activating Agent:Hydrochar:POM (4.5:1:0.5) at 750 °C

Full preparation steps are detailed in the experimental section. Briefly, the POM-AC composites were prepared by the addition of either $\{H_3W_{12}\}$ or $\{H_6W_{18}\}$ into the chemical activation of cellulose acetate-derived hydrochar. The activating agent used was potassium oxalate ($K_2C_2O_4$) in a given ratio at a set temperature. Post carbonisation, the composites were washed in deionised water for 24 hours before being filtered and dried at 100 °C.

The first set of samples were produced via chemical activation of cellulose acetate derived hydrochar by potassium oxalate and including the POMs $\{H_3W_{12}\}$ or $\{H_6W_{18}\}$ at a ratio of 4.5:1:0.5 at 750 °C. The activated carbon control sample without any POM is denoted as AC-(4.5)750. The POM@AC samples are denoted as $\{H_3W_{12}\}$@AC-(4.5)750 and $\{H_6W_{18}\}$@AC-(4.5)750.

5.4.2.2 Structural Characterisation of Set 1

Post carbonisation, the activated carbon samples were first analysed using thermogravimetric analysis (TGA). For activated carbons, increasing the temperature in air leads to a carbon burn off which manifests as a decrease in mass. Therefore, TGA can be used to assess the purity of the carbon sample in two ways; the presence of a single sharp drop in the percentage mass loss indicates that only one component is present, and secondly, if the mass drops to < 5% then it can be assumed the sample is pure. If a mass of < 10% remains, then this could be due to inorganic impurities that did not oxidise in air despite

a single mass loss. The material represented by this mass is extremely stable. TGA can also be used to verify the thermal stability of POM-substrate composites, to provide an estimate of the POM loading of the composite as well whether the presence of POMs affects the thermal stability of the substrate.

The TG curves of the control activated carbon sample and composites are shown below (Figure 13). The control sample AC-(4.5)750 is the most thermally stable as it has the highest onset temperature (486.8 °C) and is quite pure with a minimal residual weight percent (0.5%). The presence of oxidising POMs reduces the thermal stability of the composites. $\{H_3W_{12}\}$@AC-(4.5)750 and $\{H_6W_{18}\}$@AC-(4.5)750 have lower thermal stability with the onset of their degradation occurring at 324.7 °C and 370.2 °C respectively. The inorganic residues of $\{H_3W_{12}\}$@AC-(4.5)750 and $\{H_6W_{18}\}$@AC-(4.5)750 are 11.3% and 7.3% but whether these correspond to redox active POMs has to be determined.

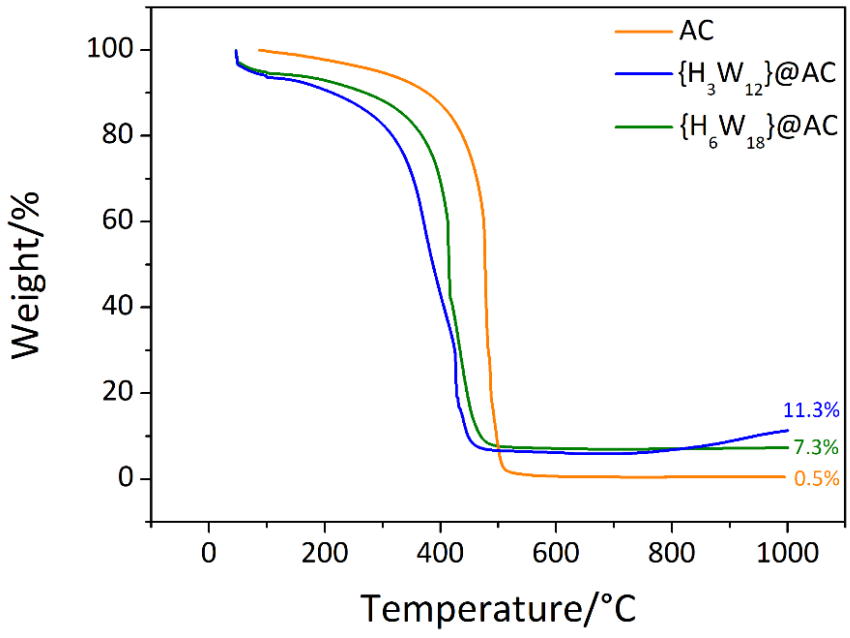


Figure 13 - TG curves for AC-(4.5)750, $\{H_3W_{12}\}$@ AC-(4.5)750 and $\{H_6W_{18}\}$ AC-(4.5)750, showing the onset temperature of their degradation and the approximate weight percent of POM within the composite.

One of the most common methods used to gain structural information of surface-immobilised POMs and confirm their attachment to a substrate is attenuated total reflectance (ATR) infrared. ATR is a more surface-sensitive method of extracting IR data, which is especially important if the POM loadings are very low. IR spectra of carbon materials can be difficult to obtain due to problems arising from poor transmission and uneven light scattering related to large particle size. Additionally, the electronic structure of carbon materials results in a complete absorption band through the visible region to the infrared. Interpretation of spectra can also be convoluted due to multiple band overlaps, so it is not always straightforward to unequivocally assign specific functional groups to observed absorption bands. It is also important to note that IR spectra for POM-substrate composites can be difficult to analyse, as often the spectra are dominated by the substrate vibrational modes.

The complex spectrum with several notable absorptions observed for the hydrochar are clearly absent in all three of the activated carbon samples prepared at 750 °C, which is indicative of complete carbonisation of the hydrochar (Figure 14). This could mean that the POM absorption bands are shrouded by the AC network as the POM is embedded deep within the pores. It is also possible that the POM has degraded during the carbonisation but nonetheless, no peaks are visible for possible degradation products such as tungsten oxide (WO_3).

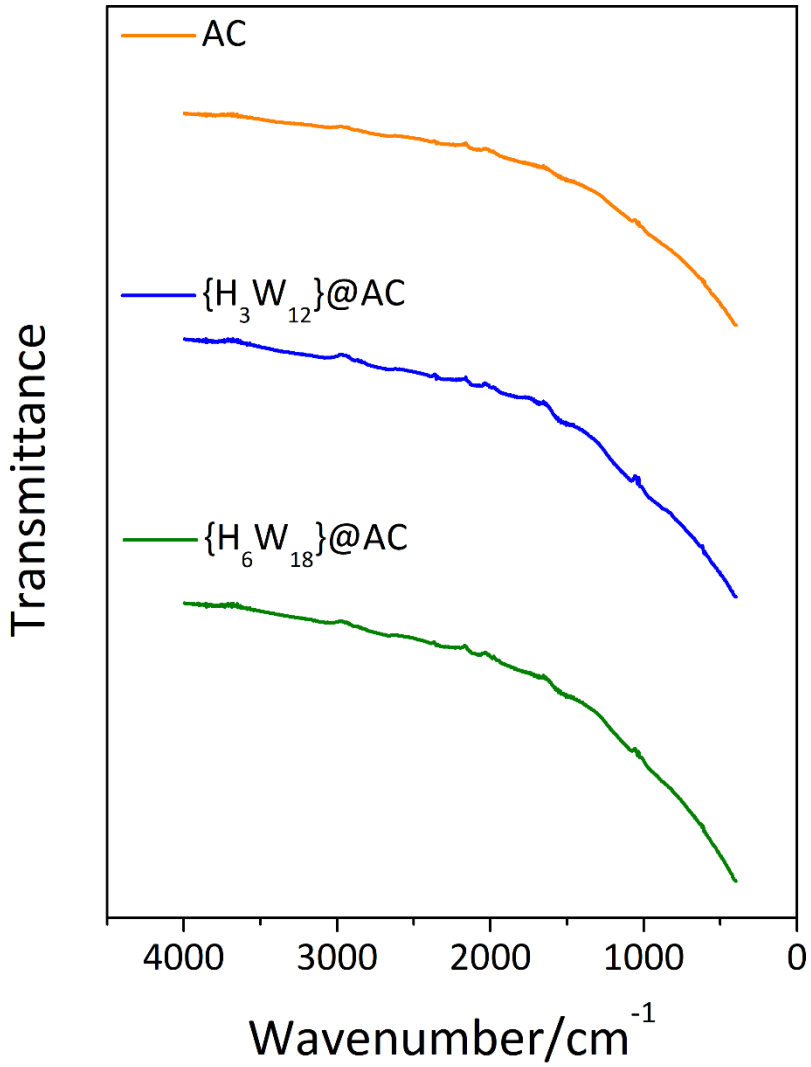


Figure 14 – IR absorption spectrums for AC-(4.5)750, $\{H_3W_{12}\}$@ AC-(4.5)750 and $\{H_6W_{18}\}$ AC-(4.5)750. No major bands were detected.

Powder X-ray diffraction (PXRD) is an analytical technique used to detect the degree of crystallisation or amporphisation of a material. Therefore, it can be useful to analyse crystalline POM-substrate composites. The absence of POM-based XRD signals is usually an indicator of the molecular dispersion of POMs on the surface. But the absence of such a signal can also be explained by the presence of larger, amorphous aggregates and thus further evidence is required in some cases.[53]

The obtained patterns are shown in Figure 15. The amorphous nature of the prepared AC-(4.5)750 material is clear. Two distinct broad peaks centered at a 2θ angle of 23.5° and 42.3° are visible, which are characteristic of carbon materials and specifically correspond to the (002) and (001) planes of graphene, respectively.[50] These diffractions are also visible in the hydrochar, which is amorphous in nature. However, the broadening of the 002-signal post carbonisation indicates an increase in the degree of disordering.

In general, the flattening of XRD signals that come from POM within a composite material prove that the POM is homogenously dispersed in the substrate matrix. However, this is not the case with the $\{H_3W_{12}\}$@AC-(4.5)750 and $\{H_6W_{18}\}$@AC-(4.5)750 composites. Both composites have many sharp diffraction peaks, indicating the materials have a crystalline component. Upon further inspection, the following peaks can be found for $\{H_3W_{12}\}$@AC-(4.5)750: 23.1°, 23.5° 24.3° and $\{H_6W_{18}\}$@AC-(4.5)750 has: 23.5°, 23.9° and 24.6°. These peaks can be ascribed to WO_3 which is a breakdown product of polyoxotungstates and have previously been reported at 2Θ = 23.14°, 23.60°, 24.40°.[49] Therefore, this analysis suggests that the in-situ carbonisation at the proposed conditions was not successful at incorporating the POM motifs within the AC network.

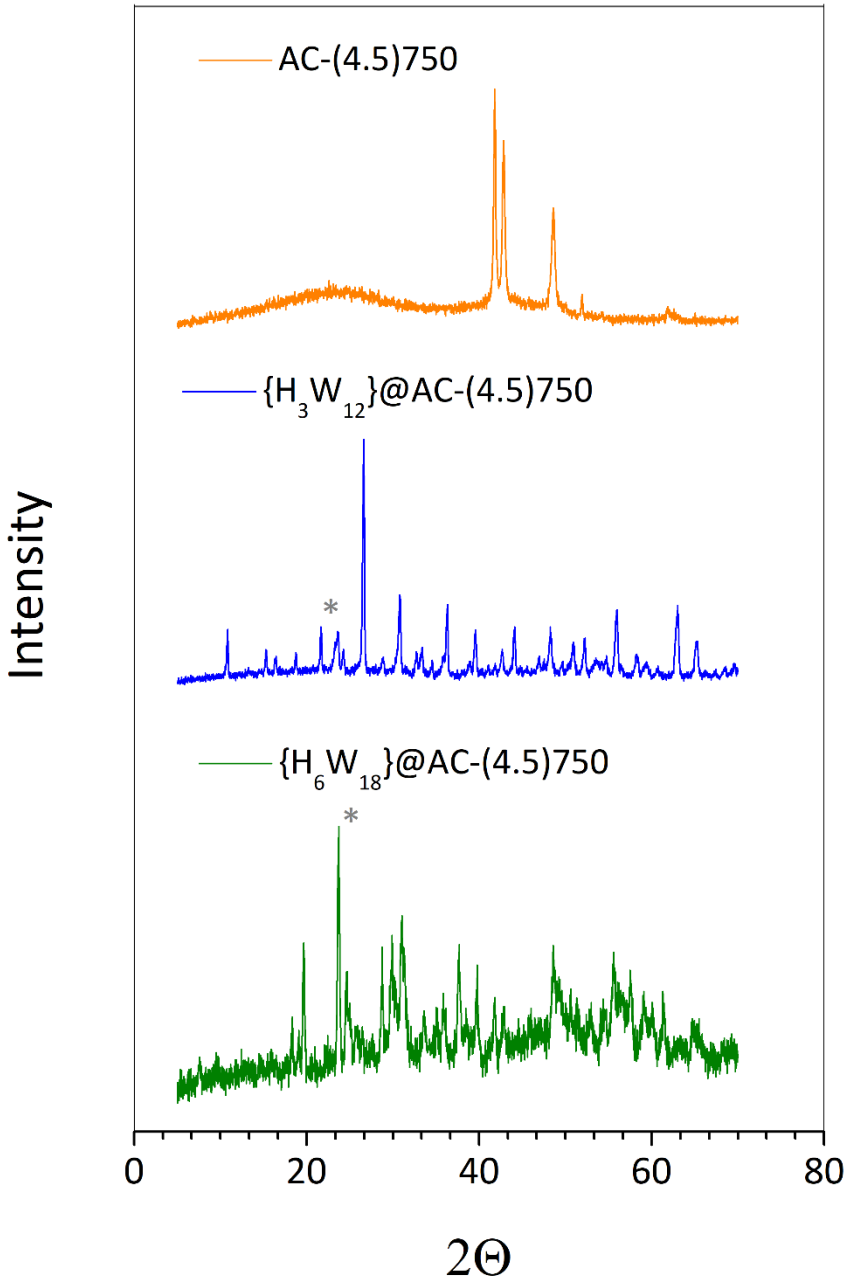


Figure 15 – PXRD patterns obtained for AC-(4.5)750, $\{H_3W_{12}\}$@ AC-(4.5)750 and $\{H_6W_{18}\}$ AC-(4.5)750. Some POM peaks are marked with an (*) that correspond to WO_3.

5.4.2.3 Textural Characterisation of Set 1

The surface area and porosity were determined by the Brunauer-Emmett-Teller method (BET) using N_2 gas as the adsorptive. An adsorption isotherm plots the quantity of gas adsorbed against the relative pressure (p/p^o).

Figures 16, 17, and 18 show the isotherms produced with an inset of the pore size distribution (incremental pore volume (cm^3/g) against pore width (Å)). The control sample AC-(4.5)750 exhibits strongly Type I(a)[54] isotherm behaviour indicating ultramicroporosity. The steep incline at low relative pressures followed by a plateau indicates that the micropores are filled rapidly. The sharp 'knee' is representative of a narrow pore size distribution. The inset for the pore size distribution (PSD) clearly shows the AC-(4.5)750 sample consisted of only narrow micropores under 10 Å and no mesopores (Figure 16). The material has a high apparent BET surface area of 1099.3 m^2 g^{-1} which reflects the ultramicroporous nature of the material. Additionally, the PXRD data indicated an increase in the disorder of the graphitic planes and such an increase in activated carbons usually leads to an increase in the porosity and internal surface area[55], which correlates well to the N_2 adsorption isotherm.

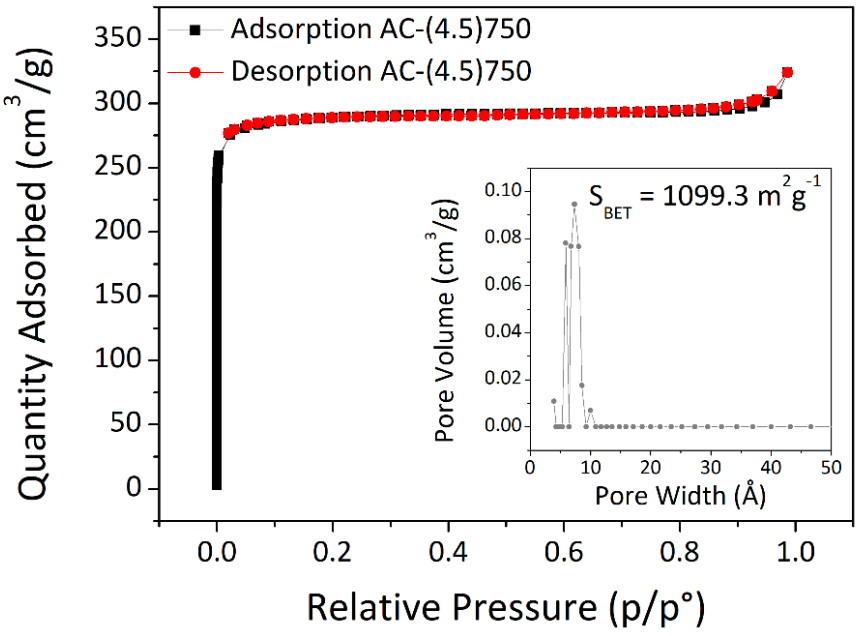


Figure 16 - N_2 adsorption isotherms of AC-(4.5)750.

$\{H_3W_{12}\}$@AC-(4.5)750 and $\{H_6W_{18}\}$@AC-(4.5)750 both show Type I isotherm behaviour, characterised by the steep uptake of N_2 at very low relative pressure (Figures 17 and 18). However, some Type II character is also shown by

the slope after the initial rapid uptake of the adsorptive. This implies that these samples had a large quantity of micropores but that mesopores were also present. A large volume of micropores is accounted for by the PSD, as well as a small but broad distribution of larger micropores and mesopores starting from 14 Å and upwards. $\{H_3W_{12}\}$@AC-(4.5)750 and $\{H_6W_{18}\}$@AC-(4.5)750 have a BET surface area of 430.7 $m^2\ g^{-1}$ and 895.6 $m^2\ g^{-1}$ respectively.

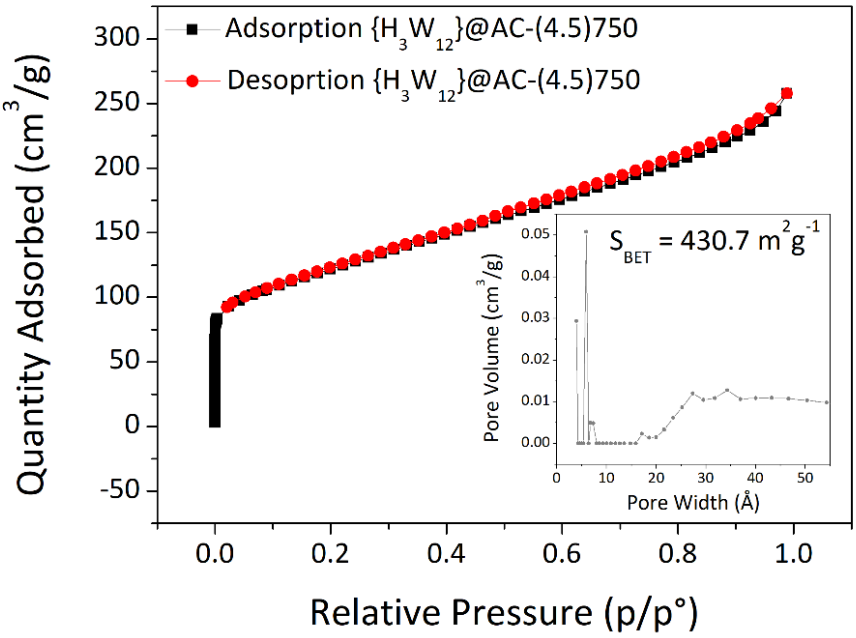


Figure 17 - N_2 adsorption isotherms of $\{H_3W_{12}\}$@AC-(4.5)750.

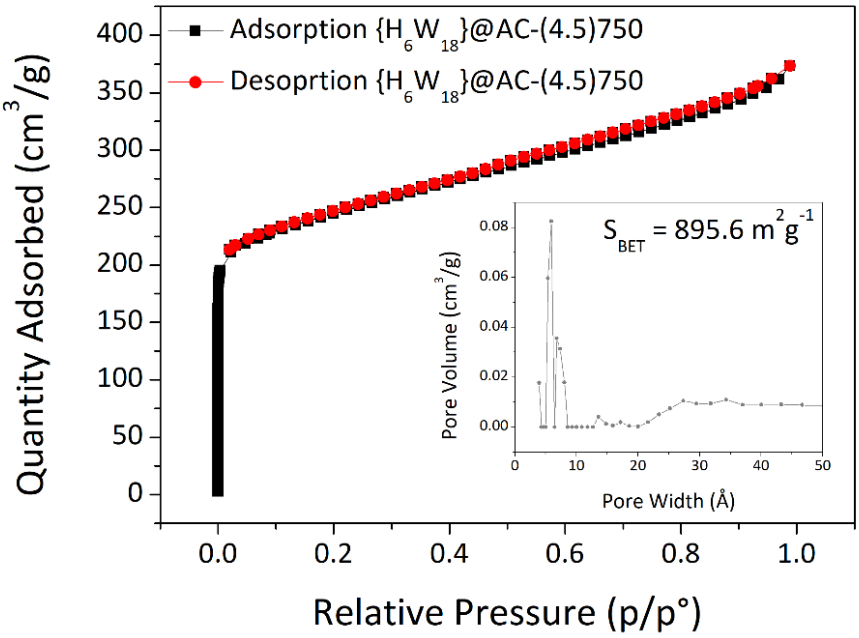


Figure 18 - N_2 adsorption isotherms of $\{H_6W_{18}\}$@AC-(4.5)750.

As evidenced by the BET data, the experimental conditions successfully produced an activated carbon with a high surface area. CA-PW_{12}@AC-(4.5)750 showed a much lower surface area and CA-P_2W_{18}@AC-(4.5)750 has a modest surface area. These results can be interpreted in several ways in which a reduced surface area would be expected. Firstly, specific surface areas will generally increase as the pore size decreases, thus it is unsurprising that the presence of mesopores in the POM-based composites reduces their surface area. Given that the carbonisation conditions are different to the control sample AC-(4.5)750, namely the presence of POM, we can consider the role of the POM during the carbon activation. The POM crystals could impede the micropore formation during activation, resulting in mesopores, and hence a reduced porosity at the end. Or we could consider that the POM has no effect on the activation process and is in fact sitting in the formed pores thereby blocking access for N_2. If the gas cannot adsorb then the porosity cannot be analysed. However, the latter hypothesis is weakened by the PXRD data which indicates the POMs are not intact post carbonisation.

Scanning Electron Microscopy (SEM) was used to investigate the morphology of the POM@Activated Carbons. Only images for $\{H_3W_{12}\}$@AC-(4.5)750 have been obtained. As revealed by Figure 19, the structure is dominated by spherical clusters. Some of the clusters appear to be perfect spheres whereas some regions contain irregular and deformed spheres. The spherical micrometre-sized particles characterise both glucose and cellulose derived hydrochar. The mechanism by which HTC modifies the starting material has previously been investigated.[56] When a polysaccharide, such as cellulose, is hydrothermally carbonised, it undergoes hydrolysis which breaks the polymer down into glucose. The glucose decomposes into organic acids, furfural-like compounds and aldehydes. These units then recombine via polymerisation and condensation reactions. The polymers formed are subjected to further aromatisation and dehydration reactions to form insoluble microspheres with hydrophobic shells. Since these spheres are not homogeneously distributed around the sample, the structural irregularities are likely due to the presence of POM crystals.

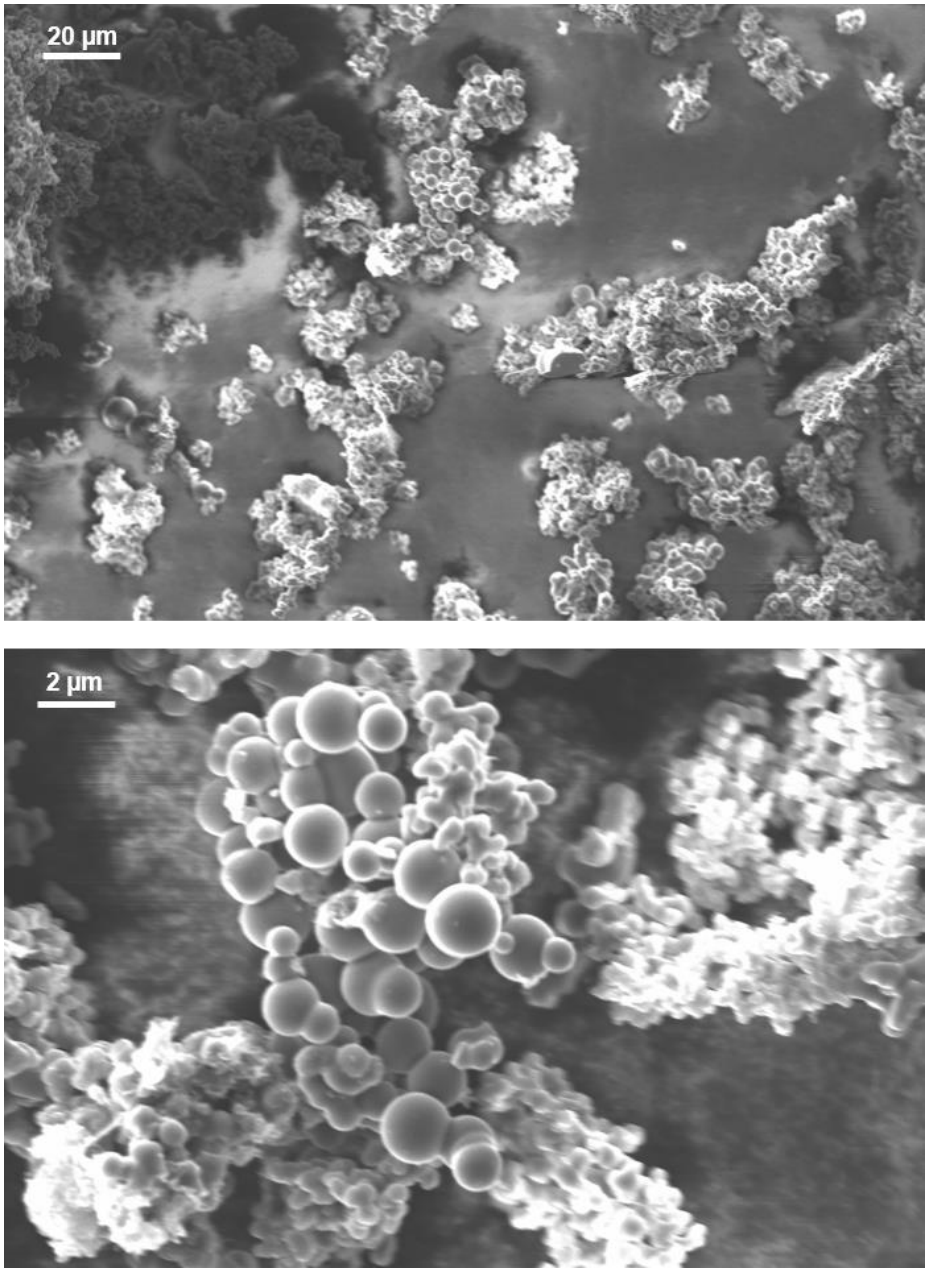


Figure 19 - SEM images of $\{H_3W_{12}\}$@AC-(4.5)750.

Elemental mapping was performed on the section shown in Figure 19. The EDX map (Figure 20) reveals the prevalent elements to be carbon, oxygen, tungsten and potassium. Figure 20 shows that the perfect spheres indeed correspond to unactivated hydrochar as the major elements are oxygen and carbon. Figure 21 shows that tungsten is spread out within the areas of structural imperfection (orange). However, the elemental map alone is not enough to ascertain whether this tungsten signature corresponds to intact POM crystals or the degradation product WO_3.

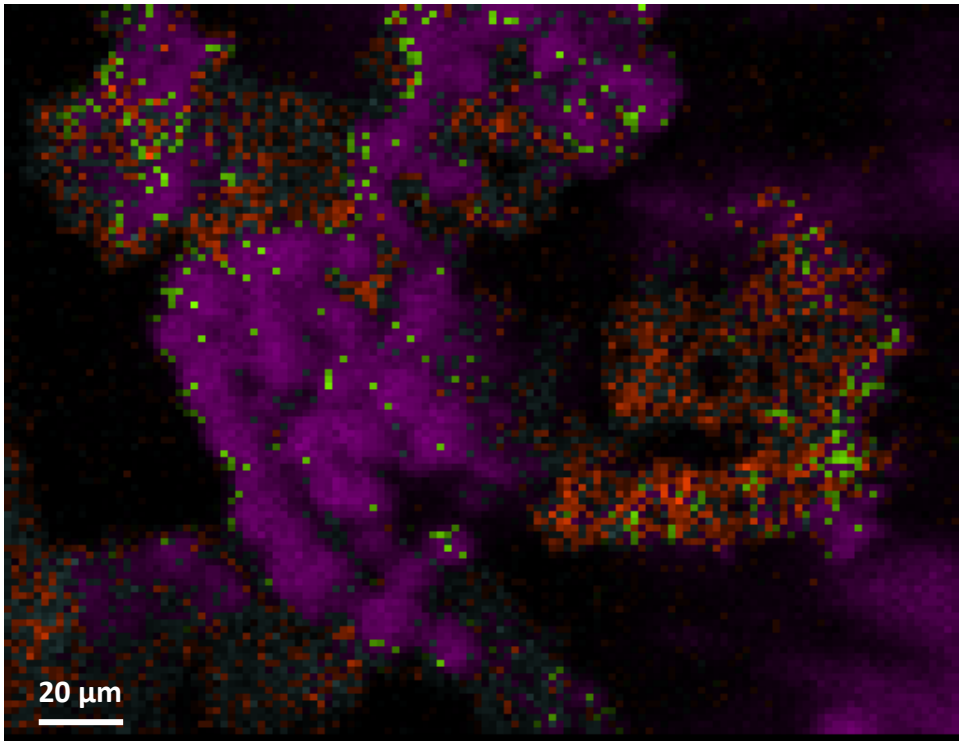


Figure 20 - Elemental mapping showing oxygen (*purple*), carbon (*green*), tungsten (*orange*) and potassium (*teal*).

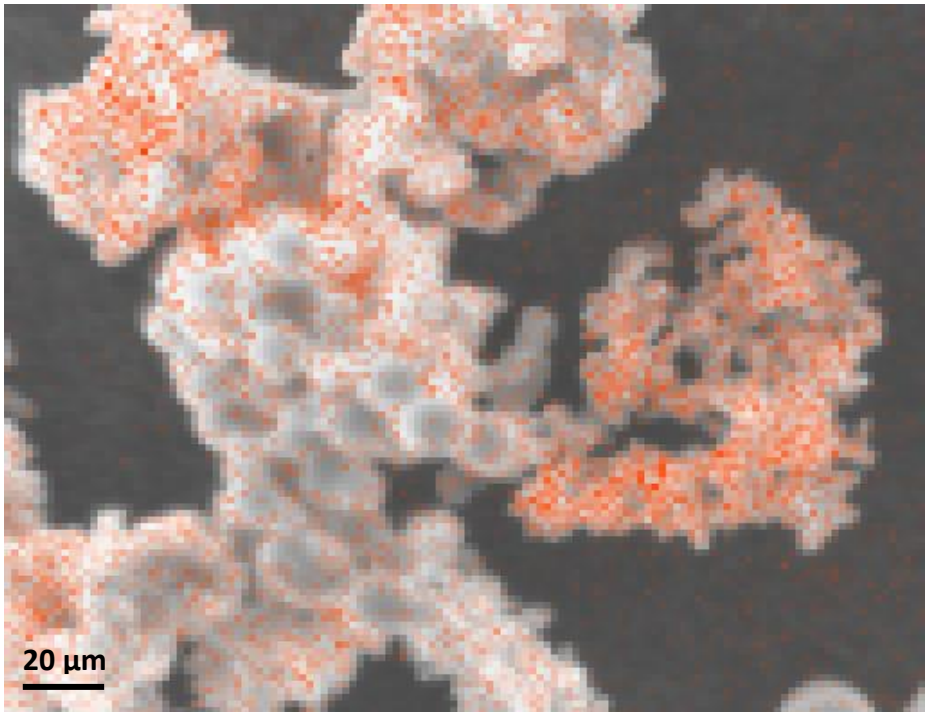


Figure 21 – EDX map highlighting tungsten rich areas (*orange*).

The appearance of potassium in the EDX map is likely due to the activating agent, potassium oxalate. Given that all the AC samples were washed in water post carbonisation, the washing step could have incited KOH formation. POMs are sensitive to degradation in alkaline conditions and thus the presence of KOH could have led to an in-situ degradation of the POMs during the washing stage. Analysis of the electrochemical behaviour of the composites will help to elucidate the nature of the tungsten moieties seen by the SEM analyses.

5.4.2.4 Electrochemical Characterisation of Set 1 in 1M Sulphuric Acid

Inks were prepared for the two POM-based AC materials and their electrochemical properties were analysed using the dropcast method outlined in the experimental section. Featureless voltammograms were observed which possess a rectangular-shaped curve, typical of capacitive behaviour of materials such as activated carbon (Figures 22 and 23). The absence of well-defined reversible redox peaks mean that the POMs did not survive the carbonisation process and had devolved into their corresponding redox-inactive metal oxides.

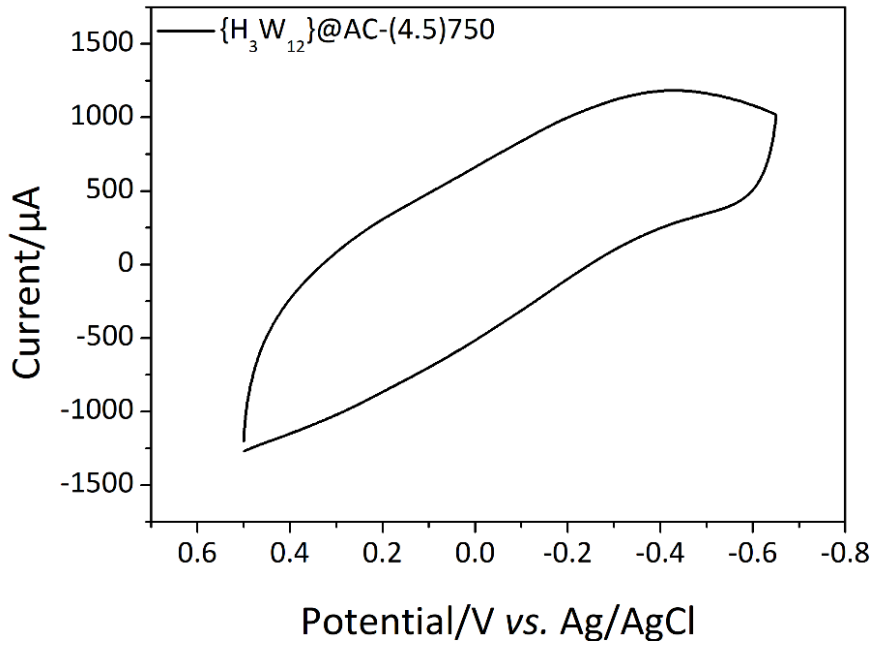


Figure 22 – Solid state CV of $\{H_3W_{12}\}$@AC-(4.5)750 in 1M H_2SO_4, recorded using a 3 mm diameter glassy carbon working electrode, a Pt counter electrode, and a Ag/AgCl reference electrode. The scan rate was 100 mv s^{-1}.

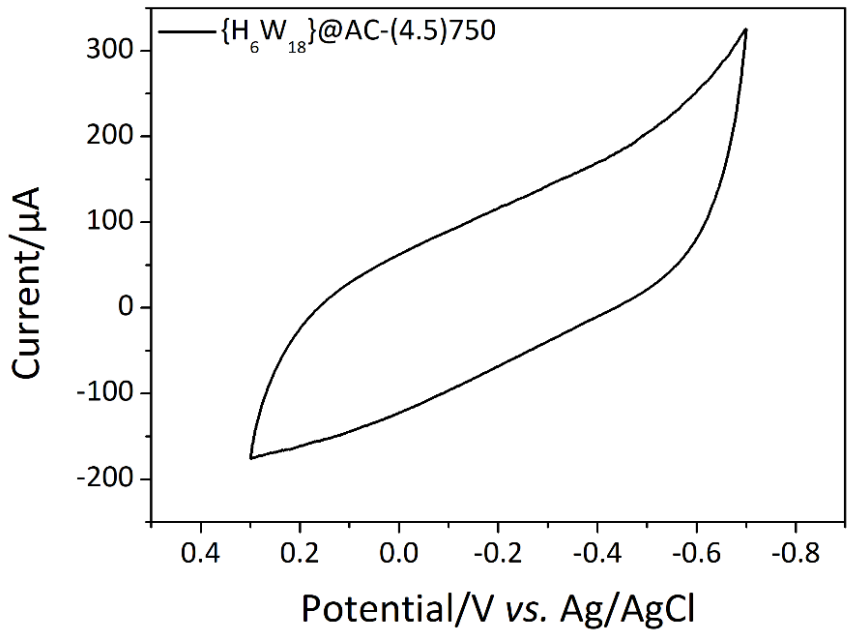


Figure 23 - Solid state Cv of $\{H_6W_{18}\}$@AC-(4.5)750 in 1M H_2SO_4, recorded using a 3 mm diameter glassy carbon working electrode, a Pt counter electrode, and a Ag/AgCl reference electrode. The scan rate was 100 mv s^{-1}.

5.4.3 In-situ Carbonisations – Set 2

5.4.3.1 Preparation of POM-AC Composites - Activating Agent:Hydrochar:POM (2:1:1) at 500 °C

This set of samples were produced in milder conditions. The chemical activation of cellulose acetate derived hydrochar using potassium oxalate and including the POMs $\{H_3W_{12}\}$ or $\{H_6W_{18}\}$ at a ratio of 2:1:1 at 500 °C. This time, the samples were washed with HCl post carbonisation, instead of water. The activated carbon control sample without any POM is denoted as AC-(2)500. The POM@AC samples are denoted as $\{H_3W_{12}\}$@AC-(2)500 and $\{H_6W_{18}\}$@AC-(2)500.

5.4.3.2 Structural Characterisation of Set 2

Post carbonisation, the activated carbon samples were analysed using thermogravimetric analysis (TGA). The TG curves of the control activated carbon sample and composites are shown below (Figure 24). The AC-(2)500 sample is

the least thermally stable in this set of samples with a burn off maxima at 366.3 °C. The residual mass is less than 5%, confirming it is virtually free of inorganic residues. This AC sample is less thermally stable than the AC sample prepared at 750 °C. And so, it appears that activated carbons prepared at higher temperatures are more thermally stable, likely due to an increase in the level of graphitisation from exposure to a higher temperature. The onset temperatures for $\{H_3W_{12}\}$@AC-(2)500 and $\{H_6W_{18}\}$@AC-(2)500 are 416.8 °C and 423.1 °C respectively. For this set of samples, the ratio of POM was increased and so an increase in POM loading is expected. Accordingly, the inorganic content of $\{H_3W_{12}\}$@AC-(2)500 and $\{H_6W_{18}\}$@AC-(2)500 is 19.2% and 44% respectively.

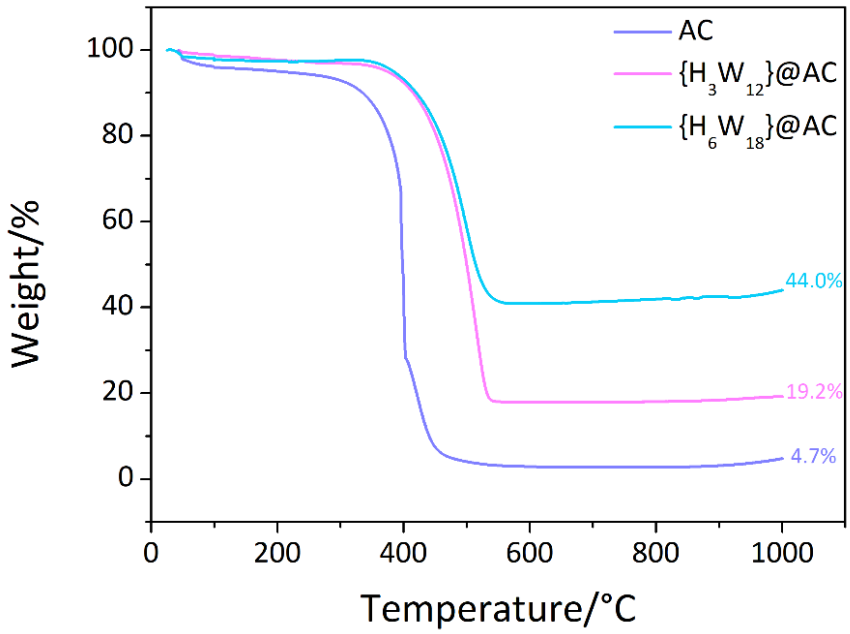


Figure 24 - TG curves for AC-(2)500, $\{H_3W_{12}\}$@ AC-(2)500 and $\{H_6W_{18}\}$ AC-(2)500, showing the onset temperature of their degradation and the approximate weight percent of POM within the composite.

The infrared spectra of AC-(2)500, $\{H_3W_{12}\}$@AC-(2)500 and $\{H_6W_{18}\}$@AC-(2)500 are shown in Figure 25. The increase and decreases in the IR spectrum peaks show how the experimental conditions affect the activated carbon structure. AC-(2)500 shows broad absorption peaks in the region of 1700 – 1400 resulting from C=O and C=C stretches. The absorption peak

between 1300 – 1000 can be attributed to C-O vibrations. These peaks indicate a mixture of functional groups such as esters, carboxylic acids, aldehydes, ketones and ethers which were seen in the raw hydrochar. Since this sample was activated at a lower temperature, the presence of unactivated hydrochar is anticipated.

With regards to the composites, both spectra show peaks pertaining to the respective POM. $\{H_3W_{12}\}$@AC-(2)500 has peaks at 1079 cm^{-1}, 981 cm^{-1}, 886 cm^{-1} and 790 cm^{-1}. $\{H_6W_{18}\}$@AC-(2)500 has peaks at 1076 cm^{-1}, 973 cm^{-1}, and 752 cm^{-1}. These absorptions match quite well to the POM peaks observed in the preliminary characterisation. Therefore, the carbonisation with this set of conditions appears to have been successful thus far.

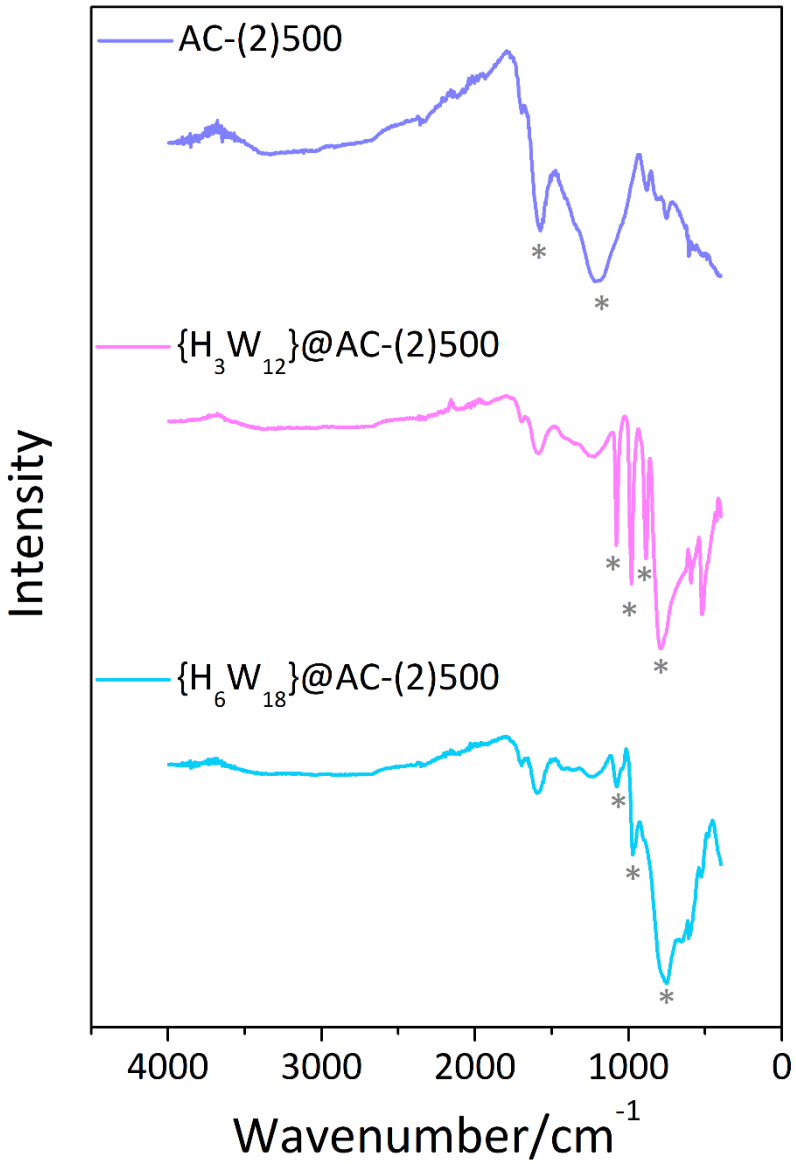


Figure 25 - IR absorption spectrums for AC-(2)500, $\{H_3W_{12}\}$@ AC-(2)500 and $\{H_6W_{18}\}$ AC-(2)500. Functional groups from unactivated hydrochar as well as characteristic POM absorption peaks are marked with an (*).

The amorphous nature of the prepared material is clear. Two distinct broad peaks centered at a 2θ angle of 23.4° and 42.3° are visible, which are characteristic of carbon materials and specifically correspond to the (002) and (001) planes of graphene, respectively.

As alluded to previously, the presence of sharp diffraction peaks indicates crystallinity within a material. Since both POM-based ACs have many sharp peaks, this could mean that the POMs are not situated within AC pores, and instead are agglomerated on the carbon surface. For $H_3PW_{12}O_{40}$, the most significant peaks are observed between 8 – 10°, 17 – 20°, 26 – 30° and 32 – 35° according to previous literature reports.[43,44,45] For $H_6P_2W_{18}O_{62}$, peaks in the ranges of 2Θ = 7 – 10° , 14 – 19°, and 24 – 30° are expected.[46,47,48] In each of these 2Θ ranges, both composites show characteristic peaks of the polyoxotungstates and the ranges in which these peaks appear are marked with an asterisk (Figure 26). Therefore, the presence of the Keggin and Dawson structures in the activated carbons was confirmed by IR and XRD.

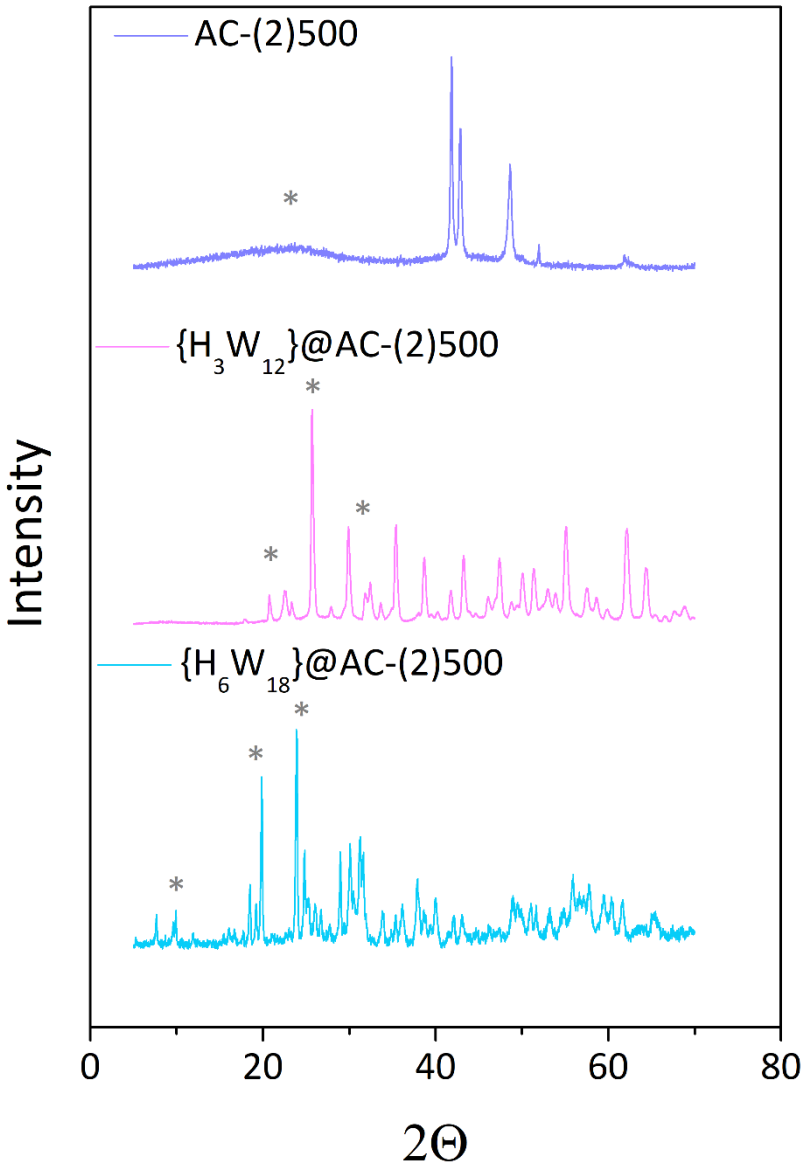


Figure 26 - PXRD patterns obtained for AC-(2)500, $\{H_3W_{12}\}$@ AC-(2)500 and $\{H_6W_{18}\}$ AC-(2)500. Characteristic graphitic and POM peaks are marked with an (*).

5.4.3.3 Textural Characterisation of Set 2

The surface area and porosity were determined by the Brunauer-Emmett-Teller method (BET) using N_2 gas as the adsorptive. Figures 27, 28, and 30 show the isotherms produced with an inset of the pore size distribution (incremental pore volume (cm^3/g) against pore width (Å)). All three samples exhibit Type II behaviour which is characteristic of non-porous solids with a wide

pore size distribution. The insets show that each sample has an extremely small amount of micropores, and generally the samples consist of mesopores (pores >20 Å). This reduced porosity is reflected in the low apparent BET surface areas where S_{BET} = 228.9 m^2g^{-1} for AC-(2)500, 42.5 m^2g^{-1} for $\{H_3W_{12}\}$@AC-(2)500 and 167.1 m^2g^{-1} for $\{H_6W_{18}\}$@AC-(2)500. Activation at lower temperatures generally results in materials which are not very microporous and therefore have lower surface areas.

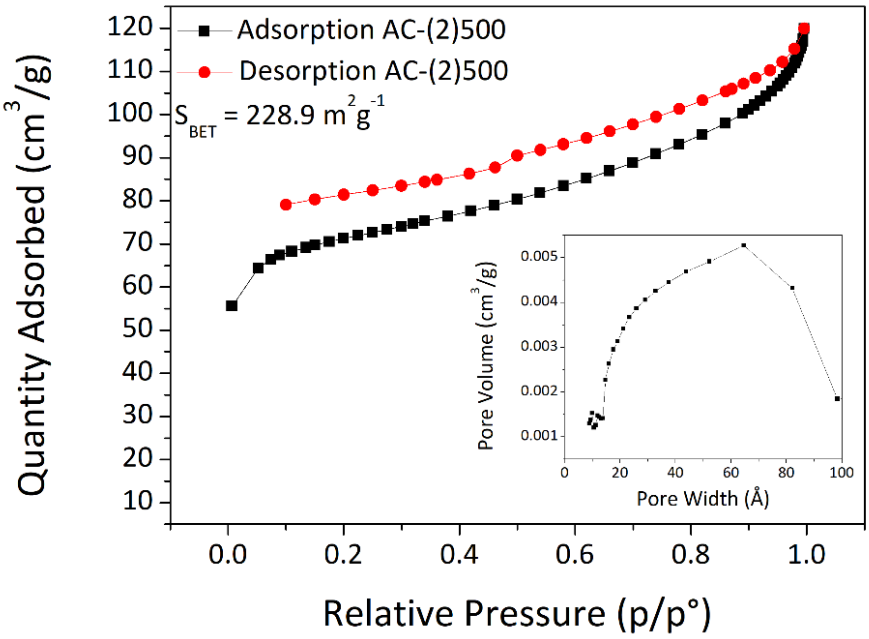


Figure 27 - N_2 adsorption isotherms of AC-(2)500.

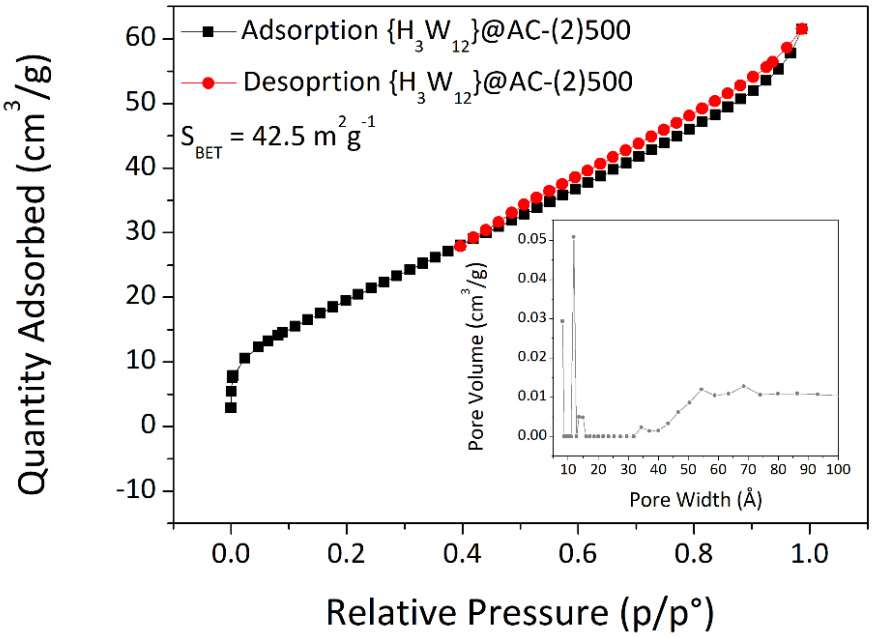


Figure 28 - N_2 adsorption isotherms of $\{H_3W_{12}\}$@AC-(2)500.

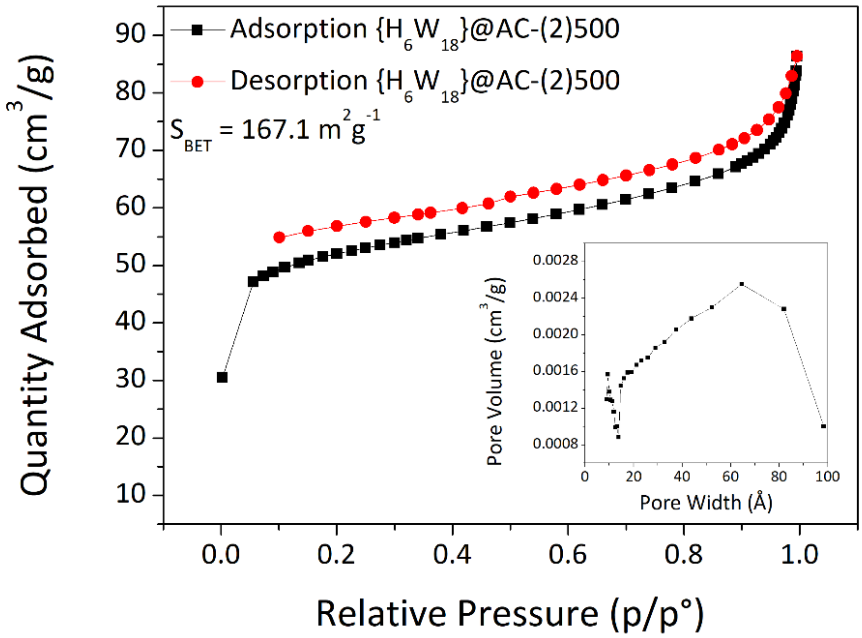


Figure 29 - N_2 adsorption isotherms of $\{H_6W_{18}\}$@AC-(2)500.

5.4.3.4 Electrochemical Characterisation of Set 2 in 1M Sulphuric Acid

The electrochemical properties of the two composites were assessed by preparing inks and using the dropcast method. This time, redox peaks were observed for both POM-based composites, confirming that the POMs were successfully incorporated into the AC matrix. $\{H_3W_{12}\}$@AC-(2)500 has two redox peaks in the range of 0.3 – 0.5 V *vs.* Ag/AgCl (Figure 30). The ΔE_p values suggest these processes are monoelectronic (Equations 10 – 11, Table 3). These peaks are less reversible than their solution counterpart ($\{H_3W_{12}\}$ in 1M H_2SO_4 vide supra) especially given that the peaks are not very well-defined and their ΔE_p values are greater than 59 mV.

$\{H_3W_{12}\}$@AC-(2)500 was sampled a further two times and the electrochemistry of the two samples was tested to ascertain the homogeneity of $\{H_3W_{12}\}$ within the AC network. Figure 31 shows the voltammogram for the second samples which shows a comparable redox profile to the first voltammogram (Figure 30). This is in good agreement with the IR and PXRD data which indicated the presence of POM moieties within the AC network. Figure 32 shows the voltammogram of the third sample and this time there is an absence of redox peaks. This highlights a flaw in the carbonisation method: that there is variability of redox active material dispersion, even within the same batch of composite.

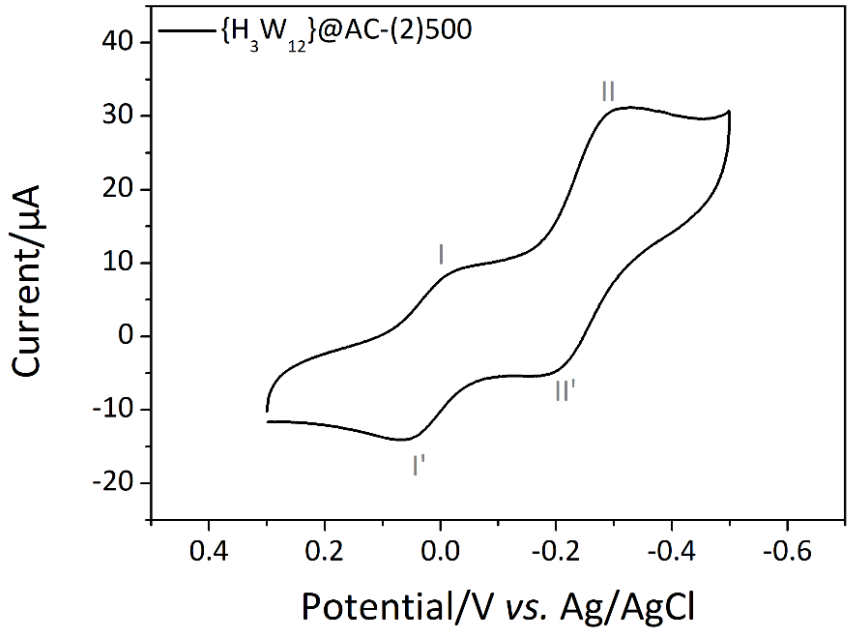


Figure 30 - Solid state CV of $\{H_3W_{12}\}$@AC-(2)500 in 1M H_2SO_4, recorded using a 3 mm diameter glassy carbon working electrode, a Pt counter electrode, and a Ag/AgCl reference electrode. The scan rate was 100 mv s^{-1}.

Equations 8 – 9 - Redox couples for $\{H_3W_{12}\}$@AC-(2)500 in 1M H_2SO_4.

$$\text{I/I'}: [PW_{12}O_{40}]^{3-} + e^- \longleftrightarrow [PW_{12}O_{40}]^{4-} \quad (8)$$

$$\text{II/II'}: [PW_{12}O_{40}]^{4-} + e^- \longleftrightarrow [PW_{12}O_{40}]^{5-} \quad (9)$$

Table 3 - Observed Midpoint Potentials (E_{mid}) and Peak-to- Peak Separations (ΔE_p) for $\{H_3W_{12}\}$@AC-(2)500 in 1M H_2SO_4.

Process	E_{mid}/V	ΔE_p/mV
I	0.018	69
II	-0.25	87

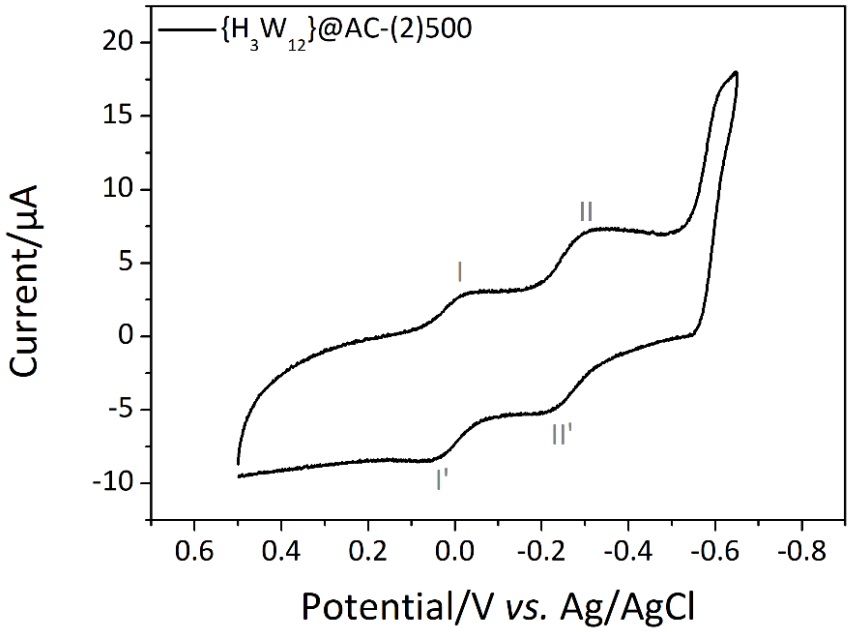


Figure 31 – Repeat solid state CV of $\{H_3W_{12}\}$@AC-(2)500 in 1M H_2SO_4, recorded using a 3 mm diameter glassy carbon working electrode, a Pt counter electrode, and a Ag/AgCl reference electrode. The scan rate was 100 mv s^{-1}.

Equations 10 – 11 - Redox couples for $\{H_3W_{12}\}$@AC-(2)500 in 1M H_2SO_4.

$$\text{I/I'}: [PW_{12}O_{40}]^{3-} + e^- \leftrightarrow [PW_{12}O_{40}]^{4-} \quad (10)$$

$$\text{II/II'}: [PW_{12}O_{40}]^{4-} + e^- \leftrightarrow [PW_{12}O_{40}]^{5-} \quad (11)$$

Table 4 - Observed Midpoint Potentials (E_{mid}) and Peak-to- Peak Separations (ΔE_p) for repeat CV of $\{H_3W_{12}\}$@AC-(2)500 in 1M H_2SO_4.

Process	E_{mid}/V	ΔE_p/mV
I	0.018	62
II	-0.25	70

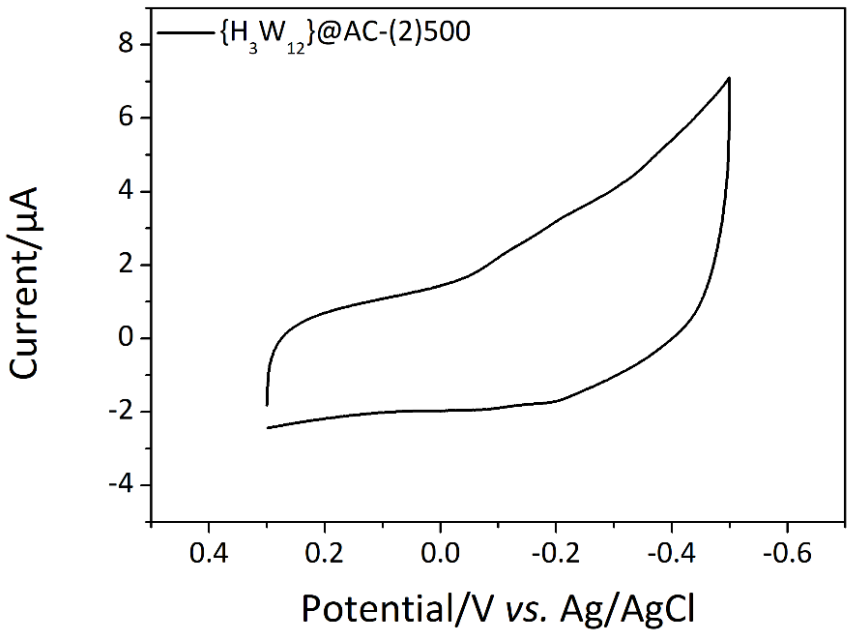


Figure 32 – Second repeat solid state CV of $\{H_3W_{12}\}$@AC-(2)500 in 1M H_2SO_4, recorded using a 3 mm diameter glassy carbon working electrode, a Pt counter electrode, and a Ag/AgCl reference electrode. The scan rate was 100 mv s^{-1}.

$\{H_6W_{18}\}$@AC-(2)500 was tested in the same fashion. Figure 33 shows the voltammogram of the first test sample within this batch. Four well-defined redox peaks are observed between the potential range of 0.2 – -0.8 V *vs.* Ag/AgCl, which are reminiscent of the solution phase voltammogram ($\{H_6W_{18}\}$ in 1M H_2SO_4 vide supra). The first two peaks are one-electron processes and the third and fourth peaks are two-electron processes, both involving protonation (Equations 12 – 15). These assignments agree closely with the observed ΔE_p values: processes I and II are 45 and 61 mV, close to the theoretical value of 59 mV for a reversible one-electron transfer in a diffusion-controlled regime. Similarly, processes III and IV are 29 and 27 mV, very close to the theoretical value of a reversible two-electron transfer in in a diffusion-controlled regime. This is a very interesting result as it would appear that the redox profile of the composite does not display symmetrical peaks which are characteristic of surface-confined electrochemistry. Thus, the redox-active POMs are being

accessed from within the AC pores and behaving as though they were dissolved in the electrolyte.

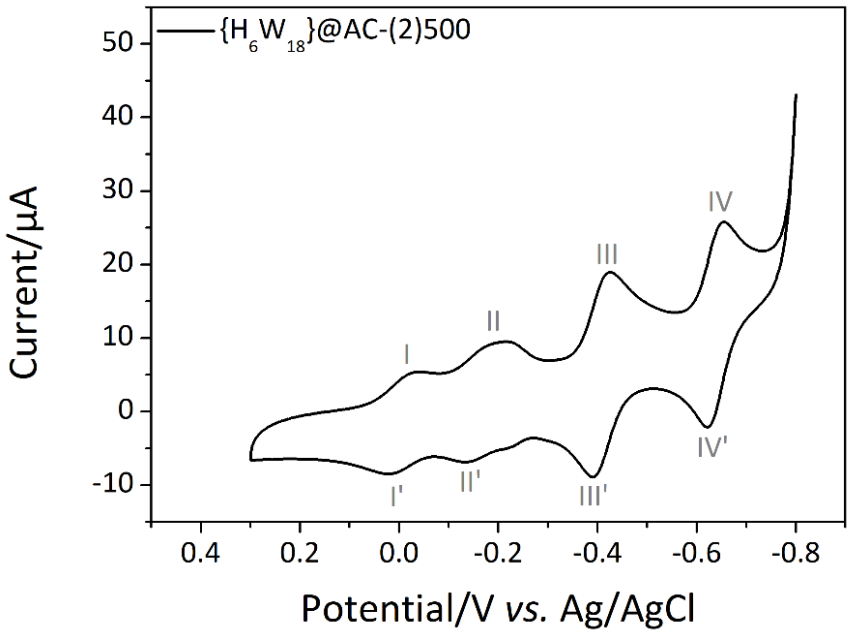


Figure 33 - Solid state CV of $\{H_6W_{18}\}$@AC-(2)500 in 1M H_2SO_4, recorded using a 3 mm diameter glassy carbon working electrode, a Pt counter electrode, and a Ag/AgCl reference electrode. The scan rate was 100 mv s^{-1}.

Equations 12 – 15 - Redox couples for $\{H_6W_{18}\}$@AC-(2)500 in 1M H_2SO_4.

$$\text{I/I'}: [P_2W_{18}O_{62}]^{6-} + e^- \leftrightarrow [P_2W_{18}O_{62}]^{7-} \quad (12)$$

$$\text{II/II'}: [P_2W_{18}O_{62}]^{7-} + e^- \leftrightarrow [P_2W_{18}O_{62}]^{8-} \quad (13)$$

$$\text{III/III'}: [P_2W_{18}O_{62}]^{8-} + 2e^- + 2H^+ \leftrightarrow [H_2P_2W_{18}O_{62}]^{8-} \quad (14)$$

$$\text{IV/IV'}: [H_2P_2W_{18}O_{62}]^{8-} + 2e^- + 2H^+ \leftrightarrow [H_4P_2W_{18}O_{62}]^{8-} \quad (15)$$

Table 5 - Observed Midpoint Potentials (E_{mid}) and Peak-to- Peak Separations (ΔE_p) for repeat CV of $\{H_6W_{18}\}$@AC-(2)500 in 1M H_2SO_4.

Process	E_{mid}/V	ΔE_p/mV
I	-0.005	45
II	-0.17	61
III	-0.41	29
IV	-0.64	27

However, when voltammograms were collected on a further two samples from the same batch of $\{H_6W_{18}\}$@AC-(2)500, the redox profiles are dissimilar. Figures 34 and 35 show ill-defined, irreversible looking redox peaks. Despite a higher loading of POM within this composite, it seems that the POM is not uniformly distributed within the AC matrix.

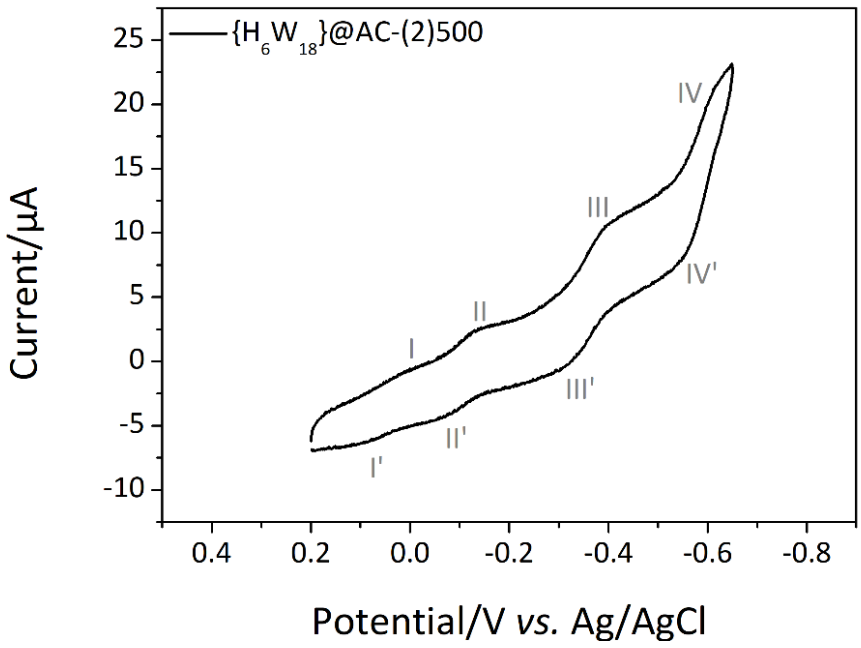


Figure 34 – Repeat solid state CV of $\{H_6W_{18}\}$@AC-(2)500 in 1M H_2SO_4, recorded using a 3 mm diameter glassy carbon working electrode, a Pt counter electrode, and a Ag/AgCl reference electrode. The scan rate was 100 mv s^{-1}.

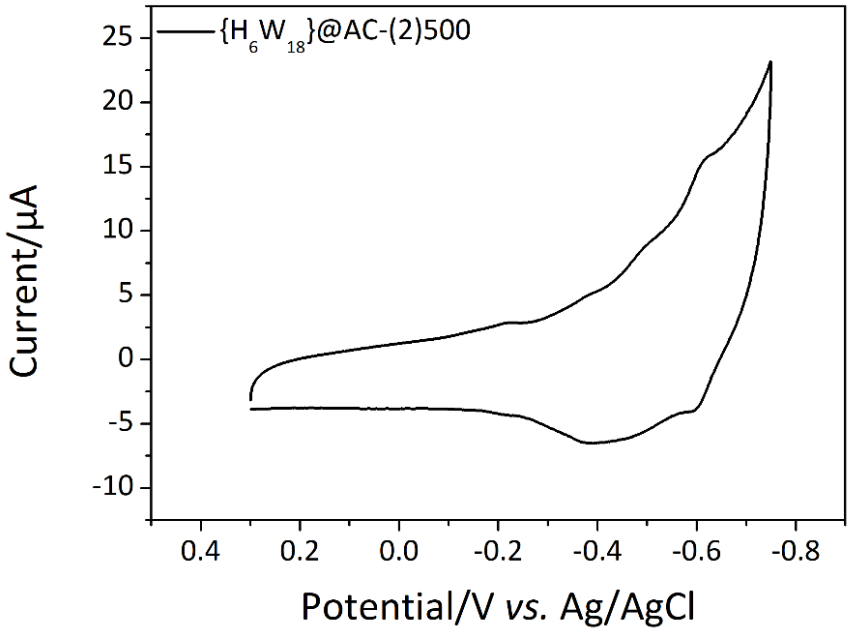


Figure 35 – 2nd repeat solid state CV of $\{H_6W_{18}\}$@AC-(2)500 in 1M H_2SO_4, recorded using a 3 mm diameter glassy carbon working electrode, a Pt counter electrode, and a Ag/AgCl reference electrode. The scan rate was 100 mv s^{-1}.

5.5 Conclusions & Future Work

Two different sets of activated carbons and POM@activated carbons were synthesised. The textural properties of the ACs were clearly influenced by parameters such as activating agent ratio and activation temperature. The addition of POMs into the carbonisation recipe led to a decrease in the BET surface area and changes in the PSD were observed. In one instance, the redox activity of the POMs was retained, however the result was not reproducible. This indicates the inefficiency of this synthetic procedure to prepare such composite materials for energy storage. Preparation of energy storage materials should be readily scalable without incurring inconsistencies between the manufacturing processes and electrochemical performance.

The characterisation for the POM@AC samples synthesised at 750 °C suggest the POMs did not survive the carbonisation procedure. The temperature may have been too high, causing the POMs to devolve into their redox-inactive metal oxides. However, the appearance of potassium in the EDX map likely arises from the activating agent, potassium oxalate. Washing the AC-(4.5)750 samples in water post carbonisation could have incited the formation of in-situ KOH. Given that POMs are sensitive to degradation in alkaline conditions, the presence of KOH could have led to an in-situ degradation of the POMs during the washing step, even if they survived the carbonisation process.

For the second set of POM@AC samples, the redox chemistry of the POMs was accessible, which could be aided by several factors. Firstly, the lowering of the activation temperature increases the likelihood that the POMs would remain intact post carbonisation. This time, the washing step involved washing the samples in 1M HCl, avoiding the formation of destructive basic media. Additionally, washing in acidic media could result in the surface oxidisation of the AC matrix, rendering it more hydrophilic, thereby providing a supplementary driving force for POM retention. However, the reproducibility of the electrochemistry of the POM@AC composites within the same batch is a

concern for the preparation of such electrode materials, where homogeneity and uniformity are imperative.

Preparing POMs supported on activated carbon using the in-situ carbonation method is not trivial, as many factors need to be taken into consideration. As reported in many studies, the properties of ACs are highly tuneable[57,58,59,60] and the general trend is that more extensive activation (higher surface area and narrow PSD) is observed when the activation temperature, activation time and ratio of activating agent is increased. However, there is a trade-off with using too harsh conditions, where the expansion and collapse of micropores creates mesopores which subsequently decreases the surface area and broadens the PSD.[61] Additionally, the high temperature treatment in an inert atmosphere leads to the decarboxylation of the AC, reducing the number of functional groups and enhancing hydrophobicity. This is something to consider when incorporating hydrophilic POMs into the matrix. The variability of biomass derived hydrochar is also limiting when attempting to modify the AC in a controlled way. Evidently, many of the AC properties are interconnected and thus difficulties arise when ascribing a particular observed change to the introduction or removal of a component in the carbonisation process.

In summary, POM-carbon composites have and will continue to influence new materials design, particularly in energy research. The aim in the future will be to garner a better understanding of the advantages and limitations of each component and how they can be assimilated for better performance.

5.6 Experimental

Materials

Solvents and reagents were purchased from either Sigma Aldrich, Acros Organics, Fischer scientific or VWR and were used without further purification.

Synthesis of $H_6[P_2W_{18}O_{62}].6H_2O$

$K_6[P_2W_{18}O_{62}].9H_2O$ (10 g, 2.57 mmol) was dissolved in deionised water (150 ml). Diethyl ether (200 ml) was then added and the flask placed in an ice bath. 12M HCl (100 ml, 400 mmol) was added slowly before sealing the flask and leaving to stir overnight. The solution formed three layers; diethyl ether (top), aqueous (middle), etherate (bottom). The etherate was isolated using a separating funnel and resembled a golden yellow oil. The etherate was left to dry at 50 °C on a hotplate, resulting in a pale yellow-green powder.

Yield: 4.06 g. ^{31}P NMR (δ, D_2O): -13.01. IR (ATR) cm^{-1}: 1085 (P-O, s), 956 (W=Od, s), 904 (W-Ob-W, s), 727 (W-Oc-W, s).

Synthesis of $H_3[PW_{12}O_{40}].3H_2O$

$Na_2WO_4.2H_2O$ (100 g, 0.303 mol) and $Na_2HPO_4.2H_2O$ (50 g, 0.281 mol) were added to deionised water (160 ml) and dissolved with vigorous stirring. The solution was refluxed at 80 °C for 1 hour. 12M HCl (100 ml, 0.4 mol) was added slowly and the solution became yellow. It was then left to reflux overnight at 80 °C. A white precipitate formed which was filtered and washed with diethyl ether. The white powder was recrystallised from a minimum amount of boiling water, yielding large white crystals.

Yield: 54.32 g, 70 %. ^{31}P NMR (δ, D_2O): -15.27. IR (ATR) cm^{-1}: 1072 (P-O, s), 973 (W=Od, s), 904 (W-Ob-W, s), 770 (W-Oc-W, s).

Hydrothermal Carbonisation

A solution of cellulose acetate powder (6.4 g) in deionised water (20 ml) was added to a stainless-steel reactor. The reactor was then heated to 250 °C at 5 °C min/1 and held at this temperature under autogenous pressure for 2 hours and then returned to room temperature. The carbonaceous material was

washed with deionised water under vacuum until the filtrate ran clear. The hydrochar was dried overnight in an oven at 100 °C. The resultant hydrochar was a black, crumbly solid.

Chemical activation to form Polyoxometalate-Activated Carbon Composites

Hydrochar, potassium oxalate and the desired polyoxometalate were physically mixed using a mortar and pestle. Different $K_2C_2O_4$: hydrochar: POM ratios were employed; 4.5:1:0.5 and 2:1:1. The mixture was introduced to an alumina boat and placed in a horizontal tube furnace. The mixture was heated to 750 °C or 600 °C at 5 °C min^{-1} under a N_2 flow and was held at the selected temperature for 1 hour before cooling. The activated carbon composite was washed in deionised water for 24 hours. The composite was then filtered and dried in an oven at 100 °C for 24 hours.

Analytical Methods

NMR

^{1}H and ^{31}P NMR spectra were obtained using a Bruker DPX 300 spectrometer or Bruker AV400 at 298 K.

Thermogravimetric Analysis

TG analysis was carried out with a TA-Q500 (TA instruments) analyser. A small quantity of sample (3 – 5 mg) was added to a platinum pan of known weight and analysed under a constant air flow. Samples were heated from room temperature to 1000 °C at a ramp rate of 10 °C min^{-1} and the % mass change was measured.

IR

Infra-red spectra were measured using a Bruker Alpha FTIR spectrometer with a platinum ATR module.

Powder X-ray Diffraction

Powder X-ray Diffraction (PXRD) measurements were performed using a PANalytical X'Pert PRO diffractometer with a Copper line focus X-ray tube (40

kV, 40 mA), with monochromator tuned to K-alpha1 (Kα1 = 1.540598) and a PIXcel detector (length 3°). The diffractometer had Bragg-Brentano geometry and was operated in reflection transmission mode with samples mounted on brass powder sample holders on a spinning stage. An incident beam Soller slit of 0.04 rad, 1° fixed anti scatter slit, incident beam mask of 10 mm and programmable automated divergence slit giving a constant illuminated path length of 5.0 mm were used.

Scanning Electron Microscopy

SEM images were taken using a ZEISS EVO MA10 SEM with an EDAX Element, at a working distance of 8.50 mm, an accelerating voltage of 8.00 kV and a beam current of 50.0 pA.

N_2 Sorption Isotherms– Brunauer-Emmett-Teller (BET)

Approximately 40 – 80 mg of each sample was added to a measurement tube of a precisely known weight. The sample was degassed for 16 h at 230 °C and the weight of the sample and tube was measured accurately. The outgassed sample was characterised using a Micrometrics Physisorption Analyser (3Flex) at 77 K with N_2 as the adsorptive gas. The specific surface area was calculated using the BET method.

Cyclic Voltammetry – Dropcasting

Carbon inks were prepared by dispersing 10 mg of the desired carbon sample into 20 µl of aqueous 3 wt % polytetrafluoroethylene (PTFE) binder and 20 µl of ethanol (Figure 36). The mixture was sonicated for 10 minutes. Blank CVs of the bare glassy carbon working electrodes were taken prior to ink addition on to the surface. 5.5 µl of carbon ink was dropcast on the GC surface and left to dry for a minimum of 2 hours. CVs were performed in 1 M H_2SO4 with a Pt wire counter electrode and Ag/AgCl reference electrode.

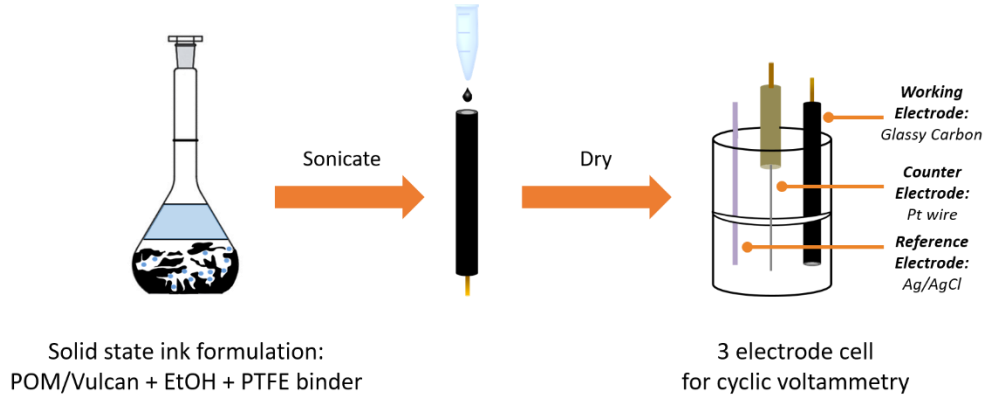


Figure 36 - Preparation of POM@activated carbon inks with binder and ethanol. Subsequent dropcasting and drying prior to use in a three electrode cell for solid state cyclic voltammetry.

5.7 References

1 Y. Zhou, G. Chen, Z. Long and J. Wang, Recent advances in polyoxometalate-based heterogeneous catalytic materials for liquid-phase organic transformations, *RSC Adv.*, 2014, **4**, 42092–42113.

2 E. Rafiee and S. Eavani, Heterogenization of heteropoly compounds: A review of their structure and synthesis, *RSC Adv.*, 2016, **6**, 46433–46466.

3 A. S. Cherevan, S. P. Nandan, I. Roger, R. Liu, C. Streb and D. Eder, Polyoxometalates on Functional Substrates: Concepts, Synergies, and Future Perspectives, *Adv. Sci.*, 2020, **7**, 1903511.

4 A. Dolbecq, E. Dumas, C. R. Mayer and P. Mialane, Hybrid Organic–Inorganic Polyoxometalate Compounds: From Structural Diversity to Applications, *Chem. Rev.*, 2010, **110**, 6009–6048.

5 A. S. Cherevan, S. P. Nandan, I. Roger, R. Liu, C. Streb and D. Eder, Polyoxometalates on Functional Substrates: Concepts, Synergies, and Future Perspectives, *Adv. Sci.*, 2020, **7**, 1903511.

6 I. Piñeiro-Prado, D. Salinas-Torres, R. Ruiz-Rosas, E. Morallón and D. Cazorla-Amorós, Design of Activated Carbon/Activated Carbon Asymmetric Capacitors, *Front. Mater.*

7 S. Kumar, M. Nehra, D. Kedia, N. Dilbaghi, K. Tankeshwar and K. H. Kim, Carbon nanotubes: A potential material for energy conversion and storage, *Prog. Energy Combust. Sci.*, 2018, **64**, 219–253.

8 M. Sevilla, G. A. Ferrero and A. B. Fuertes, Graphene-cellulose tissue composites for high power supercapacitors, *Energy Storage Mater.*, 2016, **5**, 33–42.

9 E. Frackowiak, Q. Abbas and F. Béguin, Carbon/carbon supercapacitors, *Chinese Acad. Sci. All rights Reserv. J. Energy Chem.*, 2013, **22**, 226–240.

10 M.-R. Gao, Y.-F. Xu, J. Jiang and S.-H. Yu, Nanostructured metal chalcogenides: synthesis, modification, and applications in energy conversion and storage devices, *Chem. Soc. Rev.*, 2013, **42**, 2986.

11 A. Eftekhari, L. Li and Y. Yang, Polyaniline supercapacitors, *J. Power Sources*, 2017, **347**, 86–107.

12 Y. Huang, H. Li, Z. Wang, M. Zhu, Z. Pei, Q. Xue, Y. Huang and C. Zhi, Nanostructured Polypyrrole as a flexible electrode material of supercapacitor, *Nano Energy*, 2016, **22**, 422–438.

13 D. P. Dubal, J. Suarez-Guevara, D. Tonti, E. Enciso and P. Gomez-Romero, A high voltage solid state symmetric supercapacitor based on graphene-polyoxometalate hybrid electrodes with a hydroquinone doped hybrid gel-electrolyte, *J. Mater. Chem. A*, 2015, **3**, 23483–23492.

14 M. H. Yang, B. G. Choi, S. C. Jung, Y. K. Han, Y. S. Huh and S. B. Lee, Polyoxometalate-coupled graphene via polymeric ionic liquid linker for supercapacitors, *Adv. Funct. Mater.*, 2014, **24**, 7301–7309.

15 H. Y. Chen, G. Wee, R. Al-Oweini, J. Friedl, K. S. Tan, Y. Wang, C. L. Wong, U. Kortz, U. Stimming and M. Srinivasan, A polyoxovanadate as an advanced electrode material for supercapacitors, *ChemPhysChem*, 2014, **15**, 2162–2169.

16 D. Pakulski, A. Gorczyński, W. Czepa, Z. Liu, L. Ortolani, V. Morandi, V. Patroniak, A. Ciesielski and P. Samorì, Novel Keplerate type polyoxometalate-surfactant-graphene hybrids as advanced electrode materials for supercapacitors, *Energy Storage Mater.*, 2019, **17**, 186–193.

17 M. E. Davis, Ordered porous materials for emerging applications, *Nature*, 2002, **417**, 813–821.

18 M. Sevilla and R. Mokaya, Energy storage applications of activated carbons: supercapacitors and hydrogen storage, *Energy Environ. Sci.*, 2014, **7**, 1250–1280.

19 R. A. Frenzel, G. P. Romanelli, M. N. Blanco and L. R. Pizzio, Transition metal-modified polyoxometalates supported on carbon as catalyst in 2-(methylthio)-benzothiazole sulfoxidation, *J. Chem. Sci.*, 2015, **127**, 123–132.

20 V. Ruiz, J. Suárez-Guevara and P. Gomez-Romero, Hybrid electrodes based on polyoxometalate-carbon materials for electrochemical supercapacitors, *Electrochem. commun.*, 2012, **24**, 35–38.

21 J. Suárez-Guevara, V. Ruiz and P. Gomez-Romero, Hybrid energy storage: High voltage aqueous supercapacitors based on activated carbon-phosphotungstate hybrid materials, *J. Mater. Chem. A*, 2014, **2**, 1014–1021.

22 S. Dutta, A. Bhaumik and K. C-W Wu, Hierarchically porous carbon derived from polymers and biomass: effect of interconnected pores on energy applications, *Energy Environ. Sci.*, 2014, **7**, 3445–3816.

23 M. B. Wu, L. Y. Li, J. Liu, Y. Li, P. P. Ai, W. T. Wu and J. T. Zheng, Template-free preparation of mesoporous carbon from rice husks for use in supercapacitors, *Xinxing Tan Cailiao/New Carbon Mater.*, 2015, **30**, 471–475.

24 G. S. Dos Reis, S. H. Larsson, H. P. de Oliveira, M. Thyrel and E. C. Lima, Sustainable biomass activated carbons as electrodes for battery and supercapacitors–a mini-review, *Nanomaterials*, 2020, **10**, 1–22.

25 H. Wang, Z. Xu, A. Kohandehghan, Z. Li, K. Cui, X. Tan, T. J. Stephenson, C. K. King'Ondu, C. M. B. Holt, B. C. Olsen, J. K. Tak, D. Harfield, A. O. Anyia and D. Mitlin, Interconnected carbon nanosheets derived from hemp for ultrafast supercapacitors with high energy, *ACS Nano*, 2013, **7**, 5131–5141.

26 D. Kang, Q. Liu, J. Gu, Y. Su, W. Zhang and D. Zhang, 'Egg-Box'-Assisted Fabrication of Porous Carbon with Small Mesopores for High-Rate Electric Double Layer Capacitors, *ACS Nano*, 2015, **9**, 11225–11233.

27 Y. Z. Liu, W. Yao, H. M. Gan, C. Y. Sun, Z. M. Su and X. L. Wang, Polyoxometalates-Based Metal–Organic Frameworks Made by Electrodeposition and Carbonization Methods as Cathodes and Anodes for Asymmetric Supercapacitors, *Chem. - A Eur. J.*, 2019, **25**, 16617–16624.

28 M. Wang, Y. Zhang, T. Zhang, Y. Li, M. Cui, X. Cao, Y. Lu, D. Peng, W. Liu, X. Liu, T. Wang and Y. Huang, Confinement of single polyoxometalate clusters in molecular-scale cages for improved flexible solid-state supercapacitors, *Nanoscale*, 2020, **12**, 11887–11898.

29 C. Falco, J. P. Marco-Lozar, D. Salinas-Torres, E. Morallón, D. Cazorla-Amorós, M. M. Titirici and D. Lozano-Castelló, Tailoring the porosity of chemically activated hydrothermal carbons: Influence of the precursor and hydrothermal carbonization temperature, *Carbon N. Y.*, 2013, **62**, 346–355.

30 M. Sevilla and A. B. Fuertes, The production of carbon materials by hydrothermal carbonization of cellulose, *Carbon N. Y.*, 2009, **47**, 2281–2289.

31 J. Wang and S. Kaskel, KOH activation of carbon-based materials for energy storage, *J. Mater. Chem.*, 2012, **22**, 23710–23725.

32 M. Sevilla, A. S. M. Al-Jumialy, A. B. Fuertes and R. Mokaya, Optimization of the Pore Structure of Biomass-Based Carbons in Relation to Their Use for CO_2 Capture under Low- and High-Pressure Regimes, *ACS Appl. Mater. Interfaces*, 2018, **10**, 1623–1633.

33 C. S. Cundy and P. A. Cox, The hydrothermal synthesis of zeolites: History and development from the earliest days to the present time, *Chem. Rev.*, 2003, **103**, 663–701.

34 A. Stein, Advances in microporous and mesoporous solids - Highlights of recent progress, *Adv. Mater.*, 2003, **15**, 763–775.

35 Z. Li and M. Jaroniec, Mesoporous carbons synthesized by imprinting ordered and disordered porous structures of silica particles in mesophase pitch, *J. Phys. Chem. B*, 2004, **108**, 824–826.

36 L. E. Briand, H. J. Thomas and G. T. Baronetti, Thermal stability and catalytic activity of Wells-Dawson tungsten heteropoly salts, *Appl. Catal. A Gen.*, 2000, **201**, 191–202.

37 N. V Sidgwick, *Chemical Elements and Their Compounds*, Oxford University Press, Oxford, Volume 1., 1950.

38 S. E. Elaigwu and G. M. Greenway, Chemical, structural and energy properties of hydrochars from microwave-assisted hydrothermal carbonization of glucose, *Int. J. Ind. Chem.*, 2016, **7**, 449–456.

39 M. M. Ibrahim, T. Y. A. Fahmy, E. I. Salaheldin, F. Mobarak, M. A. Youssef and M. R. Mabrook, Role of tosyl cellulose acetate as potential carrier for controlled drug release, *Life Sci. J.*, 2015, **12**, 127–133.

40 L. Xi, Z. Jin, Z. Sun, R. Liu and L. Xu, Enhanced photoelectrocatalytic performance for water oxidation by polyoxometalate molecular doping in $BiVO_4$ photoanodes, *Appl. Catal. A Gen.*, 2017, **536**, 67–74.

41 S. Xu, Y. Wang, Y. Zhao, W. Chen, J. Wang, L. He, Z. Su, E. Wang and Z. Kang, Keplerate-type polyoxometalate/semiconductor composite electrodes with light-enhanced conductivity towards highly efficient photoelectronic devices, *J. Mater. Chem. A*, 2016, **4**, 14025–14032.

42 G. Yan, X. Feng, L. Xiao, W. Xi, H. Tan, H. Shi, Y. Wang and Y. Li, Tuning of the photocatalytic performance of g-C_3N_4 by polyoxometalates under visible light, *Dalt. Trans.*, 2017, **46**, 16019–16024.

43 S. J. Yang, Y. L. Xu, W. P. Gong, Y. K. Huang, G. H. Wang, Y. Yang and C. Q. Feng, Photocatalytic degradation of organic dyes with $H_3PW_{12}O_{40}/TiO_2$–SiO_2, *Rare Met.*, 2016, **35**, 797–803.

44 M. Taghavi, M. H. Ehrampoush, M. T. Ghaneian, M. Tabatabaee and Y. Fakhri, Application of a Keggin-type heteropoly acid on supporting nanoparticles in photocatalytic degradation of organic pollutants in aqueous solutions, *J. Clean. Prod.*, 2018, **197**, 1447–1453.

45 X. Zhao, J. Yan, X. Xue, Z. Han, S. Cui, L. Zong, D. Zheng, C. Shen, H. Yu and X. Zhai, Transition-metal ion modified monolacunary tungstates: Synthesis, structural characterization and property, *Inorganica Chim. Acta*, 2014, **414**, 46–52.

46 S. R. Matkovic, M. Bosco, S. E. Collins and L. E. Briand, Tailored Brønsted and Lewis surface acid sites of the phosphotungstic Wells Dawson heteropoly-acid, *Appl. Surf. Sci.*, 2019, **495**, 143565.

47 X. Liu, W. Gong, J. Luo, C. Zou, Y. Yang and S. Yang, Selective adsorption of cationic dyes from aqueous solution by polyoxometalate-based metal-organic framework composite, *Appl. Surf. Sci.*, 2016, **362**, 517–524.

48 G. Baronetti, L. Briand, U. Sedran and H. Thomas, Heteropolyacid-based catalysis. Dawson acid for MTBE synthesis in gas phase, *Appl. Catal. A Gen.*, 1998, **172**, 265–272.

49 A. Enesca, C. Enache, A. Duta and J. Schoonman, High crystalline tungsten trioxide thin layer obtained by SPD technique, *J. Eur. Ceram. Soc.*, 2006, **26**, 571–576.

50 H. Kim, K.-Y. Park, J. Hong and K. Kang, All-graphene-battery: bridging the gap between supercapacitors and lithium ion batteries, *Sci. Rep.*, 2015, **4**, 5278.

51 A. M. Bond, J. B. Cooper, F. Marken and D. M. Way, Redox and electroinsertion processes associated with the voltammetry of microcrystalline forms of Dawson molybdate anion salts mechanically attached to graphite electrodes and immersed in aqueous electrolyte media, *J. Electroanal. Chem.*, 1995, **396**, 407–418.

52 A. Dostal, B. Meyer, F. Scholz, U. Schröder, A. M. Bond, F. Marken and S. J. Shaw, Electrochemical study of microcrystalline solid Prussian blue particles mechanically attached to graphite and gold electrodes: Electrochemically induced lattice reconstruction, *J. Phys. Chem.*, 1995, **99**, 2096–2103.

53 L. Ma, F. Li, Z. Sun, M. Liu, Y. Wang and L. Xu, Synergetic effect of polyoxoniobate and NiS as cocatalysts for enhanced photocatalytic H_2 evolution on $Cd_{0.65}Zn_{0.35}S$, *RSC Adv.*, 2014, **4**, 21369–21372.

54 M. Thommes, K. Kaneko, A. V Neimark, J. P. Olivier, F. Rodriguez-Reinoso, J. Rouquerol and K. S. W. Sing, Physisorption of gases, with special reference to the evaluation of surface area and pore size distribution (IUPAC Technical Report), *Pure Appl. Chem.*, 2015, **87**, 1051–1069.

55 G. M. S. ElShafei, I. M. A. ElSherbiny, A. S. Darwish and C. A. Philip, Artichoke as a non-conventional precursor for activated carbon: Role of the activation process, *J. Taibah Univ. Sci.*, 2017, **11**, 677–688.

56 M. Sevilla and A. B. Fuertes, Chemical and structural properties of carbonaceous products obtained by hydrothermal carbonization of saccharides, *Chem. - A Eur. J.*, 2009, **15**, 4195–4203.

57 M. Sevilla and R. Mokaya, Energy storage applications of activated carbons: Supercapacitors and hydrogen storage, *Energy Environ. Sci.*, 2014, **7**, 1250–1280.

58 J. Wang and S. Kaskel, KOH activation of carbon-based materials for energy storage, *J. Mater. Chem.*, 2012, 23710.

59 C. Falco, J. P. Marco-Lozar, D. Salinas-Torres, E. Morallón, D. Cazorla-Amorós, M. M. Titirici and D. Lozano-Castelló, Tailoring the porosity of chemically activated hydrothermal carbons: Influence of the precursor and hydrothermal carbonization temperature, *Carbon N. Y.*, 2013, **62**, 346–355.

60 C.-H. Chiang, J. Chen and J.-H. Lin, Preparation of pore-size tunable activated carbon derived from waste coffee grounds for high adsorption capacities of organic dyes, *J. Environ. Chem. Eng.*, 2020, **8**, 103929.

61 X. Zhu, Y. Gao, Q. Yue, Y. Kan, W. Kong and B. Gao, Preparation of green alga-based activated carbon with lower impregnation ratio and less activation time by potassium tartrate for adsorption of chloramphenicol, *Ecotoxicol. Environ. Saf.*, 2017, **145**, 289–294.

Conclusions & Future Prospects

Detailed conclusions for each body of work presented have been included in the relevant chapter. As such, this is a final statement about the work carried out in this thesis as well as its impact in broader context.

To date, polyoxometalates have shown promise as energy materials principally due to their multi-electron redox properties. This rich electrochemistry was showcased in this thesis in a variety of different solvents.

Surface oxidation of a conductive carbon Vulcan support was demonstrated to be an effective technique to prepare POM@Carbon composite materials. The chemical oxidation procedure introduced surface carboxylic acid functionalities which anchored POMs onto the conductive support. The $K_6[P_2W_{18}O_{62}]$@Oxidised Vulcan composite showed superior electrochemical cycling performance, POM retention and accessibility compared to its unmodified analogue. This finding will inform the future design of such composite redox active materials. The simplicity of the approach coupled with the scalability means that it could have significant implications for the development of next-generation electrode materials for electrochemical energy storage technologies.

Indeed, the superior electrochemical performance of the $K_6[P_2W_{18}O_{62}]$@Oxidised Vulcan composite translated well to a lithium metal test battery. These preliminary results provide proof of concept that such POM/Vulcan materials can be applied to battery technology.

Though the in-situ carbonisation approach was not as successful as surface modification, needless to say it was an interesting concept. The process to make activated carbons is extremely versatile as it can exploit seemingly infinite possibilities of feedstocks. Further work to optimise the preparation of consistent POM@activated carbons would be highly relevant to areas such as development of sustainable energy materials and waste valorisation.

The results from the solution phase and solid state measurements of the $K_6[P_2W_{18}O_{62}]$@Oxidised Vulcan composite in the presence of Mg^{2+} were very intriguing. The enhanced cycling stability *vs.* other metal cations alludes to the fact that no 'penalties' are incurred for the POM to ion-pair with a highly charged divalent cation. Unlike bulk oxides, the countercations for POMs are not integrated into the structure and are available for ion exchange. Therefore, the intercalation and deintercalation Mg^{2+} into POM clusters is an exciting prospect for POMs in multivalent batteries.

Much of the work surrounding POM battery chemistries in the literature is preliminary and in its infancy. Major opportunities lie in wait for applying the well understood electrochemistry of POMs into real world devices. With respect to batteries, the balance has to be found between the redox chemistry and the weight of electrode materials. Specific capacities of over 200 mAh g^{-1} need to be obtained in order to compete with current lithium-ion batteries. This means that next generation batteries will most likely consist of lithium metal as the negative electrode and focus on making the positive electrode material as light as possible.

POMs have high ionic weights which is something that must be taken into account. Although if their tuneable electrochemical properties grant access to higher energy density materials, it could compensate for the weight penalty. Of course, batteries are not just limited to portable applications. Stationary grid storage or back up power supplies do not necessarily prioritise low weight batteries. With regards to the poor electrical conductivity of POMs, there is a clear scope for developing modifiable carbon based supports as highlighted with our surface oxidation route.

The quintessential battery does not yet exist. The odyssey to superior next generation energy storage systems requires scientists from all disciplines to collaborate. The combined expertise within the fields of electrochemistry, inorganic, organic and materials chemistry will be paramount to success.